

NODYCON Conference Proceedings Series

Walter Lacarbonara
Balakumar Balachandran
Michael J. Leamy · Jun Ma
J. A. Tenreiro Machado
Gabor Stepan *Editors*


Advances in Nonlinear Dynamics

Proceedings of the Second International
Nonlinear Dynamics Conference
(NODYCON 2021), Volume 3

 Springer

NODYCON Conference Proceedings Series

Series Editor

Walter Lacarbonara , Sapienza University of Rome, Rome, Italy

The NODYCON Conference Proceedings Series presents early findings and case studies from a wide range of fundamental and applied work across multidisciplinary fields that encompass Nonlinear Dynamics. Series volumes follow the principle tracks or focus topics featured in the biennial International Nonlinear Dynamics Conference. Volumes in the series feature both well-established streams of research as well as novel areas and emerging fields of investigation.

More information about this series at <https://link.springer.com/bookseries/16666>


Walter Lacarbonara • Balakumar Balachandran
Michael J. Leamy • Jun Ma • J. A. Tenreiro Machado
Gabor Stepan
Editors


Advances in Nonlinear Dynamics


Proceedings of the Second International
Nonlinear Dynamics Conference
(NODYCON 2021), Volume 3


 Springer


Editors


Walter Lacarbonara 
Department of Structural and Geotechnical
Engineering
Sapienza University of Rome
Rome, Italy

Michael J. Leamy 
Department of Mechanical Engineering
Georgia Institute of Technology
Atlanta, GA, USA

J. A. Tenreiro Machado 
ISEP-Institute of Engineering
Polytechnic of Porto
Porto, Portugal

Balakumar Balachandran 
Department of Mechanical Engineering
University of Maryland
College Park, MD, USA

Jun Ma 
Department of Physics
Lanzhou University of Technology
Lanzhou, Gansu, China

Gabor Stepan 
Department of Applied Mechanics
Budapest University of Technology and
Economics
Budapest, Hungary

ISSN 2730-7689

ISSN 2730-7697 (electronic)

NODYCON Conference Proceedings Series

ISBN 978-3-030-81169-3

ISBN 978-3-030-81170-9 (eBook)

<https://doi.org/10.1007/978-3-030-81170-9>

© The Editor(s) (if applicable) and The Author(s), under exclusive license to Springer Nature Switzerland AG 2022

This work is subject to copyright. All rights are solely and exclusively licensed by the Publisher, whether the whole or part of the material is concerned, specifically the rights of translation, reprinting, reuse of illustrations, recitation, broadcasting, reproduction on microfilms or in any other physical way, and transmission or information storage and retrieval, electronic adaptation, computer software, or by similar or dissimilar methodology now known or hereafter developed.

The use of general descriptive names, registered names, trademarks, service marks, etc. in this publication does not imply, even in the absence of a specific statement, that such names are exempt from the relevant protective laws and regulations and therefore free for general use.

The publisher, the authors and the editors are safe to assume that the advice and information in this book are believed to be true and accurate at the date of publication. Neither the publisher nor the authors or the editors give a warranty, expressed or implied, with respect to the material contained herein or for any errors or omissions that may have been made. The publisher remains neutral with regard to jurisdictional claims in published maps and institutional affiliations.

This Springer imprint is published by the registered company Springer Nature Switzerland AG
The registered company address is: Gewerbestrasse 11, 6330 Cham, Switzerland

Preface

This volume is part of three volumes collecting the *Proceedings of the Second International Nonlinear Dynamics Conference (NODYCON 2021)* held as a virtual (online) conference, February 16–19, 2021. NODYCON was launched in 2019 to foster the tradition of the conference series originally established by Prof. Ali H. Nayfeh in 1986 at Virginia Tech, Blacksburg, VA, USA, as the Nonlinear Vibrations, Stability and Dynamics of Structures Conference. With the passing in 2017 of Prof. Nayfeh, NODYCON 2019 was organized as a collective tribute to Prof. Nayfeh. NODYCON 2019 received an extraordinary response from the community with 408 abstracts (out of 450 submissions) presented by nearly 400 participants from 68 countries.

After the successful launch of NODYCON, NODYCON 2021, originally planned to be held in Rome, February 16–19, 2021, was hosted as a virtual (online) conference given the uncertainties related to the COVID-19 world crisis. The online conference was creatively designed to help corroborate and cement the sense of cohesiveness and liveliness of the NODYCON community. The NODYCON 2021 online conference featured 16 keynotes and mini-keynotes of broad interest, a panel, two workshops, and 442 oral presentations covering recent advances in the rich spectrum of topics covered by *Nonlinear Dynamics*, including new frontiers and challenges. The Special Session and Panel Entitled “*Complex dynamics of COVID-19: modeling, prediction and control*” offered important outlooks into the nonlinear dynamic evolution and prediction of the global disease spreading across different scales by using a variety of analysis tools and modeling approaches.

For NODYCON 2021, the Organizing Committee received 478 abstracts and, after rigorous review cycles, 442 one-page abstracts were accepted and published in the [Conference Book of Abstracts](#).

The diverse topics covered by the papers were clustered along four major themes to hold the following technical sessions:

- A. Concepts and methods in nonlinear dynamics
- B. Nonlinear dynamics of mechanical and structural systems
- C. Nonlinear dynamics and control
- D. Recent trends in nonlinear dynamics

The authors of a selection of approximately 60 papers were invited to publish in the Special Issue of *Nonlinear Dynamics* entitled “NODYCON 2021 Second International Nonlinear Dynamics Conference.” At the same time, about 200 full papers were submitted to *Advances in Nonlinear Dynamics – Proceedings of the Second International Nonlinear Dynamics Conference (NODYCON 2021)* within the newly established NODYCON Conference Proceedings Series. One hundred and eighty-one papers were accepted. These papers have been collected into three volumes, which are listed below together with a sub-topical organization.

Volume 1: Nonlinear Dynamics of Structures, Systems, and Devices

- A. Fluid-structure interaction
- B. Mechanical systems and structures
- C. Computational nonlinear dynamics
- D. Analytical techniques
- E. Bifurcation and dynamic instability
- F. Rotating systems
- G. Modal interactions and energy transfer
- H. Nonsmooth systems

Volume 2: Nonlinear Dynamics and Control

- A. Nonlinear vibration control
- B. Control of nonlinear systems and synchronization
- C. Experimental dynamics
- D. System identification and SHM
- E. Multibody dynamics

Volume 3: New Trends in Nonlinear Dynamics

- A. Complex dynamics of COVID-19: modeling, prediction, and control
- B. Nonlinear phenomena in bio- and eco-systems
- C. Energy harvesting
- D. MEMS/NEMS
- E. Multifunctional structures, materials, and metamaterials
- F. Nonlinear waves
- G. Chaotic systems, stochasticity, and uncertainty

I wish to acknowledge the work and dedication of the co-editors of the NODYCON 2021 Proceedings: Prof. Bala Balachandran (University of Maryland, College Park, USA), Prof. Michael J. Leamy (Georgia Institute of Technology, USA), Prof. Jun Ma (Lanzhou University of Technology, China), Prof. Jose Antonio Tenreiro Machado (Instituto Superior de Engenharia do Porto, Portugal), and Prof. Gabor Stepan (Budapest University of Technology and Economics, Hungary).

The success of the fully online conference NODYCON 2021 is due to the efforts, talent, energy, and enthusiasm of all researchers in the field of nonlinear dynamics who wrote, submitted, and presented their papers in a very lively way. Special praise is also deserved for the reviewers who invested significant time in reading, examining, and assessing multiple papers, thus ensuring a high standard of quality for this conference proceedings.

NODYCON 2021 Chair

Walter Lacarbonara, Rome, Italy
May 2021

Preface for Volume 3: New Trends in Nonlinear Dynamics

Volume 3 of the NODYCON 2021 Proceedings is composed of 53 chapters, which are spread across the following groupings: (i) complex dynamics of COVID-19: modelling, prediction, and control (5 papers); (ii) nonlinear phenomena in bio- and eco-systems dynamics (10 papers); (iii) energy harvesting (10 papers); (iv) MEMS/NEMS (7 papers); and (v) multifunctional structures, materials, and metamaterials (6 papers), (vi) nonlinear waves (4 papers); and (vii) chaotic systems, stochasticity, and uncertainty (11 papers). Due to the cross-cutting nature of the topics, the editors acknowledge that a paper placed in one grouping could have easily been placed in another grouping as well. As one reads through these 53 contributions, one will note the use of a wide range of experimental, analytical, and numerical techniques for studying the nonlinear dynamics of a wealth of systems across different length and time scales.

In the area of complex dynamics of COVID-19 from the point of view of modelling, prediction, and control, the reader will find studies concerning the formulation of fractional-order generalized SEIR models to study and predict the spread of COVID-19 (L. Guo et al.; Y. Zhao et al.) and the extension of classical epidemiological models to include a number of social and biological conditions (Y. Ding and Y. Kang; Y. Aboelkassem and H. Taha; O. Khyar and K. Allali).

In the area of nonlinear phenomena in bio- and eco-system dynamics, the reader will find the analysis of tumour growth (D. Sourailidis et al.), the application of mathematical models in neuroscience (I. Sysoev et al.; H. Shaheen et al.; S. Ahmed et al.; S. Thottil and R. Ignatius), the dynamics of vibro-impact capsules in gastrointestinal systems (Y. Zheng et al.; J. Tian et al.; N.-T. La et al.), and the evolution of species under different conditions (S. Mishra and R. Upadhyay; M. Kumar and S. Abbas).

In the area of energy harvesting, the reader will find studies concerning the use of piezoelectric and metamaterials (A. Tusset et al.; K. Zhao et al.; P. Malaji et al.), the design of electro-mechanical systems (J. Li et al.; N. Yu et al.; M. Khasawneh and M. Daqaq; W. Wang et al.), and the performance of structures and systems including several elements (M. Vali and A. Faruque; B. Santhosh et al.; X. Wang et al.).

In the area of MEMS/NEMS, the reader will find a diversity of efforts concerning the description of the dynamic behavior (A. Opreni and A. Frangi; L. Ruzziconi et al.), and the effect of operational conditions or external signals (I. Papkova et al.; A. Alneamy et al.; M. Akbarzadeh et al.; U. Eroglu; A. Buscarino et al.).

In the area of multifunctional structures, materials, and metamaterials, the reader will find a range of perspectives concerning the modelling of asymmetric hysteresis (J.-S. Pei et al.), systems with several types of plates (A. Gawlik et al.; S. Mızrak and E. Cığeroğlu; O. Ganilova et al.), and the dynamic behavior of metamaterials (K. Chondrogiannis et al.; A. Rezaei et al.).

In the area of nonlinear waves, the reader will find studies on systems described by the Boussinesq, Korteweg-de Vries, and Schrödinger equations (P Rozmej and A. Karczewska; H. Blas et al.; S. Manna and A. Dhar; S. Carillo and C. Schiebold).

In the area of chaotic systems, stochasticity, and uncertainty, the reader will find a variety of studies following a number of distinct approaches and perspectives, namely dynamical states induced by special relativistic effects in a harmonic oscillator with sinusoidal forcing (D. Gomes and G. Ambika), high-frequency chaotic behaviour in a non-ideal amplifier (M. Bucolo et al.), multiple hysteresis jump resonance in forced oscillators (M. Bucolo et al.), chaos in neuronal network activity (E. Pankratova), chaos in close cylindrical nanoshells (I. Papkova et al.), scaling analysis based on the wavelet discrete transform (L. Reyes-López et al.), chaotic image encryption (C. Zhao and H. Ren), stochastic modelling of a crash box (B. Bhattacharyya et al.), dynamics of a cylindrical shell with Rivlin-Saunders material (W. Zhang et al.), dynamics of a nonlinear circuit including a memristor (M. Messias and A. Reinol), and the behaviour of a Mathieu oscillator with fuzzy uncertainty (X.-M. Liu et al.).

In conclusion, this volume presents studies reflecting recent advances in a variety of fields and using a plethora of distinct tools and approaches. We hope that readers will benefit from the rich work portrayed here on new trends in nonlinear dynamics and that this work will spur and inspire new ideas and future contributions.

Co-editors of the NODYCON 2021 Proceedings

Bala Balachandran, College Park, MD, USA

Walter Lacarbonara, Rome, Italy

Michael J. Leamy, Atlanta, GA, USA

Jun Ma, Lanzhou, China

J. A. Tenreiro Machado, Porto, Portugal

Gabor Stepan, Budapest, Hungary

May 2021

Contents

Part I Complex Dynamics of COVID-19: Modeling, Prediction and Control	
Prediction and Control of the Impact of the Onset Influenza Season on the Spread of COVID-19	3
Lihong Guo, Yanting Zhao, and YangQuan Chen	
A Fractional-Order Age-Structured Generalized SEIR Model: The Role of “COVID-19 Symptom Data Challenge” Dataset	13
Yanting Zhao, Lihong Guo, Yong Wang, and YangQuan Chen	
Dynamical Analysis of a COVID-19 Epidemic Model with Social Confinement and Acquired Immunity Loss	25
Yamin Ding and Yanmei Kang	
A Cooperative Epidemiological Model of Infectious Disease Dynamics: A COVID-19 Case Study	39
Yasser Aboelkassem and Haithem E. Taha	
Dynamic Analysis of a Three-Strain COVID-19 SEIR Epidemic Model with General Incidence Rates	49
Omar Khyar and Karam Allali	
Part II Nonlinear Phenomena in Bio- and Eco-Systems Dynamics	
Nonlinear Phenomena and Chaos in a Tumor Growth Model	63
Dionysios Sourailidis, Christos Volos, Lazaros Moysis, and Ioannis Stouboulos	
Modeling Limbic Seizure Initiation with an Ensemble of Delay Coupled Neurooscillator	73
Ilya V. Sysoev, Maksim V. Kornilov, Natalia A. Makarova, Marina V. Sysoeva, and Lyudmila V. Vinogradova	

Mathematical Modeling of Calcium-Mediated Exosomal Dynamics in Neural Cells	83
Hina Shaheen, Sundeep Singh, and Roderick Melnik	
Forward Sensitivity Analysis of the FitzHugh–Nagumo System: Parameter Estimation	93
Shady E. Ahmed, Omer San, and Sivaramakrishnan Lakshmivarahan	
Electromagnetic Induction on Neurons Through Field Coupling and Memristor	105
Sunsu Kurian Thottil and Rose P. Ignatius	
Variable Speed Optimization of a Vibro-impact Capsule System in Both the Forward and Backward Directions	115
Yang Zheng, Maolin Liao, Jiajia Zhang, Yang Liu, Jiapeng Zhu, and Zhiqiang Zhu	
Exploring the Dynamics of a Vibro-Impact Capsule Moving on the Small Intestine Using Finite Element Analysis	127
Jiyuan Tian, Yang Liu, and Shyam Prasad	
Vibro-Impact Capsule Under Different Conditions of Friction	137
Ngoc-Tuan La, Thanh-Toan Nguyen, Ky-Thanh Ho, Quoc-Huy Ngo, and Van-Du Nguyen	
Modeling the Fear-Induced Spatiotemporal Dynamics of Three-Species Interaction in Agroecosystems	147
Swati Mishra and Ranjit Kumar Upadhyay	
Optimal Birth Control of Population Dynamics with Time-Varying Diffusivity Coefficient	163
Manoj Kumar and Syed Abbas	
Part III Energy Harvesting	
On Energy Harvesting with Time-Varying Frequency by Using Magneto-Piezo-Elastic Oscillators with Memory	177
Angelo M. Tusset, Jose M. Balthazar, Rodrigo T. Rocha, Jorge L. P. Felix, Marcus Varanis, Mauricio A. Ribeiro, Clivaldo de Oliveira, Itamar Iliuk, and Grzegorz Litak	
Galloping Piezoelectric Energy Harvester for Low Wind Speed	189
Kaiyuan Zhao, Qichang Zhang, and Shuying Hao	
Nonlinear Resonator-Based Metastructures for Vibration Attenuation and Energy Harvesting	201
P. V. Malaji, T. Mukhopadhyay, and S. S. Chappar	
Dynamic Modeling for a Mechatronic Energy Harvesting Shock Absorber	211
Jing Li, Lei Luo, Dong Guan, Hui Shen, and Junjie Gong	

Bistable Electromagnetic Energy Harvesting Enhanced with a Resonant Circuit 221
 Ning Yu, Chuanyu Wu, Gaohong Yu, and Bo Yan

An Internally Resonant Tunable Generator for Wave Energy Harvesting 233
 Mohammad A. Khasawneh and Mohammed F. Daqaq

Nonlinear Dynamics Analysis of Electric Energy Regeneration Device Based on Vibration Energy Recovery 241
 Wei Wang, Yan Li, Kehong Wu, Yongjie Cui, and Yuling Song

Harvesting Energy from 2D Array of Harvesters 255
 Mohammad Reyaz Ahmad Vali and Ali Shaikh Faruque

Generalized Energy Balanced Method for a Combined Nonlinear Vibration Absorber Energy Harvester with Nonlinear Energy Sink..... 267
 B. Santhosh, I. R. Praveenkrishna, and Aalokeparno Dhar

Nonlinear Reduced Order Modeling of a Buckled Piezoelectric Beam for Energy Harvesting 277
 X. Q. Wang, Yabin Liao, and M. P. Mignolet

Part IV MEMS/NEMS

Full-Order Frequency-Domain Simulations of Nonlinear Piezoelectric MEMS 291
 Andrea Opreni and Attilio Frangi

Global Analysis and Experimental Dynamics of the 2:1 Internal Resonance in the Higher-Order Modes of a MEMS Microbeam 301
 Laura Ruzziconi, Nizar Jaber, Lakshmoji Kosuru, Mohammed L. Bellaredj, and Mohammad I. Younis

Nonlinear Dynamics of NEMS/MEMS Elements in the Form of Beams Taking into Account the Temperature Field, Radiation Exposure, Elastoplastic Deformations 311
 Irina Papkova, Tatiana Yakovleva, Anton Krysko, and Vadim Krysko

Single Input–Single Output MEMS Gas Sensor 321
 A. Alneamy, N. Heidari, W. Lacarbonara, and E. Abdel-Rahman

A Numerical Study of Acoustic Radiation Forces for the Contactless Excitation of a Microcantilever 335
 M. Akbarzadeh, S. Oberst, S. Sepehriahnama, Y. K. Chiang, B. J. Halkon, A. Melnikov, and D. A. Powell

Approximate Solutions to Axial Vibrations of Nanobars in Nonlinear Elastic Medium 347
 Ugurcan Eroglu

Nonlinear Modeling for Thermal Behavior on Power Integrated Circuits	357
Arturo Buscarino, Carlo Famoso, and Luigi Fortuna	
Part V Multifunctional Structures, Materials, and Metamaterials	
Modeling Asymmetric Hysteresis Inspired and Validated by Experimental Data	371
Jin-Song Pei, Biagio Carboni, and Walter Lacarbonara	
Forced Transversal Vibrations of von Karman Plates with Distributed Spring-Masses	383
Aleksandra Gawlik, Andrzej Klepka, Vsevolod Vladimirov, and Sergii Skurativskyi	
Nonlinear Free Vibrations of Functionally Graded Microplates Based on the Modified Couple Stress Theory	395
Sinem Mızrak and Ender Cigeroğlu	
The Development of a Dynamic Coupled Model for Aluminium Composite Sandwich Plates Under Thermoelastic Loading	407
Olga A. Ganilova, Matthew P. Cartmell, and Andrew Kiley	
On the Vibration Attenuation Properties of Metamaterial Design Using Negative Stiffness Elements	419
Kyriakos Alexandros Chondrogiannis, Vasilis Dertimanis, Boris Jeremic, and Eleni Chatzi	
Long-Range Resonator-Based Metamaterials	431
A. S. Rezaei, F. Mezzani, and A. Carcaterra	
Part VI Nonlinear Waves	
KdV, Extended KdV, 5th-Order KdV, and Gardner Equations Generalized for Uneven Bottom Versus Corresponding Boussinesq's Equations	443
Piotr Rozmej and Anna Karczewska	
Modified Non-linear Schrödinger Models, $\mathcal{CP}_s\mathcal{T}_d$ Symmetry, Dark Solitons, and Infinite Towers of Anomalous Charges	455
Harold Blas, Martín Cerna, and Luis dos Santos	
Effect of Vorticity on Peregrine Breather for Interfacial Waves of Finite Amplitude	467
Shibam Manna and Asoke Kumar Dhar	
Construction of Soliton Solutions of the Matrix Modified Korteweg–de Vries Equation	481
Sandra Carillo and Cornelia Schiebold	

Part VII Chaotic Systems, Stochasticity, and Uncertainty

Frequency Locking, Quasiperiodicity, and Chaos Due to Special Relativistic Effects 495
 Derek C. Gomes and G. Ambika

High Frequency Chaotic Behavior in Non-ideal Operational Amplifier ... 507
 Maide Bucolo, Arturo Buscarino, Carlo Famoso, Luigi Fortuna, and Salvina Gagliano

Multiple Hysteresis Jump Resonance in a Class of Oscillators with Nonic Polynomial Nonlinearity 513
 Maide Bucolo, Arturo Buscarino, Carlo Famoso, Luigi Fortuna, and Salvina Gagliano

Environmentally Induced Chaos and Amplitude Death in Neuronal Network Activity 523
 Evgeniya V. Pankratova

Chaos-Type Identification in the Contact Interaction of Closed Cylindrical Nanoshells Embedded One into the Other with a Gap Between Them 535
 Irina Papkova, Tatiana Yakovleva, Anton Krysko, and Vadim Krysko

Scaling Wavelet Analysis of Chaotic Systems 547
 L. E. Reyes-López, J. S. Murguía, H. González-Aguilar, and H. C. Rosu

Weakness Analyzing and Performance Improvement for Image Encryption with Chaos Across Cylinder 557
 Chaofeng Zhao and Haipeng Ren

A Surrogate Approach for Stochastic Modeling of a Crash Box Under Impact Loading in the Time Domain 569
 Biswarup Bhattacharyya, Eric Jacquelin, and Denis Brizard

Nonlinear Dynamics of a Hyperelastic Cylindrical Shell Composed of the Incompressible Rivlin-Saunders Material 581
 Wenzheng Zhang, Zhentao Zhao, and Datian Niu

Dynamical Analysis of a Memristor–Inductor–Capacitor Nonlinear Circuit..... 593
 Marcelo Messias and Alisson C. Reinol

Periodic Solutions of Mathieu Oscillator, Induced by Fuzzy Uncertainty 605
 Xiao-Ming Liu, Xiao-Ping Tian, Ling Hong, and Yue Shu

Index 617

Part I
Complex Dynamics of COVID-19:
Modeling, Prediction and Control

Prediction and Control of the Impact of the Onset Influenza Season on the Spread of COVID-19



Lihong Guo, Yanting Zhao, and YangQuan Chen

1 Introduction

Since December 2019, the coronavirus (COVID-19) epidemic is gradually changing people's lives. As of October 29, 2020, over 44 million cases have been reported, including over 11 million deaths in over 190 countries and regions [1]. At present, therapeutic drugs and vaccines are being developed [2]. In many countries and regions, the infection rate and mortality rate are still high, which shows that the spread of this infectious disease has not slowed down but is getting worse. At the same time, the flu season in the United States is also coming. According to data released by the CDC's influenza web page [3], during the 2019–2020 flu season, it is estimated that 38 million flu illnesses, 0.4 million flu hospitalizations, and 22,000 flu deaths. Therefore, it is indispensable to study the impact of the flu season's arrival on the development of the COVID-19 epidemic, such as the hospital bed capacity.

Since the trend of influenza possesses the seasonal property, we use the seasonal autoregressive integrated moving average (SARIMA) model [4–6] to simulate and predict the spread of 2020–2021 influenza season. Although the COVID-19 shares many same symptoms as the influenza, there are still many differences: the COVID-19 is a sudden infectious disease, vaccine and effective treatment were

L. Guo

Institute of Mathematics, Jilin University, Changchun, China

e-mail: guohl17@mails.jlu.edu.cn

Y. Zhao

Department of Automation, University of Science and Technology of China, Hefei, China

e-mail: zyt9lsb@mail.ustc.edu.cn

Y. Chen (✉)

Mechatronics, Embedded Systems and Automation Laboratory, Department of Engineering

University of California, Merced, CA, USA

e-mail: ychen53@ucmerced.edu

being developed, longer incubation period (averaging 5.1 days [7], which varies from person to person) than the normal influenza, meaning that a person who is infected with COVID-19 does not immediately have symptoms but can transmit to others. Investigations [8, 9] show that the transmission of COVID-19 has memory characteristics. Furthermore, as is shown in the study of small-world networks and scale-free networks [10, 11], human beings are heterogeneous in the process of interaction. As a generalized form of integer-order calculus, fractional calculus has become an indispensable tool in the field of modeling and control [12]. In particular, fractional calculus has been proved to be more effective in the modeling process with memory and heterogeneity [12]. Moreover, in many applications [13–15], it has been proved that the dynamic model based on fractional differential equation has better performance than the integer-order model.

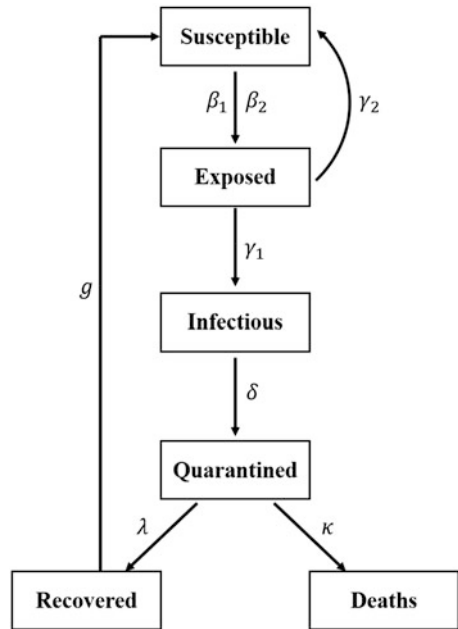
Therefore, we use a fractional generalized compartment model to study the transmission of the COVID-19. Moreover, combined with the prediction of the spread of the influenza, we examined the impact of state-level transmission on the treatment of the COVID-19, especially the impact on the utilization rate of hospital beds. Particularly, because we have an effective vaccine to prevent the spread of flu to a certain degree, we have also studied the impact of flu vaccine injection in different proportions on the utilization rate of the hospital beds.

The outline of this chapter is as follows. In Sect. 2, we introduced a new fractional-order generalized SEIQRD model. The model's parameters were estimated through real-time data of California, United States, and we gave percentile estimates of the number of active cases and deaths as of December 17, 2020. In Sect. 3, based on the seasonal property of flu transmission, we used the SARIMA model to analyze and forecast the flu trend. Furthermore, combined with the prediction of the number of COVID-19 cases and the number of influenza cases, we studied the prediction of the number of hospital beds utilization with different influenza vaccination rates. Last but not least, some conclusions and prospects are given.

2 Fractional-Order Generalized SEIQRD Model

In this section, in order to describe the transmission trend of COVID-19, we generalize the integer-order model inaugurated in Peng et al. [16] to a fractional-order generalized SEIQRD epidemic model. This model mainly includes six compartments: susceptible individuals $S(t)$, exposed individuals $E(t)$, infectious individuals $I(t)$, quarantined individuals $Q(t)$, recovered individuals $R(t)$, and death individuals $D(t)$. The total effective population size is expressed by N , which is the sum of the sizes of these five classes: $N = S(t) + E(t) + I(t) + Q(t) + R(t)$. We assumed that all members of the community are equally susceptible to this disease at the beginning, and there is a certain probability of infection after recovery, that is, there is a certain period of immunity. Moreover, for the exposed individuals, a certain proportion of the exposed population turns into infected cases

Fig. 1 The diagram of the model



after a period of incubation. A certain proportion of the exposed population is called asymptomatic infection. This part of the population can recover on their own through their own immunity and once again become susceptible. They were expressed by symptom rate γ_1 and no symptom rate γ_2 , respectively.

The transmission diagram is shown in Fig. 1 and the fractional-order generalized SEIQRD model is as follows:

$$\left\{ \begin{array}{l}
 {}_0D_t^\alpha S(t) = -\frac{\beta_1(t)}{N} S(t)I(t) - \frac{\beta_2(t)}{N} S(t)E(t) + \gamma_2 E(t) + gR(t), \\
 {}_0D_t^\alpha E(t) = \frac{\beta_1(t)}{N} S(t)I(t) + \frac{\beta_2(t)}{N} S(t)E(t) - (\gamma_1 + \gamma_2)E(t), \\
 {}_0D_t^\alpha I(t) = \gamma_1 E(t) - \delta I(t), \\
 {}_0D_t^\alpha Q(t) = \delta I(t) - (\lambda(t) + \kappa(t))Q(t), \\
 {}_0D_t^\alpha R(t) = \lambda(t)Q(t) - gR(t), \\
 {}_0D_t^\alpha D(t) = \kappa(t)Q(t).
 \end{array} \right. \quad (1)$$

Equation (1) has a non-negative initial condition $(S(0), E(0), I(0), Q(0), R(0), D(0)) = (S_0, E_0, I_0, Q_0, R_0, D_0)$, and ${}_0D_t^\alpha$ denotes the Caputo fractional derivative [12], which can capture the memory and heterogeneity properties of the transmission of the different compartments. The parameters are shown in Table 1.

Table 1 The biological meanings of parameters for system (1)

Parameter	Description	Fitted results
α	The order of fractional derivatives	0.7666
β_1	Infection rate of the infected individuals	0.3268
β_2	Infection rate of the exposed individuals	0.4566
γ_1	Symptom rate of exposed cases	0.2820
γ_2	No symptom rate of exposed cases	0.5221
δ	The rate at which infectious cases enter in quarantined cases	0.3422
$\lambda(t)$	Recovery rate of quarantined individuals	$0.8322e^{-0.0721t}$
$\kappa(t)$	Fatality rate caused by the disease	$0.0019e^{-0.0082t}$
g	Probability of infection after recovery	0.2489

Due to the end of stay-at-home order, the United States' epidemic transmission has entered a second wave. It is necessary to study the spreading trends at the state level. In particular, taking California as an example, we analyze data from Jun 1 to Oct 28. These data were provided by the Johns Hopkins University Center for Systems Science and Engineering [1], which include the number of confirmed cases and the number of deaths. From Mar 27, 2020 to now, it is reported that the United States is the country with the largest number of infections globally (<https://coronavirus.jhu.edu/map.html>). We assume that in the context of short-term disease outbreaks and policies with travel restrictions (<https://www.kff.org/coronavirus-policy-watch/stay-at-home-orders-to-fight-covid19/>), inflow rates and natural mortality rates are not taken into account in the actual model fitting process.

As the disease spreads for a long time, we can draw from the data that the recovery rate and mortality rate are not static, but a function that changes over time, as shown in first two pictures of Fig. 3 (star points are actual recorded rate). Therefore, we assume that the recovery rate and mortality rate are $\lambda(t) = \lambda_1 e^{\lambda_2 t}$ and $\kappa(t) = \kappa_1 e^{\kappa_2 t}$, respectively (as shown by the solid line in the figure), where λ_1 , λ_2 , κ_1 , and κ_2 are the constants. When the disease is spreading, for convenience, we assume that the infection rates of healthy individuals to infected individuals and exposed individuals are constants. By using the least squares method and Simulink design optimization toolbox (SLDO) [17], the parameters in the model (1) are determined (as shown in Table 1). The SLDO is a Simulink Blockset similar to Matlab Toolbox used for the fitting for COVID-19 models for the first time [18]. In the model fitting, SLDO needs zero coding effort is efficient for simulations based on Matlab 2020a.

Due to the influence of different policies, population mobility rates, and individual psychological factors in the future, the infection rates (β_1 and β_2) are selected as the random variable with normal distributions ($N(\beta_1, 0.01\beta_1^2)$ and $N(\beta_2, 0.01\beta_2^2)$) when predicting the future spread trend and scale of the disease. To estimate the validity of the results, we performed $1e4$ simulations and obtained the quantiles of active cases and deaths cases, which are shown in Fig. 2.

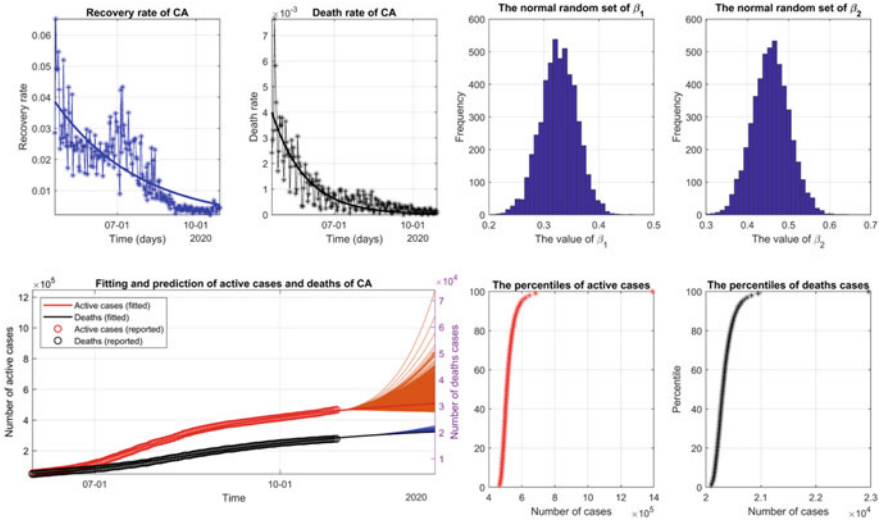


Fig. 2 The fitting results and prediction of CA

The distribution of active cases on the predicted final day (17 Dec, 2020), 5th, 25th, 50th, 75th, 95th quantiles are $4.7258e + 05$, $4.9015e + 05$, $5.0826e + 05$, $5.3436e + 05$, $5.9779e + 05$. The distribution of deaths cases on the predicted final day (17 Dec, 2020), 5th, 25th, 50th, 75th, 95th quantiles are $2.0139e+04$, $2.0225e+04$, $2.0307e+04$, $2.0417e+04$, $2.0660e+04$. From this, we can see that the predicted value of active cases and deaths is relatively concentrated, but when the infection rates in the population fluctuate, the transmission scale also has a certain probability to fluctuate greatly.

3 Influenza-Like Illness Time Series Analysis and Prediction

Influenza viruses are widespread globally, affecting people of all age groups and causing severe public health problems. Therefore, it is necessary to establish a reasonable model to study its propagation trend. Time series analysis and modeling are widely used to study the time changes in diseases to predict future trends. Generally, the ARIMA (p, d, q) model is an extension of the autoregressive (AR) model, the moving average (MA) model, and the ARMA model. If there are obvious seasonal factors in the data, we will use the seasonal ARIMA (SARIMA) model. The model has been used to fit and predict the prevalence of many infectious diseases, such as cryptosporidiosis, worm diseases, and bacterial foodborne diseases. The data preparation and model operation of the SARIMA model are relatively simple and easy to implement, and the prediction results are accurate. Therefore, it is usually used to predict short-term fluctuations in infectious diseases.

3.1 SARIMA Model

Definition 1 The seasonal autoregressive integrated moving average model (SARIMA $(p, d, q) \times (P, D, Q)_s$) of Box and Jenkins [19] is given by

$$\Phi_P(B^s)\phi(B)(1-B)^d(1-B)^D x_t = \alpha + \Theta_Q(B^s)\theta(B)\varepsilon_t, \quad (2)$$

where B is the backward operator, x_t denotes the time series, ε_t is a white noise process, and s is the seasonal period, for example, when $s = 12$, it is for monthly series. The values of d are restricted to zero when the series modeled is stationary. $\phi(B)$ is the nonseasonal AR operator of order p , and $\theta(B)$ is the nonseasonal MA operator of order q . $\Phi_P(B^s)$ and $\Theta_Q(B^s)$ are the seasonal AR and MA operators, respectively.

In order to match the above-mentioned research area, we selected the flu data from the CDC's website [3] for all flu seasons in the United States from 2002 to the present. In particular, according to the Health and Human Services (HHS) division, California belongs to the 9th division. Therefore, we use the weighted prevalence of influenza-like diseases in region 9 for analysis. In the first four data collection seasons (1997–2001), the summer months lacked surveillance data. Therefore, in order to accurately predict the results, we discard the first four data sets. The time series and its ACF and PACF are shown in Fig. 3. It can be clearly seen that this time series has a period, and its period is 52 weeks.

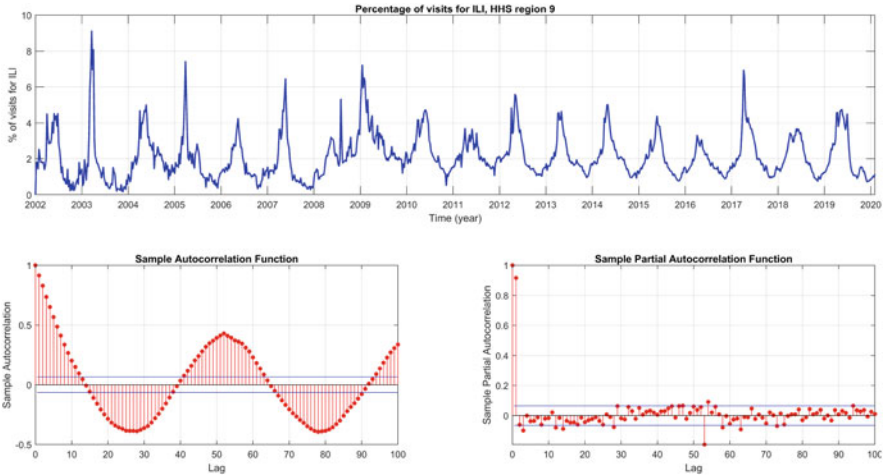


Fig. 3 The time series of ILI visit, ACF and PACF, HHS region 9

3.2 Results

We analyze the reported data of 941 weeks from Sep 22, 2002 to Oct 19, 2020, combine the use of Econometric Modeler toolbox [20], and select the model that meets the minimum AIC and BIC criterion, SARIMA(2,0,2) \times (1,0,0)₅₂, where $AIC = 1667.3166$ and $BIC = 1696.0437$. In order to ensure that the determined order is appropriate, a residual test is required. Standardized residuals are to check whether the residuals are close to the normal distribution, and the ideal residuals should be close to the normal distribution. The Q-Q plot is to test whether the residuals are close to the normal distribution. The results showed that this model fitted the seasonal fluctuation well, as shown in Figs. 4 and 5. The parameters' values can be found in Table 2.

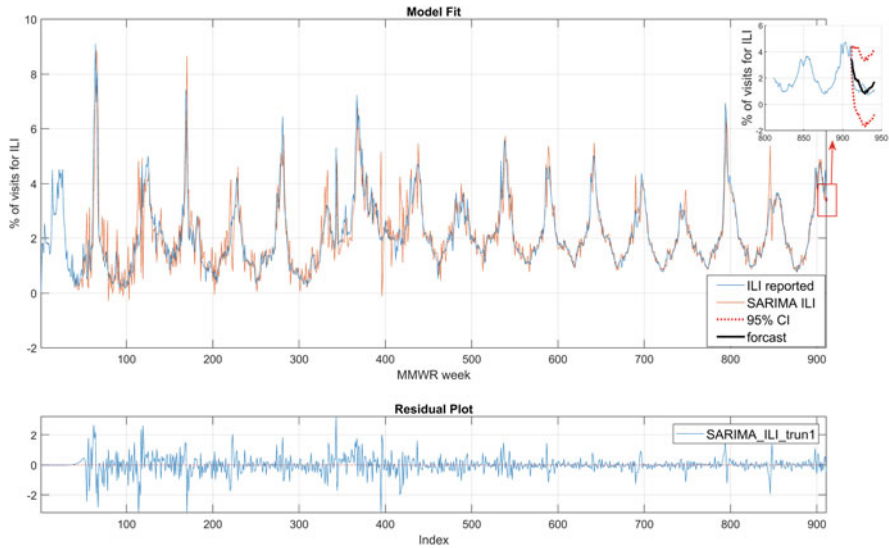


Fig. 4 Fitting and prediction results and the residuals of model SARIMA

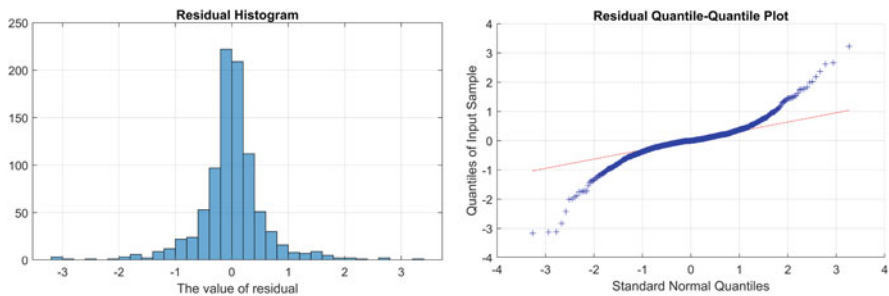


Fig. 5 The histogram of residual and Q-Q plot

Table 2 Estimation results

Parameters	Values	Standard error	<i>t</i> statistic	<i>P</i> -values
Constant	0.0037713	0.016619	0.22693	0.82048
AR{1}	1.1943	0.14947	7.9901	1.3483e-15
AR{2}	-0.31972	0.1305	-2.4499	0.014288
MA{1}	-0.22425	0.15243	-1.4712	0.14123
MA{2}	0.092713	0.026744	3.4667	0.00052684

Table 3 The hospitalization of CA

ILI vaccination rate	35%	45%	55%
ILI_hosp_CA	11,557 (95% CI: 1239, 21,875)	10,940 (95% CI: 1173, 20,706)	10322 (95% CI: 1107, 19,538)
COVID-19_hosp_CA	101,652 (95% CI: 945,16, 119,558)		
Total_hosp_CA	113,209 (95% CI: 95,755, 141,433)	112,592 (95% CI: 95,689, 140,264)	111,974 (95% CI: 95,623, 139,096)

3.3 Prediction

From the prediction results of the SARIMA model, we can know that the visit rate of influenza will increase from 1.13641% to 2.6707% (95% CI: 0.2863, 5.0550) in the seven weeks after Oct 19, 2020. According to a Feb. 21 CDC Morbidity and Mortality Weekly Report [21], the current influenza vaccine has been 45% effective overall against 2019–2020 seasonal influenza A and B viruses. In paper [22], the population-based incidence estimate for influenza-associated critical illness was 12.0 per 100,000 person-years (95% CI: 6.6, 21.6), or 1.3% (95%CI:0.7%, 2.3%) of all critical illness hospitalizations. For the COVID-19 patients, most people (about 80%) [23] recover from the disease without needing special treatment, and for the majority—especially for children and young adults—illness due to COVID-19 is generally minor.

Therefore, combined with the above research results, we studied the impact of different influenza vaccines coverage on medical resources, especially the impact on the number of hospital beds. Assuming that the test level is sufficient and that there is no misdiagnosis (i.e., no influenza cases be diagnosed as COVID-19), the number of hospital beds occupied by influenza and COVID-19 can be estimated. It can be seen from Table 3 that compared with only 35% of the population who had given the vaccine, when 55% of the population vaccinated, the use of hospital beds could be reduced by about 1200. These resources could have been provided to COVID-19 patients who need more beds. Therefore, expanding the scope of flu vaccination can alleviate and reduce the impact of the COVID-19.

4 Conclusions and Future Works

In this chapter, we not only use the fractional-order generalized SEIR model to study and predict the spread of COVID-19 but also use the SARIMA model to study and predict the spread of influenza viruses. Since we have vaccines against influenza viruses, we have also studied the impact of different proportions of vaccine injection rates on the COVID-19 epidemic, especially the number of hospital beds for detailed analysis and discussion. Our conclusion is that when there are no effective treatments and vaccines to treat COVID-19, increasing the population of influenza vaccine has a positive effect on the relief of the COVID-19, especially helping to reduce the pressure on medical resources.

In the future work, on the one hand, if the COVID-19 vaccine is put into production, we will study the optimal vaccination strategy. On the other hand, there are many kinds of analysis methods for time series, and influenza data is not only seasonal but also has long-term correlation. Therefore, we will develop new analysis methods to study and predict the trend of influenza transmission.

References

1. J. CSSE, Coronavirus COVID-19 global cases by the Center for Systems Science and Engineering (CSSE) at Johns Hopkins University (JHU) (2020). <https://github.com/CSSEGISandData/COVID-19>
2. K. Dhama, K. Sharun, R. Tiwari, M. Dadar, Y.S. Malik, K.P. Singh, W. Chaicumpa, COVID-19, an emerging coronavirus infection: advances and prospects in designing and developing vaccines, immunotherapeutics, and therapeutics. *Hum. Vaccines Immunother.* **16**(6), 1232–1238 (2020). <https://doi.org/10.1080/21645515.2020.1735227>
3. CDC: National, regional, and state level outpatient illness and viral surveillance (2020). <https://gis.cdc.gov/grasp/fluview/fluportaldashboard.html>
4. C. Qi, D. Zhang, Y. Zhu, L. Liu, C. Li, Z. Wang, X. Li, SARFIMA model prediction for infectious diseases: application to hemorrhagic fever with renal syndrome and comparing with SARIMA. *BMC Med. Res. Methodol.* **20**(1), 1–7 (2020). <https://doi.org/10.1186/s12874-020-01130-8>
5. J. Cong, M. Ren, S. Xie, P. Wang, Predicting seasonal influenza based on SARIMA model, in mainland China from 2005 to 2018. *Int. J. Environ. Res. Public Health* **16**(23), 4760 (2019). <https://doi.org/10.3390/ijerph16234760>
6. F.M. Tseng, G.H. Tzeng, et al., A fuzzy seasonal ARIMA model for forecasting. *Fuzzy Sets Syst.* **126**(3), 367–376 (2002). [https://doi.org/10.1016/S0165-0114\(01\)00047-1](https://doi.org/10.1016/S0165-0114(01)00047-1)
7. S.A. Lauer, K.H. Grantz, Q. Bi, F.K. Jones, Q. Zheng, H.R. Meredith, A.S. Azman, N.G. Reich, J. Lessler, The incubation period of coronavirus disease 2019 (COVID-19) from publicly reported confirmed cases: estimation and application. *Ann. Int. Med.* **172**(9), 577–582 (2020). <https://doi.org/10.7326/M20-0504>
8. R.M. Yulmetyev, N.A. Emelyanova, S.A. Demin, F.M. Gafarov, P. Hänggi, D.G. Yulmetyeva, Non-Markov stochastic dynamics of real epidemic process of respiratory infections. *Phys. A Statist. Mech. Appl.* **331**(1–2), 300–318 (2004). <https://doi.org/10.1016/j.physa.2003.09.023>
9. S.P. Blythe, R.M. Anderson, Variable infectiousness in HFV transmission models. *Math. Med. Biol. A J. IMA* **5**(3), 181–200 (1988). <https://doi.org/10.1093/imammb/5.3.181>

10. F.C. Santos, J.F. Rodrigues, J.M. Pacheco, Epidemic spreading and cooperation dynamics on homogeneous small-world networks. *Phys. Rev. E* **72**(5), 056,128 (2005). <https://doi.org/10.1103/PhysRevE.72.056128>
11. Y. Bai, N. Huang, L. Sun, L. Wang, Reliability-based topology design for large-scale networks. *ISA Trans.* **94**, 144–150 (2019). <https://doi.org/10.1016/j.isatra.2019.04.004>
12. I. Podlubny, *Fractional Differential Equations: An Introduction to Fractional Derivatives, Fractional Differential Equations, to Methods of Their Solution and Some of Their Applications* (Elsevier, Amsterdam, 1998)
13. S. Umarov, M. Hahn, K. Kobayashi, *Beyond the Triangle-Brownian Motion, Ito Stochastic Calculus, and Fokker-Planck Equation: Fractional Generalizations* (World Scientific Publishing, Singapore, 2018)
14. H. Sheng, Y. Chen, T. Qiu, *Fractional Processes and Fractional-Order Signal Processing: Techniques and Applications* (Springer Science & Business Media, Berlin, 2011)
15. C. Xu, Y. Yu, Q. Yang, Z. Lu, Forecast analysis of the epidemics trend of COVID-19 in the United States by a generalized fractional-order SEIR model. *Nonlinear Dyn.* **101**, 1621–1634 (2020). <https://doi.org/10.1007/s11071-020-05946-3>
16. L. Peng, W. Yang, D. Zhang, C. Zhuge, L. Hong, Epidemic analysis of COVID-19 in China by dynamical modeling (2020). Preprint arXiv:2002.06563
17. S. Documentation, Simulink design optimization toolbox (2020). <https://www.mathworks.com/products/sl-design-optimization.html>
18. Y. Zhao, L. Guo, W. Ma, S. Umarov, Y. Wang, Y. Chen, Epidemiological analysis and persistent forecast of COVID-19 by a fractional order epidemic model using SLDO. (Submitted) (2020)
19. G.E. Box, G.M. Jenkins, G.C. Reinsel, G.M. Ljung, *Time Series Analysis: Forecasting and Control* (Wiley, New York, 2015)
20. S. Documentation, Econometric Modeler toolbox (2020). <https://www.mathworks.com/products/econometrics.html>
21. F.S. Dawood, J.R. Chung, S.S. Kim, R.K. Zimmerman, M.P. Nowalk, M.L. Jackson, L.A. Jackson, A.S. Monto, E.T. Martin, E.A. Belongia, et al., Interim estimates of 2019–20 seasonal influenza vaccine effectiveness-United States, February 2020. *Morbidity Mortality Weekly Rep.* **69**(7), 177 (2020). <https://doi.org/10.15585/mmwr.mm6907a1>
22. J.R. Ortiz, K.M. Neuzil, D.K. Shay, T.C. Rue, M.B. Neradilek, H. Zhou, C.W. Seymour, L.G. Hooper, P.Y. Cheng, C.H. Goss, et al., The burden of influenza-associated critical illness hospitalizations. *Crit. Care Med.* **42**(11), 2325 (2014). <https://doi.org/10.1097/CCM.0000000000000545>
23. WHO: Media statement: Knowing the risks for COVID-19 (2020). <https://www.who.int/indonesia/news/detail/08-03-2020-knowing-the-risk-for-covid-19>

A Fractional-Order Age-Structured Generalized SEIR Model: The Role of “COVID-19 Symptom Data Challenge” Dataset



Yanting Zhao, Lihong Guo, Yong Wang, and YangQuan Chen

1 Introduction

The transmission of pneumonia associated with COVID-19 is still a worldwide epidemic. By January 1st, 2021, according to the World Health Organization, there are 84,780,171 confirmed cases and 1,853,525 confirmed deaths spreading to 235 countries, areas, or territories. With the development of globalization, traffic and environmental conditions foster the spread of the disease that breeds high economic and social costs, even in the absence of fatal forms. During the epidemic prevention war, besides medical and biological research [1], theoretical researches based on statistical, mathematical modeling, and optimal control also play essential roles. Since the outbreak of COVID-19, establishing suitable mathematical models can help understand and forecast the epidemic dynamics, integrate valid symptom

Y. Zhao

Department of Automation, University of Science and Technology of China, Hefei, China

Department of Mechanical Engineering, School of Engineering, University of California, Merced, CA, USA

e-mail: zyt9lsb@mail.ustc.edu.cn

L. Guo

Department of Mechanical Engineering, School of Engineering, University of California, Merced, CA, USA

Institute of Mathematics, Jilin University, Changchun, China

e-mail: guohl17@mails.jlu.edu

Y. Wang

Department of Automation, University of Science and Technology of China, Hefei, China

Y. Chen (✉)

Department of Mechanical Engineering, School of Engineering, University of California, Merced, CA, USA

e-mail: ychen53@ucmerced.edu

data, consider vaccine fairness priority, and determine effective mitigation and interventions to control the pandemic with an age-structured model.

Due to the long latent period of COVID-19, contacts have different spread and infection probabilities with regional and environmental differences ignored by integer-order models. Moreover, integer-order models consider the epidemic as a memoryless Markovian process, which is a non-Markovian process that reflects the prehistoric memory [2]. Based on symptom data, we find that the infection rate of COVID-19 satisfies the power-law decay, reflecting the decay of long memory [3]. Therefore, there are always errors in integer-order model fitting, and they affect the prediction accuracy [4]. Thus, the corresponding fractional-order models, which have the long-memory property to reflect the inhomogeneity, are established to consider epidemic trends and quarantine policies.

This chapter proposes a fractional-order age-structured SEIR (Fo-ASEIR) model to fit the dynamic of the COVID-19 pandemic. Based on the Facebook Symptom Data Challenge and Google mobility data, we focus on the mobility and psychological effect factors of COVID-19 to forecast the number of infected cases and deaths. In summary, the contributions of this chapter are as follows:

- (i) Proposed the Fo-ASEIR model, which can describe the epidemic trends and forecast the short-term infection cases by age groups accurately based on the long-memory property of fractional calculus.
- (ii) Analyzed control or mitigation strategies affected by mobility and psychological effect data. Piecewise functions of the infection rate and the incidence rate in our model affect the likelihood of epidemic or suppression.
- (iii) Simulink Design Optimization (SLDO) was applied to fit epidemic trends for the first time. The disturbance of infection rate was analyzed to illustrate the mitigation and intervention managements.
- (iv) Predictions of our fractional-order model, including forecasts of deaths in the United States and California, were submitted to the COVID-19 Forecast Hub in coordination with CDC (<https://viz.covid19forecasthub.org/>).

The structure of this chapter is as follows. Section 2 provides preliminary facts on fractional calculus and epidemic compartmental models. The role of symptom data challenge and incidence rate is analyzed in Sect. 3. Section 4 demonstrates the superior performance of the fractional-order model based on the fitting and short-term forecasts of models. Meanwhile, simulations examine the effects of mobility and psychological effect factors on model fitting. Section 5 gives conclusions.

2 Preliminaries

2.1 Fractional Calculus

Although various fractional-order derivatives are defined, we only consider Riemann–Liouville definitions in this chapter.

Definition 1 The fractional integral of $f(t)$ of order α is defined as follows [5]:

$${}_t \mathcal{I}_t^\alpha f(t) = \frac{1}{\Gamma(\alpha)} \int_{t_0}^t \frac{f(\tau)}{(t-\tau)^{1-\alpha}} d\tau, \tag{1}$$

where $n - 1 < \alpha < n, n \in \mathbb{N}^+$ with the Gamma function $\Gamma(z) = \int_0^{+\infty} x^{z-1} e^{-x} dx$, provided the integral on the right of (1) is finite.

Definition 2 Riemann—Liouville derivative is defined as follows [5]:

$${}^R \mathcal{D}_t^\alpha f(t) = \frac{1}{\Gamma(n-\alpha)} \frac{d^n}{dt^n} \int_{t_0}^t (t-\tau)^{n-\alpha-1} f(\tau) d\tau, \tag{2}$$

where $n - 1 < \alpha < n, n \in \mathbb{N}^+$.

To simplify the notations, ${}_0 \mathcal{I}_t^\alpha$ is replaced by \mathcal{I}^α and ${}^R \mathcal{D}_t^\alpha$ is replaced by \mathcal{D}^α when the lower endpoint $t_0 = 0$.

2.2 Fractional-Order SEIR Models

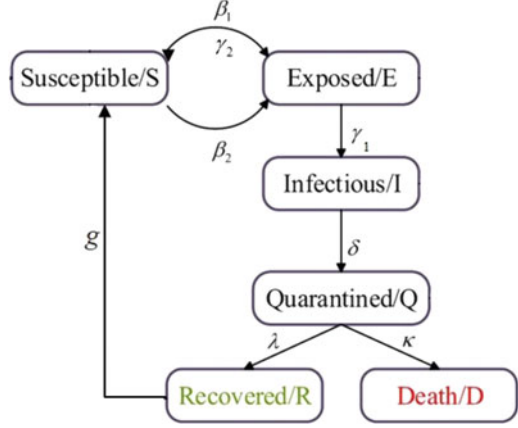
For the outbreak of the COVID-19 pandemic, the biological meanings of state variables and the transmission diagram between each compartment are shown in Table 1 and Fig. 1, respectively.

In general, the infection rate of an infectious disease is assumed to be constant. Singer [6] investigated the transmission patterns of COVID-19, indicating that the number of $E(t)$ follows the power law $n(t) = Bt^\gamma$, where $n(t)$ is the number of exposed at time t , and B and γ are constant. This pattern is consistent with the memory effects in the pandemic, which means that the dynamics of the system is dependent on both the current state and history of the system [7]. Consequently, the bilinear incidence rate $\beta_2 SE$ is changed to fractional incidence rate $\beta_2 S \mathcal{I}^{\alpha_e} E$ to characterize the phenomena of human interactions. Based on the integer-order SEIR model [8], we propose the fractional-order generalized SEIR model (Model_1) shown as follows:

Table 1 Meanings of state variables

Categories	Descriptions at time t
$S(t)$	Number of susceptible individuals
$E(t)$	Number of exposed individuals
$I(t)$	Number of infectious individuals
$Q(t)$	Number of quarantined individuals
$R(t)$	Number of recovered individuals
$D(t)$	Number of death individuals

Fig. 1 Fo-GSEIR model



$$\left\{ \begin{array}{l} \mathcal{D}^{\alpha_f} S(t) = -\frac{\beta_1 I(t)}{N} S(t) - \frac{\beta_2 \mathcal{I}^{\alpha_e} E(t)}{N} S(t) + \gamma_2 E(t) + g R(t), \\ \mathcal{D}^{\alpha_f} E(t) = \frac{\beta_1 I(t)}{N} S(t) + \frac{\beta_2 \mathcal{I}^{\alpha_e} E(t)}{N} S(t) - (\gamma_1 + \gamma_2) E(t), \\ \mathcal{D}^{\alpha_f} I(t) = \gamma_1 E(t) - \delta I(t), \\ \mathcal{D}^{\alpha_f} Q(t) = \delta I(t) - (\lambda + \kappa) Q(t), \\ \mathcal{D}^{\alpha_f} R(t) = \lambda Q(t) - g R(t), \\ \mathcal{D}^{\alpha_f} D(t) = \kappa Q(t), \end{array} \right. \quad (3)$$

with initial conditions $(S(0), E(0), I(0), Q(0), R(0), D(0)) = (s_0, e_0, i_0, q_0, r_0, d_0)$, which are non-negative. N refers to the total population of the region at the initial time. Coefficients $\{\alpha_f; \alpha_e; \beta_1; \beta_2; \gamma_1^{-1}; \gamma_2; \delta^{-1}; \lambda; \kappa; g\}$ refer to the fractional orders α_f and α_e that reflect inhomogeneity, the rate of transmission for the susceptible to infected β_1 , the rate of transmission for the susceptible to exposed β_2 , the average latent time γ_1^{-1} , no symptom rate of exposed cases γ_2 , the quarantine period that depends on the level of detection δ^{-1} , the recovery rate λ , the mortality rate κ , and the rate of recovered individuals who lose immunity and are moved back to susceptible cases g .

3 Symptom Data Challenge

As governments, researchers and universities began to mount an unprecedented worldwide response to COVID-19 in early 2020, the world lacked a standardized, global way to measure COVID-19 illness and track the pandemic that would help guide decision-making. The integration of symptom data can aid in the development and monitoring of community risk levels to guide individual and policy decision-making.

3.1 Analyses of Symptom Data

In response, there are promising signals that the symptom surveys can provide a complementary view to key, time-sensitive public health questions about COVID-19 incidence [9]. US state-level rates of COVID-like symptoms correlate with daily cases of psychological effect factor, and state-level analyses tend to show that the infection rate is roughly coincident in time with mobility data. The corresponding datasets (e.g., COVID searches on Google and related doctor visits) are collected by Facebook, which are shown in Fig. 2.

Remark 1

- (i) Using Google Health Trends, the fraction of COVID-related Google searches out of all Google searches in each area are obtained. We use searches for terms related to anosmia (loss of taste or smell) since this emerged as an unusual symptom that is indicative of COVID-19.
- (ii) Using data of COVID-related outpatient doctor visits, derived from ICD codes found in insurance claims, the percentages of daily doctor’s visits in each area that are due to COVID-like illness are estimated.
- (iii) Mobility data shows how visits to places, such as grocery stores and parks, are changing in each geographic region. Location accuracy and the understanding of categorized places vary from region to region.

According to data, we try to infer the influence of the mobility and psychological effect factors in the model to describe the performance of infectious diseases more accurately. For example, the infection rates β_1 and β_2 , which are affected by mobility in Fig. 2c of models, are fitted with piecewise function accordingly. Moreover, Fig. 2a and b reflects changes in the psychological effect factor for the COVID-19 pandemic, which is also an important factor affecting the trends. In the next subsection, we introduce the concept of incidence rate to illustrate the effects on the modified model.

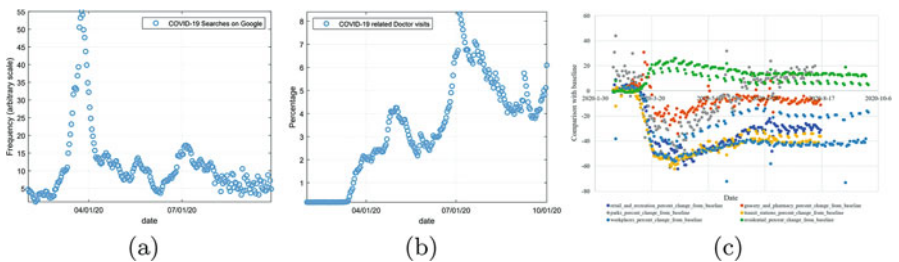


Fig. 2 COVID-19 symptom datasets in California. (a) Searches on Google. (b) Related doctor visits. (c) Google mobility

3.2 Incidence Rate and Psychological Effect

Incidence rates play important roles in epidemic models [10]. The SEIR models with saturated and nonmonotone incidence rates, in which the infection function first increases to a maximum when a new infectious disease emerges, then decreases due to psychological effect, and eventually tends to a saturation level due to crowding effect.

Case 1 Saturated incidence rate. Capasso and Serio [11] proposed a saturated incidence rate as follows:

$$g(I)S = \frac{\beta IS}{1 + \alpha I}, \quad (4)$$

where βI means the infection force of the disease and $\frac{1}{1+\alpha I}$ represents the inhibition effect from the behavioral change of S when their number increase or from the crowing effect of I . Notice that $g(I)$ eventually tends to a saturation level $\frac{\beta}{\alpha}$ when I is getting larger.

Case 2 Nonmonotone incidence rates with psychological effect. To model the effects of psychological factor and interventions when a serious disease outbreaks, Xiao and Ruan [12] proposed a nonmonotone incidence rate as follows:

$$g(I)S = \frac{\beta IS}{1 + \alpha I^2}, \quad (5)$$

where the incidence function $g(I)$ is nonmonotone when $I \geq 0$. It implies that when a new infectious disease breaks out, the probability of exposure and infection rate increases due to the lack of understanding of the disease. As the increasing number of I and the diseases worsens, psychological factor leads people to take measures to control the pandemic. For instance, during the outbreak of Severe Acute Respiratory Syndrome (SARS), aggressive mitigation and interventions were effective. So as the number of infectious cases increases, the infectivity decreases.

Two types of nonlinear incidence functions $g(I)$ with different values of parameter α are shown in Fig. 3. We can clearly see the influence of psychological factors from Fig. 3b, which is similar to the data of COVID-19-related searches on Google shown in Fig. 2a.

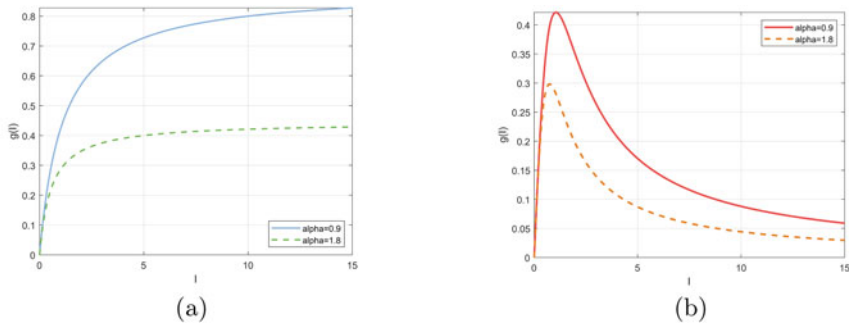


Fig. 3 Incidence functions. (a) Saturated incidence function. (b) Nonmonotone incidence function

3.3 The Age-Structured Model with Psychological Effects

When we take psychological effect factors into consideration, Model₂ with the nonmonotone incidence rate (4) is shown as

$$\begin{cases} \mathcal{I}^{\alpha} S(t) = -\frac{\beta_1 I(t)}{N(1+\alpha I^2(t))} S(t) - \frac{\beta_2 \mathcal{I}^{\alpha} E(t)}{N} S(t) + \gamma_2 E(t) + gR(t), \\ \mathcal{I}^{\alpha} E(t) = \frac{\beta_1 I(t)}{N(1+\alpha I^2(t))} S(t) + \frac{\beta_2 \mathcal{I}^{\alpha} E(t)}{N} S(t) - (\gamma_1 + \gamma_2) E(t), \\ \mathcal{I}^{\alpha} I(t) = \gamma_1 E(t) - \delta I(t), \\ \mathcal{I}^{\alpha} Q(t) = \delta I(t) - (\lambda + \kappa) Q(t), \\ \mathcal{I}^{\alpha} R(t) = \lambda Q(t) - gR(t), \\ \mathcal{I}^{\alpha} D(t) = \kappa Q(t), \end{cases} \quad (6)$$

where parameter α refers to the inhibition rate and psychological effect factors.

Afterward, we analyzed infectious cases and deaths of age groups from California Department of Public Health (<https://www.cdph.ca.gov/programs/CID-/DCDC/pages/covid-19/race-ethnicity.aspx>). The mobility data varied greatly among different age groups, and the number of deaths and infections also accounted for different proportions [13]. The parametric analysis of different age-structured models is shown in Fig. 4 and Table 2.

The fractional-order age-structured SEIR Model₃ is obtained in (7) where the parameter $a \in \{C, Y, A, E\}$ (children, young adults, adults, elderly) represents different age groups:

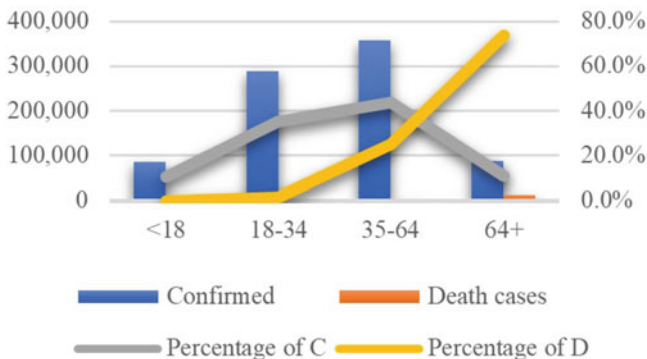


Fig. 4 Age group data of California

Table 2 Parameters of age groups

	γ_1	γ_2	λ	κ
C: < 18	$0.7\gamma_1$	$0.3\gamma_1$	0.99λ	0.01λ
Y: 18–34	$0.8\gamma_1$	$0.2\gamma_1$	0.9λ	0.1λ
A: 35–64	$0.9\gamma_1$	$0.1\gamma_1$	0.6λ	0.4λ
E: 64+	γ_1	0	0.4λ	0.6λ

$$\begin{cases}
 \mathcal{D}^{\alpha} S^a(t) = -\frac{\beta_1 I^a(t)}{N(1+\alpha(I^a(t))^2)} S^a(t) - \frac{\beta_2 \mathcal{J}^{\alpha_e} E^a(t)}{N} S^a(t) + \gamma_2 E^a(t) + g R^a(t), \\
 \mathcal{D}^{\alpha} E^a(t) = \frac{\beta_1 I^a(t)}{N(1+\alpha(I^a(t))^2)} S^a(t) + \frac{\beta_2 \mathcal{J}^{\alpha_e} E^a(t)}{N} S^a(t) - (\gamma_1 + \gamma_2) E^a(t), \\
 \mathcal{D}^{\alpha} I^a(t) = \gamma_1 E^a(t) - \delta I^a(t), \\
 \mathcal{D}^{\alpha} Q^a(t) = \delta I^a(t) - (\lambda + \kappa) Q^a(t), \\
 \mathcal{D}^{\alpha} R^a(t) = \lambda Q^a(t) - g R^a(t), \\
 \mathcal{D}^{\alpha} D^a(t) = \kappa Q^a(t).
 \end{cases} \quad (7)$$

The relationships of parameters of (7), which are affected by epidemic trends of infected cases of age groups and mobility data, are shown in Table 2.

4 Simulations and Discussions

The data of confirmed cases and deaths of COVID-19 are provided by the Johns Hopkins University (<https://github.com/CSSEGISandData/COVID-19>) for simulations. Considering that mobility data is not recommended to compare changes between countries or regions with different characteristics, so we choose data in California. For the model fitting and the analysis with zero coding effort, Simulink Design Optimization, a Simulink Blockset is used with real data.

4.1 Fitting and Forecast

To illustrate the influence of psychological effects on models, we make a comparison of the short-term forecast of COVID-19 between Model_1 and Model_2, fitting data in California from 3/5/2020 to 9/19/2020, and forecast the next 2 weeks. Fitting results of California and relative errors are shown in Fig. 5 and Table 3.

Through the analysis of mobility and infection data of age groups in California, the relationship between the parameters of latency, mortality, and the recovery rate in Model_3 is obtained, as shown in Table 2. The epidemic trends of infection and death by age groups in Model_3 are shown in Fig. 6, which can allocate resources on hospitalization, coronavirus testing, and vaccination and reopen social policies more rationally.

4.2 Mobility and Psychological Effect Factors

The fitting intervals of infection rates β_1 and β_2 are divided into complete one, two, and three segments for different policy managements in California (e.g., April 12th; April 12th, July 1st), so do the fitting intervals of piecewise function α (e.g., June 14th; May 1st, July 5th). The results are shown in Fig. 7.

Fig. 5 Fitting of California

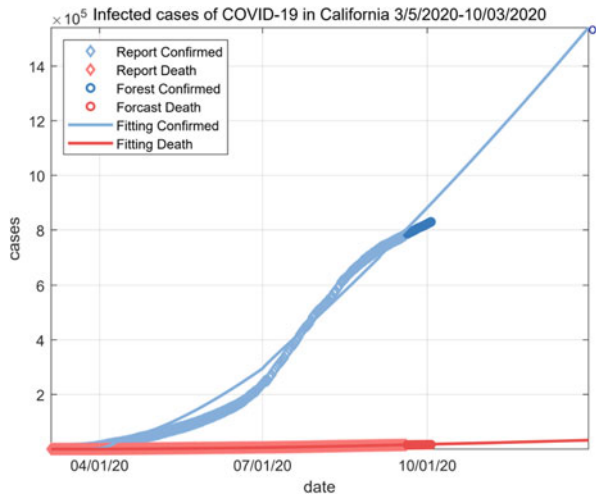


Table 3 Forecast errors of C and D

Errors	of C %		of D %	
	Model_1	Model_2	Model_1	Model_2
Average	6.32	5.38	8.08	7.81
Maximum	8.64	7.61	9.98	9.70
Minimum	4.12	3.28	6.30	6.04

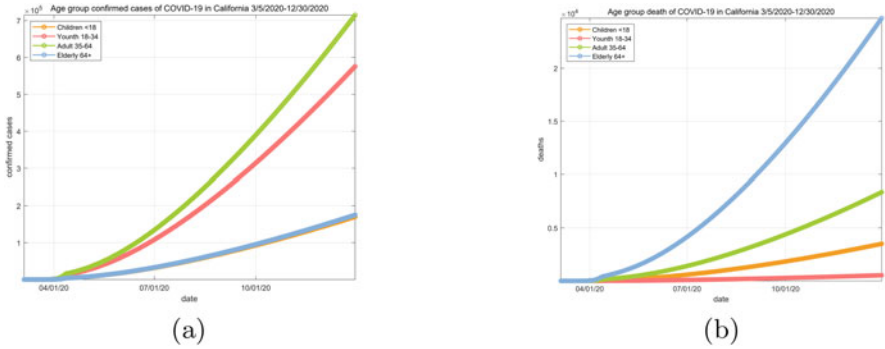


Fig. 6 COVID-19 pandemic of age groups in California 3/5/2020–12/30/2020. (a) Confirmed cases. (b) Death

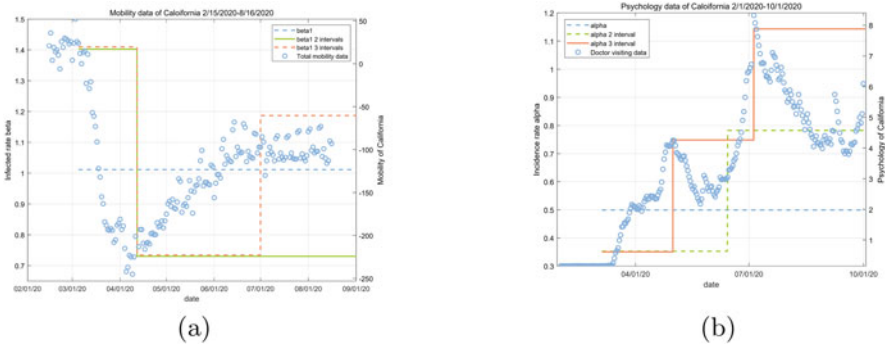


Fig. 7 Parameters fitting using symptom data 02/01/2020–10/01/2020. (a) Infection rate. (b) Psychological effect factor

We also obtain epidemic trends of uncertain models after fitting the model. After October 3rd, 2020, we set infection rates β_1 and β_2 as normal distributions of fitting values. The epidemic trends are shown in Fig. 8 till December 30th, 2020.

4.3 Analysis

Policymakers may be concerned about formulating policies related to isolation and reopening before the flu season [14]. Therefore, we will consider workplace-related and entertainment-related relaxation using Google and Facebook symptom data. Results of simulations are summarized as follows:

- (i) It is comparing 2-week forecast errors of infected cases and deaths in Table 3, and Model_2 with psychological effect factor shows better performance than Model_1 on model fitting and forecast. It means that the infection rate β_1 from

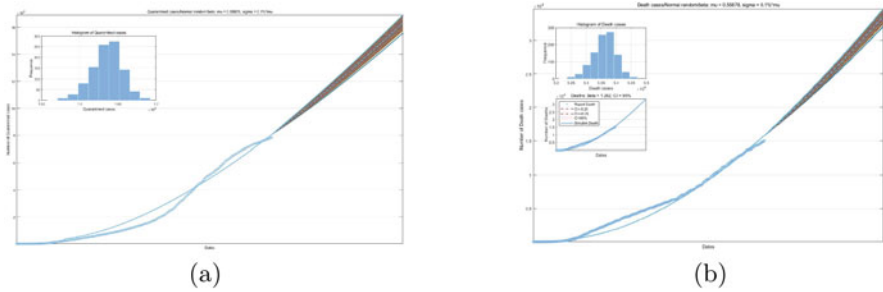


Fig. 8 Random disturbance of infection rate of California: 3/5/2020-12/30/2020. (a) Confirmed cases. (b) Deaths

S to I is not a constant. When considering $g(I)$ affected by α , the trend of infection can be depicted and predicted more accurately.

- (ii) Model_3 estimates coefficients for age modules. It is observed in Fig. 6a that the latent period of adults is the shortest, so the infected cases of adults are the largest. Policymakers should provide appropriate testing methods and locations and conduct a peak shift for working hours of adults to reduce infection. In Fig. 6b, death trends are consistent with κ . In the case of the elderly with the largest number of deaths, hospitalization and vaccination are allocated according to priority so as to minimize death.
- (iii) We analyzed symptom data and fit β_1 , β_2 , and α by piecewise functions for forecast performance in Fig. 7. (a) shows that when Californians implemented stay-at-home orders from April 12th, β_1 , $\beta_2 \downarrow$, then growth rate of I , $D \downarrow$. When reopened society on July 1st, β_1 , $\beta_2 \uparrow$. Thus, the government should continue to take subsequent quarantine and delay the reopening of social. Figure 7b shows that with the increase of the infected cases, people are constrained by psychological factors to strengthen self-isolation and increase hospital visits. Correspondingly, $\alpha \uparrow$, more symptom data should be updated, and more hospital appointments should be provided.
- (iv) Figure 8 shows that the larger the infection rates are, the larger the number of infected cases and deaths in California, then the more strict policies should be taken, so do other states. Interventions and the increase of people's cognition and fear of COVID-19 cannot only reduce the infection rate but also play a good role in controlling the pandemic.

5 Conclusions

In summary, the integration of symptom data based on the fractional-order age-structured SEIR model enables the creation of models that identify epidemic trends in state COVID-19 outbreaks with greater sensitivity, specificity, and timeliness

compared to current indicators. Our model, considering the mobility and psychological effect factors, will lead to more accurate fitting and prediction performance. Moreover, our purpose is to apply models to further investigate vaccine fairness priority problems and Multi-Model Outbreak Decision Support.

References

1. A.W. Bartik, M. Bertrand, Z. Cullen, E.L. Glaeser, M. Luca, C. Stanton, The impact of COVID-19 on small business outcomes and expectations. *Proc. Natl Acad. Sci.* **117**(30), 17656–17666 (2020)
2. R.M. Yulmetyev, N.A. Emelyanova, S.A. Demin, F.M. Gafarov, P. Hänggi, D.G. Yulmetyeva, Non-Markov stochastic dynamics of real epidemic process of respiratory infections. *Phys. Statist. Mech. Appl.* **331**(1–2), 300–318 (2004)
3. H. Singer, Short-term predictions of country-specific COVID-19 infection rates based on power law scaling exponents (2020). Preprint arXiv:2003.11997.
4. C.H. Xu, Y.G. Yu, Q.C. Yang, Z.Z. Lu, Forecast analysis of the epidemics trend of COVID-19 in the USA by a generalized fractional-order SEIR model. *Nonlinear Dyn.* **1101**, 1621–1634 (2020)
5. I. Podlubny, *Fractional Differential Equations: an Introduction to Fractional Derivatives, Fractional Differential Equations, to Methods of Their Solution and Some of Their Applications* (Academic, San Diego, 1999)
6. H.M. Singer, The COVID-19 pandemic: growth patterns, power law scaling, and saturation. *Phys. Biol.* **17**(5), 055001 (2020)
7. C.N. Angstmann, B.I. Henry, A.V. McGann, A fractional-order infectivity SIR model. *Phys. Statist. Mech. Appl.* **452**, 86–93 (2016)
8. L.R. Peng, W.Y. Yang, D.Y. Zhang, C.J. Zhu Ge, L. Hong, Epidemic analysis of COVID-19 in China by dynamical modeling (2020). arXiv:2002.06563
9. The COVID-19 Symptom Data Challenge, <https://www.symptomchallenge.org/> (2020)
10. M. Lu, J. Huang, S. Ruan, P. Yu, Bifurcation analysis of an SIRS epidemic model with a generalized nonmonotone and saturated incidence rate. *J. Differ. Eq.* **267**(3), 1859–1898 (2019)
11. V. Capasso, G. Serio, A generalization of the Kermack-McKendrick deterministic epidemic model. *Math. Biosci.* **42**(1–2), 43–61 (1978)
12. D.M. Xiao, S.G. Ruan, Global analysis of an epidemic model with nonmonotone incidence rate. *Math. Biosci.* **208**(2), 419–429 (2007)
13. A. Radulescu, K. Cavanagh, Management strategies in a SEIR model of COVID-19 community spread (2020). Preprint arXiv:2003.11150
14. K. Shea, M.C. Runge, D. Pannell, W.J. Probert, S.-L. Li, M. Tildesley, M. Ferrari, Harnessing multiple models for outbreak management. *Science* **368**(6491), 577–579 (2020)

Dynamical Analysis of a COVID-19 Epidemic Model with Social Confinement and Acquired Immunity Loss



Yamin Ding and Yanmei Kang

1 Introduction

The ongoing coronavirus disease 2019 (COVID-19) is the first global pandemic caused by a coronavirus. As of 2:45 pm CEST, September 5th, 2020, a total of 26,468,031 cases of new coronary pneumonia have been diagnosed worldwide, with a total of 871,166 deaths, of which 91 countries have confirmed cases over 10,000 [1]. At present, the epidemic has been controlled in China, but it is still spreading around the world, so fighting the epidemic is still the top priority. As of September 23th, 2020, Brazil has reported 4,624,885 confirmed cases [2], ranking third globally and still rising. Before the successful development of new drugs and vaccines, intense non-pharmaceutical interventions are particularly necessary to stop the transmission of COVID-19.

The mathematical model can help understand the nature of outbreaks and plan effective control strategies [3–6]. Many complicated mathematical models have been used to study asymptomatic infections of other infectious diseases [7–9]. These models reveal that changing the proportion of asymptomatic individuals affects mitigation strategies and thus changes the course of the epidemic. There is evidence that asymptomatic and mildly symptomatic individuals are infectious and can promote the rapid spread of the COVID-19 epidemic [10, 11]. For example, the isolation of asymptomatic cases by large-scale testing has led to a rapid decline in the number of new cases in Italian villages [12], indicating that asymptomatic individuals are somewhat infectious. Therefore, asymptomatic individuals should be considered when predicting epidemic trends and evaluating the effectiveness of confinement strategies. If social isolation is combined with individuals, the test-

Y. Ding · Y. Kang (✉)

School of Mathematics and Statistics, Xi'an Jiaotong University, Xi'an, China
e-mail: 1194170916@qq.com; ykmang@xjtu.edu.cn

track-isolation strategy will effectively control the epidemic. Particularly, Giordano et al. considered whether the infected person had been diagnosed and the severity of their symptoms and proposed a model with eight infection stages [13]. Because diagnosed individuals are typically isolated, non-diagnosed individuals are more infectious. They found that this distinction helps explain misperceptions about the spread of the COVID-19. The SIDARTHE model distinguishes different groups related to epidemics' evolution and considers more comprehensively than the SEIR model.

COVID-19 is caused by the infection of the coronavirus SARS-COV-2. Due to the lack of reliable information on the duration of the virus's acquired immunity, the risk of a surge in infection cannot be assessed [14]. A recent study shows that antibodies to the virus may only last for two months, which has caused speculation that its immunity may not exist for a long time [15]. There are also other studies that reinfection after recovery most often occurs 12 months after infection, indicating that acquired immunity is only short-lived. Particularly, antibodies rapidly decay in mild cases [16, 17]. Therefore, the loss of acquired immunity should be truly considered as a more realistic model. Nevertheless, Giordano et al. [13] omitted the impact of the acquired immunity loss. Motivated by the above discussion, we derive a modified SIDARTH model by introducing the acquired immunity loss.

The organization of this chapter is as follows. In Sect. 2, we present the modified SIDARTH model. Section 3 analyzes the global stability of the disease-free equilibrium and the endemic equilibrium by Lyapunov–LaSalle techniques and graph theory. In Sect. 4, we fit the data from Brazil to analyze the model and perform sensitivity analysis on the parameters. In the end, some concluding remarks are presented to close this chapter in Sect. 5.

2 Model and Preliminaries

2.1 Modified SIDARTH Model

Our model is extended from the work of Giordano et al. [13] but different in the following aspects: we consider the impact of acquired immunity loss; for the sake of convincing in dynamical analysis, we adopt the standard incidence rate and include the recruitment rate Λ and the natural death χ into the model; considering that the mortality rate of the disease is much smaller than the cure rate, we ignore the death rate of diseases. Therefore, the total population of individuals $N(t)$ is divided into seven different epidemic components as shown in Fig. 1. The modified SIDARTH model is as follows:

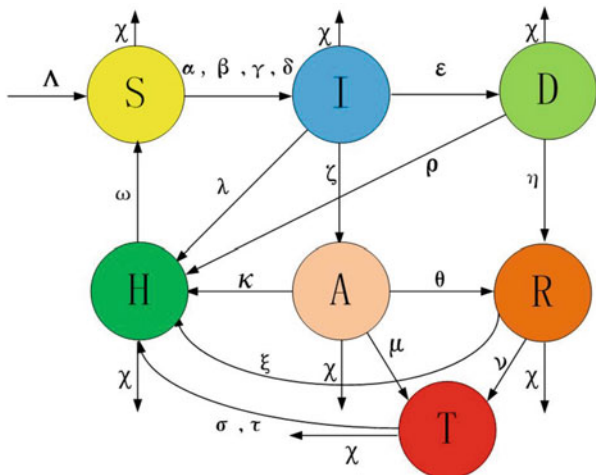


Fig. 1 Flow chart of the improved SIDARTH model

$$\begin{cases} \frac{dS}{dt} = \Lambda + \omega H - (\alpha I + \beta D + \gamma A + \delta R) \frac{S}{N} - \chi S \\ \frac{dI}{dt} = (\alpha I + \beta D + \gamma A + \delta R) \frac{S}{N} - (\epsilon + \zeta + \lambda + \chi) I \\ \frac{dD}{dt} = \epsilon I - (\eta + \rho + \chi) D \\ \frac{dA}{dt} = \zeta I - (\theta + \mu + \kappa + \chi) A \\ \frac{dR}{dt} = \eta D + \theta A - (\nu + \xi + \chi) R \\ \frac{dT}{dt} = \mu A + \nu R - (\sigma + \chi) T \\ \frac{dH}{dt} = \lambda I + \rho D + \kappa A + \xi R + \sigma T - (\chi + \omega) H, \end{cases} \quad (1)$$

where ω is the acquired immunity loss rate. Other parameters and their description can be found in Ref. [13] or Table 1. The above seven components are explained as follows:

- *S*: The class of susceptible (uninfected)
- *I*: The class of infected (asymptomatic infected, undetected)
- *D*: The class of diagnosed (asymptomatic infected, detected)
- *A*: The class of ailing (symptomatic infected, undetected)
- *R*: The class of recognized (symptomatic infected, detected)
- *T*: The class of threatened (infected with life-threatening symptoms, detected)
- *H*: The class of healed

Since $N(t) = S(t) + I(t) + D(t) + A(t) + R(t) + T(t) + H(t)$, then

$$\frac{dN}{dt} = \Lambda - \chi N \implies \lim_{t \rightarrow \infty} \sup N \leq \frac{\Lambda}{\chi}.$$

Table 1 Parameters of the model

Parameter	Description	Fitted value
α	Transmission rate between S and I	0.3328
β, δ	Transmission rate between S and D , between S and A	0.0046
γ	Transmission rate between S and R	0.1798
ε	Probability rate of asymptomatic detection	0.0849
ζ, η	Probability rate of symptoms in I, D	0.0184
λ, ρ	Recovery rate of I, D	0.2214
θ	Probability rate of symptomatic detection	0.3954
μ	The rate of life-threatening symptoms of A	0.0433
κ, ξ, σ	Recovery rate of A, R, T	0.0102
ν	The rate of life-threatening symptoms of R	0.0801
τ	Mortality rate	0.0032

Hence, the feasible region of the model (1) remains in a bounded positive invariant set Γ :

$$\Gamma = \left\{ (S, I, D, A, R, T, H) \in \mathbb{R}_+^7 : 0 < S + I + D + A + R + T + H \leq \frac{\Lambda}{\chi} \right\}.$$

2.2 Basic Reproduction Number

The basic reproduction number R_0 is the key threshold parameter, which can determine whether the infectious disease will die out or spread through the population with time increases. Here, we calculate it through the next-generation matrix method. The infection components in this model are I, D, A , and R . The new infection compartment \mathcal{F} and the transition terms \mathcal{V} are given by

$$\mathcal{F} = \begin{pmatrix} (\alpha I + \beta D + \gamma A + \delta R) \frac{S}{N} \\ 0 \\ 0 \\ 0 \end{pmatrix}, \mathcal{V} = \begin{pmatrix} (\varepsilon + \zeta + \lambda + \chi)I \\ (\eta + \rho + \chi)D - \varepsilon I \\ (\theta + \mu + \kappa + \chi)A - \zeta I \\ (\nu + \xi + \chi)R - \eta D - \theta A \end{pmatrix}.$$

The Jacobian matrices F and V for \mathcal{F} and \mathcal{V} at the disease-free equilibrium point $(\frac{\Lambda}{\chi}, 0, 0, 0, 0, 0, 0)$ are, respectively, given by

$$F = \begin{pmatrix} \frac{\alpha S_0}{N} & \frac{\beta S_0}{N} & \frac{\gamma S_0}{N} & \frac{\delta S_0}{N} \\ 0 & 0 & 0 & 0 \\ 0 & 0 & 0 & 0 \\ 0 & 0 & 0 & 0 \end{pmatrix},$$

$$V = \begin{pmatrix} \epsilon + \zeta + \lambda + \chi & 0 & 0 & 0 \\ -\epsilon & \eta + \rho + \chi & 0 & 0 \\ -\zeta & 0 & \theta + \mu + \kappa + \chi & 0 \\ 0 & -\eta & -\theta & \nu + \xi + \chi \end{pmatrix}.$$

The R_0 is defined as the spectral radius of the next-generation matrix FV^{-1} [18]:

$$\begin{aligned} R_0 &= \rho(FV^{-1}) \\ &= \frac{1}{\epsilon + \zeta + \lambda + \chi} \left(\alpha + \frac{\beta\epsilon}{\eta + \rho + \chi} + \frac{\gamma\zeta}{\theta + \mu + \kappa + \chi} \right. \\ &\quad \left. + \frac{\delta\epsilon\eta(\theta + \mu + \kappa + \chi) + \delta\zeta\theta(\eta + \rho + \chi)}{(\eta + \rho + \chi)(\theta + \mu + \kappa + \chi)(\nu + \xi + \chi)} \right). \end{aligned}$$

Notice that the R_0 consists of four parts, representing the four modes of transmission of the coronavirus.

3 Stability Analysis

The equilibrium points will provide long-term dynamic information about the epidemic. The model (1) has two equilibrium points: one is the disease-free equilibrium (DFE) $P_0 = (\frac{\Lambda}{\chi}, 0, 0, 0, 0, 0, 0)$, which exists for all parameter values, and the second is the endemic equilibrium point (EE) $P^* = (S^*, I^*, D^*, A^*, R^*, T^*, H^*)$, which is a positive solution of the following system:

$$\begin{aligned} \Lambda + \omega H^* - (\alpha I^* + \beta D^* + \gamma A^* + \delta R^*) \frac{S^*}{N} - \chi S^* &= 0 \\ (\alpha I^* + \beta D^* + \gamma A^* + \delta R^*) \frac{S^*}{N} - (\epsilon + \zeta + \lambda + \chi) I^* &= 0 \\ \epsilon I^* - (\eta + \rho + \chi) D^* &= 0 \\ \zeta I^* - (\theta + \mu + \kappa + \chi) A^* &= 0 \\ \eta D^* + \theta A^* - (\nu + \xi + \chi) R^* &= 0 \\ \mu A^* + \nu R^* - (\sigma + \chi) T^* &= 0 \\ \lambda I^* + \rho D^* + \kappa A^* + \xi R^* + \sigma T^* - (\chi + \omega) H^* &= 0. \end{aligned} \tag{2}$$

We can get

$$\begin{aligned} D^* &= \frac{\epsilon I^*}{\eta + \rho + \chi}, A^* = \frac{\zeta I^*}{\theta + \mu + \kappa + \chi}, R^* = \frac{\eta D^* + \theta A^*}{\nu + \xi + \chi}, T^* = \frac{\mu A^* + \nu R^*}{\sigma + \chi}, \\ H^* &= \frac{1}{\chi + \omega} \left(\lambda I^* + \rho \frac{\epsilon I^*}{\eta + \rho + \chi} + \kappa \frac{\zeta I^*}{\theta + \mu + \kappa + \chi} + \xi \frac{\eta D^* + \theta A^*}{\nu + \xi + \chi} + \sigma \frac{\mu A^* + \nu R^*}{\sigma + \chi} \right) := \phi I^*, \\ S^* &= \frac{N}{R_0}, I^* = \frac{\Lambda}{\epsilon + \zeta + \lambda + \chi - \omega\phi} \frac{R_0 - \chi N / \Lambda}{R_0}. \end{aligned} \tag{3}$$

For convenience, we may assume that birth and natural death are balanced (i.e., $\Lambda = \chi N$ holds). Thus, we can conclude that when $R_0 > \chi N/\Lambda > 1$, the model (1) has the unique EE P^* .

3.1 Global Stability Analysis of the Disease-Free Equilibrium

In this section, the global asymptotic stability of the disease-free equilibrium for model (1) is discussed by a matrix-theoretic method.

Theorem 1 *The disease-free equilibrium $P_0 = (\frac{\Lambda}{\chi}, 0, 0, 0, 0, 0, 0)$ of model (1) is globally asymptotically stable if $R_0 \leq 1$ or unstable if $R_0 > 1$.*

Proof We employ the method described in Ref. [19] to construct a Lyapunov function. Let $x = (I, D, A, R)^T$ and $f(x, S) := (F - V)x - \mathcal{F}(x, S) + \mathcal{V}(x, S)$; then for the disease, compartments can be written as

$$x' = (F - V)x - f(x, S).$$

Let $w^T \geq 0$ be the left eigenvector of the matrix $V^{-1}F$ corresponding to the eigenvalue $\rho(V^{-1}F) = \rho(FV^{-1}) = R_0$. It is obvious that $F \geq 0$, $V^{-1} \geq 0$, and $V^{-1}F$ is non-negative and irreducible. We construct a Lyapunov function

$$L = w^T V^{-1}x.$$

Along the trajectories of system (1), we have

$$\frac{dL}{dt} = w^T V^{-1}x' \leq w^T V^{-1}((F - V)x) = w^T (R_0 - 1)x,$$

and when $R_0 \leq 1$, we see $\frac{dL}{dt} \leq 0$, and if $\frac{dL}{dt} = 0$ implies that $x = 0$, i.e., $I = D = A = R = T = H = 0$, $S = S_0$. Hence, if $R_0 \leq 1$, the invariant set on which $\frac{dL}{dt} \leq 0$ contains only point x_0 . By LaSalle's invariance principle [20], P_0 is globally asymptotically stable.

If $R_0 > 1$, $\frac{dL}{dt} > 0$ provided $x > 0$. From the continuity of the vector field in the neighborhood of P_0 , we conclude that $\frac{dL}{dt} > 0$, which means that P_0 is unstable. \square

3.2 Global Stability Analysis of the Endemic Equilibrium

To study the global stability of the endemic equilibrium, we use a graph-theoretic method of Ref. [19]. Next, we give the basic knowledge of graph theory. For a more detailed discussion, see Ref. [21].

A *directed graph (digraph)* $\mathcal{G} = (V, E)$ contains a set $V = 1, 2, \dots, n$ of vertices and a set E of arcs (i, j) leading from initial vertex i to terminal vertex j . The in degree $d^-(i)$ is the number of arcs in \mathcal{G} whose terminal vertex is i , and the out degree $d^+(i)$ is the number of arcs whose initial vertex is i . Given a weighted digraph \mathcal{G} with n vertices, define the $n \times n$ weight matrix $A = [a_{ij}]$ with entry $a_{ij} > 0$ equal to the weight of arc (j, i) if it exists and $a_{ij} = 0$ otherwise. We denote such a weighted digraph by $(\mathcal{G}, \mathcal{A})$.

Theorem 2 *If $R_0 > 1$, the unique endemic equilibrium $P^* = (S^*, I^*, D^*, A^*, R^*, T^*, H^*)$ of model (1) is globally asymptotically stable.*

Proof Set

$$V_1 = I - I^* - I^* \log \frac{I}{I^*}, V_2 = D - D^* - D^* \log \frac{D}{D^*},$$

$$V_3 = A - A^* - A^* \log \frac{A}{A^*}, V_4 = R - R^* - R^* \log \frac{R}{R^*}.$$

Differentiating along (1) and using formula (2) to get

$$\begin{aligned} \frac{dV_1}{dt} &= \left(1 - \frac{I^*}{I}\right) \left((\alpha I + \beta D + \gamma A + \delta R) \frac{S}{N} - (\varepsilon + \zeta + \lambda + \chi) I \right) \\ &\leq -\frac{\alpha}{N} (I - I^*)^2 - \beta D \frac{(I - I^*)^2}{IN} - \gamma A \frac{(I - I^*)^2}{IN} - \delta R \frac{(I - I^*)^2}{IN} \\ &\quad + \beta D^* \frac{\left(\frac{A}{\chi} - I^*\right)}{N} \left(\frac{D}{D^*} - \frac{DI^*}{ID^*} - \frac{I}{I^*} + 1 \right) \\ &\quad + \gamma A^* \frac{\left(\frac{A}{\chi} - I^*\right)}{N} \left(\frac{A}{A^*} - \frac{AI^*}{IA^*} - \frac{I}{I^*} + 1 \right) \\ &\quad + \delta R^* \frac{\left(\frac{A}{\chi} - I^*\right)}{N} \left(\frac{R}{R^*} - \frac{RI^*}{IR^*} - \frac{I}{I^*} + 1 \right). \end{aligned}$$

Since $1 - x + \ln x \leq 0$ for $x > 0$, we get

$$\begin{aligned} \frac{dV_1}{dt} &\leq \beta D^* \left(\frac{D}{D^*} - \ln \frac{D}{D^*} - \frac{I}{I^*} + \ln \frac{I}{I^*} \right) + \gamma A^* \left(\frac{A}{A^*} - \ln \frac{A}{A^*} - \frac{I}{I^*} + \ln \frac{I}{I^*} \right) \\ &\quad + \delta R^* \left(\frac{R}{R^*} - \ln \frac{R}{R^*} - \frac{I}{I^*} + \ln \frac{I}{I^*} \right) \\ &:= a_{12}G_{12} + a_{13}G_{13} + a_{14}G_{14}, \end{aligned}$$

where

$$\begin{aligned} a_{12} &= \beta D^*, G_{12} = \frac{D}{D^*} - \ln \frac{D}{D^*} - \frac{I}{I^*} + \ln \frac{I}{I^*}, \\ a_{13} &= \gamma A^*, G_{13} = \frac{A}{A^*} - \ln \frac{A}{A^*} - \frac{I}{I^*} + \ln \frac{I}{I^*}, \\ a_{14} &= \delta R^*, G_{14} = \frac{R}{R^*} - \ln \frac{R}{R^*} - \frac{I}{I^*} + \ln \frac{I}{I^*}. \end{aligned}$$

$$\begin{aligned} \frac{dV_2}{dt} &= \left(1 - \frac{D^*}{D}\right) (\varepsilon I - (\eta + \rho + \chi)D) \\ &\leq \varepsilon I^* \left(\frac{I}{I^*} - \frac{D}{D^*} - \ln \frac{I}{I^*} + \ln \frac{D}{D^*}\right). \\ &:= a_{21}G_{21}, \end{aligned}$$

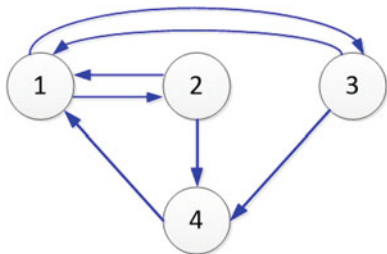
where

$$\begin{aligned} a_{21} &= \varepsilon I^*, G_{21} = \frac{I}{I^*} - \frac{D}{D^*} - \ln \frac{I}{I^*} + \ln \frac{D}{D^*}. \\ \frac{dV_3}{dt} &= \left(1 - \frac{A^*}{A}\right) (\zeta I - (\theta + \mu + \kappa + \chi)A) \\ &\leq \zeta I^* \left(\frac{I}{I^*} - \frac{A}{A^*} - \ln \frac{I}{I^*} + \ln \frac{A}{A^*}\right). \\ &:= a_{31}G_{31}, \end{aligned}$$

where

$$\begin{aligned} a_{31} &= \zeta I^*, G_{31} = \frac{I}{I^*} - \frac{A}{A^*} - \ln \frac{I}{I^*} + \ln \frac{A}{A^*}. \\ \frac{dV_4}{dt} &= \left(1 - \frac{R^*}{R}\right) (\eta D + \theta A - (v + \xi + \chi)R) \\ &= \eta D^* \left(\frac{D}{D^*} - \frac{DR^*}{D^*R} - \frac{R}{R^*} + 1\right) + \theta A^* \left(\frac{A}{A^*} - \frac{AR^*}{A^*R} - \frac{R}{R^*} + 1\right) \\ &\leq \eta D^* \left(\frac{D}{D^*} - \frac{R}{R^*} - \ln \frac{D}{D^*} + \ln \frac{R}{R^*}\right) \\ &\quad + \theta A^* \left(\frac{A}{A^*} - \frac{R}{R^*} - \ln \frac{A}{A^*} + \ln \frac{R}{R^*}\right). \\ &:= a_{42}G_{42} + a_{43}G_{43}, \end{aligned}$$

Fig. 2 The weighted digraph $(\mathcal{G}, \mathcal{A})$ constructed for the model (1)



where

$$a_{42} = \eta D^*, G_{42} = \frac{D}{D^*} - \frac{R}{R^*} - \ln \frac{D}{D^*} + \ln \frac{R}{R^*},$$

$$a_{43} = \theta A^*, G_{43} = \frac{A}{A^*} - \frac{R}{R^*} - \ln \frac{A}{A^*} + \ln \frac{R}{R^*}.$$

The associated weighted digraph $(\mathcal{G}, \mathcal{A})$ has four vertices and four cycles in Fig. 2. Simple calculations yield:

$$G_{12} + G_{21} = 0, G_{13} + G_{31} = 0, G_{14} + G_{31} + G_{43} = 0, G_{14} + G_{21} + G_{42} = 0.$$

Thus, there exist $c_i (i = 1, 2, 3, 4)$ such that $V = \sum_{i=1}^4 c_i V_i$ is a Lyapunov function satisfying $\frac{dV}{dt} \leq 0$. Since $d^-(2) = 1, d^-(3) = 1$ and $d^+(4) = 1$, we can calculate that $c_2 = c_1(\frac{\beta D^*}{\varepsilon I^*} + \frac{\delta R^*}{\varepsilon I^*(\eta D^* + \theta A^*)} \eta D^*)$, $c_3 = c_1(\frac{\gamma A^*}{\zeta I^*} + \frac{\delta R^*}{\zeta I^*(\eta D^* + \theta A^*)} \theta A^*)$ and $c_4 = \frac{c_1 \delta R^*}{\eta D^* + \theta A^*}$. We choose $c_1 = 1$, and then one can verify that

$$\frac{dV}{dt} = c_1 \frac{dV_1}{dt} + c_2 \frac{dV_2}{dt} + c_3 \frac{dV_3}{dt} + c_4 \frac{dV_4}{dt} \leq 0,$$

$\frac{dV}{dt} = 0 \iff (S, I, D, A, R, T, H) = P^*$ is the only invariant set in $\text{int}(\Gamma)$, obviously. Hence, by LaSalle's invariance principle [20], the EE P^* of system (2) is globally asymptotically stable. \square

4 Numerical Analysis of COVID-19 in Brazil

4.1 Parameters Estimation and Numerical Verification of Stability

The numerical analysis is based on the available data of the Ministry of Health of Brazil from July 5th, 2020 (day 1) to August 10th, 2020 (day 37) (diagnosed cumulative infected $(D + T + R + E + \int_0^t [\rho D(s) + \xi R(s) + \sigma T(s)] ds)$, and

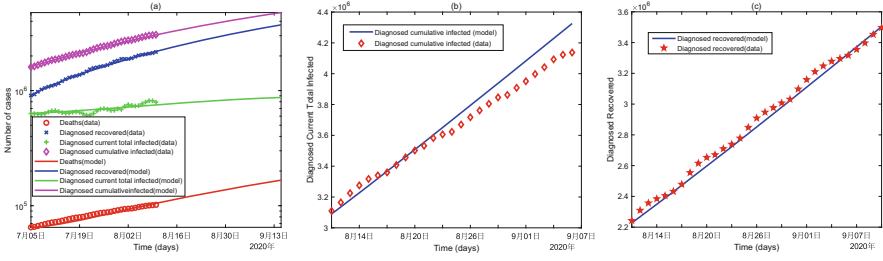


Fig. 3 (a) Brazil: reported vs. diagnosed cases of infection. The ordinate axis takes logarithmic form. (b–c) Comparison of model predictions and the official data from August 11th to September 3th, 2020: diagnosed cumulative infected and diagnosed recovered

diagnosed current total infected ($D + T + R$), diagnosed recovered ($\int_0^t [\rho D(s) + \xi R(s) + \sigma T(s)] ds$) [2]. The life expectancy in Brazil is approximately 76.6 [22]. Clearly, we can obtain that the natural death rate $\chi = 3.5767 \times 10^{-5}$ per day. Λ is approximately estimated as $2.117 \times 10^8 \times \chi \approx 7572$. Next, we use the non-linear least-squares fitting function (lsqcurvefit) to minimize the following formula to evaluate other unknown parameters of the model (1) [23]:

$$\sum_{i=1}^n (F(x, xdata_i) - ydata_i)^2,$$

where $xdata$ and $ydata$ are the given data points. The deterministic model is numerically solved by the Runge–Kutta method. Thus, the parameters of the model can be estimated as shown in Table 1. The reported and predicted number of various infections in Brazil is shown in Fig. 3a, which shows a good fitting effect.

In order to further verify the accuracy of the prediction, we collect the number of diagnosed cumulative infections and the number of diagnosed recovered individuals officially reported by Brazil from August 11th to September 3th, 2020 and compared them with the corresponding data predicted by the model in Fig. 3b and c. It can be seen that the model generally captures the short-term trend of COVID-19, but the long-term prediction requires appropriate adjustment of parameters according to changes in government strategies and medical levels.

So far, the secondary infection due to loss of acquired immunity is a sporadic phenomenon. Therefore, to obtain more accurate fitting parameters, we first assumed the immunity loss rate $\omega = 0$ in the above fitting process. If the loss of acquired immunity is considered, assume that $\omega = 0.1$. Now we verify the global stability analysis result of the equilibrium points using Theorems 1 and 2 in Sect. 3. First, we use the above ω value, other parameters are shown in Table 1, and we can calculate $R_0 = 1.0577 > 1$, so EE is globally asymptotically stable; second, we reduce α from 0.3372 to 0.2 and get $R_0 = 0.6418 < 1$, so DFE is globally asymptotically stable. Figure 4 supports our analysis results.

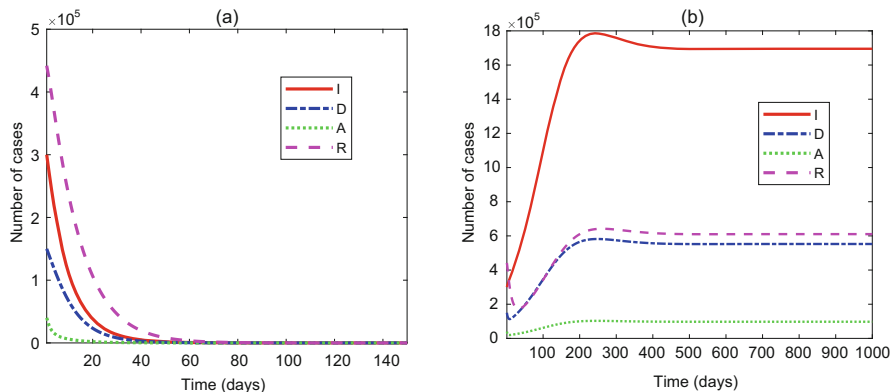


Fig. 4 The paths of $I(t)$, $D(t)$, $A(t)$, and $R(t)$ around the DFE (a) and the EE (b)

4.2 Sensitivity Analysis

Sensitivity analysis is used to determine the robustness of the parameter values predicted by the model. The sensitivity index allows us to measure the relative change of the basic reproduction number R_0 when the parameter changes, so as to formulate a prevention and control strategy based on the parameter. Here, according to Ref. [24], the normalized sensitivity index of R_0 relative to α is

$$\gamma_{\alpha}^{R_0} = \frac{\partial R_0}{\partial \alpha} \times \frac{\alpha}{R_0} = 0.9663,$$

and the sensitivity index of R_0 to other parameters can also be calculated as follows:

$$\gamma_{\beta}^{R_0} = 0.0023, \gamma_{\gamma}^{R_0} = 0.0288, \gamma_{\delta}^{R_0} = 0.0026, \gamma_{\epsilon}^{R_0} = -0.2428,$$

$$\gamma_{\zeta}^{R_0} = -0.0430, \gamma_{\eta}^{R_0} = 4.0691e-04, \gamma_{\theta}^{R_0} = -0.0248, \gamma_{\mu}^{R_0} = -0.0030,$$

$$\gamma_{\rho}^{R_0} = -0.0027, \gamma_{\xi}^{R_0} = -4.7017e-04, \gamma_{\kappa}^{R_0} = -0.0011, \gamma_{\chi}^{R_0} = -1.1258e-04.$$

Thus, it can be concluded that R_0 is positively correlated with α , β , γ , δ , η , and negatively correlated with ϵ , ζ , θ , μ , ρ , ξ , κ , χ .

We specifically analyze the sensitivity of transmission parameters (α , β , γ , δ) and detection parameters (ϵ , θ) related to strategy formulation as shown in Fig. 5(a–f). Interestingly, increasing α and ϵ will significantly increase and decrease the number of current total infected ($I + D + A + R + T$), indicating that the model is more sensitive to changes in α and ϵ . Similarly, adding other transmission parameters will also increase the number of current total infected, and increasing θ will reduce the number of current total infected, but the sensitivity is relatively

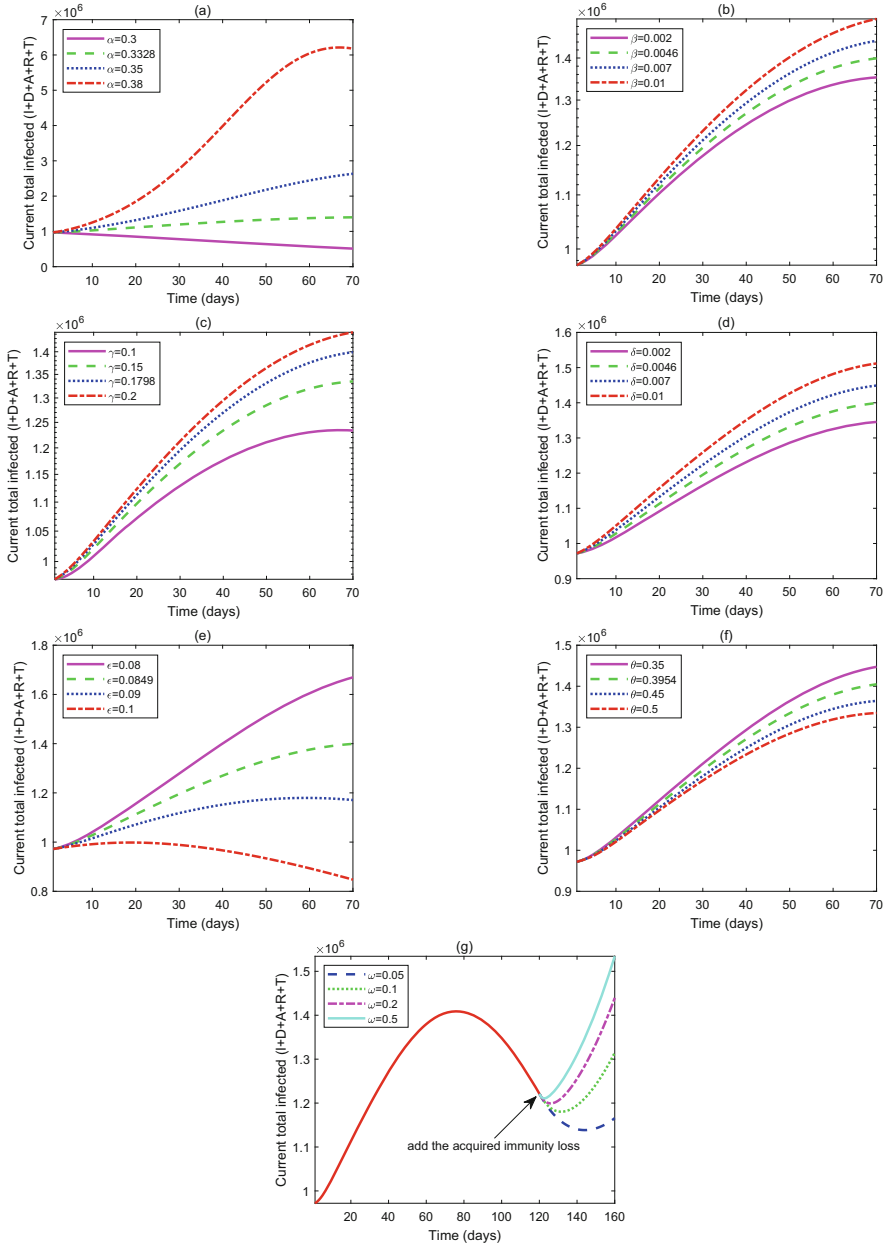


Fig. 5 (a–f) Sensitivity analysis with respect to transmission parameters ($\alpha, \beta, \gamma, \delta$) and detection parameters (ϵ, θ). (g) Current total infected ($I + D + A + R + T$) at different immunity loss rates ω after day 120. Other parameters are taken from Table 1

small. These simulation results are generally consistent with the corresponding sensitivity index. The above analysis shows that policymakers can effectively reduce the number of infections by enforcing social isolation and distancing measures, and strengthening testing and contact tracing.

Next, we analyze the impact of acquired immunity loss. We add the acquired immunity loss item to the epidemic mentioned above prediction after day 120 to simulate the number of diagnosed current total infected. As shown in Fig. 5g, with the addition of ω , a new wave of infections will appear, and the number of infections is positively correlated with ω . Effective vaccination can reduce this hidden danger and achieve long-term immunity.

5 Conclusions

We apply a SIDARTHE model to analyze the COVID-19 outbreak. After calculating the basic reproduction number by the generation matrix method, we cleverly established the global stability of the equilibrium points by combining the Lyapunov–LaSalle techniques and graph theory. Particularly, by fitting the available data of COVID-19 from Brazil, we estimated the model’s parameters and compared the official data with the model’s prediction to illustrate the latter’s effectiveness. Our main findings can be summarized as follows: (1) the DFE is globally asymptotically stable if $R_0 \leq 1$ or unstable if $R_0 > 1$, and the unique EE is globally asymptotically stable if $R_0 > 1$; (2) through sensitivity analysis, reducing the infection coefficient ($\alpha, \beta, \gamma, \delta$) and increasing the detection coefficient (ϵ, θ) play a crucial role in disease control; (3) the loss of acquired immunity might result in another wave of infection. In short, the test-track-isolation strategy and vaccination are effective methods for controlling the epidemic. We believe this research should contribute to continuous monitoring and intervention measures to control the global COVID-19 outbreak.

Acknowledgement This work is supported by the National Natural Science Foundation of China (11772241).

References

1. WHO. Coronavirus Disease 2019 (COVID-19): Situation Report 210 (2020)
2. Ministry of Health of Brazil. <https://covid.saude.gov.br/>
3. R.M. Anderson, R.M. May, *Infectious Diseases of Humans* (Oxford University Press, Oxford, 1991)
4. F. Brauer, C. Castillo-Chavez, *Mathematical Models in Population Biology and Epidemiology*, 2nd edn. (Springer, Berlin, 2012)
5. R.H. Chisholm, P.T. Campbell, Y. Wu, S.Y.C. Tong, J. McVernon, N. Geard, Implications of asymptomatic carriers for infectious disease transmission and control. *Royal Soc. Open. Sci.* **5**(2), 172341 (2018)

6. C. Fraser, S. Riley, R.M. Anderson, M.F. Neil, Factors that make an infectious disease outbreak controllable. *Proc. Natl Acad. Sci. USA* **101**(16), 6146–6151 (2004)
7. K.Y. Leung, P. Trapman, T. Britton, Who is the infector? Epidemic models with symptomatic and asymptomatic cases. *Math. Biosci.* **301**, 190–198 (2018)
8. R. Li, S. Pei, B. Chen, Y. Song, et al., Substantial undocumented infection facilitates the rapid dissemination of novel coronavirus (SARS-CoV-2). *Science* **368**(6490), 489–493 (2020)
9. Y. Li, J. Shi, J. Xia, et al., Asymptomatic and symptomatic patients with non-severe coronavirus disease (covid-19) have similar clinical features and virological courses: a retrospective single center study. *Front. Microbiol.* **11**, 1570 (2020).
10. O. Diekmann, J.A.P. Heesterbeek, *Mathematical Epidemiology of Infectious Diseases: Model Building, Analysis and Interpretation* (Wiley, Hoboken, 2000)
11. H.W. Hethcote, The mathematics of infectious diseases. *SIAM Rev.* **42**, 599–653 (2000)
12. M. Day, Covid-19: Identifying and isolating asymptomatic people helped eliminate virus in Italian village. *Brit. Med. J.* **368**, m1165 (2020)
13. G. Giordano, F. Blanchini, R. Bruno, et al., Modelling the COVID-19 epidemic and implementation of population-wide interventions in Italy. *Nat. Med.* **26**, 855–860 (2020)
14. L. López, X. Rodó, The end of social confinement and COVID-19 re-emergence risk. *Nat. Human Behav.* **4**, 1–10 (2020)
15. J. Seow, C. Graham, B. Merrick, et al., Longitudinal observation and decline of neutralizing antibody responses in the three months following SARS-CoV-2 infection in humans. *Nat. Microbiol.* **5**, 1598–1607 (2020)
16. F.J. Ibarondo, et al., Rapid decay of anti-SARS-CoV-2 antibodies in persons with mild Covid-19. *N. Engl. J. Med.* **383**, 1085–1087 (2020)
17. A.W.D. Edridge, J. Kaczorowska, A.C.R. Hoste, et al., Seasonal coronavirus protective immunity is short-lasting. *Nat. Med.* **26**, 1691–1693 (2020)
18. P. van den Driessche, J. Watmough, Reproduction numbers and sub-threshold endemic equilibria for compartmental models of disease transmission. *Math. Biosci.* **180**, 29–48 (2002)
19. Z. Shuai, P. Van den Driessche, Global stability of infectious disease models using lyapunov functions. *Siam J. Appl. Math.* **73**(4), 1513–1532 (2013)
20. J.P. LaSalle, *The Stability of Dynamical Systems*. Regional Conference Series in Applied Mathematics (SIAM, Philadelphia, 1976)
21. D.B. West, *Introduction to Graph Theory* (Prentice-Hall, Upper Saddle River, 1996)
22. Brazil Population. <https://www.worldometers.info/world-population/brazil-population/>. last Accessed 05 Sep 2020
23. Y. Ding, Y. Fu, Y. Kang, Stochastic analysis of COVID-19 by a SEIR model with Lévy noise. *Chaos* **31**, 043132 (2021)
24. N. Chitnis, J.M. Hyman, J.M. Cushing, Determining important parameters in the spread of malaria through the sensitivity analysis of a mathematical model. *Bull. Math. Biol.* **70**(5), 1272–1296 (2008)

A Cooperative Epidemiological Model of Infectious Disease Dynamics: A COVID-19 Case Study



Yasser Aboelkassem and Haithem E. Taha

1 Introduction

The coronavirus disease 2019 (COVID-19) is part of the ongoing worldwide pandemic caused by severe acute respiratory syndrome coronavirus 2 (SARS-CoV-2). This disease creates a major worldwide life threat. According to the World Health Organization (WHO) and several other data resources, as of October 27 2020, there have been more than 44M confirmed cases and more than 1.2M deaths worldwide [1, 2]. These numbers are subject to dramatic change according to the pandemic situation including the virus variants and its spread capability. The outbreak is currently under research investigations by many experts around the world, trying to forecast the virus outbreak impact on our short- and long-term health system and proposing models for pandemic analysis, control, and prevention [3].

Although the current mechanistic understanding of COVID-19 infection dynamics is still very limited. Yet, simplified probabilistic models, uncertainty quantification tools, and computational data analysis can be used to forecast an accurate measure of disease spread and its impact on our short- and long-term health system and proposing ideas for pandemic analysis, control, and prevention [4–7]. Moreover, these techniques can possibly be used to predict the number of mortalities across countries during the time course of the epidemic.

Epidemiological mathematical analysis and modeling are essential tools in the study of infectious diseases dynamics [8–10]. In fact, modeling can be used to describe the virus spread in a given population and has been critical in our response

Y. Aboelkassem (✉)

College of Innovation and Technology, University of Michigan, Flint, MI, USA

e-mail: yassera@umich.edu

H. E. Taha

University of California Irvine, Irvine, CA, USA

e-mail: hetaha@uci.edu

to the COVID-19 pandemic [11–13]. Many of these models have proven to be successful in predicting the outcome growth patterns of an epidemic and to help inform public health interventions. Data analytics and optimization algorithms are normally used to find parameters for various infectious disease models. These parameters are then used to calculate the effects of different health care actions, including but not limited to the vaccination societal programs. In other words, infectious disease models can contribute to the analysis of epidemiological environment, suggest what crucial data should be collected, and generate forecasts statistical data.

In this chapter, a novel cooperative modeling analysis of the COVID-19 pandemic is given. There are two objectives: (1) to propose a phenomenological cooperative model that can accurately capture the collected outbreak data and (2) to use that as a basis to integrate a virus-pool relationship into the classical SIRD (susceptible, infected, recovered, and death) model. This new cooperative characteristics is expected to better capture the coupling between the susceptible and infected states, hence enhancing the predictive capability of many mechanistic models of infectious disease dynamics.

2 Methods

A cooperative epidemiological mathematical model that can capture many characteristics of the infectious disease dynamics is derived. A phenomenological model that matches the total number of cases and deaths due to COVID-19 is proposed initially. The model is adopted from the well-known Hill-type sigmoidal function [14]. This particular step assumes that the virus-pool infection dynamics can be seen as a cooperative transport-mediated process. We then integrated our phenomenological virus-pool relationship into the classical SIRD. The details of the modeling approach are given in the following subsections.

2.1 Phenomenological Cooperative Model

Since many of the infectious dynamical processes can be modeled as transporter-mediated process, a phenomenological expression that is based on the Hill function (frequently used to study the kinetics of biochemistry reactions [14]) is proposed here to model the spread dynamics of COVID-19 pandemic. This modeling approach assumes that, at a given day during the outbreak, there will be a certain percentage of infection spread (concentration) that can eventually trigger new cases, which results in new deaths (reaction rates).

The development of this model is mainly based on using data inference approach and numerical optimization technique to find model parameters in the proposed phenomenological expression. The data inference step included the total cumulative numbers of confirmed cases and deaths reported from individual countries over

days. The modeling space is divided into three major steps: (1) propose a novel phenomenological Hill-type mathematical equation; (2) uncertainty propagation in the inferred data; and (3) model parameter optimization. Based on the above-mentioned assumptions and analogy with the Hill-like equation, the proposed phenomenological cooperative model can be written as

$$\frac{y}{y_{ss}} = \frac{1}{1 + \left(\frac{k_x}{t}\right)^{n_x}}, \quad y = C, D \quad \text{and} \quad x = c, d, \quad (1)$$

which can be rewritten as

$$n_x = \log\left(\frac{y_{ss} - y}{y}\right) / \log\left(\frac{k_x}{t}\right), \quad (2)$$

where y represents the total number of confirmed cumulative cases “C” or reported deaths “D.” The parameter y_{ss} refers to the steady-state (saturation) number in which there will be no more additional cases or deaths reported over time. The parameter t refers to the number of days. The parameter K (measured in days) is the time at which the cases attain half of its projected maximum reported value. The exponent n refers to the steepness “cooperativity” of this sigmoidal relationship. This cooperativity parameter is commonly known in the biochemical literature as the Hill coefficient. The subscript x is used to alternate between cases and deaths modeling scenarios. It should be noted that Eq. (1) contains three parameters: y_{ss} , K , and n that must be optimized for prediction purpose.

2.2 A Cooperative Virus-Pool-Coupled SIRD Model

The classical SIRD infectious disease model is modified to account for the cooperativity between the susceptible (S) and infected (I) states. In particular, we extend the work by Dai and Locasale [15] to include a virus-pool cooperative function $F(V(t), V_{50}, n)$ to better quantifying the dynamics of both S and I states, hence having an accurate estimate of the total number of cases (C) and deaths (D). The modified SIRD model equations are given as

$$\frac{dS}{dt} = -\alpha_1 F(V(t), V_{50}, n)S - \alpha_2 SI \quad (3)$$

$$\frac{dI}{dt} = \alpha_1 F(V(t), V_{50}, n)S + \alpha_2 SI - (\beta + \gamma)I \quad (4)$$

$$\frac{dR}{dt} = \beta I \quad (5)$$

$$\frac{dD}{dt} = \gamma I, \quad (6)$$

where $\alpha_1, \alpha_2, \beta$, and γ represent rate constants. The virus concentration is represented here using the state variable $V(t)$ with a maximal half activation parameter V_{50} . The function $F(V)$ indicates a virus pool that is assumed herein to take a cooperative form using the standard Hill-like equation as

$$F(V(t)) = \frac{V^n}{(V^n + V_{50}^n)}. \quad (7)$$

Finally, the equation that governs the coupling between the virus-pool cooperativity and the chance of a susceptible individual being infected can be given as

$$\frac{dV}{dt} = \delta_1 I - \delta_2 V, \quad (8)$$

where δ_1 and δ_2 represent rate constants at which the virus state V increases and decreases, respectively. The above system of differential equations represents a modified version of the SIRD model with virus-pool and cooperative infection dynamics. It should be noted that the model parameters (rates) must be determined to uniquely integrate the above system of equations. More specifically, we use data inference and the particle swarm optimization (PSO) techniques to find the correct model parameters.

3 Data Inference and Model Parameter Optimization

3.1 Data Inference Using Monte Carlo Simulation

The uncertainty in the input data (cases and deaths) is considered when building this model using non-intrusive approach. Each data point was assumed to be sampled from a normal distribution as described by the following probability density function:

$$f(y_{data}|\mu, \sigma^2) = \frac{1}{\sqrt{(2\pi)\sigma}} \exp\left(\frac{-1}{2} \left(\frac{x - \mu}{\sigma}\right)^2\right), \quad \mu \in R, \sigma^2 > 0, \quad (9)$$

where the parameter μ is the mean or expectation of the distribution and σ is the standard deviation with variance of σ^2 . In other words, all the collected data points for both cases and deaths will be inferred from a normal distribution to account for uncertainty in the collected data sources and the reported numbers. This is can be noted mathematically as

$$y_{data} \sim \mathcal{N}(\mu, \sigma^2) \quad y_{data} = C, D. \quad (10)$$

In the present analysis, the Monte Carlo (MC) simulations were used to sample the input data points from the normal distribution with a sample size $N_s = 50$ points. The mean (μ) value was chosen to be the average data points obtained from different sources. The standard deviation ($\sigma = 0.2\mu$) was used. The particle swarm optimization (PSO) technique is then used to find the model parameters for each sampled data set.

3.2 Model Parameters Optimization Using PSO

The parameters involved in the above mathematical model are calculated using the particle swarm optimization (PSO) technique [16]. The reported data [1, 2] that represent a simultaneous tracking of the number of cases and deaths are used in the optimization process. In particular, a cost function represented by the root mean square error (RMS) between the calculated and reported data of confirmed cases and deaths is formed. The RMS value is typically used as a quantitative measure when minimizing the error vector. The RMS is then minimized as

$$Min(RMS) = Min \left(\sqrt{\frac{1}{N} \sum_{n=0}^N |y_{model} - y_{data}|^2} \right). \quad (11)$$

The particle swarm optimization (PSO) technique is then used to find the optimal values of the proposed cooperative SIRD model parameters. The PSO method is an iterative algorithm that can be used to optimize a problem when the search space is too large. The PSO algorithm starts by distributing initial particles, which normally are known as solution candidates. These solution candidates are also assigned initial velocities. An objective function for each particle location is then formed to determine the lowest function value and the “best” position. New velocities are then computed using the current velocity, the individual particles’ best locations, and the best locations of their neighboring candidates. Iterative updates for the particle locations and their velocities are then used by replacing the new locations by the old positions. The velocity is also modified to keep particles within the specified bounds. The process repeated iteratively until the algorithm reaches a stopping criterion.

Herein we implement the abovementioned PSO approach to find the optimal parameter set for the above-modified SIRD model. Specifically, we let $\mathbf{X} = \{\alpha_1, \alpha_2, \beta, \gamma, \delta_1, \delta_2, V_{50}, n, n_c, n_d, K_c, K_d, C_{ss}, D_{ss}\}$ be a vector with unknown parameters that we aim to optimize. An initial swarm of N -particles (solution candidates) are randomly distributed. The position and velocity of each particle ($i = 1, 2, \dots, N$) are determined by the \mathbf{X}_i and \mathbf{V}_i , respectively. The equation that governs the updated velocity of each particle is given by

$$\mathbf{V}_i(t + dt) = W\mathbf{V}_i(t) + C_1 \text{rand}(\mathbf{Pbest}_i - \mathbf{X}_i) + C_2 \text{rand}(gbest - \mathbf{X}_i), \quad (12)$$

where C_1 and C_2 are constants. The function “*rand*” is a random number generator such that $\text{rand} \in (0, 1)$. The parameter $W \in (W_{min}, W_{max})$ is a constant that varies with each iteration and satisfies $W = W_{min} + j\Delta W$, with $\Delta W = (W_{max} - W_{min})/J_{max}$ and $j = 1, 2, \dots, J_{max}$, where J_{max} is the maximum iteration number. The vector \mathbf{Pbest}_i represents the personal best reported from each particle. The scalar value $gbest$ represents the global best value among all personal best values. Once the velocity is updated, the new particle positions can be obtained by

$$\mathbf{X}_i(t + \Delta t) = \mathbf{X}_i(t) + \Delta t \mathbf{V}_i(t + \Delta t), \quad (13)$$

where $\Delta t = 1$ is not physical time, but rather represents a marching index/parameter. The results obtained using the optimization parameters are then compared with the reported data sets and discussed in the following section.

4 Results and Discussion

The modeling results that show the total cumulative number of cases and deaths due to COVID-19 are given in this part. The PSO method is used to find the unknown parameters in the proposed cooperative SIRD model, Eqs. (1–8). We used $N_p = 40$ for each parameter in the model. About 100 iterations was used to achieve a residual convergence of 10^{-6} . A list of the final optimized model parameters is given in Table 1. The upper and lower ranges of each model parameter used in the PSO method are given in Table 2. Although the model equations are kept general, we however focused our results on the COVID-19 pandemic in Italy as the main case of study. The data used in the optimization process were constrained to the first pandemic wave only. We assumed a sample population $N = 1\% * N_{pop}$ of the entire Italian population (60M) can only be infected. All the states were initialized such that the $I_0 = 10$, $V_0 = 10$, $R_0 = 0$, $D_0 = 10$, and $S_0 = N - I_0$. The model performance and results are summarized as follows.

Table 1 Model parameters that are used to predict the total number of confirmed cases and deaths in Italy

Parameter	Value	Parameter	Value
n	5.2	V_{50}	1000
n_c	7.4	α_1	0.0064
n_d	7.9	α_2	0.0058
k_c	98	β	0.26
k_d	102	γ	0.04
C_{ss}	246K	δ_1	0.29
D_{ss}	35K	δ_2	0.78

Table 2 The range of each model parameter used in the PSO method

Parameter	Lower value	Upper value
α_1	0.001	0.01
α_2	0.001	0.01
β	0.01	0.5
γ	0.01	0.1
δ_1	0.1	1.0
δ_2	0.1	1.0

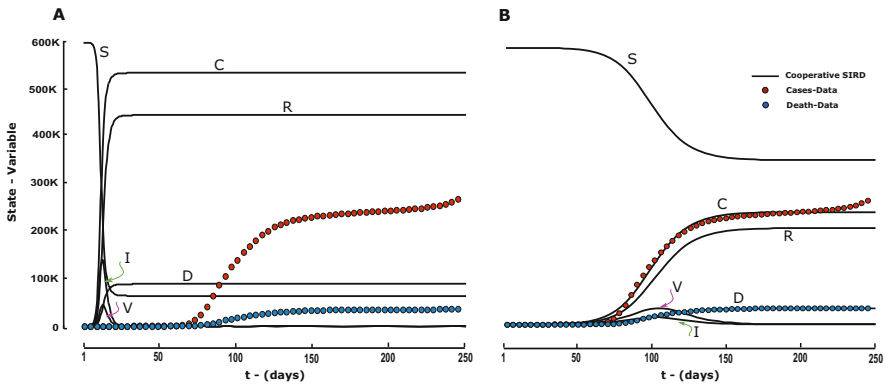


Fig. 1 The proposed cooperative SIRD model state variable distribution and PSO convergence toward the collected cases and deaths data reported from Italy during the COVID-19 first wave. (a) The state variables after a single PSO iteration using 40 particles. (b) The state variables after 100 iterations and using 40 particles. The convergence criteria were chosen such that the residual = 10^{-6} . The results show a RMS = 77.85 in each simulated case

In Fig. 1a, the cooperative SIRD model state variable distributions as a function of time are given after a single iteration using the PSO algorithm. As expected, the distribution of cases ($C = I + R + D$) and deaths (D) numbers are far from the collected data. This suggests that more iterations are required to meet the required convergence criteria. However, the state variable distribution as a function of the pandemic time seems to be heading in the right direction and very similar to the classical SIRD model behavior with an additional state to account for the virus-pool cooperativity (V). In Fig. 1b, we show the same state variable distributions after 100 iterations. The results show that both the case and the death states converged and matched well with the reported data. The results also show the interplay and coupling between the susceptible (S), infected (I), and the virus-pool (V) states. This cooperative coupling eventually helped to find an accurate estimate to the cumulative numbers of cases and deaths due to COVID-19 reported from Italy during the first-wave dynamics.

In Fig. 2a, the number of deaths per day distribution as a function of outbreak time is given. The results are given for both the classical and cooperative SIRR models. Although both models suggest that a Gaussian (bell-like) distribution can be used to represent the death rate per day, the cooperative model performed better

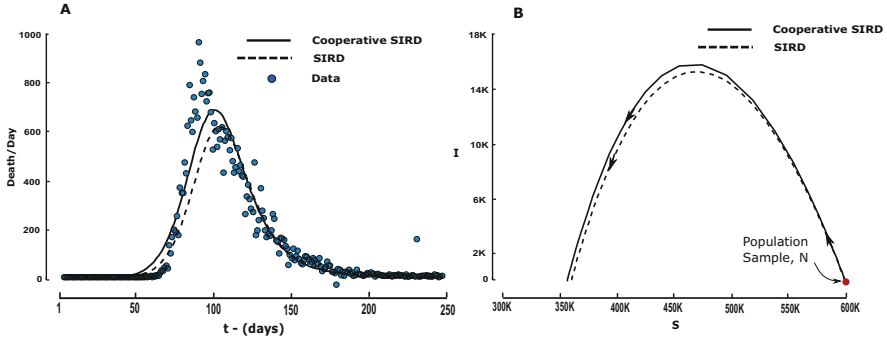


Fig. 2 A comparison between the classical SIRD and proposed cooperative SIRD models. (a) The number of deaths per day as a function time. (b) The (S-I) phase plane portrait for both the classic and cooperative SIRD epidemic models. The results are calculated using the PSO model parameters. The results show a RMS = 77.85 in each simulated case

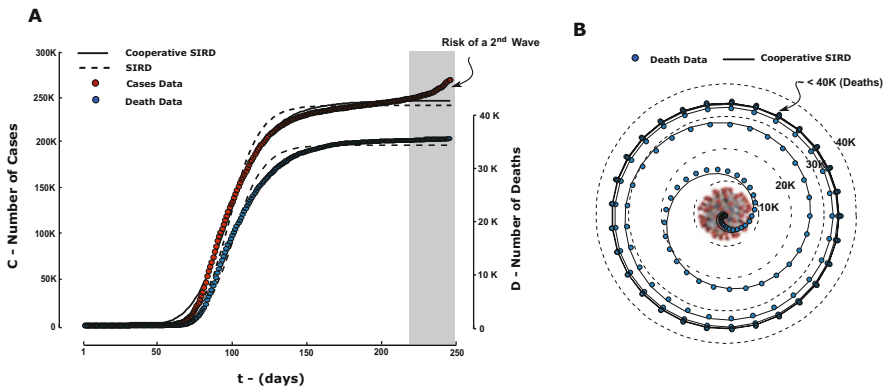


Fig. 3 Model prediction of the COVID-19 pandemic in Italy. (a) The number of infected cases (C) and deaths (D) over days is calculated using the optimized model parameters. (b) Prediction of the total number of deaths in Italy represented by polar plots. The virus illustration is created by the Centers for Disease Control and Prevention (CDC)

than the classical SIRD model in capturing the peak value of the death rate when compared with the collected data. Both models performed well during the decaying phase of the death rate distribution. In order to show the quantitative differences between the classical and cooperative SIRD models, we plot the susceptible-infected (S-I) phase plane portrait for both the classic and cooperative SIRD epidemic models in Fig. 2b. The results have shown that the classical SIRD model underestimates the maximum number of infected (I_{max}) outcomes and predicated a lower level of the final susceptible individuals.

In Fig. 3a, we show the results that describe the dynamic spread of COVID-19 transmission in Italy. A comparison between the proposed cooperative SIRD mathematical model with essential dynamics and the classical SIRD model is given.

More specifically, the total number of infected cases (C) and deaths (D) as a function of the pandemic spread time is calculated using the PSO model parameters. The results are validated using the reported data, which show that the cooperative model has performed better than the SIRD model and agreed well with the data during most of the spread time span during the COVID-19 first-wave dynamics only. The model suggested that a total number of cases $C_{ss} \approx 300K$ are expected during the first-wave dynamics only. Similarly, the number of deaths as a function of time is also calculated and is shown on the same plot, i.e., on the other y-axis of Fig. 3a. The time distribution of the number of deaths clearly exhibits a sigmoidal behavior. The steady-state value of the death curve suggests that a total number of deaths $D_{ss} \approx 40K$ are expected, unless there will be a severe second wave of the virus spread.

The cumulative total number of deaths is represented by a polar plot as shown in Fig. 3b. The filled circles indicate the data collected. The solid spiral line refers to the model prediction parameterized by the number of days. The radius of the dotted circle refers to the total number of deaths. For example, the model predicts a total death of about $D_{ss} \approx 40K$ to occur by the end of the first virus wave dynamics. This is clearly shown from the spiral trajectory that attains an almost steady-state value after about three months measured from the onset of the outbreak in Italy. It should be realized that the deaths number predicted by this model could dramatically increase due to the shortage in the necessary medical equipment (ICUs and Ventilators, etc.) or implementing the necessary health guidelines required to control the virus spread. Moreover, the number of cases and deaths is expected to increase as a result of a second wave of the virus outbreak. Regression analysis is sometimes used to create statistical models that serve as phenomenological models.

5 Model Limitation

Although the proposed cooperative virus-pool SIRD model has performed well when the results are compared with the available data, the proposed model has failed to capture any markers related to the onset of the COVID-19 second-wave dynamics in Italy. We believe that in order for this model to capture a multi-wave virus spread dynamics, the original SIRD must be modified to include complex nonlinearity.

6 Conclusions

A novel cooperative epidemiological mathematical model with essential dynamics is proposed to estimate the total number of cases and deaths in Italy due to COVID-19 pandemic. The model extends the classical SIRD model to include a cooperative coupling between the susceptible and infection state variables. The cooperativity is introduced in the model by using a sigmoidal Hill-like function.

The proposed cooperative model provides a better mechanistic understanding of the virus transmission characteristics. The model shows a good agreement with the reported cases and deaths numbers with an error value represented by the RMS = 77.85. Thus, the model results can in turn be used to propose rational health to control the spread of the virus. It should be noted that the results presented herein assumed that social distancing guideline will continue to be respected throughout the epidemic interval. Finally, although we only presented results addressing the pandemic in Italy, we however have kept our analysis general to treat data sets from other countries in the world.

References

1. World Health Organization (WHO), Coronavirus disease (COVID-2019) situation reports. <https://www.who.int/emergencies/diseases/novel-coronavirus-2019>
2. CSSE 2020. Johns Hopkins, COVID-19 Data Center. <https://coronavirus.jhu.edu/>
3. S.P. Layne, J.M. Hyman, D.M. Morens, J.K. Taubenberger, New coronavirus outbreak: Framing questions for pandemic prevention. *Sci. Transl. Med.* **12**(534), eabb1469 (2020)
4. W.W. Koczkodaja, M.A. Mansournia, W. Pedrycz, A. Wolny-Dominiak, P.F. Zabrodskii, D. Strzałka, T. Armstrong, A.H. Zolfaghari, M. Debski, J. Mazurek, 1000,000 cases of COVID-19 outside of China: the date predicted by a simple heuristic. *Global Epidemiol.* **2**, 100023 (2020).
5. M.S. Moghadas, A. Shoukat, M.C. Fitzpatrick, C.R. Wells, P. Sah, A. Pandey, J.D. Sachs, Z. Wang, L.A. Meyers, B.H. Singer, A.P. Galvani, Projecting hospital utilization during the COVID-19 outbreaks in the United States. *PNAS* **117**(16), 9122–9126 (2020)
6. C.R. Wells, P. Sah, S.M. Moghadas, A. Pandey, A. Shoukat, Y. Wang, Z. Wang, L.A. Meyers, B.H. Singer, A.P. Galvani, Impact of international travel and border control measures on the global spread of the novel 2019 coronavirus outbreak. *PNAS* **117**(13), 7504–7509 (2020)
7. N. Weinstein, T.-V. Nguyen, Motivation and preference in isolation: a test of their different influences on responses to self-isolation during the COVID-19 outbreak. *R. Soc. Open Sci.* **7**, 200458 (2020)
8. A.L. Hill, The math behind epidemics. *Phys. Today* **73**(11), 28–34 (2020)
9. H.W. Hethcote, The Mathematics of infectious diseases. *SIAM Rev.* **42**(4), 599–653 (2000)
10. Y. Aboelkassem, COVID-19 pandemic: A Hill type mathematical model predicts the US death number and the reopening date. medRxiv (2020). <https://doi.org/10.1101/2020.04.12.20062893>
11. C.A.K. Kwuimy, F. Nazari, X. Jiao, P. Rohani, C. Nataraj, Nonlinear dynamic analysis of an epidemiological model for COVID-19 including public behavior and government action. *Nonlinear Dyn.* **16**, 1–15 (2020)
12. S. He, Y. Peng, K. Sun, SEIR modeling of the COVID-19 and its dynamics. *Nonlinear Dyn.* **101**, 1667–1680 (2020)
13. K. Rajagopal, N. Hasanzadeh, F. Parastesh, I.I. Hamarash, S. Jafari, I. Hussain, A fractional-order model for the novel coronavirus (COVID-19) outbreak. *Nonlinear Dyn.* **101**, 711–718 (2020)
14. R. Gesztelyi, J. Zsuga, A. Kemeny-Beke, B. Varga, B. Juhasz, A. Tosaki, The Hill equation and the origin of quantitative pharmacology. *Arch. Hist. Exact Sci.* **66**, 427–432 (2012)
15. Z. Dai, J.W. Locasale, Cooperative virus propagation underlies COVID-19 transmission dynamics. medRxiv (2020). <https://doi.org/10.1101/2020.05.05.20092361>
16. J. Kennedy, R. Eberhart, Particle swarm optimization, in *Proceedings of the IEEE International Conference on Neural Networks* (1995), pp. 1942–1945

Dynamic Analysis of a Three-Strain COVID-19 SEIR Epidemic Model with General Incidence Rates



Omar Khyar and Karam Allali

1 Introduction

The late COVID-19 generated by the infection SARS-Cov-2 is classified as a strain of the severe acute respiratory syndrome-related coronavirus SARS-CoV-1 [1]. The classical susceptible–infected–recovered (SIR) epidemic model was first given by Kermack and McKendrick [2]. The global stability of one-strain SEIR model has been studied in [3–5] by considering bilinear or nonlinear incidence function. The global dynamics of two-strain SEIR model has been established in [6] by taking into account that the first incidence is bilinear, while the second incidence is non-monotonic. Later, the global stability of two-strain SEIR model with two incidence non-monotonic functions has been studied in [7]. Recently, a multi-strain SEIR model with two general incidence rates is studied [8]. Different researchers have revealed that the multi-strain aspect of COVID-19 is characterized by different mutation patterns [9, 10]. Therefore, it is important to study the multi-strain SEIR epidemiological models, which better describe the evolution of COVID-19 pandemic within populations, and they include the effect of long incubation period along with different infected strains. The importance of studying such multi-strain models is to check the different situations allowing the strains coexistence. In this chapter, we develop the study for a three-strain COVID-19 SEIR epidemic model

O. Khyar (✉) · K. Allali

Laboratory of Mathematics and Applications, Faculty of Sciences and Technologies, University Hassan II of Casablanca, Mohammedia, Morocco

with general incidence rates. To this end, we will consider the following three-strain generalized epidemic model:

$$\left\{ \begin{array}{l} \frac{dS}{dt} = \Lambda - f_1(S, I_1)I_1 - f_2(S, I_2)I_2 - f_3(S, I_3)I_3 - \delta S, \\ \frac{dE_1}{dt} = f_1(S, I_1)I_1 - (\gamma_1 + \delta)E_1, \\ \frac{dE_2}{dt} = f_2(S, I_2)I_2 - (\gamma_2 + \delta)E_2, \\ \frac{dE_3}{dt} = f_3(S, I_3)I_3 - (\gamma_3 + \delta)E_3, \\ \frac{dI_1}{dt} = \gamma_1 E_1 - (\mu_1 + \delta)I_1, \\ \frac{dI_2}{dt} = \gamma_2 E_2 - (\mu_2 + \delta)I_2, \\ \frac{dI_3}{dt} = \gamma_3 E_3 - (\mu_3 + \delta)I_3, \\ \frac{dR}{dt} = \mu_1 I_1 + \mu_2 I_2 + \mu_3 I_3 - \delta R, \end{array} \right. \quad (1)$$

with (S) stands for the susceptible individuals; (E_1) , (E_2) , and (E_3) are the numbers of each latent individuals class, respectively; (I_1) , (I_2) , and (I_3) are the numbers of each infectious individual class, respectively; and (R) is the number of removed individuals. The parameter Λ is the recruitment rate; δ is the death rate of the population; γ_1 , γ_2 , and γ_3 are, respectively, the latency rates of each strain; μ_1 , μ_2 , and μ_3 are, respectively, the three-strain transfer rates from infected to removed. The general incidence functions $f_1(S, I_1)$, $f_2(S, I_2)$, and $f_3(S, I_3)$ stand for the infection transmission rates for strain 1, strain 2, and strain 3, respectively. The incidence functions $f_1(S, I_1)$, $f_2(S, I_2)$, and $f_3(S, I_3)$ are assumed to be continuously differentiable and satisfy the same properties as in [11]:

$$f_1(0, I_1) = 0, \quad f_2(0, I_2) = 0, \quad f_3(0, I_3) = 0, \quad \text{for all } I_i \geq 0, \quad i = 1, 2, 3, \quad (H_1)$$

$$\frac{\partial f_1}{\partial S}(S, I_1) > 0, \quad \frac{\partial f_2}{\partial S}(S, I_2) > 0, \quad \frac{\partial f_3}{\partial S}(S, I_3) > 0, \quad \forall S > 0, \quad \forall I_i \geq 0, \quad i = 1, 2, 3, \quad (H_2)$$

$$\frac{\partial f_1}{\partial I_1}(S, I_1) \leq 0, \quad \frac{\partial f_2}{\partial I_2}(S, I_2) \leq 0, \quad \frac{\partial f_3}{\partial I_3}(S, I_3) \leq 0, \quad \forall S \geq 0, \quad \forall I_i \geq 0, \quad i = 1, 2, 3. \quad (H_3)$$

The properties (H_1) , (H_2) , and (H_3) , for all the functions f_1 , f_2 , and f_3 , are easily verified by many classical incidence rates like the bilinear incidence function βS [12], the saturated incidence function $\frac{\beta S}{1 + \alpha_1 S}$ or $\frac{\beta S}{1 + \alpha_2 I}$ [13], Beddington–

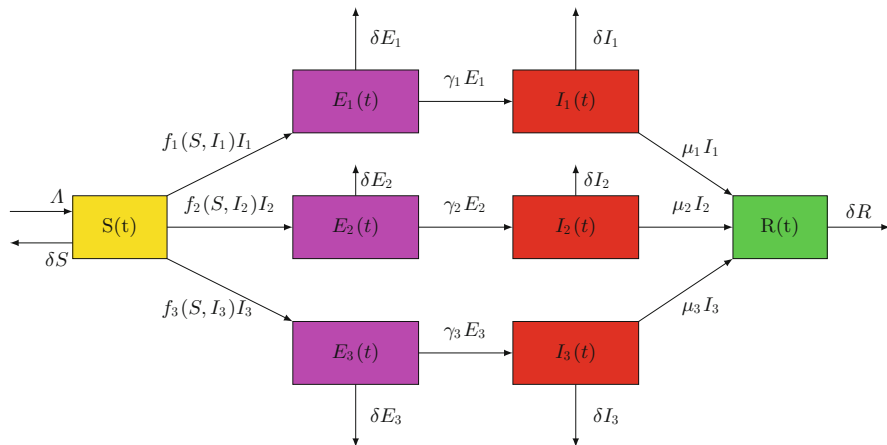


Fig. 1 The flowchart of the three-strain COVID-19 SEIR epidemic model

DeAngelis incidence function $\frac{\beta S}{1 + \alpha_1 S + \alpha_2 I}$ [14], Crowley–Martin incidence function $\frac{\beta S}{1 + \alpha_1 S + \alpha_2 I + \alpha_1 \alpha_2 SI}$ [15], the specific nonlinear incidence function $\frac{\beta S}{1 + \alpha_1 S + \alpha_2 I + \alpha_3 SI}$ [16], and non-monotonic incidence function $\frac{\beta S}{1 + \alpha I^2}$ [17].

Our main contribution centers around the global stability of a three-strain COVID-19 SEIR epidemic model without any restriction of the incidence rates. The flowchart of the three-strain COVID-19 SEIR epidemiological model is illustrated in Fig. 1.

2 The Problem Well-Posedness and Equilibria

2.1 The Problem Well-Posedness

First, we will assume that all our model parameters are positive. The main result of this subsection is given as follows:

Proposition 1 *The solutions of the problem (1) exist and remain non-negative and bounded, for every non-negative initial condition.*

Furthermore, we have $\mathcal{N}(t) \leq \frac{\Lambda}{\delta} + \mathcal{N}(0)$.

Proof From [18], we can confirm that there exists a unique local solution to our problem (1). For the positivity result, we will prove that every solution starting from the following non-negative set:

$$\begin{aligned} \mathcal{H} = \{ & (S, E_1, E_2, E_3, I_1, I_2, I_3, R) \in \mathbb{R}^8 : S \geq 0, E_1 \geq 0, E_2 \geq 0, \\ & E_3 \geq 0, I_1 \geq 0, \\ & I_2 \geq 0, I_3 \geq 0, \text{ and } R \geq 0 \} \text{ remains there.} \end{aligned}$$

First, let

$$\begin{aligned} \mathcal{T} = \sup \{ & t_0 \geq 0 \mid \forall t \in [0, t_0] : S(t) \geq 0, E_1(t) \geq 0, E_2(t) \geq 0, E_3(t) \geq 0, \\ & I_1(t) \geq 0, I_2(t) \geq 0, I_3(t) \geq 0, \text{ and } R(t) \geq 0 \}. \end{aligned}$$

Let us demonstrate that $\mathcal{T} = +\infty$. Suppose the contrary case, i.e., \mathcal{T} is finite; by continuity fact of solution, we have

$$\begin{aligned} S(\mathcal{T}) = 0 \text{ or } E_1(\mathcal{T}) = 0 \text{ or } E_2(\mathcal{T}) = 0 \text{ or } E_3(\mathcal{T}) = 0 \text{ or } I_1(\mathcal{T}) = 0 \text{ or } I_2(\mathcal{T}) = 0 \\ \text{or } I_3(\mathcal{T}) = 0 \text{ or } R(\mathcal{T}) = 0. \end{aligned}$$

If $S(\mathcal{T}) = 0$ before the other problem variables become zero. Then,

$$\frac{dS(\mathcal{T})}{dt} = \lim_{t \rightarrow \mathcal{T}^-} \frac{S(\mathcal{T}) - S(t)}{\mathcal{T} - t} = \lim_{t \rightarrow \mathcal{T}^-} \frac{-S(t)}{\mathcal{T} - t} \leq 0. \quad (2)$$

From the first equation of (1), we obtain

$$\begin{aligned} \dot{S}(\mathcal{T}) = & \Lambda - f_1(S(\mathcal{T}), I_1(\mathcal{T})) I_1(\mathcal{T}) - f_2(S(\mathcal{T}), \\ & I_2(\mathcal{T})) I_2(\mathcal{T}) - f_3(S(\mathcal{T}), I_3(\mathcal{T})) I_3(\mathcal{T}) - \delta S(\mathcal{T}); \end{aligned} \quad (3)$$

therefore,

$$\dot{S}(\mathcal{T}) = \Lambda - f_1(0, I_1(\mathcal{T})) I_1(\mathcal{T}) - f_2(0, I_2(\mathcal{T})) I_2(\mathcal{T}) - f_3(0, I_3(\mathcal{T})) I_3(\mathcal{T}). \quad (4)$$

But, from (H_1) , we have $\dot{S}(\mathcal{T}) = \Lambda > 0$, which represents a contradiction. Similar proofs for $E_1(t)$, $E_2(t)$, $E_3(t)$, $I_1(t)$, $I_2(t)$, $I_3(t)$, and $R(t)$.

We conclude then that \mathcal{T} cannot be a finite number, which implies that the solutions of our problem remain non-negative for every non-negative initial condition.

Concerning the boundedness result, let

$$\mathcal{N}(t) = S(t) + E_1(t) + E_2(t) + E_3(t) + I_1(t) + I_2(t) + I_3(t) + R(t). \quad (5)$$

From system (1), we obtain

$$\frac{d\mathcal{N}(t)}{dt} = \Lambda - \delta\mathcal{N}(t); \quad (6)$$

consequently,

$$\mathcal{N}(t) = \frac{\Lambda}{\delta} + Ke^{-\delta t}, \quad (7)$$

so

$$\mathcal{N}(0) = \frac{\Lambda}{\delta} + K; \quad (8)$$

therefore,

$$\mathcal{N}(t) = \frac{\Lambda}{\delta} + (\mathcal{N}(0) - \frac{\Lambda}{\delta})e^{-\delta t}; \quad (9)$$

then

$$\mathcal{N}(t) \leq \frac{\Lambda}{\delta} + \mathcal{N}(0)e^{-\delta t}; \quad (10)$$

since $0 < e^{-\delta t} \leq 1$, we have

$$\mathcal{N}(t) \leq \frac{\Lambda}{\delta} + \mathcal{N}(0). \quad (11)$$

Consequently, $\mathcal{N}(t)$ is bounded, and so are the variables $S(t)$, $E_1(t)$, $E_2(t)$, $E_3(t)$, $I_1(t)$, $I_2(t)$, $I_3(t)$, and $R(t)$. Hence, the local solution can be prolonged to every positive time, which means that the unique solution exists globally. \square

2.2 The Steady States

We calculated the basic reproduction number R_0 easily by using the method of the next-generation matrix. We find

$$R_0 = \max\{R_0^1, R_0^2, R_0^3\}, \quad (12)$$

with

$$R_0^1 = \frac{f_1(\frac{\Lambda}{\delta}, 0)\gamma_1}{a_1b_1}, \quad R_0^2 = \frac{f_2(\frac{\Lambda}{\delta}, 0)\gamma_2}{a_2b_2}, \quad \text{and} \quad R_0^3 = \frac{f_3(\frac{\Lambda}{\delta}, 0)\gamma_3}{a_3b_3}, \quad (13)$$

where

$$a_1 = \gamma_1 + \delta, \quad a_2 = \gamma_2 + \delta, \quad a_3 = \gamma_3 + \delta, \quad b_1 = \mu_1 + \delta, \quad b_2 = \mu_2 + \delta, \quad b_3 = \mu_3 + \delta.$$

We call R_0^i the strain i reproduction number, $i = 1, 2, 3$.

Remark 1 We omit the eighth equation of the model (1) because the first seven equations are independent of R and the total population verifies (7).

Theorem 1 *The model (1) has the disease-free equilibrium $\mathcal{E}_0 \left(\frac{\Lambda}{\delta}, 0, 0, 0, 0, 0, 0 \right)$ and seven endemic equilibria defined as follows:*

- $\mathcal{E}_1 (S_1^*, \frac{1}{a_1}(\Lambda - \delta S_1^*), 0, 0, \frac{\gamma_1}{a_1 b_1}(\Lambda - \delta S_1^*), 0, 0)$,
with $S_1^* \in]0, \frac{\Lambda}{\delta}[$, $E_{1,s_1}^* > 0$, $I_{1,s_1}^* > 0$ and $E_{2,s_1}^* = E_{3,s_1}^* = I_{2,s_1}^* = I_{3,s_1}^* = 0$.
- $\mathcal{E}_2 (S_2^*, 0, \frac{1}{a_2}(\Lambda - \delta S_2^*), 0, 0, \frac{\gamma_2}{a_2 b_2}(\Lambda - \delta S_2^*), 0)$,
with $S_2^* \in]0, \frac{\Lambda}{\delta}[$, $E_{2,s_2}^* > 0$, $I_{2,s_2}^* > 0$ and $E_{1,s_2}^* = E_{3,s_2}^* = I_{1,s_2}^* = I_{3,s_2}^* = 0$.
- $\mathcal{E}_3 (S_3^*, 0, 0, \frac{1}{a_3}(\Lambda - \delta S_3^*), 0, 0, \frac{\gamma_3}{a_3 b_3}(\Lambda - \delta S_3^*))$,
with $S_3^* \in]0, \frac{\Lambda}{\delta}[$, $E_{3,s_3}^* > 0$, $I_{3,s_3}^* > 0$ and $E_{1,s_3}^* = E_{2,s_3}^* = I_{1,s_3}^* = I_{2,s_3}^* = 0$.
- $\mathcal{E}_4 (S_4^*, \frac{1}{a_1}(\Lambda - \delta S_4^*), \frac{1}{a_2}(\Lambda - \delta S_4^*), 0, \frac{\gamma_1}{a_1 b_1}(\Lambda - \delta S_4^*), \frac{\gamma_2}{a_2 b_2}(\Lambda - \delta S_4^*), 0)$,
with $S_4^* \in]0, \frac{\Lambda}{\delta}[$, $E_{1,s_4}^* > 0$, $I_{1,s_4}^* > 0$, $E_{2,s_4}^* > 0$, $I_{2,s_4}^* > 0$
and $E_{3,s_4}^* = I_{3,s_4}^* = 0$.
- $\mathcal{E}_5 (S_5^*, \frac{1}{a_1}(\Lambda - \delta S_5^*), 0, \frac{1}{a_3}(\Lambda - \delta S_5^*), \frac{\gamma_3}{a_3 b_3}(\Lambda - \delta S_5^*), 0, \frac{\gamma_2}{a_2 b_2}(\Lambda - \delta S_5^*))$,
with $S_5^* \in]0, \frac{\Lambda}{\delta}[$, $E_{1,s_5}^* > 0$, $I_{1,s_5}^* > 0$, $E_{3,s_5}^* > 0$, $I_{3,s_5}^* > 0$
and $E_{2,s_5}^* = I_{2,s_5}^* = 0$.
- $\mathcal{E}_6 (S_6^*, 0, \frac{1}{a_2}(\Lambda - \delta S_6^*), \frac{1}{a_2 b_3}(\Lambda - \delta S_6^*), 0, \frac{\gamma_2}{a_2 b_2}(\Lambda - \delta S_6^*), \frac{\gamma_3}{a_3 b_3}(\Lambda - \delta S_6^*))$,
with $S_6^* \in]0, \frac{\Lambda}{\delta}[$, $E_{2,s_6}^* > 0$, $I_{2,s_6}^* > 0$, $E_{3,s_6}^* > 0$, $I_{3,s_6}^* > 0$
and $E_{1,s_6}^* = I_{1,s_6}^* = 0$.
- $\mathcal{E}_7 (S_7^*, E_{1,s_7}^*, E_{2,s_7}^*, E_{3,s_7}^*, I_{1,s_7}^*, I_{2,s_7}^*, I_{3,s_7}^*)$, where $E_{1,s_7}^* = \frac{b_1}{\gamma_1} I_{1,s_7}^*$,

$$E_{2,s_7}^* = \frac{b_2}{\gamma_2} I_{2,s_7}^*, \quad E_{3,s_7}^* = \frac{b_3}{\gamma_3} I_{3,s_7}^*,$$

$$S_{s_7}^* = \frac{1}{\delta} \left[\Lambda - \frac{f_1(\frac{\Lambda}{\delta}, 0)}{R_0^1} I_{1,s_7}^* - \frac{f_2(\frac{\Lambda}{\delta}, 0)}{R_0^2} I_{2,s_7}^* - \frac{f_3(\frac{\Lambda}{\delta}, 0)}{R_0^3} I_{3,s_7}^* \right]$$

with $\Lambda \geq \frac{f_1(\frac{\Lambda}{\delta}, 0)}{R_0^1} I_{1,s_7}^* + \frac{f_2(\frac{\Lambda}{\delta}, 0)}{R_0^2} I_{2,s_7}^* + \frac{f_3(\frac{\Lambda}{\delta}, 0)}{R_0^3} I_{3,s_7}^*$, $R_0^1 > 1$, $R_0^2 > 1$ and $R_0^3 > 1$.

Proof For the proof steps, we can refer to our article recently published in Nonlinear Dynamics journal [8].

3 Global Stability of Equilibria

3.1 Global Stability of Disease-Free Equilibrium

Theorem 2 *The disease-free equilibrium \mathcal{E}_0 is globally asymptotically stable (GAS) when $R_0 \leq 1$.*

Proof It is easy to prove this result by considering the following Lyapunov function in \mathbb{R}_+^7 [8]:

$$\begin{aligned} \mathcal{L}_0(S, E_1, E_2, E_3, I_1, I_2, I_3) = & S - S_0^* - \int_{S_0^*}^S \frac{f_1(S_0^*, 0)}{f_1(X, 0)} dX \\ & + E_1 + E_2 + E_3 + \frac{a_1}{\gamma_1} I_1 + \frac{a_2}{\gamma_2} I_2 + \frac{a_3}{\gamma_3} I_3. \end{aligned} \quad (14)$$

3.2 Global Stability of the Endemic Equilibria

Theorem 3 *The global stability of the endemic equilibria is given as follows:*

- The steady state \mathcal{E}_{s_1} is GAS if $1 < R_0^1$, $R_0^2 \leq 1$, and $R_0^3 \leq 1$.
- The steady state \mathcal{E}_{s_2} is GAS if $R_0^1 \leq 1 < R_0^2$, and $R_0^3 \leq 1$.
- The steady state \mathcal{E}_{s_3} is GAS if $R_0^1 \leq 1$, $R_0^2 \leq 1$, and $1 < R_0^3$.
- The steady state \mathcal{E}_{s_4} is GAS if $1 < R_0^1$, $1 < R_0^2$, and $R_0^3 \leq 1$.
- The steady state \mathcal{E}_{s_5} is GAS if $1 < R_0^1$, $R_0^2 \leq 1$, and $1 < R_0^3$.
- The steady state \mathcal{E}_{s_6} is GAS if $R_0^1 \leq 1 < R_0^2$, and $1 < R_0^3$.
- The steady state \mathcal{E}_{s_7} is GAS if $1 < R_0^1$, $1 < R_0^2$, and $1 < R_0^3$.

Proof With the aim of studying the global stability for each equilibrium \mathcal{E}_{s_j} ($\forall j \in \{1, 2, \dots, 7\}$), it will enough to follow the same steps as in [8]. Indeed, the Lyapunov functional will take the following form:

$$\begin{aligned} \mathcal{L}_j(S, E_1, E_2, E_3, I_1, I_2, I_3) &= S - S_{s_j}^* - \int_{S_{s_j}^*}^S \frac{f_i(S_{s_j}^*, I_{i,s_j}^*)}{f_i(X, I_{i,s_j}^*)} dX \\ &+ \sum_{i=1}^{i=3} E_{i,s_j}^* \left(\frac{E_i}{E_{i,s_j}^*} - \ln \left(\frac{E_i}{E_{i,s_j}^*} \right) - 1 \right) \\ &+ \sum_{i=1}^{i=3} \frac{\gamma_i + \delta}{\gamma_i} I_{i,s_j}^* \left(\frac{I_i}{I_{i,s_j}^*} - \ln \left(\frac{I_i}{I_{i,s_j}^*} \right) - 1 \right). \end{aligned}$$

The functions $f_i, i \in \{1, 2, 3\}$, are assumed to verify the following conditions [8]:

$$(1 - \Gamma) \left(\frac{1}{\Gamma} - \frac{I_i}{I_{i,s_j}^*} \right) \leq 0, \quad \forall S > 0, I_i > 0, i = 1, 2, 3,$$

with

$$\Gamma = \prod_{i=1}^{i=3} \frac{f_i(S, I_{i,s_l}^*)}{f_i(S_{s_l}^*, I_{i,s_l}^*)} \frac{f_k(S_{s_l}^*, I_{k,s_l}^*)}{f_k(S, I_{k,s_l}^*)}.$$

Such that $I_{i,s_l}^* \neq 0, I_{k,s_l}^* \neq 0, k \in \{1, 2, 3\}, l \in \{1, 2, \dots, 7\}, i \neq l, k \neq i,$ and $k \neq l$.

4 Numerical Simulations

In order to illustrate the SEIR dynamics and its comparison with the COVID-19 clinical data [19], we will restrict logically to draw the evolution of the three infected compartments with considering all incidences are bilinear. Indeed, Fig. 2 (top-left) shows the evolution of the infection for the following parameters: $\Lambda = 1, \alpha = 0.005, \beta = 0.003, \eta = 0.007, \gamma_1 = 0.3, \gamma_2 = 0.1, \gamma_3 = 0.5, \mu_1 = 0.6, \mu_2 = 0.4, \mu_3 = 0.195, \delta = 0.03$ and the initial conditions: $S^0 = 45, E_1^0 = 185, E_2^0 = 340, E_3^0 = 85, I_1^0 = 2; I_2^0 = 1; I_3^0 = 2; R^0 = 0$. Within those parameters, all the strain reproduction numbers are less than unity. More precisely, $R_0^1 = 0.2405, R_0^2 = 0.1789,$ and $R_0^3 = 0.9783$. This situation represents the die-out of the disease. Figure 2 (top-right) depicts the progression of the infection for the following parameters: $\Lambda = 1, \alpha = 0.002, \beta = 0.003, \eta = 0.05, \gamma_1 = 0.1, \gamma_2 = 0.12, \gamma_3 = 0.19, \mu_1 = 0.2, \mu_2 = 0.5, \mu_3 = 0.1, \delta = 0.03$ and the initial conditions: $S^0 = 55, E_1^0 = 225,$

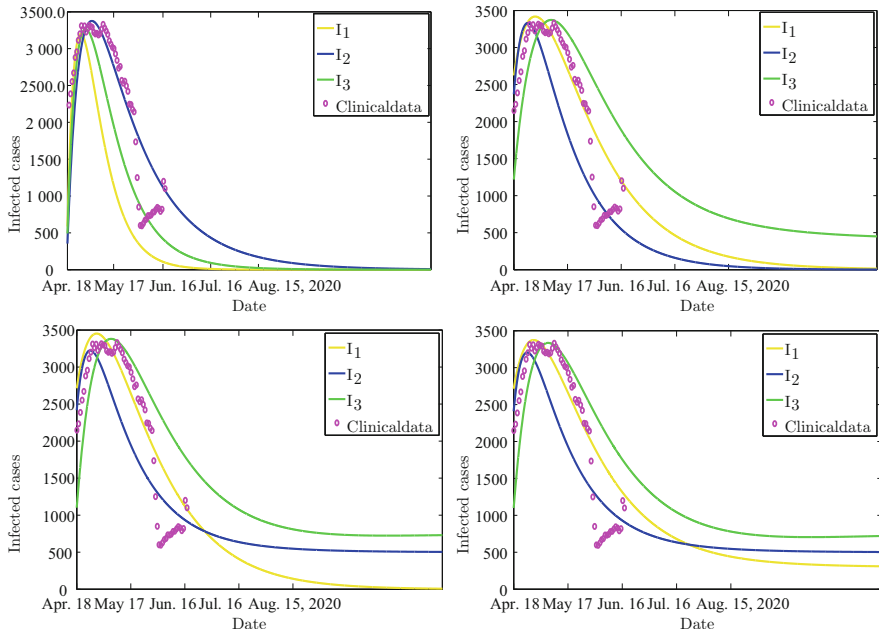


Fig. 2 The evolution of the infection for different values of the strain basic reproduction number $R_0^i, i = 1, 2, 3$

$E_2^0 = 235, E_3^0 = 92, I_1^0 = 2; I_2^0 = 1; I_3^0 = 400; R^0 = 0$. Within those parameters, the two-strain reproduction numbers R_0^1 and R_0^2 are less than unity, while the third R_0^3 are more than one. More precisely, $R_0^1 = 0.2230, R_0^2 = 0.1509$, and $R_0^3 = 11.0723$. Here, only one strain will persist. Figure 2 (bottom-left) illustrates the evolution of the infection for the following parameters: $\Lambda = 1, \alpha = 0.002, \beta = 0.1, \eta = 0.05, \gamma_1 = 0.1, \gamma_2 = 0.12, \gamma_3 = 0.19, \mu_1 = 0.2, \mu_2 = 0.3, \mu_3 = 0.1, \delta = 0.03$ and the initial conditions: $S^0 = 55, E_1^0 = 225, E_2^0 = 235, E_3^0 = 92, I_1^0 = 2; I_2^0 = 401; I_3^0 = 402; R^0 = 0$.

Within those parameters, the two-strain reproduction numbers R_0^2 and R_0^3 are superior strictly to the unity, and the third R_0^1 is less than one. More precisely, $R_0^1 = 0.2230, R_0^2 = 8.0808$, and $R_0^3 = 11.0723$. Here, only two infection strains will persist. Finally, Fig. 2 (bottom-right) shows the evolution of the infection for the following parameters: $\Lambda = 4, \alpha = 0.025, \beta = 0.013, \eta = 0.012, \gamma_1 = 0.4, \gamma_2 = 0.1, \gamma_3 = 0.4, \mu_1 = 0.43, \mu_2 = 0.9, \mu_3 = 0.1, \delta = 0.03$ and the initial conditions: $S^0 = 55, E_1^0 = 235, E_2^0 = 250, E_3^0 = 82, I_1^0 = 2; I_2^0 = 501; I_3^0 = 700; R^0 = 0$. Within those parameters, all the strain reproduction numbers are superior strictly to the unity. More precisely, $R_0^1 = 6.7408, R_0^2 = 1.4337$, and $R_0^3 = 11.4490$. Here, all the acting strains will persist. Moreover, we observe in all our numerical results a good fit between the numerical simulations and the COVID-19 clinical

data, our numerical results reveal two scenarios of evolution for this pandemic, the first happens when R_0 is less than one, and at this moment, the disease will die out. The other scenario occurs when one of the basic reproduction numbers of a strain is greater than the unity; in this case, the disease caused by the corresponding strain will persist. In this case, it will be worthy to undertake some eventual strategies such as quarantine, wearing of masks, and vaccination.

5 Conclusions

The main challenge for scientific researchers is to avoid a situation where several mutants of COVID-19 coexist in the same population. In this present work, attention is focused on this mutation phenomenon by studying the global dynamics of the COVID-19 SEIR three-strain pandemic model with general incidence rates. The proposed model included eight compartments that are the susceptible, three classes of the exposed, three classes of the infected, and the removed individuals. First, we have proved the existence, positivity, and boundedness of all solutions that ensure the SEIR model well-posedness. We have given the disease-free equilibrium and the endemic equilibria with respect to each problem strain. By using some suitable Lyapunov functions, the global stability of each equilibrium is established depending on the basic reproduction number R_0 and on each strain reproduction number R_0^i , $i = 1, 2, 3$. Numerical simulations are performed in order to confirm our different theoretical findings. We have observed that the model with generalized incidence rates can represent a large number of classical problems; furthermore, more clear view can be obtained to check the equilibria stability. In addition, numerical comparison between COVID-19 clinical data and our model infected cases has been conducted. Good fit between our numerical results and the clinical data is observed, which indicates that the multi-strain mathematical model is more appropriate to study the mutant infections.

References

1. A.E. Gobalenya, S.C. Baker, R.S. Baric, R.J. de Groot, C. Drosten, A.A. Gulyaeva, et al., The species severe acute respiratory syndrome-related coronavirus: classifying 2019-nCoV and naming it SARS-CoV-2. *Nat. Microbiol.* **5**, 536–544 (2020)
2. W.O. Kermack, A.G. McKendrick, A contribution to the mathematical theory of epidemics. *Proc. R Soc. Lond. A.* **115**, 700–721(1927)
3. M.Y. Li, J.S. Muldowney, Global stability for the SEIR model in epidemiology. *Math. Biosc.* **125** 155–164 (1995)
4. M.Y. Li, L. Wang, Global stability in some Seir epidemic models, in *Mathematical Approaches for Emerging and Reemerging Infectious Diseases: Models, Methods, and Theory* (Springer, New York, 2002), pp. 295–311
5. G. Huang, Y. Takeuchi, W. Ma, D. Wei, Global stability for delay SIR and SEIR epidemic models with nonlinear incidence rate. *Bull. Math. Biol.* **72**, 1192–1207 (2010)

6. D. Benteleb, S. Amine, Lyapunov function and global stability for a two-strain SEIR model with bilinear and non-monotone. *Int. J. Biomath.* **12**, 1950021 (2019)
7. A. Meskaf, O. Khyar, J. Danane, K. Allali, Global stability analysis of a two-strain epidemic model with non-monotone incidence rates. *Chaos Sol. Frac.* **133**, 109647 (2020)
8. O. Khyar, Allali, K. Global dynamics of a multi-strain SEIR epidemic model with general incidence rates: application to COVID-19 pandemic. *Nonlinear Dyn.* **102**, 489–509 (2020). <https://doi.org/10.1007/s11071-020-05929-4>
9. M. Pachetti, B. Marini, F. Benedetti, F. Giudici, E. Mauro, P. Storici, et al., Emerging SARS-CoV-2 mutation hot spots include a novel RNA-dependent-RNA polymerase variant. *J. Trans. Med.* **18**, 1–9 (2020)
10. D. Benvenuto, S. Angeletti, M. Giovanetti, M. Bianchi, S. Pascarella, R. Cauda, et al., Evolutionary analysis of SARS-CoV-2; how mutation of Non-Structural Protein 6 (NSP6) could affect viral autophagy. *J. Infection* **81**, 24–27 (2020)
11. K. Hattaf, N. Yousfi, A. Tridane, Mathematical analysis of a virus dynamics model with general incidence rate and cure rate. *Nonlinear Anal. Real World Appl.* **13**, 1866–1872 (2012)
12. C. Ji, D. Jiang, Threshold behaviour of a stochastic SIR model. *Appl. Math. Model.* **38**, 5067–5079 (2014)
13. X. Liu, L. Yang, Stability analysis of an SEIQV epidemic model with saturated incidence rate, *Nonlinear Anal. Real World Appl.* **13**, 2671–2679 (2012)
14. S. Sarwardi, M.M. Haque, Hossain, S. Analysis of Bogdanov–Takens bifurcations in a spatiotemporal harvested-predator and prey system with Beddington–DeAngelis-type response function. *Nonlinear Dyn.* **100**, 1755–1778 (2020)
15. P.H. Crowley, E.K. Martin, Functional responses and interference within and between year classes of a dragonfly population. *J. North. Am. Benth. Soc.* **8**, 211–221 (1989)
16. K. Hattaf, M. Mahrouf, J. Adnani, N. Yousfi, Qualitative analysis of a stochastic epidemic model with specific functional response and temporary immunity. *Phys. A* **490**, 591–600 (2018)
17. V. Capasso, G. Serio, A generalization of the Kermack–McKendrick deterministic epidemic model. *Math. Biosci.* **42**, 43–61 (1978)
18. J.K. Hale, S.M.V. Lunel, L.S. Verduyn, S.M.V. Lunel, *Introduction to Functional Differential Equations*, vol. 99 (Springer Science and Business Media, Berlin, 1993)
19. Statistics of Moroccan Health Ministry on COVID-19. <https://www.sante.gov.ma/>

Part II
Nonlinear Phenomena in
Bio- and Eco-Systems Dynamics

Nonlinear Phenomena and Chaos in a Tumor Growth Model



Dionysios Sourailidis, Christos Volos, Lazaros Moysis, and Ioannis Stouboulos

1 Introduction

In the last decade many research teams work on using dynamical system analysis for studying specific phenomena related to specific stages (avascular, vascular, and metastatic) of cancer. This happens due to the fact that the growth of malignant tumors can be described by a system of ordinary differential equations including two basic factors, the populations of effector and tumor cells.

The emergence of chaotic behavior in biological systems has long been reported in the literature [1–6]. Chaotic systems are dynamical systems in discrete or continuous time, whose prominent feature is the high sensitivity to initial conditions and parameter changes. This means that solutions starting from almost identical initial conditions will quickly diverge into different trajectories, a feature that was quoted by Edward Lorenz as the butterfly effect [7].

Understandably, the emergence of such chaotic behavior in biological systems can be somewhat expected, since biological systems are by nature complex systems having multiple interacting agents that are affected by a plethora of internal or external factors. This is also the case for dynamical models describing tumor growth [8–14]. In the early work of [9], the author argued that tumor growth is chaotic, with a fractal nature. In [14], a model for tumor growth was studied and its Lyapunov exponents were computed. In [12], the topological complexity of a tumor growth model was studied. The work [11] discussed chaos in chromosomal theory. In [13], the effect of time delays in the growth process of the hunting cells was studied.

D. Sourailidis · C. Volos (✉) · L. Moysis · I. Stouboulos
Laboratory of Nonlinear Systems - Circuits & Complexity, Physics Department, Aristotle University of Thessaloniki, Thessaloniki, Greece
e-mail: dsourail@physics.auth.gr; volos@physics.auth.gr; lmouisis@physics.auth.gr; stouboulos@physics.auth.gr

In 2016, an interesting model, which is built upon a chemical network, in order to suggest a mechanism for avascular, vascular, and metastasis cancer growth, is introduced by Llanos-Perez et al. [8]. Since then, many researchers have used this model. In more detail, 1 year later, the aforementioned model is enriched by using thermodynamic formalism for the metabolic rate of human cancer cells [10]. Montero et al. [15] worked on a biological approach of this problem. Guerra et al. [16] generalized the previously mentioned work by including the epithelial–mesenchymal transition. This is a biological process that allows a polarized epithelial cell that normally interacts with the basement membrane through its basal surface to undergo multiple biochemical changes, which empower it to assume a mesenchymal cell phenotype involving reinforced migratory capacity, invasiveness, and heightened resistance to apoptosis. Other works applied control theoretic concepts to the control of cancer growth [17–20]. Finally, some works have also considered the case of fractional-order modeling of cancer dynamics [21–24].

In this chapter, we extend the dynamical analysis for the system proposed in [8], by focusing on the bifurcation analysis of the system with respect to the population of normal cells. Interesting phenomena will be unmasked, like period-doubling route to chaos, crisis, coexisting attractors, and antimonicity. Such phenomena highlight the complex dynamics of tumor growth and can further bring light to the effect of varying the model parameters through treatment in the system. This is in essence the aim of the mathematical modeling for complex biological systems, to obtain a grasp on the interconnections between system parameters, the sensitivity of the system to parameter changes, and to understand how each parameter can be modified to bring the system under a desired performance [25–27].

The remainder of this chapter is organized as such: In Sect. 2, the dynamical model is presented. An extensive bifurcation analysis is performed and the results are discussed in Sect. 3, while Sect. 4 concludes the work with a discussion on future topics of interest.

2 The Dynamical Model for Tumor Growth

The dynamical model of tumor growth proposed in [8] is the following:

$$\begin{cases} \dot{x} = x(2N - x) - Hxz \\ \dot{y} = y(4 - 0.14y) + 0.5x^2 - Iy - 0.5Hy z + 0.001z^2 \\ \dot{z} = -Iz + 0.07y^2 + 0.5Hy z - 0.002z^2. \end{cases} \quad (1)$$

This is a three-stage system, where the variables x , y , z correspond to the concentration of tumor cells in the avascular, vascular, and metastasis phases, respectively. The system's parameters H , N , I , and T represent the populations of the host cells, normal cells, immune cells, and natural killer cells (lymphocytes).

In [8], the parameters had the values $N = 5$, $H = 3$ and considered different values for the population of immune cells I that can be considered as the control parameter. A similar approach was later considered in [28], where a bifurcation analysis was performed in terms of control parameter I , for different values of parameters N , H .

In this chapter, the behavior of the model is studied with respect to parameter N . Hence, the aim is to unmask the chaotic phenomena related to the tumor growth system, as the number of normal cells changes. Also, different choices of host and immune cells will be considered, in order to observe how they relate to the bifurcation parameter N .

3 Dynamical Analysis of the Model

To study the dynamical behavior of the system with respect to parameter N , we compute its bifurcation diagram, along with the diagram of Lyapunov exponents, for different values of host cells H , while keeping the population of immune cells steady at $I = 1$. The bifurcation diagram depicts the values of the tumor cells at the metastasis phase z , as the trajectory of the system cuts the plane $x = 1$ with $dx/dt < 0$.

For lower values of the parameter H , we observe that the system retains a periodic behavior for all values of the bifurcation parameter N . This can be seen for example in Fig. 1a where for $H = 2$ the system is periodic with period 1. As the parameter H though increases, the phenomenon of antimonicity appears, as can be seen in Fig. 1b for $H = 3.5$, in Fig. 1c for $H = 4.2$, and in Fig. 1d for $H = 4.3$. In these cases, the system starts from period-1, and then the period begins to double for values around $N = 3.5$ going up to period-2 ($H = 3.5$), period-4 ($H = 4.2$), and period-8 ($H = 4.3$) at around $N = 4$, after which the period is halved back to 1. This is signified by the characteristic formation of a bubble shape in the bifurcation diagram.

Interestingly, for larger values of H , for example $H = 4.5$, the phenomenon of antimonicity extends to chaotic behavior, as can be seen in Fig. 1e. Here, the system starts from period-1 and traverses to chaotic behavior through a period-doubling route, only to go back again to period-1 following a reverse period-halving route. In Fig. 2, various portraits of the system are depicted for $H = 4.5$, as the value of the parameter N increases and the system goes from period 1 to chaos and then back to period 1. Also, Fig. 3 depicts the 3D attractor of the system for the case of chaotic behavior, for $H = 4.5$, $I = 1$, and $N = 4$ for initial conditions $(1, 0.1, 0.1)$.

As the value of H increases even more, the chaotic behavior of the system becomes much more complex. Taking a look at the bifurcation diagrams shown in Fig. 1f–h, a plethora of chaotic bubbles are observed. Also, the system repeatedly abruptly exits or enters chaos, as can be seen from the crisp changes in the shape of the bifurcation diagram. This phenomenon is known as crisis. Also, it can be observed that the chaotic behavior appears for a much wider range of the parameters

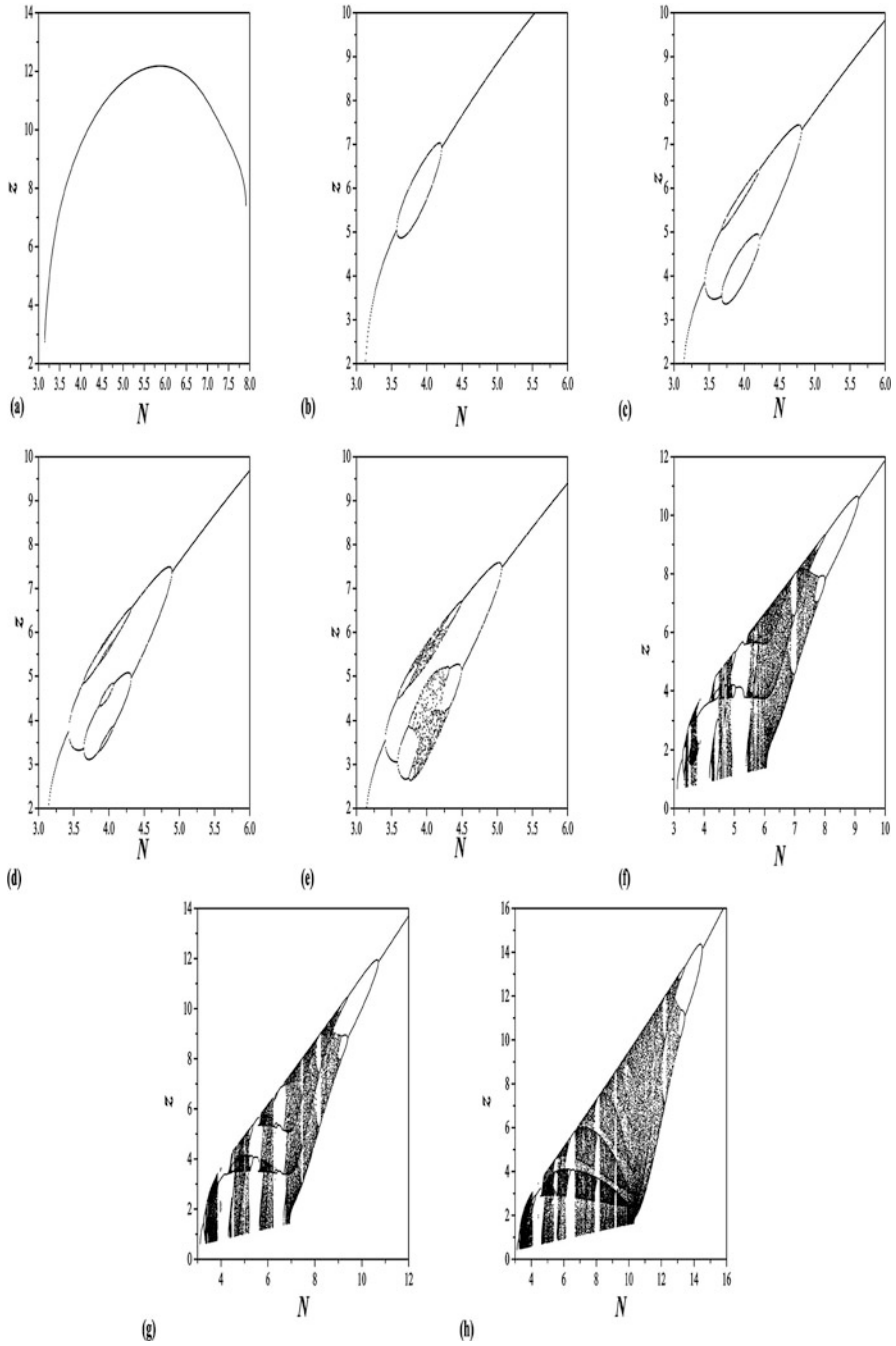


Fig. 1 Bifurcation diagram for system (1), with respect to N , for $I = 1$, and (a) $H = 2$, (b) $H = 3.5$, (c) $H = 4.2$, (d) $H = 4.3$, (e) $H = 4.5$, (f) $H = 8$, (g) $H = 9$, (h) $H = 12$

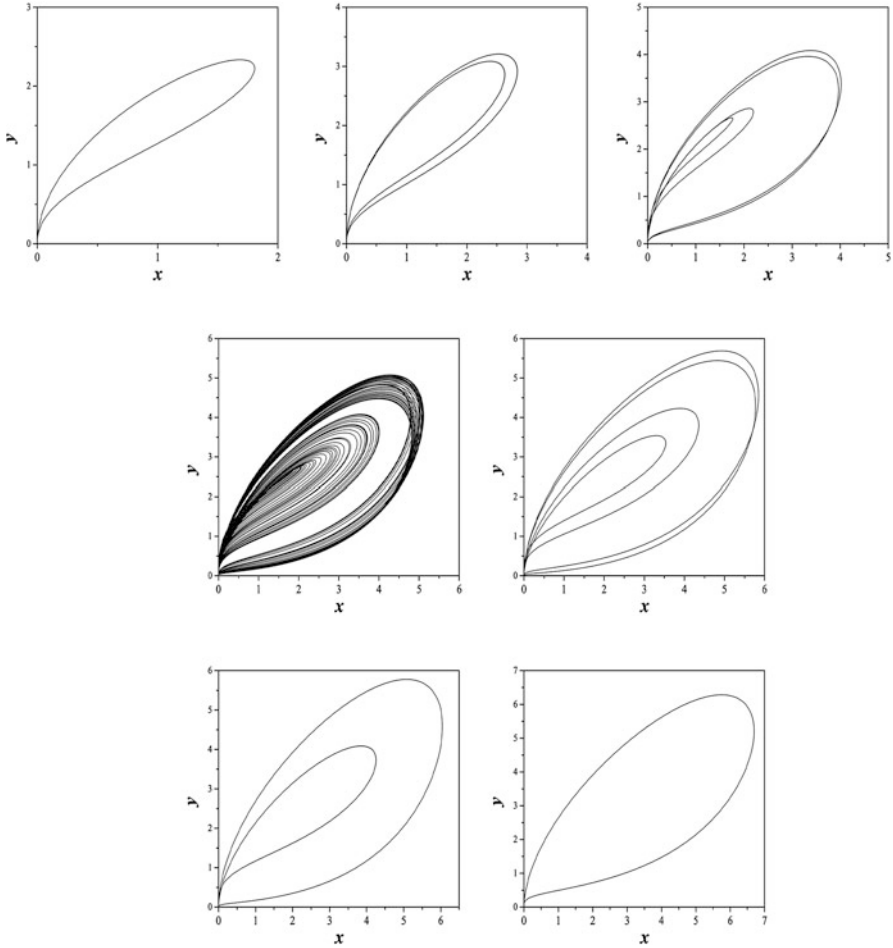


Fig. 2 Phase portraits of the system for $I = 1, H = 4.5$ and (from left to right, first line to third) $N = 3.3, N = 3.41, N = 3.6, N = 4, N = 4.4, N = 4.51, N = 5$, showcasing the antimonicity phenomenon

N than before. The diagram of the Lyapunov exponents for $H = 12$ shown in Fig. 4 also verifies the chaotic phenomena observed.

Finally, the emergence of coexisting attractors of the system is studied, by computing its continuation diagram. This diagram is similar to the bifurcation diagram, with the only difference that each time the bifurcation parameter is iterated, the initial condition of the system is taken as equal to the final state of the system from the previous simulation. Hence, in each iteration, the initial condition of the system changes, as opposed to the bifurcation diagram where it is kept steady. This is done in order to unmask any possible changes in the dynamical behavior of the system with respect to initial conditions. Indeed, as can be seen from the

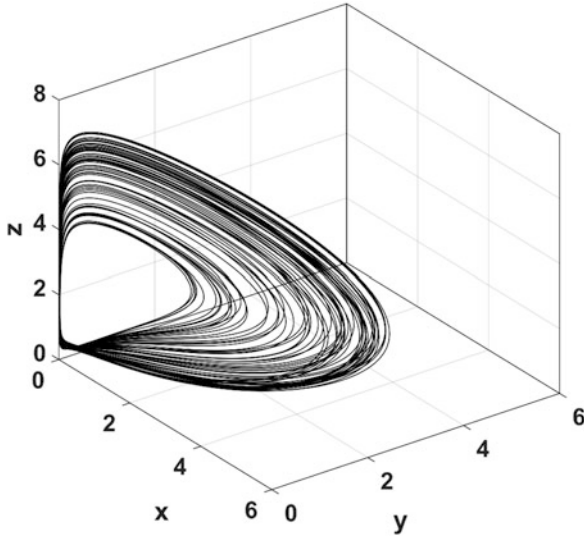


Fig. 3 Phase portrait of system (1), for $H = 4.5$, $I = 1$, and $N = 4$ and initial conditions $(x(0), y(0), z(0)) = (1, 0.1, 0.1)$

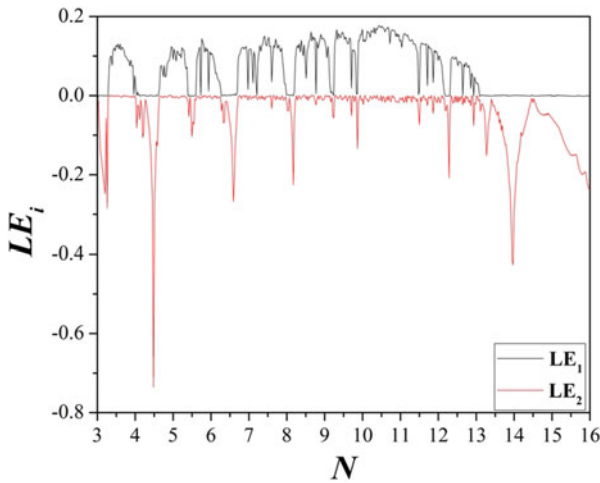


Fig. 4 Diagram of Lyapunov exponents for system (1), with respect to N , for $I = 1$, $H = 12$

overlapping of the bifurcation and the continuation diagrams shown in Fig. 5, the system showcases coexisting attractors roughly from $N = 3.76$ to $N = 3.87$. This indicates that the initial conditions can greatly affect the behavior of the system for this range of parameter values. The phase portraits of the coexisting attractors for $N = 3.778$, $H = 8$, $I = 1$ and initial conditions $(x(0), y(0), z(0)) = (1, 0, 0)$ (left) and $(x(0), y(0), z(0)) = (0, 0.101, 0.493)$ (right) are shown in Fig. 6.

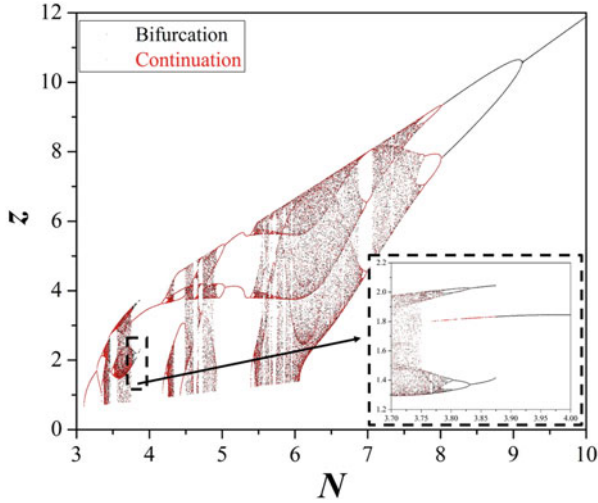


Fig. 5 Overlapping of the continuation and bifurcation diagrams of system (1) with respect to N , for $I = 1, H = 8$

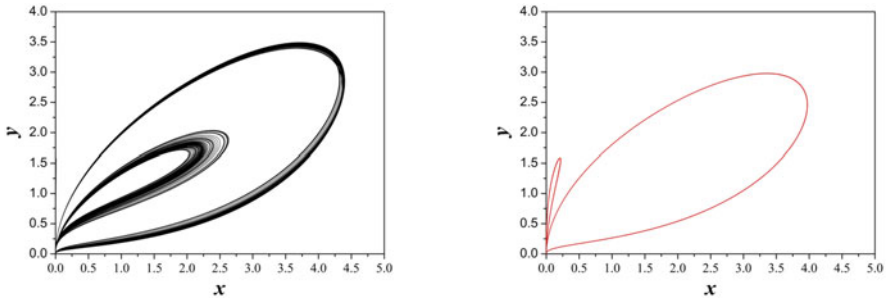


Fig. 6 Coexisting attractors of system (1) with initial conditions $(x(0), y(0), z(0))_0 = (1, 0, 0)$ (left) and $(x(0), y(0), z(0)) = (0, 0.101, 0.493)$ (right)

Overall, by comparing all of the aforementioned bifurcation diagrams, we observe that as the number of the host cells H grows, the behavior of the system exhibits more unpredictable and complex behavior, since periodic and chaotic behaviors alternate with each other abruptly, as the value of the normal cells N increases. This observation further underlines our knowledge on the complexity of the tumor dynamics and the need of robust control strategies to keep its dynamics stable around a desired level.

4 Conclusions

In this chapter, an extensive bifurcation analysis was performed for a three-stage tumor growth model, with respect to parameter N , which denotes the population of normal cells. A plethora of behaviors have been emerged for the system, from periodic to chaotic, and phenomena like antimotonicity, crisis, and coexisting attractors.

Overall, it is clear that even this simplified cancer model can showcase a very complex behavior, which further underlines the complexity of the disease and the difficulties in understanding the full spectrum of cancer dynamics in the body. Future aspects of this work will consider the design of control strategies, and also modifications of the system, where a control parameter, like the number of immune cells, can be periodically perturbed to study the effects of periodic treatment and drug regulation. Also, fractional-order versions of this model can be considered.

References

1. S.H. Strogatz, *Nonlinear Dynamics and Chaos: With Applications to Physics, Biology, Chemistry, and Engineering* (CRC Press, Boca Raton, 2018)
2. H. Degn, A.V. Holden, L.F. Olsen, *Chaos in Biological Systems*, vol. 138 (Springer Science & Business Media, New York, 2013)
3. Y. Scharf, A chaotic outlook on biological systems. *Chaos Solitons Fractals* **95**, 42–47 (2017)
4. F. Nazarimehr, S. Jafari, S.M.R.H. Golpayegani, J. Sprott, Can Lyapunov exponent predict critical transitions in biological systems? *Nonlinear Dyn.* **88**(2), 1493–1500 (2017)
5. R.J. Field, L. Gyorgyi, *Chaos in Chemistry and Biochemistry* (World Scientific, Singapore, 1993)
6. K. He, Critical phenomenon, crisis and transition to spatiotemporal chaos in plasmas, in *Advances in Space Environment Research* (Springer, Berlin, 2003), pp. 475–494
7. E. Lorenz, The butterfly effect. *World Sci. Ser. Nonlinear Sci. Ser. A* **39**, 91–94 (2000)
8. J. Llanos-Pérez, J. Betancourt-Mar, G. Cocho, R. Mansilla, J.M. Nieto-Villar, Phase transitions in tumor growth: III vascular and metastasis behavior. *Physica A Stat. Mech. Appl.* **462**, 560–568 (2016)
9. E. Ahmed, Fractals and chaos in cancer models. *Int. J. Theor. Phys.* **32**(2), 353–355 (1993)
10. J. Betancourt-Mar, J. Llanos-Pérez, G. Cocho, R. Mansilla, R. Martin, S. Montero, J. Nieto-Villar, Phase transitions in tumor growth: IV relationship between metabolic rate and fractal dimension of human tumor cells. *Physica A Stat. Mech. Appl.* **473**, 344–351 (2017)
11. P. Duesberg, Chromosomal chaos and cancer. *Sci. Am.* **296**(5), 52–59 (2007)
12. J. Duarte, C. Januário, C. Rodrigues, J. Sardanyes, Topological complexity and predictability in the dynamics of a tumor growth model with Shilnikov's chaos. *Int. J. Bifurcation Chaos* **23**(07), 1350124 (2013)
13. M. Saleem, T. Agrawal, Chaos in a tumor growth model with delayed responses of the immune system. *J. Appl. Math.* **2012**, 1–16 (2012)
14. S. Abernethy, R.J. Gooding, The importance of chaotic attractors in modelling tumour growth. *Physica A Stat. Mech. Appl.* **507**, 268–277 (2018)
15. S. Montero, R. Martin, R. Mansilla, G. Cocho, J.M. Nieto-Villar, Parameters estimation in phase-space landscape reconstruction of cell fate: a systems biology approach, in *Systems Biology* (Springer, Berlin, 2018), pp. 125–170

16. A. Guerra, D. Rodriguez, S. Montero, J. Betancourt-Mar, R. Martin, E. Silva, M. Bizzarri, G. Cocho, R. Mansilla, J. Nieto-Villar, Phase transitions in tumor growth VI: epithelial–Mesenchymal transition. *Physica A Stat. Mech. Appl.* **499**, 208–215 (2018)
17. M. Shahzad, Chaos control in three dimensional cancer model by state space exact linearization based on lie algebra. *Mathematics* **4**(2), 33 (2016)
18. J.P. Belfo, J.M. Lemos, *Optimal Impulsive Control for Cancer Therapy* (Springer, Cham, 2020)
19. I.P. Janecka, Cancer control through principles of systems science, complexity, and chaos theory: a model. *Int. J. Med. Sci.* **4**(3), 164 (2007)
20. A. El-Gohary, I. Alwasel, The chaos and optimal control of cancer model with complete unknown parameters. *Chaos Solitons Fractals* **42**(5), 2865–2874 (2009)
21. J.F. Gómez-Aguilar, M.G. López-López, V.M. Alvarado-Martínez, D. Baleanu, H. Khan, Chaos in a cancer model via fractional derivatives with exponential decay and Mittag-Leffler law. *Entropy* **19**(12), 681 (2017)
22. P.A. Naik, K.M. Owolabi, M. Yavuz, J. Zu, Chaotic dynamics of a fractional order HIV-1 model involving aids-related cancer cells. *Chaos Solitons Fractals* **140**, 110272 (2020)
23. E. Ucar, N. Özdemir, E. Altun, Fractional order model of immune cells influenced by cancer cells. *Math. Model. Nat. Phenom.* **14**(3), 308 (2019)
24. I. N'Doye, H. Voos, M. Darouach, Chaos in a fractional-order cancer system, in *2014 European Control Conference (ECC)* (IEEE, Piscataway, 2014), pp. 171–176
25. P.A. Naik, J. Zu, K.M. Owolabi, Modeling the mechanics of viral kinetics under immune control during primary infection of HIV-1 with treatment in fractional order. *Physica A Stat. Mech. Appl.* **545**, 123816 (2020)
26. P.A. Naik, Global dynamics of a fractional-order SIR epidemic model with memory. *Int. J. Biomath.* **13**(8), 2050071 (2020)
27. P.A. Naik, J. Zu, M. Ghoreishi, Stability analysis and approximate solution of SIR epidemic model with Crowley-Martin type functional response and Holling type-ii treatment rate by using homotopy analysis method. *J. Appl. Anal. Comput.* **10**(4), 1482–1515 (2020)
28. D. Sourailidis, C. Volos, L. Moysis, I. Stouboulos, Antimonotonicity, crisis and route to chaos in a tumor growth model, in *Handbook of Research on Modeling, Analysis, and Control of Complex Systems (In Press)* (IGI Global, Philadelphia, 2020)

Modeling Limbic Seizure Initiation with an Ensemble of Delay Coupled Neuroscillator



Ilya V. Sysoev, Maksim V. Kornilov, Natalia A. Makarova, Marina V. Sysoeva, and Lyudmila V. Vinogradova

1 Introduction

The limbic (temporal lobe) epilepsy is a widespread neurological disease, characterized by spontaneous seizures. Temporal lobe epilepsy is the most common form of focal epilepsy in humans [1]. Limbic seizures start as focal events able to subsequent propagation (generalization) to other brain regions [2, 3]. Seizure-associated large amplitude oscillations in different areas are highly synchronized and well studied both in humans [4] and in animal models [5]. The initial pathological activity source (epileptic focus) is frequently localized in the hippocampus, [6] but mechanisms that govern transitions from normal to pathological hypersynchronous activity of hippocampal networks and underlie seizure generalization are largely unknown.

I. V. Sysoev (✉) · M. V. Kornilov

Saratov Branch of Kotel'nikov Institute of Radioengineering and Electronics of RAS, Saratov, Russia

Saratov State University, Saratov, Russia
<http://nonlinmod.sgu.ru>

N. A. Makarova

Saratov Branch of Kotel'nikov Institute of Radioengineering and Electronics of RAS, Saratov, Russia

M. V. Sysoeva

Saratov Branch of Kotel'nikov Institute of Radioengineering and Electronics of RAS, Saratov, Russia

Yuri Gagarin State Technical University of Saratov, Saratov, Russia

L. V. Vinogradova

Saratov Branch of Kotel'nikov Institute of Radioengineering and Electronics of RAS, Saratov, Russia

Institute of Higher Nervous Activity and Neurophysiology of RAS, Moscow, Russia

Here, we hypothesize that the epileptic focus is not a spatially local phenomenon, but a partly isolated circuit consisting of relatively small number of neurons, which is distributed over large part of hippocampus (hippocampal principal neurons are known to have many long-range intra- and extra-hippocampal projections). This circuit can “sleep” for a long time and cannot be detected since it does not produce profound clinical symptoms, and moreover, even in animal models of epilepsy, local field potentials, reflecting the activity of large neuronal population [7], cannot detect the activity of the relatively small number of cells in the circuit, having small impact on the local field potentials. The single unit intra- or extracellular electrodes are unlikely to be located in the right place for the same reason, and the circuit stays unrevealed. But at some point, elements of the focal circuit begin to recruit the larger hippocampal networks and start to translate their dynamics to the other regions, forcing the synchronized oscillations. The most likely reason of pathological circuit involvement is memory processes, in which hippocampus plays the dominant role, and therefore new links between hippocampal neurons are frequently created.

Here, we propose a mesoscale model of limbic seizure initiation and generalization all over the same hippocampal half, not considering the generalization to other brain structures (entorhinal cortex, frontal cortex), and limiting with the same brain hemisphere. The models of the proposed type—network mesoscale epilepsy models—are not very popular since it is hard to find the balance between incorporation of individual cell properties like different GABA, glutamate, and CB1 receptors from one hand, and correct representation of cell numbers and networks in different brain regions. Still, some recent models were successfully constructed [8]. Recently, we proposed two models of such a type for spike-wave discharges which are the main electrographic manifestation of absence seizures [9, 10].

2 Model Design

The following simplifications are used to prove the model.

1. We assume that each model neuron (node) represents a group of neurons with similar properties and coupling, as it is usually assumed in the mesoscale models [8, 9].
2. There are many possible neuron models [11, 12], but we hypothesize that there is no significant difference if we are interested in the network effects and what they can provide for epilepsy. Therefore, we use the simplest known model for individual neurons—FitzHugh–Nagumo model [13, 14].
3. We consider only principal excitatory cells of the hippocampus that are able to orchestrate synchronicity of large neuronal populations via long-range projections here, ignoring interneurons and glial cells, as it was in [9].
4. We consider all nodes and all couplings to be completely equal (no parameter distribution).

5. We consider the neurons of the hippocampal hemisphere responsible for seizure generation to be split into two main populations: pathological (focal, smaller) and normal (surrounding, larger) one. These populations are mostly separated one from another except the moment when the pathological population starts to be involved into memory processes and the links from it to the normal population becomes active.
6. We ignore all couplings from over parts of the brain to both considered populations.

We understand that these simplifications are significant, however, they are necessary for the initial step of model development and can be overcome in future.

We used the following equations for the model:

$$\begin{aligned} \frac{dx_i}{dt} &= x_i (a - x_i) (x_i - 1) - y_i + \xi_i + \sum_{j \neq i} k_{i,j} h(x_j(t - \tau)), \\ \frac{dy_i}{dt} &= bx_i - \gamma y_i, \\ h(x) &= \frac{1 + \tanh(x)}{2}, \end{aligned} \tag{1}$$

with the same parameters $a = 0.8$, $b = 0.008$, $\gamma = 0.0033$ for all nodes. All present coupling coefficients $k_{i,j} = 0.6$ and absent coupling terms are represented by $k_{i,j} = 0$, with the coupling delay $\tau = 13$. Time delay (the term “latency” is also used) between presynaptic and postsynaptic action potential is usually considered in models [15, 16]. It can be small (1 ms delay—very fast transmission, see [17]) or large (long latency, like 26 ms in [18]). The most usual values are 2–5 ms. Since the FitzHugh–Nagumo neuron models are dimensionless, there was no possibility to set the absolute value. Instead, we considered the ratio between the main frequency of limbic seizures that is 16–40 Hz [6] (i.e. oscillation period 40–25 ms) and the delay, which should be approximately 10 times smaller. The equations were solved using Euler method with the step $\Delta t = 0.5$. In order to switch from the dimensionless time to real time scale, we propose to use the ratio 1/3400, i.e. $\Delta t = 1/1700$ s, as previously in [10]. The Euler method was used due to delay presence in couplings, therefore, the advanced Runge–Kutta or Adams methods are not directly applicable. We tested the approach for convergence.

2.1 Focal Circuit

The focal circuit consists of a small number of neurons, which are organized into the ring with possible additional elements like in Fig. 1. Here, we partly follow the idea of [19]. The used parameters correspond to no oscillations in a single node without coupling, but after the time delayed coupling is provided following the

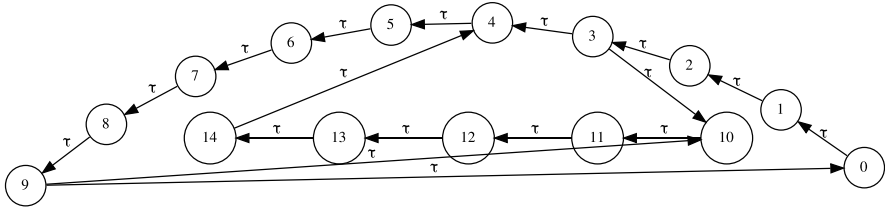


Fig. 1 A scheme of the proposed focal circuit organization with two subcircuits: the major generating the main frequency and the minor, for changing it. The neurons No. 0–9 form the major circuit, they form a one-way ring; the neurons No. 3, 10–14, 4 are included into the minor circuit and they also form a one-way ring

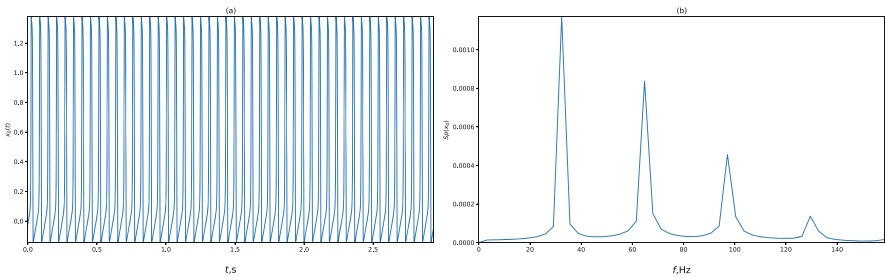


Fig. 2 Time series and spectrum of the individual neuron No. 0 of the focal circuit. The spectrum was estimated by averaging periodograms calculated from 20 time series obtained for different initial conditions. The main oscillation frequency was calculated as the first and usually the largest peak in the spectrum. All neurons of the major loop generate the similar activity with a small time delay, therefore only time series and spectrum of the neuron No. 0 were plotted

scheme Fig. 1 the individual node starts to exhibit periodic nonlinear oscillation—see Fig. 2. These oscillations are the function of the circuit organization. Their appearance and frequency are determined by the delay time τ and by the number of nodes D in the circuit, as it is shown in Fig. 3. These elements produce the principal ring. The main frequency in real data can evaluate during the seizure [6] both in humans [5] and rats [20, 21]. Such an evolution can be modeled by variation of number of circuit elements or by incorporating different $\tau_{i,j}$ for different i and j . Inclusion of additional subcircuits to the principal epileptic ring usually leads to appearance of additional spectral components.

3 Normal Circuit, Generalization

To model the normal dynamics, the larger circuit is proposed following the approach we have already used for modeling spike-wave discharges [10]. Figure 4 represents the typical complete network consisting of the normal circuit (gray nodes) and the epileptic circuit split into the principal ring (red nodes) and additional subcircuit

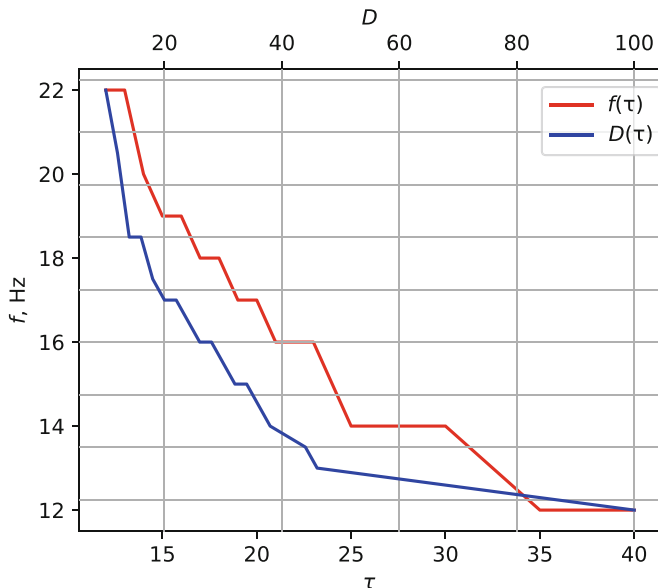


Fig. 3 Dependencies of the main oscillation frequency in the focal circuit on the number of elements in the principal ring of the epileptic circuit D and on the coupling delay time τ , τ is measured in Δt units

(blue nodes) used to initiate oscillation and, if additional links activated, to modulate the main frequency and enrich the spectrum.

The normal circuit demonstrates irregular activity being not connected to the epileptic one. When connected, the normal circuit becomes synchronized by the epileptic one (we used the same value $k_{i,j} = 0.6$ for the all types of present couplings), see time series and spectrum of summary activity of the entire network in Fig. 5. Since in most real experiments the local field potentials (summary activity) are measured. Therefore, the local filed potential synchronization is mostly considered rather than spike synchronization following [22]. Amplitude difference between Figs. 2 and 5 is due to the summary signal is plotted on Fig. 5. We consider this synchronous dynamics as a model of synchronization in the hippocampus of the same hemisphere, in which the focus is located. This step is intermediate in the process of the seizure generalization followed by propagation to entorhinal and frontal (primary motor) cortex, and then to the other hemisphere. However, modeling of the further seizure progression (and termination?) is out of aims of this study.

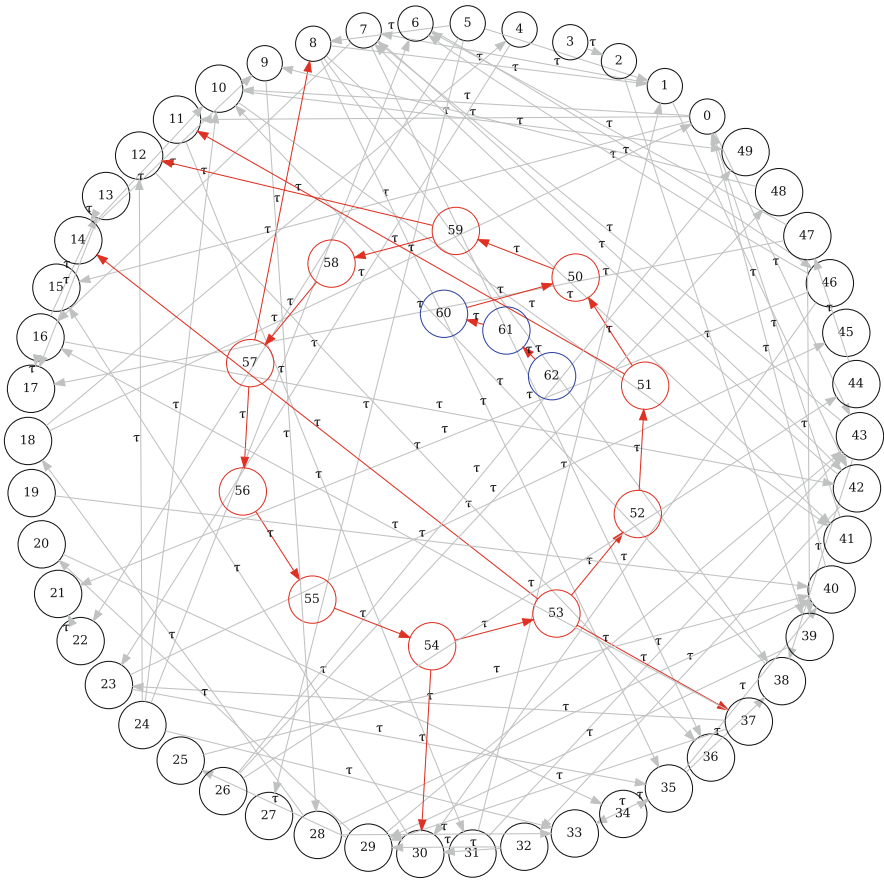


Fig. 4 Scheme of complete network for modeling limbic seizures. Red and blue nodes represent the focal matrix (principal ring and additional subcircuit), gray nodes represent the normal circuit. Red arrows are from epileptic nodes, including connections to the normal ones

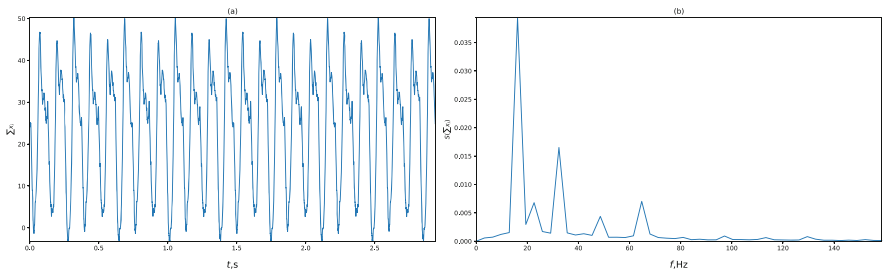


Fig. 5 Time series and spectra of network summary activity of all nodes from both circuits: epileptic and normal

4 Conclusions and Discussion

Here we propose a simple dynamical model for limbic seizure focus and primary step of generalization. The main idea is that a small neural circuit in the hippocampus in the form of a ring is responsible for main frequency and that this frequency is a function of the ring length (the larger ring is, the small frequency occurs) and the mean synaptic transition delay time in the ring. Since it is known that the main frequency of the limbic seizures is changing over time during the seizure progression, we propose a mechanism for this, by incorporating the additional subcircuits into the ring, which can be dynamically connected or disconnected. The normal dynamics of the main hippocampal networks is modeled by the larger ensemble of same nodes, but connected randomly.

The seizure generalization from the focal circuit to the entire hippocampus (the same hemisphere) can be achieved by activating the additional couplings from the focal circuit to the epileptic one [23]. These couplings may appear in the model due to some memory processes in the hippocampus, by episodically including some elements of the focal network into the memory processes.

The resulting model is a system of time delayed equations with delay located in connections (all connections are of the same weight) between nodes, which are represented by identical FitzHugh–Nagumo equations (selected as simplest oscillatory neural model). Introduction of time delay was multiply shown to allow to enrich the model dynamics significantly, see the recent review [24]. It is mostly reported that introduction of time delay provides more possibilities for chaotic behavior. But here, we are interested in activation of regular oscillations rather than in chaos. The nodes by themselves are in the excitable mode, i.e. without network they do not demonstrate any oscillatory activity. There is no noise in the system. The similar situation was shown in [25].

The chemical synapses were considered. The sigmoid coupling function is often used to describe interactions between model neurons, especially for pyramid cells which are the main type of cells in the hippocampus, see [26] and [27], for instance. In particular, the sigmoid coupling with delay as in the current work was use in [16]. We think that the same effects can be achieved with other coupling functions. We tried the simple diffusion coupling as well with similar results for the main frequency occurring in the loop due to the delay. But we did not study this question in detail.

The proposed model was made just as a proof of concept. From the physiological point of view at least inhibitory interneurons have to be incorporated. Then, the variation of node parameters (individual cells, couplings, and synaptic delays) has to be studied whether the model stays stable or not. The mechanisms of dynamically stitching connections, responsible for generalization and frequency changes, have to be modeled in detail.

Acknowledgement This work was supported by Russian Science Foundation, grant No. 19-72-10030.

References

1. A.T. Berg, S.F. Berkovic, M.J. Brodie, J. Buchhalter, J.H. Cross, W. Van Emde Boas, J. Engel, J. French, T.A. Glauser, G.W. Mathern, S.L. Moshé, D. Nordli, P. Plouin, I.E. Scheffer, *Epilepsia* **51**(4), 676 (2010). <https://doi.org/10.1111/j.1528-1167.2010.02522.x>
2. J. Engel, in *Generalized Seizures: From Clinical Phenomenology to Understanding System and Networks*, ed. by E. Hirsch, F. Andermann, P. Chauvel, J. Engel, F. Lopes da Silva, H. Luders (John Libbey Eurotext, Montrouge, 2006), pp. 305–325
3. W.T. Blume, *Epilepsy Currents* **10**(5), 115 (2010). <https://doi.org/10.1111/j.1535-7511.2010.01375.x>
4. S. Spencer, *Epilepsia* **43**(3), 219 (2002). <https://doi.org/10.1046/j.1528-1157.2002.26901.x>
5. E.H. Bertram, *Epilepsia* **38**(1), 95 (1997). <https://doi.org/10.1111/j.1528-1157.1997.tb01083.x>
6. J. Paz, J. Huguenard, *Nat. Neurosci.* **18**, 351–359 (2015). <https://doi.org/10.1038/nn.3950>
7. G. Buzsáki, C.A. Anastassiou, C. Koch, *Nat. Rev. Neurosci.* **13**(6), 407 (2012). <https://doi.org/10.1038/nrn3241>
8. G. Ullah, J.R.J. Cressman, E. Barreto, S.S. J., *J. Comput. Neurosci.* **26**, 171–183 (2009). <https://doi.org/10.1007/s10827-008-0130-6>
9. T.M. Medvedeva, M.V. Sysoeva, G. van Luijtelaar, I.V. Sysoev, *Neural Netw.* **98**, 271 (2018). <https://doi.org/10.1016/j.neunet.2017.12.002>
10. T.M. Medvedeva, M.V. Sysoeva, A. Lüttjohann, G. van Luijtelaar, I.V. Sysoev, *PLoS ONE* **15**(9), e239125 (2020). <https://doi.org/10.1371/journal.pone.0239125>
11. A.S. Dmitrichev, D.V. Kasatkin, V.V. Klinshov, S.Y. Kirillov, O.V. Maslennikov, D.S. Shchapin, V.I. Nekorkin, V.U.Z. Izvestiya, *Appl. Nonlinear Dyn.* **26**(4), 5 (2018). <https://doi.org/10.18500/0869-6632-2018-26-4-5-58>
12. E.M. Izhikevich, *IEEE Trans. Neural Netw.* **15**(5), 1063 (2004). <https://doi.org/10.1109/TNN.2004.832719>
13. R. FitzHugh, *Bull. Math. Biophys.* **17**, 257 (1955). <https://doi.org/10.1007/BF02477753>
14. J. Nagumo, S. Arimoto, S. Yoshizawa, *Proc. IRE* **50**, 2061–2070 (1962). <https://doi.org/10.1109/JRPROC.1962.288235>
15. M. Shafiei, S. Jafari, F. Parastesh, M. Ozer, T. Kapitaniak, M. Perc, *Commun. Nonlinear Sci. Num. Simul.* **84**, 105175 (2020). <https://doi.org/10.1016/j.cnsns.2020.105175>
16. N. Burić, I. Grozdanović, N. Vasović, *Chaos, Solitons Fractals* **23**(4), 1221 (2005). <https://doi.org/10.1016/j.chaos.2004.06.033>
17. D.M. Blitz, W.G. Regehr, *Neuron* **45**(6), 917 (2005). <https://doi.org/10.1016/j.neuron.2005.01.033>
18. C. Colangelo, P. Shichkova, D. Keller, H. Markram, S. Ramaswamy, *Frontiers Neural Circ.* **13**, 24 (2019). <https://doi.org/10.3389/fncir.2019.00024>
19. S.D. Glyzin, M.M. Preobrazhenskaia, in *Advances in Neural Computation, Machine Learning, and Cognitive Research IV. NEUROINFORMATICS 2020*, ed. by B. Kryzhanovsky, W. Dunin-Barkowski, V. Redko, V. Tiumentsev. Studies in Computational Intelligence, vol. 925 SCI (2021), pp. 347–356. https://doi.org/10.1007/978-3-030-60577-3_41
20. M.F.J. Perescis, N. de Bruin, L. Heijink, C. Kruse, L. Vinogradova, A. Lüttjohann, G. van Luijtelaar, C.M. van Rijn, *PLOS ONE* **12**(2), e0165363 (2017). <https://doi.org/10.1371/journal.pone.0165363>
21. I.V. Sysoev, M.F.J. Perescis, L. Vinogradova, M.V. Sysoeva, C.M. van Rijn, *Russ. Open Med. J.* **7**(4), e0404 (2018). <https://doi.org/10.15275/rusomj.2018.0404>
22. P. Jiruska, M. de Curtis, J.G.R. Jefferys, C.A. Schevon, S.J. Schiff, K. Schindler, *J. Phys.* **591**(4), 787 (2013). <https://doi.org/10.1113/jphysiol.2012.239590>
23. R.J. Morgan, I. Soltesz, *Proc. Natl Acad. Sci.* **105**(16), 6179 (2008). <https://doi.org/10.1073/pnas.0801372105>
24. H. Wernecke, B. Sándor, C. Gros, *Phys. Rep.* **824**, 1 (2019). <https://doi.org/10.1016/j.physrep.2019.08.001>. Chaos in time delay systems, an educational review

25. I.V. Sysoev, V.I. Ponomarenko, *Rus. J. Nonlin. Dyn.* **12**(4), 567–576 (2016). <https://doi.org/10.20537/nd1604002>
26. H. Hasegawa, *Phys. Rev. E* **72**, 056139 (2005). <https://doi.org/10.1103/PhysRevE.72.056139>
27. A.C. Marreiros, J. Daunizeau, S.J. Kiebel, K.J. Friston, *NeuroImage* **42**(1), 147 (2008). <https://doi.org/10.1016/j.neuroimage.2008.04.239>

Mathematical Modeling of Calcium-Mediated Exosomal Dynamics in Neural Cells



Hina Shaheen, Sundeep Singh, and Roderick Melnik

1 Introduction

The intracellular calcium (Ca^{2+}) concentration plays a critical role in synaptic transmission and neuronal excitability, along with other neural dysfunction associated with chronic brain disorders. Moreover, intracellular Ca^{2+} concentration influences multiple cellular functions, including enzyme and release activities and the signaling of numerous plasma membranes [1]. Chronic exposure to high concentrations of the Ca^{2+} can cause neurotoxicity, which is a neurological syndrome consisting of movement abnormalities that share many Parkinsonian features. Intracellular Ca^{2+} is an important neuronal signal transduction mediator, taking part in assorted biochemical reactions that evoke changes in synaptic adequacy, metabolic rate, and gene transcription. Although the measurement of intracellular Ca^{2+} in living neurons through fluorescent Ca^{2+} markers has not reliably demonstrated a link between cytosolic Ca^{2+} and the occurrence of neuronal death, excessive cytosolic calcium has been implicated as a cause of acute neuronal injury [2].

Neurodegenerative disorders represent a heterogeneous group of diseases characterized by progressive structural and functional aggregation of misfolded proteins. It has been recently shown that these aggregated proteins may be exchanged from one

H. Shaheen · S. Singh

MS2Discovery Interdisciplinary Research Institute, Wilfrid Laurier University, Waterloo, ON, Canada

e-mail: shah8322@mylaurier.ca; ssingh@wlu.ca

R. Melnik (✉)

MS2Discovery Interdisciplinary Research Institute, Wilfrid Laurier University, Waterloo, ON, Canada

BCAM - Basque Center for Applied Mathematics, Bilbao, Spain

e-mail: rmelnik@wlu.ca

cell to another through extracellular nanovesicles called exosomes [3]. Exosomes are mostly found in all kinds of biological fluids and are basically 40–100 nm sized extracellular vesicles comprising natural lipid bilayers [4]. It has been revealed that the content of the exosomes inferred from the central nervous system is altered during disease progression, making them an appealing target for biomarker development of multiple neurodegenerative disorders, viz., Alzheimer's, Parkinson, Huntington, and Creutzfeldt-Jacob [5]. Exosome release from neurons, astrocytes, and neural cell lines triggered by depolarization-induced increased intracellular Ca^{2+} leads to the interesting possibility that activity-dependent regulation of exosome release could provide a mechanism to control neural dysfunction and temporal features of exosome in the brain [6]. Owing to their biological tolerability, exosomes provide exciting opportunities for delivering chemical components to a target cell, thereby assisting in developing novel diagnostic and therapeutic approaches [7, 8].

A recent study found that when differentiated neurons and astrocytes are depolarized, specific types of Ca^{2+} channels in differentiated neurons and astrocytes are activated, resulting in increased intracellular Ca^{2+} concentration levels, which interfere with the mobilization of multivesicular bodies and exosomal release [9]. The experimental evidence demonstrates that (a) in neurons, glutamatergic movement is improved by depolarization and an increment within the intracellular Ca^{2+} which assists with upgraded exosomal secretion and (b) intracellular Ca^{2+} levels regulate vesicular secretion and release in astrocytes [9, 12]. To provide a platform toward Ca^{2+} -mediated exosomal dynamics, we propose a more realistic mathematical model for capturing the Ca^{2+} -mediated exosomal release in the neural stem cells. Here, we will focus on the novel aspects of regulated therapeutic exosomal release by introducing mathematical models as a framework for optimizing neural models that combine depolarization, intracellular Ca^{2+} concentrations, and vesicular exocytosis. The electrical activity of a depolarized neuron via membrane potential for action potential initiation and propagation is investigated using the modified Hodgkin–Huxley neuronal model. The intracellular Ca^{2+} dynamics have been modeled by coupling the neuronal electrical activity and Ca^{2+} -mediated exocytosis, taking into account the high-voltage (L-type) and low-voltage (T-type) activated Ca^{2+} channels, plasma membrane, bulk cytosol, and endoplasmic reticulum. Furthermore, the effects of temperature on the modulated Ca^{2+} -mediated exosomal release in the neurons have also been studied that could assist in developing more accurate methods for regulating neural activity [10].

2 Mathematical Model of Ca^{2+} -Mediated Exosomal Dynamics

The present study aims at modeling the Ca^{2+} -mediated exosomal dynamics in brain differentiated into neurons considering two different approaches: (1) a simplified

neuronal model consisting of intracellular Ca^{2+} dynamics with a special focus on microdomain Ca^{2+} concentrations and (2) a more realistic neuronal model accounting for temperature effects on the intracellular Ca^{2+} dynamics with gated conductances.

A better understanding of the Ca^{2+} ions dynamics in the central nervous system could serve as a testing bed for decoding synaptic exocytosis mechanism, e.g., synaptic vesicle docking, diffusion, and neurotransmitter release. In this section, we develop a comprehensive model of Ca^{2+} dynamics and exocytosis in neurons downstream of electrical activity. Exosomal release mediated by Ca^{2+} is limited to active zones, which contain voltage-gated Ca^{2+} channels that govern Ca^{2+} from the extracellular domain, mediate, and regulate exocytosis and lead to exosomal release in the brain. The proposed model is used to analyze the coupling between electrical activity and Ca^{2+} -mediated exosomal release. We first analyze the intracellular Ca^{2+} dynamics along with the microdomain Ca^{2+} concentrations surrounding high-voltage active L-type ($[Ca]_L$) and low-voltage T-type Ca^{2+} channels (when they open and close), connected beneath the plasma membrane ($[Ca]_m$), within the endoplasmic reticulum ($[Ca]_{ER}$) and in the bulk cytosol ($[Ca]_c$). The model is developed combining Watts–Sherman and Montefusco–Pedersen models for Ca^{2+} -mediated exosomal release and regulated exocytosis as [9]

$$\frac{d[Ca]_{L|opened}}{dt} = -f \left(\alpha \frac{i_{CaL}}{V_{ud}} - B_{ud}([Ca]_L - [Ca]_m) \right), \quad (1)$$

$$\frac{d[Ca]_m}{dt} = \frac{f}{V_m} \left(-\alpha i_{CaT} + N_L V_{ud} B_{ud} m_{CaL}^2 h_{CaL} ([Ca]_L - [Ca]_m) - \right. \quad (2)$$

$$\left. V_c k_{PMCA} [Ca]_m - V_c B_M ([Ca]_m - [Ca]_c) \right),$$

$$\frac{d[Ca]_c}{dt} = f(B_m([Ca]_m - [Ca]_c) + p_{leak}([Ca]_{ER} - [Ca]_c) - k_{SERCA}[Ca]_c), \quad (3)$$

$$\frac{d[Ca]_{ER}}{dt} = \frac{f V_c}{V_{ER}} (p_{leak}([Ca]_{ER} - [Ca]_c) - k_{SERCA}[Ca]_c), \quad (4)$$

where $i_{CaL} = (g_{CaL}(v_m - V_{Ca}))/N_L$ is the Ca^{2+} current entering the L-type Ca^{2+} channel, $i_{CaT} = g_{CaT} m_{CaT}^3 h_{CaT} (v_m - V_{Ca})$ is the Ca^{2+} current entering through T-type Ca^{2+} channel, g_{CaL} is the membrane conductance of the L-type Ca^{2+} channel, g_{CaT} is the membrane conductance of T-type Ca^{2+} channel, $m_{CaL}^2 h_{CaL}$ and $m_{CaT}^3 h_{CaT}$ represent the opening probability for the L-type and T-type Ca^{2+} channels, respectively, and N_L is the number of L-type Ca^{2+} channels [9]. α is the constant that converts current to flux, f is the ratio of free-to-total Ca^{2+} , B_m is the flux from sub-membrane compartment to bulk cytosol, B_{ud} is the constant flux from microdomains to sub-membrane, k_{PMCA} is the rate of Ca^{2+} adenosine

triphosphatase (ATPase) through the plasma membrane, p_{leak} is the rate of the leak current from the ER to the cytosol, and $k_{S\text{ERCA}}$ is the rate of Sarco/endoplasmic Ca^{2+} ATPase pump-dependent sequestration of Ca^{2+} into the ER, and V_d , V_m , V_c , and V_{ER} are the volumes of single microdomain, sub-membrane compartment, bulk cytosol, and ER, respectively [9]. The gating variables are defined as

$$\frac{dm_x}{dt} = \frac{m_{x,\infty}(v_m) - mx}{\tau_{mx}(v_m)}; \quad \frac{dh_x}{dt} = \frac{h_{x,\infty}(v_m) - hx}{\tau_{hx}(v_m)}, \quad (5)$$

where $x \in (Ca_L, Ca_T, Na, K)$ and

$$\begin{cases} m_{K/Na,\infty} = \frac{\alpha_{mK/Na}}{\alpha_{mK/Na} + \beta_{mK/Na}}; & h_{Na,\infty} = \frac{\alpha_{hNa}}{\alpha_{hNa} + \beta_{hNa}}, \\ \tau_{hNa} = \frac{1}{\alpha_{hNa} + \beta_{hNa}}; & \tau_{mK/Na} = \frac{1}{\alpha_{mK/Na} + \beta_{mK/Na}}, \\ \alpha_{mNa} = \frac{(0.1(v_m+40))}{(1-\exp(-(v_m+40)/10))}; & \beta_{mNa} = \frac{(4\exp(-(v_m+65)))}{18}, \\ \alpha_{mK} = \frac{(0.01(v_m+55))}{1-\exp(-(v_m+55)/10)}; & \beta_{mK} = \frac{0.125\exp(-(v_m+65))}{80}, \\ \alpha_{hNa} = \frac{(0.07\exp(-(v_m+65)))}{20}; & \beta_{hNa} = \frac{1}{1+\exp(-(v_m+35)/10)}. \end{cases} \quad (6)$$

The time constants and the gating variables in the steady state for $x \in (T, L)$ are defined as

$$\begin{cases} m_{Ca_x,\infty} = \frac{1}{1+\exp\left(\frac{-v_m - v_m Ca_x}{S m_{Ca_x}}\right)}; & h_{Ca_x,\infty} = \frac{1}{1+\exp\left(\frac{-v_m - v_h Ca_x}{S h_{Ca_x}}\right)}, \\ \tau_{m_{Ca_x}} = \frac{\tau_m v_{Ca_x}}{\exp\left(\frac{-(v_m - v_m Ca_x)}{S \tau_m Ca_x}\right) + \exp\left(\frac{(v_m - v_m Ca_x)}{S \tau_m Ca_x}\right)} + \tau_m 0_{v_{Ca_x}}, \\ \tau_{h_{Ca_x}} = \frac{\tau_h v_{Ca_x}}{\exp\left(\frac{-(v_m - v_h Ca_x)}{S \tau_h Ca_x}\right) + \exp\left(\frac{(v_m - v_h Ca_x)}{S \tau_h Ca_x}\right)} + \tau_h 0_{v_{Ca_x}}. \end{cases} \quad (7)$$

The relative exosomal release rate in neurons depending on L-type Ca^{2+} microdomain concentrations and plasma membrane Ca^{2+} concentrations can be represented, respectively, as follows [9]:

$$R_{Ca_L} = m_{Ca_L}^2 h_{Ca_L} F_H([Ca]_{L|opened}, K_L, n_L) + (1 - m_{Ca_L}^2 h_{Ca_L}) F_H([Ca]_{L|closed}, K_L, n_L), \quad (8)$$

$$R_{Ca_m} = F_H([Ca]_m, K_m, n_m), \quad (9)$$

where $F_H(x, K, n) = \phi \frac{x^n}{x^n + K^n}$ is the Hill function, $[Ca]_{L|closed} = [Ca]_m$, and ϕ is a fusion constant given in s^{-1} [9]. Experimental evidences have revealed that Ca^{2+} -mediated exocytosis by neurons is regulated by intracellular Ca^{2+} where Ca^{2+} threshold of exocytosis depends on the pattern of electrical activity [9]. The electrical activity triggered by the neuron depolarization includes the activation of

voltage-gated Ca^{2+} channels upon cell depolarization, due to increased intracellular Ca^{2+} concentration levels, which interfere with the mobilization of multivesicular bodies, resulting in exosome release and exocytosis. As mentioned, we adopt the modified Hodgkin–Huxley neuron model for describing the neural signals of a depolarized neuron via membrane potential (v_m) that depends on voltage-gated potassium (K^+) channel, voltage-gated sodium (Na^+) channel, leak current, and induced control signal/current (i_{ind}) as [9]

$$\frac{dv_m}{dt} = \frac{-1}{C_m} \left[g_K (v_m - V_K) + g_{Na} (v_m - V_{Na}) + g_L (v_m - V_L) - i_{ind} \right], \quad (10)$$

where C_m is the membrane capacitance, V_K , V_{Na} , V_{Ca} , and V_L are Nernst potentials for K^+ , Ca^{2+} , and Na^+ ions and other ions clubbed as a leak channel, respectively, and g_K , V_{Na} , and g_L are the corresponding membrane conductances. Voltage-gated conductances ($g_K = \bar{g}_K m_K^4$ and $g_{Na} = \bar{g}_{Na} m_{Na}^3 h_{Na}$) change with time during the action potential initiation and dissemination. Moreover, m_K^4 and $m_{Na}^3 h_{Na}$ represent the opening probability for K^+ and Na^+ channels. The gating variables m_K , m_{Na} , and h_{Na} are defined in Eq. (7). Furthermore, we will construct a more realistic neuronal model where the main characteristics account for temperature effects on Ca^{2+} -mediated exosomal release in the neurons. Potassium currents exceed sodium currents at higher temperatures, resulting in action potential failure. Thermal inhibition may, however, be explained by other temperature-dependent alterations [10]. Therefore, understanding the effects of temperature on Ca^{2+} -mediated exosomal release may be extremely useful in developing more accurate methods of regulating neural activity in the brain. We will use the modified Hodgkin–Huxley model to capture the response of Ca^{2+} -mediated exosomal release in the neurons by varying the peak sodium and potassium conductances with temperature. It has been shown that the resting potential varies with the temperature [10]. In the simplified neuronal model, the peak sodium and potassium conductances \bar{g}_{Na} and \bar{g}_K were assumed to be constant and independent of temperature, but these values vary with temperature for a more realistic neuronal model, i.e., $g_K = g_{Kmax}(T) m_K^4$ and $g_{Na} = g_{Namax}(T) m_{Na}^3 h_{Na}$, where $g_{Kmax}(T) = 1.60e^{-\left(\frac{T-27.88}{12.85}\right)^2}$ and $g_{Namax}(T) = 0.42e^{-\left(\frac{T-31.83}{31.62}\right)^2}$ [9]. Thus, while modeling the temperature effects, only the membrane potential, given in Eq. (10), will be modified, and the values of peak conductances will be computed from the temperature-dependent gating variables defined as

$$\begin{cases} \frac{dm_{K/Na}}{dt} = \phi_{m_{K/Na}}(T)(\alpha_{m_{K/Na}}(1 - m_{K/Na}) - \beta_{m_{K/Na}} m_{K/Na}), \\ \frac{dh_{Na}}{dt} = \phi_{h_{Na}}(T)(\alpha_{h_{Na}}(1 - h_{Na}) - \beta_{h_{Na}} h_{Na}), \end{cases} \quad (11)$$

where

$$\begin{cases} \phi_{m_K}(T) = 3^{\frac{10-6.3}{10}} 3^{\frac{15-10}{10}} 2.8^{\frac{20-15}{10}} 2.7^{\frac{T-20}{10}}, \\ \phi_{m_{Na}}(T) = 3^{\frac{10-6.3}{10}} 2.9^{\frac{15-10}{10}} 3^{\frac{20-15}{10}} 3^{\frac{T-20}{10}}, \\ \phi_{h_{Na}}(T) = 3^{\frac{10-6.3}{10}} 2.8^{\frac{15-10}{10}} 2.4^{\frac{20-15}{10}} 2.3^{\frac{T-20}{10}}, \end{cases} \quad (12)$$

are adopted from [10] for the considered temperature of 25 °C.

3 Results and Discussion

In this chapter, a numerical study has been performed for quantifying the effects of a control signal, membrane potential, gated conductances, and temperature on Ca^{2+} -mediated exosomal dynamics in the neurons. Notably, Ca^{2+} -mediated exocytosis has been quantified on the membrane potential with particular attention given to microdomain Ca^{2+} concentrations that surrounds the high-voltage L-type and low-voltage T-type Ca^{2+} channels that links to the description of Ca^{2+} within the bulk cytosol and the endoplasmic reticulum under the plasma membrane using the simplified neuronal model. Whereas the effects of temperature on the Ca^{2+} -mediated exosomal dynamics have been investigated utilizing the more realistic neuronal model. The numerical results presented in this section have been obtained using the parameter values collected from [9] and [10], as presented in Table 1. A finite element method implemented via [11] has been used to solve the set of coupled ordinary differential equations of the simplified and more realistic neuronal model.

Motivated by Veletić et al. [9], an external stimulus has been applied to excite the neurons by applying the current pulses ranging from amplitudes of 5–20 $\mu\text{A}/\text{cm}^2$ for a duration of 500 ms, as depicted in Fig. 1a. The effects of the induced pulse of 20 $\mu\text{A}/\text{cm}^2$ on the membrane potential with temperature ($T = 25^\circ\text{C}$) and without the temperature effects have been presented in Fig. 1b. As evident from this figure, the rate of generated sequences of the action potentials is proportional to both the magnitude and the duration of the external stimuli. Not only this, but also the spiking sequences are also significantly reduced when the temperature effects are incorporated within the numerical model. Importantly, the voltage-gated calcium channels in the membrane are regulated by these spiking sequences [9].

The effects of the temperature on the microdomain calcium concentrations have been presented in Fig. 2. As seen from the analysis of this figure, the intracellular Ca^{2+} concentrations in the closed and open channels of L-type, plasma membrane, bulk cytosol, and endoplasmic reticulum are significantly overestimated if the effect of temperature is neglected. Moreover, the exosomal release rate in neurons directly linked with the Ca^{2+} concentrations in different compartments has been presented in Fig. 3. Again, there prevail significant deviations among the two considered cases. The exosomal release rate is relatively higher when temperature effects are

Table 1 Parameter set for calcium-mediated exosomal dynamics

Parameter	Value	Parameter	Value	Parameter	Value
V_K	-70 (mV)	V_L	-54.4 (mV)	V_{hCa_T}	-52 (mV)
$V_{\tau_{hCa_T}}$	-50 (mV)	$V_{\tau_{mCa_T}}$	-50 (mV)	$V_{\tau_{hCa_L}}$	0 (mV)
V_{mCa_T}	-49 (mV)	V_{hCa_L}	-33 (mV)	V_{mCa_L}	-30 (mV)
$V_{\tau_{mCa_L}}$	-23 (mV)	S_{hCa_L}	-5 (mV)	S_{hCa_T}	-5 (mV)
$\tau_{m0V_{Ca_T}}$	0 (ms)	V_{ud}	2.62×10^{-19} (L)	α	5×10^{-15} ($\mu\text{molpm}/\text{As}$)
V_m	5×10^{-14} (L)	V_c	5.7×10^{-13} (L)	p_{leak}	3×10^{-4} (ms^{-1})
f	0.01	$\tau_{m0V_{Ca_L}}$	0.05 (ms)	k_{SERCA}	0.100 (ms^{-1})
B_m	0.128 (ms^{-1})	g_L	0.3 (mS/cm^3)	k_{PMCA}	0.300 (ms^{-1})
g_{Ca_T}	0.4 (nS)	g_{Ca_L}	0.7 (nS)	C_m	1 ($\mu\text{F}/\text{cm}^2$)
$\tau_{mV_{Ca_I}}$	1 (ms)	K_m	2 (μM)	n_L	4
n_m	4	S_{mCa_T}	4 (mV)	$\tau_{h0V_{Ca_T}}$	5 (ms)
S_{mCa_L}	10 (mV)	T	10°C	$S_{\tau_{mCa_T}}$	12 (mV)
$\tau_{mV_{Ca_T}}$	15 (ms)	$S_{\tau_{hCa_T}}$	15 (mV)	$S_{\tau_{mCa_I}}$	20 (mV)
$S_{\tau_{hCa_L}}$	20 (mV)	$\tau_{hV_{Ca_T}}$	20 (ms)	$\frac{V_c}{V_{ER}}$	31
\bar{g}_K	36 (mS/cm^3)	V_{Na}	50 (mV)	K_L	50 (μM)
$\tau_{h0V_{Ca_L}}$	51 (ms)	$\tau_{hV_{Ca_L}}$	60 (ms)	V_{Ca}	65 (mV)
\bar{g}_{Na}	120 (mS/cm^3)	N_L	200	B_{ud}	264 (ms^{-1})

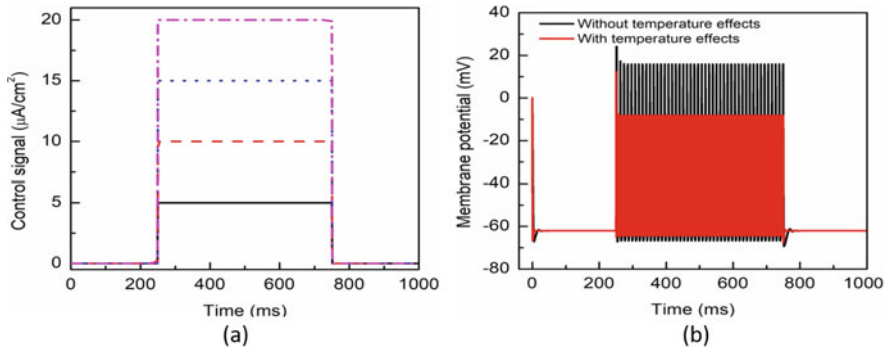


Fig. 1 (Color online) (a) Induced control signals/currents and (b) the effect of temperature on the responses/spiking sequence in the depolarized neurons for $i_{ind} = 20 \mu\text{A}/\text{cm}^2$

incorporated within the model. This can be attributed to the fact that an increase in temperature values will lead to corresponding increase in the net hyperpolarizing current. Although due to the increased speed of sodium/potassium ions gated conductances, the sodium inward current became shorter and the potassium outward current became stronger and wider. As the membrane was depolarized by the action potential, the net current became steadily outward (hyperpolarizing) with increasing temperature. Thus, the exosomal release rate of the targeted neuron is significantly

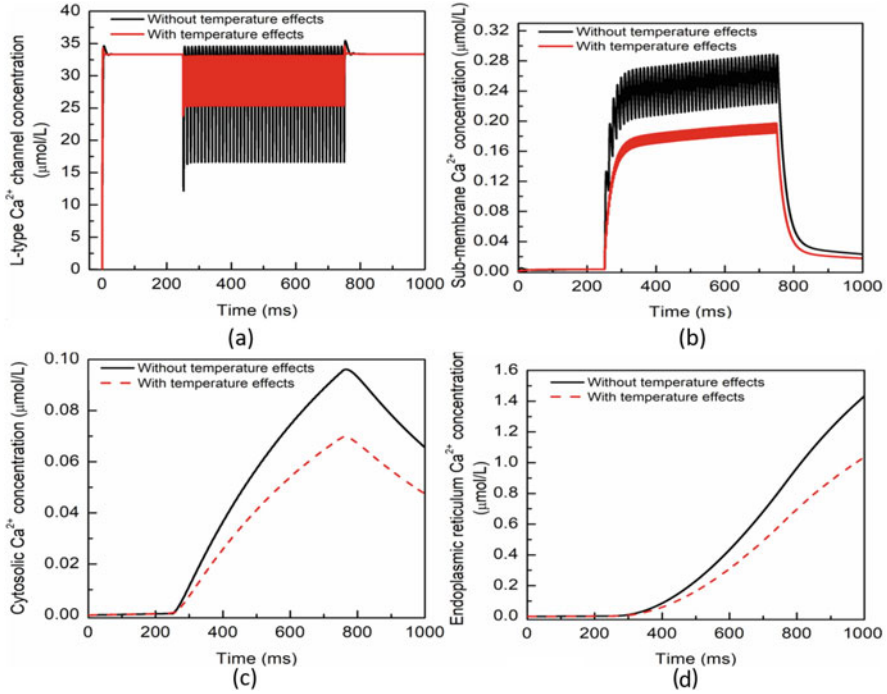


Fig. 2 (Color online) Microdomain calcium concentrations: (a) $[Ca]_L$, (b) $[Ca]_m$, (c) $[Ca]_c$, and (d) $[Ca]_{ER}$ with and without temperature effects corresponding to control signal of $i_{ind} = 20 \mu A/cm^2$

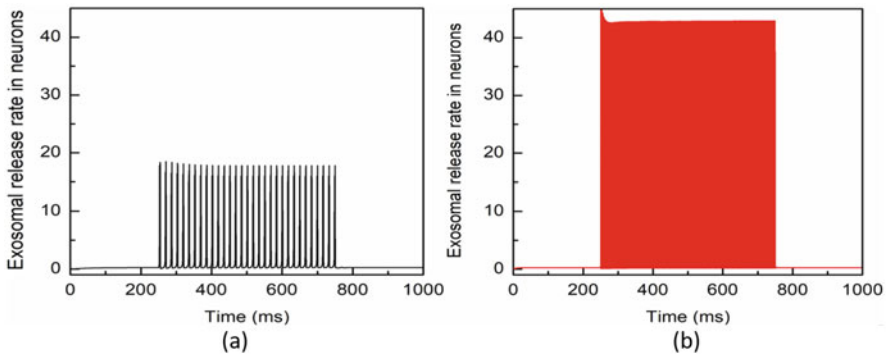


Fig. 3 (Color online) The rate of released exosomes in neurons: (a) without temperature and (b) with temperature corresponding to control signals of $i_{ind} = 20 \mu A/cm^2$

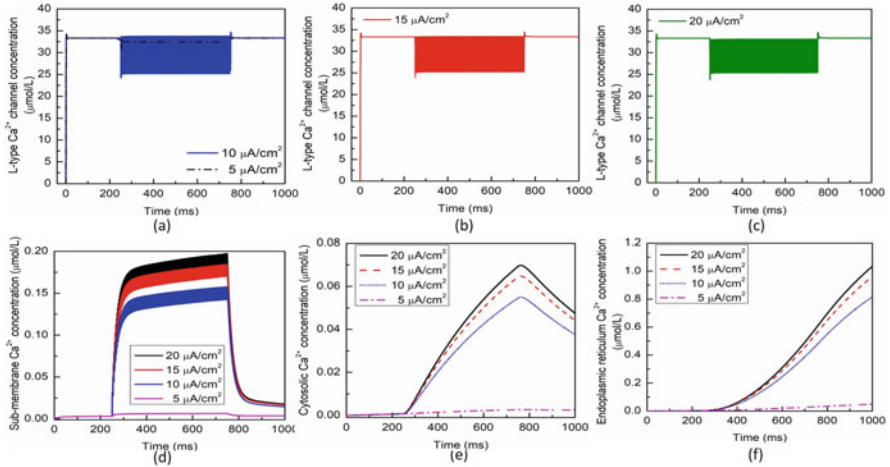


Fig. 4 (Color online) Microdomain calcium concentrations for (a–c) $[Ca]_L$, (d) $[Ca]_m$, (e) $[Ca]_c$, and (f) $[Ca]_{ER}$ corresponding to control signal shown in Fig 1a ranging from $i_{ind} = 5\text{--}20 \mu\text{A/cm}^2$ incorporating temperature effects

affected by the changes in temperature. Furthermore, the effect of the control signal presented in Fig. 1a on the microdomain calcium concentrations has been depicted in Fig. 4. As evident, the increase in the amplitude of the control signal stimuli from 5 to $20 \mu\text{A/cm}^2$ results in a corresponding increase in the concentration of $[Ca]_{ER}$, $[Ca]_m$, $[Ca]_c$ concentrations, while the effect on the $[Ca]_L$ concentration is quite negligible.

4 Conclusions

In this chapter, we proposed a new numerical model for accurately quantifying the Ca^{2+} -mediated exosomal release influenced by the externally applied stimulus to the neurons accounting for temperature effects, a feature that lends potentially more realistic predictions. Our predictions suggest that cell depolarization in neurons is directly related to the exosomal release which is further proportional to the applied stimulation. The novelty of the present research is in the development of Ca^{2+} -mediated exosomal dynamics model of neurons accounting for the temperature effects. Furthermore, it has been observed that calcium concentrations in the respective compartments and thus the overall Ca^{2+} -mediated exosomal dynamics are significantly affected by the changes in temperature. The developed neuronal model and the results presented in this study provide an important initial step for our better understanding of the exosomal dynamics. The authors believe that the developed model would provide a pathway for the generation of new models for optimizing and designing exosomes based drug delivery systems for the treatment

of brain pathologies. Future studies will be focused on the inclusion of other calcium compartments, as well as on the development of a new stochastic model based on the ideas highlighted here.

Acknowledgments Authors are grateful to the NSERC and the CRC Program for their support. RM is also acknowledging support of the BERC 2018-2021 program and Spanish Ministry of Science, Innovation and Universities through the Agencia Estatal de Investigacion (AEI) BCAM Severo Ochoa excellence accreditation SEV-2017-0718, and the Basque Government fund AI in BCAM EXP. 2019/00432.

References

1. Y. Buskila, A. Bellot-Saez, J.W. Morley, Generating brain waves, the power of astrocytes. *Front. Neurosci.* **13**, 1125 (2019)
2. K.K. Jain, Neuroprotection in Alzheimer disease, in *The Handbook of Neuroprotection*, 2nd edn. (Humana Press, New York, 2019), pp. 465–585
3. F. Ferrantelli, C. Chiozzini, P. Leone, F. Manfredi, M. Federico, Engineered extracellular vesicles/exosomes as a new tool against neurodegenerative diseases. *Pharmaceutics* **12**(6), 529 (2020)
4. J.E. Pullan, M.I. Confeld, J.K. Osborn, J. Kim, K. Sarkar, S. Mallik, Exosomes as drug carriers for cancer therapy. *Mol. Pharm.* **16**(5), 1789–1798 (2019)
5. S. Luo, L. Du, Y. Cui, Potential therapeutic applications and developments of exosomes in Parkinson's disease. *Mol. Pharm.* **17**(5), 1447–1457 (2020)
6. Z. Deng, J. Wang, Y. Xiao, F. Li, L. Niu, X. Liu, L. Meng, H. Zheng, Ultrasound-mediated augmented exosome release from astrocytes alleviates amyloid- β -induced neurotoxicity. *Theranostics* **11**(9), 4351 (2021)
7. Y.S. Kim, J.S. Ahn, S. Kim, H.J. Kim, S.H. Kim, J.S. Kang, The potential theragnostic (diagnostic+therapeutic) application of exosomes in diverse biomedical fields. *Korean J. Physiol. Pharmacol.* **22**(2), 113–125 (2018)
8. M. Veletić, M.T. Barros, I. Balasingham, S. Balasubramaniam, A molecular communication model of exosome-mediated brain drug delivery, in *NANOCOM '19* (ACM, New York, 2019), pp.1–7. <https://doi.org/10.1145/3345312.3345478>
9. M. Veletić, M.T. Barros, H. Arjmandi, S. Balasubramaniam, I. Balasingham, Modeling of modulated exosome release from differentiated induced neural stem cells for targeted drug delivery. *IEEE Trans. Nanobiosci.* **19**(3), 357–367 (2020)
10. M. Ganguly, M.W. Jenkins, E.D. Jansen, H.J. Chiel, Thermal block of action potentials is primarily due to voltage-dependent potassium currents: a modeling study. *J. Neural Eng.* **16**(3), 036020 (2019)
11. COMSOL Multiphysics® v. 5.5. www.comsol.com. COMSOL AB, Stockholm
12. A. Mizuma, J.Y. Kim, R. Kacimi, K. Stauderman, M. Dunn, S. Hebbar, M.A. Yenari, Microglial calcium release-activated calcium channel inhibition improves outcome from experimental traumatic brain injury and microglia-induced neuronal death. *J. Neurotrauma* **36**(7), 996–1007 (2019)

Forward Sensitivity Analysis of the FitzHugh–Nagumo System: Parameter Estimation



Shady E. Ahmed, Omer San, and Sivaramakrishnan Lakshmivarahan

1 Introduction

Dynamical systems are ubiquitous around us and in every scientific discipline. Examples from physical sciences include atmospheric and oceanic flows, heat and mass transfer, the behavior of moving objects (e.g., cars, ships, airplanes, rockets, pendulums, etc.), chemical reactions, and signal transmission. In social sciences, the population increase and distribution, human interactions, and cultural developments over centuries have been following interesting dynamical patterns. Researchers and practitioners in life sciences have also found that the application of dynamical systems theories to the bodies, organs, and cells yields significant advancement in our understanding and treatment of the body. In neurosciences, the understanding of brain performance and response to external stimulus has been critical for epilepsy prevention and treatment. Several dynamical models have been historically proposed and investigated to study and analyze the neuronal activity (e.g., see [1]). The FitzHugh–Nagumo (FHN) equations [2–4] represent one of the very popular and simple models in the study of neurophysiology. In addition to its utility for the modeling of biological behavior, it is considered a prototypical model in the study of nonlinear dynamics due to its interesting characteristics such as the bifurcation properties [5].

S. E. Ahmed (✉) · O. San
School of Mechanical & Aerospace Engineering, Oklahoma State University, Stillwater,
OK, USA
e-mail: shady.ahmed@okstate.edu; osan@okstate.edu
<https://go.okstate.edu/>

S. Lakshmivarahan
School of Computer Science, University of Oklahoma, Norman, OK, USA
e-mail: varahan@ou.edu
<https://www.ou.edu/>

The two-equation FHN model, describing neuronal spike discharges, can be defined as

$$\frac{dv}{dt} = v - \frac{1}{3}v^3 - w + I, \quad (1)$$

$$\tau \frac{dw}{dt} = v + a - bw, \quad (2)$$

where v defines the membrane potential, w stands for a recovery variable, and τ is the time scale. I represents the external input current, while a and b are controlling parameters. The FHN model might appear in various forms, which can be related to Eqs. (1)–(2) by a set of changes of variables and coordinate transformations. It describes the dynamics of excitable systems, which can be observed in various natural systems such as neuronal dynamics, electrocardiology, chemical reactions, and climate dynamics. However, the parameters in the FHN model are difficult to be computed directly in a real-world experimentation, and the estimation of these parameters has gained the interest of a lot of researchers in physiological sciences. We shall see in the following discussions that the specification of the model parameters is crucial for the prediction of the system's behavior. For instance, the system can either converge to a stable fixed point or exhibit a limit cycle. Thus, the knowledge of such parameters can be very useful for diagnostic and prediction purposes, and the objective of the current study is to estimate the model's parameters from a few (possibly noisy) measurements of the system's state.

The parameter estimation framework for FHN model can be generally formulated via standard techniques such as simulated annealing, genetic algorithms, differential evolution, and Kalman filtering extensions. Besides, the known model's structure and characteristics can be utilized to customize an algorithm to estimate the parameters of the respective model. For example, the time-scale separation in the FHN model has been exploited to infer the model's parameters [6]. Che et al. [7] solved the parameter estimation problem by deriving a second-order differential equation for the membrane potential, being the observed quantity. A least-squares-based regression was then applied and equipped by a wavelet denoising technique to reduce the effect of noise contamination. Geng et al. [8] applied an expectation maximization-based algorithm to identify generic FHN model parameters and estimate the variance of the interfering Gaussian noise. Jensen et al. [9] applied a Markov chain Monte Carlo method to infer the parameters in a stochastic FHN model, constructed by adding a noise term governed by a Brownian motion. Melnykova [10] proposed a contrast estimator technique to infer the model's parameters in the asymptotic setting.

In this chapter, we utilize a variational data assimilation technique, namely the forward sensitivity method (FSM) [11, 12], to identify the correct parameter values. The inherent sensitivity analysis reveals the relative dependence of the cost functional, defined by the discrepancy between the identified model's predictions and the actual observations, onto the respective parameters. We also investigate the effect of observation placement instants on the shape of the cost functional and the

corresponding sensitivities. We finally highlight measurement collection guidelines that potentially improve the parameter inference iterations.

2 Parameter Estimation Framework

The FHN model can be described as

$$\dot{\mathbf{x}} = f(\mathbf{x}, \boldsymbol{\alpha}), \quad (3)$$

where $\mathbf{x} = [v(t), w(t)]^T$ denotes the system's state, $\boldsymbol{\alpha} = [a, b]^T$ is the model's parameters, and f represents the continuous-time dynamics of the FHN model (i.e., $f(\mathbf{x}; \boldsymbol{\alpha}) = [v - \frac{1}{3}v^3 - w + I, (v + a - bw)/\tau]^T$). Assuming that the model f is continuously differentiable in its arguments (i.e., \mathbf{x} and $\boldsymbol{\alpha}$), its Jacobians with respect to the state \mathbf{x} and the parameter $\boldsymbol{\alpha}$ can be defined as below:

$$Df_{\mathbf{x}} = \begin{bmatrix} 1 - v^2 & -1 \\ 1/\tau & -b/\tau \end{bmatrix}, \quad Df_{\boldsymbol{\alpha}} = \begin{bmatrix} 0 & 0 \\ 1/\tau & -w/\tau \end{bmatrix}, \quad (4)$$

where $Df_{\mathbf{x}}$ and $Df_{\boldsymbol{\alpha}}$ define the model's sensitivity with respect to the state \mathbf{x} and the parameters $\boldsymbol{\alpha}$, respectively.

2.1 Forward Sensitivities

Using a suitable temporal integration scheme, the FHN can be rewritten in a discrete-time form as follows:

$$\mathbf{x}(k+1) = \mathbf{M}(\mathbf{x}(k), \boldsymbol{\alpha}), \quad (5)$$

where $\mathbf{x}(k) = [v(t_k), w(t_k)]^T \in \mathbb{R}^2$ defines the system's state at time t_k , and $\mathbf{M} : \mathbb{R}^2 \times \mathbb{R}^2 \rightarrow \mathbb{R}^2$ represents the one-step state transition map. Thus, the following discrete-time Jacobians can be computed:

$$\mathbf{DM}_{\mathbf{x}}(k) = \left[\frac{\partial M_i(\mathbf{x}, \boldsymbol{\alpha})}{\partial x_j} \right]_{\mathbf{x}=\mathbf{x}(k)}, \quad \mathbf{DM}_{\boldsymbol{\alpha}}(k) = \left[\frac{\partial M_i(\mathbf{x}, \boldsymbol{\alpha})}{\partial \alpha_j} \right]_{\mathbf{x}=\mathbf{x}(k)}. \quad (6)$$

Furthermore, we define the sensitivity of the model forecast at any time t_k with respect to the model's parameters as follows:

$$\mathbf{V}(k) = \left[\frac{\partial x_i(k)}{\partial \alpha_j} \right] \in \mathbb{R}^{2 \times 2}. \quad (7)$$

Equation (5) can be used to evaluate the forward sensitivity matrices at different times in a recursive way as

$$\mathbf{V}(k+1) = \mathbf{D}\mathbf{M}_x(k)\mathbf{V}(k) + \mathbf{D}\mathbf{M}_\alpha(k), \quad (8)$$

with $\mathbf{V}(0) = \mathbf{0}$ since the initial condition $\mathbf{x}(0)$ is independent of the model's parameters α .

2.2 Forecast Error

In order to approximate the forecast error, we assume that we have a set of measurements so that we can assess the model predictions. In particular, the measurement vector $\mathbf{z}(k) \in \mathbb{R}^m$ at time t_k is defined as

$$\mathbf{z}(k) = \mathbf{h}(\bar{\mathbf{x}}(k)) + \boldsymbol{\xi}(k), \quad (9)$$

where $\mathbf{h} : \mathbb{R}^2 \rightarrow \mathbb{R}^m$ is the observational operator that relates the model space to the observation space, and $\bar{\mathbf{x}}$ stands for the *true* system's state while $\boldsymbol{\xi}$ denotes the measurement noise. For simplicity, we suppose that we directly measure the system's state (i.e., $\mathbf{h}(\bar{\mathbf{x}}(k)) = \bar{\mathbf{x}}(k)$). We also assume that $\boldsymbol{\xi}$ is a white Gaussian noise with zero mean and a covariance matrix \mathbf{R} (i.e., $\boldsymbol{\xi}(k) = \mathcal{N}(\mathbf{0}, \mathbf{R}(k))$).

We define the difference between the model forecast and measurements as $\mathbf{e}(k) = \mathbf{z}(k) - \mathbf{h}(\mathbf{x}(k))$, which is called the innovation or forecast error (computed in the observation space). With the assumption that the dynamical model is perfect (i.e., correctly encapsulates all the relevant processes) and the initial condition $\mathbf{x}(0)$ is known, then the deterministic part of the forecast error can be attributed to the inaccuracy of the values of model's parameters, defined as $\delta\alpha = \bar{\alpha} - \alpha$, where $\bar{\alpha}$ denotes the true values of the parameters. Thus, we can define a cost functional $J : \mathbb{R}^2 \rightarrow \mathbb{R}$ as

$$J(\alpha) = \sum_{k=1}^N \frac{1}{2} \|\mathbf{e}(k)\|_{\mathbf{R}^{-1}(k)}^2 = \sum_{k=1}^N \frac{1}{2} \mathbf{e}(k)^T \mathbf{R}^{-1}(k) \mathbf{e}(k), \quad (10)$$

where N is the number of measurement instants. The minimization of the cost function J can be solved as a strong constrained problem with the standard Lagrangian multiplier method, resulting in the adjoint framework. Alternatively, we utilize the forward sensitivity matrices to evaluate an optimal estimate for the parameters α . Let $\delta\mathbf{x}(k) = \bar{\mathbf{x}}(k) - \mathbf{x}(k)$ be the difference between the model's forecast and the true state, with $\delta\mathbf{x}(0) = \mathbf{0}$ since the initial conditions are perfectly known. With first-order Taylor expansions of $\mathbf{e}(k)$ and $\delta\mathbf{x}(k)$, the following expressions can be defined:

$$\mathbf{e}(k) = \mathbf{D}\mathbf{h}(k)\delta\mathbf{x}(k), \quad \delta\mathbf{x}(k) = \mathbf{V}(k)\delta\alpha, \quad (11)$$

where \mathbf{Dh} is the Jacobian of the observational operator \mathbf{h} . Therefore, the forecast error can be related to the correction to the model's parameters as $\mathbf{e}(k) = \mathbf{Dh}(k)\mathbf{V}(k)\delta\boldsymbol{\alpha}$. Since we assume that $\mathbf{h}(\mathbf{x}(k)) = \mathbf{x}(k)$, we deduce that \mathbf{Dh} reduces to the identity matrix. The previous forecast error formulation can be written for all N time instants at which observations become available, and the following linear equation is obtained:

$$\mathbf{H}\delta\boldsymbol{\alpha} = \mathbf{e}_F, \quad (12)$$

where the matrix $\mathbf{H} \in \mathbb{R}^{Nm \times 2}$ and the vector $\mathbf{e}_F \in \mathbb{R}^{Nm}$ are defined as follows:

$$\mathbf{H} = \begin{bmatrix} \mathbf{Dh}(1)\mathbf{V}(1) \\ \mathbf{Dh}(2)\mathbf{V}(2) \\ \vdots \\ \mathbf{Dh}(N)\mathbf{V}(N) \end{bmatrix}, \quad \mathbf{e}_F = \begin{bmatrix} \mathbf{e}(1) \\ \mathbf{e}(2) \\ \vdots \\ \mathbf{e}(N) \end{bmatrix}. \quad (13)$$

The inverse problem can be solved in a weighted least-squares sense to find an optimal correction vector $\delta\boldsymbol{\alpha}$, with \mathbf{R}^{-1} as a weighting matrix, where \mathbf{R} is an $Nm \times Nm$ block diagonal matrix with $\mathbf{R}(k)$ being its k -th diagonal block. We assume that \mathbf{R} is a diagonal matrix defined as $\mathbf{R} = \sigma^2 \mathbf{I}_{Nm}$, where \mathbf{I}_{Nm} is the $Nm \times Nm$ identity matrix. Then, the solution to Eq. (12) can be written as

$$\delta\boldsymbol{\alpha} = \left(\mathbf{H}^T \mathbf{R}^{-1} \mathbf{H} \right)^{-1} \mathbf{H}^T \mathbf{R}^{-1} \mathbf{e}_F. \quad (14)$$

2.3 Placement of Observations Using Forward Sensitivity

In order to select the time instants at which measurement data are collected, we relate the cost functional given in Eq. (10) to the forward sensitivity matrix $\mathbf{V}(k)$. This is based on the method proposed by Lakshmivarahan et al. [13] to control the shape of the cost functional and keep its gradient away from zero. By substituting $\mathbf{e}(k) = \mathbf{Dh}(k)\mathbf{V}(k)\delta\boldsymbol{\alpha}$ into Eq. (10), we get the following:

$$J(\boldsymbol{\alpha}) = \sum_{k=1}^N \frac{1}{2} \delta\boldsymbol{\alpha}^T \left(\mathbf{E}(k)^T \mathbf{R}^{-1}(k) \mathbf{E}(k) \right) \delta\boldsymbol{\alpha} = \sum_{k=1}^N \frac{1}{2} \delta\boldsymbol{\alpha}^T \mathbf{G}(k) \delta\boldsymbol{\alpha}, \quad (15)$$

where $\mathbf{E}(k) = \mathbf{Dh}(k)\mathbf{V}(k)$ and $\mathbf{G}(k) = \mathbf{E}(k)^T \mathbf{R}^{-1}(k) \mathbf{E}(k)$. We note that $\mathbf{G}(k)$ is called the observability Gramian. The gradient of the cost functional with respect to the parameter vector $\boldsymbol{\alpha}$ can be written as below:

$$\nabla_{\alpha} J(\alpha) = \sum_{k=1}^N -\mathbf{G}(k)\delta\alpha, \quad (16)$$

which relates the gradient of the cost functional and the parameterization error/correction. From Eq. (16), a necessary condition for the minimization of the cost functional is that $\mathbf{G}(k)$ is positive definite. For the case considered here, $\mathbf{Dh}(k) = \mathbf{I}$ and $\mathbf{R}^{-1}(k) = \frac{1}{\sigma^2}\mathbf{I}$. Thus, $\mathbf{G}(k) = \frac{1}{\sigma^2}\mathbf{V}(k)^T\mathbf{V}(k)$, where $\mathbf{V}(k) = \begin{bmatrix} V_{11} & V_{12} \\ V_{21} & V_{22} \end{bmatrix}$. Therefore, one way to guarantee that the gradient of the cost functional does not hit zero is to select the measurement instants in such a way that the diagonal entries (i.e., $V_{11}^2 + V_{21}^2$ and $V_{12}^2 + V_{22}^2$) are as large as possible.

3 Results and Discussions

We analyze the capability of the forward sensitivity approach to identify the FHN model's parameters. In particular, we study an arbitrary case where the true parameters' values are $a = 0.15$ and $b = 0.35$. Initial conditions of $(v(0), w(0)) = (0.0, 1.0)$ are considered, and the fourth-order Runge–Kutta scheme is applied for time integration with a time step of $\Delta t = 0.1$, time scale $\tau = 10$, and a maximum time of $t_m = 100$. We assume that the measurements are collected every 200 time steps, corrupted by an additive Gaussian noise with a zero mean and a standard deviation of $\sigma = 0.1$.

3.1 Fixed Input

As a first investigation, we study the case with zero input (i.e., $I = 0$). This corresponds to a fixed point of $(v^*, w^*) = (-0.229, -0.225)$ with a model Jacobian of $\begin{bmatrix} 0.948 & -1 \\ 0.1 & -0.035 \end{bmatrix}$. The eigenvalues of this matrix are $\lambda_1 = 0.832$ and $\lambda_2 = 0.080$, implying unsteady equilibrium points. However, a Lyapunov function analysis reveals that the solution of this system is bounded and exhibits an attractive limit cycle [14–18]. In Fig. 1, we plot the time evolution of the membrane potential, v , and the recovery variable, w , for the true system compared to the case with the inferred parameters' values. Starting from a prior guess of $a = 0.2$ and $b = 0.2$ to initiate the FSM iterations, a parameterization of $a = 0.159$ and $b = 0.364$ is identified, very close to the true values. Thus, we can see that the adopted FSM approach is adequately capable of assimilating these noisy data to estimate the model's parameters for this case.

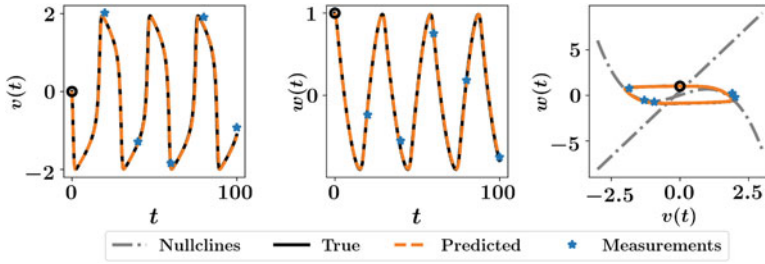


Fig. 1 Results for $a = 0.15$, $b = 0.35$, and $I = 0$, with measurements every 200 time steps and $\sigma = 0.1$. Estimated parameters are $a = 0.159$ and $b = 0.364$

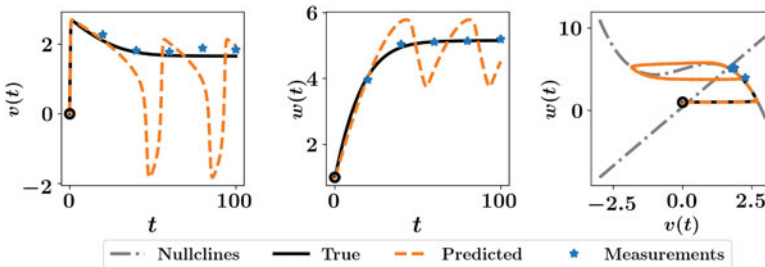


Fig. 2 Results for $a = 0.15$, $b = 0.35$, and $I = 5$, with measurements every 200 time steps and $\sigma = 0.1$. Estimated parameters are $a = -0.930$ and $b = -0.021$, starting from an initial guess of $(0.2, 0.2)$

A second testing situation is to apply a constant input of $I = 5$, with the same parameters’ values as before. We find that this case corresponds to a stable fixed point. In other words, the solution trajectory converges to the equilibrium point (which is $(v^*, w^*) = (1.652, 5.149)$) and resides there. We apply the same procedure to estimate the model’s parameters starting with an initial guess of $a = 0.2$ and $b = 0.2$. The plots in Fig. 2 show that the iterative algorithm fails to correctly approximate the parameters’ values and produces a periodic solution, instead. To understand this, we compute the fixed point and the eigenvalues of the corresponding model’s Jacobian. We find that with $I = 0$ (the previous case), both the true values $(a, b) = (0.15, 0.35)$ and the initial guess $(a, b) = (0.2, 0.2)$ induce a periodic limit cycle. On the other hand, for $I = 5$, the true parameter values correspond to a stable fixed point, while the initial guess still yields a cyclic behavior. Therefore, the estimation process should cross the bifurcation points in order to predict the correct parameterization, which is a common problem in parameter estimation frameworks.

In order to mitigate this issue, prior information about the regime of the solution trajectory can be utilized to make an intelligent guess. For instance, an initial guess of $(a, b) = (0.5, 0.5)$ with $I = 5$ yields a stable fixed point and hence can be chosen as an alternative starting point. Results are presented in Fig. 3, where we can see that

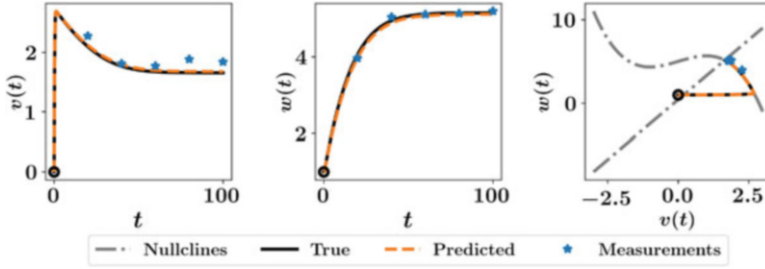


Fig. 3 Results for $a = 0.15$, $b = 0.35$, and $I = 5$, with measurements every 200 time steps and $\sigma = 0.1$. Estimated parameters are $a = 0.0344$ and $b = 0.334$, starting from an initial guess of $(0.5, 0.5)$

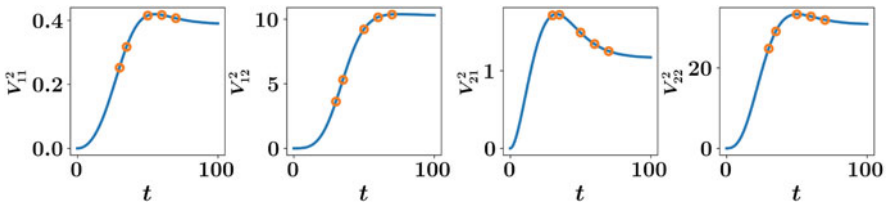


Fig. 4 Forward sensitivities for $a = 0.15$, $b = 0.35$, and $I = 5$. Selected observation instants are denoted with orange circles

both the true and predicted trajectories converge to the equilibrium state. However, the estimated parameters’ values ($a = 0.0344$ and $b = 0.334$) are slightly far from the true ones.

In order to explore the effect of the measurements on the forward sensitivities, we plot the variation of V_{ij}^2 for $i, j \in \{1, 2\}$ with time in Fig. 4. We observe that the initial period has the least influence on the forward sensitivities, while the measurements around and after $t = 50$ have the largest effects. Therefore, we redistribute our measurement instants based on the approach described in Sect. 2.3. In particular, we collect data at $t \in \{30, 35, 50, 60, 70\}$ and apply the FSM framework to estimate the model’s parameter. Starting from an initial guess of $(a, b) = (0.5, 0.5)$, a parameterization of $(a, b) = (0.128, 0.355)$ is estimated, showing significant improvement with respect to the case with equispaced measurement signals. Results are shown in Fig. 5 for the true and predicted trajectories. We can also notice that the optimized measurements are concentrated toward the equilibrium state.

3.2 Varying Input

Finally, we vary the input excitation as $I = 5t/t_m$ (i.e., linearly increasing from 0 to 5). This corresponds to a moving fixed point, beginning with a cyclic trajectory

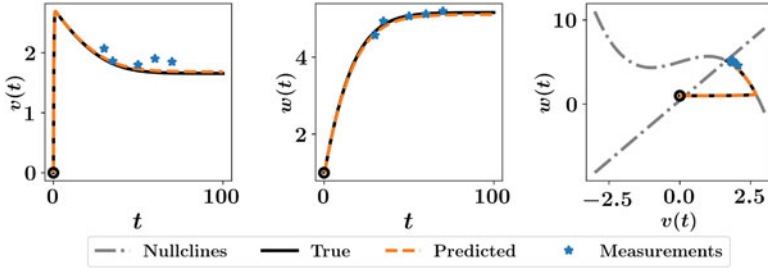


Fig. 5 Results for $a = 0.15$, $b = 0.35$, and $I = 5$, with measurement instants selected based on the forward sensitivity criteria. Estimated parameters are $a = 0.128$ and $b = 0.355$, starting from an initial guess of $(0.5, 0.5)$

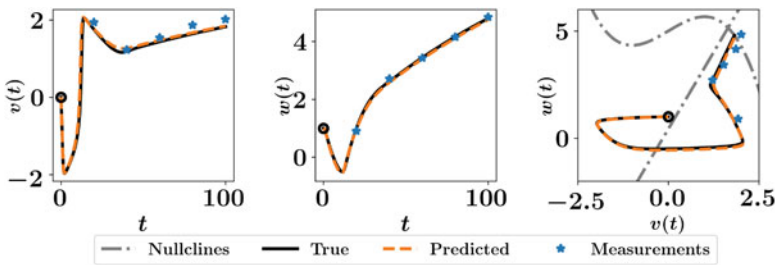


Fig. 6 Results for $a = 0.15$, $b = 0.35$, and varying I , with measurements every 200 time steps and $\sigma = 0.1$. Estimated parameters are $a = 0.023$ and $b = 0.330$, starting from an initial guess of $(0.2, 0.2)$

and followed by a convergence to the stable equilibria. Parameter estimation results for equidistant measurement instants are depicted in Fig. 6 beginning from an initial guess of $(a, b) = (0.2, 0.2)$. We find that the predicted trajectory sufficiently matches the true one, but the estimated parameters are not very accurate.

We then investigate the effects of observation times on the forward sensitivities of the model predictions. We find a spike in the sensitivity of v predictions with respect to the v measurements around $t = 12.5$. We also see a relatively large dependence on the w measurements about $t = 37.5$. On the other hand, the w predictions show an increasing sensitivity on either v or w measurements at final times. Therefore, we reallocate our observation times to capture these trends as demonstrated in Fig. 7. Results based on this enhanced parameter estimation methodology are described in Fig. 8, where the approximated parameters' values ($a = 0.128$ and $b = 0.356$) are closer to the true values.

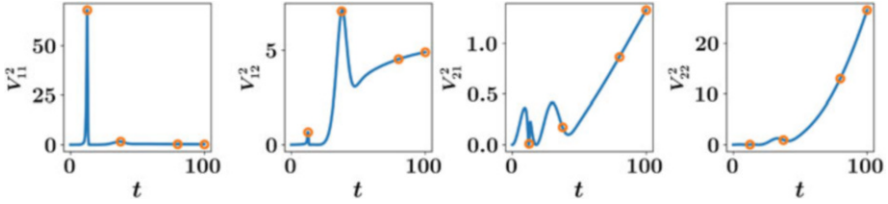


Fig. 7 Sensitivities for $a = 0.15$, $b = 0.35$, and varying I . Selected observation instants are denoted with orange circles

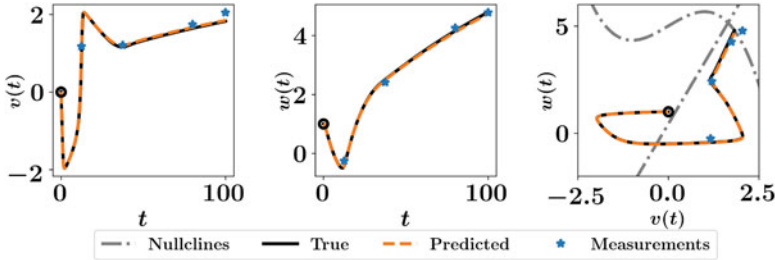


Fig. 8 Results for $a = 0.15$, $b = 0.35$, and varying I , with measurement instants selected based on the forward sensitivity criteria. Estimated parameters are $a = 0.128$ and $b = 0.356$ starting from an initial guess of $(0.2, 0.2)$

4 Concluding Remarks

We put forth a forward sensitivity analysis for the FitzHugh–Nagumo (FHN) system to infer the model’s parameterization from sparse observations. The approach relies on the investigation of the forward sensitivity matrices that encapsulates the temporal dependence of model’s predictions onto its parameters. The presented methodology shows substantial success in assimilating noisy observational data to identify the unknown parameters. We find that the convergence of the predicted parameters to the true values relatively depends on the first guess used to initialize the algorithm. In particular, the initial guess has to yield equilibrium points with similar stability characteristics to the true one. We study three test cases, including zero input, constant nonzero current, and time-dependent excitation. We also formulate measurement collection guidelines based on the relation between the cost functional and the forward sensitivity components. We demonstrate that this approach provides more accurate estimates of unknown parameters than those resulting with arbitrary measurement placements.

Acknowledgments This material is based upon work supported by the U.S. Department of Energy, Office of Science, Office of Advanced Scientific Computing Research under Award Number DE-SC0019290. O.S. gratefully acknowledges their support.

Data Availability

The data that supports the findings of this study are available within the article. The codes to reproduce the presented results are publicly accessible at our GitHub repository: <https://github.com/Shady-Ahmed/FSM-FHN>

References

1. E.M. Izhikevich, *Dynamical Systems in Neuroscience: The Geometry of Excitability and Bursting* (MIT Press, Cambridge, 2007)
2. R. FitzHugh, *Bull. Math. Biophys.* **17**(4), 257 (1955)
3. R. FitzHugh, *Biophys. J.* **1**(6), 445 (1961)
4. J. Nagumo, S. Arimoto, S. Yoshizawa, *Proc. IRE* **50**(10), 2061 (1962)
5. S. Sehgal, A. Foulkes, *Phys. Rev. E* **102**(1), 012212 (2020)
6. R.T. Faghih, K. Savla, M.A. Dahleh, E.N. Brown, in *2010 Annual International Conference of the IEEE Engineering in Medicine and Biology* (IEEE, Piscataway, 2010), pp. 4116–4119
7. Y. Che, L.H. Geng, C. Han, S. Cui, J. Wang, *Chaos Interdiscip. J. Nonlinear Sci.* **22**(2), 023139 (2012)
8. L.H. Geng, T.B. Ayele, J.C. Liu, B. Ninness, in *2020 Chinese Control and Decision Conference (CCDC)* (IEEE, Piscataway, 2020), pp. 2167–2172
9. A.C. Jensen, S. Ditlevsen, M. Kessler, O. Papaspiliopoulos, *Phys. Rev. E* **86**(4), 041114 (2012)
10. A. Melnykova, *Stat. Infer. Stoch. Process* **23**(3), 595 (2020)
11. S. Lakshmivarahan, J.M. Lewis, *Adv. Meteorol.* **2010**, 1–12 (2010)
12. S. Lakshmivarahan, J.M. Lewis, R. Jabrzemski, *Forecast Error Correction Using Dynamic Data Assimilation* (Springer, Cham, 2017)
13. S. Lakshmivarahan, J.M. Lewis, J. Hu, *J. Atmos. Sci.* **77**(8), 2969 (2020)
14. M. Ringkvist, On dynamical behaviour of FitzHugh–Nagumo systems. Ph.D. thesis, Department of Mathematics, Stockholm University (2006)
15. E. Kaumann, U. Staude, in *Equadiff 82* (Springer, Berlin, 1983), pp. 313–321
16. K. Hadelér, U. An Der Heiden, K. Schumacher, *Biol. Cybern.* **23**(4), 211 (1976)
17. S. Treskov, E. Volokitin, *Q. Appl. Math.* **54**(4), 601 (1996)
18. M. Ringkvist, Y. Zhou, *Nonlinear Anal. Theory Methods Appl.* **71**(7–8), 2667 (2009)

Electromagnetic Induction on Neurons Through Field Coupling and Memristor



Sunsu Kurian Thottil  and Rose P. Ignatius 

1 Introduction

Neuron is the basic unit in neuronal system, and its electrical activities show distinct nonlinear properties. Various biological neuron models and their modified versions have confirmed their effectiveness for recognizing and understanding the electrical activities in neurons. External forcing can induce mode transition in electrical activities in neurons from quiescent state to spiking, bursting, and even chaotic states. Recent researches showed that field coupling between neurons can also give a new sight to understand the collective behaviors in neuronal networks. This problem is examined in this paper. Studies on biological Hodgkin–Huxley neuron model is helpful to understand the occurrence mechanism of neuronal systems induced by electromagnetic radiation [1]. Researches based on collective responses in electrical activities of neurons under field coupling have been reported [2], where the contribution of field coupling from each neuron is described by introducing appropriate weight dependent on the distance between two neurons. Such studies have shown that the synchronization degree is much dependent on the coupling intensity. Also, the synchronization or pattern selection of network connected with gap junction can be modulated by field coupling [2–4].

S. K. Thottil

Department of Physics, St. Teresa's College, Ernakulam, Kerala, India

R. P. Ignatius (✉)

Department of Physics, Al-Ameen College, Edathala, Aluva, Kerala, India

2 Model and Scheme

An improved H-R neuron model is selected to represent local kinetics of neuron model. This model incorporates the magnetic flux as fourth variable. Based on an improved neuron model, the effect of field coupling on electromagnetic induction is analyzed, and the modulation of magnetic flux on membrane potential is realized by using cubic flux-controlled memristor coupling.

The dynamic equations for improved Hindmarsh–Rose neuron with field coupling are given by the following:

$$\begin{aligned}
 \dot{x}_{1i} &= x_{2i} - ax_{1i}^3 + bx_{2i}^3 - x_{3i} + I_{ext} - k\rho(\varphi_i)x_{1i} \\
 \dot{x}_{2i} &= c - dx_{1i}^2 - x_{2i} \\
 \dot{x}_{3i} &= r(s(x_{1i} - x_0)) - x_{3i} \\
 \dot{\varphi} &= k_1x_{1i} + g \left(\sum_{i \neq j}^N \varphi_j - \varphi_i \right)
 \end{aligned} \tag{1}$$

Field coupling is used to exchange signals between neurons. $\sum_{j \neq i}^N \varphi_j - \varphi_i$ represents the field and magnetic contribution of other neurons to the i th neuron. The coupling intensity is represented by g . The membrane potential, slow current associated with recovery variable, and adaption current are represented by x_1 , x_2 , and x_3 , respectively. The memductance $\rho(\varphi_i)$ is cubic flux-controlled memristor term and can be expressed as $\rho(\varphi_i) = \alpha + 3\beta\varphi_i^2$. It can act as coupling synapse between neurons. The parameter values are selected as $a = 1$, $b = 3$, $c = 1$, $d = 5$, $r = 0.006$, $s = 4$, and $x_0 = -1.6$. Here, kx_{1i} denotes the changes in magnetic flux due to membrane potential. Hence, the interaction between membrane potential and magnetic flux is represented by the variables k and k_1 . Relation between memristor magnetic flux, membrane potential, and current is as follows:

$$i = \frac{dq(\varphi)}{dt} = \frac{dq(\varphi)}{d\varphi} \frac{d\varphi}{dt} = \rho(\varphi)V = k\rho(\varphi)x_1 \tag{2}$$

3 Modes of Electrical Activity of Isolated Improved H-R Neuron Under Field Coupling

Sampled time series analysis is done using MATLAB platform for the isolated neuron [5] by changing control parameters. As the intensity of external current I_{ext} increases, the dynamics of single H-R neuron model under field coupling shows

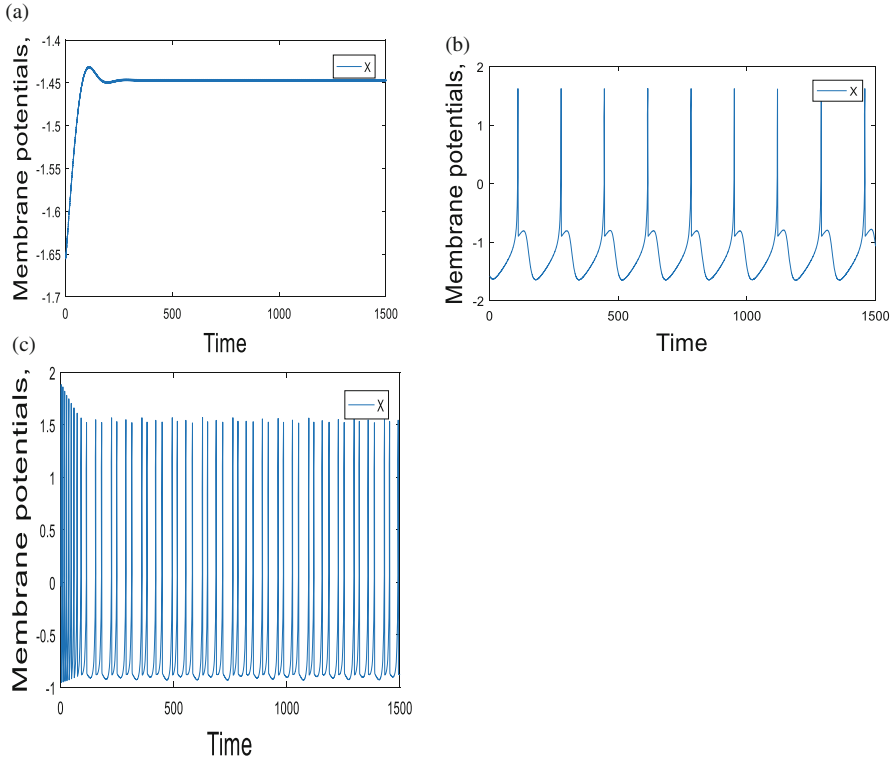


Fig. 1 Time series plot of membrane potentials for coupling strength $g = 0.5$. (a) Oscillation suppression of neuron under $I_{\text{ext}}=0.5$. (b) Spiking activity $I_{\text{ext}}=1.5$. (c) Tonic spiking for $I_{\text{ext}}=3.5$

distinct behaviors. For the external current $I_{\text{ext}}=0.5$ mA, the neuron shows the suppression of activity. But as current changes to 1.5 mA, its activity gets changed to sudden spiking behavior. For higher values of external current, it shows a tonic or continuous spiking activity. Figure 1 shows the different dynamics of the system.

Further, the study is done for coupled neurons. Here, the two improved H-R neurons are selected, and the dynamics is analyzed under field coupling. The corresponding mode transitions of electrical activities under electromagnetic induction due to field coupling are analyzed [2]. Figure 2 shows distinct dynamics such as suppression of activity, spiking and death of neuron, antiphase state, and synchronization under the variation of external forcing currents.

Further, the study is extended with high value of coupling strength ($g = 1$). The system dynamics changes to quiescent state and then to oscillation death as the value of external current increases. The result is quite different compared to that of low coupling intensity. For low coupling strength, the oscillation death occurs in low values of external stimulating current. But as coupling strength increases, suppression of oscillation takes place at high stimulating current. Hence, we can reign the dynamic behaviors under field coupling by selecting appropriate control parameters.

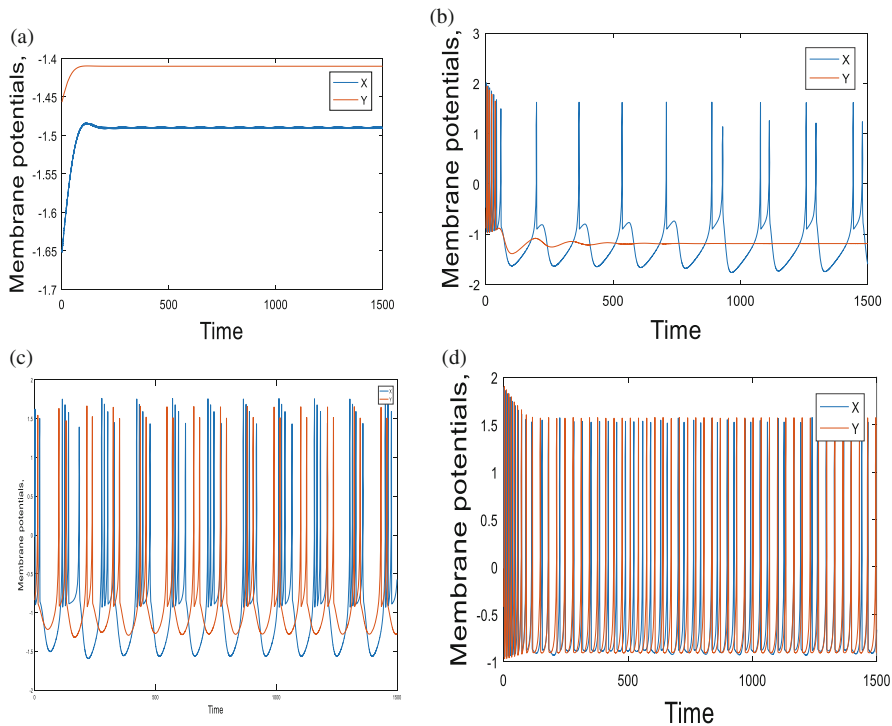


Fig. 2 The time series analysis of coupled neuron for coupling strength $g = 0.6$. (a) Two neurons are in oscillation death state for $I_{ext}=0.5$. (b) For the current $I_{ext}=1.5$, one of the neuron spikes, while the other one experiences oscillation death. (c) Antiphase synchronization/desynchronization observed for $I_{ext}=2.5$. (d) Some synchronization occurs at $I_{ext}=3.5$

4 Collective Responses in Electrical Activities of Improved H-R Neurons Under Field Coupling

The effect of field coupling on the collective behaviors of neurons in neuronal network is analyzed. Here, adjacent neurons are connected by field coupling.

Transition to synchronized state with increase in coupling strength is observed for 300 H-R neurons (Figs. 3 and 4).

5 Analysis of Improved H-R Neuron Under Field Coupling with Control Inputs

The control law is used to find out the unknown parameters of the neuronal model [5]. This represents a disease condition in the biological neurons and can be used to create a connection network in between the abnormal and normal network. The

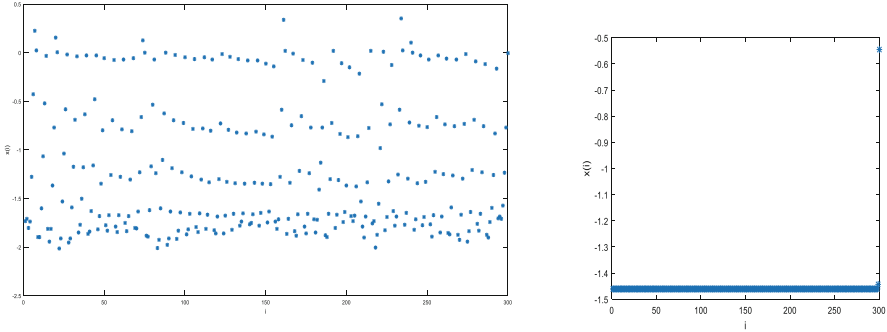


Fig. 3 Transition from incoherent state to synchronous state is observed with increase in coupling strength, where i denotes the neuron number and x_i denotes the membrane potential of neuron. **(a, b)** Represent the dynamics of 300 H-R neurons for low and high coupling strengths. Desynchrony is observed for $g = 0.1$, and synchronous behavior is for $g = 1.0$

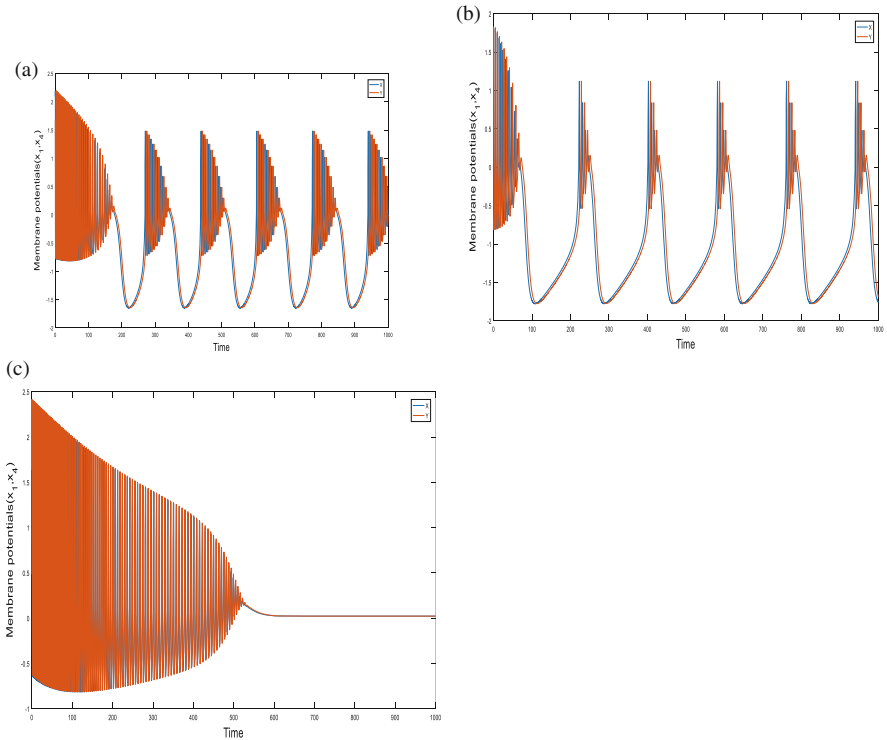


Fig. 4 The time series analysis of coupled neuron for coupling strength $g = 1$. **(a)** Two neurons are in in quiescent state for $I_{ext} = 0.5$. **(b)** For the current $I_{ext} = 2.5$, two neurons exhibit quiescent state with increase in number of spikes in each quiescent state. **(c)** Oscillation suppression occurs at $I_{ext} = 3.5$ after a time at around 50

method of deriving control laws for synchronization can be used in many complex networks. It is used as a potential method for adjusting neuronal rhythm to cure mental disorders. In the following section, the synchronization condition for the model is developed with the control inputs added to the neuronal network. Control inputs for system can be analyzed by Lyapunov function method. The dynamics of the system with control input can be written as follows:

$$\begin{aligned}
 \dot{x}_{1i} &= x_{2i} - ax_{1i}^2 + bx_{2i}^3 - x_{3i} + I_{\text{ext}} - k\rho(x_{4i})x_{1i} + u(i, x_{1i}). \\
 \dot{x}_{2i} &= c - dx_{1i}^2 - x_{2i} + u(i, x_{2i}) \\
 \dot{x}_{3i} &= r(s(x_{1i} - x_0)) - x_{3i} + u(i, x_{3i}) \\
 \dot{x}_{4i} &= k_1x_{1i} + g \left(\sum_{i \neq j}^N x_{4j} - x_{4i} \right) + u(i, x_{4i}) \quad (3)
 \end{aligned}$$

The synchronization errors are defined as follows:

$$e(i, x_{1i}) = x_{1ni} - x_{1i}, e(i, x_{2i}) = x_{2ni} - x_{2i}, e(i, x_{3i}) = x_{3ni} - x_{3i}, e(i, x_{4i}) = x_{4ni} - x_{4i}$$

The error dynamics are given by the following:

$$\begin{aligned}
 \dot{e}(i, x_{1i}) &= e(i, x_{2i}) - a(x_{1ni} - x_{1i})^2 + b(x_{2ni} - x_{2i})^3 - (x_{3ni} - x_{3i}) - k\rho e(i, x_{1i}) - u(i, x_{1i}) \\
 \dot{e}(i, x_{2i}) &= -d(x_{1ni} - x_{1i})^2 - e(i, x_{2i}) - u(i, x_{2i}) \\
 \dot{e}(i, x_{3i}) &= rs(x_{1ni} - x_{1i}) - e(i, x_{3i}) - u(i, x_{3i}) \\
 \dot{e}(i, x_{4i}) &= k_1(x_{1ni} - x_{1i}) - g e(i, x_{4i}) - u(i, x_{4i}) \quad (4)
 \end{aligned}$$

Considering the Lyapunov function using the difference variable we get,

$$V = \frac{1}{2} \sum_{i=1}^{N-1} e(i, x_{1i})^2 + e(i, x_{2i})^2 + e(i, x_{3i})^2 + e(i, x_{4i})^2 \quad (5)$$

$\dot{V} = e(i, x_{2i}) e(i, x_{1i}) - a(x_{1ni} - x_{1i})^2 e(i, x_{1i}) + b(x_{2ni} - x_{2i})^3 e(i, x_{1i}) - (x_{3ni} - x_{3i}) e(i, x_{1i}) - k\rho e(i, x_{1i})^2 - u(i, x_{1i}) e(i, x_{1i}) - d(x_{1ni} - x_{1i})^2 e(i, x_{2i}) - e(i, x_{2i})^2 - u(i, x_{2i}) e(i, x_{2i}) + rs(x_{1ni} - x_{1i}) e(i, x_{3i}) - e(i, x_{3i})^2 - u(i, x_{3i}) e(i, x_{3i}) + k_1(x_{1ni} - x_{1i}) e(i, x_{4i}) - g e(i, x_{4i})^2 - u(i, x_{4i}) e(i, x_{4i})$
 Here,

$$i = 1 \dots \dots \dots n - 1 \tag{6}$$

The controllers are chosen to ensure that the time derivative of Lyapunov function is negative definite. Then, the errors converge to zero as $t \rightarrow \infty$, and this leads to asymptotically stable synchronization manifold.

So controllers are chosen as follows:

$$\begin{aligned}
 u(i, x_{1i}) &= e(i, x_{2i}) a(x_{1ni} - x_{1i})^2 + b(x_{2ni} - x_{2i})^3 - (x_{3ni} - x_{3i}) - k\rho e(i, x_{1i}) \\
 u(i, x_{2i}) &= -d(x_{1ni} - x_{1i})^2 + e(i, x_{2i}) \\
 u(i, x_{3i}) &= rs(x_{1ni} - x_{1i}) - e(i, x_{3i}) \\
 u(i, x_{4i}) &= k_1(x_{1ni} - x_{1i}) - g e(i, x_{4i})
 \end{aligned} \tag{7}$$

Then,

$$\dot{V} = -g \sum_{i=1}^{n-1} e(i, x_{4i})^2 \tag{8}$$

Hence, the H-R neuron network with field coupling has the negative Lyapunov function derivative. This is observed with in the presence of the controller for the system.

6 Stability of Synchronization for Improved H-R Neuron Under Field Coupling

The stability of synchronization of the selected model can be analyzed using the master stability approach [5]. The synchronization is stable if the corresponding master stability function is negative for each of the transverse eigenvalues.

For complete stable synchronization, the difference between neural oscillator coordinates vanishes in the limit of $t \rightarrow \infty$, and there exists a synchronous solution. Hence, the stability of equations for perturbations transverse to synchronization corresponding to given equation can be calculated.

The minimal condition for the stability of synchronized state [5] is the negative-ness of the transverse Lyapunov exponents (TLEs) associated with Eq. (3).

Variation of two largest TLEs ($\lambda_{\perp 1}$ and $\lambda_{\perp 2}$) with increase in coupling strength are shown in Fig. 5. As the coupling strength is increased, the largest TLE ($\lambda_{\perp 1}$) increases initially; then, it reaches a peak and finally decreases. The largest TLE crosses zero and becomes negative indicating a transition from incoherent state to complete synchrony.

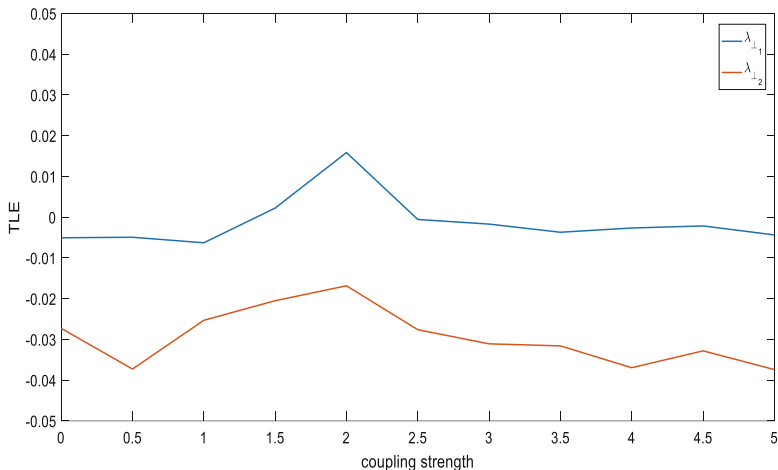


Fig. 5 The TLEs of coupled H-R neural network. (a) Coupling strength is plotted along x-axis and TLE along y-axis. The largest (blue color) TLE ($\lambda_{\perp 1}$) becomes positive under coupling strength $1.1 < g < 2.7$

7 Conclusions

In the complex physical and biological condition like noise and electromagnetic radiation, complete synchronization between neurons becomes more difficult, while the phase synchronization or rhythm becomes available. It is also observed that magnetic coupling is an effective way to realize synchronization. The effect of field coupling on the electromagnetic induction and corresponding modes of electrical activities with cubic flux-controlled memristor are examined by finding the influence of the magnetic flux on membrane potential.

For isolated and coupled neurons, multiple modes in electrical activities are analyzed by increasing the intensity of field coupling. As the external forcing current increases, the system shows diversity in behavior. Various dynamics such as oscillation death, tonic spiking, desynchronization, and synchronizations are resulted in. Further, it is observed that under the high coupling strength, the oscillation suppression of coupled systems can be achieved by high value of external current. It is observed that for a network of 300 H-R neurons, the neuron oscillator shows incoherent as well as synchronization behavior. Control inputs for the system are analyzed, and the stability of the system is confirmed by the negative value of transverse Lyapunov exponent plot.

The field coupling contributes magnetic flux and induction current; as a result, the mode in electrical activities is controlled. The excitability of neuron mainly depends on the external forcing current, and also, the larger external stimuli are much helpful to excite neurons. This is well understood through the numerical studies. So present

studies give instructive clues to understand the signal encoding and exchange when the synapse coupling is absent.

References

1. M. Lv, J. Ma, Multiple modes of electrical activities in a new neuron model under electromagnetic radiation. *Neurocomputing* **205**, 375–381 (2016)
2. L.M. Pecora, T.L. Carroll, Master stability functions for synchronized coupled systems. *Phys. Rev. Lett.* **80**(10), 2109 (1998)
3. A.L. Hodgkin, A.F. Huxley, A quantitative description of membrane current and its application to conduction and excitation in nerve. *J. Physiol. Lond.* **117**, 500–544 (1952)
4. Y. Xu, Y. Jia, J. Ma, T. Hayat, A. Alsaedi, Collective responses in electrical activities of neurons under field coupling. *Sci. Rep.* **8**(1), 1349 (2018)
5. K. Usha, P.A. Subha, C.R. Nayak, The route to synchrony via drum head mode and mixed oscillatory state in star coupled Hindmarsh–Rose neural network. *Chaos, Solitons Fractals* **108**, 25–31 (2018)

Variable Speed Optimization of a Vibro-impact Capsule System in Both the Forward and Backward Directions



Yang Zheng, Maolin Liao, Jiajia Zhang, Yang Liu, Jiapeng Zhu, and Zhiqiang Zhu

1 Introduction

The wireless capsule endoscopy detection technology was proposed about 20 years ago [1]. Due to its significant advantages on being painless, noninvasive, and free of anesthesia and having no cross infection, the wireless capsule endoscopy thoroughly changed the traditional endoscopy detection by using wired endoscopy. At present, the capsule endoscope for clinical application either moves passively depending on gastrointestinal motility or is controlled by an external magnetic field [2, 3]; thus, the capsule does not own the independent capacity of movement. Under such circumstances, the research about the self-propulsion capsule has gradually become a hotspot. Liu et al. proposed a model about the vibro-impact capsule system [4–6] and conducted a series of experimental studies to demonstrate the numerical results obtained according to their dynamic model [7–9]. Based on their work, the further consideration is how to effectively control the movement direction and speed of the self-propulsion capsule, which will be discussed in this paper.

Y. Zheng · M. Liao (✉) · J. Zhu · Z. Zhu

School of Mechanical Engineering, University of Science and Technology Beijing, Beijing, China
e-mail: liaomaolin@ustb.edu.cn

J. Zhang · Y. Liu

College of Engineering, Mathematics, and Physical Sciences, University of Exeter, Exeter, UK

2 Mathematical Modelling

In this section, a mathematical model about the vibro-impact self-propulsion capsule system is introduced. The physical model is simplified from the actual capsule, based on which the dynamic model is developed.

2.1 Physical Model

The physical model of a vibro-impact self-propulsion capsule is shown in Fig. 1, where M_c and M_m are the masses of the capsule and the magnet, respectively. k_1 and c represent the stiffness of the helical spring connecting the magnet and the capsule and the damping coefficient of the energy dissipation led by the relative speed between the capsule and the magnet, respectively. The springs with stiffness k_2 and k_3 represent the primary and the secondary constraints, and their gaps between the magnet and the constraints are G_2 and G_3 , respectively. A pre-compressed distance of the physical spring is defined as G_1 . X_c and X_m are the displacements of the capsule and the magnet, and their velocities are V_c and V_m , respectively. In addition, F_f , F_e , and F_i are the external frictional force, the inner excitation force, and the impact force between the capsule and the magnet, respectively. All the structure parameters for the capsule system are listed in Table 1.

2.2 Dynamic Model

Based on the physical model shown in Fig. 1, the corresponding mathematical model can be developed as [10].

$$\begin{cases} M_m \ddot{X}_m = F_i \\ M_c \ddot{X}_c = F_f - F_i \end{cases} \quad (1)$$

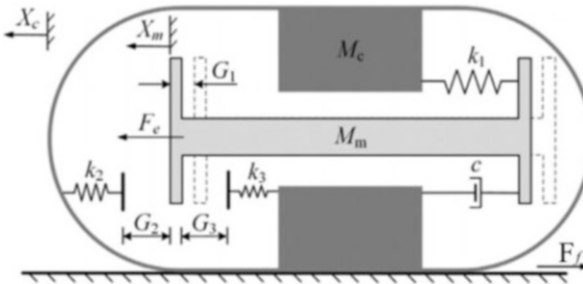


Fig. 1 Physical model of a vibro-impact self-propulsion capsule [10]

Table 1 Structure parameters of the capsule system

Parameters	Unit	Values
M_c	g	1.8
M_m	g	1.67
G_1	mm	0
G_2	mm	1.6
G_3	mm	0
k_1	kN/m	0.062
k_2	kN/m	27.9
k_3	kN/m	53.5
c	Ns/m	0.0156

where

$$F_f = \begin{cases} -\text{sign}(V_c) \cdot \mu (M_m + M_c) g, & V_c \neq 0 \\ \text{sign}(F_i) \cdot \mu (M_m + M_c) g, & V_c = 0, |F_i| \geq \mu (M_m + M_c) g \\ F_i, & V_c = 0, |F_i| \leq \mu (M_m + M_c) g \end{cases} \quad (2)$$

$$F_i = \begin{cases} F_e - F_1 - c(V_m - V_c) - F_3, & X_m - X_c \leq -G_3 \\ F_e - F_1 - c(V_m - V_c), & -G_3 \leq X_m - X_c \leq G_2 \\ F_e - F_1 - c(V_m - V_c) - F_2, & X_m - X_c \geq G_2 \end{cases} \quad (3)$$

$$F_e(t) = \begin{cases} P_d, & t \in \left[n \frac{1}{f}, n \frac{1}{f} + D \frac{1}{f} \right] \\ 0, & t \in \left(n \frac{1}{f} + D \frac{1}{f}, n \frac{1}{f} + \frac{1}{f} \right) \end{cases} \quad (4)$$

$$\begin{cases} F_1 = k_1 (X_m - X_c + G_1) \\ F_2 = k_2 (X_m - X_c - G_2) \\ F_3 = k_3 (X_m - X_c + G_3) \end{cases} \quad (5)$$

where n is the period number and P_d , f , and D are the amplitude, frequency, and duty cycle ratio of the excitation signal, respectively. Moreover, in order to compare the variable speed of the vibro-impact capsule, its average velocity is calculated as follows:

$$v_{\text{avg}} = \frac{f}{n} \left(X_c \left(n \frac{1}{f} \right) - X_c(0) \right) \quad (6)$$

3 Optimization Design

The precise control of both the speed and the direction for the capsule movement in uncertain small-bowel circumstance is a challenging task. For such a purpose, to better describe the dynamic responses of the capsule, seven variable speed steps are proposed, including fast backward and forward movements, medium-speed backward and forward movements, slow backward and forward movements, and hover movement under gastrointestinal motility. In addition, for a given capsule system, the excitation signal is convenient to be adjusted; hence, the optimization parameters consist of the frequency (f), amplitude (P_d), and duty cycle ratio (D) of the excitation square signal. Moreover, the uncertainty of the friction coefficient (μ) due to the varied structure and lubrication of the practical small bowel is also considered as an environment variable. The purpose of optimization is to find the best combination of parameters within the respective ranges of the given parameters to make the capsule move with the speed closest to the proposed speed step. To conduct the speed optimization, the dynamic model built in MATLAB is introduced into Isight, since Isight integrates a group of optimization algorithms which can be redesigned and combined to complete an optimization task with high efficiency and high accuracy.

3.1 Optimization Algorithms and Flow Path

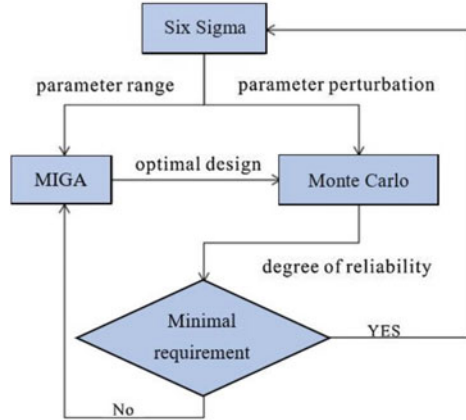
As aforementioned, there are three optimization parameters, one environment variable, and one optimization objective; hence, this is a multiparameter and single-objective optimization. Furthermore, in order to secure the reliability of the obtained optimization solutions in uncertain practical small-bowel environmental, parameter perturbations should be considered accompanying with the optimization. Therefore, a combination of the optimization algorithms is considered. Specifically, Multi-Island Genetic Algorithm (MIGA) is chosen to conduct the optimization, while Monte Carlo algorithm is applied in measuring the degrees of reliability of the optimal solutions provided by MIGA. Moreover, both the MIGA and the Monte Carlo method are driven by the Six Sigma algorithm which secures that all the confirmed optimal solutions satisfy a predefined minimal degree of reliability, which is set as 99% in this present work, and finally, the steady optimization designs can thus be extracted from massive parameter combinations. The flow path of this combined optimization is illustrated in Fig. 2.

The detailed optimization model for this combined optimization algorithms can be introduced as follows:

$$X_L + \Delta X \leq X \leq X_U - \Delta X \quad (7)$$

$$Z_L \leq Z \leq Z_U \quad (8)$$

Fig. 2 Flow chart of the combined optimization algorithms



$$\text{Lower limit} \leq G = \mu_Y(X, Z) + n\sigma_Y(X, Z) \leq \text{Upper limit} \tag{9}$$

$$\text{Minimize } F(\mu_Y(X, Z), \sigma_Y(X, Z)) = \left[(\mu_Y(X, Z) - M)^2 - \sigma_Y(X, Z)^2 \right] \tag{10}$$

where X represents the design variables, including the frequency, amplitude, and duty cycle ratio of the excitation square signal, and X_L , X_U , and $\pm\Delta X$ are the lower and upper limits and the fluctuation range for the design parameters, respectively. Z represents the environmental variable, namely, the uncertainty of the friction coefficient in the small bowel; Z_L and Z_U are its lower and upper limits. G is the constraint condition, where the accepted velocity range for the capsule movement in each optimization case can be set. $\mu_Y(X, Z)$ and $\sigma_Y(X, Z)$ represent the average velocity of the capsule and its standard deviation, respectively. n is the number of sigma; when $n = 6$, the reliability of the optimization result is the highest; hence, this method is called Six Sigma algorithm. F is the objective function, and M is the target speed of the capsule; hence, the purpose of the optimization is to make the capsule speed be close to the proposed speed step.

3.2 Optimization Case: Forward Movement with Medium Speed

The optimization case for the capsule moving forward with medium speed (5 mm/s) is taken as an example to introduce the whole optimization process. Primarily, all the parameter ranges for the environmental variable and the three optimization parameters are listed in Table 2. In particular, the optimized Latin square method

Table 2 Parameter settings for optimization

Parameters	Unit	Signs	Mode	Lower	Upper
Friction coefficient	–	μ	Input	0.2	0.5
Frequency	Hz	f	Input	1	50.0
Amplitude	N	P_d	Input	0.001	0.03
Duty cycle ratio	%	D	Input	10.0	90.0
Velocity of capsule	mm/s	V_{avg}	Output	0.1	10.0

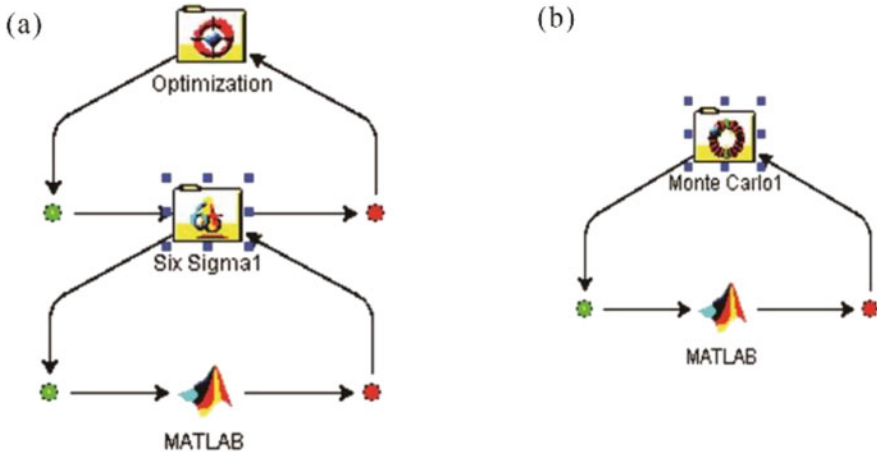


Fig. 3 Optimization by integrating Isight and MATLAB. (a) Combination of optimization algorithms; (b) reliability verification of the obtained optimal solution

is applied to build a uniform distribution for the uncertainty friction coefficient, which is an array with 50 different friction coefficients whose values are within 0.2 and 0.5. Furthermore, the lower and upper boundaries for the capsule speed are set as 0.1 mm/s and 10 mm/s, respectively; namely, as a fundamental requirement, the capsule should keep moving forward. Based on the optimization flow built in Isight (see Fig. 3a), in total, 50 combinations of the design parameters were tested, and for each combination, 50 different friction coefficients were simulated; eventually, the average velocity for such combination under the 50 different friction coefficients was calculated. The variations of both the three design parameters and the obtained average velocity of capsule are shown in Fig. 4. From Fig. 4, the average velocity of the capsule cannot be stabilized exactly as 5 mm/s; however, if the design parameters shown in Table 3 are used to excite the capsule system, an approximate speed of 4.5840136 mm/s can be obtained, which can be accepted as the medium speed for the capsule moving forward.

Subsequently, both the variation range of the friction coefficient and the boundaries of the capsule speed are kept to be consistent with that in the optimization process, while the optimization parameters are set to fluctuate slightly near the obtained optimal result; see Table 4. Based on the flow path for the reliability

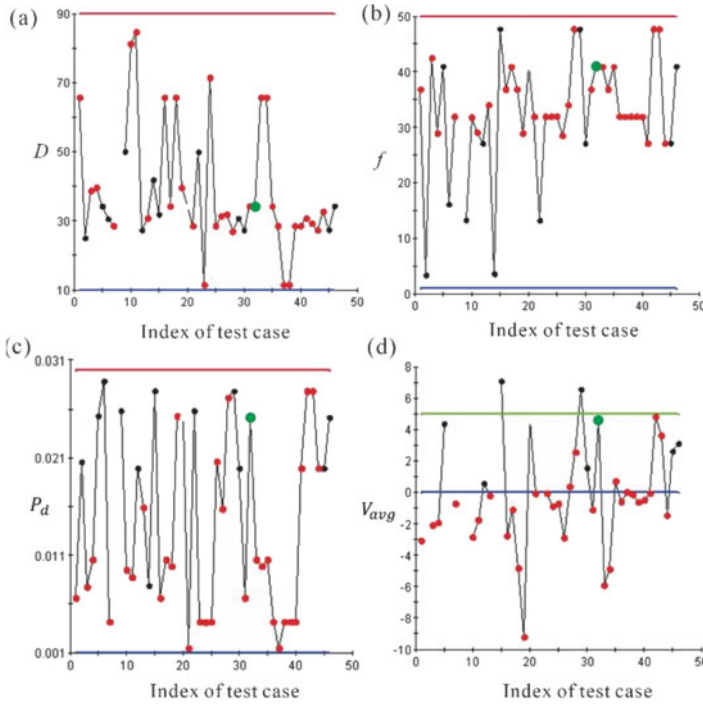


Fig. 4 Variations of the parameters and the capsule speed in the optimization process and the green point in each subplot corresponds to the optimal solution

Table 3 Result of optimization

Parameters	Unit	Values
D	%	34.233768
f	Hz	40.949187
P_d	N	0.0251731
V_{avg}	mm/s	4.5840136

Table 4 Parameter settings for reliability verification

Parameters	Mode	Mean	Lower	Upper	Distribution
μ	Input	0.35	0.2	0.5	Uniform
P_d	Input	0.0251731	0.02473	0.02561	Uniform
f	Input	40.949187	40.2398	41.6584	Uniform
D	Input	34.233768	33.6408	34.8267	Uniform
V_{avg}	Output	4.5840136	0.1	10.0	—

verification shown in Fig. 3b, 1000 combinations of the optimization parameters, whose distributions are shown in Fig. 5, are simulated numerically to check whether the capsule speed crosses the defined boundaries 0.1 mm/s or 10 mm/s. The obtained distribution of the capsule speed is displayed in Fig. 6, and the corresponding

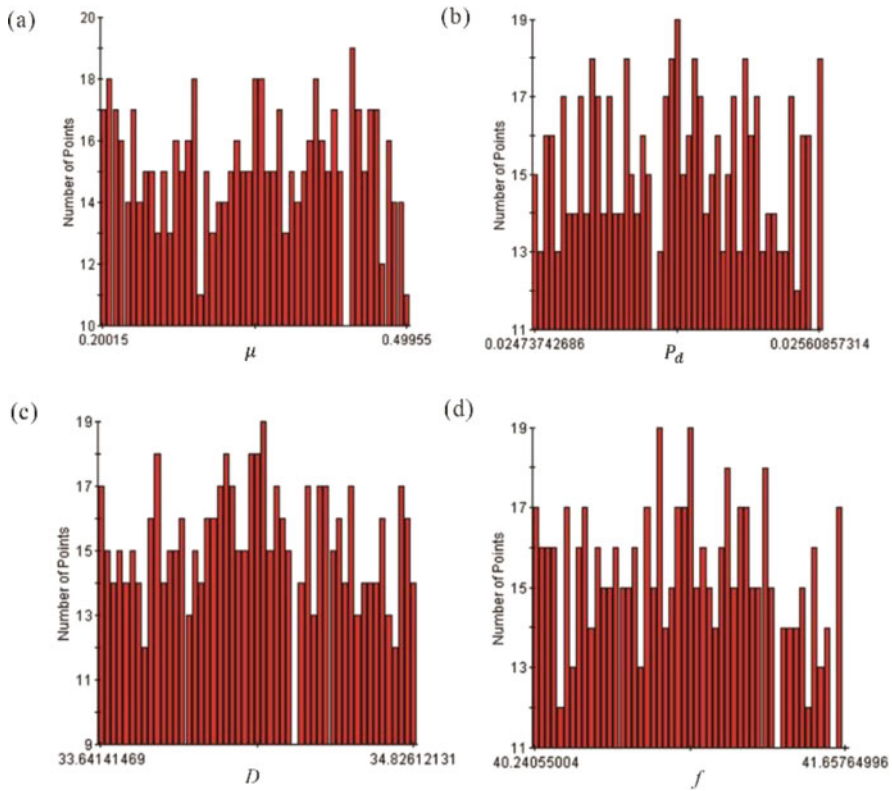


Fig. 5 Distributions of parameters for reliability verification

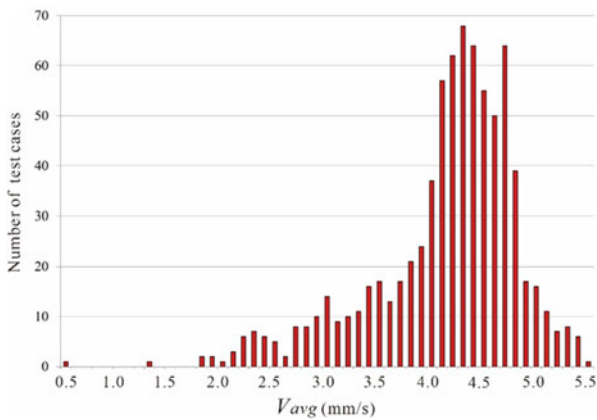


Fig. 6 Distributions of average velocity of capsule for reliability verification

Table 5 Results of reliability verification

Type	Value
Mean velocity	4.091490737
Standard deviation	0.685242201
Minimum velocity	0.505602717
Maximum velocity	5.473377537
Probability between limits	100%

Table 6 Optimization results of seven speed steps for the capsule movement

Speed steps	Target speed (mm/s)	Allowed speed (mm/s)	Optimized parameters			Obtained speed (mm/s)
			f (Hz)	P_d (N)	D (%)	
Fast backward	-10	(-15, -5)	33.77	0.0223	66.86	-9.01
Medium backward	-5	(-10, -0.1)	44.14	0.0242	14.66	-5.05
Slow backward	-1	(-3, -0.1)	44.14	0.0044	25.70	-0.91
Hover	0	(-0.1, 0.1)	21.84	0.0043	86.75	0
Slow forward	1	(0.5, 1.5)	Failed			
Medium forward	5	(0.1, 10)	40.95	0.0251	34.23	4.58
Fast forward	10	(5, 15)	Failed			

statistical result is listed in Table 5, where the reliability for the capsule moving forward is verified as 100%, since, when setting the excitation signal as the obtained optimal combination of parameters, the minimal velocity is around 0.51 mm/s; moreover, the average velocity is 4.1 mm/s which is still close to the predefined medium speed (5 mm/s).

3.3 Optimization Results

By using the same way introduced in Subsection 3.2, the proposed seven speed steps are optimized one by one, and the obtained results are listed in Table 6. Specifically, according to the optimization of excitation parameters for the vibro-impact capsule, five speed steps for the capsule moving steady under uncertain small-bowel environment are explored. However, given the current excitation parameter ranges, the steady slow and fast-forward movements cannot be achieved by the studied capsule. Therefore, if the rest two speed steps are required for the practical application of the capsule system, both the modification of the structure parameters and the broader ranges of control parameters deserve to be tried.

According to the obtained parameter combinations for five different speed steps, the numerical simulations are conducted to observe the changes of the capsule

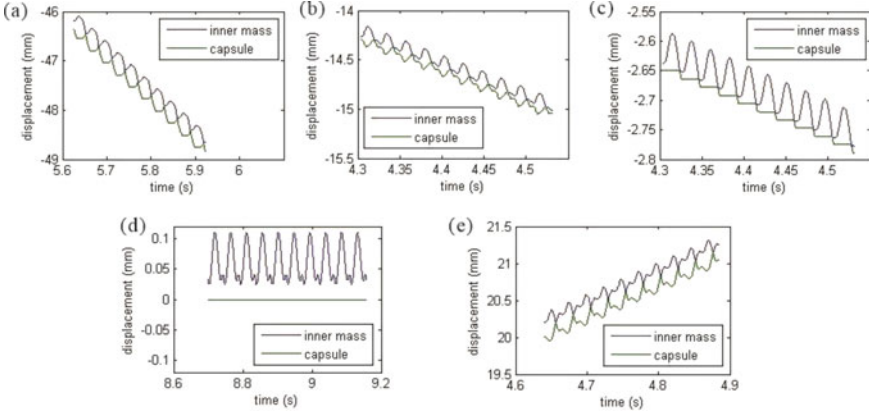


Fig. 7 Results of numerical simulations with different parameter combinations for five different speed steps: (a) fast backward, (b) medium backward, (c) slow backward, (d) hover, and (e) medium forward

speed. For all the five cases, the friction factor is set the same as 0.2293. Eventually, the simulated results are shown in Fig. 7 where the corresponding velocities of the capsule are (a) $v_{\text{avg}} = -8.3068$ mm/s for fast backward, (b) $v_{\text{avg}} = -3.3368$ mm/s for medium backward, (c) $v_{\text{avg}} = -0.6142$ mm/s for slow backward, (d) $v_{\text{avg}} = 0$ mm/s for hover, and (e) $v_{\text{avg}} = 4.28$ mm/s for medium forward. All the obtained five velocities of capsule are close to the predefined targets of speed steps.

4 Concluding Remarks

1. In this paper, a graded variable speed design for a self-propulsion capsule system was carried out, in which three types of movements, including forward, backward, and hover, were considered; meanwhile, the fast, medium, and slow speeds were classified for both the forward and backward movements of the capsule; thus, in total, seven speed steps were defined for the further optimization.
2. According to the seven speed steps defined in this paper, the optimization was conducted via the combination of the MATLAB and Isight software. Specifically, three controllable parameters, including frequency, amplitude, and duty cycle ratio, were optimized, and the influence of the friction coefficient in the uncertain small-bowel environment was also introduced in the optimization process. Finally, it was demonstrated that the capsule can achieve five speed steps: fast backward, medium speed backward, slow backward, hover, and medium speed forward; however, it was also found that for the given structure parameters of the capsule, the stable fast-forward movements and the stable slow forward movements cannot be obtained by the optimization of the three controllable parameters.

3. In future work, by resorting on the guidance of the numerical simulation conducted in this paper, the corresponding variable speed steps will be experimentally tested, and the optimization design method will also be improved according to the obtained experimental results.

References

1. Y. Lee, A. Erdogan, S. Rao, How to assess regional and whole gut transit time with wireless motility capsule. *J. Neuro Gastroenterol. Motil.* **20**(2), 265–270 (2014)
2. F. Carpi, N. Kastelein, M. Talcott, et al., Magnetically controllable gastrointestinal steering of video capsules. *I.E.E.E. Trans. Biomed. Eng.* **58**(2), 231–234 (2011)
3. J. Keller, C. Fibbe, F. Volke, et al., Remote magnetic control of a wireless capsule endoscope in the esophagus is safe and feasible: results of a randomized, clinical trial in healthy volunteers. *Gastrointest. Endosc.* **72**(5), 941–946 (2010)
4. Y. Liu, M. Wiercigroch, E. Pavlovskaja, et al., Modelling of a vibro-impact capsule system. *Int. J. Mech. Sci.* **66**, 2–11 (2013)
5. Y. Liu, E. Pavlovskaja, M. Wiercigroch, Vibro-impact responses of capsule system with various friction models. *Int. J. Mech. Sci.* **72**, 39–54 (2013)
6. Y. Yan, Y. Liu, M. Liao, A comparative study of the vibro-impact capsule systems with one-sided and two-sided constraints. *Nonlinear Dyn.* **89**, 1063–1087 (2017)
7. Y. Liu, E. Pavlovskaja, M. Wiercigroch, Experimental verification of the vibro-impact capsule model. *Nonlinear Dyn.* **83**, 1029–1041 (2013)
8. Y. Yan, Y. Liu, J. Páez Chávez, et al., Proof-of-concept prototype development of the self-propelled capsule system for pipeline inspection. *Meccanica* **53**(8), 1997–2012 (2017)
9. Y. Liu, J. Paez Chavez, J. Zhang, et al., The vibro-impact capsule system in millimetre scale: numerical optimisation and experimental verification. *Meccanica* **55**, 1885–1902 (2020)
10. B. Guo, E. Ley, J. Tian, et al., Experimental and numerical studies of intestinal frictions for propulsive force optimisation of a vibro-impact capsule system. *Nonlinear Dyn.* **101**(1), 65–83 (2020)

Exploring the Dynamics of a Vibro-Impact Capsule Moving on the Small Intestine Using Finite Element Analysis



Jiyuan Tian, Yang Liu, and Shyam Prasad

1 Introduction

Since its introduction into clinical practice two decades ago, capsule endoscopy has become established as the primary modality for examining the surface lining of the small intestine, an anatomical site previously considered to be inaccessible to clinicians. However, its reliance on peristalsis for passage through the intestine leads to significant limitations, in particular due to the unpredictable and variable locomotion speeds. Significant abnormalities may be missed, due to intermittent high transit speeds that lead to incomplete visualisation of the intestinal surface. Furthermore, each case produces up to 100,000 still images, from which video footage is generated, taking between 30 and 90 min for the clinician to examine in its entirety. The procedure is therefore considered both time consuming and burdensome for clinicians. There is, therefore, in gastrointestinal (GI) endoscopic practice a desperate need for new modalities that are safe, painless, accurate and reliable, which require minimal training for practitioners.

Leveraging their pioneering work in the field of controllable capsule endoscopy, the Applied Dynamics and Control Lab at the University of Exeter has developed a novel untethered, self-propelled, endoscopic capsule [1], with the aim of enabling cost-effective small-bowel examination. Design innovations include self-propulsion for mobility and visualisation, facilitated manipulation, real-time screening and short examination time. Building upon their successful pilot studies,

J. Tian · Y. Liu (✉)

College of Engineering, Mathematics and Physical Sciences, University of Exeter, Exeter, UK

e-mail: jt535@exeter.ac.uk; y.liu2@exeter.ac.uk

<http://blogs.exeter.ac.uk/adce/>

S. Prasad

Royal Devon and Exeter NHS Foundation Trust, Exeter, UK

e-mail: shyamprasad@nhs.net

including capsule–bowel contact modelling [2], experimental and numerical studies of intestinal frictions [3], capsule dynamics in the bowel environment [4] and their proof-of-concept validations [5, 6], with this further research, the present work will study the dynamic response of the vibro-impact capsule when it moves in the intestinal environment with the consideration of tissue’s mechanical properties by using finite element (FE) methods. This model can then be utilised to describe the detailed locomotion of the capsule and capsule–intestine interaction under vibro-impact dynamics.

The principle of the vibro-impact self-propulsion technique is that the rectilinear motion of the capsule can be obtained using a periodically driven inner mass interacting with the main capsule body in the presence of environmental resistance [7]. The merit of such a system is its simplicity in mechanical design and control, which does not require any external driving accessories, while allowing independent movement in a complex environment inaccessible for the legged and wheeled robots [8]. Imagine, for example, a miniaturised vibro-impact capsule, which is moving inside the small intestine by adopting this method. In this case, many complications induced by external driving accessories, e.g. [9], can be avoided. However, understanding of the dynamics and efficient control of such a driving mechanism are critical, and the researchers have been working on the modelling [10, 11], bifurcation analysis [12] and proof-of-concept verification [13]. So, it is critical to study the complex dynamics of the capsule in a real intestinal environment by considering the intestinal anatomy and mechanical properties, such as the viscoelasticity, the hoop stress and the haustral folds of the intestine.

In this chapter, a new FE model of capsule–intestine contact coupling with the vibro-impact mechanism in the capsule was studied. Material properties of the intestinal tissue (e.g. viscoelasticity) and the geometry of the capsule (e.g. the arced shape) were considered in the model. The dynamic response of the capsule and the capsule–intestine interaction were studied through FE analysis in order to complement the insufficient consideration of environmental influence in the previous models [10, 12]. Some new phenomena of the capsule were observed, which were not discovered in the literature before. The rest of the chapter is organised as follows. In Sect. 2, FE modelling of the vibro-impact capsule moving on the small intestine is studied. A brief introduction of the experimental apparatus and procedure is provided in Sect. 3. In Sect. 4, FE results are compared with the simulation and the experimental results. Finally, conclusions are drawn in Sect. 5.

2 Finite Element Modelling

In this section, the material properties, the geometry and the boundary conditions of the capsule and the small intestine are elaborated. The FE model was developed using ANSYS WORKBENCH Transient Structural module for which an implicit dynamics was applied.

Table 1 Material properties of the FE model obtained from [2, 3]

Parameters	Values	Units	Parameters	Values	Units
E_c	0.11	GPa	ρ_c	0.95	$\text{g} \cdot \text{mm}^{-3}$
E_a	71	GPa	ρ_a	2.77	$\text{g} \cdot \text{mm}^{-3}$
E_s	200	GPa	ρ_s	7.85	$\text{g} \cdot \text{mm}^{-3}$
E_i	25	kPa	ρ_i	1	$\text{g} \cdot \text{mm}^{-3}$
E_1	196.43	kPa	ν_c	0.42	–
E_2	757.48	kPa	ν_a	0.33	–
η_1	5.36	MPa	ν_s	0.3	–
μ_a	0.3117	–	ν_i	0.49	–
μ_i	0.2293	–			

2.1 Material Properties

Since it fits better with our stress relaxation experiment [2], the three-element Maxwell model that contains two elastic springs and one viscous dashpot was adopted to describe the viscoelasticity of the synthetic small intestine. The three-element Maxwell model can be expressed as

$$E(t) = E_1 e^{-\frac{E_1}{\eta_1} t} + E_2, \quad (1)$$

where E_1 , E_2 and η_1 are the Young's moduli of the springs and the damping coefficient, respectively. In order to compare different supporting substrates for the capsule, aluminium bench was also tested in the FE model. Table 1 summarises all the parameters used in the FE model, where E is the Young's modulus, ρ is the material density, ν is the Poisson's ratio, μ is the friction coefficient and the subscripts 'c', 'a', 's' and 'i' represent the capsule, the aluminium bench, the inner mass and the intestine, respectively. It is worth noting that E_i is the Young's modulus of the intestine for compression, and $E(t)$ is the one for tension. In this study, only E_i was used in the FE model as the capsule was placed on a cut-open intestine.

2.2 Model Description and Hypotheses

The 3D conceptual design of the capsule prototype is presented in Fig. 1a, where the capsule has a primary and a secondary impact constraints and a linear bearing. The linear bearing holds a T-shaped magnet (inner mass) and restricts its motion in the axial direction of the capsule. The magnet is controlled by an external magnetic field excited by a pulse-width modulation signal. A helical spring connecting the magnet and the bearing was used to push the magnet back to its original position after each external excitation. The two impact constraints restrict the axial motion of the magnet within a limited distance but magnify the excitation force through the

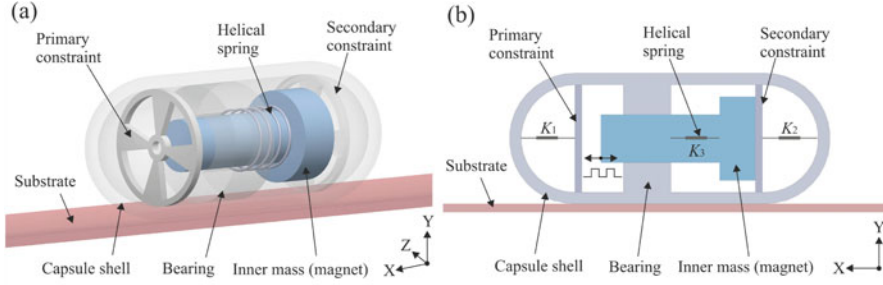


Fig. 1 (a) 3D conceptual design and (b) 2D FE model of the vibro-impact capsule moving on a cut-open small intestine

Table 2 Physical parameters for the FE model obtained from [1]

Parameters	Values	Units	Parameters	Values	Units
M_1	1.80	g	M_2	1.67	g
K_1	14.24	$\text{N} \cdot \text{mm}^{-1}$	C_1	0.01	$\text{Ns} \cdot \text{m}^{-1}$
K_2	97.06	$\text{N} \cdot \text{mm}^{-1}$	C_2	0.35	$\text{Ns} \cdot \text{m}^{-1}$
K_3	0.06	$\text{N} \cdot \text{mm}^{-1}$	C_3	0.01	$\text{Ns} \cdot \text{m}^{-1}$

vibro-impact dynamics. Due to the nonlinear characteristics of the small intestine and the nonlinear nature of the capsule system, computing a 3D FE model is time consuming. So, the 2D FE model shown in Fig. 1b was developed, and the following hypotheses were introduced:

1. The stress of the 2D plane along the Z -axis of the 3D model is zero.
2. The primary and the secondary constraints in the 3D model were replaced by using the springs connecting with two rigid plates in the 2D model.
3. The inner mass can move in the axial direction of the capsule along the frictionless bearing only.

All the identified parameters of the 2D FE model were listed in Table 2, where M_1 and M_2 are the weights of the magnet and the capsule, K_1 , K_2 and K_3 are the stiffness and C_1 , C_2 and C_3 are the damping coefficients of the primary constraint, the secondary constraint and the helical springs, respectively.

2.3 FE Setup and Mesh Convergence Test

The dimension of the FE model is presented in Fig. 2a, where the total length, the diameter and the thickness of the capsule are 26, 11 and 1 mm, respectively. The total weight of the capsule is 3.47 g, including the capsule 1.67 g and the inner mass (magnet) 1.8 g. The thickness of the small intestine is 0.69 mm measured from the synthetic small intestine used in [3]. In order to consider the energy loss by the

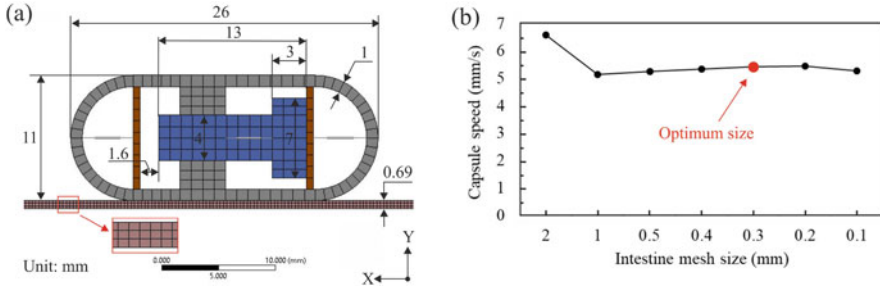


Fig. 2 (a) Dimension of the FE model and (b) mesh convergence tests: the capsule moving on the intestine at the excitation frequency of 30 Hz, the duty cycle 0.8 and the excitation amplitude 6.8 mN. Red dot marks the chosen mesh size for the intestine

collisions between the inner mass and the primary and the secondary constraints, they were set as quasi-rigid bodies in the FE model, so the primary spring K_1 and the secondary spring K_2 were more accurate to represent the constraints in the 3D model. The contact pair between the capsule and the substrate was set as frictional with their corresponding coefficients listed in Table 1. In order to get a more accurate simulation, the capsule–intestine contact algorithm was configured as pure penalty, the normal contact stiffness factor was set as 1 and the sliding motion between the internal mass and the bearing was frictionless.

Due to the requirement of deformation, two types of elements were used to mesh the proposed model. The 4-node plane element (PLANE182) was used for modelling the capsule, the inner mass and the aluminum bench. The higher order 8-node plane element (PLANE183) that exhibits quadratic displacement behaviour was used to simulate the viscoelasticity of the intestine. Convergence tests using different mesh sizes were implemented, and their results were summarised in Fig. 2b. It can be seen from the movement speed of the capsule that when the small intestine mesh is less than 1 mm, the FE result tends to converge. In order to obtain the best performance for the FE model, the mesh sizes for the capsule and the small intestine were set to 1 and 0.3 mm, respectively, and the three-layer small intestine mesh was considered as presented in Fig. 2a. For the boundary condition of the FE model, the substrates were fixed on the bottom surface. For the first 0.3 s of the simulation, the standard gravity was applied to the capsule, and the external excitation was applied to the inner mass after the capsule settled down along the Y axis.

3 Experimental Apparatus and Procedure

The prototype of the vibro-impact capsule is presented in the left panels of Fig. 3, and its experimental rig is shown in the right panel. The magnet inside the capsule was excited through an on–off electromagnetic field \vec{B} and the helical spring to

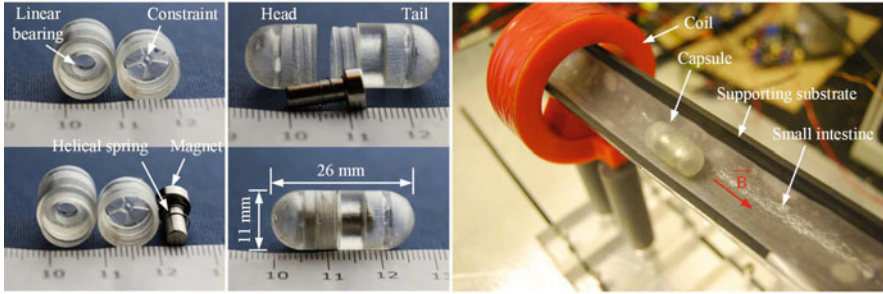


Fig. 3 [1] Left panels: components and dimension of the prototype. Right panel: photograph of the experimental setup

generate forward and backward impact motion, leading to the locomotion of the prototype. The on–off external excitation was generated using a signal generator producing a pulse-width modulation signal via a power amplifier, and the amplifier can control the voltage applied to the coil by adjusting a DC power supply. The prototype was put on a piece of cut-open synthetic small intestine supported by a halved black plastic tube, which was placed along the axis centre of the coil. On the top of the experimental setup, a video camera was used to record the motion of the capsule, and recorded videos were analysed by using an open-source software to generate the time history of capsule’s displacement and velocity. A detailed experimental study and identification of the physical parameters can be found from [1].

4 Results and Analysis

FE results for the capsule moving on the small intestine are compared with the simulation obtained using MATLAB and experimental results [1] in Fig. 4. It can be seen that both forward and backward progressions are in good agreement. In Fig. 4a, the progression speed of the capsule obtained from FE simulation is slightly higher than the other two results, which might be due to the experimental inaccuracy in measuring the friction coefficient between the capsule and the intestinal surface. In Fig. 4b, a backward progression of the capsule was recorded, but it was a chaotic motion in FE and experiment while was a periodic motion in simulation. This reveals that the FE model is more realistic than the simulation model in terms of the asymmetries caused by the impact constraint and the capsule–intestine contact.

One of the merits of the FE model is that it allows a close monitoring of different variables of the capsule system, which cannot be obtained from Matlab simulation or even be measured from experiment. Figure 5 presents such variables as the functions of time by using the excitation parameters in Fig. 4a. In Fig. 5a, capsule’s displacements in Y -axis at different positions of the capsule are presented, where

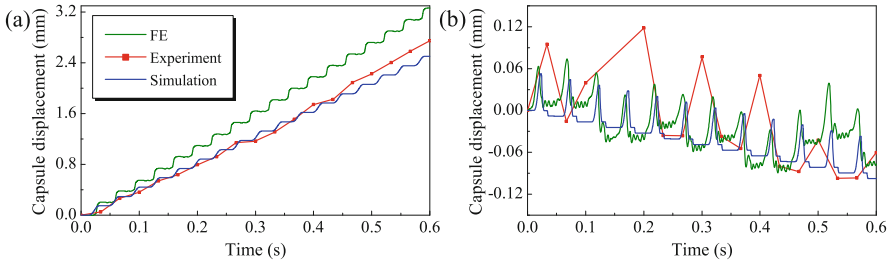


Fig. 4 (a) Time histories of capsule’s displacements in X -axis obtained at the excitation of frequency 30 Hz, the amplitude 6.8 mN and the duty cycle 0.8. (b) Time histories of capsule’s displacements in X -axis obtained at the excitation frequency of 20 Hz, the amplitude 5.8 mN and the duty cycle 0.3

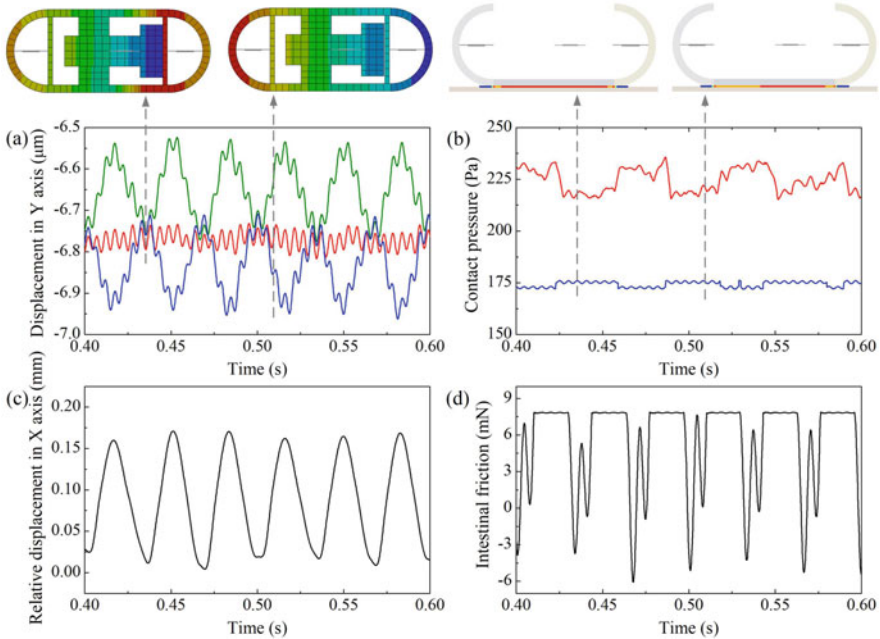


Fig. 5 (a) FE time histories of capsule’s displacements in Y -axis measured at the front (green line), middle (red line) and back (blue line) of the capsule, (b) capsule–intestine maximum (red line) and average (blue line) contact pressures, (c) magnet–capsule relative displacement and (d) intestinal friction obtained at the excitation frequency of 30 Hz, the amplitude 6.8 mN and the duty cycle 0.8. Extra panels in (a) present the contour map of displacement of the capsule in Y -axis, where red and blue colours denote large and small displacements, respectively. Extra panels in (b) present the contour map of pressure distribution on the small intestine, where red and blue colours represent high and low pressure, respectively

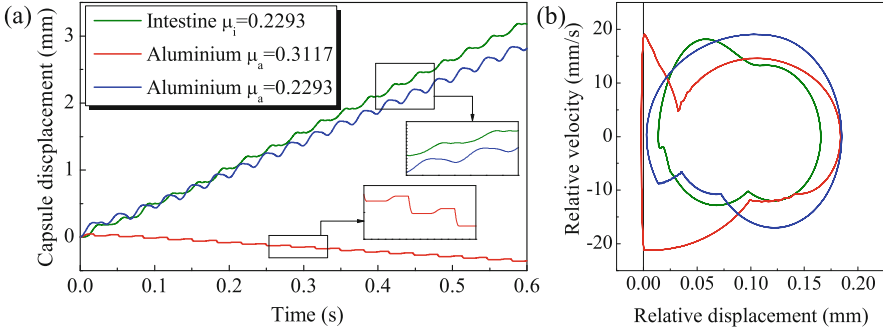


Fig. 6 (a) FE time histories of capsule's displacement in X -axis and (b) phase trajectories obtained at the excitation frequency of 30 Hz, the amplitude 6.8 mN and the duty cycle 0.8. Green, red and blue lines represent the FE results obtained on the intestine ($\mu_i = 0.2293$) and the aluminium bench ($\mu_a = 0.3117$ and 0.2293), respectively. The vertical black line stands for the back impact boundary

intestinal deformation at about $6.8 \mu\text{m}$ due to the capsule's weight was recorded. Compared with the relative displacement between the magnet and the capsule in Fig. 5c, it reveals that the capsule tilts up when their relative displacement increases, while it moves down if the magnet reverses back to its original position, which can be demonstrated in the extra panels of Fig. 5a. This tilted motion affects the distribution of the contact pressure between the capsule and the intestine as shown in Fig. 5b and its extra panels, so leading to a quasi-periodic intestinal friction on the capsule as presented in Fig. 5d. This reason also explains the discrepancies observed in Fig. 4.

To further investigate the influence of the friction coefficient and intestinal deformation on the capsule, FE simulations under different friction coefficients and supporting substrates are compared in Fig. 6. Experimental identification of the friction coefficients was carried out by lifting one side of the supporting surface slowly until the stationary capsule started to move. So the friction coefficient was determined by the angle of the surface slope at that moment. It can be seen from Fig. 6a that although their friction coefficients were set the same, the capsule moved faster on the intestine as the intestinal deformation can prevent its backward motion at each period of excitation. While when the capsule moved on the rigid aluminium bench, it had backward motion at each period of excitation. When the capsule moved on the aluminium bench with a larger friction coefficient ($\mu_a = 0.3117$) measured from experiment, the capsule bifurcated from a period-one forward motion without any impact (at $\mu_a = 0.2293$) to a period-one backward motion with one back impact. Such a qualitative change was due to the grazing-induced bifurcation as demonstrated in Fig. 6b, where the capsule's phase trajectory crossed over the back impact boundary indicating the contact between the magnet and the secondary constraint.

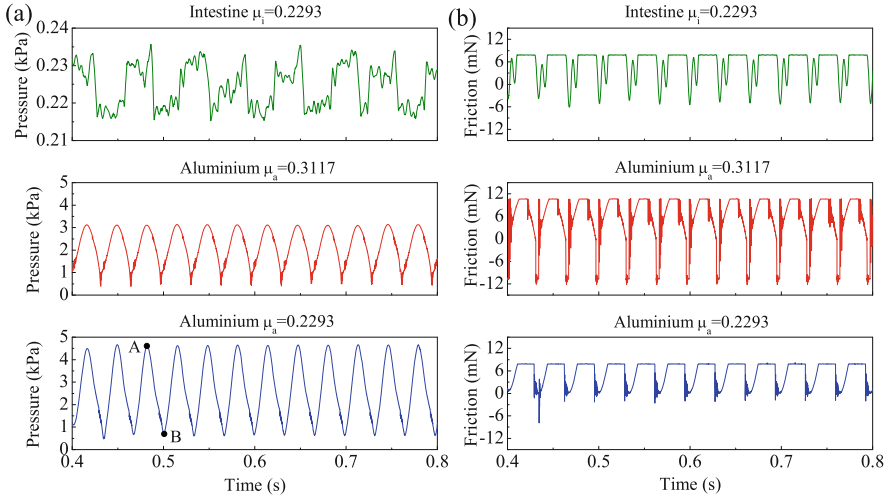


Fig. 7 (a) Maximum contact pressures and (b) intestinal frictions obtained at the excitation frequency 30 Hz, the amplitude 6.8 mN, and the duty cycle 0.8. Green, red and blue lines represent the FE results obtained on the intestine ($\mu_i = 0.2293$) and the aluminium bench ($\mu_a = 0.3117$ and 0.2293), respectively

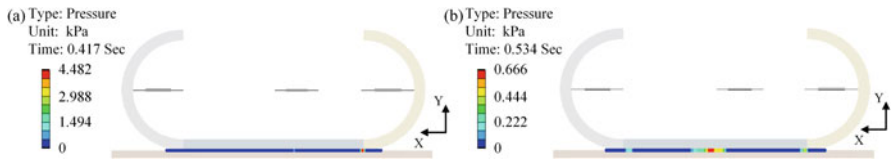


Fig. 8 The contour map of pressure distribution on the aluminium bench corresponding to points (a) A and (b) B marked in Fig. 7a

To compare the tilted motion of the capsule on different substrates, Fig. 7 presents the maximum contact pressures on the substrates and its relevant intestinal frictions on the capsule. As can be seen from Fig. 7a, the maximum contact pressure on the aluminium bench is much larger than the one on the intestine. This is due to the rigidity of the aluminium bench as illustrated in Fig. 8 such that when the capsule tilts up, it has much less contact area with the bench, while the intestine is “soft” resulting in a large contact area. Hence, such a difference in the supporting materials led to different frictions on the capsule.

5 Conclusions

This chapter studied a realistic 2D FE model to depict the nonlinear motion of the vibro-impact capsule moving on the small intestine. FE results were validated by using the simulation results obtained using non-smooth differential equations and

the experimental results in [1]. Comparative analysis indicates that the FE model can better represent the capsule's dynamics and the contact with its substrate. It was found that the titled motion of the capsule during progression may cause asymmetric pressure on the substrate leading to quasi-periodic friction on the capsule. Therefore, a comprehensive bifurcation study for fully understanding its dynamics under intestinal peristalsis is recommended for future development.


Acknowledgments This work has been supported by EPSRC under grant no. EP/R043698/1. Mr. Jiyuan Tian would like to acknowledge the financial support from the China Scholarship Council (award no. 201908060172) for his PhD scholarship.

References

1. Y. Liu, J. Páez Chávez, J. Zhang, J. Tian, B. Guo, S. Prasad, The vibro-impact capsule system in millimetre scale: numerical optimisation and experimental verification. *Meccanica* **55**, 1885–1902 (2020)
2. B. Guo, Y. Liu, S. Prasad, Modelling of capsule–intestine contact for a self-propelled capsule robot via experimental and numerical investigation. *Nonlinear Dyn.* **98**, 3155–3167 (2019)
3. B. Guo, E. Ley, J. Tian, J. Zhang, Y. Liu, S. Prasad, Experimental and numerical studies of intestinal frictions for propulsive force optimisation of a vibro-impact capsule system. *Nonlinear Dyn.* **101**, 65–83 (2020)
4. Y. Yan, Y. Liu, L. Manfredi, S. Prasad, Modelling of a vibro-impact self-propelled capsule in the small intestine. *Nonlinear Dyn.* **96**, 123–144 (2019)
5. B. Guo, Y. Liu, R. Birler, S. Prasad, Self-propelled capsule endoscopy for small-bowel examination: proof-of-concept and model verification. *Int. J. Mech. Sci.* **174**, 105506 (2020)
6. Y. Liu, J. Páez Chávez, B. Guo, R. Birler, Bifurcation analysis of a vibro-impact experimental rig with two-sided constraint. *Meccanica* **55**, 2505–2521 (2020)
7. F.L. Chernous'ko, Two- and three-dimensional motions of a body controlled by an internal movable mass. *Nonlinear Dyn.* **99**, 793–802 (2020)
8. A. Nunuparov, F. Becker, N. Bolotnik, I. Zeidis, K. Zimmermann, Dynamics and motion control of a capsule robot with an opposing spring. *Arch. Appl. Mech.* **89**, 2193–2208 (2019)
9. P. Glass, E. Cheung, M. Sitti, A legged anchoring mechanism for capsule endoscopes using micropatterned adhesives. *IEEE Trans. Biomed. Eng.* **55**, 2759–2767 (2008)
10. Y. Liu, E. Pavlovskaja, M. Wiercigroch, H. Yu, Modelling of a vibro-impact capsule system. *Int. J. Mech. Sci.* **66**, 2–11 (2013)
11. X. Zhan, J. Xu, H. Fang, A vibration-driven planar locomotion robot—shell. *Robotica* **36**, 1402–1420 (2018)
12. Y. Liu, E. Pavlovskaja, M. Wiercigroch, Z. Peng, Forward and backward motion control of a vibro-impact capsule system. *Int. J. Non-Linear Mech.* **70**, 30–46 (2015)
13. Y. Liu, E. Pavlovskaja, M. Wiercigroch, Experimental verification of the vibro-impact capsule model. *Nonlinear Dyn.* **83**, 1029–1041 (2015)

Vibro-Impact Capsule Under Different Conditions of Friction



Ngoc-Tuan La, Thanh-Toan Nguyen, Ky-Thanh Ho, Quoc-Huy Ngo,
and Van-Du Nguyen 

1 Introduction

Recently, the application of vibration-driven locomotion in capsule robots has been widely considered. A capsule robot is a platform that can self-propel in a resistive environment but can be encapsulated in a smooth form, without any external propellers [1]. The design of the locomotion systems is based on the two major mechanics of the interaction between the internal mass and the system body, known as vibration-driven and vibro-impact-driven principles.

In vibration-driven locomotion systems, initially proposed by Chernous'ko [2], the rectilinear motion can be achieved by using an additional internal mass interacting with the body frame. On the one hand, the simplicity in structure of the system makes it well suitable to form capsule robots. On the other hand, it is required that the relative motion of the internal mass must be controlled to have an exact form of multiphase accelerations. The vibration-driven platforms have been extensively investigated from various aspects, such as designing, modeling, and experimental validation [3–10]; dynamical analysis [11–16]; and optimal progression and motion control [14, 17–24]. The internal mass can connect with the body by means of an elastic spring to enhance the resonant characteristics. Various methods have been proposed to actuate the internal drives, including DC-motor-driven pendulum [25], unbalance rotor [10, 26], electromagnetic mechanisms [14, 27–29], and solenoid [15], [28]. Several useful guidelines for the design and control of bistable vibration-driven locomotion systems were also provided. However, for periodic relative

N.-T. La
Vinh University of Technology Education, Vinh, Vietnam

T.-T. Nguyen · K.-T. Ho · Q.-H. Ngo · V.-D. Nguyen (✉)
Thai Nguyen University of Technology, Thai Nguyen University, Thai Nguyen, Vietnam
e-mail: vandu@tnut.edu.vn

motion of the internal mass, the friction must be anisotropic, i.e., friction force in the forward direction is smaller than that in backward trend (e.g., [7, 15, 18, 30, 31]). As a whole, the major concerns of the first design option would be the complex motion control and special demand of anisotropic friction.

In a vibro-impact-driven locomotion system, the internal mass oscillates and has periodical impacts with the system body [32], resulted in a jump-up of the inertial force. When the impact force exceeds the friction force, the system is displaced. The drifting oscillator proposed by Pavlovskaja et al. [33] provided a fundamental model for distinctive locomotion systems. The internal mass (impact oscillator) has been driven by various ways, for example, a system of motor and cam mechanism [34], solenoid working with sinusoidal in an RLC circuit [35, 36], electromagnetic device [37, 38], linear motor [9], and electrodynamic shaker [16, 22]. The system can be either position feedback controlled [23] or reverse the impact side [5] to obtain the expected direction of motion.

In previous experimental studies on the locomotion platforms, the friction force was considered as either an isotropic [13] or an anisotropic [18] resistance. Several experimental studies have been investigated. However, the effect of various friction levels on the system behavior was not fully examined.

With isotropic assumption, the excitation force was usually compared with the friction force magnitude, using the force ratio between the excited amplitude and the friction force. The motion of the system was examined for different levels of the excitation by varying such force ratio (see, e.g., in [5, 9, 25, 32, 33]). In experimental studies, a preset and unchanged dry friction was usually implemented (see [8, 9, 22, 39, 40]). The dependence of the system response as a function of the friction variable has rarely been experimentally examined [35, 41]. Several interesting phenomena have been observed [9, 23]. For example, when the elastic force acting on the system body becomes greater than the friction threshold, the system may move backward [23]. In some situations, applying a larger excited amplitude would not improve the performance of the system [9]. It is regretted that such interesting interpretations were carried out at a certain value of friction. Besides, the magnitude of excitation force was counted by comparing it with the friction. The results of our study revealed that with the same force ratio, different values of friction provided different average velocities and also the direction of the progression. Recently, several interesting investigations were implemented, focusing on the efficacy of the model and its feasibility under various isotropic frictional conditions [42, 43]. Various capsule-intestine contact conditions for which the capsule moves include four cases of isotropic friction: flat-open synthetic small intestine in a flat form and in a curve form, collapsed and loose synthetic small intestine, and contractive synthetic intestine whose inner diameter was smaller than the capsule's external diameter.

Several studies were made for anisotropic friction, where the friction force in forward motion is different from that in backward motion. However, most of the experimental studies assumed that the forward friction is smaller than the backward friction [18, 30]. Such systems either were built with asymmetric legs [30] or were able to move downward on an inclined chute only [18]. In our study, the response

of the locomotion system was experimentally examined under a more general case of anisotropic friction, where the resistant force in the forward direction is larger than that in the backward motion. The experimental setup was built similar to the one implemented in [18], but the forward direction was considered to be the upward trend on an inclined chute. Moreover, the resistant force consisted of two contents: one preset and an adjustable level.

This report presents an experimental study on the vibro-impact-driven capsule, working under different friction conditions, including isotropic and anisotropic resistant forces. The experimental setup made it possible to vary the friction force easily.

2 Experimental Setup

The model of a vibro-impact locomotion system is shown in Fig. 1a.

An internal mass m_1 is connected with the system frame mass m_2 by a spring with stiffness k and a linear viscous damper c . A harmonic sinusoidal force F_m acts on both masses as an interaction force. The impact stiffness is modeled as a linear spring k_0 . X_1 and X_2 are the absolute displacements of the two masses m_1 and m_2 , respectively. At the initial stage, the two masses gave a gap G . Whenever $X_1 - X_2$ overcomes the gap G , impact happens, and thus, the system can move forward. A dry friction force F_S presents the environment resistance acting against the motion of the system frame.

In this study, the experimental apparatus was made to provide either isotropic friction or anisotropic friction resistance. When the system is arranged horizontally, as shown in Fig. 1a, the resistant forces in forward and backward motions are considered to be the same, i.e., the friction force is isotropic. The setup was then developed to examine the anisotropic friction, referring to previous studies [7, 18],

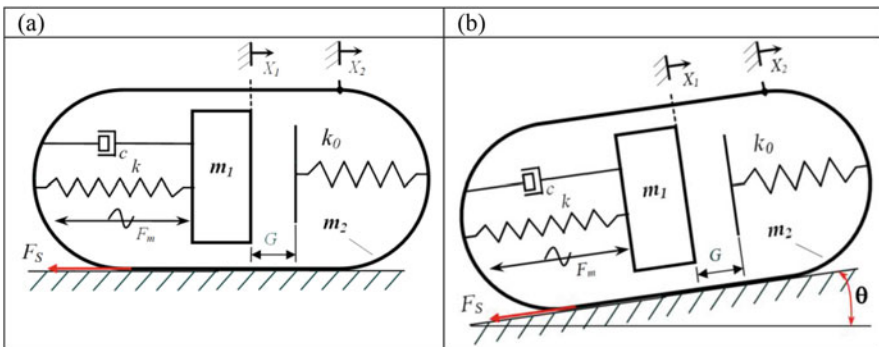


Fig. 1 Models of the vibro-impact locomotion system with (a) isotropic friction and (b) anisotropic friction

where the forward resistance is smaller than the backward resistance. When the prototype is placed on an inclined surface, as shown in Fig. 1b, the anisotropy characteristic of the friction coefficients can be achieved by making use of the gravity effect.

When the prototype is moving on the chute, the equivalent friction force consists of two parts: one is the dry friction force F_S , and the other is the gravitational force component along the inclined chute direction. In contrast to [7, 18], this study assigned the upward direction as the forward motion, i.e., the forward resistance force is larger than the backward resistance. Increasing the inclined angle, θ leads to increase in the ratio between forward friction and backward friction. In this study, such ratio will be called the anisotropic ratio. Two levels of the ratio were examined, represented by two values of the inclined angle, θ .

The detailed experimental setup is described in Fig. 2, where the experimental schema is depicted in Fig. 2a and a photograph of the realized apparatus is shown in Fig. 2b.

In Fig. 2, a mini electrodynamic shaker (1) was used to provide relative oscillations between the two masses. The shaker was fixed on a rolling slider guide (4), provided that a tiny rolling friction force is available when the system moves. The slider can be adjusted to provide a certain inclined angle θ , with respect to the horizontal surface. An additional mass (2) was fixed on the shaker shaft. Exciting the shaker by a sinusoidal current, a linear oscillation of the shaker shaft with respect to the shaker body was generated. The internal mass m_1 involves the addition of mass and the shaker shaft weight. A noncontact position sensor (7) was used to measure the relative motion of the internal mass m_1 . The displacement of the shaker body was collected by a linear variable displacement transformer (LVDT). The body shaker, including the sensors and the carbon tube, is denoted as the mass m_2 . An obstacle block (3) was used to absorb the impact force. A carbon tube (5), which has a tiny weight, is connected with the shaker body by means of a flexible joint and can be slid inside a coupled V-block. This mechanism provided the ability to adjust the resistance (friction) force when the system is moving. The detailed mechanism of providing preset friction is depicted in Fig. 3.

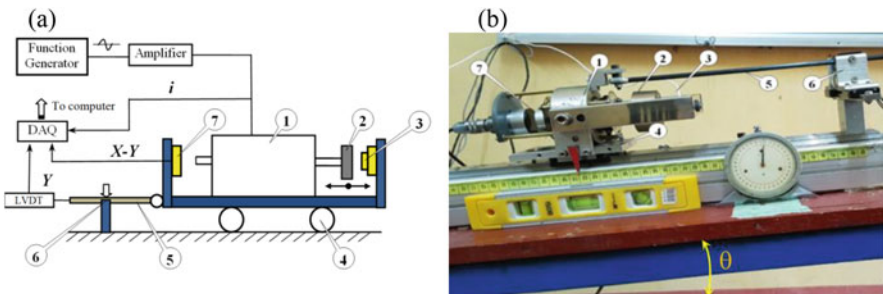


Fig. 2 Models of the vibro-impact locomotion system with (a) isotropic friction and (b) anisotropic friction

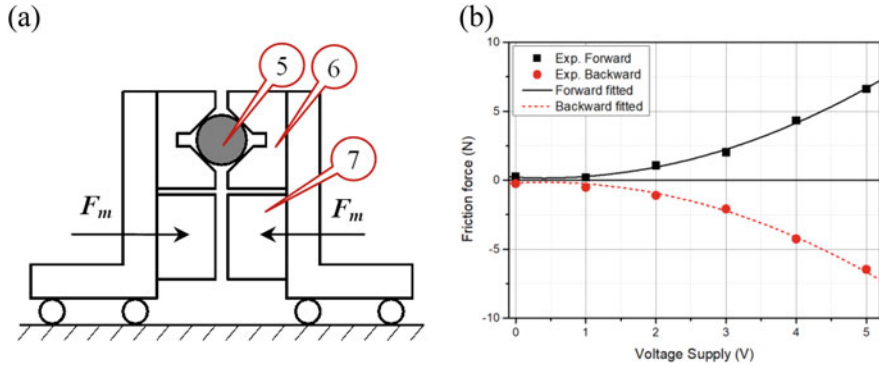


Fig. 3 Varying the friction force: (a) apparatus structure and (b) the dependency of friction force on the supplied voltage

Table 1 Experimental factors

Factor	Notation	Value	Unit
Internal mass	m_1	0.518	Kg
Body mass	m_2	1.818	Kg
Impact gap	G	0.5	mm
Friction force	F_S	2.4; 6.8; and 13.6	N
Force ratio	$\alpha = A/F_S$	0.59; 0.79; 0.99; and 1.19	–
Inclined angle	θ	0; 2.5 and 5	°
Excitation frequency	f_{exc}	15	Hz

As depicted in Fig. 3a, the carbon tube (5) connects with and moves together with the system body. The tube is clamped by means of two aluminum V-block (6), which are fixed on two electromagnets (7). By adjusting the electrical current supplied to the electromagnets, it is able to obtain the expected force clamping the carbon tube. As a result, the sliding friction force exerting on the tube when moving can be predetermined. Moving the body at a slow and steady speed, the preset friction force corresponding to the voltage supplied can be collected (see more details in [41]). Figure 3b presents the relationship between the control voltage and the slide friction force. Based on such relationship, the preset friction between the system and the environment can be adjusted, without changing the weight of the system. Table 1 shows the values of experimental parameters.

3 Results and Discussions

Figure 4 shows the time history of the motion X_1 of the internal mass and the motion X_2 of the whole body for various preset friction levels and inclined angles.

Overall, the system works under higher preset friction force would have more ability to move forward. Besides, increasing the inclined angle θ resulted in either

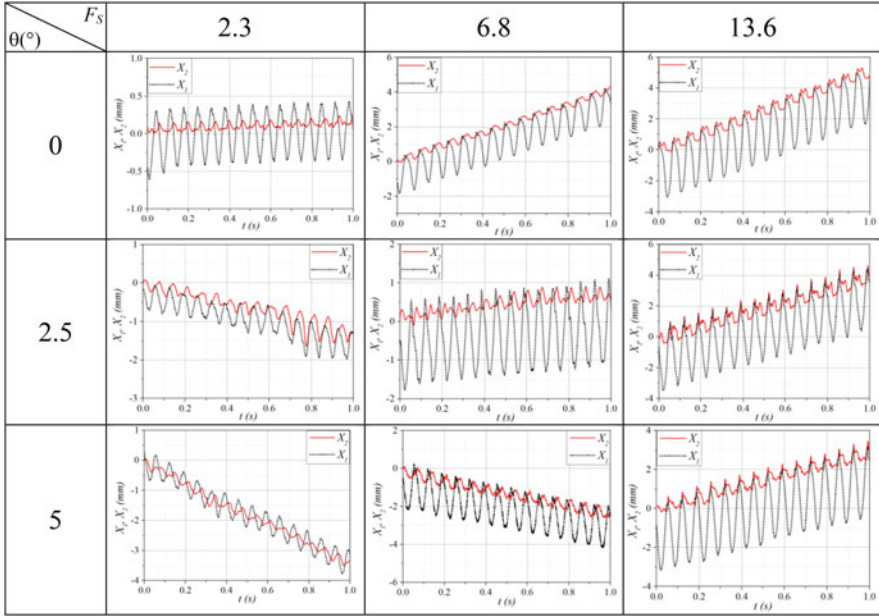


Fig. 4 Time history of the motions of the two masses for various values of preset friction and inclined angle; a force ratio $\alpha = 0.59$ and an excitation frequency of 15 Hz were applied

backward motion or a lower forward progression rate. It is reasonable due to the effect of the gravity force, which always tends to draw the system to move backward.

As shown in the first-row subplots of Fig. 4, under the isotropic friction ($\theta = 0^\circ$), increasing the preset friction would provide a higher progression rate. For anisotropic friction ($\theta = 2.5^\circ$ and $\theta = 5^\circ$), a low preset friction resulted in a backward motion, whereas the highest preset friction provided the fastest forward motion.

In order to examine the moving direction as well as the progression rate of the system under the concurrent effect of the force ratio and the preset friction, three sets for inclined angles of 0° , 2.5° , and 5° were implemented. Each set includes 12 runs, combining three levels of friction ($F_S = 2.3$ N, 6.8 N, and 13.6 N), and four levels of the force ratio ($\alpha = 0.59, 0.79, 0.99$, and 1.19) were implemented. The progression velocity obtained is represented by two-parameter contour plots in Fig. 5. The plots were made directly from experimental data by OriginLab[®] software. In Fig. 5, the areas of backward motion (denoted by the sign “-”) were represented by gray, dark grey, violet, blue, purple, and navy, whereas the areas of forward motion (denoted by the sign “+”) were shown in green, yellow, orange, and magenta.

As can be seen, in the investigated ranges of the two parameters, for isotropic friction (Fig. 5a), the system had forward motion for most combination values of the preset friction force and the force ratio. The system moved backward in a small range of the force ratio $\alpha \in [1.05, 1.19]$ combined with a large range of friction force

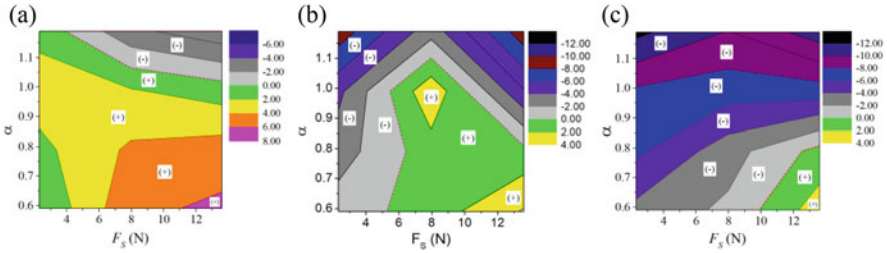


Fig. 5 (Color online) Contour plots of the progression rate with respects to the preset friction force F_s and the force ratio α for (a) $\theta = 0^\circ$, (b) $\theta = 2.5^\circ$, and (c) $\theta = 5^\circ$

$F_s \in [4.5, 13.6]$ N. With higher inclined angles, the areas of backward motion became larger, and the forward motion appeared in smaller ranges of the parameters. With an inclined angle of 5° , the system had forward motion in small ranges of $F_s \in [10, 13.6]$ N and $\alpha \in [0.59, 0.79]$. Generally, larger friction combined with a smaller value of the force ratio would result in faster moving forward.

4 Conclusions

This paper presented experimental results of a vibro-impact-driven locomotion system under different friction conditions, including both isotropic and anisotropic friction.

The following remarks would be useful for further studies:

- For the system working with isotropic friction, the level of preset friction force would have significant effects both on the rate and the direction of the progression.
- For the system working with anisotropic friction, the vibro-impact would provide forward motion of the whole system. Larger friction combined with a smaller value of the force ratio would result in faster moving forward.

Acknowledgments This research is funded by Vietnam National Foundation for Science and Technology Development (NAFOSTED) under grant number 107.01-2017.318.

References

1. A. Garg, C.S. Vikram, S. Gupta, M.K. Sutar, P.M. Pathak, N.K. Mehta, A.K. Sharma, V.K. Gupta, Design and development of in vivo robot for biopsy. *Mech. Based Design Struct. Mach.* **42**(3), 278–295 (2014). <https://doi.org/10.1080/15397734.2014.898587>
2. F.L. Chernous'ko, The optimum rectilinear motion of a two-mass system. *J. Appl. Math. Mech.* **66**(1), 1–7 (2002). [https://doi.org/10.1016/S0021-8928\(02\)00002-3](https://doi.org/10.1016/S0021-8928(02)00002-3)

3. Y. Yan, Y. Liu, L. Manfredi, S. Prasad, Modelling of a vibro-impact self-propelled capsule in the small intestine. *Nonlinear Dyn.* **96**(1), 123–144 (2019). <https://doi.org/10.1007/s11071-019-04779-z>
4. J. Ju, Q. Wang, K. Zhang, Design and analysis of a novel micro-robot driving platform. *Proc. Inst. Mech. Eng. C J. Mech. Eng. Sci.* **233**(11), 3849–3857 (2018). <https://doi.org/10.1177/0954406218802314>
5. T.-H. Duong, V.-D. Nguyen, H.-C. Nguyen, N.-P. Vu, N.-K. Ngo, V.-T. Nguyen, A new design for bidirectional autogenous mobile systems with two-side drifting impact oscillator. *Int. J. Mech. Sci.* **140**, 325–338 (2018). <https://doi.org/10.1016/j.ijmecsci.2018.01.003>
6. Y. Yan, Y. Liu, J. Páez Chávez, F. Zonta, A. Yusupov, Proof-of-concept prototype development of the self-propelled capsule system for pipeline inspection. *Meccanica* **53**(8), 1997–2012 (2018). <https://doi.org/10.1007/s11012-017-0801-3>
7. Z. Du, H. Fang, X. Zhan, J. Xu, Experiments on vibration-driven stick-slip locomotion: A sliding bifurcation perspective. *Mech. Syst. Signal Process.* **105**, 261–275 (2018). <https://doi.org/10.1016/j.ymsp.2017.12.001>
8. V.-D. Nguyen, H.-C. Nguyen, N.-K. Ngo, N.-T. La, A new design of horizontal electro-Vibro-impact devices. *J. Comput. Nonlinear Dyn.* **12**(6), 061002 (2017). <https://doi.org/10.1115/1.4035933>
9. Y. Liu, E. Pavlovskaia, M. Wiercigroch, Experimental verification of the vibro-impact capsule model. *Nonlinear Dyn.* **83**(1–2), 1029–1041 (2015). <https://doi.org/10.1007/s11071-015-2385-6>
10. N.A. Sobolev, K.S. Sorokin, Experimental investigation of a model of a vibration-driven robot with rotating masses. *J. Comput. Syst. Sci. Int.* **46**(5), 826–835 (2007). <https://doi.org/10.1134/s1064230707050140>
11. P. Liu, H. Yu, S. Cang, Modelling and analysis of dynamic frictional interactions of vibro-driven capsule systems with viscoelastic property. *Eur. J. Mech. A-Solids* **74**, 16–25 (2019). <https://doi.org/10.1016/j.euromechsol.2018.10.016>
12. P. Liu, H. Yu, S. Cang, On the dynamics of a vibro-driven capsule system. *Arch. Appl. Mech.* **88**(12), 2199–2219 (2018). <https://doi.org/10.1007/s00419-018-1444-0>
13. Y. Liu, E. Pavlovskaia, D. Hendry, M. Wiercigroch, Vibro-impact responses of capsule system with various friction models. *Int. J. Mech. Sci.* **72**, 39–54 (2013). <https://doi.org/10.1016/j.ijmecsci.2013.03.009>
14. A. Nunuparov, F. Becker, N. Bolotnik, I. Zeidis, K. Zimmermann, Dynamics and motion control of a capsule robot with an opposing spring. *Arch. Appl. Mech.* **89**(10), 2193–2208 (2019). <https://doi.org/10.1007/s00419-019-01571-8>
15. X. Zhan, J. Xu, H. Fang, A vibration-driven planar locomotion robot—Shell. *Robotica* **36**(9), 1402–1420 (2018). <https://doi.org/10.1017/S0263574718000383>
16. V.-D. Nguyen, T.-H. Duong, N.-H. Chu, Q.-H. Ngo, The effect of inertial mass and excitation frequency on a Duffing vibro-impact drifting system. *Int. J. Mech. Sci.* **124–125**, 9–21 (2017). <https://doi.org/10.1016/j.ijmecsci.2017.02.023>
17. J. Fan, C. Li, Z. Yang, S. Chen, J. Cao, C. Dou, On discontinuous dynamics of a 2-DOF oscillator with an one-sided rigid obstacle. *Int. J. Non-Linear Mech.* **118**, 103261 (2020). <https://doi.org/10.1016/j.ijnonlinmec.2019.103261>
18. J. Xu, H. Fang, Improving performance: recent progress on vibration-driven locomotion systems. *Nonlinear Dyn.* **98**(4), 2651–2669 (2019). <https://doi.org/10.1007/s11071-019-04982-y>
19. P. Liu, H. Yu, S. Cang, Optimized adaptive tracking control for an underactuated vibro-driven capsule system. *Nonlinear Dyn.* **94**(3), 1803–1817 (2018). <https://doi.org/10.1007/s11071-018-4458-9>
20. M.V. Golitsyna, Periodic regime of motion of a vibratory robot under a control constraint. *Mech. Solids* **53**(1), 49–59 (2018). <https://doi.org/10.3103/S002565441803007X>
21. F.L. Chernousko, Optimal control of two-dimensional motions of a body by a movable mass. *IFAC-PapersOnLine* **51**(2), 232–235 (2018). <https://doi.org/10.1016/j.ifacol.2018.03.040>

22. V.-D. Nguyen, H.-D. Ho, T.-H. Duong, N.-H. Chu, Q.-H. Ngo, Identification of the effective control parameter to enhance the progression rate of vibro-impact devices with drift. *J. Vib. Acoust.* **140**(1), 011001 (2017). <https://doi.org/10.1115/1.4037214>
23. Y. Liu, E. Pavlovskaja, M. Wiercigroch, Z. Peng, Forward and backward motion control of a vibro-impact capsule system. *Int. J. Non-Linear Mech.* **70**, 30–46 (2015). <https://doi.org/10.1016/j.ijnonlinmec.2014.10.009>
24. B. He, B.R. Wang, T.H. Yan, Y.Y. Han, A distributed parallel motion control for the multi-thruster autonomous underwater vehicle. *Mech. Based Des. Struct. Mach.* **41**(2), 236–257 (2013). <https://doi.org/10.1080/15397734.2012.726847>
25. P. Liu, M. Nazmul Huda, Z. Tang, K. Sun, A self-propelled robotic system with a visco-elastic joint: Dynamics and motion analysis. *Eng. Comput.* **36**(2), 655–669 (2019). <https://doi.org/10.1007/s00366-019-00722-3>
26. H. Yu, Y. Liu, T. Yang, Closed-loop tracking control of a pendulum-driven cart-pole underactuated system. *Proc. Inst. Mech. Eng. Part I J. Syst. Control Eng.* **222**(2), 109–125 (2008). <https://doi.org/10.1243/09596518JSCE460>
27. M.N. Huda, H. Yu, Trajectory tracking control of an underactuated capsbot. *Auton. Robot.* **39**(2), 183–198 (2015). <https://doi.org/10.1007/s10514-015-9434-3>
28. G. Su, C. Zhang, R. Tan, H.A. Li, Design of the electromagnetic driver for the internal force-static friction capsbot. In: *2009 IEEE/RSJ International Conference on Intelligent Robots and Systems*, 10–15 Oct. 2009 2009, pp 613–617. <https://doi.org/10.1109/IROS.2009.5354587>
29. H. Li, K. Furuta, F.L. Chernousko, Motion generation of the capsbot using internal force and static friction. In: *Proceedings of the 45th IEEE Conference on Decision and Control*, 13–15 Dec. 2006 2006, pp. 6575–6580. <https://doi.org/10.1109/CDC.2006.377472>
30. J. Xu, H. Fang, Stick-slip effect in a vibration-driven system with dry friction: sliding bifurcations and optimization. *J. Appl. Mech.* **81**, 061001 (2014). <https://doi.org/10.1115/1.4025747>
31. F.L. Chernous'ko, The optimal periodic motions of a two-mass system in a resistant medium. *J. Appl. Math. Mech.* **72**(2), 116–125 (2008). <https://doi.org/10.1016/j.jappmathmech.2008.04.014>
32. Y. Yan, Y. Liu, M. Liao, A comparative study of the vibro-impact capsule systems with one-sided and two-sided constraints. *Nonlinear Dyn.* **89**(2), 1063–1087 (2017). <https://doi.org/10.1007/s11071-017-3500-7>
33. E. Pavlovskaja, M. Wiercigroch, C. Grebogi, Modeling of an impact system with a drift. *Phys. Rev. E Stat. Nonlin. Soft Matter Phys.* **64**(5 Pt 2), 056224 (2001). <https://doi.org/10.1103/PhysRevE.64.056224>
34. E. Pavlovskaja, M. Wiercigroch, K.-C. Woo, A.A. Rodger, Modelling of ground Miling dynamics by an impact oscillator with a frictional slider. *Meccanica* **38**(1), 85–97 (2003). <https://doi.org/10.1023/a:1022023502199>
35. V.-D. Nguyen, K.-C. Woo, E. Pavlovskaja, Experimental study and mathematical modelling of a new of vibro-impact miling device. *Int. J. Non-Linear Mech.* **43**(6), 542–550 (2008). <https://doi.org/10.1016/j.ijnonlinmec.2007.10.003>
36. V.D. Nguyen, K.C. Woo, New electro-vibroimpact system. *Proc. Inst. Mech. Eng. C J. Mech. Eng. Sci.* **222**(4), 629–642 (2008). <https://doi.org/10.1243/09544062jmes833>
37. A.N. Grankin, S.F. Yatsun, Investigation of vibroimpact regimes of motion of a mobile microrobot with electromagnetic drive. *J. Comput. Syst. Sci. Int.* **48**(1), 155–163 (2009). <https://doi.org/10.1134/S1064230709010158>
38. K.A. Sapronov, A.A. Cherepanov, S.F. Yatsun, Investigation of motion of a mobile two-mass vibration-driven system. *J. Comput. Syst. Sci. Int.* **49**(1), 144–151 (2010). <https://doi.org/10.1134/S1064230710010156>
39. J.-H. Ho, V.-D. Nguyen, K.-C. Woo, Nonlinear dynamics of a new electro-vibro-impact system. *Nonlinear Dyn.* **63**(1–2), 35–49 (2010). <https://doi.org/10.1007/s11071-010-9783-6>
40. G. Su, C. Zhang, R. Tan, H.A. Li, Design of the electromagnetic driver for the “internal force-static friction” capsbot. In: *The 2009 IEEE/RSJ International Conference on Intelligent Robots and Systems*, 2009. IEEE, pp 613–617

41. V.-D. Nguyen, N.-T. La, An improvement of vibration-driven locomotion module for capsule robots. *Mech. Based Des. Struct. Mach.*, 1–15 (2020). <https://doi.org/10.1080/15397734.2020.1760880>
42. B. Guo, Y. Liu, R. Birler, S. Prasad, Self-propelled capsule endoscopy for small-bowel examination: proof-of-concept and model verification. *Int. J. Mech. Sci.* **174**, 105506 (2020). <https://doi.org/10.1016/j.ijmecsci.2020.105506>
43. B. Guo, E. Ley, J. Tian, J. Zhang, Y. Liu, S. Prasad, Experimental and numerical studies of intestinal frictions for propulsive force optimisation of a vibro-impact capsule system. *Nonlinear Dyn.* **101**(1), 65–83 (2020). <https://doi.org/10.1007/s11071-020-05767-4>

Modeling the Fear-Induced Spatiotemporal Dynamics of Three-Species Interaction in Agroecosystems



Swati Mishra and Ranjit Kumar Upadhyay

1 Introduction

Herbivory can be very overpricing as it significantly removes the valuable photosynthesis material of plants required for the growth and reproduction of plants. Every year millions of dollars losses occur in the agricultural industry due to herbivory. Usually, pesticides are used to reduce herbivory. These synthetic chemicals have an adverse effect on the environment. For environment-friendly concern, utilizing natural methods for controlling pest density is the need of the day. A good number of biological control agents showed promising results as an alternative to pesticides [1]. In the agricultural ecosystem, “non-web building” wolf spider of family Lycosidae is often the dominant predatory arthropods [2] and a good candidate for biological control measures.

The presence of spiders in an agroecosystem impacts insect pests not only through direct predation but also through the fear effects. Silk draglines and pheromones produced by wolf spiders serve as chemical cues [3]. These cues cause fear among the herbivores, and they avoid the plants bearing the spiders or their cues. Thus, it alters the foraging behavior of herbivores insects [4]. Recently, Suraci et al. [5] manipulated the fear of large carnivores (wolves, cougars, and black bears) on the mesocarnivore (raccoons) on several small coastal Gulf Islands by using the month-long vocalizations of large carnivore in their field experiment. They reported 66% less time foraging over the course of the month. This dramatic reduction in mesocarnivore foraging in turn dramatically benefits the mesocarnivore’s prey (intertidal crabs, intertidal fish, polychaete worms, and subtidal red rock crabs). They observed that due to the month-long large carnivore playbacks, there were

S. Mishra · R. K. Upadhyay (✉)

Department of Mathematics & Computing, Indian Institute of Technology (ISM), Dhanbad, India

97% more intertidal crabs, 81% more intertidal fish, 59% more polychaete worms, and 61% more subtidal red rock crabs.

Fear effects in predator–prey interaction models are first introduced by Wang et al. [6]. After this work, various studies have been done to investigate the impact of fear in predator–prey systems [7–10]. Recently, Panday et al. [11] studied a tri-trophic food chain model with a specialist top predator in which they have incorporated the lowered foraging behavior due to the fear of top predator. In this work, we have proposed mathematical model for wolf spiders, insect pests, and plant community interactions in an agroecosystem. Experimental studies [4] have reported that the chemical cues by wolf spiders affect the behavior of herbivore insects and thus limit their feeding activities in agriculture systems. To model the reduced foraging time due to fear of wolf spiders, we have multiplied the predation rate of insect pests by the factor $f(k, S) = \frac{1}{1+kS}$, where k is the level of fear.

Populations are rarely homogeneously distributed in space what makes the study of pattern formation a very important issue. Turing’s seminal work [12] explained that a stationary stable homogeneous distribution of two chemical substances in the absence of diffusion can be destabilized by heterogeneous perturbations when diffusion is present. Segel and Jakson [13] have presented Turing’s idea of instability induced by diffusion in ecological context. Gierer and Meinhardt [14] identified the “activator–inhibitor mechanism.” Since then various studies have been done on pattern formation scenario via Turing instability [15–17]. These studies have not considered the impact of fear in species interactions. Recently, Wang and Zou [8] first time explored pattern formation scenario in a predator–prey model with fear effect. After that Upadhyay and Mishra [9] have illustrated the spatiotemporal dynamics and pattern formation in a system with fearful prey and predator population. Pattern formation and pattern selection in the modified Leslie–Gower (LG) predator–prey model with fear effect are studied by Han et al. [18]. All these works have explored the pattern formation in the two-species predator–prey model with fear effect. In this work, we have investigated the pattern formation and Turing instability conditions in a three-species plant community–insect pests–wolf spiders interaction model in an agroecosystem.

In this chapter, we have studied the temporal and spatiotemporal dynamics of a tri-trophic food-chain model with fear effect in an agroecosystem. We have discussed the stability and Turing instability analysis of the proposed system. It is obtained that fear level k has stabilizing impact on the temporal dynamics and destabilizing impact on the spatial dynamics. We have presented 1D and 2D Turing patterns. We have explored the “wave of chaos” phenomenon first time in the food-chain model with fear effect. The chapter is organized as follows. In Sect. 2, we have given model formulation. Analysis of the temporal system is performed in Sect. 3. In Sect. 4, we have analyzed the spatiotemporal system and obtained the Turing instability conditions. Numerical simulations are carried out in Sect. 5. Finally, the chapter ends with brief discussions and conclusions.

2 Model Formulation

The proposed model system is given by the following reaction–diffusion system:

$$\begin{aligned} \frac{\partial P}{\partial t} &= r_1 P \left(1 - \frac{P}{K_1} \right) - \frac{\omega_1 P I}{(1 + kS)(P + D)} + d_1 \Delta P, \quad t > 0, (u, v) \in \Omega, \\ \frac{\partial I}{\partial t} &= -(\delta + m)I + \frac{\omega_1 P I}{(1 + kS)(P + D)} - \frac{\omega_2 I^2 S}{(I^2 + D_1^2)} + d_2 \Delta I, \quad t > 0, (u, v) \in \Omega, \\ \frac{\partial S}{\partial t} &= r_2 S \left(1 - \frac{S}{K_2} \right) + \frac{\omega_3 I^2 S}{(I^2 + D_1^2)} + d_3 \Delta S, \quad t > 0, (u, v) \in \Omega, \end{aligned} \tag{1}$$

with the initial conditions

$$P(0, u, v) > 0, \quad I(0, u, v) > 0, \quad S(0, u, v) > 0, \quad (u, v) \in \Omega \tag{2}$$

and the zero-flux boundary conditions

$$\frac{\partial P}{\partial \nu} = \frac{\partial I}{\partial \nu} = \frac{\partial S}{\partial \nu} = 0, \quad t > 0, \quad (u, v) \in \partial\Omega, \tag{3}$$

where $P(t, u, v)$, $I(t, u, v)$, and $S(t, u, v)$ be the population densities of plant community, insect pests, and wolf spiders at time t and position $(u, v) \in \Omega$. All the system parameters, r_1 , K_1 , ω , k , D , δ , m , ω_1 , ω_2 , D_1 , r_2 , K_2 , and ω_3 , are positive and their definitions are given in Table 1. Also, d_1 , d_2 , and d_3 are self-diffusion coefficients for the species P , I , and S , respectively, and ν is the outward normal to the $\partial\Omega$. Zero-flux boundary conditions specify that population is self-contained, and there is no population flux across the boundary of the domain.

3 Analysis of the Temporal System

3.1 Boundedness

Theorem 1

$$\Omega_1 = \left\{ (P(t), I(t), S(t)) \in \mathbb{R}_+^3 : 0 \leq P(t) \leq K_1, 0 \leq I(t) \leq \frac{K_1 \omega_1}{\omega} \left(1 + \frac{r_1}{4(\delta + m)} \right), \right. \\ \left. K_2 \leq S(t) \leq K_2 \left(1 + \frac{\omega_3}{r_2} \right) \right\}$$

is a region of attraction for all the solutions of the system (1) without diffusion initiating in the interior of \mathbb{R}_+^3 .

Table 1 Meaning of the system parameters used in the model system (1)

Parameters	Biological meaning
r_1	Intrinsic growth rate of plant community
K_1	Environmental carrying capacity of plant community
ω	Maximum predation rate of insect pests on plant community
D	Half saturation constant of insect pests
k	Reflects the level of fear of wolf spiders
δ	Natural death rate of insect pests
m	Migration rate of insect pests due to fear of wolf spiders
ω_1	Conversion rate of plant biomass to insect pests biomass
ω_2	Maximum predation rate of wolf spiders on insect pests
r_2	Intrinsic growth rate of wolf spiders
K_2	Environmental carrying capacity of wolf spiders
ω_3	Conversion rate of insect pests biomass to wolf spiders biomass
D_1	Insect pests density at which the population killed by wolf spiders reached half of its maximum value

Proof Proof directly follows from the article [19] and hence omitted.

3.2 Equilibria and Stability Analysis

1. The trivial equilibrium point $E_0(0, 0, 0)$ always exists. The eigenvalues corresponding to E_0 are $r_1 > 0$, $-(m + \delta) < 0$, and $r_2 > 0$. Therefore, E_0 is a saddle point.
2. The insect pests and wolf spiders population-free axial equilibrium point $E_1(K_1, 0, 0)$ always exists. The eigenvalues corresponding to E_1 are $-r_1 < 0$, $-(m + \delta) + \frac{K_1\omega_1}{K_1 + D}$, and $r_2 > 0$. Therefore, E_1 is a saddle point.
3. The axial equilibrium point $E_2(0, 0, K_2)$ always exists. The eigenvalues corresponding to E_2 are $r_1 > 0$, $-(m + \delta) < 0$, and $-r_2 < 0$. Therefore, E_2 is a saddle point.
4. The planer equilibrium point $E_3(\hat{P}, \hat{I}, 0)$, where $\hat{P} = \frac{(\delta+m)D}{\omega_1 - (\delta+m)}$ and $\hat{I} = \frac{r_1(K_1 - \hat{P})(\hat{P} + D)}{K_1\omega}$, exists provided $\omega_1 > \delta + m$. The eigenvalues corresponding to E_3 are

$$\lambda_1 = \frac{\omega_3 \hat{I}^2 + r_2 \hat{\beta}_1}{\hat{\beta}_1} > 0,$$

$$\text{and } \lambda_{2,3} = \frac{\omega K_1 \hat{\beta}_1 \hat{P} \hat{I} - r_1 \hat{\beta}_1 \hat{\beta}_2^2 \hat{P} \pm \sqrt{(r_1 \hat{\beta}_1 \hat{\beta}_2^2 \hat{P} - \omega K_1 \hat{\beta}_1 \hat{P} \hat{I})^2 - 4\omega\omega_1 D K_1^2 \hat{\beta}_1^2 \hat{\beta}_2 \hat{P} \hat{I}}}{2K_1 \hat{\beta}_1 \hat{\beta}_2^2},$$

where $\hat{\beta}_1 = \hat{P} + D$ and $\hat{\beta}_2 = \hat{I}^2 + D_1^2$. Therefore, E_3 is unstable.

- The planer equilibrium point $E_4(K_1, 0, K_2)$ always exists. The eigenvalues corresponding to E_4 are $-r_1 < 0$, $-(m + \delta) + \frac{K_1\omega_1}{(1+kK_2)(K_1+D)}$ and $-r_2 < 0$. E_4 is locally asymptotically stable if $(\delta + m) > \frac{K_1\omega_1}{(1+kK_2)(K_1+D)}$ and a saddle point if $(\delta + m) < \frac{K_1\omega_1}{(1+kK_2)(K_1+D)}$.
- The interior equilibrium point $E^*(P^*, I^*, S^*)$ exists if and only if there is a positive solution to the following set of equations:

$$\begin{aligned} r_1 \left(1 - \frac{P}{K_1} \right) - \frac{\omega I}{(1+kS)(P+D)} &= 0, \\ -(\delta + m) + \frac{\omega_1 P}{(1+kS)(P+D)} - \frac{\omega_2 I S}{(I^2 + D_1^2)} &= 0, \\ r_2 \left(1 - \frac{S}{K_2} \right) + \frac{\omega_3 I^2}{(I^2 + D_1^2)} &= 0. \end{aligned} \tag{4}$$

It seems difficult to find values of P^* , I^* , and S^* explicitly. The existence of interior equilibrium point $E^*(P^*, I^*, S^*)$ can be established with the help of graphical method technique. Readers may refer [20] for better understanding. Here, we have shown the existence of $E^*(P^*, I^*, S^*)$ numerically taking the following set of parameter values:

$$\begin{aligned} r_1 &= 1.2, \quad K_1 = 100, \quad \omega = 5.89, \quad D = 10, \quad k = 0.015, \\ \delta &= 0.05, \quad m = 0.001, \quad \omega_1 = 2.58, \\ \omega_2 &= 0.25, \quad D_1 = 20, \quad r_2 = 0.05, \quad K_2 = 20, \quad \omega_3 = 0.8. \end{aligned}$$

We obtained the interior equilibrium point $E^*(P^*, I^*, S^*)$ as $E^*(0.582489, 3.01515, 27.1113)$ for the above set of parameter values. Jacobian matrix \mathbf{J} at $E^*(P^*, I^*, S^*)$ is given below:

$$\mathbf{J} = \begin{pmatrix} -\frac{r_1 P^*}{K_1} + \frac{\omega P^* I^*}{\beta_1 \beta_2^2} & -\frac{\omega P^*}{\beta_1 \beta_2} & \frac{\omega k P^* I^*}{\beta_1^2 \beta_2} \\ \frac{\omega_1 D I^*}{\beta_1 \beta_2^2} & \frac{\omega_2 (I^{*2} - D_1^2) S^* I^*}{\beta_3^2} & -\frac{\omega_1 k P^* I^*}{\beta_1^2 \beta_2} - \frac{\omega_2 I^{*2}}{\beta_3} \\ 0 & \frac{2\omega_3 D_1^2 S^* I^*}{\beta_3^2} & -\frac{r_2 S^*}{K_2} \end{pmatrix} = \begin{pmatrix} a_{11} & a_{12} & a_{13} \\ a_{21} & a_{22} & a_{23} \\ 0 & a_{32} & a_{33} \end{pmatrix}.$$

The characteristic equation of Jacobian matrix \mathbf{J} is given by

$$\lambda^3 + A_1 \lambda^2 + A_2 \lambda + A_3 = 0, \tag{5}$$

where

$$A_1 = -(a_{11} + a_{22} + a_{33}), \quad A_2 = a_{11}a_{22} - a_{12}a_{21} + a_{22}a_{33} - a_{23}a_{32} + a_{11}a_{33},$$

$$A_3 = -a_{13}a_{21}a_{32} + a_{11}a_{23}a_{32} + a_{12}a_{21}a_{33} - a_{11}a_{22}a_{33}.$$

According to the Routh–Hurwitz criterion, $E^*(P^*, I^*, S^*)$ is locally asymptotically stable provided that $A_1 > 0$, $A_3 > 0$ and $A_1A_2 - A_3 > 0$. After simple mathematical manipulations, stability condition about $E^*(P^*, I^*, S^*)$ is summarized in the theorem below.

Theorem 2 *The interior equilibrium point $E^*(P^*, I^*, S^*)$ is locally asymptotically stable, provided the following conditions are satisfied:*

$$D_1 \geq I^*, \quad (1 + kS^*) > \frac{\omega P^* I^* K_1 K_2 \beta_3^2}{\beta_2^2 \left(\beta_3^2 (r_1 K_2 P^* + r_2 K_1 S^*) + \omega_2 S^* I^* K_1 K_2 (D_1^2 - I^{*2}) \right)}, \quad (6)$$

$$\begin{aligned} & \frac{r_1 \beta_4 \beta_6 P^*}{K_1} + \frac{r_2 \beta_1 \beta_5 S^*}{K_2} + \frac{r_1 P^* \beta_8 (D_1^2 - I^{*2})}{K_1} \\ & > \beta_4 \beta_6 \beta_7 + k \beta_5 \beta_6 I^* + \beta_7 \beta_8 (D_1^2 - I^{*2}), \end{aligned} \quad (7)$$

$$\begin{aligned} & \frac{r_2 S^*}{K_2} \left(1 + \frac{\beta_8 K_2^2 (D_1^2 - I^{*2})}{r_2^2 S^{*2}} \right) \left(\beta_4 \beta_6 + \left(\frac{r_1 P^*}{K_1} - \beta_7 \right)^2 \right) \\ & + \frac{\beta_8^2 K_2^2 (D_1^2 - I^{*2})^2}{r_2^2 S^{*2}} \left(\frac{r_1 P^*}{K_1} + \frac{r_2 S^*}{K_2} \right) \\ & + \left(\frac{r_2^2 S^{*2}}{K_2^2} + \beta_1 \beta_5 \right) \left(\frac{r_1 P^*}{K_1} + \frac{(D_1^2 - I^{*2}) \beta_8 K_2}{r_2 S^*} \right) + \frac{2r_1 \beta_8 P^* (D_1^2 - I^{*2})}{K_1} \\ & > \beta_7 \left(\beta_1 \beta_5 + 2\beta_8 (D_1^2 - I^{*2}) \right) \\ & + \frac{r_2^2 S^{*2}}{K_2^2} + \frac{\beta_8^2 K_2^2 (D_1^2 - I^{*2})^2}{r_2^2 S^{*2}}, \end{aligned} \quad (8)$$

where

$$\begin{aligned} \beta_1 &= (1 + kS^*), \quad \beta_2 = (P^* + D), \quad \beta_3 = (I^{*2} + D_1^2), \\ \beta_4 &= \left(\frac{k\omega_1 P^* I^*}{\beta_1^2 \beta_2} + \frac{\omega_2 I^{*2}}{\beta_3} \right), \\ \beta_5 &= \frac{D\omega\omega_1 P^* I^*}{\beta_1^3 \beta_2^3}, \quad \beta_6 = \frac{2D_1^2 \omega_3 S^* I^*}{\beta_3^2}, \quad \beta_7 = \frac{\omega P^* I^*}{\beta_1 \beta_2^2}, \quad \beta_8 = \frac{r_2 \omega_2 I^* S^{*2}}{\beta_3^2 K_2}. \end{aligned}$$

4 Stability Analysis of the Spatiotemporal System

To understand the dynamics of the spatiotemporal system (1), we linearize the system (1) about the interior equilibrium point $E^*(P^*, I^*, S^*)$ by introducing the following transformations:

$$P = P^* + \hat{P}(u, v, t), \quad I = I^* + \hat{I}(u, v, t), \quad S = S^* + \hat{S}(u, v, t), \quad (9)$$

where $|\hat{P}(u, v, t)| \ll P^*$, $|\hat{I}(u, v, t)| \ll I^*$, and $|\hat{S}(u, v, t)| \ll S^*$. In the linearized form, the model system (1) is given by

$$\begin{aligned} \frac{\partial \hat{P}}{\partial t} &= a_{11}\hat{P} + a_{12}\hat{I} + a_{13}\hat{S} + d_1\Delta\hat{P}, \\ \frac{\partial \hat{I}}{\partial t} &= a_{21}\hat{P} + a_{22}\hat{I} + a_{23}\hat{S} + d_2\Delta\hat{I}, \\ \frac{\partial \hat{S}}{\partial t} &= a_{32}\hat{I} + a_{33}\hat{S} + d_3\Delta\hat{S}. \end{aligned} \quad (10)$$

Conventionally, we choose

$$\begin{aligned} \hat{P}(u, v, t) &= \varepsilon_1 e^{\lambda_K t + i(K_u u + K_v v)}, \quad \hat{I}(u, v, t) = \varepsilon_2 e^{\lambda_K t + i(K_u u + K_v v)}, \\ \hat{S}(u, v, t) &= \varepsilon_3 e^{\lambda_K t + i(K_u u + K_v v)}, \end{aligned} \quad (11)$$

where ε_i , $i = 1, 2, 3$, are the corresponding amplitudes of perturbations, λ_K is the wavelength, $\mathcal{K} = (K_u, K_v)$ is the wave number vector, and $K = |\mathcal{K}|$ is the wave number.

Now, the characteristic equation of the linearized system (10) is given by

$$(J_{E^*} - \lambda I - K^2 d) \begin{bmatrix} \varepsilon_1 \\ \varepsilon_2 \\ \varepsilon_3 \end{bmatrix} = 0, \quad \text{where } J_{E^*} = \begin{bmatrix} a_{11} & a_{12} & a_{13} \\ a_{21} & a_{22} & a_{23} \\ 0 & a_{32} & a_{33} \end{bmatrix}, \quad d = \begin{bmatrix} d_1 & 0 & 0 \\ 0 & d_2 & 0 \\ 0 & 0 & d_3 \end{bmatrix}, \quad (12)$$

and I is the 3×3 identity matrix. Now, for a nonzero solution of (12), we require that $\det(J_{E^*} - \lambda I - K^2 d) = 0$, which yields the following dispersion relation:

$$\begin{aligned} & \lambda^3 + \left\{ K^2(d_1 + d_2 + d_3) + A_1 \right\} \lambda^2 + \left\{ K^4(d_1d_2 + d_2d_3 + d_3d_1) + K^2(-a_{11}(d_2 + d_3) \right. \\ & \quad \left. - a_{22}(d_1 + d_3) - a_{33}(d_1 + d_2)) + A_2 \right\} \lambda \\ & + \left\{ K^6(d_1d_2d_3) + K^4(-a_{11}d_2d_3 - a_{22}d_1d_3 - a_{33}d_1d_2) \right. \\ & \quad \left. + K^2(d_1(a_{22}a_{33} - a_{23}a_{32}) + d_2(a_{11}a_{33}) + d_3(a_{11}a_{22} - a_{12}a_{21})) + A_3 \right\} = 0. \end{aligned}$$

We rewrite the dispersion relation as

$$\lambda^3 + \mu_2(K^2)\lambda^2 + \mu_1(K^2)\lambda + \mu_0(K^2) = 0, \quad (13)$$

where

$$\begin{aligned} \mu_2(K^2) &= K^2(d_1 + d_2 + d_3) + A_1, \\ \mu_1(K^2) &= \{K^4(d_1d_2 + d_2d_3 + d_3d_1) \\ & \quad + K^2(-a_{11}(d_2 + d_3) - a_{22}(d_1 + d_3) - a_{33}(d_1 + d_2)) + A_2, \\ \mu_0(K^2) &= K^6(d_1d_2d_3) + K^4(-a_{11}d_2d_3 - a_{22}d_1d_3 - a_{33}d_1d_2) \\ & \quad + K^2(d_1(a_{22}a_{33} - a_{23}a_{32}) + d_2(a_{11}a_{33}) \\ & \quad + d_3(a_{11}a_{22} - a_{12}a_{21})) + A_3. \end{aligned} \quad (14)$$

Next, we obtain the value of $(\mu_1\mu_2 - \mu_0)(K^2)$, which is given in the expression below:

$$\begin{aligned} (\mu_2\mu_1 - \mu_0)(K^2) &= \{(d_1 + d_2)(d_2 + d_3)(d_3 + d_1)\} K^6 \\ & + \{-a_{11}(d_2 + d_3)(2d_1 + d_2 + d_3) \\ & - a_{22}(d_1 + d_3)(d_1 + 2d_2 + d_3) - a_{33}(d_1 + d_2)(d_1 + d_2 + 2d_3)\} K^4 \\ & + \left\{ (-a_{12}a_{21} + a_{22}^2 + 2a_{22}a_{33} + a_{33}^2 + 2a_{11}(a_{22} + a_{33}))d_1 \right. \\ & + (a_{11}^2 - a_{12}a_{21} - a_{23}a_{32} + 2a_{22}a_{33} + a_{33}^2 + 2a_{11}(a_{22} + a_{33}))d_2 \\ & \left. + (a_{11}^2 + a_{22}^2 - a_{23}a_{32} + 2a_{22}a_{33} + 2a_{11}(a_{22} + a_{33}))d_3 \right\} K^2 + A_1A_2 - A_3. \end{aligned} \quad (15)$$

According to the Routh–Hurwitz criterion for stability, $\text{Re}(\lambda) < 0$, iff the following conditions hold:

$$\mu_2(K^2) > 0, \quad \mu_0(K^2) > 0, \quad \text{and} \quad [\mu_2\mu_1 - \mu_0](K^2) > 0. \quad (16)$$

Theorem 3 *The interior equilibrium point $E_3(x^*, y^*, z^*)$ is locally asymptotically stable in the presence of diffusion provided the condition (16) holds.*

4.1 Turing Instability

Turing instability breaks the spatial symmetry of the system and leads to formation of spatial patterns, which are stationary in time and oscillatory in space. It is also known as diffusion-driven instability. Turing instability occurs when the model system without diffusion is stable and model system with diffusion becomes unstable for small perturbations about the homogeneous steady state $E^*(P^*, I^*, S^*)$. That is, if $\mu_2(0) > 0$, $\mu_0(0) > 0$, $[\mu_2\mu_1 - \mu_0](0) > 0$, and any one of these conditions $\mu_2(K^2) > 0$, $\mu_0(K^2) > 0$, $[\mu_2\mu_1 - \mu_0](K^2) > 0$ fails to hold.

It can be easily seen that diffusion-driven instability cannot occur by contradicting the condition $\mu_2(K^2) > 0$ as d_1, d_2, d_3, K^2 are all positive and $A_1 > 0$ from the stability condition of interior equilibrium point $E^*(P^*, I^*, S^*)$. Hence, we are dependent on the signs of $\mu_0(K^2)$ and $[\mu_2\mu_1 - \mu_0](K^2)$ for Turing instability to occur in the system (1)–(3). The expressions of $\mu_0(K^2)$ and $[\mu_2\mu_1 - \mu_0](K^2)$ are both cubic polynomials in K^2 of the form

$$\sigma(K^2) = \sigma_3 K^6 + \sigma_2 K^4 + \sigma_1 K^2 + \sigma_0, \quad \text{such that } \sigma_3 > 0, \sigma_0 > 0.$$

The coefficients σ_i 's ($i = 0, 1, 2, 3$) for expressions of $\mu_0(K^2)$ and $[\mu_2\mu_1 - \mu_0](K^2)$ are the same as those given in the third equation of (14) and (15), respectively. For $\sigma(K^2)$ to be negative for some positive real number $K^2 \neq 0$, the minimum must be negative. The minimum of $\sigma(K^2)$ occurs at $K^2 = K_{cr}^2 = \frac{-\sigma_2 + \sqrt{\sigma_2^2 - 3\sigma_3\sigma_1}}{3\sigma_3}$. Now, K_{cr}^2 is real and positive if

$$\sigma_1 < 0 \quad \text{or} \quad (\sigma_2 < 0 \quad \text{and} \quad \sigma_2^2 > 3\sigma_1\sigma_3). \tag{17}$$

Hence,

$$\sigma_{min} = \sigma(K_{cr}^2) = \frac{2\sigma_2^3 - 9\sigma_1\sigma_2\sigma_3 - 2(\sigma_2^2 - 3\sigma_1\sigma_3)^{\frac{3}{2}} + 27\sigma_3^2\sigma_0}{27\sigma_3^2}.$$

Thus,

$$\sigma(K_{cr}^2) < 0, \quad \text{if } 2\sigma_2^3 - 9\sigma_1\sigma_2\sigma_3 - 2(\sigma_2^2 - 3\sigma_1\sigma_3)^{\frac{3}{2}} + 27\sigma_3^2\sigma_0 < 0. \tag{18}$$

Theorem 4 *The spatial model system (1)–(3) will undergo the Turing instability at the homogeneous steady state $E^*(P^*, I^*, S^*)$ provided the following conditions are satisfied:*

$$\sigma_1 < 0 \text{ or } (\sigma_2 < 0 \text{ and } \sigma_2^2 > 3\sigma_1\sigma_3)$$

and

$$\left(\sigma_2^3 + \frac{27}{2}\sigma_3^2\sigma_0 - \frac{9}{2}\sigma_1\sigma_2\sigma_3\right)^2 < (\sigma_2^2 - 3\sigma_1\sigma_3)^3. \tag{19}$$

Example 1 To explore the above phenomenon numerically, we have chosen the following set of parameter values:

$$\begin{aligned} r_1 &= 1.2, K_1 = 100, \omega = 5.89, D = 10, k = 0.015, \\ \delta &= 0.05, m = 0.001, \omega_1 = 2.58, \\ \omega_2 &= 0.25, D_1 = 20, r_2 = 0.05, K_2 = 20, \omega_3 = 0.8, \\ d_1 &= 0.0001, d_2 = 0.001, d_3 = 1. \end{aligned} \tag{20}$$

For this set of parameter values, $\mu_2(0) = -(a_{11} + a_{22} + a_{33}) = 0.056836 > 0$, $\mu_0(0) = -a_{13}a_{21}a_{32} + a_{11}a_{23}a_{32} + a_{12}a_{21}a_{33} - a_{11}a_{22}a_{33} = 0.006219 > 0$ and $[\mu_2\mu_1 - \mu_0](0) = 0.000205 > 0$. Thus, model system (1) without diffusion is locally asymptotically stable about homogeneous steady state $E^*(0.582489, 3.01515, 27.1113)$. $\sigma_2 = -2.46006 < 0$, $\sigma_2^2 = 6.05189 > 3\sigma_1\sigma_3 = 0.015555$ and $\left(\sigma_2^3 + \frac{27}{2}\sigma_3^2\sigma_0 - \frac{9}{2}\sigma_1\sigma_2\sigma_3\right)^2 = 219.942 < (\sigma_2^2 - 3\sigma_1\sigma_3)^3 = 219.948$. Thus, Turing instability conditions are satisfied. In Fig. 1a, we have shown the plot of $[\mu_2\mu_1 - \mu_0](K^2)$ with respect to wave number K . From this figure, it is clear that $[\mu_2\mu_1 - \mu_0](K^2) < 0$ for some values of wave number K , and this implies that Turing instability occurs in the system (1) for the given set of parameter values. In Fig. 1b, we have shown $[\mu_2\mu_1 - \mu_0](K^2)$ vs. K^2 plot for three different values of fear level $k = 0.015, 0.018, 0.023$, and the other parameter values

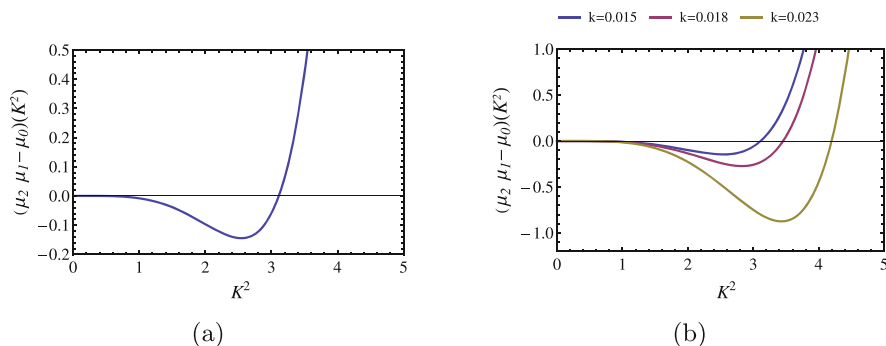


Fig. 1 (a) Plot of $[\mu_2\mu_1 - \mu_0](K^2)$ with respect to K^2 , showing occurrence of Turing instability, (b) $[\mu_2\mu_1 - \mu_0](K^2)$ vs. K^2 plot for three different values of fear level $k = 0.015, 0.018, 0.023$

are the same as given in Eq. (20). It is observed that the interval of negativity of $[\mu_2\mu_1 - \mu_0](K^2)$ increases with increase in the value of fear level k . Thus, the level of fear k has a destabilizing impact on the spatial dynamics.

5 Numerical Simulations

In this section, we have performed simulation experiments to validate the analytical findings and to illustrate the various dynamical behaviors. We have taken the same set of parameter values as given in Eq. (20). For this set of parameter values, model system (1) without diffusion is showing stable dynamics (cf. Fig. 2a). Increasing the value of migration coefficient m to 0.01, system loses its stability and goes to limit cycle oscillations (cf. Fig. 2b). Further increasing the value of m to 0.4, system again becomes stable (cf. Fig. 2c); thus, migration coefficient m has a significant impact on the temporal dynamics of the system (1). In Fig. 3a, we have presented the bifurcation diagram with respect to fear level k . For small values of fear level k , system (1) without diffusion is showing oscillatory behaviors and becomes stable

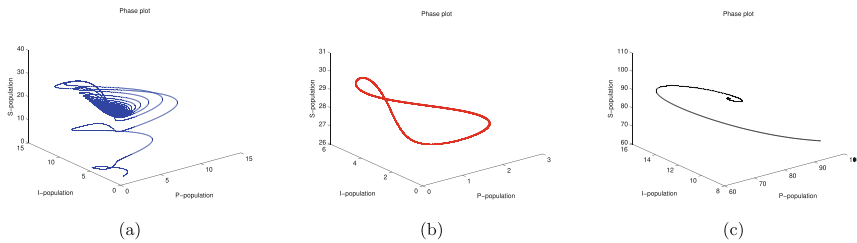


Fig. 2 Phase diagram of the system (1) without diffusion at (a) $m = 0.001$, asymptotically stable, (b) $m = 0.01$, limit cycle, and (c) $m = 0.4$, stable focus. Other parameter values are given in Eq. (20)

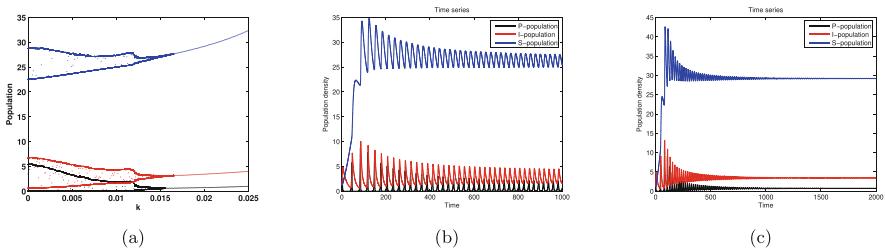


Fig. 3 (a) Bifurcation diagram of $P(t)$, $I(t)$, and $S(t)$ populations with respect to fear level k , (b) time series plot at $k = 0.01$, and (c) time series plot at $k = 0.02$. Other parameter values are given in Eq. (20)

with increase in the value of fear level k (cf. Fig. 3a). In Fig. 3b, c, we have given time series plots at $k = 0.01$ and $k = 0.02$. At $k = 0.01$, we obtained periodic oscillations, and at $k = 0.02$, system is stable.

Next, we have numerically explored the dynamics of the spatiotemporal system (1) with one- and two-dimensional diffusions. Simulation experiments are performed in Matlab (R2013a). The temporal part of the system (1) is solved by using Euler’s methods, central difference scheme is used for one-dimensional case, and standard five-point explicit finite difference scheme is used for two-dimensional diffusion terms. Space and time steps are taken as $\Delta h = 1$ and $\Delta t = 0.01$. In every pattern, blue color corresponds to low density and red color corresponds to high density of the species.

1D Diffusion In this subsection, we have presented the space vs. population density plots (cf. Fig. 4). We have assumed that the domain is of size 7000. We have considered a nonmonotonic form of initial condition as $P(u, 0) = P^* + \epsilon(u - u_1)(u - u_2)$, $I(u, 0) = I^*$, $S(u, 0) = S^*$, where $E^*(P^*, I^*, S^*)$ is the interior equilibrium point, and $\epsilon = 10^{-8}$, $u_1 = 1200$, and $u_2 = 2800$ are the parameters affecting the system dynamics. We have taken the same set of parameter values as given in Eq. (20) except at $k = 0.1$ and $d_1 = 0.01$. Initially, at time level $t = 100$, plant community $P(t)$ and insect pests $I(t)$ populations are distributed in form of regular patterns (cf. Fig. 4a). Increasing time level to $t = 3000$, irregular patterns representing chaotic behavior are observed (cf. Fig. 4c). It is found that the irregular chaotic patterns grows steadily with time (cf. Fig. 4d, e). At $t = 10,000$,

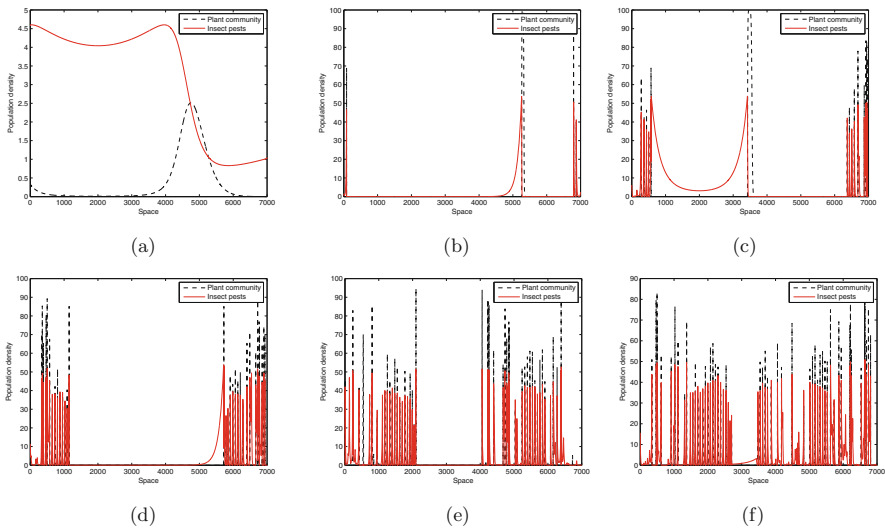


Fig. 4 Spatial distribution of plant community and insect pests populations at different time levels: (a) $t = 100$, (b) $t = 1500$, (c) $t = 3000$, (d) $t = 5000$, (e) $t = 8000$, and (f) $t = 10,000$

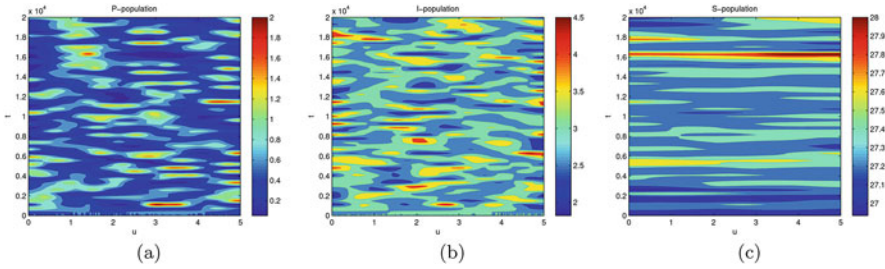


Fig. 5 (a)–(c) Contour plots showing the population density of plant community, insect pests, and wolf spiders in $u - t$ plane

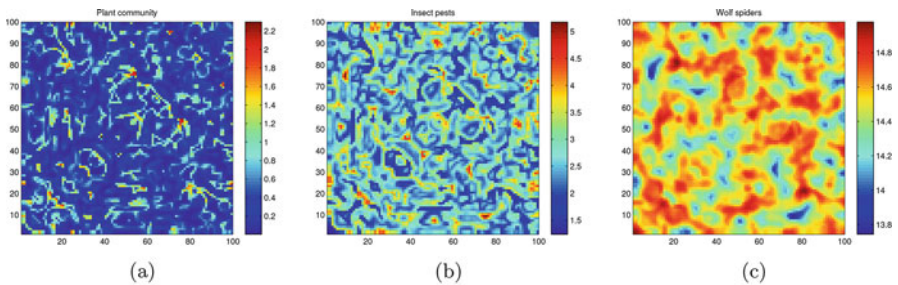


Fig. 6 (a–c) Snapshots of Turing patterns at 1950 days, for parameters given in Eq. (20)

almost whole domain is occupied by these irregular chaotic patterns (cf. Fig. 4f). This phenomenon is called wave of chaos (WOC) [21].

To investigate the spatiotemporal dynamics of the system (1), we have presented spatial patterns of plant community, insect pests, and wolf spiders as contour plots in Fig. 5a–c. From this figure, it is clear that these populations are distributed in the form of patches in the physical domain.

2D Diffusion In this subsection, we have presented Turing pattern formation for the system (1). The initial distribution of the species is considered to be a small spatial perturbation of the form $P(0, u, v) = P^* + 0.5 \cos^2(10u) \cos^2(10v)$, $I(0, u, v) = I^* + 0.5 \cos^2(10u) \cos^2(10v)$, $S(0, u, v) = S^* + 0.5 \cos^2(10u) \cos^2(10v)$.

In Fig. 6, we have presented Turing patterns of the system (1) for the parameter set given in Eq. (20) at 1950 days. It is observed that plant community and insect pests are distributed in the form of small patches over two-dimensional domain (Fig. 6a, b). Wolf spiders are distributed in the form of large patches (Fig. 6c). In Fig. 7, we have shown evolutionary process of patterns shown in Fig. 6c at different time levels $t = 25,000, 55,000, 95,000, 155,000, 195,000,$ and $225,000$. Initially, at $t = 25,000$, high density of wolf spiders is located at the boundary of the domain (Fig. 7a). Increasing time level to $t = 55,000$, high-density region increases (Fig. 7b). Further increasing time level to $t = 95,000$, almost the whole domain is

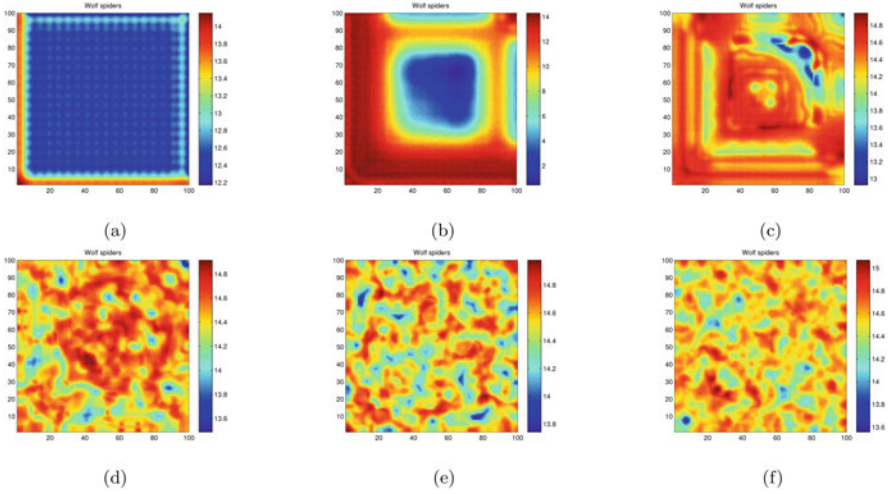


Fig. 7 Snapshots of contour pictures of time evaluation of wolf spiders at (a) $t = 250$ days, (b) $t = 550$ days, (c) $t = 950$ days, (d) $t = 1550$ days, (e) $t = 1950$ days, and (f) $t = 2250$ days. Parameter values are the same as given in (20)

occupied with high density of wolf spiders (Fig. 7c). At $t = 195,000$, wolf spiders are distributed in form of large patches over the whole domain (Fig. 7e). Further increasing time level to $t = 225,000$, distribution remains unaltered (Fig. 7f).

6 Discussions and Conclusions

In herbivorous insects, the indirect trait-mediated effects of predators have been repeatedly shown to reduce herbivory and consequently plant damage; the examples of this include the effect of spiders on the feeding of grasshoppers [22]. In this work, we have investigated the three-species food chain model of plant community, insect pests, and wolf spiders interactions, incorporating the cost of fear in predation rate of insect pests. Spatial random movement of species in one and two dimensions is considered. We have analyzed the proposed system analytically as well as numerically, and the main findings are as follows:

1. We have presented time series, phase plots, and bifurcation diagram for the temporal system. It is observed that the fear level of wolf spiders has stabilizing impact on the temporal dynamics of the system.
2. We have obtained the Turing instability conditions and shown the interesting Turing patterns. It is found that plant community, insect pests, and wolf spiders are distributed in the form of patches over the physical domain.
3. We have explored the wave of chaos phenomenon, which is not discussed yet in the food-chain model with fear effects.

4. It is observed that the fear level k of wolf spiders has destabilizing effect on the spatial system.

In this work, we have first time explored a three-species food chain model in an agroecosystem with fear effects. Our results are general in nature and will help to understand the plant community, insect pests, and wolf spiders interactions in the agroecosystem.

References

1. R.P. Prasad, W.E. Snyder, Diverse trait-mediated interactions in a multi-predator, multi-prey community. *Ecology* **87**(5), 1131–1137 (2006)
2. A. Sih, K.J. Mathot, M. Moirón, P.O. Montiglio, M. Wolf, N.J. Dingemanse, Animal personality and state–behaviour feedbacks: a review and guide for empiricists. *Trends Ecol. Evol.* **30**(1), 50–60 (2015)
3. M.C. Barnes, M.H. Persons, A.L. Rypstra, The effect of predator chemical cue age on antipredator behavior in the wolf spider *Pardosa milvina* (Araneae: Lycosidae). *J. Insect Behav.* **15**(2), 269–281 (2002)
4. S.L. Lima, L.M. Dill, Behavioral decisions made under the risk of predation: a review and prospectus. *Can. J. Zool.* **68**(4), 619–640 (1990)
5. J.P. Suraci, M. Clinchy, L.M., Dill, D. Roberts, L.Y. Zanette, Fear of large carnivores causes a trophic cascade. *Nat. Commun.* **7**, 10,698 (2016)
6. X. Wang, L. Zanette, X. Zou, Modelling the fear effect in predator–prey interactions. *J. Math. Biol.* **73**(5), 1179–1204 (2016)
7. J. Wang, Y. Cai, S. Fu, W. Wang, The effect of the fear factor on the dynamics of a predator–prey model incorporating the prey refuge. *Chaos Interdiscip. J. Nonlinear Sci.* **29**(8), 083,109 (2019)
8. X. Wang, X. Zou, Pattern formation of a predator-prey model with the cost of anti-predator behaviors. *Math. Biosci. Eng.* **15**, 775–805 (2018)
9. R.K. Upadhyay, S. Mishra, Population dynamic consequences of fearful prey in a spatiotemporal predator-prey system. *Math. Biosci. Eng.* **16**(1), 338–372 (2018)
10. P. Panday, N. Pal, S. Samanta, J. Chattopadhyay, Stability and bifurcation analysis of a three-species food chain model with fear. *Int. J. Bifurcat. Chaos* **28**(01), 1850,009 (2018)
11. P. Panday, N. Pal, S. Samanta, J. Chattopadhyay, A three species food chain model with fear induced trophic cascade. *Int. J. Appl. Comput. Math.* **5**(4), 100 (2019)
12. A.M. Turing, The chemical basis of morphogenesis. *Bull. Math. Biol.* **52**(1–2), 153–197 (1990)
13. L.A. Segel, J.L. Jackson, Dissipative structure: an explanation and an ecological example. *J. Theor. Biol.* **37**(3), 545–559 (1972)
14. A. Gierer, H. Meinhardt, A theory of biological pattern formation. *Kybernetik* **12**(1), 30–39 (1972)
15. M. Baurmann, T. Gross, U. Feudel, Instabilities in spatially extended predator–prey systems: spatio-temporal patterns in the neighborhood of Turing–Hopf bifurcations. *J. Theor. Biol.* **245**(2), 220–229 (2007)
16. M. Banerjee, Turing and non-Turing patterns in two-dimensional prey-predator models, in *Applications of Chaos and Nonlinear Dynamics in Science and Engineering*, vol. 4 (Springer, Berlin, 2015), pp. 257–280
17. R.K. Upadhyay, S. Mishra, R.D. Parshad, J. Lyu, A.A. Basheer, Investigation of an explosive food chain model with interference and inhibitory effects. *IMA J. Appl. Math.* **82**(6), 1209–1237 (2017)

18. R. Han, L.N. Guin, B. Dai, Cross-diffusion-driven pattern formation and selection in a modified Leslie–Gower predator–prey model with fear effect. *J. Biol. Syst.* **28**(01), 27–64 (2020)
19. Y. Kang, L. Wedekin, Dynamics of a intraguild predation model with generalist or specialist predator. *J. Math. Biol.* **67**(5), 1227–1259 (2013)
20. R.K. Upadhyay, S. Kumari, Bifurcation analysis of an e-epidemic model in wireless sensor network. *Int. J. Comput. Math.* **95**(9), 1775–1805 (2018)
21. S.V. Petrovskii, H. Malchow, Wave of chaos: new mechanism of pattern formation in spatio-temporal population dynamics. *Theor. Popul. Biol.* **59**(2), 157–174 (2001)
22. O.J. Schmitz, K.B. Suttle, Effects of top predator species on direct and indirect interactions in a food web. *Ecology* **82**(7), 2072–2081 (2001)

Optimal Birth Control of Population Dynamics with Time-Varying Diffusivity Coefficient



Manoj Kumar and Syed Abbas

1 Introduction

Birth control is among the most effective control strategies to reduce the population of harmful or invading species. There are only few papers concerned with optimal control problems in size-structured population models (see [1–4] and references therein). Size-structured population models play a significant role in mathematical analysis and control of a biological population. Size can be considered as a variable, which is continuous and shows statistical or physiological characteristics of population. Depending on the population under study, age, mass, maturity, diameter, and length can be taken as size.

Using semigroup theory, N. Kato [5] qualitatively analyzed the abstract differential equations arising from a population model with spatial diffusion. The semigroup approach [6] enables to describe a population process as a dynamical system in a state space. Rong et al. [1] studied an optimal birth control problem for a size-structured population model without diffusion term. Ze-Rong et al. [2] also studied similar kind of problem but with a different form of cost functional. In this work, we extend the model of N. Kato [5] and S. Abbas et al. [3]. S. Abbas et al. [3] also studied optimal control problem for a population model but with a constant diffusivity coefficient.

Using semigroup theory and fixed point arguments, we obtained important estimates on the mild solution of given population model with time-varying diffusion rate. By fixing fertility rate on three sets, we obtained optimality conditions to our model. Using Ekeland's variational principle, we have shown the existence of an optimal birth controller, which is also unique under some conditions.

M. Kumar · S. Abbas (✉)

School of Basic Sciences, Indian Institute of Technology Mandi, Mandi, Himachal Pradesh, India
e-mail: d18004@students.iitmandi.ac.in; abbas@iitmandi.ac.in

2 Model Formulation

Let us consider a biological population living in a habitat $\Gamma \subset \mathbb{R}^n$ with smooth boundary $\partial\Gamma$. Let $u(s, t, x)$ be the population density of size $s \in [0, s_m]$ individuals at time $t \in [0, T]$ in spatial position $x \in \Gamma$.

Size will increase in the similar manner for all individuals, and the individuals do not move outside of their habitat through boundary.

Let $V(s, t)$ be the growth rate of individuals of size s at time t and $m(s, t, x)$ and $v(s, t, x)$ be mortality and reproduction rates, respectively. Let $f_s(s, t, x)$ and $C_0(t, x)$ be the inflow of s size and zero size individuals, respectively, from outside of the environment. Let $\Gamma_T = (0, T) \times \Gamma$, $\Gamma_s = (0, s_m) \times \Gamma$, $\Gamma_{Ts} = (0, s_m) \times (0, T) \times \Gamma$, and $\Sigma_{Ts} = (0, s_m) \times (0, T) \times \partial\Gamma$. Then, the evolution with respect to size and time is given by the following system:

$$\frac{\partial u}{\partial t} + \frac{\partial}{\partial s}(V(s, t)u) = k(t)\Delta u - m(s, t, x)u + f_s(s, t, x) \text{ in } \Gamma_{Ts} \tag{1}$$

$$V(0, t)u(0, t, x) = C_0(t, x) + \int_0^{s_m} v(s, t, x)u(s, t, x)ds \text{ in } \Gamma_T \tag{2}$$

$$\frac{\partial u}{\partial v}(s, t, x) = 0 \text{ in } \Sigma_{Ts}, \quad u(s, 0, x) = u_0(s, x) \text{ in } \Gamma_s. \tag{3}$$

Let $U = \{v \in L^\infty(\Gamma_{Ts}) \mid v_l(s, t, x) \leq v(s, t, x) \leq v_m(s, t, x) \text{ a.e. in } \Gamma_{Ts}\}$,

where v_l and v_m are functions that are non-negative and lie in $L^\infty(\Gamma_{Ts})$. Let $u^v(s, t, x)$ be the solution of (1)–(3), and then optimal birth control problem can be stated as

$$\text{minimize } E(v) = \int_0^T \int_0^{s_m} \int_\Gamma \left[u^v(s, t, x) + \frac{1}{2}\rho(v(s, t, x)^2) \right] ds dt dx \tag{4}$$

subject to $v \in U$ (v is a control variable). Here, ρ is a weight factor, which is a positive constant. Let us take realization of $\mathcal{A}(t)$ of $-k(t)\Delta$ in $L^p(\Gamma)$, p in $(1, \infty)$. For each $t \in [0, T]$,

$$D(\mathcal{A}(t)) = \left\{ v \in W^{2,p}(\Gamma) \mid \frac{\partial v}{\partial \nu} = 0 \text{ a.e. on } \partial\Gamma \right\}.$$

For $\varphi \in L^p(\Gamma)$, operators $M(s, t)$ and $\mathcal{V}(s, t)$, which are bounded linear, are defined according to [5].

So, our model in operator form can be written as

$$\frac{\partial u}{\partial t} + \frac{\partial}{\partial s}(V(s, t)u) = [-\mathcal{A}(t) - M(s, t)]u + f_s(s, t), \quad (s, t) \in \bar{S}_T = [0, s_m] \times [0, T] \tag{5}$$

$$V(0, t)u(0, t) = C_0(t) + \int_0^{s_m} \mathcal{V}(s, t)u(s, t)ds, \quad t \in [0, T] \tag{6}$$

$$u(s, 0) = u_0(s), \quad s \in [0, s_m]. \tag{7}$$

3 Estimates on Mild Solution

Here, we have taken some assumptions. Some of the assumptions have biological significance, and some are required to derive mild solution.

- (H1) $V: \bar{S}_T \mapsto [0, \infty)$ is of class C^1 w.r.t. both s, t and $V(s, t) > 0$ on S_T . Here, growth is the rate of change in size with respect to time and for most of the species size either remains constant or increases. So, it makes sense to consider the growth rate as non-negative function. Also, for each $t \in [0, T]$, we consider the following cases:
 - (a) $V(0, t) > 0$ and $V(s_m, t) > 0$; (b) $V(0, t) > 0$ and $V(s_m, t) = 0$;
 - (c) $V(0, t) = 0$ and $V(s_m, t) > 0$; (d) $V(0, t) = 0$ and $V(s_m, t) = 0$.
- (H2) For each $t \geq 0$, $-\mathcal{A}(t)$ generates a C_0 semigroup $\{S_t(r) | r \geq 0\}$ in Z . Here, semigroup is the solution operator corresponding to Laplacian.
- (H3) It would be a strange model if suddenly infinitely many animals are die/born. Therefore, we take $\mathcal{V}(s, t)$ and $M(s, t)$ as bounded linear operators in Z for $(s, t) \in S_T$.
- (H4) $f_s \in L^1(S_T; Z)$, $C_0 \in L^1(0, T; Z)$, and $u_0 \in L^1(0, s_m; Z)$. This assumption also makes sense biologically because initial population and individuals coming from outside of the environment cannot be infinite.

The extension of function $V(s, t)$ on $\mathbb{R} \times [0, T]$ is done according to [5].

Assumption (H1) guarantees the existence and uniqueness of solution of IVP (initial value problem)

$$\frac{d}{dt}s(t) = V(s(t), t), \quad s(t_0) = s_0 \quad \text{where } s_0 \in \mathbb{R}. \tag{8}$$

Let us denote the solution of above initial value problem by $s(t) = \varphi(t; t_0, s_0)$, $s_1(t) = \varphi(t; 0, 0)$, and $s_2(t) = \varphi(t; T, s_m)$.

Initial time τ_0 and final time τ_1 are defined according to [5]. Suppose $u(s, t)$ satisfies (5)–(7) in strict sense, and let

$$p(\eta; t, s) = \exp \left[\int_{\tau_0}^{\tau_1} \partial_s V(\varphi(\sigma; t, s), \sigma) d\sigma \right] u(s(\eta), \eta), \quad \text{where } \varphi(\sigma; t, s) = s(\sigma).$$

Differentiation of $p(\eta; t, s)$ with respect to η gives

$$\begin{aligned} \frac{d}{d\eta}(p(\eta; t, s)) &= [-\mathcal{A}(\eta) - M(s(\eta), \eta)]p(\eta; t, s) \\ &+ \exp\left(\int_{\tau_0}^{\eta} \partial_s V(\varphi(\sigma; t, s), \sigma) d\sigma\right) f_s(s(\eta), \eta). \end{aligned} \tag{9}$$

To carry out further analysis, we assume that the assumptions given in parabolic case [6, Section 5.6] hold. Under those assumptions, the homogeneous system

$$\frac{dp(t)}{dt} + \mathcal{A}(t)p(t) = 0, \quad 0 \leq r < t < T \text{ with } p(r) = z \tag{10}$$

has a unique evolution system $\{X(t, r) \mid 0 \leq r < t \leq T\}$ with some properties (for more details, see Pazy [6]).

Variation of constant formula and substitution of $\eta = t$ give us

$$\begin{aligned} u(s, t) &= Q(\tau_0)X(t, \tau_0)u(0, \tau_0) \\ &+ \int_{\tau_0}^t Q(\sigma)X(t, \sigma)[-M(s(\sigma), \sigma)u(s(\sigma), \sigma) + f_s(s(\sigma), \sigma)]d\sigma, \end{aligned}$$

$$\text{where } Q(\tau_0) = \exp\left(-\int_{\tau_0}^t \partial_s g(\varphi(\sigma; t, s), \sigma) d\sigma\right).$$

For the case (H1)-(a) and (H1)-(b), $V(0, t) > 0$, so $u(0, t)$ is defined by

$$u(0, t) = \frac{1}{V(0, t)} \left[C_0(t) + \int_0^{s_m} \mathcal{V}(s, t)u(s, t)ds \right] \text{ for } t \in (0, T). \tag{11}$$

In the case (H1)-(a) and (H1)-(b), initial time will be given by

$$\tau_0(t, s) = \tau_0 \text{ for } s \in (0, s_1(t)) \text{ and } \tau_0(t, s) = 0 \text{ for } s \in (s_1(t), s_m).$$

For this case a.e. $t \in (0, T)$, mild solution $u(s, t)$ is given by

$$u(s, t) = \begin{cases} Q(\tau_0)X(t, \tau_0)u(0, \tau_0) \\ + \int_{\tau_0}^t X(t, \eta) \{-M(s(\eta), \eta)u(s(\eta), \eta) + f_s(s(\eta), \eta)\} Q(\eta)d\eta & , \text{ a.e. } s \in (0, s_1(t)) \\ Q(0)X(t, 0)u_0(\varphi(0; t, s)) \\ + \int_0^t X(t, \eta) \{-M(s(\eta), \eta)u(s(\eta), \eta) + f_s(s(\eta), \eta)\} Q(\eta)d\eta & , \text{ a.e. } s \in (s_1(t), s_m) \end{cases}$$

Note that $u_0 = u_0(\varphi(0; t, s))$, and for the case (H1)-(c) and (H1)-(d), there is no fecundity rate, so $u(s, t)$ will be defined accordingly. $C_\varphi^k(S_T; Z)$ is the collection

of functions with values in Banach space Z and continuously differentiable along curve φ , and $D_\varphi u(s, t)$ is the derivative along curve (characteristic) φ .

Theorem 1 *Let $u \in L^\infty(0, T; L^1(0, s_m; Z))$ be mild solution of (1)–(3); then, in the Case (H1)-(a) and Case (H1)-(b), it is of class $C_\varphi^k(S_T; Z)$ and satisfies*

$$D_\varphi u(s, t) = -A(t)u(s, t) - \partial_s V(s, t)u(s, t) - M(s, t)u(s, t) + f_s(s, t) \quad a.e. \quad (s, t) \in S_T, \tag{12}$$

$$V(0, t)u(0, t) = C_0(t) + \int_0^{s_m} \mathcal{V}(s, t)u(s, t)ds, \quad a.e. \quad t \in (0, T), \tag{13}$$

$$u(s, 0) = u_0(s), \quad a.e. \quad s \in (0, s_m). \tag{14}$$

Proof The proof follows the same steps as given in [5].

Theorem 2 *Under the assumptions (H1)–(H4), let $u^{v_1}, u^{v_2} \in L^\infty(0, T; L^1(0, s_m; Z))$ be mild solutions with birth rates v_1 and v_2 , respectively. Then,*

$$\|u^{v_1}(\cdot, t) - u^{v_2}(\cdot, t)\|_{L^1(0, s_m; Z)} \leq \tilde{N} e^{(T\|\mathcal{V}_1 - \mathcal{V}_2\|_{L^\infty(S_T; \mathcal{L}(Z))})}, \tag{15}$$

where \tilde{N} is a generic constant which depends on L^∞ norm of M , constant T , and the bound of the evolution system $\{X(t, r), 0 \leq r < t \leq \infty\}$.

Also, if $\tilde{N} \leq \frac{\tilde{C}}{\|\mathcal{V}_1 - \mathcal{V}_2\|_{L^\infty(S_T; \mathcal{L}(Z))}} \forall v_1, v_2 \in U$ for some positive constant \tilde{C} ,

$$\text{then } \|u^{v_1}(\cdot, t) - u^{v_2}(\cdot, t)\|_{L^1(0, s_m; Z)} \leq M_1 \|\mathcal{V}_1 - \mathcal{V}_2\|_{L^\infty(S_T; \mathcal{L}(Z))} \tag{16}$$

for some positive constant M_1 .

Proof Let $0 \leq t \leq T$ and $u^{v_1}, u^{v_2} \in L^\infty(0, T; L^1(0, s_m; Z))$, and then we have

$$\begin{aligned} & \|u^{v_1}(\cdot, t) - u^{v_2}(\cdot, t)\|_{L^1(0, s_m; Z)} \\ & \leq \int_0^{s_1(t)} \|Q(\tau_0)X(t, \tau_0)(u^{v_1}(0, \tau_0) - u^{v_2}(0, \tau_0))\|_Z ds \\ & \quad + \int_0^{s_1(t)} \int_{\tau_0}^t \|Q(\sigma)X(t, \sigma)M(s(\sigma), \sigma)(u^{v_1} - u^{v_2})\|_Z d\sigma ds \\ & \quad + \int_{s_1(t)}^{s_m} \int_0^t \|Q(\sigma)X(t, \sigma)M(s(\sigma), \sigma)(u^{v_1} - u^{v_2})\|_Z d\sigma ds \\ & = T_1 + T_2 + T_3. \end{aligned}$$

In the integral T_1 , let us use the substitution $s = \eta = \tau_0(t, s)$, and then we have

$$\frac{ds}{d\eta} = -V(0, \eta)\exp\left(-\int_{\eta}^t \partial_s g(\varphi(\sigma; \eta, 0), \sigma)d\sigma\right).$$

$$\begin{aligned} \text{So, } T_1 \leq & \int_0^t \left\| X(t, \eta) \left(\int_0^{s_m} U_1(s(\sigma), \sigma)u^{v_1}(s(\sigma), \sigma)d\sigma \right. \right. \\ & \left. \left. - \int_0^{s_m} U_2(s(\sigma), \sigma)u^{v_2}(s(\sigma), \sigma)d\sigma \right) \right\|_Z d\eta. \end{aligned}$$

The authors of [5] have proved that if $v_2 \leq v_1$, then $u^{v_2} \leq u^{v_1}$. Using this, we will derive a new inequality. Let us assume that $v_2 \geq v_1$; then,

$$v_1 u^{v_1} - v_2 u^{v_2} \leq v_1 u^{v_1} + v_2 u^{v_2} - v_1 u^{v_2} - v_2 u^{v_1} = (v_1 - v_2)(u^{v_1} - u^{v_2}).$$

$$\text{Therefore, } T_1 \leq \tilde{N} \|\mathcal{V}_1 - \mathcal{V}_2\|_{L^\infty(S_T; \mathcal{L}(Z))} \int_0^t \|u^{v_1}(\cdot, \eta) - u^{v_2}(\cdot, \eta)\|_{L^1(0, s_m; Z)} d\eta.$$

Now, let $s = \xi = \varphi(\eta; t, s)$; then,

$$\frac{ds}{d\xi} = \exp\left(\int_{\eta}^t \partial_s V(\varphi(\sigma; t, s), \sigma)d\sigma\right),$$

and we can always find \tilde{N} such that

$$T_2 + T_3 \leq \tilde{N} \|\mathcal{V}_1 - \mathcal{V}_2\|_{L^\infty(S_T; \mathcal{L}(Z))} \int_0^t \|u^{v_1}(\cdot, \eta) - u^{v_2}(\cdot, \eta)\|_{L^1(0, s_m; Z)} d\eta.$$

Therefore,

$$\begin{aligned} \|u^{v_1}(\cdot, t) - u^{v_2}(\cdot, t)\|_{L^1(0, s_m; Z)} & \leq C + \tilde{N} \|\mathcal{V}_1 - \mathcal{V}_2\|_{L^\infty(S_T; \mathcal{L}(Z))} \\ & \quad \times \int_0^t \|u^{v_1}(\cdot, \eta) - u^{v_2}(\cdot, \eta)\|_{L^1(0, s_m; Z)} d\eta, \end{aligned} \tag{17}$$

where C is an arbitrary constant which is positive, and \tilde{N} is also a constant (generic constant), which depends on $\|M\|_{L^\infty(S_T; \mathcal{L}(Z))}$, T , and the bound of the evolution system $\{X(t, r), 0 \leq r < t \leq \infty\}$. Now, using the Gronwall inequality, we get

$$\|u^{v_1}(\cdot, t) - u^{v_2}(\cdot, t)\|_{L^1(0, s_m; Z)} \leq C e^{\left(\tilde{N}T \|\mathcal{V}_1 - \mathcal{V}_2\|_{L^\infty(S_T; \mathcal{L}(Z))}\right)}.$$

We can always find constant C such that

$$C \leq C \|\mathcal{V}_1 - \mathcal{V}_2\|_{L^\infty(S_T; \mathcal{L}(Z))}.$$

Because of the bound of \tilde{N} , we have

$$\|u^{v_1}(\cdot, t) - u^{v_2}(\cdot, t)\|_{L^1(0, s_m; Z)} \leq C \|\mathcal{V}_1 - \mathcal{V}_2\|_{L^\infty(S_T; \mathcal{L}(Z))} e^{\tilde{C}T}.$$

Taking $M_1 = C e^{\tilde{C}T}$, results of the theorem will hold. \square

Now, let us consider the dual problem to (12)–(14).

In the case (H1)-(a) and (H1)-(c),

$$\begin{cases} D_\varphi q(s, t) = \mathcal{A}^*(t)q(s, t) + M^*(s, t)q(s, t) - \mathcal{V}^*(s, t)q(0, t) + f_s^*(s, t) & \text{a.e. } (s, t) \in S_T \\ q(s_m, t) = \lim_{h \rightarrow +0} q(\varphi(t - h; t, s_m), t - h) = 0 & \text{a.e. } t \in (0, T) \\ q(s, T) = \lim_{h \rightarrow +0} q(\varphi(T - h; T, s), T - h) = 0, & \text{a.e. } s \in (0, s_m), \end{cases} \quad (18)$$

and for the case (H1)-(b) and (H1)-(d), it will satisfy (19)(i) and (19)(ii).

Here, $q \in L^\infty(S_T; D(\mathcal{A}^*)) \cap C_\varphi^1(S_T; Z^*)$ is unknown. In dual problem (adjoint system), \mathcal{A}^* , M^* , and \mathcal{V}^* are adjoint operators of \mathcal{A} , M , and \mathcal{V} , respectively. For $t \in [0, T]$, let us assume that $\mathcal{A}^*(t)$ also satisfies the assumptions (A1)–(A3) and $\{X^*(t, r); 0 \leq r < t < T\}$ be evolution system corresponding to $\mathcal{A}^*(t)$.

M^* and \mathcal{V}^* will be defined by $[M^*(s, t)q](x) = m(s, t, x)q(x)$,

$$[\mathcal{V}^*(s, t)q](x) = v(s, t, x)q(x).$$

Also, $\|M^*\|_{L^\infty(S_T; L(Z^*))} \leq \|m\|_{L^\infty(\Gamma_{T_s})}$, $\|\mathcal{V}^*\|_{L^\infty(S_T; L(Z^*))} \leq \|v\|_{L^\infty(\Gamma_{T_s})}$.

Using the transformation $\bar{q}(s, t) = q(s_m - s, T - t)$, we can transform the data $q(s_m, t) = q(s, t) = 0$ into the data $q(0, t) = q(s, 0) = 0$. Also, following the same procedure as we followed in Theorem 1, we can show the existence of unique solution to the dual problem.

Theorem 3 *Let us assume that the assumptions (H1)–(H4) hold and q^{v_1} and q^{v_2} be solutions to the adjoint equation with birth rates v_1 and v_2 , respectively; then,*

$$\|q^{v_1}(s, t) - q^{v_2}(s, t)\|_{Z^*} \leq M_2 \|\mathcal{V}_1^* - \mathcal{V}_2^*\|_{L^\infty(S_T; \mathcal{L}(Z^*))}. \quad (19)$$

4 Optimal Birth Control Problem

Here, our objective functional (also called energy functional) is given by

$$E(v) = \int_0^T \int_0^{s_m} \int_{\Gamma} \left[u^v(s, t, x) + \frac{1}{2} \rho(v(s, t, x))^2 \right] dx ds dt, \quad (20)$$

and our task is to minimize it. Let Φ be the functional which is equal to $E(v)$ if $v \in U$ and $+\infty$ otherwise.

Theorem 4 *Let (v_*, u^{v*}) be optimal pair which minimizes $E(v)$ and q^{v*} be the solution of dual problem (18).*

Then, for $f_s^(s, t, x) = -c, c > 0$*

$$v_*(s, t, x) = \mathcal{F} \left(\frac{q^{v*}(0, t, x) u^{v*}(s, t, x)}{c\rho} \right)$$

$\mathcal{F}: L^1(\Gamma_{T_s}) \mapsto L^\infty(\Gamma_{T_s})$ is defined by

$$(\mathcal{F}\zeta)(s, t, x) = \begin{cases} v_l, & \text{if } \zeta(s, t, x) < v_l \\ \zeta(s, t, x), & \text{if } v_l \leq \zeta(s, t, x) \leq v_m \\ v_m, & \text{if } \zeta(s, t, x) > v_m. \end{cases} \quad (21)$$

Proof Let $w_\epsilon = \frac{1}{\epsilon} [u^{v_* + \epsilon \delta_*} - u^{v_*}]$, where $\delta_* = v - v_*$; then, w_ϵ converges to $w \in L^\infty(S_T; Z)$, and w satisfies

$$\begin{cases} D_\varphi w(s, t) = \mathcal{A}(t)w(s, t) - \partial_s V(s, t)w(s, t) - \mathcal{M}(s, t)w(s, t) & \text{a.e. } (s, t) \in S_T \\ V(0, t)w(0, t) = \int_0^{s_m} \mathcal{V}^*(s, t)w(s, t)ds + \int_0^{s_m} \delta_* u^{v_*}(s, t)ds, & \text{a.e. } t \in (0, T) \\ w(s, 0) = 0, & \text{a.e. } s \in (0, s_m), \end{cases} \quad (22)$$

where $\delta_* u^{v_*}(s, t) = \delta^*(s, t, \cdot) u^{v_*}(s, t, \cdot)$, and also $\delta_* u^{v_*} \in L^\infty(S_T; Z)$.

Because $w(s, t)$ is a weak solution of (22), we have

$$\begin{aligned} & \int_0^T \int_0^{s_m} \int_{\Gamma} w(s, t, x) (-D_\varphi q(s, t, x) - k(t)\Delta q(s, t, x) \\ & \quad + m(s, t, x)q(s, t, x) - v(s, t, x)q(0, t, x)) dx ds dt \\ & = \int_0^T \int_0^{s_m} \int_{\Gamma} \delta_*(s, t, x) u^{v_*}(s, t, x) q(s, t, x) dx ds dt. \end{aligned}$$

As $q(s, t)$ satisfies

$$D_\varphi q(s, t) = -\mathcal{A}^*(t)q(s, t) - M^*(s, t)q(s, t) + \mathcal{V}^*(s, t)q(0, t) + f_s^*(s, t),$$

we have

$$\begin{aligned} & \int_0^T \int_0^{s_m} \int_\Gamma w(s, t, x) f_s^*(s, t, x) dx ds dt \\ &= \int_0^T \int_0^{s_m} \int_\Gamma \delta_* r^*(s, t, x) u^{v_*}(s, t, x) q(0, t, x) dx ds dt. \end{aligned} \tag{23}$$

Because (v_*, u^{v_*}) is a pair with optimal controller, we have

$$\lim_{\epsilon \rightarrow +0} \frac{1}{\epsilon} [\Phi(v_* + \epsilon \delta_*) - \Phi(v_*)] \geq 0,$$

which implies
$$\lim_{\epsilon \rightarrow +0} \int_0^T \int_0^{s_m} \int_\Gamma \left[\frac{u^{v_* + \epsilon \delta_*} - u^{v_*}}{\epsilon} - \frac{\rho \epsilon (\delta_*)^2}{2} + \rho v_* \delta_* \right] dx ds dt \geq 0,$$

which further implies
$$\int_0^T \int_0^{s_m} \int_\Gamma (w(s, t, x) + \rho v_* \delta_*) dx ds dt \geq 0.$$

For $f_s^*(s, t, x) = -c$, $c > 0$ and using (23), we get

$$\int_0^T \int_0^{s_m} \int_\Gamma (v - v_*) \left(\rho v_* - \frac{u^{v_*}(s, t, x) q^{v_*}(0, t, x)}{c} \right) dx ds dt \geq 0,$$

which implies
$$\int_0^T \int_0^{s_m} \int_\Gamma \rho (v - v_*) \left(v_* - \frac{u^{v_*}(s, t, x) q^{v_*}(0, t, x)}{c\rho} \right) dx ds dt \geq 0.$$

$$\text{Let } \Psi_1 = \left\{ (s, t, x) \in \Gamma_{Ts} \mid \frac{u^{v_*}(s, t, x) q^{v_*}(0, t, x)}{c\rho} < v_l \right\}.$$

Choose $v = v_l$ on Ψ_1 . So, in this case,

$$\int_{\Psi_1} \rho (v_l - v_*) \left(v_* - \frac{u^{v_*}(s, t, x) q^{v_*}(0, t, x)}{c\rho} \right) dx ds dt = 0,$$

because ρ cannot be zero, we have $v_* = v_l$.

Similarly, let $\Psi_2 = \left\{ (s, t, x) \in \Gamma_{Ts} \mid \frac{u^{v_*}(s, t, x) q^{v_*}(0, t, x)}{c\rho} > v_m \right\},$

and choose $v = v_m$ on Ψ_2 . Then, $v_* = v_m$ on Ψ_2 .

$$\text{If } \Psi_3 = \left\{ (s, t, x) \in \Gamma_{T_s} \mid v_l \leq \frac{u^{v_*}(s, t, x)q^{v_*}(0, t, x)}{c\rho} \leq v_m \right\},$$

$$\text{then on } \Psi_3, v_* = \frac{q^{v_*}(0, t, x)u^{v_*}(s, t, x)}{c\rho}.$$

□

Theorem 5 Under the assumptions (H1)–(H4) and assumptions of Theorem 4 with

$$\frac{M_1 P_2 + M_2 P_1}{c\rho} < 1,$$

uniqueness of optimal birth controller $\bar{v} \in \Gamma_{T_s}$ is guaranteed for the optimal birth control problem (4), where P_1 and P_2 are supremum of $|u|$ and $|q|$, respectively.

Proof The lower semicontinuity of functional Φ is easy to check, so using Ekeland’s variational principle, for every $\epsilon > 0$, we can find $v_\epsilon \in U$ such that

$$\Phi(v_\epsilon) \leq \inf_{v \in U} \Phi(v) + \epsilon \tag{24}$$

$$\Phi(v_\epsilon) \leq \inf_{v \in U} \{ \Phi(v) + \sqrt{\epsilon} \|v - v_\epsilon\|_{L^1(\Gamma_{T_s})} \}. \tag{25}$$

Thus, the functional in perturbed form

$$\Phi_\epsilon(v) = \Phi(v) + \sqrt{\epsilon} \|v - v_\epsilon\|_{L^1(\Gamma_{T_s})} \tag{26}$$

will attain its infimum at v_ϵ . Therefore,

$$\lim_{\epsilon' \rightarrow 0} \frac{1}{\epsilon'} [\Phi_\epsilon(v_\epsilon + \epsilon' \delta_*) - \Phi_\epsilon(v_\epsilon)] \geq 0,$$

$$\text{therefore, } \lim_{\epsilon' \rightarrow 0} \frac{1}{\epsilon'} [\Phi(v_\epsilon + \epsilon' \delta_*) + \sqrt{\epsilon} \|\epsilon' \delta_*\| - \Phi(v_\epsilon)] \geq 0.$$

The procedure followed in Theorem 4 will help us to obtain the following:

$$\begin{aligned} & \int_0^T \int_0^{s_m} \int_\Gamma \rho \delta_* \left(v_\epsilon + \frac{u^{v_\epsilon}(s, t, x)q^{v_\epsilon}(0, t, x)}{c\rho} \right) dx ds dt \\ & + \sqrt{\epsilon} \int_0^T \int_0^{s_m} \int_\Gamma |\delta_*| dx ds dt \geq 0. \end{aligned} \tag{27}$$

δ_* lies in tangent cone $\mathcal{T}_u(U)$ and also $\delta_* = v - v_\epsilon$ is dependent on the control variable v which lies in U , which implies (27) holds for any $\delta_* \in \mathcal{T}_u(U)$.

Therefore, according to the structure of normal cones [3, Proposition 5.3], there exists $\theta(s, t, x) \in L^\infty(\Gamma_{T_s})$, which lies in unit ball, and the following holds:

$$\rho v_\epsilon + \frac{u^{v_\epsilon}(s, t, x)q^{v_\epsilon}(0, t, x)}{c} + \sqrt{\epsilon}\theta \in \mathcal{N}_u(v_\epsilon).$$

$$\text{Therefore, } v_\epsilon(s, t, x) = \mathcal{F}\left(-\frac{u^{v_\epsilon}(s, t, x)q^{v_\epsilon}(0, t, x)}{c\rho} + \frac{\sqrt{\epsilon}\theta}{\rho}\right).$$

Now, we will prove the uniqueness part. For this purpose, firstly let us define

$$\mathcal{G}: U \subset L^\infty(\Gamma_{T_s}) \mapsto U \text{ by}$$

$$(\mathcal{G}v)(s, t, x) = \mathcal{F}\left(-\frac{u^v(s, t, x)q^v(0, t, x)}{c\rho} + \frac{\sqrt{\epsilon}\theta}{\rho}\right).$$

Then, for any $(s, t, x) \in \Gamma_{T_s}$, we have

$$\begin{aligned} & |(\mathcal{G}v_1)(s, t, x) - (\mathcal{G}v_2)(s, t, x)| \\ & \leq \left| \frac{1}{c\rho} \right| (|u^{v_1}(s, t, x) - u^{v_2}(s, t, x)| |q^{v_1}(0, t, x)| \\ & \quad + |u^{v_2}(s, t, x)| |q^{v_1}(0, t, x) - q^{v_2}(0, t, x)|) \\ & \leq \frac{1}{c\rho} (M_1 P_2 + M_2 P_1) \|v_1 - v_2\|_{L^\infty(\Gamma_{T_s})}. \end{aligned}$$

Therefore, \mathcal{G} is a contraction mapping, and the existence of unique fixed point is assured. Uniqueness of the optimal control will be due to optimality conditions in Theorem 4. Now, our task is to show the existence of optimal controller.

$$\text{Let } \Phi(\bar{v}) = \inf \{ \Phi(v) : v \in U \}.$$

$$\text{Clearly, } \|\mathcal{G}v_\epsilon - v_\epsilon\|_{L^\infty(\Gamma_{T_s})} \leq \frac{\sqrt{\epsilon}}{\rho}.$$

$$\begin{aligned} \text{Therefore, } \|\bar{v} - v_\epsilon\|_{L^\infty(\Gamma_{T_s})} &= \|\mathcal{G}\bar{v} - v_\epsilon\|_{L^\infty(\Gamma_{T_s})} \\ &\leq \|\mathcal{G}\bar{v} - \mathcal{G}v_\epsilon\|_{L^\infty(\Gamma_{T_s})} + \|\mathcal{G}v_\epsilon - v_\epsilon\|_{L^\infty(\Gamma_{T_s})} \\ &\leq \frac{1}{c\rho} (M_1 P_2 + M_2 P_1) \|\bar{v} - v_\epsilon\|_{L^\infty(\Gamma_{T_s})} + \frac{\sqrt{\epsilon}}{\rho}. \end{aligned}$$

$$\text{That is, } \|\bar{v} - v_\epsilon\|_{L^\infty(\Gamma_{T_s})} \leq \frac{1}{\rho} \left(1 - \frac{1}{c\rho} (M_1 P_2 + M_2 P_1) \right)^{-1} \sqrt{\epsilon},$$

which implies $v_\epsilon \rightarrow \bar{v}$ in $L^\infty(\Gamma_{T_s})$ as $\epsilon \rightarrow 0^+$. Hence, by (24), we have

$$\Phi(\bar{v}) = \inf_{v \in U} \Phi(v).$$

□

5 Conclusions

Optimal birth control for a structured population model with time-varying diffusion rate is qualitatively analyzed. The existence and uniqueness of mild solution is shown with the help of semigroup of operators and characteristic method. We take fertility rate as a control variable to study the optimal control problem which minimizes a given cost functional. Necessary optimality conditions of first order are established in the form of an Euler–Lagrange system. The existence and uniqueness of optimal birth controller is shown with the help of Ekeland’s variational principle.

References

1. R. Liu, G. Liu, Optimal birth control problems for a nonlinear vermin population model with size-structure. *J. Math. Anal. Appl.* **449**(1), 265–291 (2017)
2. Z.R. He, Y. Liu, An optimal birth control problem for a dynamical population model with size-structure. *Nonlinear Anal. Real World Appl.* **13**(3), 1369–1378 (2012)
3. V. Barbu, M. Iannelli, Optimal control of population dynamics. *J. Optim. Theory Appl.* **102**(1), 1–14 (1999)
4. S. Anita, *Analysis and Control of Age-Dependent Population Dynamics, Mathematical Modelling: Theory and Applications*, vol. 11 (Kluwer, Dordrecht, 2000)
5. N. Kato, Abstract linear partial differential equations related to size-structured population models with diffusion. *J. Math. Anal. Appl.* **436**(2), 890–910 (2016)
6. A. Pazy, *Semigroups of Linear Operators and Applications to Partial Differential Equations*. Applied Mathematical Sciences (Springer, New York, 1983)
7. M. Kumar, S. Abbas, Optimal birth control for a size-structured population model with diffusion (2021). Preprint, arXiv:2103.08399

Part III

Energy Harvesting

On Energy Harvesting with Time-Varying Frequency by Using Magneto-Piezo-Elastic Oscillators with Memory



Angelo M. Tuset, Jose M. Balthazar, Rodrigo T. Rocha, Jorge L. P. Felix,
Marcus Varanis, Mauricio A. Ribeiro, Clivaldo de Oliveira, Itamar Iliuk,
and Grzegorz Litak

1 Introduction

With the increasing demand for energy consumption in recent years, several areas of science have been looking for the production of clean and renewable energy. In this context, several devices are used, such as converting mechanical movement of sea waves [1–3] and portal frame systems [4–7].

However, many of these devices contain piezoceramic patches (PZT). These materials have the ability to generate electrical tension when under a mechanical stress. This deformation of the material allows the creation of electrical energy. The reverse is also possible, that is, the application of an electrical voltage to these

A. M. Tuset · M. A. Ribeiro · I. Iliuk

Federal University of Technology of Parana – UTFPR, Department of Electronics, Ponta Grossa, PR, Brazil

J. M. Balthazar (✉)

Federal University of Technology of Parana – UTFPR, Department of Electronics, Ponta Grossa, PR, Brazil

São Paulo State University, Faculty of Mechanical Engineering of Bauru – UNESP, Bauru, SP, Brazil

R. T. Rocha

UTFPR, Federal University of Technology, Paraná, Electronic Department, Ponta Grossa, Brazil

J. L. P. Felix

Universidade Federal de Fronteira do Sul-UFFS, Cerro Largo, RS, Brazil

M. Varanis · C. de Oliveira

Federal University of Grand Dourados-UFGD, Dourados, MS, Brazil

G. Litak

Lublin University of Technology, Faculty of Mechanical Engineering, Lublin, Poland

materials causes a mechanical deformation in the system. Therefore, following this line of thought, we can define the term energy generation or harvesting [1–6].

In this context, we highlight the devices in which we can apply an external excitation force to the system and thus converting the PZT deformation into electrical voltage. According to [8], we propose a system for collecting energy based on a structure with two bars, in which one of its ends is embedded in the moving system frame and the other end is under the action of magnetic fields. The recessed tips are connected to an electrical system in which a resistor generates a voltage due to the current produced by the PZT deformations. However, the external force comprises a harmonic oscillation of the type, being applied to the oscillators and showing the conditions for the behavior of the system.

In [8], the authors discuss the production of energy with a structure comprising a bar under the action of two magnetic poles, forming coupled bistable oscillators. The external force applied for energy production is characterized as excitation at the base of the system. The energy is accumulated in mechanical nonlinear resonators and transduced into the electrical power output by the piezoelectric elements. Nonlinear effects from the magnetic field assure the increase of the energy harvesting efficiency in variable source conditions (frequency and amplitude) through the so-called frequency broadband effect. Such nonlinear effects were discussed previously for a single degree of freedom [9–12]. For systems with multiple oscillators [8], dynamics and synchronization of the oscillator responses were studied for various system parameters.

Note also other forms of a multiple-degree-of-freedom harvesting device for collecting energy were proposed including piezoelectric or electromagnetics transduction laws with various mass distributions [13–15]. Harmonic excitation force is applied to the system and also under the action of multiple power wells [16]. Thus, describing the dynamic behavior of the structure with phase portraits and bifurcation diagrams, the model is validated using an experimental device with three different tip masses, representing three interesting cases: a linear system; a non-curved beam of natural low frequency, and a deformed beam.

However, many studies explore systems for the collection of energy-containing harmonic excitation forces in the system and analyzed the nonlinear dynamics of the system and its energy production. Alternatively, they analyze the systems with optimization techniques to obtain parameters in which the system is taken to more energetic orbits. Based on these discussions of external forces acting on the system, Ref. [5] proposes the investigation of energy collection on a portal frame system composed of PZT material. The authors consider the variable of the motor that produces the external force that is determined by the parameters that determine the active interaction between the oscillatory system and the excitation source. In this way, we analyzed a system with two degrees of freedom with a similar structure proposed by [8, 10], in which the system is coupled to two cantilevers with PZT patches that undergo the deformation of magnetic fields that form the potential well; these piezoceramic patches contain an electrical circuit for collecting energy. Therefore, this paper is an extension of the mathematical model proposed by [8, 10], considering that beams have some hysteresis properties. For this behavior, we

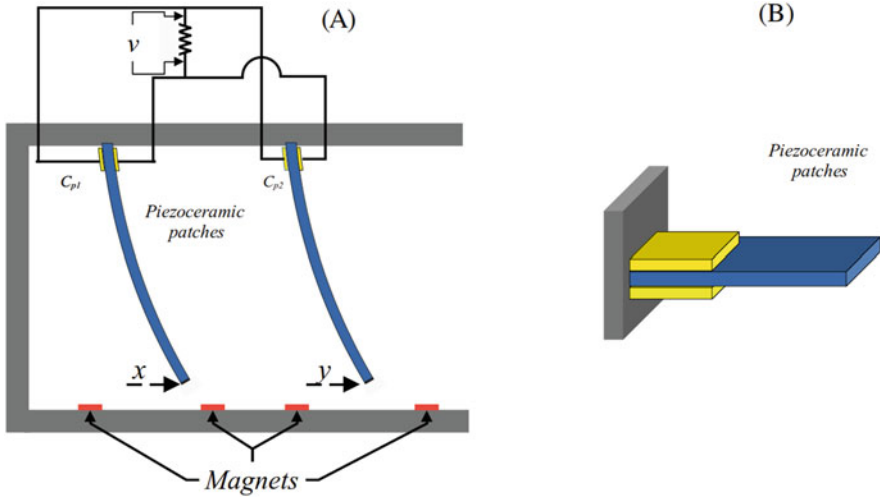


Fig. 1 (a) Scheme of a magnetoelastic system for energy harvesting consisting of two beams with applied the external force $F(t)$. R is the load resistance, and v is the voltage. Dampers are not indicated and (b) represent the patches of the piezoceramic material in beam

use Bouc-Wen damping to numerical simulation the hysteresis behavior. In [25], the authors investigate the effect of hysterical in a beam containing PZT patches for use in vibration-based energy harvesting. In Fig. 1a represents a schematic of the structure under the action of the acting force and that couples two beams with patches of PZT materials submitted to the potential caused to magnetic poles in the base, and Fig. 1b represents the patches PZT material in the beam.

1.1 Mathematical Modeling

For the mathematical model, we consider the system based on the structures described in Fig. 1. However, we consider the potential wells in their mathematical form described. In our case, we have two potentials: the first described in Eq. (1) for the displacement in x and for the displacement y in Eq. (2), for the displacement of mechanical oscillators, as follows. Equations (1) and (2) are based on the approximate description of the potential wells formed by the magnetic poles of the system [8].

$$V_1(x) = -x^2 + \frac{x^4}{2} \tag{1}$$

$$V_2(y) = \alpha \left(-y^2 + \frac{y^4}{2} \right) \quad (2)$$

where α is the parameter that regulates the amplitude of the powers acting in the system and are the displacements of the tips subjected to the magnetic compound. However, considering the actuation and coupling force as [10, 13]:

$$F(t) = f_0 \cos(\omega t + a_0 \sin(b_0 \omega t)) \quad (3)$$

where f_0 is the amplitude of the excitation force, it is the system frequency, and they define the interaction constants between the oscillatory system and the excitation force. Therefore, if we consider $a_0 = 0$, in Eq. (3), we will have a force external to $F(t) = f_0 \cos(\omega t)$ the type oscillatory system. However, we consider Bouc-Wen Damping, described as follows [23, 24]:

$$\begin{cases} \Phi^{BW}(x)(t) = k_1 x(t) + (1 - \eta) D k_1 z(t) \\ \dot{z}(t) = D^{-1} (A \dot{x} - \beta |\dot{x}| |z|^{n-1} z - \gamma x |\dot{z}|^n) \end{cases} \quad (4)$$

where ≥ 1 , $D > 0$, $k_1 > 0$, $0 < \alpha < 1$, α is the ratio between post-flow and pre-flow stiffness, and $x(t)$ is the yield displacement [20, 21]. Therefore, considering Eqs. (1)–(4), we obtain the mathematical model that describes the movement of the two coupled beams, together with the equation of the electric current produced, which are given by:

$$\begin{cases} \ddot{x} + 2\zeta x (1 - x^2) - Xv + \Phi^{BW}(x)(t) = f_0 \cos(\omega t + a_0 \sin(b_0 \omega t)) \\ \ddot{y} + \frac{1}{2}\alpha y (1 - y^2) - Xv + \Phi^{BW}(y)(t) = f_0 \cos(\omega t + a_0 \sin(b_0 \omega t)) \\ \dot{v} + \lambda v + \kappa \dot{x} + \kappa \dot{y} = 0 \\ \dot{z}_x(t) = D^{-1} (A \dot{x} - \beta |\dot{x}| |z_x|^{n-1} z_x - \gamma x |\dot{z}_x|^n) \\ \dot{z}_y(t) = D^{-1} (A \dot{y} - \beta |\dot{y}| |z_y|^{n-1} z_y - \gamma y |\dot{z}_y|^n) \end{cases} \quad (5)$$

where x and y are the transverse displacements of the beam, v is the voltage across the resistor, X is the coupling term of the piezoelectric system in electrical equations, κ is the reciprocal temporal constant of the electrical circuit, R is the resistance, and $e C_p = C_{p1} + C_{p2}$ is the capacitance of the piezoelectric material and finally is the stiffness mistuning parameter which should be considered in any realistic system.

2 Numerical Results

For the numerical analysis, we considered the constants in Table 1 [12, 20, 21]:

We also consider for numerical analysis the following initial condition $x_0 = [0.01, 0, 0.01, 0, 0, 0]$, and for the integration of the system of differential

Table 1 Parameter of numerical simulation (for a dimensionless model)

Parameter	Values	Parameter	Values
X	0.05	D	1.0
κ	0.5	k_1	0.25
ζ	0.01	β	0.55
f_0	0.2	A	1.0
α	1.1	γ	0.45
λ	0.01	n	3.0

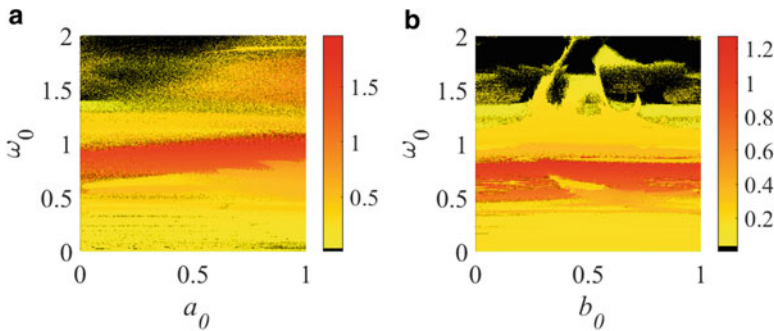


Fig. 2 (a) Color plot of $\sigma(x - y)$ versus $(\omega_0 \times a_0)$ in which the black region represents values in which the system is $\sigma(x - y) \approx 0$, with a value of $b_0 = 0.5$; (b) $\sigma(x - y)$ versus $(\omega_0 \times b_0)$ in which the black region represents values in which the system is $\sigma(x - y) \approx 0$, with the parameter $a_0 = 0.2$ and initial condition $x_0 = [0.01, 0, 0.01, 0, 0, 0]$

equations, it is the method of Runge-Kutta of fourth order implicitly [12], with an integration step $h = 0.001$ and a time of convergence of the system trajectories in $t = 300,000$ s (dimensionless units) with a transient time of 40% of the total time. Therefore, we analyze the dynamic behavior of the structure by doing some sweeps with the parameters $\omega_0 \in [0, 2]$, $a_0 \in [0, 1]$, and $b_0 \in [0, 1]$. We check the behavior of the system coupling, calculating $\sigma(x - y)$ from Eq. (4), the standard deviation between the displacements. Thus, if $\sigma(x - y) \approx 0$, the value of the synchronization process occurs. According to [8–10], for values $a_0 = 0$ in the force, the frequency is $\omega = 1.1$, the system has a maximum power, and the system is decoupled. Then, Fig. 2 represents the coupling behavior between the two trajectories x and y , so we use the standard deviation between the trajectories and, that is, when the trajectories are in sync. Therefore, the black regions of Fig. 2a, b represent the accompaniment of the trajectories of the PZT energy harvesting subsystems with the variation in $(\omega_0 \times a_0)$ and $(\omega_0 \times b_0)$, respectively.

Thus, we analyze the behavior of the $\langle v^2 \rangle$ as an approximation of the power of the system, i.e., $\propto \langle v^2 \rangle$ [22]. We can observe that Fig. 3a, b represents an approximation of the behavior of the power for $(\omega_0 \times a_0)$ and $(\omega_0 \times b_0)$, respectively. The black region represents the minimum power obtained by the system; however, for the values in white to red, the maximum power values stand out. Therefore, we can see that the regions of possible synchronization have the black regions in Fig. 2

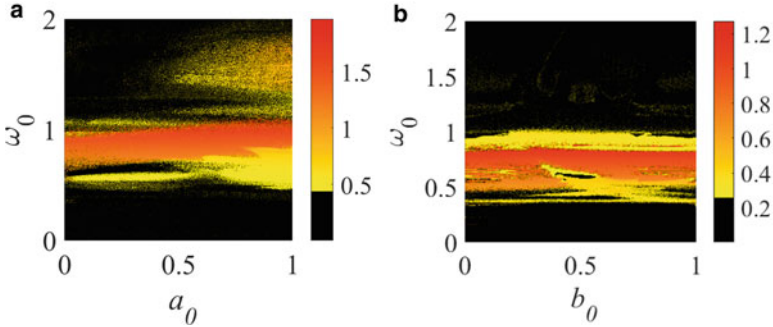


Fig. 3 (a) Color plot of power output P versus $(\omega_0 \times a_0)$ in which the black region represents maximum values for P (brown region), with a value of $b_0 = 0.5$; (b) Similarly, power output P versus $(\omega_0 \times a_0)$ in which the black region represents maximum values for P (brown region), with the parameter $a_0 = 0.2$. Initial conditions and the system parameters are the same as in Fig. 2

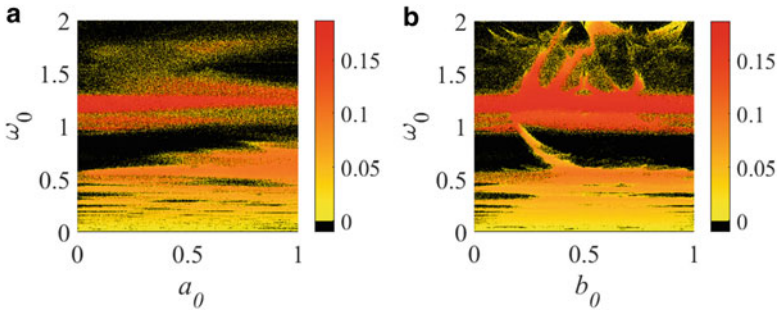


Fig. 4 (a) Color plot of maximum Lyapunov exponent λ_{\max} versus $(\omega_0 \times a_0)$ in which the black region represents $\lambda_{\max} < 0$ (periodic region) and yellow to brown region $\lambda_{\max} > 0$ (chaotic region), with parameter $b_0 = 0.5$. (b); similarly, maximum Lyapunov exponent λ_{\max} versus $(\omega_0 \times b_0)$ in which the black region represents $\lambda_{\max} < 0$ (periodic region) and yellow to brown region $\lambda_{\max} > 0$ (chaotic region), with parameter $a_0 = 0.2$. Initial conditions and the system parameters are the same as in Fig. 2

that are approximately compatible with the maximum average power regions of the system.

The synchronous behavior of the system is linked to the production of average power and results of the dynamics of the system. We analyze the dynamic behavior of the energy collection structure, with the maximum exponents of Lyapunov and determine the possible regions in which the system has a chaotic behavior and the regions that have a periodic behavior [17–19]. Figure 4 shows the regions in which $\lambda_{\max} > 0$, which represents a chaotic behavior for the system which are the regions $\lambda_{\max} \in [0, 0.16]$, and for the regions $\lambda_{\max} < 0$, we can observe a periodic behavior. Determining the periodic and chaotic regions is important to contribute to the regions found in the coupling and the power.

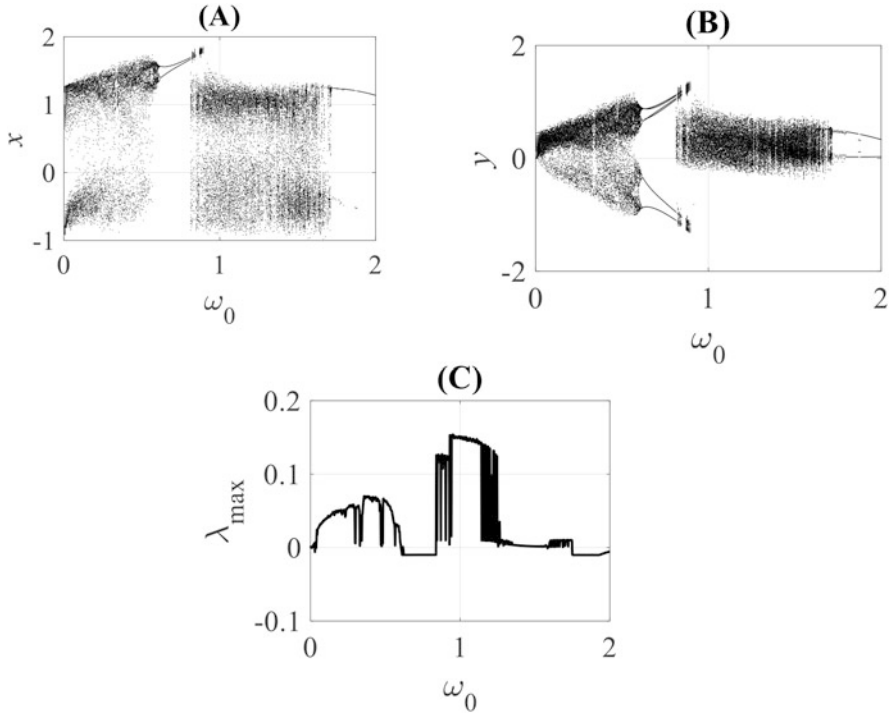


Fig. 5 (a) Bifurcation diagram for x , (b) bifurcation diagram for y , and (c) Lyapunov's maximum exponent with $\omega_0 \in [0, 2]$. Initial conditions $x_0 = [0.01, 0, 0.01, 0, 0, 0]$ and the system parameters are the same as in Fig. 2

Thus, we consider the following parameters $a_0 = 0.2$ and $b_0 = 0.5$ to determine the bifurcation diagrams. Figure 5a, b represents the bifurcation diagram of variables x_1 and x_3 determining the time series maximums, and thus, we can observe the periodic windows for $\omega_0 \in [0.6097; 0.8242]$ and $\omega_0 \in [1.716; 2]$; the other intervals had a chaotic behavior. These interleavings are confirmed with the Lyapunov's maximum exponent, which demonstrated the same periodic ones in Fig. 5c.

Typically, Figs. 6, 7, 8, and 9 represent the phase portrait of the structures for the values of $\omega_0 = 0.7468, 1.061, 1.897,$ and 1.179 , respectively. Thus, we observe the nonlinear dynamics behavior of ω_0 in the Eq. (4).

3 Conclusions

In this paper, we analyze the nonlinear dynamic behavior of an oscillator-type structure using elastic magneto under the action of the external force of an eccentric rotating mass-motor. As the structure has two oscillators under the action of

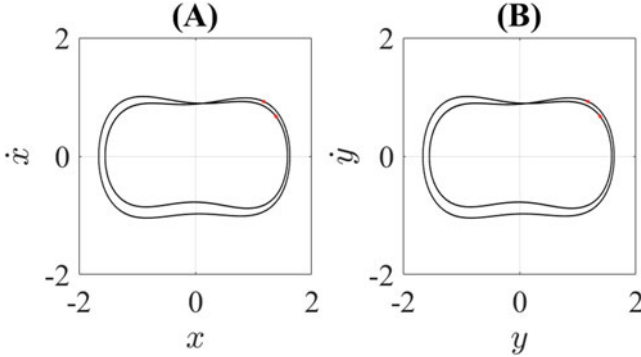


Fig. 6 Phase portrait with Poincare points for the value of $\omega_0 = 0.7468$ using Eq. (4) with 2-periodic behavior. (a) $x - \dot{x}$ and (b) $y - \dot{y}$

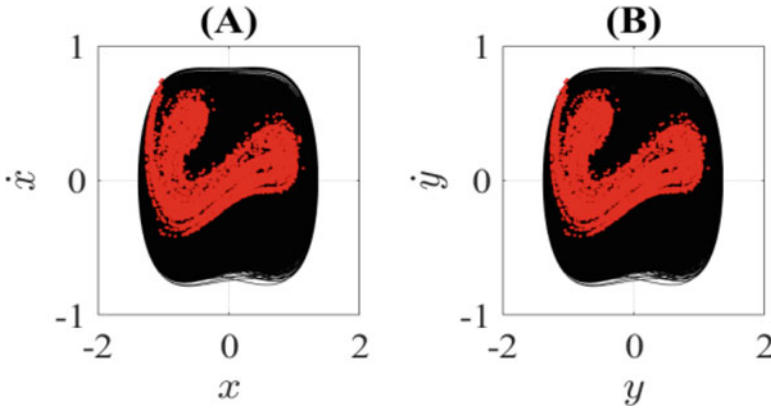


Fig. 7 Phase portrait with Poincare points for the value of $\omega_0 = 1.061$ using Eq. (4) with chaotic behavior. (a) $x - \dot{x}$ and (b) $y - \dot{y}$

magnetic potential wells, we analyzed the coupling of this system based on the parameters of the external force eccentric rotating mass motor a_0 and b_0 in relation to the frequency ω_0 da acting force and thus determining the regions in which $\delta(x_1 - x_3) \approx 0$ in which the trajectory of the system is in sync. Another amount that we calculated was the average power for the same parameters, and we observed that for maximum average power, they are for values close to $\omega_0 \approx 1.1$; the regions of maximum power are close to the regions where the oscillators are synchronous, that is, $\delta(x_1 - x_3) \approx 0$ Thus, we calculate the dynamic parameters of the Eq. (4); the first to be calculated was the maximum exponent of Lyapunov, making a scan for the same parameters, and we observed that the region of maximum power and synchronism of the system is close to the periodicity region, that is, $\lambda_{\max} < 0$ This analysis allowed us to observe regions where the system's orbits can produce more power from this system under the action of magnetic poles. And for the values of $a_0 = 0.2$ and $b_0 = 0.5$, we calculate the bifurcation diagram and observe the

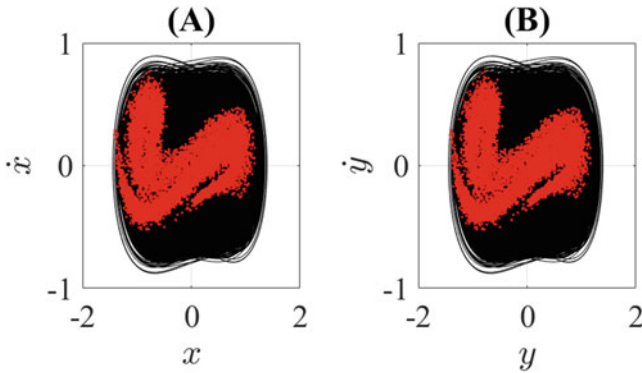


Fig. 8 Phase portrait with Poincare points for the value of $\omega_0 = 1.082$ using Eq. (4) with chaotic behavior. (a) $x - \dot{x}$ and (b) $y - \dot{y}$

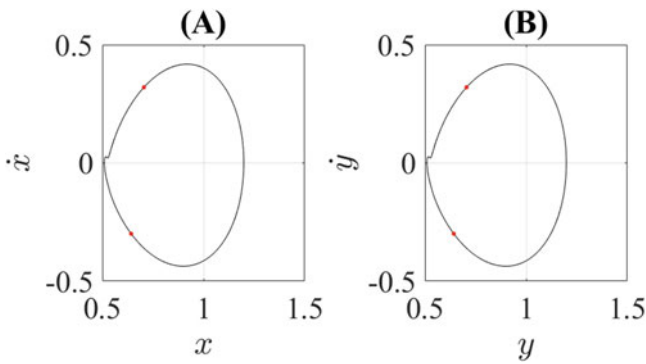


Fig. 9 Phase portrait with Poincare points for the value of $\omega_0 = 1.897$ using Eq. (4) with 2-periodic behavior. (a) $x - \dot{x}$ and (b) $y - \dot{y}$

periodic windows that have been confirmed with the Lyapunov exponent. In both calculations, we use the frequency scan. Once this analysis is done, we determine the phase diagrams and the Poincare maps close to the regions of maximum power as observed in Figs. 2 and 3.

Acknowledgments This work was supported by the program of the Polish Ministry of Science and Higher Education under the project DIALOG 0019/DLG/2019/10 in the years 2019–2021.

Conflict of Interest The authors declare that they have no conflict of interest.

References

1. X.D. Xie, Q. Wang, N. Wu, Potential of a piezoelectric energy harvester from sea waves. *J. Sound Vib.* **333**(5), 1421–1429 (2014)
2. N. Wu, Q. Wang, X.D. Xie, Ocean wave energy harvesting with a piezoelectric coupled buoy structure. *Appl. Ocean Res.* **50**, 110–118 (2015)
3. A. Jbaily, R.W. Yeung, Piezoelectric devices for ocean energy: a brief survey. *J. Ocean Eng. Mar. Energy* **1**(1), 101–118 (2015)
4. X. Xie, Q. Wang, A mathematical model for piezoelectric ring energy harvesting technology from vehicle tires. *Int. J. Eng. Sci.* **94**, 113–127 (2015)
5. J.M. Balthazar, A.M. Tusset, R.M.L.R.F. Brasil, J.L.P. Felix, R.T. Rocha, F.C. Jansen, A. Nabarreta, C. Oliveira, An overview on the appearance of the Sommerfeld effect and saturation phenomenon in non-ideal vibrating systems (NIS) in macro and MEMS scales. *Nonlinear Dyn.* **93**(1), 19–40 (2018)
6. I. Iliuk, J.M. Balthazar, A.M. Tusset, J.R.C. Piqueira, B.R. de Pontes, J.L.P. Felix, Á.M. Bueno, A non-ideal portal frame energy harvester controlled using a pendulum. *Eur. Phys. J. Spec. Top.* **222**(7), 1575–1586 (2013)
7. R.T. Rocha, J.M. Balthazar, A.M. Tusset, V. Piccirillo, F.C. Janzen, J.L. Felix, On mode coupling analysis and stability regions to energy harvesting in a two-degrees-of-freedom portal frame platform. In: *International Design Engineering Technical Conferences and Computers and Information in Engineering Conference*. (58202), V006T10A053. American Society of Mechanical Engineers (2017)
8. G. Litak, M.I. Friswell, C.A.K. Kuwimy, S. Adhikari, M. Borowiec, Energy harvesting by two magnetopiezoelectric oscillators with mistuning. *Theor. Appl. Mech. Lett.* **2**(4), 043009 (2012)
9. A. Erturk, D.J. Inman, *Piezoelectric Energy Harvesting*, 1st edn. (Wiley, United Kingdom, 2011)
10. A. Erturk, J. Hoffmann, D.J. Inman, A piezomagnetoelastic structure for broadband vibration energy harvesting. *Appl. Phys. Lett.* **94**(25), 254102 (2009)
11. F. Cottone, H. Vocca, L. Gammaitoni, Nonlinear energy harvesting. *Phys. Rev. Lett.* **102**(8), 080601 (2009)
12. M.F. Daqaq, R. Masana, A. Erturk, D.D. Quinn, On the role of nonlinearities in vibratory energy harvesting: a critical review and discussion. *Appl. Mech. Rev.* **66**, 40801 (2014)
13. J.L.P. Felix, R.P. Bianchin, A. Almeida, J.M. Balthazar, R.T. Rocha, R.M. Brasil, On energy transfer between vibration modes under frequency-varying excitations for energy harvesting, in *Applied Mechanics and Materials*, (Trans Tech Publications Ltd, India, 2016), pp. 65–75
14. P.V. Malaji, S.F. Ali, Analysis of energy harvesting from multiple pendulums with and without mechanical coupling. *Eur. Phys. J. Spec. Top.* **224**(14–15), 2823–2838 (2015)
15. P.V. Malaji, M.I. Friswell, S. Adhikari, G. Litak, Enhancement of harvesting capability of coupled nonlinear energy harvesters through high energy orbits. *AIP Adv.* **10**, 085315 (2020)
16. D. Huang, S. Zhou, G. Litak, Theoretical analysis of multi-stable energy harvesters with high order stiffness terms. *Commun. Nonlinear Sci. Numer. Simul.* **69**, 270–286 (2019)
17. S.P. Beeby, M.J. Tudor, N.M. White, Energy harvesting vibration sources for microsystems applications. *Meas. Sci. Technol.* **17**(12), 175 (2006)
18. L.F. Shapine, M.W. Reichelt, The matlab ode suite. *SIAM J. Sci. Comput.* **18**(1), 1–22 (1997)
19. R.T. Rocha, A.M. Tusset, M.A. Ribeiro, W.B. Lenz, J.M. Balthazar, Remarks on energy harvesting of nonlinear charge and voltage piezoelectric models in a two-degrees-of-freedom nonlinear portal frame model. *Proc. Inst. Mech. Eng. C J. Mech. Eng. Sci.* (2020). United Kingdom. <https://doi.org/10.1177/0954406220939994>
20. A. Wolf, J.B. Swift, H.L. Swinney, J.A. Vastano, Determining Lyapunov exponents from a time series. *Phys. D Nonlinear Phenom.* **16**(3), 285–317 (1985)
21. H. Kantz, T. Schreiber, *Nonlinear Time Series Analysis*, 1st edn. (Cambridge University Press, 2004)

22. L. Cvetivanin, M. Zukovic, J.M. Balthazar, *Dynamics of Mechanical Systems with Non-ideal Excitation*, 1st edn. (Springer International Publishing, Switzerland, 2018)
23. A.M. Solovyov, M.E. Semenov, P.A. Meleshenko, A.I. Barsukov, Bouc-Wen model of hysteretic damping. *Proc. Eng.* **201**, 549–555 (2017)
24. N.M. Kwok, Q.P. Ha, M.T. Nguyen, J. Li, B. Samali, Bouc–Wen model parameter identification for a MR fluid damper using computationally efficient GA. *ISA Trans.* **46**(2), 167–179 (2007)
25. L.L. Silva, M.A. Savi, P.C. Monteiro Jr., T.A. Netto, Effect of the piezoelectric hysteretic behavior on the vibration-based energy harvesting. *J. Intell. Mater. Syst. Struct.* **24**(10), 1278–1285 (2013)

Galloping Piezoelectric Energy Harvester for Low Wind Speed



Kaiyuan Zhao, Qichang Zhang, and Shuying Hao

1 Introduction

Energy harvester is customarily the procedure of converting light, heat, solar energy, and vibration energy into electric energy. Its ultimate goal is to develop self-powered sensors, actuators, and other electronic devices. Wind is one of the main natural energy sources that cause structural vibration. In the past few years, wind-induced vibration clean energy harvesters have been investigated in small-scale applications for the purpose of converting unused aeroelastic vibrations to usable amount of electric power [1]. These wind-induced vibration energy harvesters can be used to power important and sensitive electronic devices without the need of a main power grid. The design and optimization of wind-induced vibration energy harvester are mainly divided into three parts: wind energy harvesting, kinetic energy harvesting, and electric energy harvesting.

In order to collect wind-induced vibration energy more efficiently, researchers showed quantitatively and qualitatively that the structure subjected to gallop oscillations is more efficient than vortex-induced vibration (VIV) and flutter-based vibration. In addition to that, since the galloping system is the one single free system, the structural design of the galloping energy harvester is simpler than that of the flutter one, which makes it easier to miniaturize, integrate, and mass produce the galloping energy harvester. Furthermore, it was indicated that compared with the vortex-induced vibration energy collector, galloping vibration energy collector

K. Zhao · Q. Zhang (✉)

Tianjin Key Laboratory of Nonlinear Dynamics and Control, Department of Mechanics, School of Mechanical Engineering, Tianjin University, Tianjin, China
e-mail: qzhang@tju.edu.cn

S. Hao

Tianjin Key Laboratory of Advanced Electromechanical System Design and Intelligent Control, Tianjin University of Technology, Tianjin, China

can work in a wider wind speed range which is due to the fact that the galloping harvester is useful for any speed higher than the onset speed of galloping. Several investigations have been performed in order to accurately predict the response of the galloping energy harvester with the influences of the cross-sectional geometry [2], Reynolds number [3], and base excitation [4]. The main purpose of these studies is to improve the efficiency of converting wind energy into kinetic energy. However, the object of study is mainly focused on the section of the basic shape of the column, such as D-shaped [5], triangle [6], square [7], and circular [8]. This is mainly because the expression of flow force is the difficulty in this part. In our study, a square prism with a V-shaped groove on the windward side is used to optimize wind energy harvesting. One of the challenging tasks in this analytical modeling of the galloping systems is the representation of galloping force. First, we establish the mathematical model of energy harvester based on study of Abdelmoula [9]. Then, the empirical parameters of dance power in the model are set as undetermined parameters. Then, the sparse identification algorithm is used to establish the parameters to be determined by combining the wind tunnel experimental data and mathematical model. Finally, the theoretical analysis results of the system are improved.

A large number of literatures show that the piezoelectric cantilever beam can realize the efficient collection of kinetic energy in the vibration energy harvester [10]. At present, the optimization of cantilever beam mainly focuses on the length thickness ratio of beam [11], trapezoid beam, triangle beam, and so on [12]. There are still some limitations in these optimizations. Therefore, how to break through the conventional shape and optimize the shape of beam based on big data calculation has become the main content of this part of research. In this part of the study, we use semi-analytical method to analyze the energy harvester with variable cross-sectional piezoelectric cantilever beam and then use particle swarm optimization (PSO) method to optimize the topology of piezoelectric cantilever beam.

The direct output of piezoelectric vibration energy harvester is AC with large voltage and small current. But in engineering application, DC voltage is often needed for various electric loads. Therefore, AC-DC conversion and power storage must be carried out. This part is mainly based on the nonlinear rectifier interface circuit of synchronous switch to optimize [10]. Because of the reverse piezoelectric effect, there is coupling between the piezoelectric generator and the interface circuit. The coupling phenomenon directly affects the efficiency of DC voltage conversion to AC voltage. Therefore, this part mainly optimizes the system efficiency, output power, and critical flow rate of the energy harvester based on the analysis of rectifier circuit.

2 Optimization of Wind Energy

We proposed the concept of the galloping piezoelectric energy harvester with a V-shaped groove (GPEH-V). The GPEH-V system consisting of a square prismatic with a V-shaped groove and subjected to wind flow is considered, as shown in

Fig. 1 Schematic of GPEH-V

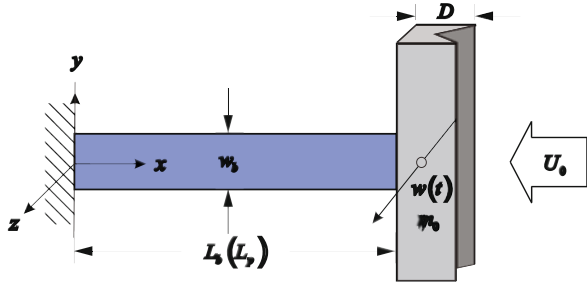


Fig. 1. It is mainly composed of a square prismatic with a V-groove on windward side and a piezoelectric cantilever beam. The piezoelectric cantilever beam consists of a beryllium bronze support layer with length, width, and thickness of 110 mm, 15 mm, and 0.8 mm, respectively, and its bonded piezoelectric composite (MFC M8507 P2). The free end of the piezoelectric cantilever beam is attached to the square prismatic having a mass of m_0 , a width of 2×20 mm, a moment of inertia J , and a V-groove with α degrees. In addition, the piezoelectric cantilever is connected to an electric impedance composed of a load resistance R and a capacitance C in parallel connection. From the analysis of mathematical principles, it is clear that the vibration phenomenon is possible when the derivative of the steady-state aerodynamic lift coefficient is negative. As the wind speed increases, there may be a critical speed, named galloping critical speed, at which single-mode self-excited vibration takes place. The main reason for this phenomenon is that the structural damping is insufficient to damp out motions due to the aerodynamic effects.

The response behavior of the galloping energy harvester is modeled based on the Lagrangian equation and the virtual work principle, combined with the Galerkin discrete method:

$$EI \frac{\partial^4 w(x,t)}{\partial x^4} + c \frac{\partial w(x,t)}{\partial t} + meq \frac{\partial^2 w(x,t)}{\partial t^2} + \theta V(t) \left(\frac{d\delta(x-x_1)}{dx} - \frac{d\delta(x-x_1-L_p)}{dx} \right) = \frac{1}{2} \rho_a D_c L_c U_0^2 \times \sum_{i=1}^3 a_i \left[\frac{1}{U_0} \frac{\partial w(x,t)}{\partial t} + \frac{D_c}{U_0} \right]^i \left(\delta(x-L_b) + \frac{D}{2} \frac{d\delta(x-L_b)}{dx} \right). \tag{1}$$

To improve the accuracy of the calculation, the torque of the square prismatic is taken into account in the boundary conditions, and the associated boundary conditions are given by the following:

$$\begin{aligned} w(0,t) &= 0, \quad \frac{\partial w(0,t)}{\partial x} = 0, \\ EI \frac{\partial^3 w(L_b,t)}{\partial x^3} &= m_c \frac{\partial^2 w(L_b,t)}{\partial t^2} + m_c \frac{D_c}{2} \frac{\partial^3 w(L_b,t)}{\partial x \partial t^2}, \\ EI \frac{\partial^2 w(L_b,t)}{\partial x^2} &= -m_c \frac{D_c}{2} \frac{\partial^2 w(L_b,t)}{\partial t^2} - \left(J + m_c \left(\frac{D_c}{2} \right)^2 \right) \frac{\partial^3 w(L_b,t)}{\partial x \partial t^2}. \end{aligned} \tag{2}$$

According to the first-order modal ordinary differential equations, when the energy input from the fluid is equal to the energy consumed by the damping, the critical velocity can be calculated as follows:

$$U_g = \frac{4\zeta_1\omega_1}{\rho_0DL_0a_1[\varphi_1(L_b) + \frac{D}{2}\varphi'_1(L_b)]^2}. \tag{3}$$

It can be seen from Eq. (3) that the galloping critical velocity U_g is closely related to seven parameters, which are damping, intrinsic frequency, prismatic density, length, section edge length, and piezoelectric cantilever beam modal function. When the mass of the prismatic and the piezoelectric cantilever beam is constant, the key factor affecting the critical flow velocity is the shape of the windward side of the prismatic. The fluid force coefficients a_1 change significantly with the shape of the windward surface, which in turn affects the change of the critical flow velocity. Figure 2 shows the trend between the critical flow velocity and the fluid force parameters for different masses of the column. Figure 3 shows the cross-sectional shape of the prismatic with a V-groove on the windward side. Starting from model 2, the values of α are 13° , 20° , 27° , 34° , 45° , and 64° , respectively.

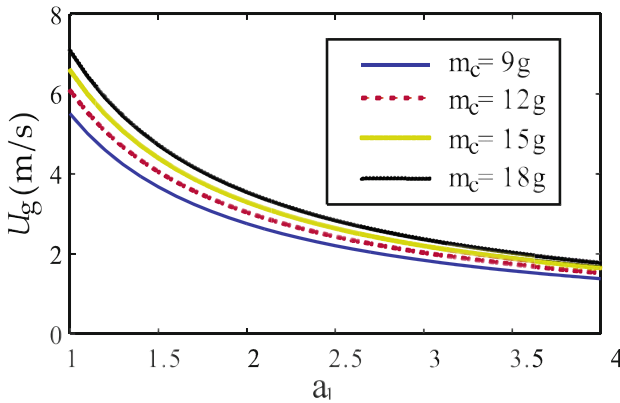


Fig. 2 The relationship between a_1 and U_g of different mass cylinders

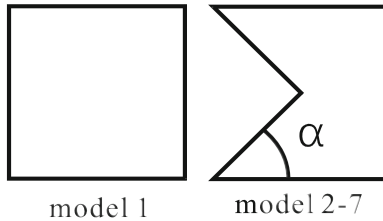


Fig. 3 Column section model

Fig. 4 Relationship between models and the critical velocity

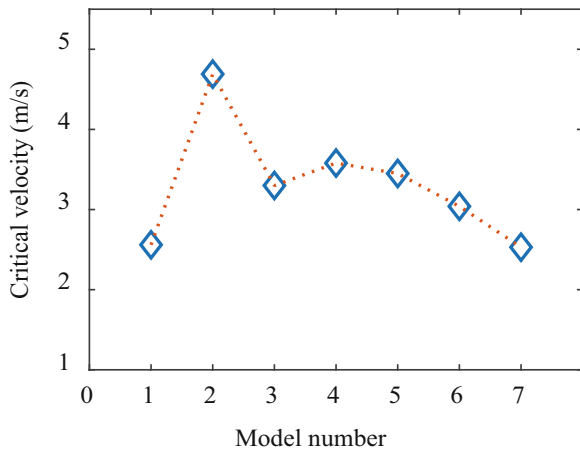


Fig. 5 Output power of the model at a flow velocity of 10 m/s

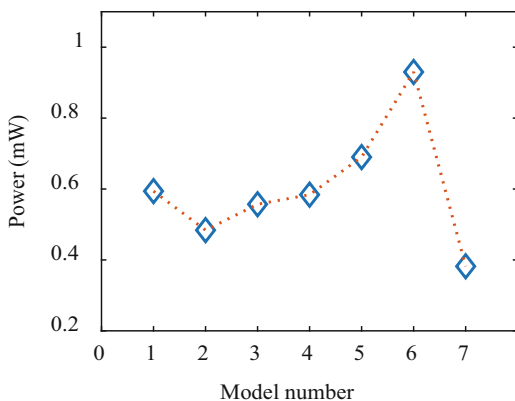


Figure 4 shows the critical flow rate of the GPEH-V system for different models. Figure 5 shows the output energy of the GPEH-V system for different models.

3 Optimization of Kinetic Energy

As shown in Fig. 6, the schematic diagram of variable cross-sectional piezoelectric wind-induced vibration energy harvester system is shown, and the beam width can be expressed as a function $w_b(x)$ of position coordinate x . The governing equation of the energy harvester can be written as follows:

$$\frac{\partial^2 M(x,t)}{\partial x^2} + c \frac{\partial w(x,t)}{\partial t} + \text{meq}(x) \frac{\partial^2 w(x,t)}{\partial t^2} = \frac{1}{2} \rho_a D_c L_c U_0^2 \times \sum_{i=1}^3 a_1 \left[\frac{1}{U_0} \frac{\partial w(x,t)}{\partial t} + \frac{D_c}{U_0} \right]^i \left(\delta(x - L_b) + \frac{D}{2} \frac{d\delta(x-L_b)}{dx} \right), \tag{4}$$

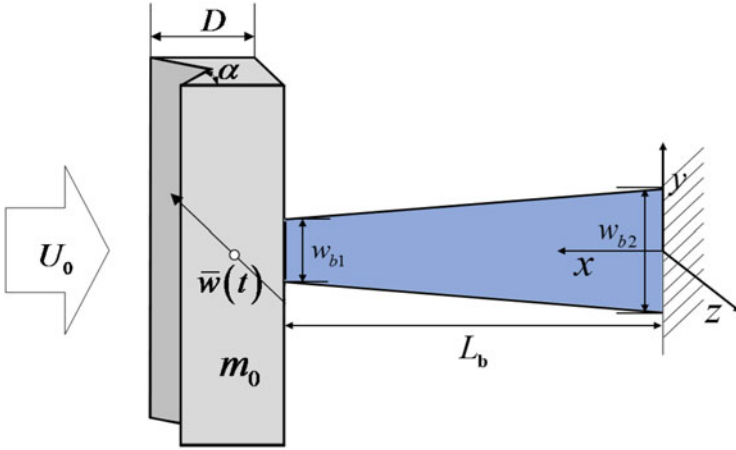


Fig. 6 Schematic diagram of variable cross-sectional energy harvester

where

$$M(x, t) = E_b I(x) \frac{\partial^2 w(x, t)}{\partial x^2} + \theta(x) V(t), \quad (5)$$

$$\text{meq}(x) = \frac{w_b(x) (\rho_b L_p t_b + 2\rho_p L_p t_p)}{L_p}, \quad (6)$$

$$I(x) = \frac{2w_b(x)}{E_b 3} \left[E_b \left(\frac{t_b}{2} \right)^3 + 3E_p \left(\frac{t_b}{2} \right)^2 t_p + 3E_p \left(\frac{t_b}{2} \right) t_p^2 + t_p^3 \right], \quad (7)$$

$$\theta(x) = \frac{d_{31} E_p w_p(x)}{2t_p} \left[\left(\frac{t_b}{2} \right)^2 - \left(t_p + \frac{t_b}{2} \right)^2 \right]. \quad (8)$$

The variable cross-sectional beam is divided into several connected segments. When the number of segments is enough, each segment is regarded as a uniform section. Based on the analytical expression of the modal function of the beam, the modal function of the i segment of the beam is obtained as follows:

$$\phi_i(x) = A_i \cos X_i + B_i \cosh X_i + C_i \sin X_i + D_i \sinh X_i, \quad (9)$$

where

$$X_i = \beta_i (x - x_{i-1}), x_{i-1} \leq x \leq x_i, i = 1, 2, \dots, N, x_0 = 0. \quad (10)$$

According to the continuity of displacement, rotation angle, bending moment, and shear force at the connection point of segments i and $i + 1$, the following relationship is obtained:

$$\begin{bmatrix} \phi_{i+1}(x_i) \\ \phi'_{i+1}(x_i) \\ (E_b I_b(x))_{i+1} \phi''_{i+1}(x_i) \\ ((E_b I_b(x))_{i+1} \phi''_{i+1}(x_i))' \end{bmatrix} = \begin{bmatrix} \phi_i(x_i) \\ \phi'_i(x_i) \\ (E_b I_b(x))_i \phi''_i(x_i) \\ ((E_b I_b(x))_i \phi''_i(x_i))' \end{bmatrix}. \tag{11}$$

By substituting the i -order mode and $i + 1$ mode into Eq. (9), the relationship between the undetermined coefficients of adjacent modal functions can be obtained as follows:

$$A_{(i+1)} = Z_{(i)} A_{(i)}. \tag{12}$$

$A_{(N)}$ and $A_{(1)}$ can be obtained by iteration:

$$A_{(N)} = \mathbf{Z} A_{(1)}, \tag{13}$$

where

$$\mathbf{Z} = Z_{(N-1)} Z_{(N-1)} \dots Z_{(2)} Z_{(1)}. \tag{14}$$

Each element in \mathbf{Z} matrix is a function of the natural circle frequency ω , which establishes the relationship between the undetermined coefficient $A_{(1)}$ of the first equivalent segment and the undetermined coefficient $A_{(N)}$ of the equivalent segment N . Therefore, as long as the four boundary conditions at the left and right ends of the beam are given, the expression of the natural circular frequency ω can be obtained, and then, the modal function of each segment can be obtained from the boundary conditions and Eq. (11). The modal function of the cantilever beam with variable cross-sectional $\phi(x)$ is obtained by orthogonalization and normalization of the modal function of the segment. Finally, the ordinary differential equations of the system are obtained:

$$\begin{aligned} & \ddot{r} + 2\xi\omega\dot{r} + \omega^2 r - \\ & \frac{1}{2}\rho_0 D L_0 U_0 a_1 \left(\phi(L_b) + \frac{D}{2}\phi'(L_b) \right) \left[\phi(L_b) + \frac{D}{2}\phi'(L_b) \right] \dot{r} - \\ & \frac{1}{2U_0}\rho_0 D L_0 a_3 \left(\phi(L_b) + \frac{D}{2}\phi'(L_b) \right) \left[\phi(L_b) + \frac{D}{2}\phi'(L_b) \right]^3 \dot{r}^3 + \\ & \theta_1 V(t) = 0, \end{aligned} \tag{15}$$

$$C_p \dot{V} - \theta_1 \dot{r} + \frac{V}{R} = 0, \tag{16}$$

where

$$C_p = \int_0^{L_b} \frac{\varepsilon_{33} w_b(x)}{2t_p} dx, \quad (17)$$

$$\theta_1 = \int_0^{L_b} \theta(x) \phi''(x) dx, \quad (18)$$

$$\theta(x) = \frac{d_{31} E_p w_p(x)}{2t_p} \left[\left(\frac{t_b}{2} \right)^2 - \left(t_p + \frac{t_b}{2} \right)^2 \right]. \quad (19)$$

With this method, the natural frequency with variable cross section can be solved directly from the stiffness and linear density functions along the axis direction. This method can be used to solve any kind of variable cross-sectional beam quickly, but if the finite element method is used, the model needs to be rebuilt and meshed for calculation, which increases a lot of time calculation cost for the purpose of using big data method for optimization.

We first define the width function of the beam by defining the width of the beam at a finite number of locations. Then, the width function of the beam is optimized by particle swarm optimization algorithm. When the wind speed is 11 m/s, the beam model is optimized. The maximum width of setting beam is 40 mm, and the minimum width is 8 mm. In the optimization, the population size is 50 and the evolution times are 50. Figure 7 shows the iteration results of PSO optimization process. By about 30 generations, the collected power has converged to a maximum. The shape of the optimized beam is shown in Fig. 8. At this time, the collected electric energy is 65.5 mW.

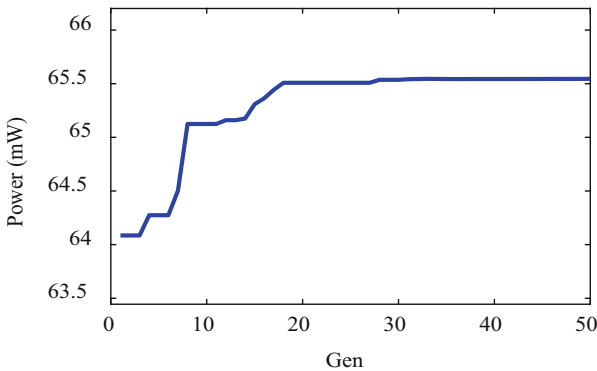


Fig. 7 Iteration results of PSO optimization process

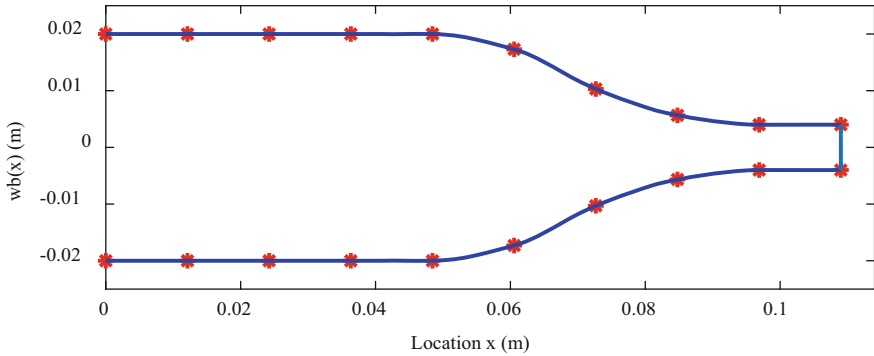


Fig. 8 Optimal beam model

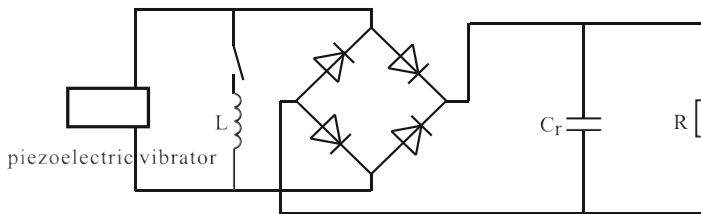


Fig. 9 Parallel synchronous switch interface circuit

4 Energy Collection Interface Circuit

The energy harvester interface circuit adopts parallel synchronous switch interface circuit, as shown in Fig. 9. Its basic principle is as follows: first, the cantilever piezoelectric vibrator starts to vibrate from the initial position, and the switch is in the off state, and the parallel synchronous switch interface circuit is equivalent to the standard bridge rectifier interface circuit. Without considering the diode voltage drop, the output voltage V_P of the piezoelectric harvester is equal to the voltage V_s at both ends of the load. When the vibration displacement of the cantilever piezoelectric vibrator reaches the maximum value, the switch is closed, and the inductance and capacitance constitute a vibration circuit. After half an oscillation cycle, the switch automatically opens, and the output voltage V_P turns over. When the output voltage is reversed and keeps synchronous with the vibration speed, V_P will increase to $-V_s$. After that, the voltage reversal process will be repeated periodically. The conversion efficiency of the parallel synchronous switch interface circuit is closely related to the load, and there is an optimal load to maximize the conversion efficiency. Through numerical calculation, the optimal load of the system is $180\text{ K } \Omega$.

5 Conclusions

By changing the shape of the windward side of the square cylinder, not only the critical velocity of the cylinder galloping but also the amplitude of the cylinder vibration can be changed. When the sharp angle of the windward side is around 45° , the falling-off speed of the vortex will accelerate the pressure difference of the cylinder in the direction perpendicular to the incoming flow, and the increase of the pressure difference will increase the lift coefficient of the cylinder and the amplitude of the cylinder. More electric energy is collected in the same environment. This study provides a new idea and a more concise analysis method for the study of wind-induced vibration energy harvester.

The use of optimized piezoelectric cantilever beam can effectively improve the efficiency of electromechanical conversion, reduce the deformation fatigue at the root of the cantilever beam, increase the life of piezoelectric materials, and increase the deformation at the end of the cantilever beam, so that the system can generate greater voltage.

References

1. J. Wang, L. Geng, L. Ding, H. Zhu, D. Yurchenko, The state-of-the-art review on energy harvesting from flow-induced vibrations. *Appl. Energy* **267**, 114902 (2020)
2. L. Ding, L. Zhang, C. Wu, X. Mao, D. Jiang, Flow induced motion and energy harvesting of bluff bodies with different cross sections. *Energy Convers. Manag.* **91**, 416–426 (2015)
3. C.-C. Chang, R. Ajith Kumar, M.M. Bernitsas, Viv and galloping of single circular cylinder with surface roughness at $3.0 \times 10^4 \leq re \leq 1.2 \times 10^5$. *Ocean Eng.* **38**(16), 1713–1732 (2011)
4. H. Abdelmoula, A. Abdelkefi, Investigations on the presence of electrical frequency on the characteristics of energy harvesters under base and galloping excitations. *Nonlinear Dyn.* **89**(4), 2461–2479 (2017)
5. L. Zhao, Synchronization extension using a bistable galloping oscillator for enhanced power generation from concurrent wind and base vibration. *Appl. Phys. Lett.* **116**(5), 053904 (2020)
6. H.-X. Zou, L.-C. Zhao, Q.-H. Gao, L. Zuo, F.-R. Liu, T. Tan, K.-X. Wei, W.-M. Zhang, Mechanical modulations for enhancing energy harvesting: Principles, methods and applications. *Appl. Energy* **255**, 113871 (2019)
7. M. Zhang, G. Zhao, J. Wang, Study on fluid-induced vibration power harvesting of square columns under different attack angles. *Geofluids* **2017**, 1–18 (2017)
8. J. Wang, G. Hu, Z. Su, G. Li, W. Zhao, L. Tang, L. Zhao, A cross-coupled dual-beam for multi-directional energy harvesting from vortex induced vibrations. *Smart Mater. Struct.* **28**(12), 12LT02 (2019)
9. H. Abdelmoula, A. Abdelkefi, The potential of electrical impedance on the performance of galloping systems for energy harvesting and control applications. *J. Sound Vib.* **370**, 191–208 (2016)
10. C. Wei, X. Jing, A comprehensive review on vibration energy harvesting: Modelling and realization. *Renew. Sust. Energ. Rev.* **74**, 1–18 (2017)

11. R. Nowak, M. Pietrzakowski, P. Rumianek, Influence of design parameters on bending piezoelectric harvester effectiveness: Static approach. *Mech. Syst. Signal Process.* **143**, 106833 (2020)
12. R. Naseer, H. Dai, A. Abdelkefi, L. Wang, Comparative study of piezoelectric vortex-induced vibration-based energy harvesters with multi-stability characteristics. *Energies* **13**(1), 71 (2019)

Nonlinear Resonator-Based Metastructures for Vibration Attenuation and Energy Harvesting



P. V. Malaji, T. Mukhopadhyay, and S. S. Chappar

1 Introduction

Mitigation of vibration is a serious concern for most of the practical applications across different disciplines. For example, machines are subjected to huge dynamic loading during operation. Tall buildings and bridges are subjected to the large amplitude of vibration due to wind, earthquake, water waves, and traffic motions. Keeping structures safe and improving durability are crucial to economic progress and sustainability [1]. Application of vibration absorbers or tuned mass dampers is the conventional method for suppressing vibrations. These absorbers are tuned to the frequency of a structure where the structure is under a high level of vibrations. Such absorbers can considerably minimize the vibrations at that frequency. This approach of vibration mitigation has multiple limitations such as these absorbers would add mass up to 30% to the host structure and are effective only at frequency they have been tuned. Though nonlinear energy sinks use relatively smaller masses compared to vibration absorbers and cover a wider range of frequencies for vibration mitigation [2, 3], such systems do not perform adequately for sophisticated lightweight structural systems.

Artificial materials such as metamaterials/metastructures exhibit unique properties such as negative stiffness, negative density, and negative modulus. Bandgap enhancement and control is one of the attractive applications of the metastructure [4]. Bandgap is the ability to restrict the wave transmission over a specified

P. V. Malaji (✉) · S. S. Chappar

Vibration, Energy Harvesting and IoT Lab, BLDEA's V P Dr. P G Halakatti College of Engineering and Technology, Vijayapur, Karnataka, India
e-mail: pradeepmalaji@bldeacet.ac.in

T. Mukhopadhyay

Department of Aerospace Engineering, IIT Kanpur, Kanpur, Uttar Pradesh, India
e-mail: tanmoy@iitk.ac.in

frequency range. Within this bandgap, vibration attenuation of a primary structure can be attained. The metastructure for such applications consists of a number of small absorber unit cells, which allow distribution and integration of absorbers into the structure. With many absorbers in place, it gives the flexibility of tuning more parameters to attain the desirable bandgap [5].

Huang and Sun [6] proposed a two-resonator mass in mass lattice system with a multi-resonator acoustic metamaterial to attain multiple bandgaps. They reported that the major bandgap was created by the outer mass of the mass-in-mass lattice system, whereas the minor bandgap can be achieved by changing the inner mass-spring constants. A dual-resonator metamaterial design was proposed by Tan et al. [7] to optimize the bandgap. This dual-resonator design proved to have a wider bandgap and reduced vibration amplitude than that of the single-resonator design.

Most of the literature has considered linear local resonators. This results in limited attenuation bandgap which is controlled by added mass [5]. Nonlinear local resonators exhibit rich dynamics such as chaotic behavior and sub-harmonic and super-harmonic resonances. Yiwei et al. [8] investigated metastructure with nonlinear local resonators to enhance amplitude-dependent frequency bandwidth both numerically and experimentally. They demonstrated that bandgap offered by nonlinear attachments is significantly higher than the corresponding linear resonators. Similarly, Mohammad and Oumar [9] investigated the nonlinear metamaterials with nonlinear chains along with multiple nonlinear local resonators to understand spectro-spatial properties of wave propagation. They used numerical results to validate analytical results. Similarly way, various researches have been conducted on metamaterials regarding bandgap enhancement for vibration suppression.

An interesting aspect is that the metastructures for vibration mitigation can be simultaneously used for energy harvesting to power the necessary sensors for health monitoring and low-powered autonomous devices, essentially replacing conventional batteries. Energy harvesting has potential applications in the fields of industrial automation, structural monitoring, and medical implants. The objective is to harvest energy from the ambient environment and serve as the power source for wireless electronic devices instead of conventional batteries [10, 11]. Metamaterials have shown promising applications in energy harvesting. Carrara et al. [12] used three concepts: wave focusing, energy localization, and waveguiding to develop metamaterial for energy harvesting. The wave energy is converted into electrical energy by coupling the metamaterial and electroelastic domains. Shen et al. [13] used an array of spiral beams to design a phononic crystal plate for energy harvesting. They reported enhanced energy output at a dozen of resonant frequencies. An energy harvesting system using a series of spring loaded magnets was proposed by Mikoshiba et al. [14]. The magnet oscillation inside the fixed coils induced the current over a broad frequency range. Ahmed et al. [15] proposed AEMM-based energy harvester, which served the dual purpose of wave filtering and energy harvesting.

Many of the literatures have studied metastructures with repeated similar nonlinear resonators for vibration attenuation and energy harvesting. In this chapter, we consider resonators with spring softening and spring hardening effect with

different linear natural frequencies to understand its effect on vibration attenuation and energy harvesting. The chapter is organized as follows: Sect. 2 presents the model description and electromechanical equations. Section 3 presents numerically simulated results for various parameters. A brief discussion of the work along with conclusions of the work is provided in Sect. 4.

2 System Model

Schematic of a harmonically excited metastructure with nonlinear resonators is shown in Fig. 1. The primary system is considered as a chain of linear spring (k_1), damper (c_1), and mass (m_1) system. Each main mass (m_1) consists of local nonlinear resonator with nonlinear spring (with linear stiffness k_{li} and nonlinear cubic stiffness k_{ni}), damping (c_2), and mass (m_2). These resonators are attached with a piezoelectric patch for energy harvesting with electromechanical coupling coefficient θ , capacitance C , and resistance R . The system is subjected to harmonic base excitation $x_g \cos(\omega t)$ of amplitude x_g . The electromechanical equations of the system are given as

$$\begin{aligned}
 m_1 \ddot{x}_{1i} + c_1(-\dot{x}_{1(i-1)} + 2\dot{x}_{1i} - \dot{x}_{1(i+1)}) + c_2(\dot{x}_{1i} - \dot{x}_{2i}) + k_1(-x_{1(i-1)} + \\
 2x_{1i} - x_{1(i+1)}) + k_{li}(x_{1i} - x_{2i}) + k_{ni}(x_{1i} - x_{2i})^3 = -m_1 \ddot{x}_g \\
 m_n \ddot{x}_{1n} + c_1(-\dot{x}_{1(n-1)} + \dot{x}_{1n}) + c_2(\dot{x}_{1n} - \dot{x}_{2n}) + k_n(-x_{1n} - 1 + x_{1n}) + \\
 k_{ln}(x_{1n} - x_{2n}) + k_{nn}(x_{1n} - x_{2n})^3 = -m_1 \ddot{x}_g \tag{1} \\
 m_2 \ddot{x}_{2i} + c_2(\dot{x}_{2i} - \dot{x}_{1i}) + k_{li}(x_{2i} - x_{1i}) + k_{ni}(x_{2i} - x_{1i})^3 + \theta v_i = -m_2 \ddot{x}_g \\
 \frac{V_i}{R} + C \dot{v}_i + \theta(x_{2i} - x_{1i}) = 0
 \end{aligned}$$

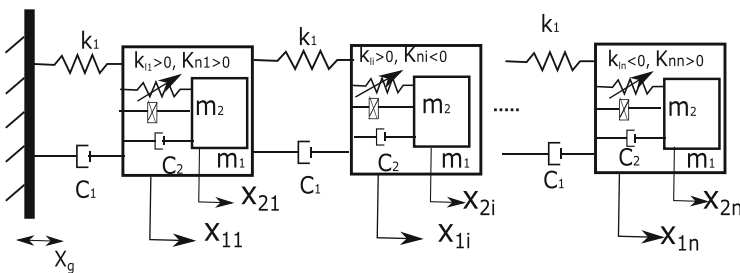


Fig. 1 Schematic representation of metastructure model

The value of nonlinear cubic stiffness can be changed to get spring hardening ($k_{li} > 0$) and spring softening ($k_{li} < 0$) effect. The nondimensional form of the above electromechanical equations is given as

$$\begin{aligned}
& X''_{1i} + \zeta_1(-X'_{1(i-1)} + 2X'_{1i} - X'_{1(i+1)}) + \zeta_2\Gamma_{li}\mu(X'_{1i} - X'_{2i}) + (-X_{1(i-1)} + \\
& 2X_{1i} - X_{1(i+1)}) + \Gamma_{li}^2\mu(X_{1i} - X_{2i}) + \lambda_{ni}\Gamma_{li}^2\mu(X_{1i} - X_{2i})^3 = \Omega^2 X_g \cos(\omega\tau) \\
& X''_{1n} + \zeta_1(-X'_{1(n-1)} + X'_{1n}) + c_2\zeta_2\Gamma_{ln}\mu(X'_{1n} - X'_{2n}) + (-X_{1n} - 1 + X_{1n}) + \\
& \Gamma_{ln}^2\mu(X_{1n} - X_{2n}) + \lambda_{nn}\Gamma_{ln}^2\mu(X_{1n} - X_{2n})^3 = \Omega^2 X_g \cos(\omega\tau) \\
& X''_{2i} + \zeta_2\Gamma_{li}(X'_{2i} - X'_{1i}) + \Gamma_{li}^2(X_{2i} - X_{1i}) + \lambda_{ni}\Gamma_{li}^2(X_{2i} - X_{1i})^3 \\
& + \Gamma_{li}^2\beta V_i = \Omega^2 f \cos(\omega\tau) \\
& V'_i + \eta V_i + \kappa(X'_{2i} - X'_{1i}) = 0
\end{aligned} \tag{2}$$

The nondimensional parameters used are $\zeta_1 = \frac{c_1}{m_1\omega_1}$, $\zeta_2 = \frac{c_2}{m_2\omega_{2i}}$, $\Gamma_{li} = \frac{\omega_{2i}}{\omega_1}$, $\lambda = \frac{k_{li}}{k_{ni}}$, $\mu = \frac{m_2}{m_1}$, $\Omega = \frac{\omega}{\omega_1}$, $\omega_1 = \sqrt{\frac{k_1}{m}}$, $\beta = \frac{\theta}{k_{li}}$, $\eta = \frac{1}{CR\omega_{2i}}$, $\kappa = \frac{\theta}{C}$, and $X_g = \frac{x_g}{l}$. $\tau = \omega_1 t$ is the nondimensional time.

Equations (2) will be solved numerically using the Runge–Kutta method and results are presented in the next section.

3 Results and Discussion

This section presents the numerical results for two unit cell (four degrees of freedom) system to show the influence of parameters on the amplitude of the primary system and the energy harvested by resonators. The simulation is considered for 1000 time length; first 75% of them were eliminated to count transient time. The following parameters were used unless otherwise mentioned; $X_g = 0.1$, $\zeta_1 = 0.03$, $\zeta_2 = 0.1$, $\mu = 0.2$, $\eta = 1$, and $\beta = \kappa = 0.05$. A forward frequency sweep is considered for the frequency response analysis of the system over the nondimensional frequency range of $0.2 < \Omega < 2$.

3.1 Effect of Nonlinear Stiffness Coefficient λ

Nondimensional numerical results of frequency RMS response for the second mass and the total RMS voltage generated (open circuit) are presented in Fig. 2a, b, respectively. The response ratio X/X_g represents transmissibility (the ratio of steady state response of end mass to base excitation amplitude). The plain beam refers to the primary system without the resonators. The first mode of the plain beam is

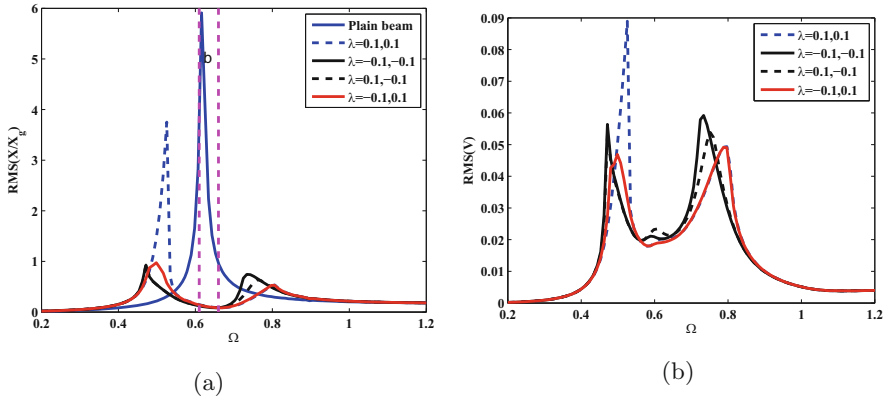


Fig. 2 (a) Primary system response of second mass and (b) total voltage generated by resonators, with $\Gamma_{11} = \Gamma_{12} = 0.61$

identified to be at $\Omega = 0.61$, and this will be the target mode to be attenuated. The region between two dotted lines shows the theoretical linear bandgap for metamaterial given by $\Omega_t < \Omega < \Omega_t \sqrt{1 + \mu}$ [16]. With the addition of nonlinear resonators the target mode of the plain beam is attenuated. An additional resonances around the target mode is observed. An enhancement in bandgap can be observed with a hardening effect in both the resonators ($\lambda_1 = \lambda_2 = 0.1$) with a higher peak at the lower frequency as shown in Fig. 2a. Spring softening effect ($\lambda_1 = \lambda_2 = -0.1$) in both the resonators shows frequency response similar to the fixed point method of linear absorber explained by Den Hartog [17]. The softening effect has shown more promising effects compared to the hardening effect on attenuation. Many of the literatures on metastructures have considered repeated unit cells (similar resonators as explained above), in order to check the robustness of metastructure with different unit cells (functionally graded metastructure), both softening ($\lambda = -0.1$) and hardening ($\lambda = 0.1$) spring effects are considered. This mixed hardening and softening have shown promising effects on attenuation and bandgap. Around 200% enhancement in bandgap with mixed effect can be obtained compared to linear bandgap.

Simultaneous energy harvesting from resonators was the secondary function of the metastructure, and the effect of nonlinear stiffness on the voltage generated is shown in Fig. 2b. Hardening spring configuration has a higher magnitude voltage compared to other configurations. The bandwidth at $V = 0.02$ of all configurations is nearly the same. With the primary objective being attenuation mixed configuration is preferred over others. The effect of other parameters on this mixed configuration is presented in the next subsections.

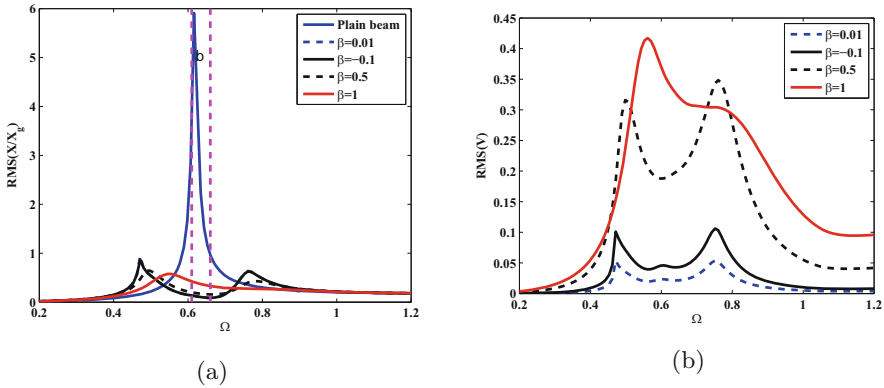


Fig. 3 (a) Primary system response and (b) total voltage generated by resonators, with $\Gamma_{11} = \Gamma_{12} = 0.61$, $\lambda_1 = 0.1$, and $\lambda_2 = -0.1$

3.2 Effect of Coupling Coefficient β

The frequency response of the primary system and the voltage for different values of coupling coefficient β are shown in Fig. 3a, b. From the frequency response plot, it is observed that the amplitude of the primary system decreases by a small amount with the increase in coupling coefficient as shown in Fig. 3a. This is due to the added damping to the system due to coupling. A large increment in the voltage generated with the increase in coupling coefficient can be observed in Fig. 3b.

3.3 Effect of Excitation Amplitude X_g

The frequency response of the primary system and the voltage for a higher value of excitation amplitudes X_g are shown in Fig. 4a, b. From the frequency response plot, it is observed that with the increase in excitation amplitude, the nonlinear resonators can enhance bandgap at target frequency although the peak at lower frequency is a bit higher. This shows the robustness of nonlinear resonators against excitation amplitude as shown in Fig. 4a. With the increase in excitation amplitude, the voltage generated increases as expected with clear jump phenomenon appearing as shown in Fig. 4b.

3.4 Effect of Linear Stiffness Coefficient of Resonator Γ

The frequency response of the primary system and the voltage with different values of linear stiffness coefficient (linear resonance of nonlinear resonators) Γ are shown

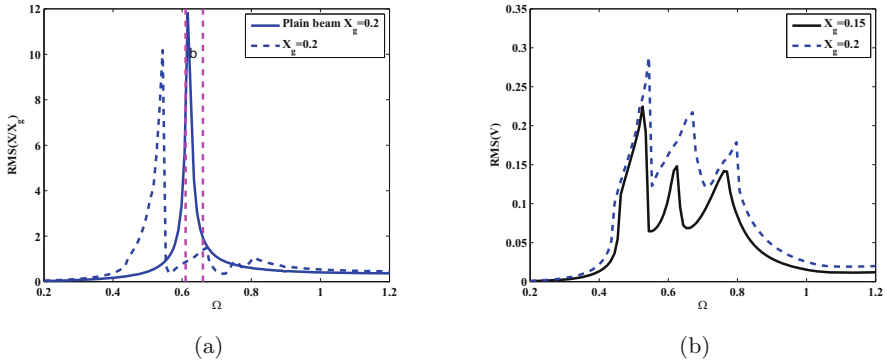


Fig. 4 (a) Primary system response and (b) total voltage generated by resonators, with $\Gamma_{11} = \Gamma_{12} = 0.61, \lambda_1 = 0.1, \lambda_2 = -0.1,$ and $\beta = 0.1$

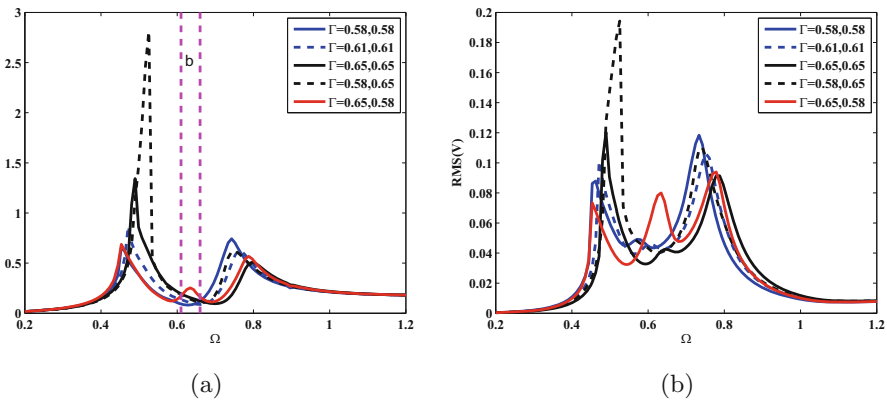


Fig. 5 (a) Primary system response and (b) total voltage generated by resonators, with $\lambda_1 = 0.1, \lambda_2 = -0.1, \beta = 0.1,$ and $X|_g = 0.1$

in Fig. 5a, b. From the frequency response plot, it is observed that the higher bandgap is obtained with the $\Gamma = 0.65, 0.58$ for resonator 1 and 2 respectively. This also gives rise to an extra peak at target frequency as shown in Fig. 5a. This extra peak can also be observed in the voltage frequency response plot with compromise in voltage amplitude as shown in Fig. 5b.

4 Summary and Conclusions

A metastructure with nonlinear resonators is analyzed parametrically to attenuate the primary structure and harvest energy simultaneously in this chapter. A primary structure with n masses and resonators is considered. Parameters like nonlinear stiffness, linear stiffness, excitation, and coupling coefficient are considered for

the study. A different combination of parameters representing functionally graded metastructure is reported.

In conclusion, the frequency bandgap with nonlinear resonator metastructures is enhanced when the optimal combination of different parameters is used (functionally graded metastructure). Purely spring hardening resonators are found to be less effective. Optimal values to obtain a higher bandgap of primary structure and a higher bandwidth for voltage generated are to be considered in the future study. The results presented here are the initial analysis of a bigger problem. In the future analysis, a higher number of masses and optimal combination of parameters will be considered.

Acknowledgments P V Malaji acknowledges Vision Group on Science and Technology (VGST), Government of Karnataka (grant no. KSTePS/VGST-K-FIST L2/GRD No.765) for supporting the research.

References

1. S.F. Ali, A. Ramaswamy, Optimal dynamic inversion-based semi-active control of benchmark bridge using MR dampers. *Struct. Control. Health Monit.* **16**(5), 564–585 (2009)
2. A.F. Vakakis, O.V. Gendelman, L.A. Bergman, M. McFarland, G. Kerschen, Y.S. Lee, *Nonlinear Targeted Energy Transfer in Mechanical and Structural Systems*, vol. 156 (Springer, Dordrecht, 2009)
3. P.V. Malaji, M. Rajarathinam, V. Jaiswal, S.F. Ali, I.M. Howard, *Energy Harvesting from Dynamic Vibration Pendulum Absorber*. Recent Advances in Structural Engineering, vol. 2 (Springer, Singapore, 2019), pp. 467–478
4. G. Hu, L. Tang, A. Banerjee, R. Das, Metastructure with piezoelectric element for simultaneous vibration suppression and energy harvesting. *J. Vib. Acoust.* **139**(1) (2016)
5. R. Zhu, X.N. Liu, G.K. Hu, C.T. Sun, G.L. Huang, A chiral elastic metamaterial beam for broadband vibration suppression. *J. Sound Vib.* **333**(10), 2759–2773 (2014)
6. H.H. Huang, C.T. Sun, Wave attenuation mechanism in an acoustic metamaterial with negative effective mass density. *New J. Phys.* **11**(1), 013003 (2009)
7. K.T. Tan, H.H. Huang, C.T. Sun, Optimizing the band gap of effective mass negativity in acoustic metamaterials. *Appl. Phys. Lett.* **101**(24), 241902 (2012)
8. Y. Xia, M. Ruzzene, A. Erturk, Dramatic bandwidth enhancement in nonlinear metastructures via bistable attachments. *Appl. Phys. Lett.* **114**(9), 093501 (2019)
9. M. Bukhari, O. Barry, Spectro-spatial analyses of a nonlinear metamaterial with multiple nonlinear local resonators. *Nonlinear Dyn.* **99**, 1539–1560 (2020)
10. C. Williams, R. Yates, Analysis of a micro-electric generator for microsystems, in *Proceedings of the International Solid-State Sensors and Actuators Conference - Transducers*, vol. 1 (1995), pp. 8–11
11. P.V. Malaji, M.I. Friswell, S. Adhikari, G. Litak, Enhancement of harvesting capability of coupled nonlinear energy harvesters through high energy orbits. *AIP Adv.* **10**(8), 085315 (2020)
12. M. Carrara, M.R. Cacan, J. Toussaint, M.J. Leamy, M. Ruzzene, A. Erturk, Metamaterial-inspired structures and concepts for elastoacoustic wave energy harvesting. *Smart Mater. Struct.* **22**(6), 065004 (2013)

13. L. Shen, J.H. Wu, S. Zhang, Z. Liu, J. Li, Low-frequency vibration energy harvesting using a locally resonant phononic crystal plate with spiral beams. *Mod. Phys. Lett. B* **29**(01), 1450259 (2015)
14. K. Mikoshiba, J.M. Manimala, C.T. Sun, Energy harvesting using an array of multifunctional resonators. *J. Intell. Mater. Syst. Struct.* **24**(2), 168–179 (2013)
15. R.U. Ahmed, A. Adiba, S. Banerjee, Energy scavenging from acousto-elastic metamaterial using local resonance phenomenon, in *Active and Passive Smart Structures and Integrated Systems 2015*, vol. 9431 (International Society for Optics and Photonics, SPIE, Bellingham, 2015), pp. 45–54
16. C. Sugino, S. Leadenham, M. Ruzzene, A. Erturk, On the mechanism of bandgap formation in locally resonant finite elastic metamaterials. *J. Appl. Phys.* **120**(13), 134501 (2016)
17. J.P. Den Hartog, *Mechanical Vibrations* (McGraw Hill, New York, 1934)

Dynamic Modeling for a Mechatronic Energy Harvesting Shock Absorber



Jing Li, Lei Luo, Dong Guan, Hui Shen, and Junjie Gong

1 Introduction

Traveling on roads, vehicles are subjected to different disturbances such as road irregularities, braking force, acceleration forces, and centrifugal forces on a curved road. Those disturbances not only cause discomfort to the driver and passengers but also reduce the energy efficiency of vehicles. The shock absorber is widely used in vehicles, for vibration absorption and system stability [1]. The vibration energy dissipated by shock absorber is nearly 400 watts in the typical passenger vehicles traveling at 60 miles h^{-1} on good and average roads [2]. The energy efficiency can reach 2.5% by harvesting the vibration energy in shock absorber, which can not only improve fuel economy of petrol vehicles but also increase the range of electric vehicle [3]. Recently, energy harvesting shock absorbers, composed of transmission structure and electromagnetic generator, have been analyzed and tested to verify the capabilities of energy harvesting. There are several types of transmission structure which convert a translation into a rotation, such as hydraulic [3], rack and pinion [4, 5], ball screw [6, 7], multi-connecting rods [8, 9], and cable transmission [10]. In order to keep good contact with roads and reduce vibration to the vehicle body, the shock absorber with asymmetric damping coefficients is designed. By shunting the EHSA with different electric loads during the upward and downward stroke, Li et al. [5] presented the EHSA with asymmetric damping coefficients. Wang et al. [6] designed an EHSA with asymmetric transmission chain. Because of the different transmission paths in two strokes, this kind of EHSA has asymmetric damping coefficients. Although existing regenerative shock absorbers can provide the different damping coefficients in upward stroke and downward

J. Li (✉) · L. Luo · D. Guan · H. Shen · J. Gong
College of Mechanical Engineering, Yangzhou University, Yangzhou, Jiangsu, China
e-mail: yzlijing@yzu.edu.cn

stroke, the other dynamic performances of such EHSA still challenge researchers. This paper seeks to demonstrate an asymmetric characteristics of EHSA. For this, the EHSA with asymmetric transmission chain is designed; dynamic modeling of EHSA is established. This work focuses on the relationship between the asymmetric transmission chain and asymmetric characteristics of EHSA, in which a computational model is developed.

This paper is divided into four sections. The second section describes the structure of the EHSA, along with its lumped model and dynamic model carried out. The third section shows the force-displacement and the force-velocity loops of the EHSA, the variations of the equivalent stiffness and the equivalent damping coefficient in two strokes, and the output voltage of the EHSA in time domain. In Sect. 4, some conclusions have been given.

2 Modeling for EHSA

The structure of EHSA is shown in Fig. 1. It is mainly composed of generator, gearbox, coupling, rack and pinion, and overrun clutch. The rack and pinion converts a translation into a rotation. The overrun clutch keeps the unidirectional rotation. The coupling connects the overrun clutch with the gearbox. The gearbox is used to magnify the motion and reduce the torque. The electric generator will generate the electricity from the motion of the rotor.

By using the overrun clutch, the transmission paths in upward stroke and downward stroke are different. In order to analyze the transmission paths, a lumped EHSA transmission model is built and shown in Fig. 2. In the downward stroke, the displacement excitation drives the rack downward, which causes a counterclockwise

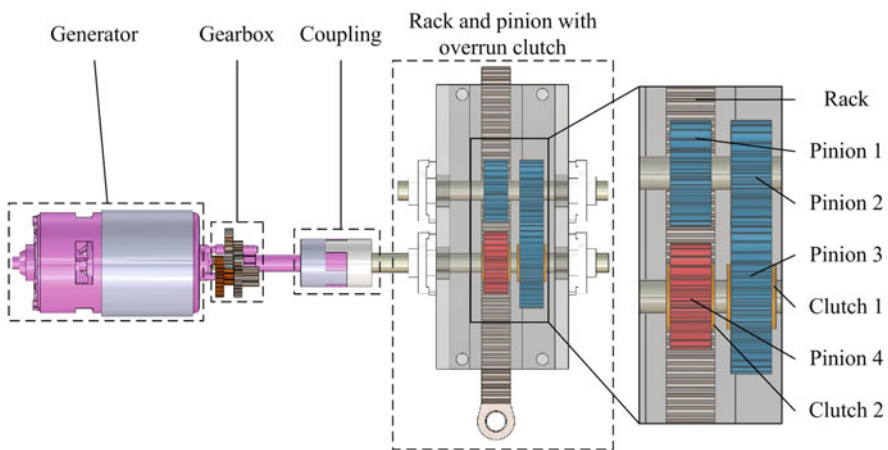


Fig. 1 Structure of EHSA

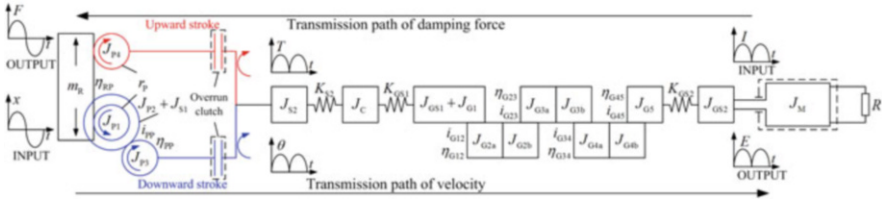


Fig. 2 Lumped model of EHSA

rotation (as viewed from left to right in Fig. 1) of the pinion 1, the pinion 2, and the pinion 4. Then, the pinion 3 rotates in clockwise direction. Thus, the overrun clutch 1 between the pinion 3 and the shaft will provide the actual torque and the velocity transmitted when the pinion 3 rotates clockwise, and the overrun clutch 2 between the pinion 4 and the shaft will be disengagement to keep the pinion 4 and the shaft in independent rotation. As a result, the torque and the velocity will be transmitted through the blue path as shown in Fig. 2. Conversely, in the upward stroke, the upward movement of the rack causes the clockwise rotation (as viewed from left to right in Fig. 1) of the pinion 1, the pinion 2, and the pinion 4. Therefore, the pinion 3 rotates counterclockwise, and the overrun clutch 1 is disengagement. The pinion 4 rotates clockwise and drives the shaft through the overrun clutch 2. As a result, the torque and the velocity will be transmitted through the red path as shown in Fig. 2.

In Fig. 2, m and J represent the mass and inertia of the corresponding components, respectively. η and i represent the transmission efficiency and transmission ratio of the EMSA, respectively. r_p is the radius of the pinion 1 and pinion 4. R is the effective resistance of load circuit. K is the stiffness of shafts. Considering that the output force induced by EHSA is usually in the range from 0 to 1000 N, which makes very small torsional deformation of shafts, the influence of the shafts' stiffness can be neglected. Due to the low-frequency small amplitude of applied vibration and small rotational inertia of moving parts, Sommerfeld effect phenomenon is ignored as well. Because of the high transmission efficiency of gear transmission, we assume that the transmission efficiency between gears is 0.99, and the transmission efficiency between rack and pinion is 0.95. Table 1 shows the parameters used in the model.

The vibration induced by the road irregularities can be equivalent to the sum of the simple harmonic oscillations. And the harmonic oscillations can be expressed as

$$\begin{cases} x = X_0 \cos(\omega t) \\ \dot{x} = -\omega X_0 \sin(\omega t) \\ \ddot{x} = -\omega^2 X_0 \cos(\omega t) \end{cases} \quad (1)$$

where x , \dot{x} , and \ddot{x} are displacement, velocity, and acceleration, respectively. ω represents angular velocity, $\omega = 2\pi f$. X_0 , ωX_0 , and $-\omega^2 X_0$ denote the amplitude of displacement, velocity, and acceleration, respectively.

Table 1 Key parameters used in the model

Symbol	Name	Value
m_{P0}	Rack	0.491 kg
J_{P1}	Pinion 1	$3.140e-6 \text{ kg}\cdot\text{m}^2$
J_{P2}	Pinion 2	$7.066e-6 \text{ kg}\cdot\text{m}^2$
J_{P3}	Pinion 3	$3.140e-6 \text{ kg}\cdot\text{m}^2$
J_{P4}	Pinion 4	$3.140e-6 \text{ kg}\cdot\text{m}^2$
J_{S1}	Pinion shaft 1	$0.279e-6 \text{ kg}\cdot\text{m}^2$
J_{S2}	Pinion shaft 2	$0.420e-6 \text{ kg}\cdot\text{m}^2$
J_C	Coupling	$3.106e-6 \text{ kg}\cdot\text{m}^2$
J_M	Rotor in motor	$11.212e-6 \text{ kg}\cdot\text{m}^2$
J_{G1}	Gear 1	$0.105e-6 \text{ kg}\cdot\text{m}^2$
$J_{G2a} + J_{G2b}$	Gear 2	$0.185e-6 \text{ kg}\cdot\text{m}^2$
$J_{G3a} + J_{G3b}$	Gear 3	$0.149e-6 \text{ kg}\cdot\text{m}^2$
$J_{G4a} + J_{G4b}$	Gear 4	$0.148e-6 \text{ kg}\cdot\text{m}^2$
J_{G5}	Gear 5	$7.066e-6 \text{ kg}\cdot\text{m}^2$
J_{GS1}	Gear shaft 1	$0.064e-6 \text{ kg}\cdot\text{m}^2$
J_{GS2}	Gear shaft 2	$0.147e-6 \text{ kg}\cdot\text{m}^2$
r_P	Pinion 1 and pinion 4	12 mm
i_P	Pinion 2 to pinion 3	1.5
i_{G12}	Gear 1 to gear 2	1.9
i_{G23}	Gear 2 to gear 3	2.7
i_{G34}	Gear 3 to gear 4	2.7
i_{G45}	Gear 4 to gear 5	3.2
R	Resistance	1.5Ω

As analyzed before, the transmission chain changes with the direction of rack movement. In the upward stroke, the output force F_U can be expressed as

$$F_U = \left(m_R + \frac{J_{URP}}{\eta_{RP} r_P^2} \right) \ddot{x} + \frac{T_C}{\eta_{RP} r_P} \quad (2)$$

where T_C is the torque from the coupling, J_{URP} denotes the total inertial of the shafts and the pinions in the upward stroke, and J_{URP} can be calculated by

$$J_{URP} = J_{P1} + J_{P2} + J_{P4} + J_{S1} + J_{S2} + \frac{J_{P3}}{\eta_{PP} i_P^2} \quad (3)$$

Similarly, the output force F_D in the downward stroke can be expressed as

$$F_D = \left(m_R + \frac{J_{DRP}}{\eta_{RP} r_P^2} \right) \ddot{x} + \frac{T_C}{\eta_{RP} \eta_{PP} r_P i_P} \quad (4)$$

where J_{DRP} denotes the total inertial of the shafts and the pinions in the downward stroke, and it can be calculated by

$$J_{DRP} = J_{P1} + J_{P2} + J_{P4} + J_{S1} + \frac{J_{P3} + J_{S2}}{\eta_{PP} i_P^2} \quad (5)$$

The transmission chain after the overrun clutch is unchanged in both stroke. Thus, the torque T_C can be calculated by

$$\begin{pmatrix} \alpha_C \\ T_C \end{pmatrix} = \begin{pmatrix} \frac{i_{Gearbox}}{J_{CGM}} & 0 \\ \frac{1}{\eta_{Gearbox} i_{Gearbox}} & \frac{1}{\eta_{Gearbox} i_{Gearbox}} \end{pmatrix} \begin{pmatrix} \alpha_M \\ T_M \end{pmatrix} \quad (6)$$

where J_{CGM} denotes the total inertial of the coupling, the gearbox, and the rotor in the motor. α_C and α_M denote the angular acceleration of the coupling and the rotor, respectively. $\eta_{Gearbox}$ and $i_{Gearbox}$ denote the total transmission efficiency and the transmission ratio in the gearbox, respectively. T_M represents the torque which is produced by the motor, and it can be calculated by

$$T_M = k_t I \quad (7)$$

where k_t is the torque constant, and it equals to 0.044. I is the electric current. Based on Ohm's law, we can get

$$I = \frac{E}{R} \quad (8)$$

where E is the back electromotive force voltage, and it can be written as

$$E = k_e \dot{\theta}_M \quad (9)$$

where k_e is the back electromotive voltage constant, and it equals to 0.045. $\dot{\theta}_M$ is the angular velocity of the rotor, and it is determined by the transmission ratio and the velocity of the rack. Substitution of Eqs. (1), (3), and (5)–(9) into Eqs. (2) and (4), the output force of the EHSA in two strokes can be obtained:

$$\begin{cases} F_U = M_U \ddot{x} + \frac{k_e k_t}{\eta_U i_U^2 R} \dot{x} \\ F_D = M_D \ddot{x} + \frac{k_e k_t}{\eta_D i_D^2 R} \dot{x} \end{cases} \quad (10)$$

where M represents the effective inertial mass of the EHSA and η and i are the total transmission efficiency and the ratio of the transmission chain, respectively. The subscripts U and D denote the parameters in the upward stroke and the downward stroke, respectively. From Eq. (10), we can find that the output force consists of two parts: one is the inertial force and the other is the damping force. The inertial force depends on the effective inertial mass. And the electromagnetic damping

force is affected by the transmission efficiency η , the transmission ratio i , the back electromotive voltage constant k_e , the torque constant k_t , and the effective resistance of load circuit R .

3 Results and Discussion

Figure 3 shows the force-displacement loops and the force-velocity loops under the harmonic vibration, respectively. The frequency and the amplitude of this vibration are 0.5 Hz and 10 mm, respectively. From Fig. 3a, we can find that the curve of the damping force is the ellipse which is symmetric around the Y-axis and asymmetric around the X-axis. The maximum and the minimum of the damping force are 223 N and -94 N, respectively. And both of them are at zero point of displacement. The curve of the inertial force is the broken line which passes through the origin twice. Under the combination of the damping force and the inertial force, the curve of the output force is elliptic and deflects in a clockwise direction. From Fig. 3b, we can find that the curve of the inertial force is the ellipse which is symmetric around the X-axis and asymmetric around Y-axis, and the right half of the curve is larger than the left half. The curve of the damping force consists of two lines with different slopes. The sum of the damping force and the inertial force gives the output force. Thus, the shape and the position of the output force curve are determined by the inertial force and the damping force.

By comparing Fig. 3a, b, we can find that the curve of the inertial force in Fig. 3a and the curve of the damping force in Fig. 3b are both lines, which means the inertial force and the damping force are linearly related to the displacement and the velocity, respectively. The relationship between the inertial force and the displacement can be expressed as the equivalent stiffness, and the relationship between the damping force

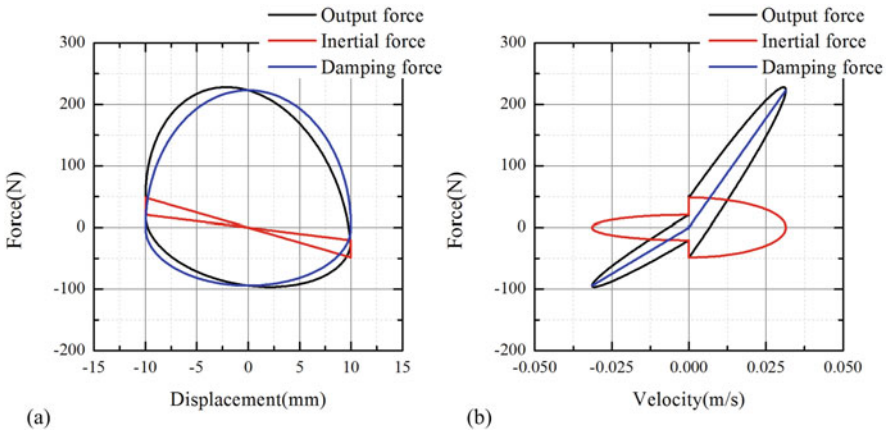


Fig. 3 Force-displacement loops (a) and force-velocity loops (b) of EHSA

and the velocity can be expressed as the equivalent damping coefficient. Therefore, in order to investigate the dynamic performance of the EHSA in depth, the equivalent stiffness and the damping coefficient are calculated by using the force-displacement and the force-velocity results, respectively. The equivalent stiffness and the damping coefficient can be expressed as follows [4]:

$$\begin{cases} k = \frac{F_{inertial}}{x} \\ c = \frac{F_{damping}}{\dot{x}} \end{cases} \tag{11}$$

Substitute the data of Fig. 3 into Eq. (11), the variations of the equivalent stiffness and the equivalent damping coefficient at time domain can be obtained. Moreover, substitute the Eq. (10) into Eq. (11); the relationship between the parameters of the structure and the equivalent parameters can be obtained, as shown in Eq. (12):

$$\begin{cases} k_{eff} = -\omega^2 M_S \\ c_{eff} = \frac{k_e k_t}{\eta s i_s^2 R} \end{cases} \tag{12}$$

From Eq. (12), we can find that the equivalent stiffness is determined by the angular frequency and the effective inertial mass of the transmission chain, and the equivalent damping coefficient is determined by the transmission efficiency, the transmission ratio, and the resistance of the load circuit.

Figure 4a shows the variations of the equivalent stiffness at time domain, under three different frequencies of 0.25 Hz, 0.5 Hz, and 1 Hz. The amplitude of those applied vibrations are 10 mm, and the resistance of the load circuit is 10 Ω. In Fig. 4a, we can find that the equivalent stiffness curves at time domain are almost square wave, where the high level of each curve is the equivalent stiffness in the

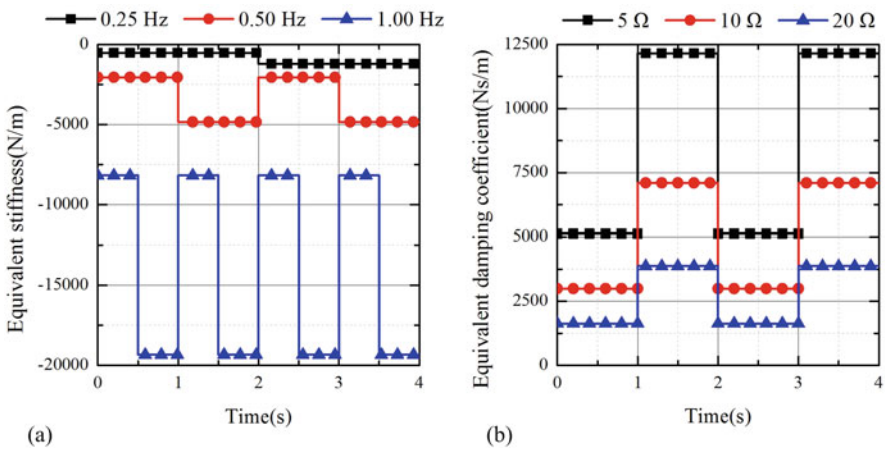


Fig. 4 Equivalent stiffness (a) and equivalent damping coefficient (b) at time domain

downward stroke and the low level of each curve is the equivalent stiffness in the upward stroke. And the high level and the low level both decrease with the increase of frequency. To observe Eqs. (3) and (5), we can find that the inertia is related to the square of transmission ratio i_p . Therefore, the ratio of the high level to the low level in different excitation frequencies is 2.36, which is very similar to the square of transmission ratio i_p . Figure 4b shows the variations of the equivalent damping coefficient at time domain, under three different resistances of 5 Ω , 10 Ω , and 20 Ω . The frequency and the amplitude of the applied vibration are 0.5 Hz and 10 mm, respectively. In Fig. 4b, we can find that the equivalent damping coefficient curves at time domain are also square wave. However, the high level of each curve is the equivalent damping coefficient in the upward stroke, and the low level of each curve is the equivalent damping coefficient in the downward stroke. The high level and the low level both decrease with the increase of resistance. The ratio of the high level to the low level in different resistances is 2.37, which is also very similar to the square of transmission ratio i_p . This can be explained by using Eq. (12), where we can find the square of transmission ratio i_p in the denominator.

Figure 5 shows the variations of the output voltage at time domain. The resistance in the load circuit is 10 Ω . The amplitude of the applied harmonic vibration in Fig. 5a is 10 mm. The frequency of the applied harmonic vibration in Fig. 5b is 0.5 Hz. To observe Fig. 5, we can find that the shape of the output voltage is the rectified sine curve where the two adjacent amplitudes are different. This can be explained by using the overrun clutch and the transmission path. Due to the use of the overrun clutch, the reciprocating motion of the rack is converted to the unidirectional rotation of the rotor in motor. Thus, the output voltage is positive, while the harmonic vibration excites the EHSA. Because of the different transmission paths in the upward stroke and the downward stroke, the transmission ratio in the upward stroke is larger than that in the downward stroke. Therefore, the

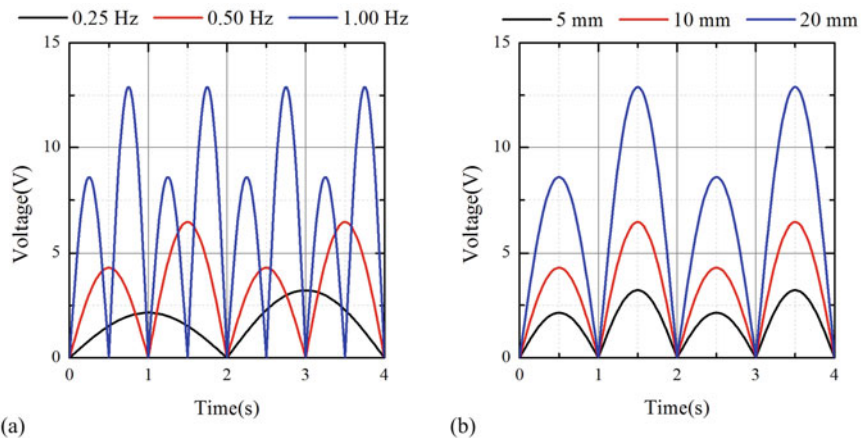


Fig. 5 Effect of frequency (a) and amplitude (b) on output voltage at time domain

angular velocity in the downward stroke is smaller than that in the upward stroke. Thus, the output voltages in those two strokes are different. The ratio between the peak values in those two strokes is 1.5, which equals to the transmission ratio i_p . To compare the different curves in Fig. 5a, b, we can find that the output voltage increases with the frequency and the amplitude of applied vibration.

4 Conclusions

In this paper, The EHSA with asymmetric performance is presented, and the lumped model and the dynamic model of the EHSA are presented and analyzed. The results show that the transmission paths in the upward stroke and the downward stroke are different because of the use of the overrun clutch and the rack and pinion. The output force of the EHSA is composed of the inertial force and the damping force, where the inertial force and the damping force can be converted into the equivalent stiffness and the equivalent damping coefficient. The shapes of the equivalent stiffness and the equivalent damping coefficient in time domain are the square wave. And the ratio between the high level and the low level in this square wave equals to the square of transmission ratio i_p . The output voltage at time domain is the rectified sine curve in which two adjacent amplitudes are different. And the ratio between two adjacent amplitudes equals to the transmission ratio i_p .

Acknowledgments This work was supported by the financial support of National Natural Science Foundation of China (grant no. 52005433), Jiangsu Province Natural Science Foundation (no. 20180933), Natural Science Foundation of Jiangsu Higher Institutions (no. 20KJB460001 and no. 19KJB460028), Special Cooperation Foundation for Yangzhou & YZU (no. 2020182), and Qing Lan Project from Yangzhou University. Thanks for the suggestions from the reviewers to help us in improving the paper in depth.

References

1. D. Guan, X. Jing, H. Shen, L. Jing, J. Gong, Test and simulation the failure characteristics of twin tube shock absorber. *Mech. Syst. Signal Process.* **122**, 707–719 (2019)
2. L. Zuo, P. Zhang, Energy harvesting, ride comfort, and road handling of regenerative vehicle suspensions. *J. Vib. Acoust.* **135**(1), 011002 (2013)
3. S. Guo, L. Xu, Y. Liu, X. Guo, L. Zuo, Modeling and experiments of a hydraulic electromagnetic energy-harvesting shock absorber. *IEEE-ASME Trans. Mechatron.* **22**(6), 2684–2694 (2017)
4. Z. Li, L. Zuo, G. Luhrs, L. Lin, Y. Qin, Electromagnetic energy-harvesting shock absorbers: design, modelling, and road tests. *IEEE Trans. Veh. Technol.* **62**(3), 1065–1074 (2013)
5. Z. Li, L. Zuo, J. Kuang, G. Luhrs, Energy-harvesting shock absorber with a mechanical motion rectifier. *Smart Mater. Struct.* **22**, 025008 (2013)
6. Z. Wang, T. Zhang, Z. Zhang, Y. Yuan, Y. Liu, A high-efficiency regenerative shock absorber considering twin ball screws transmissions for application in range-extended electric vehicles. *Energy Built Environ.* **1**, 36–49 (2020)

7. S. Li, J. Xu, X. Pu, T. Tao, H. Gao, X. Mei, Energy-harvesting variable/constant damping suspension system with motor based electromagnetic damper. *Energy* **189**, 116199 (2019)
8. Q. Xie, T. Zhang, Y. Pan, Z. Zhang, Y. Yuan, Y. Liu, A novel oscillating buoy wave energy harvester based on a spatial double X-shaped mechanism for self-powered sensors in sea-crossing bridges. *Energy Convers. Manag.* **204**, 112286 (2020)
9. A. Maravandi, M. Moallem, Regenerative shock absorber using a two-leg motion conversion mechanism. *IEEE-ASME Trans. Mechatron.* **20**(6), 2853–2861 (2015)
10. L. Bowen, J. Vinolas, J.L. Olazagoitia, Design and potential power recovery of two types of energy harvesting shock absorbers. *Energies* **12**(24), 4710 (2019)

Bistable Electromagnetic Energy Harvesting Enhanced with a Resonant Circuit



Ning Yu, Chuanyu Wu, Gaohong Yu, and Bo Yan 

1 Introduction

Recently, energy harvesting is attractive for their good application potential in the field of powering the microelectronic components in the ambient environment of broad frequency range [1]. Electromagnetic vibration energy harvesting technology has the advantages of high efficiency, low cost, and strong durability. However, conventional electromagnetic energy harvesters are designed as linear resonant oscillators. The limited frequency range results linear energy harvester in a narrow effective working range [2]. In this case, nonlinearity has been proposed to fill this shortcoming.

Possessing the ability of tuning dynamic stiffness characteristic, nonlinear energy harvesting has attracted widely attentions. For the bistable energy harvesters (BEHs) under random base excitations, the dynamic response mechanism and enhanced energy harvesting were numerically and experimentally verified by Litak [3]. The tristable energy harvesters (TEHs) can be optimally designed so that it increases the frequency bandwidth and achieves a high energy harvesting efficiency at coherence resonance under a low-level excitation.

The previous scholars mainly concentrated on a pure external load resistance to harvest the ambient vibration. Yan et al. [4] analyzed the TEH with a series resistor-inductor (RL) resonant. The result shows the TEH with the RL circuit can greatly enhance energy harvesting efficiency. And it provides another method to improve the energy harvesting efficiency of nonlinear energy harvesters. Zhou et al. [5] made a further analysis for a TEH with the RL resonant circuit. It found the effect of the excitation amplitude and the electromechanical coupling coefficient

N. Yu · C. Wu · G. Yu · B. Yan (✉)

Faculty of Mechanical Engineering and Automation, Zhejiang Sci-Tech University, Hangzhou, China

e-mail: yanbo@zstu.edu.cn

on the energy harvesting performance. Chen et al. [6] used various values of inductance and excitation frequencies to calculate the output voltage of the unit cell. They found inserting an inductor parallel with the clamped capacitor of the piezoelectric patch can generate a new dispersion curve, enlarge the first-order bandgap, and decrease the frequency band region, which is more beneficial for low-frequency and broadband harvesting. Pei et al. [7] proposed two multi-resonant electromagnetic shunts, to effectively mitigate the vibration for the isolations, and simultaneously harvest the vibrational energy generated by the dampers. The practical tests validated the effectiveness of multi-resonant electromagnetic shunts in both vibration damping and energy harvesting.

This paper proposes the theoretical model and simulated investigation of a broadband vibration electromagnetic energy harvester with twin-well potential. The effects of various initial conditions and the resonant frequency of the circuit on the energy harvesting characteristics of the bistable energy harvester are discussed. The performance of the output voltage of the energy harvester with resonant circuit is compared to the one with pure resistance. It can be seen from Fig. 2 that the maximum output voltage of the harvester with resonant circuit is bigger than the conventional one. It demonstrates that the proposed harvester has a larger bandwidth for harvesting the high energy interwell oscillation.

2 Modeling of the Bistable Electromagnetic Energy Harvester (BEEH) with the Resonance Circuit

Figure 1 presents the schematic diagram of the proposed BEEH with the resonant circuit. A group of permanent magnets are used to build nonlinear force. The nonlinear restoring force can be simplified as $k_1z + k_3z^3$. This paper focuses on numerically exploring the influence mechanism of the resonant circuit on bistable energy harvesting via a basic model.

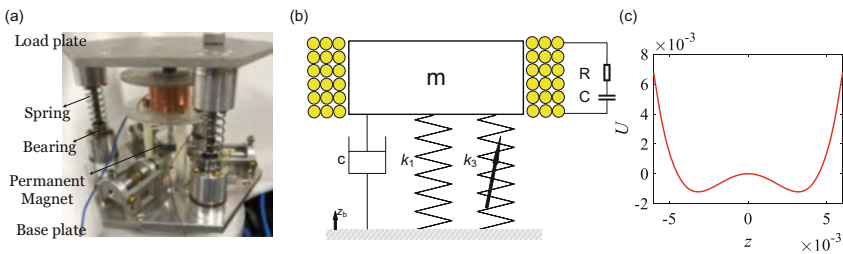


Fig. 1 The BEEH with resonance circuit: (a) picture, (b) schematic diagram, and (c) the potential energy

2.1 Electromagnetic Coupling

According to Faraday's law, an induced emf $V_e(t)$ writes in the following form:

$$V_e(t) = C_e \dot{z} \quad (1)$$

where C_e denotes the electromechanical coupling coefficient of the BEEH.

The Lorenz force will be generated correspondingly when the coil and the resistance compose a closed loop circuit, which can be expressed as

$$F_e = C_m i(t) \quad (2)$$

where $i(t)$ is the induced current flowing in the circuit. C_m is the electromagnetic coupling coefficient of the nonlinear electromagnetic isolator that can be measured experimentally, and C_m is equal to C_e . C_e is equal to $2\pi N r_g B_g$, where N is the turns of coil, r_g is the internal diameter of working air gap, and B_g is magnetic induction intensity [8]. C_e and C_m mainly depended on the turns of coil and the arrangement of magnets in simulation. The wire diameter of the coils used in the test is 0.1 mm. And the internal resistance of the coils is constant when we change the value of inductance in simulation to obtain different circuit resonant frequencies.

When a resistor R is connected to the terminals of the coil, the electrical governing equation is

$$V_e = L_e \frac{di}{dt} + (R_e + R) i(t) + \frac{\int i dt}{C} \quad (3)$$

where L_e and R_e denote the inherent inductance and impedance of the coil.

2.2 Equation of Motion

According to the analysis above, the BEEH can be simplified into a one degree of freedom (1-DOF) system. If the BEEH is subjected to a base motion $z_b \cos(\omega t + \theta)$, the equation of motion of the BEEH is as follows:

$$m\ddot{z} + c\dot{z} + k_1 z + k_2 z^2 + k_3 z^3 + F_e = m z_b \omega^2 \cos(\omega t + \theta) \quad (4)$$

where m , c , and k_1 denote the mass, the structural damping coefficient, and the linear stiffness, respectively. z is the relative displacement. z_b and ω indicate the amplitude and angular frequency of the base excitation, respectively. θ is the phase of the response. The superscript dots ($\dot{}$) and ($\ddot{}$) are the first-order and second-order derivatives with respect to time variable t , respectively.

Substituting (1) into (3), (3) will be as follows:

$$L_e \frac{di}{dt} + (R + R_e) i(t) + \frac{\int i dt}{C} - C_e \dot{z} = 0 \quad (5)$$

Substituting (2) into (4), the equation of motion will be as follows:

$$m\ddot{z} + c\dot{z} + k_1 z + k_2 z^2 + k_3 z^3 + C_e i(t) = m z_b \omega^2 \cos(\omega t + \theta) \quad (6)$$

3 Energy Harvesting Performance of the BEEH with the Resonance Circuit

In this section, the nonlinear dynamics of the BEEH with the resonant circuit is numerically analyzed using frequency sweep excitations, and the generated voltage is discussed. Bifurcation diagrams, frequency response curves, and Poincaré maps are presented to analyze the influence of the two-order electrical circuit on the dynamic response and energy harvesting performance of the BEEH. Simulation parameters of the BEEH with the resonant circuit are given in Table 1. The coefficient of stiffness k_1 is -480 N/m, while k_3 is $4.74e7$; the corresponding figure of potential well is shown in Fig. 1c.

Figure 2 presents energy harvesting comparison of the BEEH with the resonant circuit and that with a pure resistor ($R = 500 \Omega$), where the electrical governing equation of the resonant circuit is defined by Eq. (3). The result shows that the displacement of the BEEH is almost the same with the resonant circuit and pure resistor circuits when f_f is 4.24. The maximum voltage is only 3.4 V for the pure resistor, while the maximum generated voltage increases to 4 V according to the resonant circuit. It implies the performance of the BEEH with resonance circuit can be changed by adjusting the parameters of the circuit.

When the circuit resonance frequency is 9.48 while the capacitance is set as 470 nF, the performance of two cases is shown in Fig. 3. It can be seen that the output voltage of the BEEH with the resonant circuit can reach up to 3.62 V while the pure resistance one is only 0.21 V. It is demonstrated that the output voltage increased a lot by the resonant circuit while the displacement of the BEEH of the two

Table 1 Parameters of the BEEH with resonant circuit

Parameter	Value
$m(\text{kg})$	0.5
$c(\text{Ns/m})$	2.81
$k_1(\text{N/m})$	-480
$R(\Omega)$	500
$R_e(\Omega)$	500

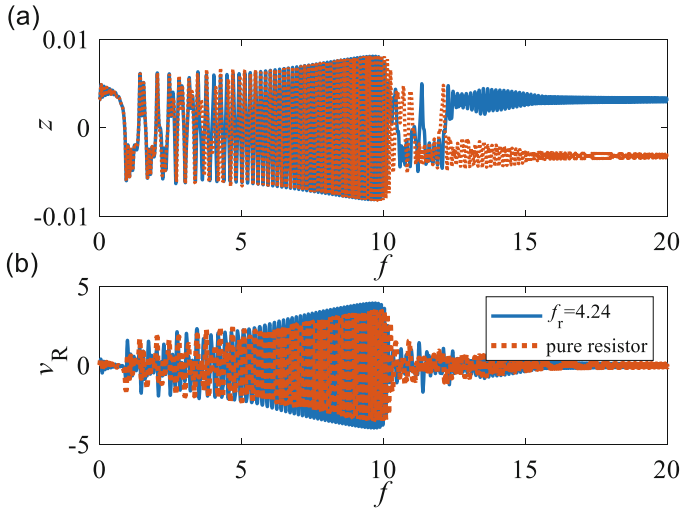


Fig. 2 (a) Displacement and (b) output of the BEEH with resonant circuit (blue solid line) and with a pure resistance (red dash line), $R = 500 \Omega$

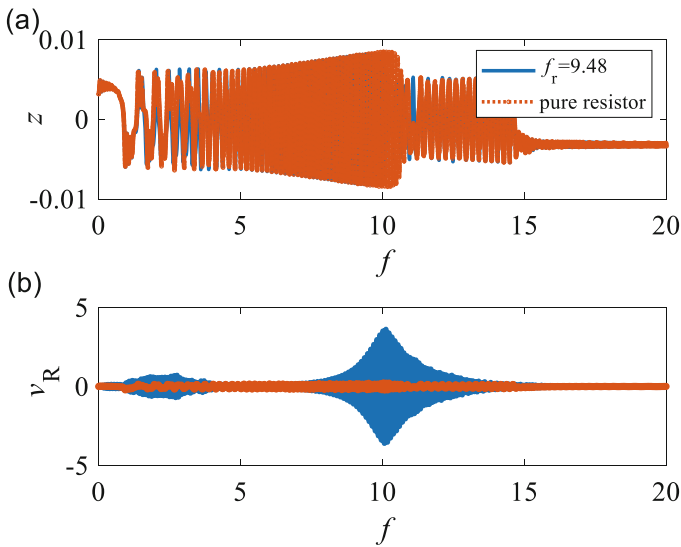


Fig. 3 Comparison of the BEEH with the resonant circuit and with a pure resistor, $R = 500 \Omega$: (a) displacement and (b) the output voltage

cases is almost the same. We can harvest a large voltage by changing the resonance frequency when other conditions are the same.

The internal resistance of the coils is constant when we change the value of inductance in simulation to obtain different circuit resonant frequencies. The

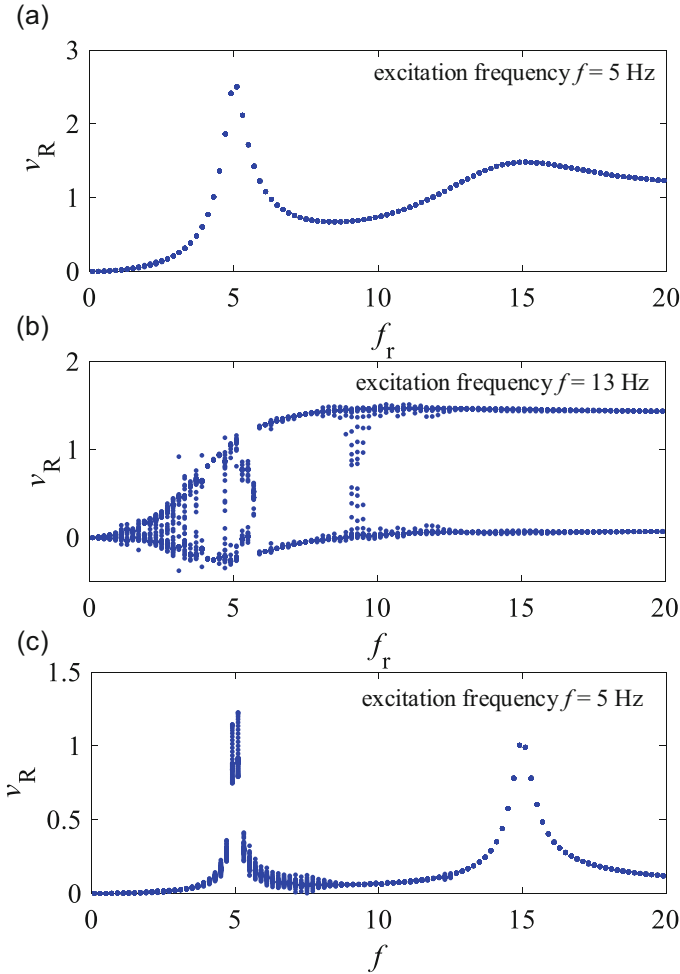


Fig. 4 Bifurcation diagram of the output voltage of the BEEH with the resonant circuit under the excitation condition of $A = 0.3$ g and (a) $f = 5$ Hz, $C = 4700$ nF, (b) $f = 13$ Hz, $C = 47$ μ F, (c) $f = 5$ Hz, and $C = 470$ nF

relationship between the output voltage and resonance frequency is as follows. Figure 4a shows the bifurcation diagram of the output voltage with respect to the circuit resonance frequency when $C = 4700$ nF and the excitation frequency f is 5 Hz. The excitation amplitude A is 0.3 g. It shows that the output voltage increases with the increase of f_r until 5 Hz. Then, the value of v_R in bifurcation diagram experiences from decreasing to increasing and finally tending to be stable, while the output voltage reaches up to 1.48 V when $f_r = 14.9$ Hz. When the excitation frequency f is 13 Hz and $C = 47$ μ F, the output voltage is increasing with the increase of f_r . The output voltage of the BEEH is less than 1.6 V with the change of

f_r . The motion of BEEH undergoes the periodic and chaotic responses comparing with Fig. 4a when the excitation frequency $f = 5$ Hz and $C = 470$ nF. There are also two peaks appearing in the diagram while the performance of the output voltage and the bandwidth is worse. It implies the performance of the BEEH also depends on the value of the circuit parameters even if the circuit resonance frequency is the same.

Figure 5 shows the bifurcation diagram of v_R with respect to excitation frequency f under the excitation amplitude $A = 0.3$ g. It shows that the motion of BEEH with resonant circuit enters into periodic when the excitation frequency increases from 4.3 to 7.2 Hz. It also experiences chaotic motion in other excitation frequency. The output voltage reaches a maximum value as 3.97 V when the excitation frequency is 7.4 Hz.

Figure 6 shows the bifurcation diagram of the output power versus the load resistance R . It can be seen that the output power increases with the increase of

Fig. 5 Bifurcation diagram of the output voltage of the BEEH with the resonant circuit under the excitation condition of $A = 0.3$ g and resonance frequency $f_r = 9.48$ Hz

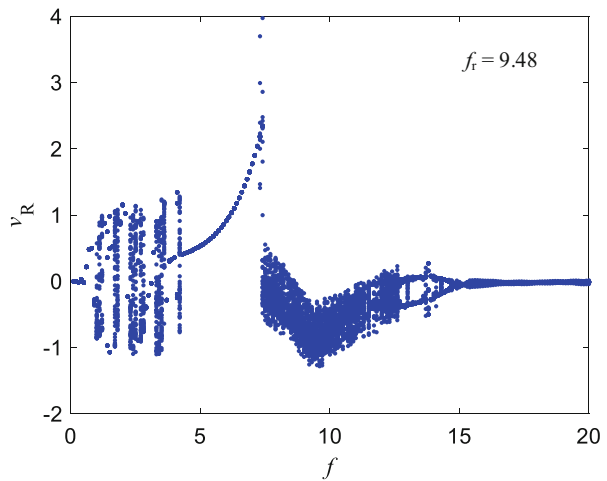
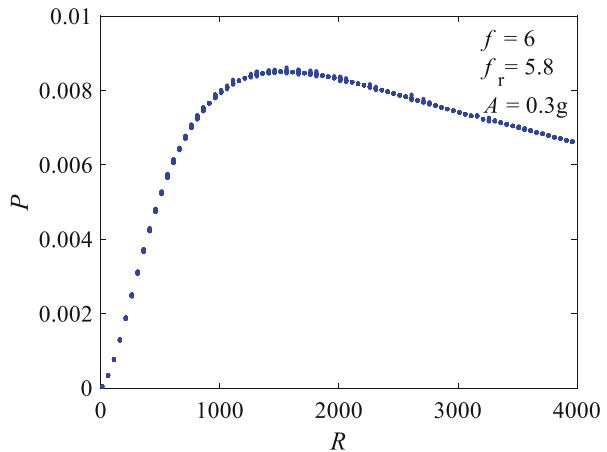


Fig. 6 Bifurcation diagram of output power of the BEEH with resonant circuit versus the load resistance



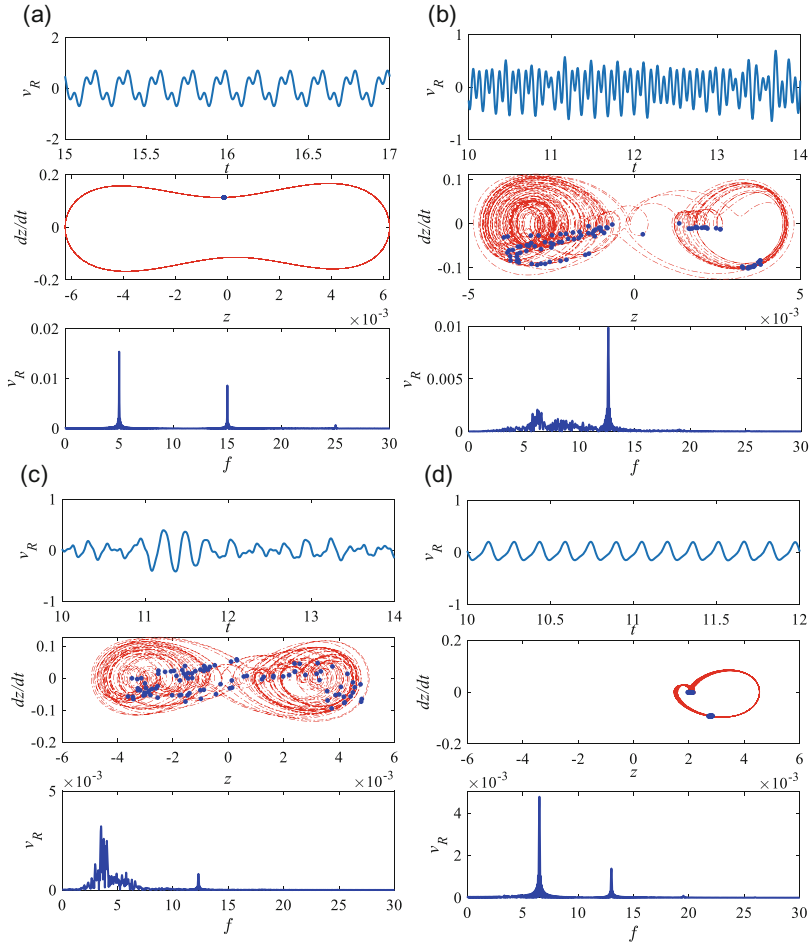


Fig. 7 BEEH with the resonant circuit: output voltage, phase orbit, Poincaré map, and frequency response for **(a)** $f = 5$, $f_r = 9.48$, $A = 0.3$ g, **(b)** $f = 12.6$, $f_r = 9.48$, $A = 0.3$ g, **(c)** $f = 12.3$, $f_r = 3.67$, $A = 0.3$ g and **(d)** $f = 13$, $f_r = 4.74$, and $A = 0.3$ g

R at the beginning. The output power reaches a maximum value when R is 1560 Ω . Then, the output power decreases and tends to be a stable value.

The dynamic response of the BEEH with resonant circuit is discussed for the further analyzing of the influence of f_r on the energy harvesting. Figure 7a presents the output voltage, the frequency response, the phase orbit, Poincaré map, and frequency response of the BEEH when $A = 0.3$ g, $f = 5$ Hz, and $f_r = 9.48$. It can be seen that the motion of the BEEH is in the interwell oscillation and the steady-state voltage can reach up to 0.7 V. The BEEH is in a periodic motion for there is only one point in Poincaré map. The corresponding Fourier spectrum indicates the subharmonic component of the order 3.

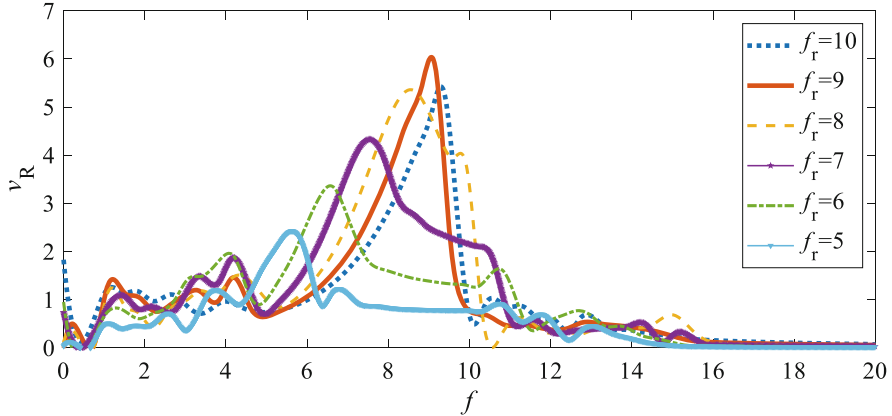


Fig. 8 Output voltage of the BEEH with the resonant circuit under different resonance frequencies

The output voltage, the frequency response, the phase orbit, Poincaré map, and frequency response is shown in Fig. 7b when the excitation frequency increases to 12.6 Hz as other conditions remain unchanged. It is seen that the BEEH enters into the chaos-dominated parametric region and is also in the interwell oscillation. In this case, the output voltage is smaller than 0.8 V. The continuous frequency band is also shown in the frequency response curve.

When f is 12.3 Hz and f_r is 3.67, Fig. 7c shows the output voltage, phase orbit, and Poincaré map and frequency response of the BEEH. It is seen that there is a strange attractor appearing in the Poincaré map, which indicates that the BEEH is in the chaotic motion.

When the excitation frequency increases to 13 Hz, Fig. 7d indicates that the motion of the BEEH transforms from interwell oscillation to intrawell oscillation. The corresponding Fourier spectrum shows the subharmonic resonance. The output voltage is 0.2 V for the small amplitude of oscillation under the period of intrawell vibration.

Figure 8 shows the relationship between the output voltage of the harvester and the resonance frequency of the circuit. It can be seen from Fig. 8 that the frequency of the resonant peak is close to the resonance frequency of the circuit, which means that the selection of the circuit parameters can influence the performance of the BEEH with resonance circuit. The maximum value of output voltage reaches up to 6 V when the resonance frequency f_r is 9 Hz. The maximum output voltage of the harvester decreases with the decrease of the f_r . When the resonance frequency of the circuit exceeds 9 Hz, the harvester begins to underperform, which means the ideal resonance frequency of the circuit is around 9 Hz.

When the resonant frequency f_r is relatively small, there is some interesting phenomenon occurring under the forward sweeping frequency response comparing to the BEEH with a pure resistor. When f_r is 5 Hz, there is only one single resonance peak as shown in Fig. 9a. The curve of the output voltage appears as two resonant

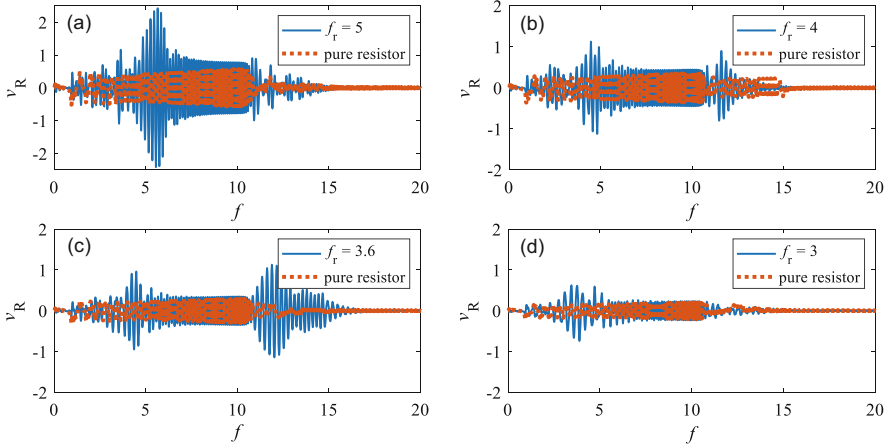


Fig. 9 Comparison of the output voltage between the BEEH with the resonant circuit and the pure resistance when (a) $f_r = 5$, (b) $f_r = 4$, (c) $f_r = 3.6$, and (d) $f_r = 3$

peaks when the circuit resonance frequency f_r decreases to 4 Hz. The second resonance peak surpasses the first resonance peak while f_r is 3.6 Hz. But the curve of the output voltage returns to one single peak when f_r is 3 Hz.

4 Conclusions

This paper analyzes the bistable electromagnetic energy harvester with a resonance circuit to improve the performance of energy harvesting. The resonance circuit is conducted by attaching a capacitance to the induction coil comparing to the normal circuit which contain a pure resistance. The numerical simulations under frequency sweep excitation indicate that the BEEH with the resonant circuit can improve the performance of energy harvesting to some extent. The influence of the resonant frequency f_r and the excitation frequency on dynamic behaviors is analyzed using the bifurcation diagram, the phase trajectory, the power spectrum, and the Poincaré map.

Under some excitation frequencies, the results show that the BEEH with the resonance circuit undergoes periodic and chaotic motion. Under the same excitation conditions, the maximum output voltage can be obtained when f_r is around 9 Hz. As for the BEEH with resonance circuit being a two degree of freedom system, the output voltage of the harvester can get two resonance peaks when f_r is relatively small. It means that the working bandwidth can be broadened comparing to the one with pure resistance. It demonstrates that it is a feasible method to enhance the performance of energy harvesting via adjusting the frequency of the resonant circuit.

References

1. Z. Yang, S. Zhou, J.W. Zu, et al., High-performance piezoelectric energy harvesters and their applications. *Joule* **2**(4), 642–697 (2018)
2. W. Liu, C. Liu, B. Ren, et al., Bandwidth increasing mechanism by introducing a curve fixture to the cantilever generator. *Appl. Phys. Lett.* **109**(4), 043905 (2016)
3. G. Litak, M.I. Friswell, S. Adhikari, Magnetopiezoelastic energy harvesting driven by random excitations. *Appl. Phys. Lett.* **96**(21), 214103 (2010)
4. B. Yan, S. Zhou, G. Litak, Nonlinear analysis of the Tristable energy harvester with a resonant circuit for performance enhancement. *Int. J. Bifurcat. Chaos* **28**(07), 1850092 (2018)
5. D. Huang, S. Zhou, G. Litak, Analytical analysis of the vibrational Tristable energy harvester with a RI resonant circuit. *Nonlinear Dyn.* **97**(1), 663–677 (2019)
6. Z. Chen, Y. Xia, J. He, et al., Elastic-electro-mechanical modeling and analysis of piezoelectric metamaterial plate with a self-powered synchronized charge extraction circuit for vibration energy harvesting. *Mech. Syst. Signal Pr.* **143**, 106824 (2020)
7. Y. Pei, Y. Liu, L. Zuo, Multi-resonant electromagnetic shunt in base isolation for vibration damping and energy harvesting. *J. Sound Vib.* **423**, 1–17 (2018)
8. B. Yan, X. Zhang, Y. Luo, et al., Negative impedance shunted electromagnetic absorber for broadband absorbing: experimental investigation. *Smart Mater. Struct.* **23**(12), 125044 (2014)

An Internally Resonant Tunable Generator for Wave Energy Harvesting



Mohammad A. Khasawneh and Mohammed F. Daqaq

1 Introduction

Point wave energy absorbers (PWAs) are considered to be the simplest, most efficient, and widely-utilized approach to harness wave energy. They currently occupy 40% of the market share and are often preferred over other types because they can be scaled down without considerably reducing efficiency. However, PWAs suffer from a main shortcoming which limits their efficacy. This shortcoming emanates from their very fundamental principle of operation which is based on establishing resonance conditions between the sea waves and the absorber [1]. This occurs when the natural frequency of the converter is close to one of the dominant frequencies in the wave energy spectrum. Establishment of resonance however leads to three main issues. (1) Because of the high stiffness of the hydrostatic restoring force resulting from buoyancy, the natural frequency of the absorber is typically higher than that of the dominant frequencies in the wave energy spectrum [2]. As a result, to reduce its natural frequency, the absorber has to be augmented with a heavy submerged body [3] or other complex mechanical and control solutions [4]. (2) Even when incorporating the proper design means to reduce the frequency of the PWA such that it matches the dominant frequencies in the spectrum of the incident waves, much of the available wave energy is still lost. This is because the resonant bandwidth of the PWA is narrower than the spectrum of the incident waves

M. A. Khasawneh (✉)
New York University, Brooklyn, NY, USA

New York University, Abu Dhabi, United Arab Emirates
e-mail: mak1011@nyu.edu

M. F. Daqaq
New York University, Abu Dhabi, United Arab Emirates
e-mail: mfd6@nyu.edu

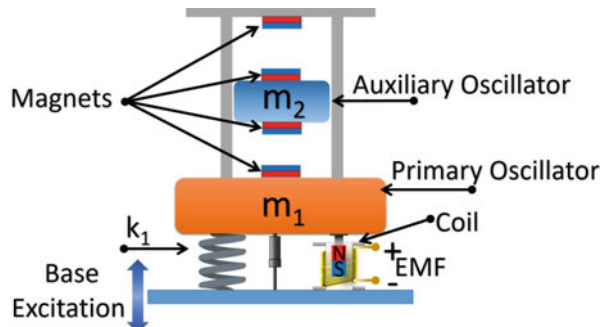
whose energy is distributed over a wide range of frequencies [5, 6]. (3) Operating the absorber at the linear resonance can also sometimes lead to very large amplitude motions that adversely influence the structural integrity of the absorber [7].

To overcome the abovementioned issues, we propose a new design of PWAs that has (1) a broader bandwidth and lesser sensitivity to variations in the excitation frequency, (2) can respond to excitation frequencies that are as low as half its fundamental frequency, and (3) does not exhibit the large-amplitude small-bandwidth resonance peak typical of the linear PWAs. The absorber consists of two coupled oscillators. The first, denoted here as the primary oscillator, comprises a partially submerged buoy. Here, the mass of the buoy provides the inertial forces while the hydrostatic buoyancy provides the restoring force. The primary oscillator has a high natural frequency due to the high stiffness of the hydrostatic restoring force. The second oscillator, denoted here as the auxiliary oscillator, consists of a moving mass and a nonlinear restoring force element created by magnetic levitation. The auxiliary oscillator is mounted inside the buoy and has its natural frequency tuned to the dominant frequency in the wave spectrum and to half the natural frequency of the primary oscillator. When the buoy is subjected to the low-frequency wave excitation, the auxiliary oscillator resonates with the wave excitation and starts to move. Energy is then channeled to the primary oscillator due to the 2-to-1 internal resonance between the two oscillators. This results in a reasonably large-amplitude relative motion between the two oscillators over a wide spectrum of frequencies. This motion can then be channeled into electricity as per Faraday's law.

2 Mathematical Formulation

The schematic for the 2-to-1 internally resonant wave energy harvester is shown in Fig. 1. The system consists of two degrees-of-freedom, y_1 , and y_2 , where y_1 stands for the displacement of the primary oscillator while y_2 stands for the displacement of the auxiliary oscillator. The primary oscillator has a mass, m_1 , and a linear stiffness k_1 . The primary oscillator is also coupled to a power take-off unit (PTO) which comprises an electromagnetic linear generator. The auxiliary oscillator has a mass, m_2 , and a nonlinear stiffness resulting from repulsive magnetic forces as shown in

Fig. 1 A schematic diagram of the harvester



the figure. The magnets also serve to limit the amplitude of oscillations so that it does not cause damage to the energy harvesting unit.

2.1 Governing Equations

The dynamics of the aforementioned system is captured by the following set of equations:

$$m_1 y_1'' + c_1 y_1' - c_2 (y_2' - y_1') + k_1 y_1 - \sum_{i=1}^3 d_i (y_2 - y_1)^i + \alpha V_L = m_1 A_f \cos(\Omega t) \quad (1)$$

$$m_2 y_2'' + c_2 (y_2' - y_1') + \sum_{i=1}^3 d_i (y_2 - y_1)^i = m_2 A_f \cos(\Omega t) \quad (2)$$

$$V_L' + \omega_c V_L = \delta_c \omega_c y_1' \quad (3)$$

where the overprime represents a temporal derivative, m_1 and m_2 are, respectively, the effective masses of the primary and auxiliary oscillators, k_1 is the effective linear stiffness of the primary oscillator, d_i represent the effective stiffness components resulting from the magnetic field, c_1 and c_2 are the effective damping coefficients, A_f and Ω are respectively the magnitude and frequency of a harmonic base acceleration used to mimic excitation forces imparted by regular ocean incident waves. Equation (3) represents the response of the electrical subsystem associated with the PTO. Here, V_L is the voltage across the load resistance, ω_c is the cut-off frequency of the circuit, α is the coupling parameter, and δ_c is the conversion factor [8].

2.2 Natural Frequencies

In order to obtain the natural frequencies of the system and create the 2-to-1 tuning between the modal frequencies, the restoring force of the auxiliary oscillator was measured using a force gauge. Figure 2 shows variation of the nonlinear magnetic restoring force with the deflection and the corresponding potential energy function. Due to the asymmetric nature of the magnetic forces imposed by using two different magnets as shown in Fig. 1, the nonlinear restoring force has quadratic nonlinearities resulting in an asymmetric potential function. These nonlinearities are crucial to activate the 2-to-1 internal resonance between the two vibration modes. The best fit of the experimental data yields a cubic polynomial: $F = d_1 y + d_2 y^2 + d_3 y^3$ with $d_1 = 795.5 \text{ N} \cdot \text{m}^{-1}$, $d_2 = -23,660 \text{ N} \cdot \text{m}^{-2}$, and $d_3 = 439,300 \text{ N} \cdot \text{m}^{-3}$. Using the experimental parameters listed in Table 1, we evaluated the natural frequencies of

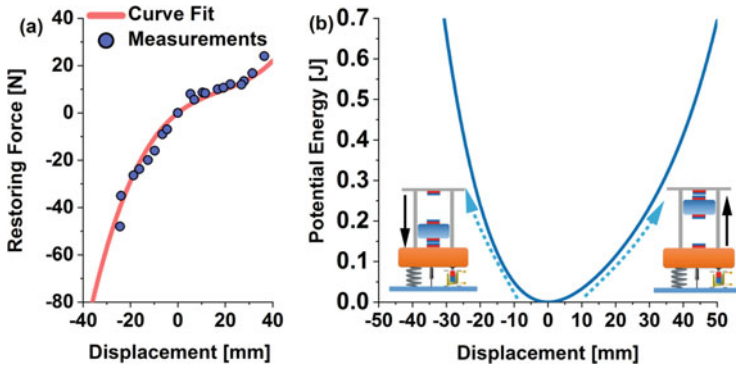


Fig. 2 (a) Nonlinear restoring force of the auxiliary oscillator fitted to third order polynomial. (b) The corresponding potential function

Table 1 Parameters used in the experiment

Parameter	Value
m_1	1.8 [kg]
m_2	0.665 [kg]
k_1	5922 [$\text{N} \cdot \text{m}^{-1}$]
d_1	795.5 [$\text{N} \cdot \text{m}^{-1}$]
d_2	-23,660 [$\text{N} \cdot \text{m}^{-2}$]
d_3	439,300 [$\text{N} \cdot \text{m}^{-3}$]
c_1	2 [$\text{N} \cdot \text{s} \cdot \text{m}^{-1}$]
c_2	1.26 [$\text{N} \cdot \text{s} \cdot \text{m}^{-1}$]
A_f	0.981 [$\text{m} \cdot \text{s}^{-2}$]
ω_c	13 [$\text{rad} \cdot \text{s}^{-1}$]
α	0.0987 [$\text{N} \cdot \text{V}^{-1}$]
δ_c	98.7 [$\text{V} \cdot \text{s} \cdot \text{m}^{-1}$]

the two modes as $\omega_1 = 31.66 \text{ rad} \cdot \text{s}^{-1}$ and $\omega_2 = 62.65 \text{ rad} \cdot \text{s}^{-1}$, which are nearly commensurate in 2-to-1 ratio.

3 Experiment

An overview of the experimental setup is shown in Fig. 3. The setup is mounted on a LabWorks electrodynamic shaker which excites the system harmonically. The frequency sweep experiment is conducted quasi-statically at constant acceleration around the primary resonant frequency of the auxiliary oscillator. The magnitude of the base acceleration provided by the shaker is maintained at a constant value by implementing a feedback algorithm using an accelerometer mounted on the shaker's base. The displacements y_1 and y_2 of the primary and secondary oscillators, respectively, are measured using two micro-epsilon laser Doppler vibrometers.

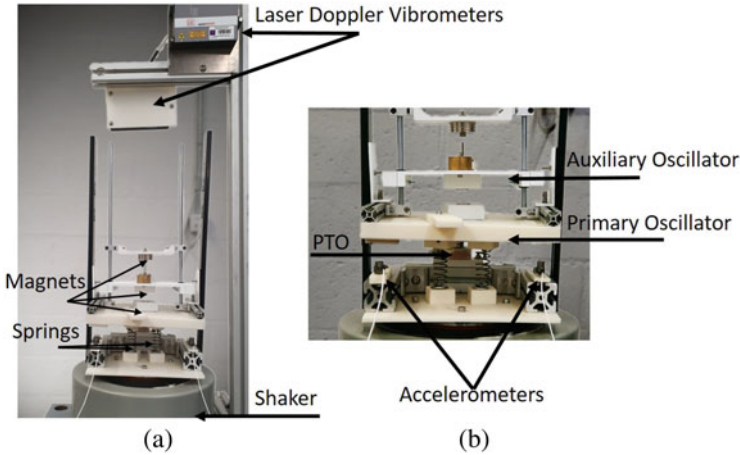


Fig. 3 (a) An overview of the experimental setup. (b) Primary and auxiliary oscillators

A PTO unit which consists of a multi-turns coil and a cylindrical magnet was used to induce current in a purely resistive load. In order to create the relative displacement between the magnet and the coil, the cylindrical magnet was mounted on the primary oscillator's plate while the coil is fixed on the base such that they are concentrically aligned. The coil was fabricated by winding 5000 turns of grade 36-AWG enameled copper wire. All measurement were logged in sync to a computer using NI-DAQ data acquisition system.

4 Results and Discussion

In order to verify the theoretical model, a direct numerical simulation was carried out and compared to the experimental results as shown in Fig. 4. A fairly good qualitative agreement between the numerical simulation and experimental results can be observed. However, due to many uncertainties in this complex nonlinear system, full quantitative agreement could not be achieved. In particular, the theoretical results under-predicted the size of the actual harvester's bandwidth. We attribute this disagreement to the sensitivity of the response bandwidth to variations in the nonlinear coefficients, d_2 , and d_3 . It is also worth noting that, over the frequency range of interest, both experimental and theoretical results had revealed no hysteresis jumps in the response and almost identical frequency response curves were obtained for both forward and backward frequency sweeps.

A comparison between the system's response with and without the 2-to-1 internal resonance tuning is illustrated in Fig. 5. The comparison clearly reveals a significant enhancement in the effective voltage bandwidth of the converter. Unlike the detuned case, it was also observed that the internally resonant case does not exhibit a

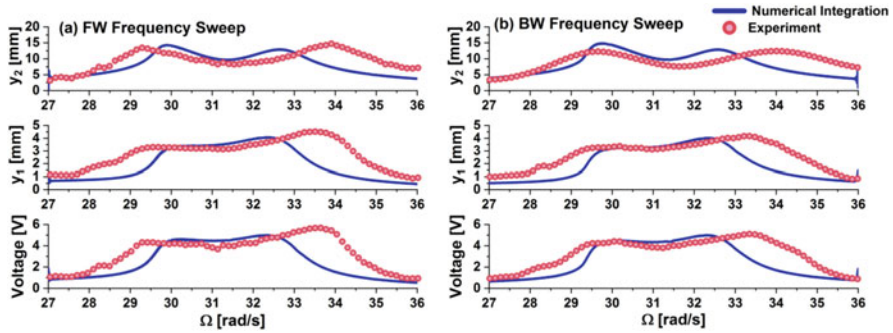


Fig. 4 Comparison between the theoretical and experimental results. (a) Forward frequency sweep, and (b) Backward frequency sweep

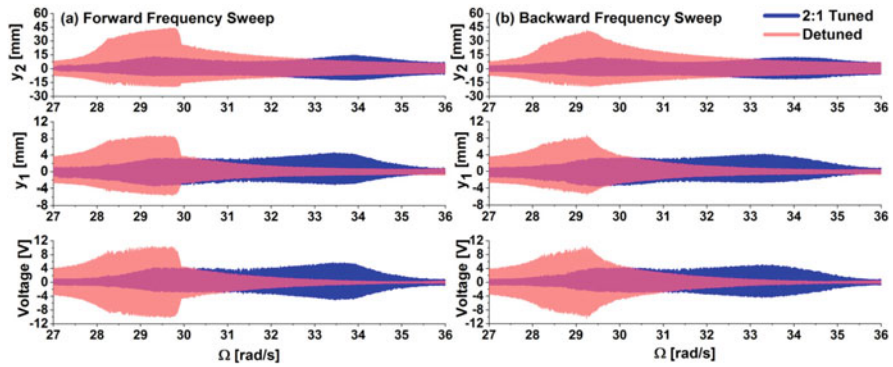


Fig. 5 Comparison between the system's response with and without 2-to-1 internal resonance tuning. (a) Forward frequency sweep. (b) Backward frequency sweep

hysteretic jump as the driving frequency is changed in both directions of the frequency sweep. Upon inspecting the induced voltage plots in Fig. 5, it becomes evident that the response is almost flat around the primary resonance. This wide and almost flat response bandwidth is one of the key advantages in exploiting the 2-to-1 nonlinear interactions in wave energy harvesting. Since incident waves come in a wide frequency spectrum and conventional point wave energy absorbers possess a distinct and a narrow resonance peak, only a small portion of the wave energy can be harnessed which leaves most of the energy inefficiently exploited. The current system overcomes this issue by providing a response that is less sensitive to the shape of the incoming waves spectrum. Moreover, it was reported by various researchers that, operating at resonance is not desirable because the amplitude of oscillations becomes too large that it influences the structural integrity of the converter specially at high sea states [1]. The proposed system operates at a reasonably medium-amplitude response over a wide spectrum of incoming waves frequencies, and in return contributes to alleviating the heavy loads exerted on the structure at resonance.

5 Conclusions

This chapter presented a theoretical and experimental proof of concept for a proposed PWA that exploits the 2-to-1 internal resonance phenomenon. The system is proposed in order to address some of the shortcomings which are associated with the conventional linear PWAs. The main advantages of the current system are (1) reducing the resonant frequency to match the dominant frequency of the incoming waves, and (2) obtaining a broader flat effective resonant bandwidth that is less sensitive to variations in the frequency of the incident waves. In addition to that, unlike the typical linear PWA, the proposed system operates at a reasonably medium-amplitude response over a wide spectrum of incoming waves frequencies, and, in return, contributes to alleviating the heavy loads exerted on the structure at resonance. This had been achieved through exploiting 2:1 internal resonance energy pump.

References

1. E. Al Shami, R. Zhang, X. Wang, Point absorber wave energy harvesters: a review of recent developments. *Energies* **12**(1), 47 (2019). <https://doi.org/10.3390/en12010047>
2. J.H. Todalshaug, Hydrodynamics of WECs, in *Handbook of Ocean Wave Energy* (Springer, Cham, 2017), pp. 139–158. https://doi.org/10.1007/978-3-319-39889-1_6
3. N.Y. Sergiienko, B.S. Cazzolato, B. Ding, P. Hardy, M. Arjomandi, Performance comparison of the floating and fully submerged quasi-point absorber wave energy converters. *Renew. Energy* **108**, 425–437 (2017). <https://doi.org/10.1016/j.renene.2017.03.002>
4. J. Hals, J. Falnes, T. Moan, A comparison of selected strategies for adaptive control of wave energy converters. *J. Offshore Mech. Arct. Eng.* **133**(3) (2011). <https://doi.org/10.1115/1.4002735>
5. B. Drew, A.R. Plummer, M.N. Sahinkaya, A review of wave energy converter technology. *Proc. Inst. Mech. Eng. A J. Power Energy* **223**(8), 887–902 (2009). <https://doi.org/10.1243/09576509JPE782>
6. B. Czech, P. Bauer, Wave energy converter concepts: design challenges and classification. *IEEE Ind. Electron. Mag.* **6**(2), 4–16 (2012). <https://doi.org/10.1109/MIE.2012.2193290>
7. J. Engström, M. Eriksson, J. Isberg, M. Leijon, Wave energy converter with enhanced amplitude response at frequencies coinciding with Swedish west coast sea states by use of a supplementary submerged body. *J. Appl. Phys.* **106**(6), 064512 (2009). <https://doi.org/10.1063/1.3233656>
8. C. Wei, X. Jing, A comprehensive review on vibration energy harvesting: modelling and realization. *Renew. Sust. Energ. Rev.* **74**, 1–18, 47 (2017). <https://doi.org/10.1016/j.rser.2017.01.073>

Nonlinear Dynamics Analysis of Electric Energy Regeneration Device Based on Vibration Energy Recovery



Wei Wang, Yan Li, Kehong Wu, Yongjie Cui, and Yuling Song

1 Introduction

The energy crisis has attracted more and more attention to energy-saving and environmentally friendly technologies, and related research on vibration energy recovery of electric vehicles has become a current research hotspot [1]. At present, research scholars mainly carry out research on energy recovery devices for vehicle suspension systems [2, 3]. The feasibility of energy recovery for the shock absorber has been studied and analyzed [4]; a variety of different types of devices have been proposed based on the vehicle's suspension system.

Taghavifar [2] researched the recovery of vibration energy of off-road vehicles, mainly considering the suspension system based on hybrid electromagnetic, and combined with the circuit dynamics of the electromagnetic energy recovery system to analyze the effectiveness of energy recovery. Through the acceleration response of chassis in the frequency domain and time domain, the influence of the vibration energy recovery system on driver/passenger riding comfort is studied and analyzed. Li et al. [5] proposed a new vibration energy collecting suspension system based on a generator and ball screw mechanism. Vehicle vibration energy is collected

W. Wang · Y. Li · K. Wu · Y. Cui

College of Mechanical and Electronic Engineering, Northwest A&F University, Yangling, Shaanxi, China

Y. Song (✉)

College of Mechanical and Electronic Engineering, Northwest A&F University, Yangling, Shaanxi, China

Key Laboratory of Agricultural Internet of Things, Ministry of Agriculture, Yangling, Shaanxi, China

Key Laboratory of Agricultural Information Perception and Intelligent Services, Yangling, Shaanxi, China

from the suspension system, and stored in the battery. Zhang et al. [3] integrated an arm-tooth drive electric energy regeneration device based on the vehicle suspension system to obtain a more accurate power output response. Through the 1/4, 1/2, and full-vehicle electric energy regeneration system models reveal the influence of road unevenness on the system power output. Unlike the above method, vibration energy recovery by functional materials has great advantages for small-amplitude vibration. Tavares and Ruderman [6] used piezoelectric ceramics to convert mechanical energy into electrical energy. The piezoelectric ceramic sensor's ability and efficiency of electric energy regeneration under two different types of external excitations are studied. Genovese et al. [7] studied the recovery of wasted energy from the vibration of train air suspension, design and develop an energy collection system integrated into a pneumatic spring. The boundary volume of the new equipment is defined mainly through reverse engineering technology, and the energy is collected by means of a resonance system and a temporary conversion mechanism located in a defined enclosed space.

On the basis of existing research, this paper proposes an electromechanical energy regeneration device with two one-way clutches for the reduction vibration of the power battery pack of an electric vehicle and extending the cruising range of electric vehicles. The transmission system in this device converts the two-way vibration of the rack into one-way rotation of the input shaft of the generator, thereby greatly improving reliability and efficiency. The generator will be driven in one direction to convert kinetic energy into electrical energy. In the movement process, the meshing of gears and racks, the transmission of bevel gears, the working process of a one-way clutch, and the process of contact, paired contact impact and separation processes occur at all times. In theory, chaos may occur in the system, which will lead to the decline of the motion stability of the electric energy regeneration device. The stability of system motion depends on whether the design of key parameters in the device is reasonable [8–10]. Many researches have been conducted on the influence of gear transmission system design parameters on performance.

Yang et al. [11] established a one-DOF gear pair model including time-varying meshing stiffness, static transmission error, and nonlinear backlash, and analyzed the stability of the gear system to obtain stable and unstable boundary conditions of the area. Finally, a parameter study is carried out to reveal the influence of several key parameters on the system performance. Xiao et al. [12] installed a dumbbell-shaped damper in the damping hole. Based on the nonlinear energy dissipation mechanism, the damping force is used as an external excitation and its damping effect is discussed. Using the dynamic coupling method of continuum and discontinuity, the equivalent displacement mapping of the contact load from the discontinuous domain of the gear to the node of the continuous element is realized. Zhu et al. [13] established the nonlinear dynamic model of the segmented bending and pendulum of the gear transmission system and studied its nonlinear dynamic characteristics and dynamic characteristics. Based on three different Poincaré maps, defined by bifurcation diagram, Lyapunov exponent diagram, phase diagram, and dynamic change curve, the effects of the load factor, meshing frequency, comprehensive transmission error on system dynamics and nonlinear dynamics are studied. Shin and Palazzolo [14] proposed a new method for modeling and analyzing

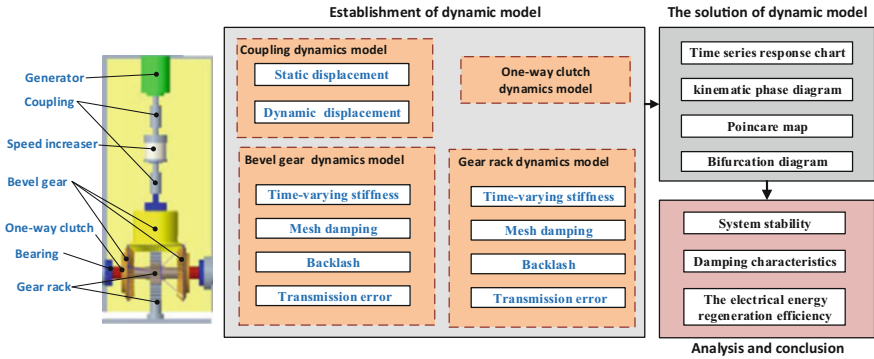


Fig. 1 Flow chart of nonlinear dynamic analysis of electric energy regeneration device

gear rotor-bearing systems. Considering the nonlinear force in the gear set and the supporting liquid film journal bearing, a rotor dynamic model with five degrees of freedom is established. Yi et al. [15] proposed a new nonlinear dynamic model of the spur gear system, which considered the time-varying behavior of pressure angle and gear clearance, as well as the influence of gear gravity, unbalanced mass, and internal/external excitation. The motion equation of the system is derived strictly by the Lagrange method and solved by the numerical integration method.

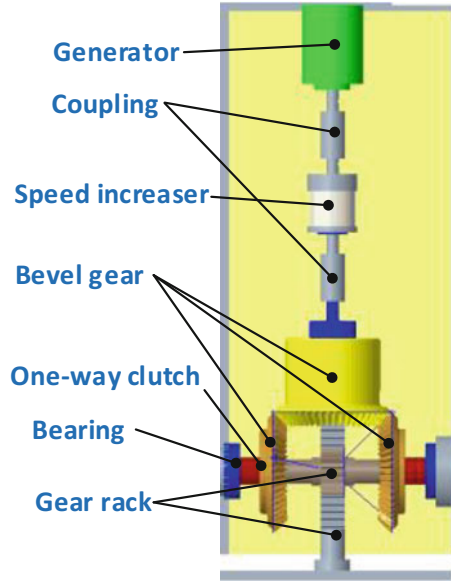
To sum up, this paper proposes a mechanical electromagnetic electric energy regeneration device. The layout design of two one-way clutches transforms the reciprocating vibration into a one-way rotation of the generator. In order to improve the motion stability of the electric energy regeneration device, the analysis of the nonlinear parameters in the device, considering the time-varying meshing stiffness, meshing damping, tooth side clearance, comprehensive transmission error of the meshing pair, and the reserve clearance of the one-way clutch. The mass concentration method is used to establish a multi-degree-of-freedom nonlinear dynamic model. The effects of excitation frequency, reserve gap, and integrated transfer error on the nonlinear dynamic performance were analyzed by time-series response diagrams, phase diagrams, Poincaré diagrams, and bifurcation diagrams, revealing the law of influence of parameters on the damping characteristics of the device. The research will lay a profound theoretical foundation and practical significance for improving the stability of the power regeneration system. Figure 1 shows the technical route studied in the paper.

2 Dynamic Model of Electric Energy Regeneration Device

2.1 Device Structure Design

This paper proposes an electromagnetic electric energy regeneration device using two one-way clutches. As shown in Fig. 2, it mainly has four parts: a rack and pinion

Fig. 2 Schematic diagram of electromagnetic energy regeneration device structure



mechanism, a bevel gear transmission mechanism, a generator, and an electric energy storage module. When an electric vehicle is driving on a road, the unevenness of the road elevation will cause a vibration of the electric vehicle. In order to alleviate the vibration of the battery pack, an electric energy regeneration device is installed between the battery pack and the chassis of the electric vehicle. The function of the rack and pinion transmission mechanism is to convert the relative linear motion between the battery pack and the chassis into the rotational motion of the generator. The bevel gear transmission mechanism includes two one-way clutches and three bevel gears. Its function is to convert the bidirectional rotation of the gears in the rack and pinion mechanism into unidirectional rotation of the bevel gears and drive the speed increaser and generator to rotate in one direction so that the generator can output electricity. The electric energy storage module is directly connected to the generator and contains three components of the filter circuit, voltage stabilizing circuit, and supercapacitor. The purpose is to store the electrical electric energy by the electrical energy regeneration system to increase the mileage of electric vehicles. The device can recover energy from vibrations with a large range of amplitude, effectively improve the cruising range of electric vehicles, take into account the safety of the power battery pack, and increase the rate of the energy regeneration and vibration energy recovery of the device.

2.2 Road Incentive and Time Domain Description

In the design process of the electric energy regeneration device, not only the strength and rigidity of the components must be considered, but also the vibration caused by

the unevenness of the road during the road driving process [16, 17]. The unevenness of the road is unpredictable, and the excitation to the car body is random, belonging to random loads. This kind of load cannot be used to express the load time history with a function, but this relationship can be described by statistics and probability theory. Bearing this kind of random load for a long time may cause large vibrations in the electrical energy regeneration device, which may affect the safety of the power battery pack and may cause cracks or fractures in the structure due to fatigue, shortening the service life of the device as a whole [18, 19].

The external excitation of the device comes from the unevenness of the road elevation. When performing device simulation research and performance evaluation, it is necessary to obtain accurate road information. The road unevenness input of vehicle vibration mainly adopts the form of road power spectrum density. The most direct method to obtain the road surface spectrum is measurement, but it is laborious, time-consuming, and uneconomical. Many scholars have measured road surface unevenness and determined that the power spectrum density function and variance of the road surface describe its statistical characteristics. In 1984, the International Organization for Standardization put forward the “Draft Representation Method for Descriptive Roughness” in the document ISO/TC108/SC2N67. China also formulated the corresponding national standards by referring to it. The Changchun Automobile Research Institute drafted and formulated GB/T7031-1986 “Vehicle Vibration Input-Standard for Road Surface Roughness Representation Method. The formula (1) is used in the documents to fit and describe the road power spectrum density [17].

$$G_q(n) = G_q(n_0) \left(\frac{n}{n_0}\right)^{-w} \tag{1}$$

where n is spatial frequency, n_0 is reference spatial frequency, $G_q(n_0)$ is the road power spectral density at the reference spatial frequency, and $G_q(n)$ is the road roughness coefficient. w is the frequency index, which is the slope of the diagonal line in double logarithmic coordinates and usually takes the value of 2. The document divides the road into eight classes, and in this paper, we mainly use class D road for the study. The roughness coefficient of class D road is $1024 \times 10^{-6} \text{ m}^3$, and the root mean square value is $30.45 \times 10^{-3} \text{ m}$.

There is no speed influence factor present in the spatial frequency power spectrum description. But for vehicle vibration systems, the vehicle speed is a factor that must be considered [18]. When a car travels on a road surface with a spatial frequency n at speed u , the equivalent time-frequency is $f = un$.

Therefore, the time-frequency power spectral density is

$$G_q(f) = \frac{1}{u} G_q(n_0) \left(\frac{n}{n_0}\right)^{-w} = G_q(n_0) n_0^2 \frac{u}{f^2} \tag{2}$$

Since the road surface is regarded as a superposition of a group of sine waves with different wavelengths, amplitudes, and phases, it can be assumed that the spatial frequency range of the group of waves is (n_1, n_2) and the interval (n_1, n_2) is divided

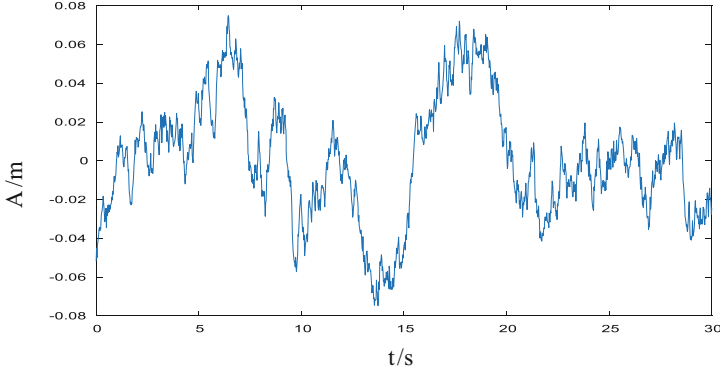


Fig. 3 Time-domain displacement excitation for class D road ($u = 5$ m/s)

into N cells. The center frequency between i th cell is $n_{\text{mid-}i}$, the interval width is $\Delta n = (n_2 - n_1)/N$, then the corresponding road surface displacement power spectrum density is:

$$G_q(f_i) = G_q(n_0) n_0^2 \frac{1}{un_{\text{mid-}i}^2} \tag{3}$$

Therefore, the expression of the sine signal corresponding to this interval is

$$\sqrt{2G_q(f_i)} \Delta n \sin(2\pi un_{\text{mid-}i}x + \alpha_i) \tag{4}$$

As shown in Fig. 3, multiple sine signal waveforms are superimposed to obtain an expression for the random excitation of farm pavements:

$$q(x) = \sum_{i=1}^N \sqrt{2G_q(f_i)} u \Delta n \sin(2\pi un_{\text{mid-}i}x + \alpha_i) \tag{5}$$

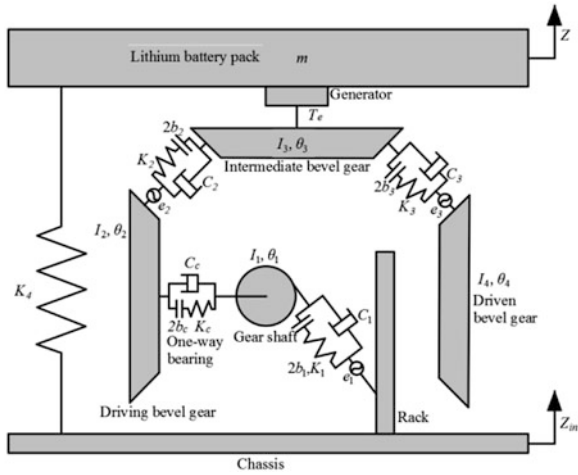
where α_i is a random number uniformly distributed in $[0, 2\pi]$. In this study, the first harmonic term of the road displacement excitation is selected, and the time domain road displacement excitation is:

$$q(t) = A \sin(\omega t + \phi) \tag{6}$$

2.3 System Dynamics Model

The dynamic model of the mechanical electromagnetic power regeneration system is shown in Fig. 4. In the figure, Z_{in} is the displacement excitation of the soil road

Fig. 4 Dynamic model of electric energy regeneration device



surface; Z is the vertical displacement of the lithium battery pack; and r_i, I_i, θ_i ($i = 1,2,3,4$) are the base radius, inertia, and angular displacement of torsional vibration of the gear, respectively. C_1, K_1, b_1 , and e_1 are the meshing damping, time-varying meshing stiffness, tooth side clearance, and comprehensive transmission error of the rack and pinion meshing pair respectively. C_i, K_i, b_i , and e_i ($i = 2,3$) are the meshing damping, time-varying meshing stiffness, tooth side clearance, and comprehensive transmission error of the i th gear meshing pair respectively. C_c, K_c, b_c are the torsional damping, torsional stiffness, and reserve clearance when the one-way clutch is in contact. T_e is the induced torque generated during the operation of the generator.

Considering the time-varying meshing stiffness, meshing damping, tooth side clearance, and comprehensive transmission error of the meshing pair, as well as the reserve clearance of the one-way clutch, the mass concentration method [20] is used to establish the nonlinear vibration equation of the dynamic model shown in Fig. 4 as

$$\begin{cases} I_1\ddot{\theta}_1 = r_1(K_1f_1 + C_1\dot{X}_1) - K_cfc - C_c\dot{X}_c \\ I_2\ddot{\theta}_2 = K_cfc + C_c\dot{X}_c - r_2(K_2f_2 + C_2\dot{X}_2) \\ I_3\ddot{\theta}_3 = r_3(K_2f_2 + C_2\dot{X}_2) - r_3(K_3f_3 + C_3\dot{X}_3) - T_e \\ I_4\ddot{\theta}_4 = r_4(K_3f_3 + C_3\dot{X}_3) \\ m\ddot{Z} = K_4X_4 + K_1f_1 + C_1\dot{X}_1 \end{cases} \quad (7)$$

Among them, the relative displacement of each meshing pair is:

$$\begin{cases} X_1 = Z_{in} - r_1\theta_1 - Z \cos \alpha - \bar{e}_1 \\ X_c = \theta_1 - \theta_2 \\ X_2 = r_2\theta_2 - r_3\theta_3 - \bar{e}_2 \\ X_3 = r_3\theta_3 - r_4\theta_4 - \bar{e}_3 \\ X_4 = Z_{in} - Z \end{cases} \quad (8)$$

$f_i(t)$ is the nonlinear function of the side clearance of the gear meshing pair, then:

$$f_i(t) = \begin{cases} X_i - \bar{b}_i, & X_i > \bar{b}_i, i = 1, 2, 3; \\ 0, & |X_i| \leq \bar{b}_i, i = 1, 2, 3; \\ X_i + \bar{b}_i, & X_i < -\bar{b}_i, i = 1, 2, 3. \end{cases} \quad (9)$$

The nonlinear function of the reserve clearance of the roller one-way clutch is:

$$f_c(t) = \begin{cases} X_c r_c - b_c, & X_c r_c > b_c \\ 0, & |X_c r_c| \leq b_c \\ X_c r_c + b_c, & X_c r_c < -b_c \end{cases} \quad (10)$$

where r_c is the radius of movement of the one-way bearing roller.

Taking the first harmonic component of the meshing stiffness of the gear meshing pair, the time-varying meshing stiffness is

$$K_i = k_{avi} + k_{mi} \cos(\omega_i t + \varphi_i) \quad i = 1, 2, 3; \quad (11)$$

where $\omega_1 = 4A\omega/p$, p is the tooth pitch of the driving gear in the meshing pair, A is the amplitude of the displacement excitation, and $\omega_i = \mu\omega_1, i = 2, 3$.

In order to solve the problem smoothly, relative coordinates are introduced to eliminate rigid body displacements:

$$\begin{cases} \ddot{X}_1 = \ddot{Z}_{in} - \frac{r_1}{I_1} (r_1 K_1 f_1 + r_1 C_1 \dot{X}_1 - K_c f_c - C_c \dot{X}_c) \\ \quad - \frac{1}{m} (K_4 X_4 + r_1 K_1 f_1 \cos \alpha + r_1 C_1 \dot{X}_1 \cos \alpha) \cos \alpha - \bar{e}_1 \\ \ddot{X}_c = \frac{1}{I_1} (r_1 K_1 f_1 + r_1 C_1 \dot{X}_1 - K_c f_c - C_c \dot{X}_c) - \frac{1}{I_2} (K_c f_c + C_c \dot{X}_c - r_2 K_2 f_2 - r_2 C_2 \dot{X}_2) \\ \ddot{X}_2 = \frac{r_2}{I_2} (K_c f_c + C_c \dot{X}_c - r_2 K_2 f_2 - r_2 C_2 \dot{X}_2) \\ \quad - \frac{r_3}{I_3} (r_3 K_2 f_2 + r_3 C_2 \dot{X}_2 - r_3 K_3 f_3 - r_3 C_3 \dot{X}_3 - T_e) - \bar{e}_2 \\ \ddot{X}_3 = \frac{r_3}{I_3} (r_3 K_2 f_2 + r_3 C_2 \dot{X}_2 - r_3 K_3 f_3 - r_3 C_3 \dot{X}_3 - T_e) - \frac{r_4}{I_4} (r_4 K_3 f_3 + r_4 C_3 \dot{X}_3) - \bar{e}_3 \\ \ddot{X}_4 = \ddot{Z}_{in} - \frac{1}{m} (K_4 X_4 + K_1 f_1 + C_1 \dot{X}_1) \end{cases} \quad (12)$$

Defining the nominal time scale $\omega_c = \sqrt{k_{av1}/m}$, let $\tau = \omega_c t, \omega_{hi} = \omega_i/\omega_c. \ddot{x}_i$ is the derivative of x_{to} . Using characteristic length b , let $x_i = \frac{X_i}{b}, b_i = \frac{\bar{b}_i}{b}, e_i(t) = \frac{\bar{e}_i(t)}{b}, e_{ai} = \frac{\bar{e}_{ai}}{b}$.

Defining dimensionless parameters:

$$\begin{aligned} \xi_{11} &= \frac{r_1^2 C_1}{I_1 \omega_c} + \frac{C_1 \cos \alpha}{m \omega_c} & K_{11} &= \frac{r_1^2 k_{av1}}{I_1 \omega_c^2} + \frac{k_{av1} \cos \alpha}{m \omega_c^2} & \xi_{1c} &= -\frac{r_1 C_c}{I_1 \omega_c} & K_{1c} &= -\frac{r_1 K_c}{I_1 \omega_c^2} & K_{14} &= \frac{K_4 \cos \alpha}{m \omega_c^2} \\ \xi_{c1} &= -\frac{r_1 C_1}{I_1 \omega_c} & K_{c1} &= -\frac{r_1 k_{av1}}{I_1 \omega_c^2} & \xi_{cc} &= \frac{C_c}{I_1 \omega_c} + \frac{C_c}{I_2 \omega_c} & K_{cc} &= \frac{K_c}{I_1 \omega_c^2} + \frac{K_c}{I_2 \omega_c^2} & \xi_{c2} &= -\frac{1}{I_2 \omega_c} r_2 C_2 & K_{c2} &= -\frac{r_2 k_{av2}}{I_2 \omega_c^2} \\ \xi_{2c} &= -\frac{r_2 C_c}{I_2 \omega_c} & K_{2c} &= -\frac{r_2 K_c}{I_2 \omega_c^2} & \xi_{22} &= \frac{r_2^2 C_2}{I_2 \omega_c^2} + \frac{r_3^2 C_2}{I_3 \omega_c^2} & K_{22} &= \frac{r_2^2 k_{av2}}{I_2 \omega_c^2} + \frac{r_3^2 k_{av2}}{I_3 \omega_c^2} & \xi_{23} &= -\frac{r_3^2 C_3}{I_3 \omega_c} & K_{23} &= -\frac{r_3^2 k_{av3}}{I_3 \omega_c^2} \\ \xi_{32} &= -\frac{r_3^2 C_2}{I_3 \omega_c} & K_{32} &= -\frac{r_3^2 k_{av2}}{I_3 \omega_c^2} & \xi_{33} &= \frac{r_3^2 C_3}{I_3 \omega_c} + \frac{r_4^2 C_3}{I_4 \omega_c} & K_{33} &= \frac{r_3^2 k_{av3}}{I_3 \omega_c^2} + \frac{r_4^2 k_{av3}}{I_4 \omega_c^2} \\ \xi_{41} &= \frac{C_1}{m \omega_c} & K_{41} &= \frac{k_{av1}}{m \omega_c^2} & K_{44} &= \frac{K_4}{m \omega_c^2} \end{aligned} \quad (13)$$

The dimensionless differential equation of motion for the electrical energy regeneration system is obtained by transforming:

$$\begin{cases} \ddot{x}_1 + \xi_{11}\dot{x}_1 + K_{11}k_1(\tau) f_1(\tau) + \xi_{1c}\dot{x}_c + K_{1c}f_c(\tau) + K_{14}x_4 = p_1(\tau) \\ \ddot{x}_c + \xi_{c1}\dot{x}_1 + K_{c1}k_1(\tau) f_1(\tau) + \xi_{cc}\dot{x}_c + K_{cc}f_c(\tau) + \xi_{c2}\dot{x}_2 + K_{c2}k_2(\tau) f_2(\tau) = 0 \\ \ddot{x}_2 + \xi_{2c}\dot{x}_c + K_{2c}f_c(\tau) + \xi_{22}\dot{x}_2 + K_{22}k_2(\tau) f_2(\tau) + \xi_{23}\dot{x}_3 + K_{23}k_3(\tau) f_3(\tau) = p_2(\tau) \\ \ddot{x}_3 + \xi_{32}\dot{x}_2 + K_{32}k_2(\tau) f_2(\tau) + \xi_{33}\dot{x}_3 + K_{33}k_3(\tau) f_3(\tau) = p_3(\tau) \\ \ddot{x}_4 + \xi_{41}\dot{x}_1 + K_{41}k_1(\tau) f_1(\tau) + K_{44}x_4 = p_4(\tau) \end{cases} \tag{14}$$

Where, $p_1 = \ddot{Z}_{in} - \ddot{e}_1$ $p_2 = \frac{r_3}{l_3 b \omega_c^2} T_e - \ddot{e}_2$ $p_3 = -\ddot{e}_3 - \frac{r_3}{l_3 b \omega_c^2} T_e$ $p_4 = \ddot{Z}_{in}$.

$$f_i(\tau) = \begin{cases} x_i - b_i, & x_i > b_i, i = 1, 2, 3; \\ 0, & |x_i| \leq b_i, i = 1, 2, 3; \\ x_i + b_i, & x_i < -b_i, i = 1, 2, 3. \end{cases}$$

3 Simulation Investigation

Taking the two one-way clutches mechanical electromagnetic power regeneration system as the research object, considering the time-varying meshing stiffness, meshing damping, tooth side clearance, and comprehensive transmission error of the meshing pair, as well as the reserve clearance of the one-way clutch, based on the above differential equation of motion group, using variable step size Runge-Kutta algorithm for the numerical solution of system dynamics [21]. The parameters used in the calculation are shown in Tables 1 and 2.

The bifurcation diagram of the dimensionless displacement of the first-stage bevel gear with the meshing frequency is shown in Fig. 5. It can be seen from Fig. 5 that when the meshing frequency ω is less than 2.56 Hz, the electric energy regeneration system exhibits a stable single-cycle motion. Taking $\omega = 2.02$ Hz as an example, the dimensionless time-domain response diagram, phase diagram, and Poincaré cross-sectional diagram of the first-stage bevel gear are shown in Fig. 6. The movement process of the gear is expressed from the tooth surface meshing to the disengagement then to the tooth surface meshing. When the meshing frequency continues to increase, the single-period motion becomes unstable, and the motion state of the system is transformed into quasiperiodic motion from periodic motion. Taking $\omega = 2.58$ Hz as an example, the dimensionless time-domain response diagram, phase diagram, and Poincaré cross-sectional diagram of the first-stage bevel gear are shown in Fig. 7. The phase diagram is shown as an annular band with a certain width, and the Poincaré cross-section is shown by a circle composed of points. Continue to increase the meshing frequency, and the system motion is transformed from quasiperiodic motion to chaotic motion. Taking $\omega = 4.54$ Hz as an example, the dimensionless time-domain response diagram, phase diagram, and

Table 1 Gear system parameters

Parameter	Symbol	Value	Parameter	Symbol	Value
Battery quality	$m(\text{kg})$	90		z_2	50
Gear shaft quality	$m_1(\text{kg})$	0.6691	Number of bevel gear teeth	z_3	50
Number of rack teeth	z	20		z_4	50
Number of gear shaft teeth	z_1	18		$I_2(10^{-6}\text{kg} \cdot \text{m}^2)$	819.7169
Moment of inertia of gear shaft	$I_1(10^{-6}\text{kg} \cdot \text{m}^2)$	56.5730	Bevel gear moment of inertia	$I_3(10^{-6}\text{kg} \cdot \text{m}^2)$	2050.2
Gear shaft radius	$r_1(\text{m})$	0.018		$I_4(10^{-6}\text{kg} \cdot \text{m}^2)$	819.7169
One-way clutch damping	$C_c(\text{N} \cdot \text{m} \cdot \text{s}/\text{rad})$	400		$r_2(\text{m})$	0.05
One-way clutch stiffness	$K_c(\text{N} \cdot \text{m}/\text{rad})$	3.5×10^4	Bevel gear radius	$r_3(\text{m})$	0.05
One-way clutch clearance	$b_c(\text{m})$	8×10^{-6}		$r_4(\text{m})$	0.05
Gear rack clearance	$b_1(\text{m})$	5×10^{-6}	Bevel gear meshing clearance	$b_2b_3(\text{m})$	2×10^{-6}

Table 2 Generator parameters

Parameter	Value
Generator rotor inertia	$0.4 \times 10^{-4} \text{ kg} \cdot \text{m}^2$
Internal resistance	0.45Ω
External load	5Ω
Back electromotive voltage constant	$0.0458 \text{ V} \cdot \text{s}/\text{rad}$
Speed increaser transmission ratio	1:10

Poincaré cross-sectional diagram of the first-stage bevel gear are shown in Fig. 8. The Chaotic motion causes the unstable vibration of the electric energy regeneration system.

4 Conclusions

A mechanical electromagnetic energy regeneration device using two one-way clutches is proposed to extend the range of electric vehicles. The transmission system converts the bidirectional vibration of the rack into unidirectional rotation of the input shaft of the generator, which greatly increases reliability and efficiency. The generator will be driven in one direction to convert the kinetic energy into electrical energy. Nonlinear parameters in the energy regeneration device will affect

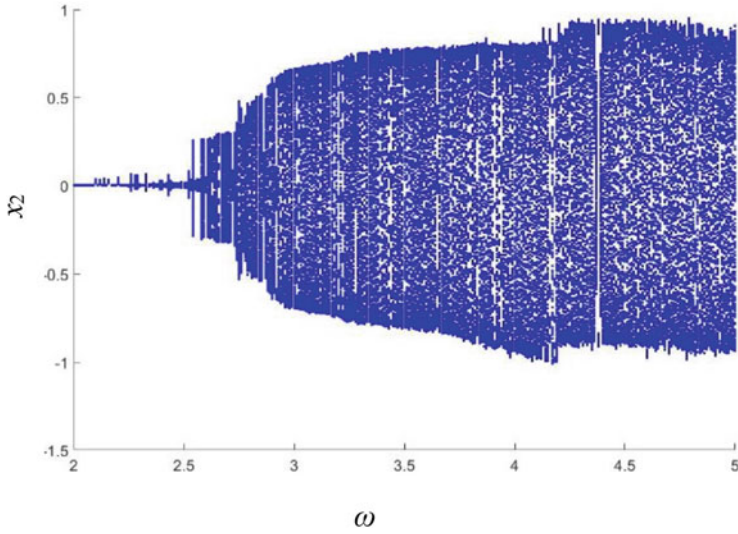


Fig. 5 Bifurcation diagram of the system changing with the meshing frequency

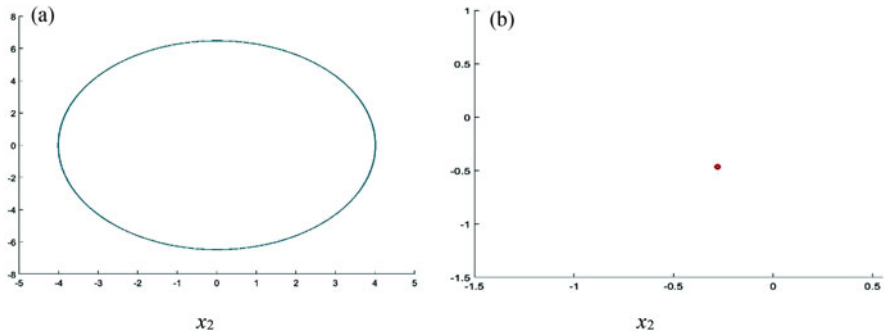


Fig. 6 Phase diagram (a) and Poincaré cross section (b) ($\omega = 2.02$ Hz)

the stability of the system and the efficiency of electric energy regeneration. Through the analysis of the nonlinear parameters in the device, considering the time-varying mesh stiffness, mesh damping, backlash and dynamic transmission error of the meshing pair, and the reserve clearance of the one-way clutch, using the mass centralized method to establish the multiple degrees of freedom nonlinear dynamic model. The Runge-Kutta method is used to calculate the nonlinear differential equation. The time-series response chart, kinematic phase diagram, Poincare map, and bifurcation diagram are used to analyze the influence of parameters. The results show that as the meshing frequency changes, the system response changes from period-doubling bifurcation to chaotic motion. In addition, The influence law of parameters on the damping characteristics of the device is revealed. The research results can improve the stability and the efficiency of electric energy regeneration

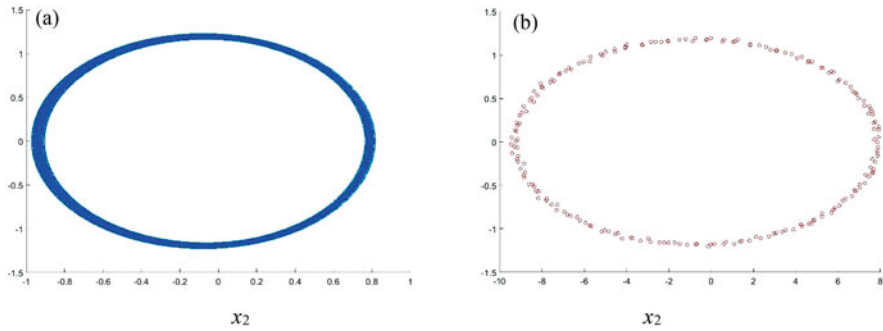


Fig. 7 Phase diagram (a) and Poincaré cross section (b) ($\omega = 2.58$ Hz)

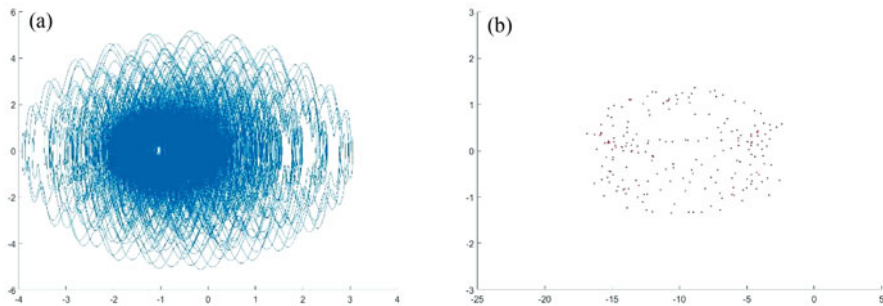


Fig. 8 Phase diagram (a) and Poincaré cross section (b) ($\omega = 4.54$ Hz)

devices and achieve the goals of prolonging the cruising mileage. It can lay a profound theoretical foundation and reality significance for the research of electric energy regeneration devices.

Acknowledgments This study was funded by the National Key Research and Development Program of China (grant number 2016YFD0700800), and the International Cooperation Project of Qilu University of Technology (grant number QLUTGJHZ2018022). The authors would like to appreciate all the authors listed in the references, and would also like to thank the funding organizations that provided financial support and anonymous reviewers for helpful comments and suggestions. The authors declare no potential conflicts of interest with respect to the research, authorship, and/or publication of this article.

References

1. Z. Zhang et al., A high-efficiency energy regenerative shock absorber using supercapacitors for renewable energy applications in range extended electric vehicle. *Appl. Energy* **178**, 177–188 (2016)
2. H. Taghavifar, A novel energy harvesting approach for hybrid electromagnetic-based suspension system of off-road vehicles considering terrain deformability. *Mech. Syst. Signal Process.* **146**, 106988 (2021)

3. R. Zhang et al., A comprehensive comparison of the vehicle vibration energy harvesting abilities of the regenerative shock absorbers predicted by the quarter, half and full vehicle suspension system models. *Appl. Energy* **272**, 115180 (2020)
4. M.A.A. Abdelkareem et al., Vibration energy harvesting in automotive suspension system: A detailed review. *Appl. Energy* **229**, 672–699 (2018)
5. S. Li et al., Energy-harvesting variable/constant damping suspension system with motor based electromagnetic damper. *Energy* **189**, 116199 (2019)
6. R. Tavares, M. Ruderman, Energy harvesting using piezoelectric transducers for suspension systems. *Mechatronics* **65**, 102294 (2020)
7. A. Genovese, S. Strano, M. Terzo, Design and multi-physics optimization of an energy harvesting system integrated in a pneumatic suspension. *Mechatronics* **69**, 102395 (2020)
8. X. Wang, Stability research of multistage gear transmission system with crack fault. *J. Sound Vib.* **434**, 63–77 (2018)
9. J. Chen et al., Study on reliability of shearer permanent magnet semi-direct drive gear transmission system. *Int. J. Fatigue* **132**, 105387 (2020)
10. K. Huang et al., Bifurcation and chaos analysis of a spur gear pair system with fractal gear backlash. *Chaos, Solitons Fractals* **142**, 110387 (2020)
11. Y. Yang et al., Nonlinear dynamic response of a spur gear pair based on the modeling of periodic mesh stiffness and static transmission error. *Appl. Math. Model.* **72**, 444–469 (2019)
12. W. Xiao et al., Effect of particle damping on high-power gear transmission with dynamic coupling for continuum and non-continuum. *Appl. Acoust.* **173**, 107724 (2021)
13. L.-Y. Zhu, J.F. Shi, X.F. Gou, Modeling and dynamics analyzing of a torsional-bending-pendular face-gear drive system considering multi-state engagements. *Mech. Mach. Theory* **149**, 103790 (2020)
14. D. Shin, A. Palazzolo, Nonlinear analysis of a geared rotor system supported by fluid film journal bearings. *J. Sound Vib.* **475**, 115269 (2020)
15. Y. Yi et al., Nonlinear dynamic modelling and analysis for a spur gear system with time-varying pressure angle and gear backlash. *Mech. Syst. Signal Process.* **132**, 18–34 (2019)
16. C.H. Chin et al., Durability assessment of suspension coil spring considering the multifractality of road excitations. *Measurement* **158**, 107697 (2020)
17. X. Shao et al., Coupling effect between road excitation and an in-wheel switched reluctance motor on vehicle ride comfort and active suspension control. *J. Sound Vib.* **443**, 683–702 (2019)
18. B. Huang et al., Development and optimization of an energy-regenerative suspension system under stochastic road excitation. *J. Sound Vib.* **357**, 16–34 (2015)
19. J. Yao et al., Analysis of the stability of nonlinear suspension system with slow-varying sprung mass under dual-excitation. *J. Sound Vib.* **425**, 124–136 (2018)
20. V. Roda-Casanova, F. Sanchez-Marin, Contribution of the deflection of tapered roller bearings to the misalignment of the pinion in a pinion-rack transmission. *Mech. Mach. Theory* **109**, 78–94 (2017)
21. D. Wei et al., Chaos vibration of pinion and rack steering trapezoidal mechanism containing two clearances. *Mech. Syst. Signal Process.* **92**, 146–155 (2017)

Harvesting Energy from 2D Array of Harvesters



Mohammad Reyaz Ahmad Vali and Ali Shaikh Faruque

1 Introduction

The dream of smart facilities across the world with information at everyone's hand requires sensing all around. This requires millions of sensors to be employed measuring different sets of data. Running these sensors requires electrical power. Thousands of wireless sensors are used for structural health monitoring, environmental control, military applications, etc. Powering them using batteries poses challenges in replacement, maintenance, and disposal. This can be overcome by directly powering them by ambient sources of energy. Vibrational energy from ambient sources is tapped to convert it into electrical energy by means of electromagnetic, electrostatic, and piezoelectric transduction [1–3]. In this study, electromagnetic principle is used to tap the ambient energy by means of 2D array of interconnected pendulums. Magnets are attached at the end of pendulums, and magnetic coil placed just below each of them serves the purpose of harvesting energy. The magnetic interaction among the neighboring pendulums is assumed to be small and is therefore neglected. Equations of motion are obtained from Lagrange's method, and voltage generated in each harvester is calculated by voltage equation for the coil [4]. Numerical solution of this system is obtained which provides time histories of displacement and velocity of harvesters. Mistuning of pendulum lengths is introduced to study the broadband harvesting characteristics of the system [5, 6]. Operating bandwidth of frequency is analyzed for different sets of values of mistuned lengths for 10×10 array for relatively optimal harvesting characteristics.

M. R. A. Vali (✉) · A. S. Faruque
Indian Institute of Technology Madras, Chennai, India

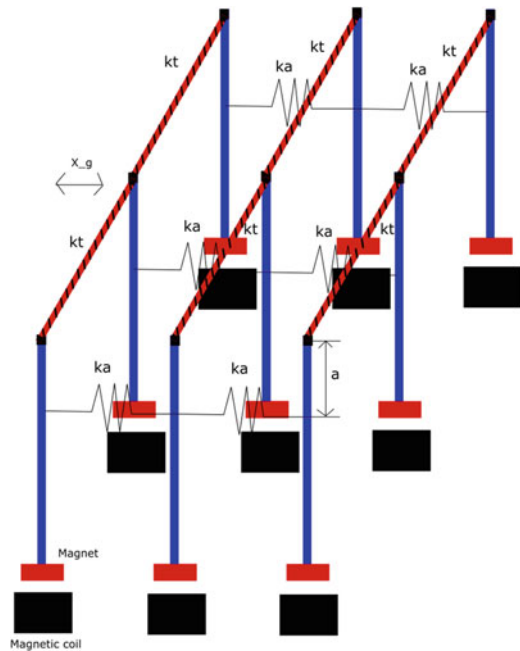
2 System Model and Mathematical Formulation

In this section, model of the system is explained with the schematic diagram, and governing equations of motion of the system is derived.

2.1 System Model

Figure 1 shows the schematic of the system which has been considered for study in this manuscript. It consists of a series of electromagnetic pendulum harvesters connected to the same base, and harmonic base excitation is given to the system. Each pendulum harvester has a magnet attached to its free end, and an electric coil is placed beneath it. Further, each pendulum is connected with another pendulum by a spring of stiffness “ ka ” at a distance of “ a ” from the hinge of the pendulum along the row wise, and torsional spring with stiffness of “ kt ” is attached to the base of the system along the column wise. Support excitation generates a relative motion between the coil and the magnet attached with the pendulum, and the change in magnetic field due to pendulum motion generates electricity in the coils. Voltage is received across each coil through a load resistor (R) connected to it. In Fig. 1, x_g denotes the amplitude of support motion which has been assumed to be harmonic in the current study. As standalone harvester produces less power, to generate

Fig. 1 Schematic of 2D array of harvesters



higher power, an array of tuned (lengths are the same) electromagnetic pendulum harvesters are used in this study. In practice, manufacturing a set of tuned harvesters is difficult. Further, due to operational non-similarity, tuning may get lost. There may be power loss from the designed power due to loss in tuning.

2.2 Mathematical Formulation

The mathematical equations for the abovementioned system is developed here. The magnetic interaction among the neighboring pendulums is assumed to be small and is, therefore, neglected.

Equations of Motion The equations are framed using Lagrange's equations [4, 7]. Final formulated equations are shown as below:

$$ml^2\ddot{\theta}_{i,j} + cl^2\ddot{\theta}_{i,j} + mgl \sin \theta_{i,j} + m\ddot{x}_g l \cos \theta_{i,j} - k_a a^2 \cos \theta_{i,j} (S_{j+1} + S_{j-1}) + k_t (T_{i+1} + T_{i-1}) = 0$$

$$i = 1, 2, \dots, z; j = 1, 2, \dots, n \quad (1)$$

where $S_{j+1} = \sin \theta_{i,j+1} - \sin \theta_{i,j}$; $S_{j-1} = \sin \theta_{i,j-1} - \sin \theta_{i,j}$; $T_{i+1} = \theta_{i+1,j} - \theta_{i,j}$; $T_{i-1} = \theta_{i-1,j} - \theta_{i,j}$; $z = \text{no. of rows}$; $n = \text{no. of columns}$.

The terms containing indices outside the ranges of i and j vanish for a given particular equation of the harvester.

Electrical Equation for Harvester The electrical equation of harvester is given as below where the equation of voltage developed in the individual harvester is given [7]:

$$V = BLD\omega \quad (2)$$

L = Coil length.

B = Magnetic flux density.

D = Distance between coil and magnet.

ω = Angular velocity of harvester.

3 Different Types of Mistuning Patterns

In this section, different patterns of mistuning considered for numerical simulations are discussed here for analyzing broadband harvesting characteristics of 10×10 array.

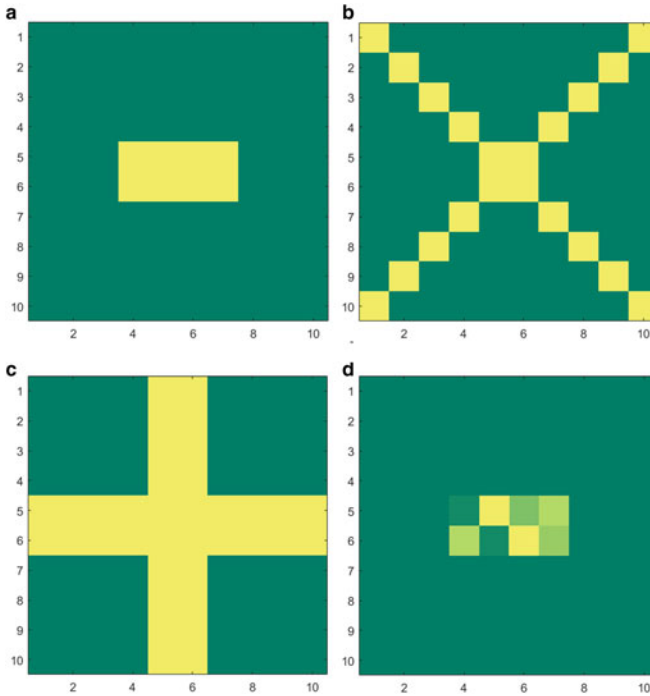


Fig. 2 Different types of mistuning patterns considered for study. **(a)** Rectangular mistuning. **(b)** Diagonal mistuning. **(c)** Middle rows and columns mistuned. **(d)** One of unsymmetric mistuning pattern

Study is done on 10×10 array. Mistuning in lengths of harvesters is considered for study. Random mistuning patterns based on positioning of mistuning and mistuning values of harvesters are designed and the mistuning patterns are divided as rectangular (sub-array of harvesters in center are mistuned), diagonal, middle rows and columns mistuned and unsymmetric mistuning. The matching of colors in the mistuned harvesters for Fig. 2a–c corresponds that the mistuned lengths are equal for those harvesters.

In symmetric mistuning patterns, it is considered that positions of mistuned harvesters are symmetric about the center of the array and percentage of mistuning is equal in the mistuned harvesters. In the present study, Fig. 2a–c types of symmetric mistuning patterns are studied. For unsymmetric mistuning patterns, positions of mistuning may or may not be symmetric, but the percentage of mistuning is different among them. The color deviation in the mistuned rectangular array at the center of Fig. 2d corresponds to different lengths of mistuned harvesters.

4 Results and Discussions

In this section, different results and observations from the numerical simulations are discussed. Unless otherwise mentioned, $k_a = 2 \text{ N/m}$ and $k_t = 0.02 \text{ N-m/rad}$ (Table 1).

4.1 Response of the System to Harmonic Excitation

For each type of mistuning pattern, simulations are ran for different positions and values of mistuning. These simulations are done for all types of mistuning patterns mentioned in Sect. 3. Harmonic excitation sweep is carried out from 0.8^* (natural frequency of tuned individual harvester) to 1.2^* (natural frequency of tuned individual harvester) for each of the mistuning pattern. From these sweeps, time histories of few harvesters at certain frequencies are shown in Fig. 3 to depict that the system is operating in nonlinear zone.

4.2 Power and Peak Power Plots

Different power plots showing the variation of maximum, minimum, and average power of individual harvesters and total power for each mistuning pattern for the entire frequency sweep are plotted. Peak power coming from each harvester is plotted with color code representing the distribution of peak power among the harvesters.

Figure 4 shows the power plots for one of rectangular mistuning pattern where the center 4×4 array is mistuned as -2% , and Fig. 5 represents its corresponding peak power plot.

Table 1 Values of parameters used in the simulations

Parameter	Value
Axial spring stiffness (k_a)	2 N/m
Torsional spring stiffness (k_t)	0.02 N-m/rad
Offset of axial spring (a)	0.02 m
Excitation amplitude (x_g)	2.3 mm
Distance between coil and magnet (D)	3 mm
Mechanical damping constant (c)	0.004 N-s/m
Magnetic flux density (B)	0.2094 T
Coil length (L)	10 m
Coil resistance (R)	120 Ω
Tuned pendulum length (l), Mass of each pendulum (m)	0.06 m 13 g

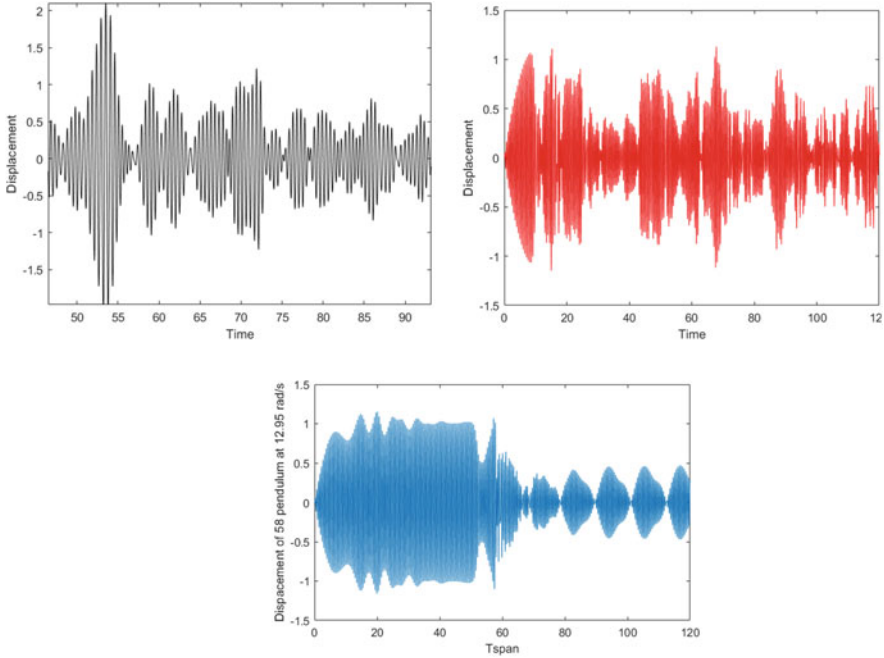


Fig. 3 Time histories of few harvesters from different mistuning patterns

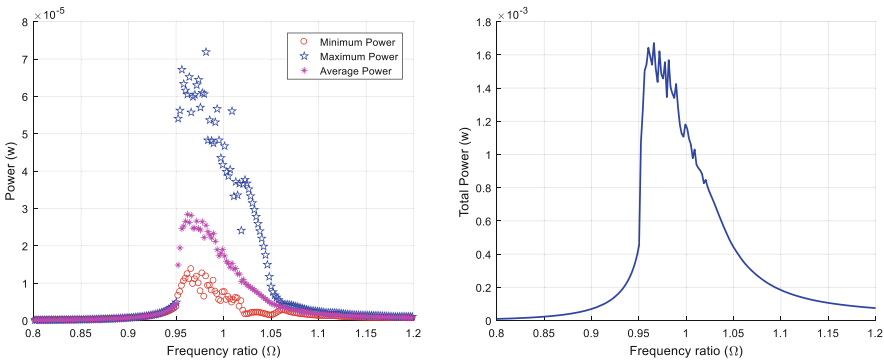


Fig. 4 Power plots for 4×4 mistuning in the center of 10×10 harvesters array

4.3 Observations in Peak Power Plots

- For symmetric mistuning patterns, the power FRFs of harvesters which are symmetric about rows' center line in peak power graph were found to be matching. So, the peak powers are also matching. These observations can be seen in the Figs. 6 and 7 for a few types of symmetric mistuning pattern.

Fig. 5 Peak power plot for 4×4 mistuning in the center of 10×10 harvesters array

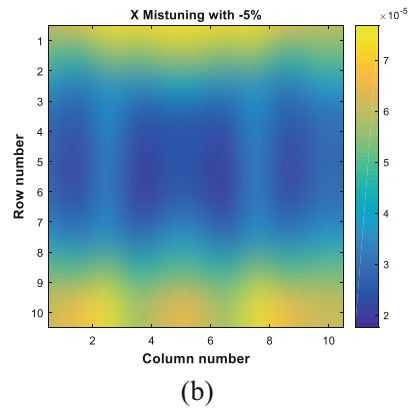
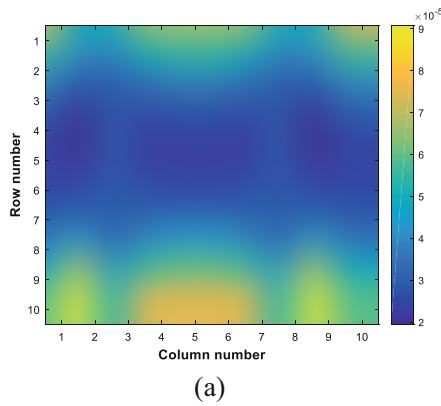
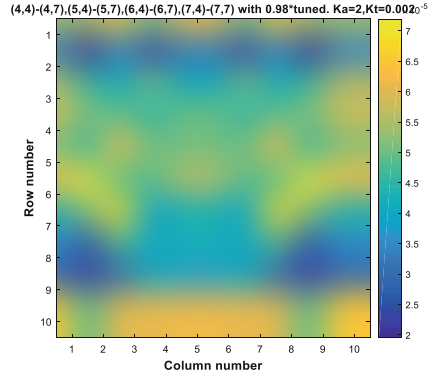


Fig. 6 Peak power distribution of (a) middle harvesters (center four harvesters) mistuned by -2% and (b) diagonal harvesters mistuned as -5%

- For the unsymmetric mistuning pattern, the power FRFs of harvesters which are not symmetric about rows' center line in peak power graph were found to be not matching. This can be seen in the Fig. 8 for a particular type of unsymmetric mistuning pattern.
- The time histories of symmetric harvesters along rows' center line for few mistuning patterns are showing frequency sync or almost frequency sync or complete sync at close to natural frequencies for visibly color matching of symmetric harvesters in peak power plot. This can be seen in Fig. 9 where frequencies or time scales were matching for few of the harvesters.
- For all mistuning patterns, given $ka = 2 \text{ N/m}$, and for certain values of kt , energy is getting concentrated in some local regions. For all mistuning patterns, at $ka = 2 \text{ N/m}$ and $kt = 0.02 \text{ N-m/rad}$, maximum peaks and close to maximum

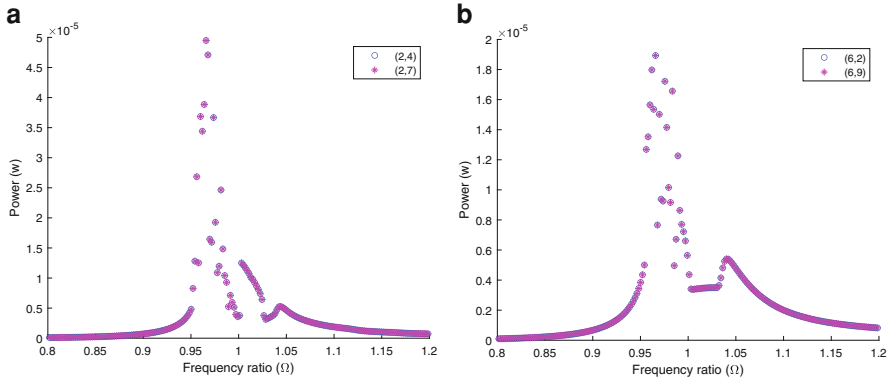
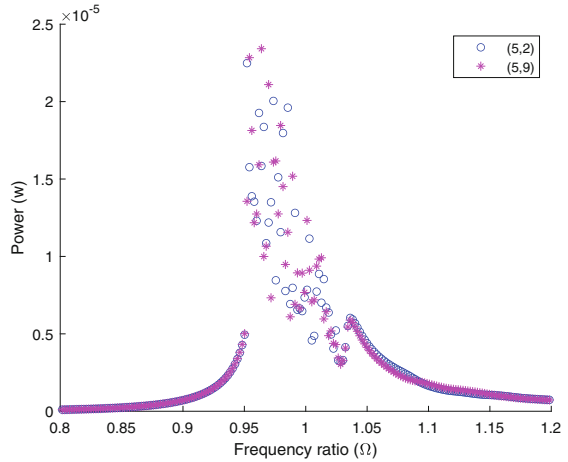


Fig. 7 Power FRFs for a set of symmetric harvesters for (a) middle harvesters (center four harvesters) mistuned by -2% and (b) diagonal harvesters mistuned as -5%

Fig. 8 Peak power distribution of unsymmetric mistuning with rectangular subset at center mistuned



peak are observed in the first two rows and last two rows, i.e., energy is getting concentrated in the first two rows and last two rows. This is shown in Fig. 10. This phenomenon of localization of energy can be made use by utilizing high-energy concentration pendulums as harvesters and remaining as oscillators to save the material for coils. So, in Fig. 10, the first two rows and last two rows can be harvesters, and the remaining pendulums can be oscillators.

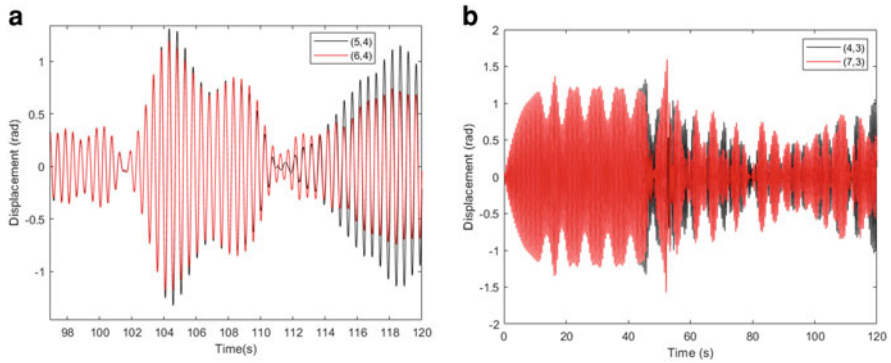


Fig. 9 Time histories of few of symmetric harvesters

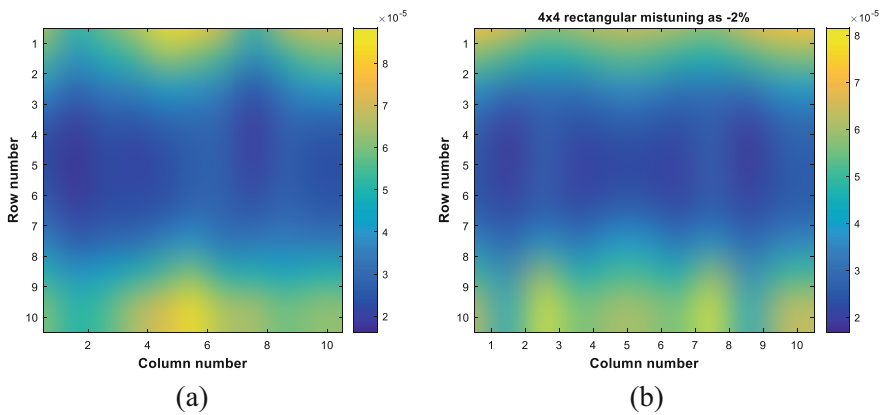


Fig. 10 Peak power distribution of (a) one of unsymmetric mistuning patterns (b) Peak power plots for 4×4 mistuning as -2% in the center of 10×10 harvesters array

4.4 Bandwidths Observed in Different Mistuning Patterns

Bandwidths are also calculated for these mistuning patterns, and from those, maximum bandwidth giving pattern for the required targeted power of 900 microwatts is identified. The maximum bandwidth pattern is middle two rows and columns mistuned as -2% .

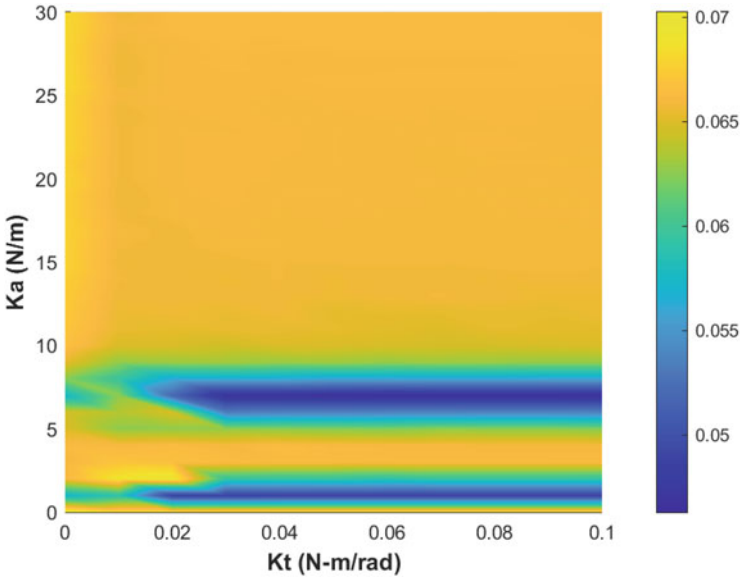


Fig. 11 Nondimensional bandwidth distribution at 900 mW with variation of stiffness values

4.5 Optimization of Bandwidth

The maximum bandwidth pattern is middle two rows and columns mistuned as -2% . For this mistuning pattern, the variation in bandwidth with change in values of stiffness is plotted. Torsional stiffness is varied from 0 to 0.1 N-m/rad, and axial stiffness is varied from 0 to 30 N/m. The distribution of nondimensional bandwidth (bandwidth/tuned pendulum natural frequency) at 900 mW can be seen in Fig. 11. From all these stiffness pairs, the stiffness pairs giving maximum bandwidth are identified. Optimum stiffness pairs are identified as $k_t = 0$ N-m/rad and $k_a = 0$ N/m. These pairs of stiffness, i.e., uncoupled configuration, gives maximum bandwidth.

5 Conclusions

The system under different patterns of mistuning is studied. Different observations from them are noted. Energy localization phenomenon is observed which can be used to save the material by removing electric coils below the harvesters which are giving less power. Later, the bandwidth for a mistuning pattern giving largest value of bandwidth among mistuning patterns is optimized for stiffness values, and it came out to be uncoupled configuration, which further reduces material used in form of springs.

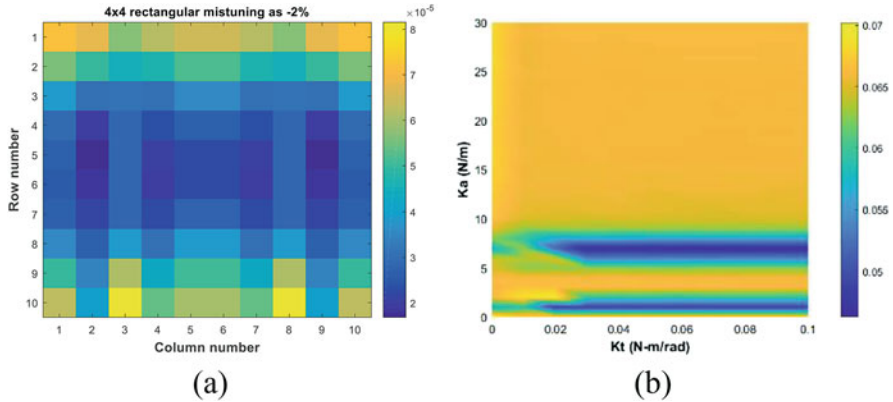


Fig. 12 (a) Energy localization phenomenon. (b) Distribution of bandwidth ratio with stiffness values

References

1. M. Rajarathinam, S.F. Ali, Energy generation in a hybrid harvester under harmonic excitation. *Energy Convers. Manag.* **155**, 10–19 (2018)
2. C.B. Williams, R.B. Yates, Analysis of a micro-electric generator for microsystems. *Sens. Actuators, A* **52**(1–3), 8–11 (1996)
3. Z. Hadas, M. Kluge, V. Singule, C. Ondrusek, Electromagnetic vibration power generator. In: *2007 IEEE International Symposium on Diagnostics for Electric Machines, Power Electronics and Drives*, pp. 451–455. IEEE (2007)
4. D. Bitar, N. Kacem, N. Bouhaddi, Multistability and modal interactions in periodic 2D coupled pendulums array. In: *ASME 2016 International Mechanical Engineering Congress and Exposition*, Phoenix (2016)
5. P.V. Malaji, S.F. Ali, Broadband energy harvesting with mechanically coupled harvesters. *Sensors Actuators A Phys.* **255**, 1–9 (2017)
6. A.V. Mohammad Reyaz, S.F. Ali, Harvesting energy from a series of harvesters, in *ICCMS 2020, Recent Advances in Computational Mechanics and Simulations*, ed. by K. S. Sandip, M. Mousumi, vol. 2, (Springer Nature, Singapore, 2021), pp. 573–585
7. A. Jallouli, N. Kacem, N. Bouhaddi, Nonlinear dynamics of a 2D array of coupled pendulums under parametric excitation. In: *5th ECCOMAS Thematic Conference on Computational Methods in Structural Dynamics and Earthquake Engineering (COMPdyn 2015)*, p. 8 p (2015)

Generalized Energy Balanced Method for a Combined Nonlinear Vibration Absorber Energy Harvester with Nonlinear Energy Sink



B. Santhosh, I. R. Praveenkrishna, and Aalokeparno Dhar

1 Introduction

Enhancing the performance of physical system considering nonlinearities leads to new design concepts in vibration absorption, vibration isolation, and energy harvesting [1]. Linear vibration absorbers without or with damping are effectively used to reduce the vibrations of primary systems in different applications [2, 3]. Nonlinear vibration absorbers are also effectively used in vibration attenuation. Nonlinear energy sink (NES) is a special type of absorber which has an essentially nonlinear element, a small mass and a damper is used in number of applications to effectively channelize the energy from the primary system [4]. NES facilitates irreversible transfer of energy through the process of targeted energy transfer (TET). Dynamics of NES based absorber systems were investigated using numerical and analytical methods to understand the energy transfer in such systems [5].

Energy harvesting from vibrations can be used in low power devices like sensors used in remote locations and in condition monitoring and bio-applications [6]. Linear vibration energy harvesters are more effective in a region close to the resonance. It is understood that nonlinear vibration energy harvesters do not have a preferential natural frequency and thus effective over a larger band of excitation frequencies [7]. Piezoelectric transduction mechanism is found to be the most effective way for the conversion of mechanical energy to electrical energy. Attempts were made in a direction to combine the vibration absorber and energy harvester

B. Santhosh (✉)

Department of Mechanical Engineering, Amrita School of Engineering, Amrita Vishwa Vidyapeetham, Coimbatore, India
e-mail: b_santhosh@cb.amrita.edu

I. R. Praveenkrishna · A. Dhar

Department of Aerospace Engineering, Indian Institute of Space Science and Technology, Valiamala, Thiruvananthapuram, India

system to develop a multifunctional energy harvesting system [8–10]. In this case, the vibrational energy transferred to the absorber can be harvested using a suitable transduction mechanism.

This work considers a combined vibration absorber energy harvester system and investigated using numerical and semi-analytical methods. The vibration absorber is used in as NES, and it is combined with a piezoelectric transduction mechanism for energy harvesting. The primary system is excited harmonically. The non-dimensional equations of motion are derived and the generalized harmonic energy balance method (HEBM) [11] is used along with numerical integration and conventional harmonic balance method (HBM) to investigate the dynamics of the system through phase plots, time history, and frequency response. The paper is organized as follows. The mathematical model is discussed in Sect. 2. The procedure involved in the formulation of HEBM is explained in Sect. 3. Important results based on HEBM, numerical integration, and HBM are discussed in Sect. 4. Conclusions and references are provided at the end.

2 Mathematical Model

The model of a harmonically excited linear primary system with nonlinear energy sink (NES) absorber and piezoelectric energy harvester is shown in Fig. 1. The primary linear system is with mass m_1 , stiffness k_1 , and damping c_1 . It is excited harmonically with a forcing function $F(t) = F_0 \cos \omega t$ with F_0 and ω as the amplitude and frequency of the external excitation. The NES system consists of a small mass m_2 , an essentially nonlinear stiffness element k_{2nl} , and viscous damping c_2 . The piezoelectric transduction mechanism attached to the NES is characterized by its capacitance C_p and internal resistance R_l . The response of the primary and NES systems is given by the coordinates X_1 and X_2 , and the voltage generated across the resistance is given by V . The equation of motion for the combined vibration absorber energy harvester system in dimensional form is given by

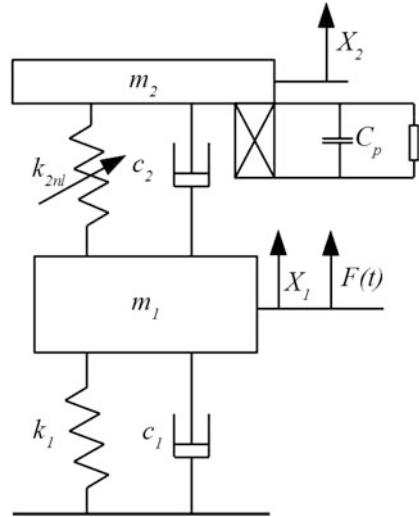
$$m_1 \ddot{X}_1 + c_1 \dot{X}_1 + k_1 X_1 + c_2 (\dot{X}_1 - \dot{X}_2) + k_{2nl} (X_1 - X_2)^3 = F_0 \cos \omega t \quad (1)$$

$$m_2 \ddot{X}_2 - c_2 (\dot{X}_1 - \dot{X}_2) - k_{2nl} (X_1 - X_2)^3 - \Theta_1 V = 0 \quad (2)$$

$$C_p \dot{V} + \frac{V}{R_l} + \Theta_2 \dot{X}_2 = 0 \quad (3)$$

Equation of motion can be expressed in the non-dimensional form by assuming the non-dimensional parameters, $x_1 = \frac{X_1}{X_{st}}$, $x_2 = \frac{X_2}{X_{st}}$, $X_{st} = \frac{F_0}{k_1}$, $\zeta_1 = \frac{c_1}{m_1 \omega_{n1}}$, $\zeta_2 = \frac{c_2}{m_1 \omega_{n1}}$, $\mu = \frac{m_2}{m_1}$, $\alpha_2 = \frac{k_{2nl}}{k_1} X_{st}^2$, $X_0 = \frac{F_0}{k_1 X_{st}}$, $\lambda = \frac{\omega}{\omega_{n1}}$, $v = \frac{V}{V_0}$, $\epsilon = \frac{1}{C_p R_l \omega_{n1}}$, $\chi = \frac{\Theta_1 V_0}{k_2 X_{st}}$, $\kappa = \frac{\Theta_2 X_{st}}{C_p V_0}$ with V_0 as a reference voltage and $\omega_{n1} = \sqrt{\frac{k_1}{m_1}}$. The order of primes denotes the differentiation with the non-dimensional time $\tau = \omega_{n1} t$. In the

Fig. 1 Harmonically excited primary system with NES absorber and piezoelectric energy harvester



next section, the computational methods used for the solution of the system are explained.

3 Generalized Harmonic Energy Balance Method

In this section, the generalized harmonic energy balance method (HEBM) used to find the periodic solutions of externally excited multi-degree of freedom nonlinear system is explained. The equation of motion for a general multi-degree of freedom system is given by

$$\mathbf{M}\ddot{\mathbf{x}} + \mathbf{C}\dot{\mathbf{x}} + \mathbf{K}\mathbf{x} + \mathbf{F}_{nl} = \mathbf{F}_{ext} \tag{4}$$

where \mathbf{M} , \mathbf{C} , and \mathbf{K} are the linear mass, damping, and stiffness matrices, \mathbf{x} is the displacement vector, \mathbf{F}_{nl} is the vector of nonlinear functions, and \mathbf{F}_{ext} is the vector of external excitation. The solution and its derivatives are expressed in a truncated Fourier series as

$$\mathbf{x} = \mathbf{X}^T \mathbf{n} \tag{5}$$

$$\dot{\mathbf{x}} = \omega \mathbf{X}^T \mathbf{n}' \tag{6}$$

$$\ddot{\mathbf{x}} = \omega^2 \mathbf{X}^T \mathbf{n}'' \tag{7}$$

where $\mathbf{n}(\tau)$ is the vector of Fourier functions with τ as the non-dimensional time and \mathbf{X} is the Fourier coefficient vector. Applying the approximation and time scaling, the equation of motion can be expressed as

$$r = \left(\omega^2 \mathbf{M} \mathbf{X}^T \mathbf{D}^{(2)T} + \omega \mathbf{C} \mathbf{X}^T \mathbf{D}^{(1)T} + \mathbf{K} \mathbf{X}^T \mathbf{D}^{(0)T} + \mathbf{F}_{\text{nl}}^T \mathbf{D}^{(0)T} - \mathbf{F}_{\text{ext}}^T \mathbf{D}^{(0)T} \right) \mathbf{n} \quad (8)$$

where $\mathbf{D}^{(0)} = \frac{1}{2\pi} \int_0^{2\pi} \mathbf{n} \mathbf{n}^T d\tau = \mathbf{I}$, $\mathbf{D}^{(1)} = \frac{1}{2\pi} \int_0^{2\pi} \mathbf{n}' \mathbf{n}^T d\tau$, $\mathbf{D}^{(2)} = \frac{1}{2\pi} \int_0^{2\pi} \mathbf{n}'' \mathbf{n}^T d\tau$.
Applying Galerkin procedure

$$\mathbf{R}_{HBM} = \frac{1}{2\pi} \int_0^{2\pi} \mathbf{r} d\tau \quad (9)$$

$$\mathbf{R}_{HBM} = \omega^2 \mathbf{M} \mathbf{X}^T \mathbf{D}^{(2)T} + \omega \mathbf{C} \mathbf{X}^T \mathbf{D}^{(1)T} + \mathbf{K} \mathbf{X}^T + \mathbf{F}_{\text{nl}}^T - \mathbf{F}_{\text{ext}}^T \quad (10)$$

The energy equation can be obtained as

$$\mathbf{y}^T (\mathbf{M} \ddot{\mathbf{x}} + \mathbf{C} \dot{\mathbf{x}} + \mathbf{K} \mathbf{x} + \mathbf{F}_{\text{nl}} - \mathbf{F}_{\text{ext}}) = 0 \quad (11)$$

where \mathbf{y} is the vector containing functions of \mathbf{x} , $\dot{\mathbf{x}}$. Using the Fourier approximation, the equation of motion can now be expressed as

$$r_E = \mathbf{n}^T \mathbf{Y} \left(\omega^2 \mathbf{M} \mathbf{X}^T \mathbf{D}^{(2)T} + \omega \mathbf{C} \mathbf{X}^T \mathbf{D}^{(1)T} + \mathbf{K} \mathbf{X}^T \mathbf{D}^{(0)T} + \mathbf{F}_{\text{nl}}^T \mathbf{D}^{(0)T} - \mathbf{F}_{\text{ext}}^T \mathbf{D}^{(0)T} \right) \mathbf{n} \quad (12)$$

Applying the Galerkin procedure to the new residue

$$R_E = \frac{1}{2\pi} \int_0^{2\pi} r_E d\tau \quad (13)$$

On combining the residues for original equation of motion r and the residue for the energy equation r_E , the new residue can be expressed as

$$\mathbf{R}_{HEBM} = \begin{bmatrix} R_{HBM} \\ R_E \end{bmatrix} \quad (14)$$

Minimizing the above residue using Galerkin procedure and subsequent application of Newton Raphson method to the resulting nonlinear equations results in actual Fourier coefficients. This method can be easily programmed and can be implemented with less computational effort.

4 Results and Discussions

In this section, the response of the combined vibration absorber harvester system considered in this paper is investigated using the energy balanced method, numerical integration, and conventional HBM.

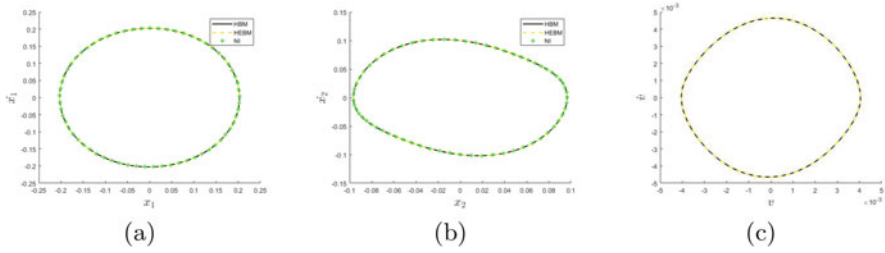


Fig. 2 Phase plane plots for (a) response of primary system (b) NES (c) voltage for $\lambda = 1$

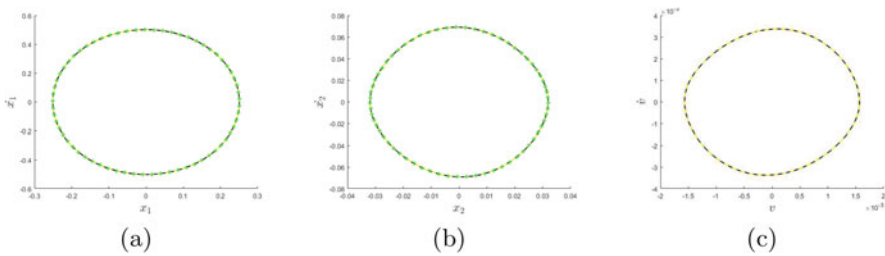


Fig. 3 Phase plane plots for (a) response of primary system (b) NES (c) voltage for $\lambda = 2$

4.1 HEBM Results

The phase plane plot of the response for $\zeta_1 = \zeta_2 = 0.01, \mu = 0.05, \alpha_2 = 0.25, \chi = 0.0467, \kappa = 0.0515, \epsilon = 0.6501, \lambda = 1,$ and $X_0 = 0.2$ is obtained by HEBM and is shown in Fig. 2a–c. The phase plane plots for $\lambda = 2$ and $X_0 = 1$ are shown in Fig. 3a–c. The HEBM results are found to match exactly with the numerical integration (NI) and harmonic balance method (HBM).

4.2 Numerical Analysis

To get further insight into the vibration absorption capability of the NES, the equations of motion are integrated numerically to understand the dynamics with $\zeta_1 = \zeta_2 = 0.01, \alpha_2 = 0.25, \mu = 0.05, \chi = 0.0467, \kappa = 0.0515, \epsilon = 0.6501, X_0 = 0.1,$ and $\lambda = 0.5$. The time histories of the primary system amplitude, NES amplitude, and voltage are shown in Fig. 4a, b. It is found that the amplitude of the primary system is less compared to the NES. Energy transfer takes place from the primary system to NES. The voltage generated also show substantial amplitude. The dynamics is investigated close to the linear resonance of the system by taking $\lambda = 1$ and retained the other parameters the same. The time history of the primary system response, NES, and the voltage obtained are shown in Fig. 5a, b. NES performs better in this frequency region also, and the voltage generated also has

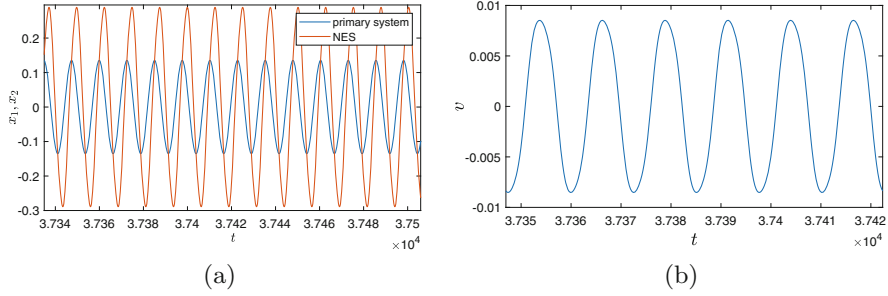


Fig. 4 Time history of (a) response of primary system and NES (b) voltage for $\lambda = 0.5$

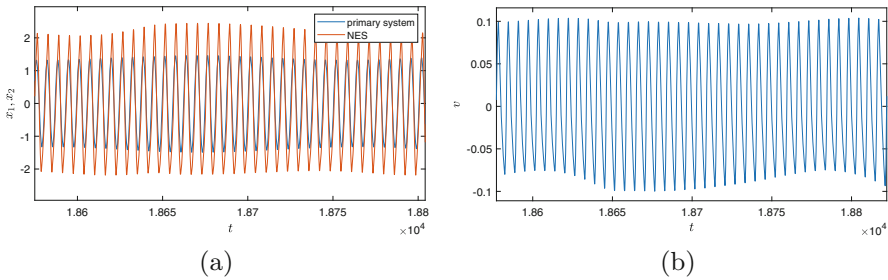


Fig. 5 Time history of (a) response of primary system and NES (b) voltage for $\lambda = 1$

substantial amplitude. The response of the NES is similar to the beat phenomenon and is known as the strongly modulated response (SMR). The transfer of energy from the primary system to NES takes place effectively when SMR is initiated [12].

4.3 Harmonic Balance Method for Frequency Response

In this section, the harmonic balance method (HBM) is used to find the periodic solutions of the system considered in this paper. In HBM, the response and its derivatives are assumed as a truncated Fourier series. The Fourier expressions are substituted in the equation of motion to find the residual. The residual is made orthogonal with respect to the basis function using the Galerkin procedure. This process generates a set of algebraic equations which will be solved numerically to find the unknown Fourier coefficients. There are variants of HBM like incremental harmonic balance (IHBM) and Fourier–Galerkin–Newton method (FGNM) which are successfully used to find periodic solutions of systems with continuous and discontinuous nonlinearities [13, 14]. HBM can be combined with a path tracing algorithm to generate the frequency response plots. In this section, HBM along with the arc length continuation method is used to obtain the frequency response plots for the response of the primary system, NES, and voltage generated. Frequency

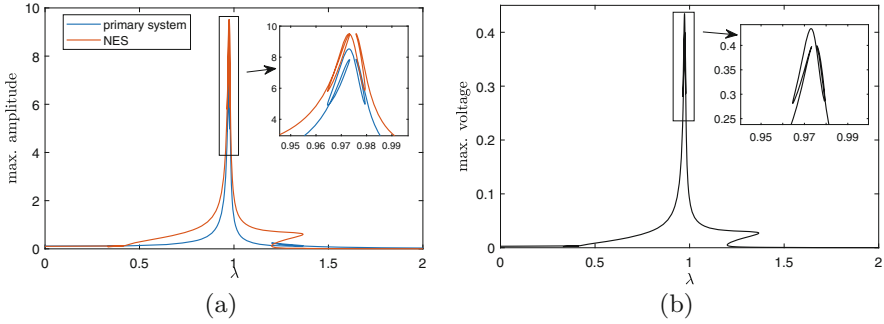


Fig. 6 Frequency response (a) amplitude of primary system and NES (b) maximum amplitude of voltage for $X_0 = 0.1$

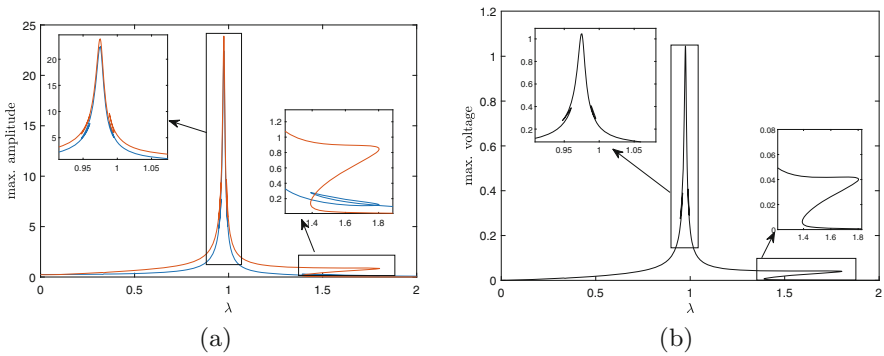


Fig. 7 Frequency response (a) amplitude of primary system and NES (b) maximum amplitude of voltage for $X_0 = 0.25$

response plots are generated for three values of excitation amplitudes $X_0 = 0.1, 0.25,$ and 0.5 and are shown in Figs. 6, 7, and 8. All the other parameters are retained as in the previous section.

The following observations were made with reference to the frequency response plots. The nonlinear behavior of the system is evident from the response plots with multiple solutions observed at different frequency ranges. The amplitude of NES is larger compared to the primary system indicating that the energy transfer takes place effectively in the system. The zoomed view of the multiple solution regions is shown in the inset. The frequency response of the voltage generated is also given, which shows substantial improvement with increase in the value of forcing amplitude.

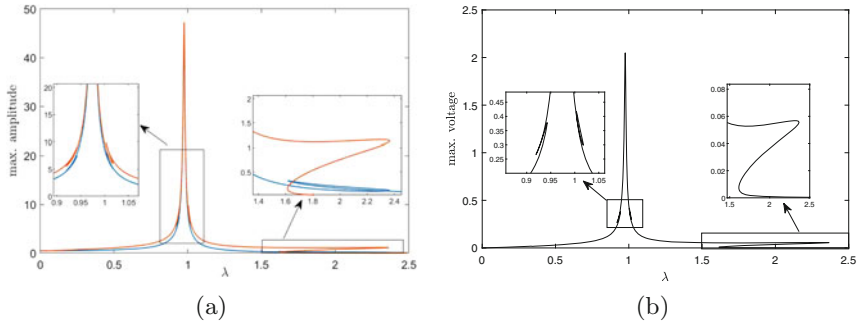


Fig. 8 Frequency response (a) amplitude of primary system and NES (b) maximum amplitude of voltage for $X_0 = 0.5$

5 Conclusions

The dynamics of an NES based vibration absorption system with a piezoelectric energy harvesting mechanism is investigated in this paper. The periodic solutions of the combined system are found using the generalized harmonic energy balance method. This is the first time that such a method is used to find the solution of multifunctional energy harvesting systems. The method is found to be a computationally efficient way to investigate dynamics of such systems. The time histories of the NES and primary system reveal the existence of strongly modulated response (SMR), which facilitate effective energy transfer close to the resonant region of the linear system. The frequency response plots obtained by harmonic balance method in combination with a continuation technique show multiple solution regions and also reveal the effectiveness of the NES in reducing the vibrations of the primary system. The generalized energy balance method along with the numerical solution and HBM is an effective tool for the analysis of multifunctional energy harvesting systems.

Acknowledgments The first two authors would like to acknowledge the research grant received under the TARE scheme of Science Engineering and Research Board (SERB), Department of Science and Technology (DST), Govt. of India under the sanction number :TAR/2019/000190.

References

1. D. Wagg, L. Virgin (eds.), *Exploiting Nonlinear Behavior in Structural Dynamics*, vol. 536 (Springer Science & Business Media, Wien, 2012)
2. G. Habib, G. Kerschen, G. Stepan, Chatter mitigation using the nonlinear tuned vibration absorber. *Int. J. Non-Linear Mech.* **91**, 103–112 (2017)
3. E. Verstraelen, G. Kerschen, G. Dimitriadis, Flutter and limit cycle oscillation suppression using linear and nonlinear tuned vibration absorbers, in *Shock & Vibration, Aircraft/Aerospace, Energy Harvesting, Acoustics & Optics*, vol. 9 (Springer, Cham, 2017), pp. 301–313

4. O.V. Gendelman, Y. Starosvetsky, M. Feldman, Attractors of harmonically forced linear oscillator with attached nonlinear energy sink I: description of response regimes. *Nonlinear Dyn.* **51**(1–2), 31–46 (2008)
5. Y. Starosvetsky, O.V. Gendelman, Vibration absorption in systems with a nonlinear energy sink: nonlinear damping. *J. Sound Vib.* **324**(3–5), 916–939 (2009)
6. N.G. Stephen, On energy harvesting from ambient vibration. *J. Sound Vib.* **293**(1–2), 409–425 (2006)
7. M.F. Daqaq, R. Masana, A. Erturk, D. Dane Quinn, On the role of nonlinearities in vibratory energy harvesting: a critical review and discussion. *Appl. Mech. Rev.* **66**(4), 040801 (2014)
8. A.S. Das, B. Santhosh, Energy harvesting from nonlinear vibration absorbers. *Procedia Eng.* **144**, 653–659 (2016)
9. P.V.R. Raj, B. Santhosh, Parametric study and optimization of linear and nonlinear vibration absorbers combined with piezoelectric energy harvester. *Int. J. Mech. Sci.* **152**, 268–279 (2019)
10. P.V.R. Raj, B. Santhosh, A comparative study on the primary system response and energy harvesting from linear and nonlinear tuned vibration absorbers, in *Advances in Rotor Dynamics, Control, and Structural Health Monitoring* (Springer, Singapore, 2020), pp. 429–440
11. N.N. Balaji, I.R.P. Krishna, C. Padmanabhan, A multi-harmonic generalized energy balance method for studying autonomous oscillations of nonlinear conservative systems. *J. Sound Vib.* **422**, 526–541 (2018)
12. Y. Starosvetsky, O.V. Gendelman, Strongly modulated response in forced 2DOF oscillatory system with essential mass and potential asymmetry. *Physica D Nonlinear Phenom.* **237**(13), 1719–1733 (2008)
13. B. Santhosh, C. Padmanabhan, S. Narayanan, Numeric-analytic solutions of the smooth and discontinuous oscillator. *Int. J. Mech. Sci.* **84**, 102–119 (2014)
14. I.R.P. Krishna, C. Padmanabhan, Improved reduced order solution techniques for nonlinear systems with localized nonlinearities. *Nonlinear Dyn.* **63**(4), 561–586 (2011)

Nonlinear Reduced Order Modeling of a Buckled Piezoelectric Beam for Energy Harvesting



X. Q. Wang, Yabin Liao, and M. P. Mignolet

1 Introduction

Piezoelectric energy harvesting from ambient vibrations has attracted extensive research interest as a potential solution to continuous and convenient energy supply for consumer electronics, wireless sensors, portable health monitors, etc. Earlier studies were focused on the harvesting of vibratory energy around a dominant natural frequency. This linear energy harvester performs well when the ambient vibration is narrow-banded close to the natural frequency but is less efficient when the environmental vibration has a wide frequency spectrum. In recent years, more and more research has been shifting to the utilization of nonlinear vibration behaviors to broaden the effective bandwidth of energy harvesting [1]. One such way is to use the buckling responses of the structure as a baseline configuration [2].

The study of nonlinear energy harvester motivated the development of efficient computational methods for the coupled electromechanical analysis of nonlinear energy harvesters. The technique of reduced order modeling appears to be an attractive one [3] since it significantly reduces the computational cost while essentially preserving the accuracy of prediction. As a matter of fact, a nonintrusive reduced order modeling methodology has been well developed for nonlinear geometric vibration, see the review paper [4]. This method is particularly noteworthy since the reduced order model is constructed using data from commercial finite element software; hence, it is applicable to practical and complex configurations. The method has been extended to include the thermal effects [5] and the piezoelectric

X. Q. Wang (✉) · M. P. Mignolet
Arizona State University, Tempe, AZ, USA
e-mail: xiaoquan.wang.1@asu.edu; xwang138@asu.edu

Y. Liao
Penn State Erie, The Behrend College, Erie, PA, USA

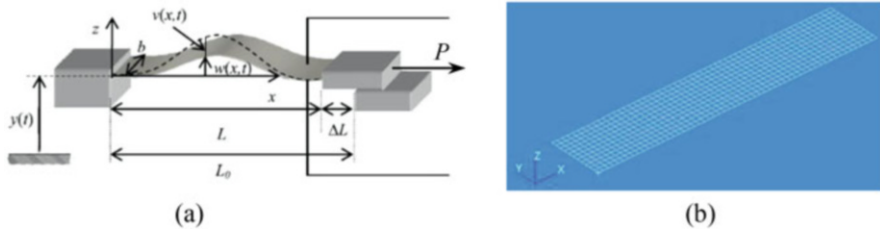


Fig. 1 The buckled piezoelectric beam for energy harvesting of [2]. (a) Beam configuration; (b) finite element model

effects through the piezoelectric-thermal analogy [6] and is also used for strongly nonlinear behavior such as the snap-through of curved structures [7, 8].

In this study, this nonintrusive reduced order modeling method is applied to the buckled piezoelectric beam configuration for energy harvesting of [2], as shown in Fig. 1a. The beam is subjected to an axial compressive force so that it would operate in a buckling status and a dynamic random acceleration is simulated as the source of energy harvesting. A finite element model of this beam structure is firstly constructed with Nastran, then the structural reduced order model including the piezoelectric effect is developed following the approach proposed in [6]. The reduced order model is next validated against Nastran results of nonlinear static and dynamic responses to the aforementioned load, then used to predict structural vibrations for various axial forces and corresponding voltage output assuming an open circuit.

2 Reduced Order Modeling of the Piezoelectric Beam

2.1 Finite Element Model

A finite element model of the piezoelectric beam was constructed with Nastran using CQUAD4 shell elements, as shown in Fig. 1b.

The geometric and material properties of the beam are essentially the same as those [2] listed in Table 1. These multilayer piezoelectric properties are defined using the composite material card with the CQUAD4 shell element. The beam is clamped at both ends, except for the right end which is free to move in the axial direction.

The thermal analogy is invoked with Nastran to implement the piezoelectric properties. This analogy is based on the similarity in the strain induced by the piezoelectric and thermal effects. For the current beam model, considering the piezoelectric material with direction 1 defined along the axial (X-) direction and direction 3 defined along the transverse (Z-) direction, the normal strain in the 1-

Table 1 Geometric and material properties of the beam

Property	Symbol	Value
Length	L_0	55 mm
Width	b	11 mm
Thickness of steel shim	h_s	0.1 mm
Thickness of piezo layer	h_p	0.08 mm
Density of steel shim	ρ_s	7850 kg/m ³
Density of piezo layer	ρ_p	4000 kg/m ³
Young's modulus of steel shim	E_s	2.03e+11 Pa
Young's modulus of piezo layer	E_p	4.00e+10 Pa
Damping ratio	ζ	0.02
Coupling coefficient	D_{31}	-10 pC/N
Electrical permittivity	ε_{33}^T	100 ε_0
Vacuum permittivity	ε_0	8.854e-12 F/m

direction induced by the piezoelectric effect, i.e., ε_1 , due to an applied electric field in the 3-direction, E_3 , is given as

$$E_{11}^{(s)} = d_{31} E_3^{(p)}, \quad (1)$$

where d_{31} is the piezoelectric coefficient. Assume that the electrical field is uniform and given as $E_3^{(p)} = V/h_p$, where V is the voltage across the PZT element (between the electrodes on the top and bottom surfaces) and h_p is the thickness of the PZT. Equation (1) can be rewritten as

$$E_{11}^{(s)} = d_{31} \cdot V/h_p, \quad (2)$$

On the other hand, the thermal strain induced by a temperature change is given as

$$E_{11}^{(s)} = \alpha_1 \cdot (T - T_{\text{ref}}), \quad (3)$$

where α_1 is the coefficient of thermal expansion, T the current temperature, and T_{ref} is the reference temperature.

Comparing Eqs. (2) and (3) and setting $T_{\text{ref}} = 0$ lead to the piezoelectric-thermal analogy

$$T = V \quad \text{when} \quad \alpha_1 = d_{31}/h_p, \quad (4)$$

that is, the piezoelectric effect can be equivalently modeled by a temperature change when the thermal expansion coefficient is set according to Eq. (4).

2.2 Reduced Order Modeling

Formulation. In the present nonlinear reduced order modeling approach, a set of basis functions are constructed so that the nonlinear structural displacements of the finite element model $\underline{u}(t)$, which are supposed to be well predicted by the developed reduced order model, are expressed as

$$\underline{u}(t) = \sum_{n=1}^N q_n(t) \underline{\phi}_n \quad (5)$$

where $q_n(t)$ is the time-dependent generalized coordinates and $\underline{\phi}^{(n)}$ are the set of basis functions. Noting that the nonlinear reduced order model is supposed to predict structural responses in both transverse and inplane directions, the basis functions should represent both with sufficient accuracy.

Assuming the material is linearly elastic and including the piezoelectric effect, the constitutive equation can be written as

$$S_{ij}^{(s)} = C_{ijkl} E_{kl}^{(s)} + e_{kij} E_k^{(p)}, \quad (6)$$

where $\underline{S}^{(s)}$ is the second Piola-Kirchhoff stress tensor, $\underline{E}^{(s)}$ is the Green strain tensor related to the structural displacement, \underline{u} , e_{kij} is the electromechanical coupling coefficients, and $\underline{E}^{(p)}$ is the electric field vector.

The electric field can be expressed as, in terms of a set of electric basis functions

$$\underline{E}^{(p)}(t) = \sum_{m=1}^{N_p} \tau_m^{(p)}(t) \cdot \underline{\phi}_m^{(p)}. \quad (7)$$

Substituting Eqs. (5) and (7) into Eq. (6) and using the Galerkin approach, the governing equation of the nonlinear reduced order model is obtained as

$$M_{ij} \ddot{q}_j(t) + D_{ij} \dot{q}_j(t) + K_{ij}^{(1)} q_j(t) + K_{ijl}^{(2)} q_j(t) q_l(t) + K_{ijlp}^{(3)} q_j(t) q_l(t) q_p(t) - K_{ijm}^{(p)} q_j(t) \tau_m^{(p)}(t) = F_i(t) + F_{im}^{(p)} \tau_m^{(p)}(t), \quad (8)$$

$i, j=1, 2, \dots, N$; $l=j, j+1, \dots, N$; $p=l, l+1, \dots, N$; and $m=1, 2, \dots, N_p$,

where M_{ij} denotes the elements of the mass matrix, $K_{ij}^{(1)}$, $K_{ijl}^{(2)}$, and $K_{ijlp}^{(3)}$ are the linear, quadratic, and cubic stiffness coefficients, $K_{ijm}^{(p)}$, and $F_{im}^{(p)}$ are the electromechanical coupling coefficients, and $F_i = \underline{\phi}_i^T \underline{F}$ is the modal force associated

with mode i . The damping matrix D_{ij} is added to collectively represent various energy dissipation mechanisms. One commonly used damping model, the Rayleigh damping model, is adopted in this paper, defined as $D_{ij} = \alpha M_{ij} + \beta K_{ij}^{(1)}$, where α and β are the Rayleigh damping coefficients. Summation over repeated indices is implied here.

In nonintrusive reduced order models, the ROM matrices in Eq. (8) are identified using data from commercial finite element software. The computation of the mass and linear stiffness matrices is straightforward once their finite element counterparts $M^{(FE)}$ and $K^{(FE)}$ are extracted from the finite element software, as the following

$$M = \Phi^T M^{(FE)} \Phi \quad \text{and} \quad K^{(1)} = \Phi^T K^{(FE)} \Phi. \tag{9}$$

The damping matrix can then be computed using the Rayleigh damping model.

The evaluation of the nonlinear stiffness coefficients, $K_{ijl}^{(2)}$, and $K_{ijlp}^{(3)}$, has to proceed differently since the global nonlinear stiffness operator is typically not computed/not available in a commercial finite element code. The evaluation is carried out without electromechanical or thermal-structural coupling.

In one proposed approach, the displacement-force method [9, 10], a set of designed static displacements are imposed to the structure, and the corresponding nonlinear forces are obtained from the finite element code. They are then used to compute the corresponding modal forces F_i . Finally, imposing the same modal displacements and modal forces to the ROM governing equation, Eq. (8), leads to the conditions

$$K_{ij}^{(1)} q_j + K_{ijl}^{(2)} q_j q_l + K_{ijlp}^{(3)} q_j q_l q_p = F_i, \tag{10}$$

which can be used to determine the stiffness coefficients $K_{ijl}^{(2)}$ and $K_{ijlp}^{(3)}$.

When the basis of a ROM is large, this displacement-force method requires a large number of static solutions, i.e., $O(N^3/6)$. To resolve this issue, a method using the tangent stiffness matrix denoted as $K^{(T)}$, in the identification has been developed [11]. This displacement- $K^{(T)}$ method relies on the availability of the tangent stiffness matrix for each imposed displacement. Once this matrix has been obtained, it is projected on the basis and then matched to its ROM counterpart of iu element given by

$$K_{iu}^{(T)} = \frac{\partial F_i}{\partial q_u} = K_{iu}^{(1)} + [K_{iju}^{(2)} + K_{iuj}^{(2)}] q_j + [K_{ijlu}^{(3)} + K_{ijul}^{(3)} + K_{iujl}^{(3)}] q_j q_l. \tag{11}$$

Construction of the Current ROM. From the above formulation, it can be seen that there remain two key issues in the nonlinear reduced order modeling: (a) the construction of basis functions, and (b) the identification of electromechanical coupling coefficients.

(a) *Construction of Basis Functions.* The basis functions of the reduced order model should account for both transverse and inplane displacements. For the present beam structure, the following basis functions are included:

1. For the transverse displacements, linear modes of the structure are usually the first choice. For the present beam structure, the first two symmetric “beam-like” linear modes are taken as transverse basis functions since they are dominant in transverse structural responses.
2. Noting that the beam buckles in the current study under the action of an axial compressive force, the linear response of the beam to such an axial force, normalized with respect to the mass matrix of the beam, is taken as the third basis function. This basis function included only inplane displacements.
3. Finally, for the inplane displacements due to the nonlinear geometric effect (membrane stretching), some “dual modes” are constructed, see [4] and [5–9, 11, 12]. The dual modes are extracted from a set of nonlinear static displacements which are the responses to the loadings that, in the linear case, would induce the displacements along a single or combination of two selected transverse basis functions. To this end, these loadings are generated as the forces on the finite element mesh of the form

$$\underline{F}_{ij,s}^{(FE)} = K^{(FE)} \left[\pm \alpha_{ij,s} \left(\underline{\phi}_i + \underline{\phi}_j \right) / 2 \right], \quad (12)$$

where i and j are the indices of the two transverse basis functions (the case $i = j$ emulates the single basis function case). In this equation, $\alpha_{ij,s}$ are a set of scaling factors selected so that the corresponding structural response spans a given range of levels. In this study, three combinations out of the two transverse basis functions taken in (1), i.e., combo $i - j = 1-1, 1-2,$ and $2-2,$ are considered, and s spans 10 levels with the maximum transverse displacement of about six thicknesses. Once these responses have been obtained from Nastran, their transverse components are first removed by making the displacements orthogonal to the two transverse basis functions. Next, a proper orthogonal decomposition (POD) analysis is carried out and dominant POD eigenvectors are retained as dual modes. For the current beam structure, one dual mode is taken from each combination, and totally three dual modes are constructed.

The final basis has six basis functions.

(b) *Identification of Stiffness and Electromechanical Coupling Coefficients*

The identification of electromechanical coupling coefficients is performed as follows. For the $K_{ijm}^{(p)}$ coefficients, the displacement- $K^{(T)}$ method is used with the applied electric (temperature) field from each electric (thermal) mode, $\tau_m^{(p)} \underline{\phi}_m^{(p)}$, instead of the imposed displacement. The corresponding tangent stiffness matrix is expressed as

$$K_{iu}^{(T)} = K_{iu}^{(1)} - K_{ium}^{(p)} \tau_m^{(p)}. \tag{13}$$

The coefficient $K_{ijm}^{(p)}$ is then obtained as $K_{ijm}^{(p)} = [K_{ij}^{(1)} - K_{ij}^{(T)}] / \tau_m^{(p)}$.

For the $F_{im}^{(p)}$ coefficients, the same electric field, $\tau_m^{(p)} \phi_m^{(p)}$, is applied to the Nastran mesh with all degrees of freedom blocked. The corresponding reaction forces of a linear static solution are then output, from which the corresponding modal forces F_i are computed. They are related to the $F_{im}^{(p)}$ coefficients by $F_i = F_{im}^{(p)} \tau_m^{(p)}$, from which the coefficient $F_{im}^{(p)}$ is computed as $F_{im}^{(p)} = F_i / \tau_m^{(p)}$.

3 Results and Discussions

3.1 Validation Results

Critical Buckling Load and Modes. Firstly, a buckling analysis is carried out using the constructed ROM. The predicted inplane critical buckling force is $P = -10.78$ N (see Fig. 1a), matching very well the Nastran result of -10.75 N. The agreement of the predicted buckling mode shape, not present here for brevity, is also very good.

Nonlinear Static Responses. The constructed ROM is then validated against the Nastran results for combined transverse and axial static forces. The transverse force is equivalent to the amplitude of the force due to the base acceleration at the level of 3 g. The single axial compressive force P of Fig. 1a is also applied with increasing magnitude so that the beam will buckle eventually.

Shown in Fig. 2 are the ROM predictions as compared to the Nastran results. The agreement is very good for both the transverse (Z-) and the inplane (X-) displacements until the beam starts to buckle.

It should be noted that the structural response in this region is very sensitive to the key stiffness coefficients. In fact, shown in Fig. 2 are the predictions of two ROMs, the first one with stiffness coefficients as identified and the other with the

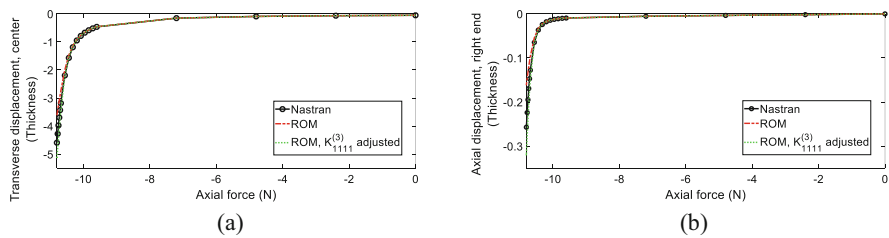


Fig. 2 Comparison of static displacements, ROM versus Nastran, as a function of axial force P . (a) Transverse displacement, center point, and (b) Inplane displacement right end point

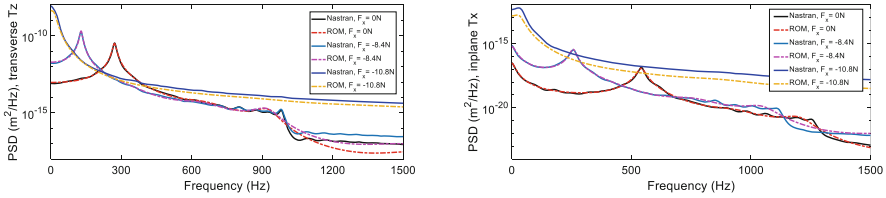


Fig. 3 Comparison of the power spectral density (PSD) of the center displacement in dynamic response. ROM versus Nastran. (a) Transverse (Z-direction); and (b) Inplane (X-direction)

key stiffness coefficient $K_{1111}^{(3)}$, the cubic coefficient of linear mode 1, reduced by a tiny amount, i.e., 0.035%. One can see that the response has a significant change due to this very small adjustment. This has been discussed in [12], where a tuning technique was developed to cope with this high sensitivity issue. In this study, the original ROM is retained, and the tuning technique will be implemented in the subsequent extensive studies.

Nonlinear Dynamic Responses. The constructed ROM is used to predict the dynamic structural responses which are the source of energy harvesting. Spatially, the dynamic load is the same as the previous static load, but temporally, the transverse force has a random time-variant part, given as the bounded white noise with the cutoff frequency of 1000 Hz.

Shown in Fig. 3 are the power spectral densities of transverse and inplane displacements at the beam center point predicted by the ROM, as compared to Nastran results, for three axial forces $P = 0$ N, -8.4 N, and -10.8 N. When the axial force is zero, there is a clear frequency peak in the spectra. When the force is increased to -8.4 N, the peak is shifted to the lower frequency due to the softening effect of the axial force. When the force is further increased to -10.8 N, just above the buckling force, the peak in the transverse PSD almost disappears, suggesting the buckling is occurring. For the first two axial force levels, the ROM predictions match Nastran results very well, and for the last axial force, the matching of the transverse PSD is still good although that of the inplane PSD becomes a little worse. Based on these results and the static ones of Fig. 2, it is concluded that the constructed ROM is very good to excellent up to the buckling.

3.2 Electromechanical Analysis: Voltage Output with Open Circuit

The time histories of the structural generalized coordinates obtained from the constructed ROM are further used to predict the voltage output of the piezoelectric layers. This is done by assuming an open-loop circuit and ignoring the piezoelectric feedback effect on the structural vibration. Specifically, the formula derived in [6] is

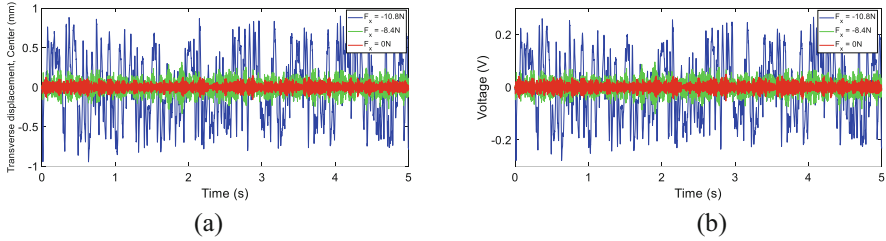
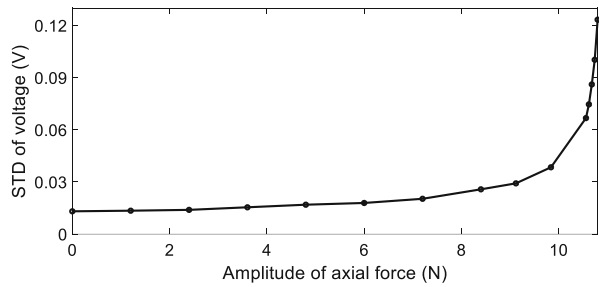


Fig. 4 Time history of (a) beam center structural displacement and (b) output voltage

Fig. 5 The standard deviation (STD) of voltage output induced by the structural dynamic vibration, as a function of the applied axial force



revised for the current uniform electric field, and the voltage output due to structural vibration is then

$$V(t) = \left[\frac{1}{2} K_{ijm}^{(p)} q_i(t) q_j(t) + F_{im}^{(p)} q_i(t) \right] / C_p, \tag{14}$$

where $K_{ijm}^{(p)}$ and $F_{im}^{(p)}$ are the electromechanical coupling coefficients in Eq. (8), $m = 1$ corresponding to the uniform electric field, and C_p is the total electric capacity of the piezoelectric patch. This effort is carried out for the dynamic base acceleration of 3 g and a set of applied axial forces P .

Shown in Fig. 4 are the time histories of the beam center transverse displacement and the output voltage for three representative axial forces, $P = 0$ N, -8.4 N, and -10.8 N, as in Fig. 3. The time history plots clearly show that the buckling occurs when the applied axial force exceeds the buckling threshold ($P = -10.78$ N) and that the vibration magnitude and the corresponding output voltage are significantly increased. The time variations of these two entities are very similar because the effect of nonlinear coupling, dictated by $K_{ijm}^{(p)}$, is, in fact, very small here.

Furthermore, the standard deviation (STD) of the time-variant voltage output is computed and shown in Fig. 5. It can be seen that when the axial force is small and well below the buckling value, the output voltage is small. However, when the force is increased to approach the buckling threshold, the output voltage becomes larger, and once the force exceeds the buckling value, there is a significant increase in the output voltage. This is consistent with the observation in the literature [13].

4 Summary

A nonlinear reduced order model (ROM) has been developed for a piezoelectric energy harvesting beam structure subjected to a random base acceleration and an axial compressive force for potential operation around the buckled configuration. The nonintrusive ROM is constructed using a finite element model and data from commercial software (Nastran). The ROM predictions are shown to match very well for the critical buckling force and shape and the static and dynamic responses to the aforementioned working load. Given the ROM computed structural responses for a set of axial forces, the corresponding voltage outputs are also determined. It is shown that the voltage is significantly increased when the beam is right on the buckling configuration, which is consistent with the observation in the literature. The developed ROM provides a computationally efficient tool for the analysis of the piezoelectric energy harvester and can be further used in the fully coupled electromechanical analysis.

References

1. M.F. Daqaq, R. Masana, A. Erturk, D.D. Quinn, On the role of nonlinearities in vibratory energy harvesting: A critical review and discussion. *ASME Appl. Mech. Rev.* **66**, 040801 (2014)
2. F. Cottone, L. Gammaitoni, H. Vocca, M. Ferrari, V. Ferrari, Piezoelectric buckled beams for random vibration energy harvesting. *Smart Mater. Struct.* **21**, 035021 (2012)
3. M.F. Daqaq, T. Seuaciuc-Osorio, On the reduced order modeling of energy harvesters. *J. Intell. Mater. Syst. Struct.* **20**, 2003–2016 (2009)
4. M.P. Mignolet, A. Przekop, S.A. Rizzi, S.M. Spottswood, A review of indirect/non-intrusive reduced order modeling of nonlinear geometric structures. *J. Sound Vib.* **332**, 2437–2460 (2013)
5. R.A. Perez, X.Q. Wang, M.P. Mignolet, Nonlinear reduced order models for thermoelastodynamic response of isotropic and FGM panels. *AIAA J.* **49**, 630–641 (2011)
6. V. Vyas, X.Q. Wang, A. Jain, M.P. Mignolet, Nonlinear geometric reduced order model for the response of a beam with a piezoelectric actuator, in Proceedings of the 56th SDM Conference (AIAA SciTech), Kissimmee, Florida, USA, January 5–9, 2015. AIAA Paper AIAA-2015-0692 (2015)
7. S.M. Spottswood, T.G. Eason, X.Q. Wang, M.P. Mignolet, Nonlinear reduced order modeling of curved beams: A comparison of methods, in Proceedings of the 50th SDM Conference (AIAA SciTech), Palm Springs, California, USA, May 4–7, 2009. AIAA Paper AIAA-2009-2433 (2009)
8. J. Lin, X.Q. Wang, M.P. Mignolet, On the detection and capturing of strongly nonlinear geometric events with reduced order models, in Proceedings of the 38th IMAC, Conference and Exposition on Structural Dynamics, Houston, Texas, USA, Feb 10–13, 2020. Paper 8471 (2020)
9. K. Kim, A.G. Radu, X.Q. Wang, M.P. Mignolet, Nonlinear reduced order modeling of isotropic and functionally graded plates. *Int. J. Non Linear Mech.* **49**, 100–110 (2013)
10. A. Przekop, S.A. Rizzi, A reduced order method for predicting high cycle fatigue of nonlinear structures. *Comput. Struct.* **84**, 1606–1618 (2006)

11. R.A. Perez, X.Q. Wang, M.P. Mignolet, Non-intrusive structural dynamic reduced order modeling for large deformations: Enhancements for complex structures. *J. Comput. Nonlinear Dyn.* **9**, 031008 (2014)
12. J. Lin, X.Q. Wang, M.P. Mignolet, Non-intrusive identification of nonlinear reduced order models: Symmetry and tuning, in *Proceedings of the 38th IMAC, Conference and Exposition on Structural Dynamics*, Houston, Texas, USA, Feb 10–13, 2020. Paper 8656 (2020)
13. H. Vocca, F. Cottone, I. Neri, L. Gammaitoni, A comparison between nonlinear cantilever and buckled beam for energy harvesting. *Eur. Phys. J. Spec. Top.* **222**, 1699–1705 (2013)

Part IV
MEMS/NEMS

Full-Order Frequency-Domain Simulations of Nonlinear Piezoelectric MEMS



Andrea Opreni and Attilio Frangi

1 Introduction

Scanning micromirrors belong to the family of optical Micro-Electro-Mechanical Systems (MEMS), i.e. MEMS that involve sensing or manipulating optical signals on a very small size scale, using integrated mechanical, optical, and electrical systems [1]. Successful applications range from consumer pico projectors to holographic lenses [2].

Several actuation systems have been proposed in the past. In [3, 4] prototypes of electrostatic micromirrors have been thoroughly analyzed, with particular emphasis on the phenomenon of parametric resonance which governs their dynamical response. However, mainly due to the high level of voltage bias required to control the device and to the strong nonlinearities in the response, the attention has progressively shifted towards magnetic- [5] and piezo-actuation [6]. One of the expected benefits is an enhanced linear behavior, even if the large rotations experienced by the mirror generally prevent reaching a perfectly linear regime.

Focusing on piezoelectric actuation, this is achieved exploiting piezoelectric materials as Lead-Zirconate Titanate (PZT) [7] or Aluminum Nitride [8], the former being the preferred choice since it has large electromechanical coupling coefficients [9].

Even if piezoelectric actuation develops higher forces compared to electrostatic actuation at moderate voltages, the electric fields generated within thin piezoelectric films reach values that deny the validity of the linearized theory of piezoelectric materials [10]. Indeed, assuming a voltage bias of 10 V, across a piezoelectric film with a thickness of 1 μm , electric fields of the order of 10^7 V/m are generated within

A. Opreni (✉) · A. Frangi

Department of Civil and Environmental Engineering, Politecnico di Milano, Milano, Italy

e-mail: andrea.opreni@polimi.it; attilio.frangi@polimi.it

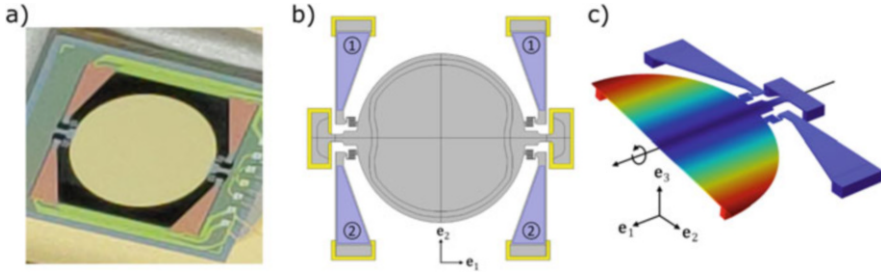


Fig. 1 Optical image of the device (a), schematic representation of the tested device (b), and displacement field of the excited mode (c)

the material, hence electromechanical nonlinearities arise. Therefore, a complete model for predicting the dynamic response of piezoelectric micromirrors should account for two main types of nonlinearities: geometric and piezoelectric.

In the present work, a fully nonlinear model to describe the nonlinear dynamic behavior of piezo MEMS subjected to finite transformations is detailed. The model is an extension of the technique presented in [11, 12] and it aims at adding the effect of large displacements of the piezoelectric films upon device actuation. Validation of the model is performed on the device depicted in Fig. 1a. The full-order model is derived using the finite element approximation of the differential equation that stems from the approach in [11] for MEMS actuated with thin films of piezoelectrics, and the resulting system of differential equations is solved using the Harmonic Balance Method (HBM) to compute the steady dynamic response of the system.

The remainder of the paper is organized as follows. In Sect. 2 we introduce the nonlinear model for piezoelectric MEMS developed in [11, 12]. Next, in Sect. 3 we provide a comprehensive description of the device and its experimental characterization. In Sect. 4 we report the comparison between the proposed model and the experimental data. At last, in Sect. 5 we summarize the outcomes the present work.

2 Full-Order Nonlinear Piezoelectric Model and Numerical Methods

We start our derivation from the principle of virtual power written in spatial configuration for a mechanical system:

$$\int_{\Omega} \rho \mathbf{u}_{tt} \cdot \mathbf{w} \, d\Omega + \int_{\Omega} \boldsymbol{\sigma}[\mathbf{u}, \mathbf{p}] : \nabla \mathbf{w} \, d\Omega = 0 \quad \forall \mathbf{w} \in \mathcal{C}(\mathbf{0}) \quad (1)$$

where ρ is the density in spatial configuration, \mathbf{u} is the displacement field, $(\cdot)_{tt}$ is the time derivative operator applied twice, $\boldsymbol{\sigma}[\mathbf{u}, \mathbf{p}]$ is the Cauchy's stress tensor, \mathbf{w} is a

suitable test function belonging to the space $\mathcal{C}(\mathbf{0})$, that is the space of functions that vanish on the boundary where Dirichlet boundary conditions on the displacement field are prescribed, Ω is the domain in spatial configuration, and $\nabla(\cdot)$ is the spatial gradient operator. Square brackets highlight that in the application at hand the stress tensor is a function of both displacement vector \mathbf{u} and polarization vector \mathbf{p} .

In piezoelectric materials, in accordance with the Landau-Devonshire theory of ferroelectrics [13], the polarization field induces inelastic stresses within the material. Therefore, we operate an additive decomposition of $\boldsymbol{\sigma}[\mathbf{u}, \mathbf{p}]$ in an elastic term $\boldsymbol{\sigma}^e[\mathbf{u}]$, and an inelastic one $\boldsymbol{\sigma}^p[\mathbf{p}]$, that is $\boldsymbol{\sigma}[\mathbf{u}, \mathbf{p}] = \boldsymbol{\sigma}^e[\mathbf{u}] - \boldsymbol{\sigma}^p[\mathbf{p}]$. This allows rewriting Eq. (1) as:

$$\int_{\Omega} \rho \mathbf{u}_{tt} \cdot \mathbf{w} \, d\Omega + \int_{\Omega} \boldsymbol{\sigma}^e[\mathbf{u}] : \nabla \mathbf{w} \, d\Omega = \int_{\Omega} \boldsymbol{\sigma}^p[\mathbf{p}] : \nabla \mathbf{w} \, d\Omega \quad \forall \mathbf{w} \in \mathcal{C}(\mathbf{0}) \quad (2)$$

We introduce the assumption that the orientation of the polarization field is not affected by the motion of the system. This assumption is introduced since in MEMS the piezoelectric patches used for actuation are placed in sections of the structure that do not undergo large strains. Furthermore, we describe the system with respect to reference configuration using the well known transformation derived from the theory of finite elasticity:

$$\begin{aligned} \int_{\Omega_0} \rho_0 \mathbf{u}_{tt} \cdot \mathbf{w} \, d\Omega_0 + \int_{\Omega_0} \mathbf{S}^e[\mathbf{u}] : (\mathbf{F}^T \nabla_0 \mathbf{w}) \, d\Omega_0 = \\ \int_{\Omega_0} \mathbf{S}^p[\mathbf{p}] : (\mathbf{F}^T \nabla_0 \mathbf{w}) \, d\Omega_0 \quad \forall \mathbf{w} \in \mathcal{C}(\mathbf{0}) \end{aligned} \quad (3)$$

where Ω_0 is the domain in reference configuration, ρ_0 is the density of the material in reference configuration, \mathbf{F} is the deformation gradient, i.e. $\mathbf{I} + \nabla_0 \mathbf{u}$ with \mathbf{I} identity tensor, $\mathbf{S}^e[\mathbf{u}]$ is the elastic second Piola-Kirchhoff stress tensor, $\mathbf{S}^p[\mathbf{u}]$ is the inelastic second Piola-Kirchhoff stress tensor, and $\nabla_0(\cdot)$ is the gradient operator with respect to reference configuration. The superscript $(\cdot)^T$ denotes the transpose operator.

The right-hand side of Eq. (3) is split in two terms, one that is constant with respect to the displacement, and one that is linear with respect to the displacement:

$$\int_{\Omega_0} \mathbf{S}^p[\mathbf{p}] : (\mathbf{F}^T \nabla_0 \mathbf{w}) \, d\Omega_0 = \int_{\Omega_0} \mathbf{S}^p[\mathbf{p}] : \nabla_0 \mathbf{w} + (\nabla_0 \mathbf{u} \cdot \mathbf{S}^p[\mathbf{p}]) : \nabla_0 \mathbf{w} \, d\Omega_0 \quad (4)$$

The relation between inelastic stresses and polarization field is taken from the Landau-Devonshire theory of ferroelectrics [13] assuming that the electrostrictive effect dominates the electromechanical response of the piezoelectric material, as usually happens in structures excited at finite voltage amplitudes:

$$\mathbf{S}^p[\mathbf{p}] = \mathbb{C} : \mathbb{Q} : (\mathbf{p} \otimes \mathbf{p}) \quad (5)$$

where \mathbb{C} is the fourth-order elasticity tensor, \mathbb{Q} is the fourth-order tensor that collects the electrostrictive coefficients of the piezoelectric material, and \otimes denotes the tensor product.

Finally, we operate one last approximation on Eq. (3) derived from the analysis reported in [11]. Piezoelectric patches exploited for actuation are thin, hence upon application of a potential difference between the two sides of the patch the electric field \mathbf{E} is oriented along the thickness direction, that is $\mathbf{E} = E[V] \mathbf{e}_3$, with $E[V]$ scalar proportional to the applied voltage V and \mathbf{e}_3 unit vector oriented along the thickness direction. Since piezoelectric materials used in thin films have cubic symmetry, with at least one symmetry axis oriented along the deposition direction, we have $\mathbf{p} = P[V] \mathbf{e}_3$, with $P[V]$ scalar function of the applied voltage. We did not include any dependence of the polarization on the displacement field since in actuators applied voltages are so high that any dependence of the polarization field on the displacement would be negligible. Furthermore, the polarization within the film is assumed uniform over the patch. This last assumption is not true from a physical standpoint since piezoelectric films are characterized by domains of uniform polarization, yet from a macroscopic standpoint we can interpret $P[V]$ as the averaged value of the polarization within the film. Using these last assumptions, and by restraining the integral of the right-hand side of Eq. (3) to the portion of the domain where piezoelectric materials are defined, we simplify Eq. (3) to:

$$\int_{\Omega_0} \rho_0 \mathbf{u}_{tt} \cdot \mathbf{w} d\Omega_0 + \int_{\Omega_0} \mathbf{S}^e[\mathbf{u}] : (\mathbf{F}^T \nabla_0 \mathbf{w}) d\Omega_0 = \sum_{i=1}^{N_p} P_i^2[V_i] \int_{\Omega_{0,p}^i} \mathbf{\Lambda} : \nabla_0 \mathbf{w} + (\nabla_0 \mathbf{u} \cdot \mathbf{\Lambda}) : \nabla_0 \mathbf{w} d\Omega_{0,p}^i \quad \forall \mathbf{w} \in \mathcal{C}(\mathbf{0}) \quad (6)$$

where $\Omega_{0,p}^i$ denotes the i th-piezoelectric material domain, and N_p is the number of piezoelectric domains. Equation (6) highlights that the different actuation patches of the system can be subjected to different actuation voltage histories. In cartesian coordinates, the second-order tensor $\mathbf{\Lambda}$ has the form:

$$\mathbf{\Lambda} = \alpha_1(\mathbf{e}_1 \otimes \mathbf{e}_1) + \alpha_1(\mathbf{e}_2 \otimes \mathbf{e}_2) + \alpha_3(\mathbf{e}_3 \otimes \mathbf{e}_3) \quad (7)$$

with α_1 and α_3 material constants derived from the elasticity and the electrostrictive tensors.

The formulation presented in Eq. (6) offers several interesting features that make it appealing from a numerical and academic standpoint. First, the piezoelectric force is nonlinear with respect to the polarization field. Second, the piezoelectric force is made by two terms: the first term is constant with respect to the displacement, while the second is linear with respect to the displacement itself. This last term implies that since the polarization is a function of time, then the stiffness of the system is modulated in time by the piezoelectric force. This aspect is not investigated in the present work but it is subject of future studies. Furthermore, the piezoelectric

force introduces integrals that are already implemented in most commercial finite element software since the mathematical formulation of the piezoelectric force coincides with the formulation used for prestressed structures. Finally, since the polarization field is interpreted as the average value of the polarization field within the piezoelectric film, direct characterization of $P[V]$ within the film can be operated with simple experimental setups, as, for instance, a Sawyer-Tower circuit.

Numerical solution of Eq. (6) is performed using a finite element discretization of the problem that leads to the following system of time-dependent coupled differential equations:

$$[M]\{U_{tt}\} + \{F(U)\} = \sum_{i=1}^{N_p} P_i^2[V_i] (\{F^p\}_i + [K^p]_i\{U\}) \tag{8}$$

where $[M]$ is the mass matrix, $\{U_{tt}\}$ is the nodal acceleration vector, $\{U\}$ is the nodal displacement vector, $\{F(U)\}$ is the nonlinear internal force vector, and the right-hand side defines the nodal piezoelectric forces $\{F^p\}_i$ and stiffness $[K^p]_i$. Rayleigh damping proportional to the mass matrix is added to the system:

$$[M]\{U_{tt}\} + \frac{\omega_0}{Q}[M]\{U_t\} + \{F(U)\} = \sum_{i=1}^{N_p} (P_i^2[V_i]\{F^p\}_i + [K^p]_i\{U\}) \tag{9}$$

where ω_0 is the resonance frequency of the mode of interest and Q is the so-called quality factor. The term $(\omega_0/Q)[M]$ denotes the damping matrix $[C]$.

2.1 Harmonic Balance Method

Solving Eq. (9) through direct time integration to compute the steady dynamic response of the system would be prohibitively costly. Therefore, we exploit the HBM. The displacement field $\{U\}$ is expanded as Fourier series:

$$\{U\} = \{U\}_0 + \sum_{n=1}^N \{U\}_c^n \cos(n\omega t) + \{U\}_s^n \sin(n\omega t) \tag{10}$$

with $\{U\}_0$, $\{U\}_c^n$, and $\{U\}_s^n$ unknowns, and N expansion order. The new problem is formulated by substituting Eq. (10) in Eq. (9) and by imposing orthogonality with the Fourier basis. This yields the following system of nonlinear algebraic equations:

$$\begin{aligned}
 & - (n\omega)^2[M]\{U\}_c^n + n\omega[C]\{U\}_s^n + \frac{1}{\pi} \int_0^{2\pi} \{F(U)\} \cos(n\tau) d\tau = \\
 & \frac{1}{\pi} \sum_{i=1}^{N_p} \int_0^{2\pi} \left[(P_i^2[V_i]\{F^p\}_i + [K^p]_i\{U\}) \right] \cos(n\tau) d\tau \quad \forall n = 1, \dots, N
 \end{aligned} \tag{11a}$$

$$\begin{aligned}
& - (n\omega)^2 [\mathbb{M}]\{\mathbb{U}\}_s^n - n\omega [\mathbb{C}]\{\mathbb{U}\}_c^n + \frac{1}{\pi} \int_0^{2\pi} \{\mathbb{F}(\mathbb{U})\} \sin(n\tau) d\tau = \\
& \frac{1}{\pi} \sum_{i=1}^{N_p} \int_0^{2\pi} \left[\mathbb{P}_i^2[V_i] (\{\mathbb{F}^p\}_i + [\mathbb{K}^p]_i \{\mathbb{U}\}) \right] \sin(n\tau) d\tau \quad \forall n = 1, \dots, N
\end{aligned} \tag{11b}$$

$$\int_0^{2\pi} \{\mathbb{F}(\mathbb{U})\} d\tau = \frac{1}{\pi} \sum_{i=1}^{N_p} \int_0^{2\pi} \left[\mathbb{P}_i^2[V_i] (\{\mathbb{F}^p\}_i + [\mathbb{K}^p]_i \{\mathbb{U}\}) \right] d\tau \tag{11c}$$

where the change of variable $\tau = \omega t$ was used.

The accuracy of the solution computed through the HBM is directly proportional to the order of the expansion. Nevertheless, the number of unknowns of the problem scales as $2N + 1$, hence the computational cost for solving the problem dramatically increases by increasing the expansion order. In this work, the expansion order was chosen based on a simple consideration regarding the system motion. Assuming a rotation θ of the device around a fixed axis, the cartesian coordinates of the displacement of a point on the mirror surface is expressed as:

$$\begin{aligned}
u_x &= r\theta(\cos(\theta) - 1) = r\theta \left(\frac{1}{2}\theta + O(\theta^3) \right) \\
u_y &= r\theta \sin(\theta) = r\theta \left(1 - \frac{1}{6}\theta^2 + O(\theta^4) \right)
\end{aligned} \tag{12}$$

Therefore, we need to include terms at least up to $N = 3$ to reach an order of accuracy greater or equal than $O(\theta^3)$.

3 Device Overview and Characterization

The device under investigation is a piezoelectric micromirror developed by STMicroelectronicsTM. A picture of the device is reported in Fig. 1a, and a schematic representation of the device geometry is visible in Fig. 1b. The central circular reflective surface of the device is attached to the substrate by means of two torsional beams, while actuation is achieved by means of two pairs of trapezoidal beams that act as mechanical hinges. The structure of the device is made by monocrystalline silicon with the [110] orientation aligned with the torsional springs. The sol-gel-deposited piezoelectric patches used for actuation are deposited on the trapezoidal beams and they are highlighted in light purple in Fig. 1b. The patches are deposited together with electrodes and passivation layers through the Petra Thin-Film-Piezoelectric technology developed by STMicroelectronicsTM.

The device is actuated at its first resonant mode, that is a rotation around an axis parallel to e_1 . The displacement field of the torsional mode is reported in Fig. 1c.

To excite this mode, piezoelectric patches are organized in two actuation groups. The two groups are labeled as 1 and 2 and they are highlighted by the markers in Fig. 1b. During actuation, the voltage laws applied to the patches groups are $V_1(t) = (V_0/2)(1 + \cos(\omega t))$ and $V_2(t) = (V_0/2)(1 - \cos(\omega t))$.

3.1 Frequency Response Measurements

The Frequency Response Function (FRF) of the device was experimentally determined from the opening angle. Its characterization was performed by measuring the deflection of a laser beam incident on the device. The experimental apparatus is reported in Fig. 2a. The actuation signal was produced by the function generator

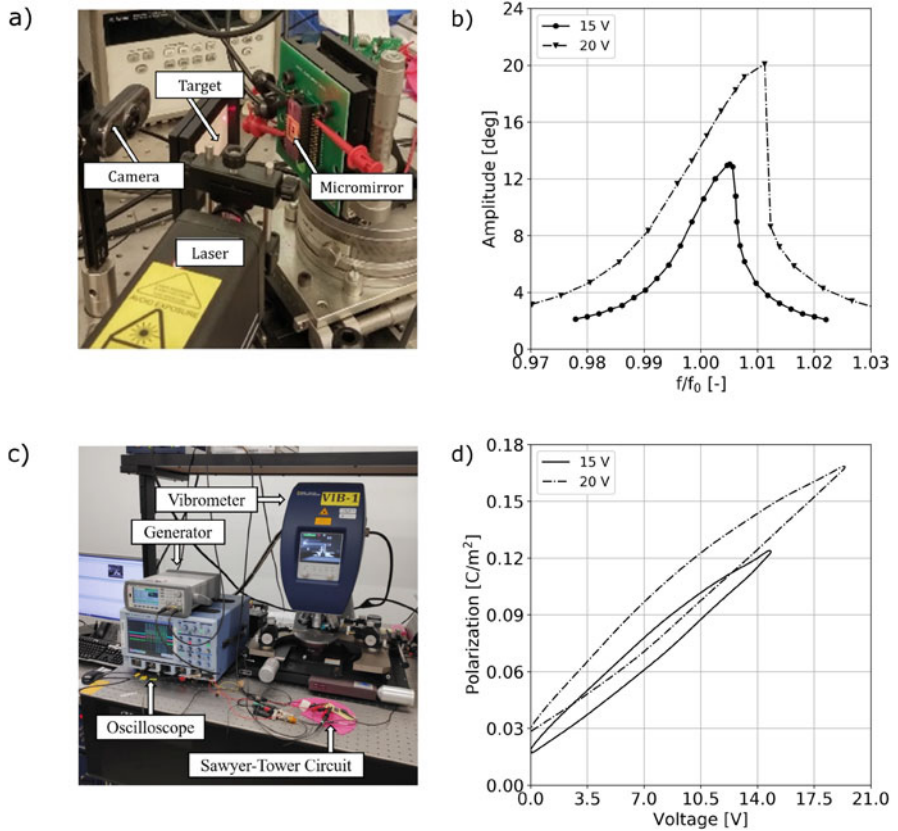


Fig. 2 Optical setup used to characterize the FRFs of the device (a), measured FRFs (b), polarization measurements setup (c), and measured polarization curves (d)

“Agilent 33521A”. A He-Ne laser was used to measure the rotation angle. The device was mounted on an optical alignment bench to provide a 45° laser beam incidence and a perpendicular projection of the reflected beam on the millimetric target. The resonant movement of the mirror spanned a segment that was acquired by a camera and processed using LabView™.

The FRF of the device is reported in Fig. 2b, where the maximum tilting angle for a given frequency is reported. The frequency axis is normalized by the eigenfrequency of the torsional mode. As highlighted in the chart, the micromirror shows hardening behavior with formation of an unstable branch for V_0 equal to 20 V. Only stable branches were measured during the experiment since the data were collected under frequency control.

3.2 Piezoelectric Film Measurements

The devices were actuated using a prescribed potential law, yet the model reported in Eq. (6) requires the polarization field within the patches $P[V]$. Its value can be either computed using numerical simulations of the film microstructure, or it can be experimentally measured. In this work we chose the second technique, i.e. we experimentally characterized the polarization history of the piezoelectric film. This was performed by resorting to a Sawyer-Tower circuit. The experimental setup is shown in Fig. 2c. The experimental test was performed by applying first a constant potential equal to V_0 to the piezoelectric patches for 5 min. Then, five bipolar and five unipolar cycles were applied to the patches. Bipolar cycles follow the law $V(t) = V_0 \cos(\omega t)$, while unipolar potential cycles are prescribed as $V(t) = (V_0/2)(1 + \cos(\omega t))$. Only data corresponding to the last unipolar cycle were collected. The $P[V]$ curves are reported in Fig. 2d. We remark the nonlinear response of the piezoelectric patches with respect to the applied voltage, as highlighted by the hysteresis of the polarization curves.

4 Results

Numerical simulations are performed by solving Eq. (11) for two V_0 values: 15 and 20 V. For each voltage value, the corresponding polarization history $P[V(t)]$ is expressed as a function of time and fed to the model to compute the corresponding piezoelectric force. This approach is based on the assumption that the polarization of the patches is not affected by the frequency of excitation, that is reasonable for devices working in the range of tens of kilohertz.

The damping in the model is calibrated from experimental data using the relation provided in equation 14 of the work by Davis [14] for each V_0 value under the assumption of linear damping, as the one adopted in the present work. Measured quality factors are collected in Table 1. Regarding constitutive models,

Table 1 Quality factor values computed from experimental data

V_0 [V]	15	20
Q[-]	133.1	104.1

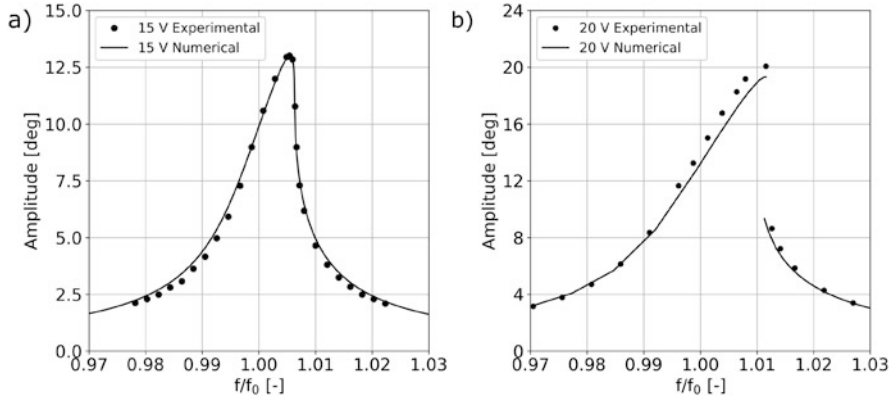


Fig. 3 Comparison between numerical and experimental FRFs

all materials are treated with a Saint-Venant Kirchhoff model. The monocrystalline silicon mechanical parameters are taken from the work by Hopcroft [15], while PZT patches are modeled as isotropic with a Young’s modulus of 64 GPa and a Poisson’s ratio of 0.34. Lastly, the electrostrictive coefficients of the PZT are taken from the work by Haun [7].

We developed a harmonic balance finite element code to solve the proposed model. The resulting solution of the numerical model is compared with the experimental data for the two V_0 values in Fig. 3. Figure 3a shows a mild hardening response, while Fig. 3b shows for both numerical and experimental data the formation of an unstable branch. For both actuation voltages the piezoelectric model predicts the correct actuation force, as highlighted by the excellent agreement between numerical and experimental data far from the resonance peak. Overall, the numerical analyses accurately reproduce the nonlinear response of the device for both excitation voltages.

5 Conclusions

In the present work we extended the thin piezoelectric film model presented in [11, 12] to handle the large displacements the piezoelectric patches are subjected to during device actuation. The model is developed starting from the conservation of linear momentum and from the theory of ferroelectrics developed by Landau-Devonshire. The model embeds both geometric nonlinearities caused by the finite

rotation amplitudes of the structure, and material nonlinearities induced by excitation of the piezoelectric material at high electric potentials.

The model is then applied to study a piezoelectric scanning micromirror excited at large voltages and consequently at large rotation amplitudes. Solution of the models is performed using the HBM for direct computation of the steady dynamic response of the system. The results of the analyses show that the proposed technique efficiently predicts the nonlinear dynamic response of the device, hence it proves reliable and efficient for modeling piezo MEMS.

Acknowledgments The authors express their gratitude towards STMicroelectronics™ for the device exploited for this study.

References

1. G. Silva, F. Carpignano, F. Guerinoni, S. Costantini, M. De Fazio, S. Merlo, Optical detection of the electromechanical response of MEMS micromirrors designed for scanning picoprojectors, *IEEE J. Sel. Top. Quantum Electron.* **21**(4), 147–156 (2014)
2. K. Ikegami, T. Koyama, T. Saito, Y. Yasuda, H. Toshiyoshi, A biaxial piezoelectric MEMS scanning mirror and its application to pico-projectors, in *IEEE 2014 International Conference on Optical MEMS and Nanophotonics* (2014), pp. 95–96
3. A. Frangi, A. Guerrieri, R. Carminati, G. Mendicino, Parametric resonance in electrostatically actuated micromirrors, *IEEE Trans. Ind. Electron.* **64**(2), 1544–1551 (2017)
4. A. Frangi, A. Guerrieri, N. Boni, Accurate simulation of parametrically excited micromirrors via direct computation of the electrostatic stiffness. *Sensors* **17**(4), 779 (2017)
5. J.H. Kim, H. Jeong, S.K. Lee, C.H. Ji, J.H. Park, Electromagnetically actuated biaxial scanning micromirror fabricated with silicon on glass wafer. *Microsyst. Technol.* **23**(6), 2075–2085 (2017)
6. Y. Zhu, W. Liu, K. Jia, W. Liao, H. Xie, A piezoelectric unimorph actuator based tip-tilt-piston micromirror with high fill factor and small tilt and lateral shift. *Sens. Actuators A Phys.* **167**(2), 495–501 (2011)
7. M.J. Haun, E. Furman, S.J. Jang, H.A. McKinstry, L.E. Cross, Thermodynamic theory of PbTiO₃. *J. Appl. Phys.* **62**(8), 3331–3338 (1987)
8. K. Meinel, C. Stoeckel, M. Melzer, S. Zimmermann, R. Forke, K. Hiller, T. Otto, Piezoelectric scanning micromirror with built-in sensors based on thin film aluminum nitride. *IEEE Sens. J.* **21**(8), 9682–9689 (2020)
9. J. Rödel, W. Jo, K.T.P. Seifert, E.M. Anton, T. Granzow, D. Damjanovic, Perspective on the development of lead-free piezoceramics. *J. Am. Ceram. Soc.* **92**(6), 1153–1177 (2009)
10. M.I. Younis, *MEMS Linear and Nonlinear Statics and Dynamics* (Springer Science & Business Media, New York, 2011)
11. A. Frangi, A. Opreni, N. Boni, P. Fedeli, R. Carminati, M. Merli, G. Mendicino, Nonlinear response of PZT-actuated resonant micromirrors. *J. Microelectromech. Syst.* **29**(6), 1421–1430 (2020)
12. A. Opreni, A. Frangi, N. Boni, G. Mendicino, M. Merli, R. Carminati, Piezoelectric micromirrors with geometric and material nonlinearities: experimental study and numerical modeling, in *Proceeding of IEEE SENSORS 2020*, online conference, 25–28 Oct 2020
13. A.F. Devonshire, Theory of ferroelectrics. *Adv. Phys.* **3**(10), 85–130 (1954)
14. W.O. Davis, Measuring quality factor from a nonlinear frequency response with jump discontinuities. *J. Microelectromech. Syst.* **20**(4), 968–975 (2011)
15. M.A. Hopcroft, W.D. Nix, T.W. Kenny, What is the Young’s modulus of silicon? *J. Microelectromech. Syst.* **19**(2), 229–238 (2010)

Global Analysis and Experimental Dynamics of the 2:1 Internal Resonance in the Higher-Order Modes of a MEMS Microbeam



Laura Ruzziconi, Nizar Jaber, Lakshmoji Kosuru, Mohammed L. Bellaredj, and Mohammad I. Younis

1 Introduction

In micro and nano-electromechanical systems, nonlinear phenomena are extensively investigated to be implemented in novel devices and satisfy increasingly more sophisticated requirements [1]. Ruzziconi et al. [2] acquire extensive experimental data of MEMS devices and compare the experimental response with the simulated dynamical integrity charts. Kacem et al. [3] examine the problem of overcoming the limitations of nano-mechanical resonators and, to this extent, make use of simultaneous resonance. Alcheikh et al. [4] fabricate curved resonators and track multiple modes of vibration, which are used to develop resonant pressure sensors of high sensitivity. Settimi and Rega [5] explore the feasibility of different control techniques for controlling the dynamics of a cantilever microbeam used for atomic force microscopy. Medina et al. [6] consider curved bistable microbeams exhibiting latching phenomenon and demonstrate dynamic releases as the beam is subjected to transverse loading. Jaber et al. [7] release a smart switch via the fabrication of a resonant gas sensor, which presents metal-organic frameworks coating. Bassinello et al. [8] explore the possibility of driving a MEMS resonator in the nonlinear regime and exhibit both chaotic and periodic motion. Kumar et al. [9] make use of the dynamic transitions across saddle-node bifurcations to develop an alternative

L. Ruzziconi (✉)

Faculty of Engineering, eCampus University, Novedrate, Italy
e-mail: laura.ruzziconi@uniecampus.it

N. Jaber

Mechanical Engineering Department and the Center for Communication Systems and Sensing,
King Fahd University of Petroleum & Minerals (KFUPM), Dhahran, Saudi Arabia

L. Kosuru · M. L. Bellaredj · M. I. Younis

King Abdullah University of Science and Technology (KAUST), Thuwal, Saudi Arabia

sensing approach. Alneamy et al. [10] present an electrostatic micro-tweezers based on the multistability related to the snap-through phenomenon. Lenci and Rega [11] propose a control method for increasing the operational range of a MEMS device, suggesting to shift the safe basin erosion toward excitations of higher amplitudes. Hafiz et al. [12] consider an arch resonator and apply the nonlinearity arising in the response to develop mechanical memory operation.

Different vibration modes may exhibit nonlinear interactions, which are raising increasing interest in the research community due to the variety of their possible applications [13, 14]. Yang and Towfighian [15] take advantage of the internal resonance to develop a nonlinear energy harvester. Internal resonances are analyzed in Vyas et al. [16] between flexural-torsional modes of a microresonator, in Potekin et al. [17] in multifrequency atomic force microscopy, in Nathamgari et al. [18] in a nanoresonator, where multiple internal resonances are detected. In magnetic resonance force microscopy, Hacker and Gottlieb [19] address the mechanism of energy transfer related to the two-to-one internal resonance. Kirkendall et al. [20] analyze the internal resonance in a quartz crystal resonator at large forcing amplitudes. Daqaq et al. [21] investigate the internal resonance in a micromirror. Simulations are reported in Ouakad et al. [22] for internal resonances between symmetric and antisymmetric modes of MEMS with half-electrode actuation. Sarrafan et al. [23] fabricate a nonlinear rate microsensors based on the internal resonance phenomenon. Hajjaj et al. [24] tune the electrothermal voltage in MEMS arches in order to experimentally excite different internal resonances. Ruzziconi et al. [25] explore the coexistence of attractors at internal resonance and the related nonlinearities in the experimental dynamics of a MEMS.

This study considers a MEMS device electrically actuated, where the third-mode dynamics exhibit internal resonance with fifth mode. Tracking each single branch, the main attractors are examined, up to final disappearance. Simulations and data are compared. We analyze the bifurcational behavior related to the internal resonance activation, and we alert that this may actually shrink the operational range.

This paper is organized as follows. In Sect. 2, we report on the forward and the backward frequency sweeps experimentally acquired, and we analyze the numerical simulations developed via shooting technique. Section 3 investigates the activation of the 2:1 internal resonance by performing sections of basins of attraction. Section 4 summarizes the main conclusions.

2 Experimental 2:1 Internal Resonance

2.1 MEMS Device

An optical image showing the microbeam-based MEMS device considered in the present work is reported in Fig. 1. The microbeam has a length of 400 μm . It is clamped-clamped and presents rectangular cross section. The width is 50 μm . To

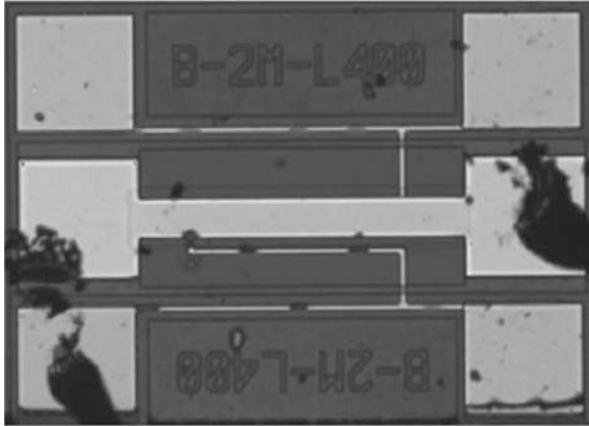


Fig. 1 MEMS device

excite both symmetric and antisymmetric modes, the lower electrode covers half of the length of the microbeam. The device is electrically actuated, and the separation gap is $2.5 \mu\text{m}$.

The first (first symmetric) natural frequency occurs at $f_1 = 145.2 \text{ kHz}$, the second (first antisymmetric) at $f_2 = 314.8 \text{ kHz}$, the third (second symmetric) at $f_3 = 526.6 \text{ kHz}$, the fourth (second antisymmetric) at $f_4 = 787 \text{ kHz}$, and the fifth (third symmetric) at $f_5 = 1105 \text{ kHz}$.

2.2 *Experimental and Simulated Response*

We analyze the experimental behavior at the third-mode dynamics, for $V_{AC} = 21.5 \text{ V}$. In Fig. 2a, we show the frequency response diagram, where the maximum oscillation amplitude versus the driving frequency is reported, while in Fig. 2b, we show the FFT diagram, which reports the corresponding FFT amplitude. The device exhibits hardening bending.

As forward sweeping, the resonant branch P_{res} progressively raises the oscillation amplitude up to about $\Omega = 573.5 \text{ kHz}$. After that, we can observe the activation of the 2:1 internal resonance with the fifth mode. This phenomenon induces a visible change in the oscillation amplitude, which continues up to the disappearance of the attractor occurring at about $\Omega = 589.7 \text{ kHz}$. In the following, this second part of the resonant branch where the 2:1 internal resonance is taking place is denoted S_{Ires} . Analyzing the FFT diagram, along this range, the third mode saturates and performs a practically constant plateau, while the dynamics of the fifth mode progressively raise, still exhibiting hardening bending. The amplitude gradually reached by the fifth mode component is rather elevated, although its contribution remains smaller than the third mode one.

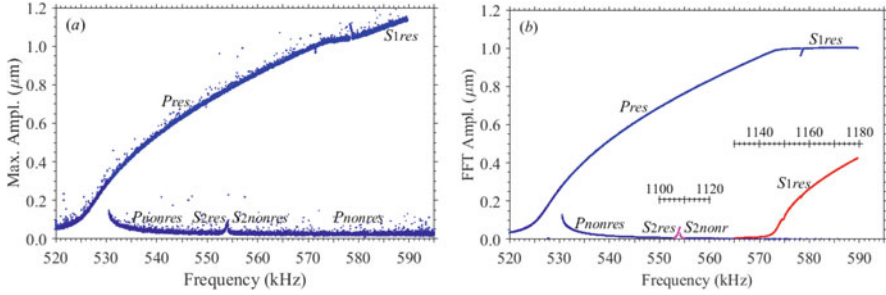


Fig. 2 Experimental dynamics at $V_{AC} = 21.5$ V, with $V_{DC} = 30$ V. (a) Frequency response diagram. (b) FFT diagram. Scale of response frequency for the fifth mode is shown above the corresponding curve

As backward sweeping, we can see the nonresonant branch P_{nonres} , which, at about $\Omega = 530.5$ kHz, performs a saddle-node bifurcation after which it disappears and the dynamics jump to the resonant branch P_{res} . Also, the nonresonant branch is involved in the 2:1 internal resonance. In fact, at about $\Omega = 554$ kHz, the experimental data show the nonresonant branch evolving into resonant dynamics (S_{2res}) and nonresonant ones ($S_{2nonres}$). This activation involves a narrow frequency range, $\Omega = [552.8; 555.0]$ kHz. Since only the backward sweep is acquired for the nonresonant branch, we have no information about the experimental length of S_{2res} .

It is worth noting that the 2:1 internal resonance is activated along the nonresonant branch P_{nonres} at about half of the value of the fifth-mode natural frequency. Conversely, the activation in the resonant branch P_{res} is shifted and takes place at higher frequencies, which is related to the nonlinearities of the system.

To simulate the experimental behavior, we derive a reduced-order model. This is based on the Galerkin technique, where 2 d.o.f. are considered to take into account both the third and the fifth mode ([Appendix](#)).

The simulated frequency response diagram is shown in Fig. 3a, and the simulated FFT diagram is in Fig. 3b. To detect the periodic orbits and their stability, these results are obtained via self-developed codes based on shooting technique and Floquet theory [26]. Simulations detect all the main features arising in the experimental data. We can observe the activation of the 2:1 internal resonance along both the resonant branch and the nonresonant one. The theoretical results alert on the coexistence of additional attractors. There is the novel P_{res} , which appears by saddle-node bifurcation after the 2:1 internal resonance activation along P_{res} and shares very similar features with this branch. There is $S_{1res-ph}$, which similarly appears at about the same range by saddle-node bifurcation, and its development presents similar aspects to S_{1res} , except for a phase shift between the coupling modes [27]. Overall, close is the correspondence between simulations and experimental data.

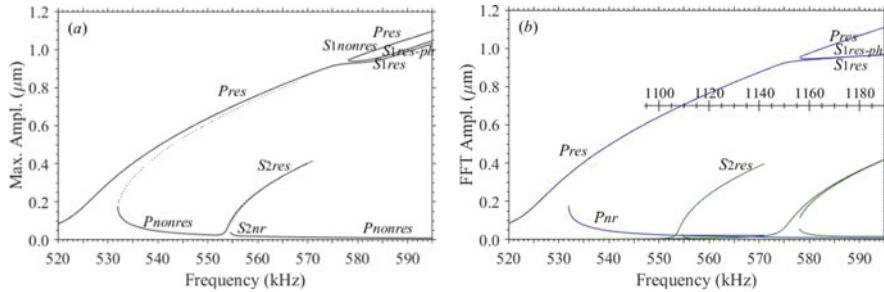


Fig. 3 Numerical simulations at $V_{AC} = 21.5$ V, with $V_{DC} = 30$ V. (a) Frequency response diagram. (b) FFT diagram

3 Basins of Attraction

We focus on the progression of the basins of attraction at the activation of the 2:1 internal resonance. We mainly investigate the basin of S_{1res} , of which we analyze its metamorphoses along the fifth-mode plane (u_3, u_4) , as increasing the driving frequency. The basin of this attractor along this plane is computed by considering as initial conditions along the third-mode plane the ones of its Poincaré map [28]. All simulations are developed via long-time integration.

The scenario at $\Omega = 580$ kHz, i.e., soon after the 2:1 internal resonance activation, is reported in Fig. 4a. The basin of S_{1res} (yellow) is close to the one of $S_{1nonres}$, i.e., the novel P_{res} (blue). These basins are spiraling around each other, and both of them are provided with an evident compact core, which suggests that both these attractors may be safely operated under realistic conditions [1]. We can observe the appearance of the basin of $S_{1res-ph}$ (pink), which develops close to the compact core of the novel P_{res} . Although this section of attractor basins is soon after its appearance by saddle-node bifurcation, its basin is clearly evident, despite being smaller than the others, denoting that the basin of this attractor is rapidly enlarging after its appearance. The basins of all these three attractors jointly extend for a large part of the reported phase space. This area is about the same area that previously was of the basin of P_{res} , before the 2:1 internal resonance activation. Outside this area, the phase space is mainly covered by the basin of P_{nonres} (green), although this is tangled with the basins of the other attractors.

As increasing the driving frequency, the region formed by the aforementioned three basins progressively widens. The attractor-basin scenario around S_{1res} at $\Omega = 590$ kHz is reported in Fig. 4b. The basin of S_{1res} (yellow) is progressively shifted toward the right-hand side, while the basin of $S_{1res-ph}$ (pink) toward the opposite direction. The shape of these basins appears very similar, and their wideness is increased. In the central part of the phase space, there is the basin of the novel P_{res} (blue), which progressively widens. A minor attractor (gray) appears, whose basin presents two main disconnected parts. Even if the three main basins

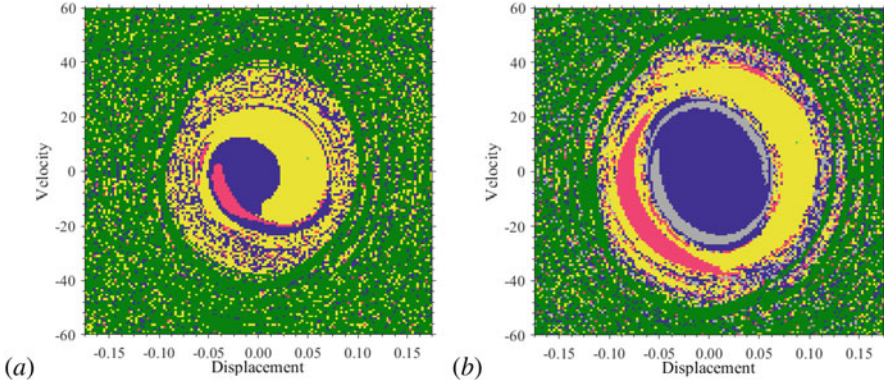


Fig. 4 Attractor basins at 2:1 internal resonance, at $V_{AC} = 21.5$ V, with $V_{DC} = 30$ V. The figure shows the scenario around S_{Ires} , assuming the fifth-mode plane. The basins of S_{Ires} , novel P_{res} , $S_{Ires-ph}$, and P_{nonres} are yellow, blue, pink, and green, respectively. The basin of a minor attractor is gray, and the escape is white. The Poincaré map of S_{Ires} is in green asterisk. (a) $\Omega = 580$ kHz; (b) $\Omega = 590$ kHz

are still close to each other, their compact cores are progressively separated by non-compact parts of their own basins.

Up to about the values of Ω previously considered, the initial conditions of $S_{Ires-ph}$ and of the novel P_{res} in the third mode plane are about close to the ones of S_{Ires} ; thus, the attractor-basin scenario drawn around this attractor in the present plane is about similar to the one drawn around the other attractors (not reported). As further increasing Ω , instead, differences become more evident. We continue to analyze sections centered at S_{Ires} .

At $\Omega = 625$ kHz in Fig. 5a, the three basins are no further close to each other. The basin of S_{Ires} (yellow) and the basin of $S_{Ires-ph}$ (pink) are increasingly located toward the right- and the left-hand side of the present section of the phase space, respectively. From this section, we can observe only two main compact portions of the basin of the novel P_{res} (blue). The central part of the section is covered by the basin of P_{nonres} (green), which further spans not only the outer region of the phase space section but also the inner one, denoting wide robustness for this attractor. All these aspects become further evident as increasing Ω , Fig. 5b.

4 Conclusions

We have analyzed a microbeam-based MEMS device exhibiting internal resonance in the higher-order modes, in particular between the third and fifth modes. Experimental data and numerical simulations have been performed, which have emphasized the interesting dynamics induced by the 2:1 internal resonance. We have observed the coexistence of different attractors undergoing qualitatively different

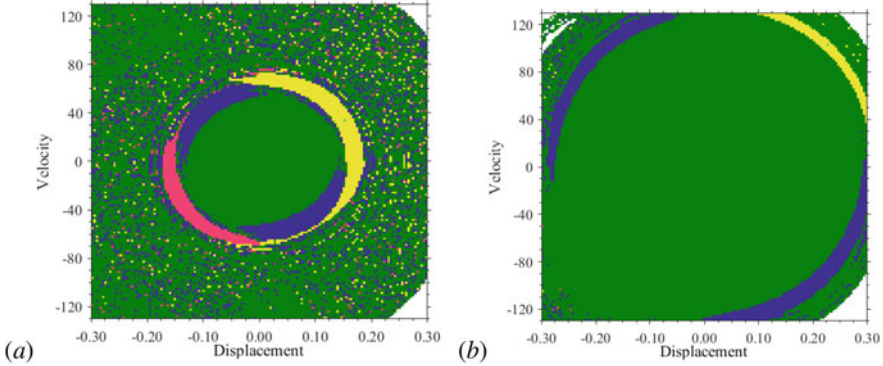


Fig. 5 Attractor basins at 2:1 internal resonance, at $V_{AC} = 21.5$ V, with $V_{DC} = 30$ V. Scenario around S_{1res} , in the fifth-mode plane. **(a)** $\Omega = 625$ kHz; **(b)** $\Omega = 725$ kHz

behaviors. The attractors involved in the 2:1 internal resonance present a non-negligible safe basin, which remains moderately large and compact for a substantial range of the driving parameters. This suggests the possibility of designing novel devices deliberately making use of the internal resonance and of the concurrent nonlinear features related to its activation. We have shown that the microbeam may be operated actively at internal resonance, as confirmed by the data experimentally acquired.

A.1 Appendix: Mechanical Model

We model the device as a parallel plate capacitor. The upper electrode is represented by a clamped-clamped microbeam with a rectangular cross section and straight configuration. To model the residual stresses, we assume a constant axial load P . To represent the half-electrode configuration, only half of the microbeam length is supposed to provide the electric contribution. The governing equation of motion is [29]

$$\ddot{v} + \xi \dot{v} + v'''' + \alpha v'' = -\gamma F_e \quad (\text{A.1})$$

with

$$\alpha = n - ka \int_0^1 \frac{1}{2} (v')^2 dz \quad F_e = \frac{(V_{DC} + V_{AC} \cos(\Omega t))^2}{(1 - v)^2} [H(z_1) - H(z_2)] \quad (\text{A.2})$$

with $H(z_1)$ and $H(z_2)$ unit step functions, which are used to define the length and the position of the lower electrode. The considered nondimensional parameters are

Table A.1 Coefficients of the model in Eq. (A.4)

Eq.	u_1	u_2	u_1^3	u_2^3	$u_1u_2^2$	$u_2u_1^2$
1st	28,904.48	0	137,150	74,958	388,510	81,656
2nd	0	127,495.86	27,219	1,040,200	224,870	388,510

$$\begin{aligned}
 ka &= (EA)d^2/(EJ) & n &= (EA)Lw_B/(EJ) & \xi &= cL^4/(EJT) \\
 \gamma &= \frac{1}{2}\varepsilon_0\varepsilon_r A_c L^3 / (d^3 E J) & T &= \sqrt{(\rho AL^4)/(EJ)} & \tilde{\Omega} &= \Omega T
 \end{aligned}
 \tag{A.3}$$

where L is length, A and J are respectively area and moment of inertia, ρ is the material density, E is the effective Young’s modulus, c is damping coefficient, d is the capacitor gap, ε_0 is dielectric constant in the free space, ε_r is the relative permittivity of the gap space medium (air) with respect to the free space, and A_c is the area overlapping between the electrodes.

The dynamics of the microbeam are approximated as $v(z, t) \cong \sum_{i=1}^n \phi_i(z)u_i(t)$, where $\phi_i(z)$ are the mode shapes under consideration (third and fifth). We derive the reduced-order model by applying the Galerkin procedure, which yields the 2 d.o.f. system [25]

$$\begin{aligned}
 \ddot{u}_n + c\dot{u}_n + \omega_n^2 u_n - ka (a_{n1}u_1^3 + a_{n2}u_2^3 + a_{n3}u_1u_2^2 + a_{n4}u_2u_1^2) \\
 = -\gamma V^2 \int_0^{0.5} \frac{\phi_n}{(1-\phi_1u_1-\phi_2u_2)^2} dz \quad \text{for } n = 1, 2
 \end{aligned}
 \tag{A.4}$$

where numerical integration is applied to evaluate the electric force term. Table A.1 reports the coefficients used in the model.

References

1. L. Ruzziconi, S. Lenci, M.I. Younis, Interpreting and predicting experimental responses of micro- and nano-devices via dynamical integrity, in *Global Nonlinear Dynamics for Engineering Design and System Safety*, ed. by S. Lenci, G. Rega, (Springer, 2019), pp. 113–166
2. L. Ruzziconi, M.I. Younis, S. Lenci, An electrically actuated imperfect microbeam: Dynamical integrity for interpreting and predicting the device response. *Meccanica* **48**, 1761–1775 (2013)
3. N. Kacem, S. Baguet, L. Duraffourg, G. Jourdan, R. Dufour, S. Hentz, Overcoming limitations of nanomechanical resonators with simultaneous resonances. *Appl. Phys. Lett.* **107**(7), 073105 (2015)
4. N. Alcheikh, A.Z. Hajjaj, M.I. Younis, Highly sensitive and wide-range resonant pressure sensor based on the veering phenomenon. *Sens. Actuators A Phys.* **300**, 111652 (2019)
5. V. Settimi, G. Rega, Exploiting global dynamics of a noncontact atomic force microcantilever to enhance its dynamical robustness via numerical control. *Int. J. Bifurcat. Chaos* **26**(7), 1630018 (2016)
6. L. Medina, R. Gilat, S. Krylov, Dynamic release condition in latched curved micro beams. *Commun. Nonlinear Sci. Numer. Simul.* **73**, 291–306 (2019)
7. N. Jaber, S. Ilyas, O. Shekhah, M. Eddaoudi, M.I. Younis, Resonant gas sensor and switch operating in air with metal-organic frameworks coating. *J. Microelectromech. Syst.* **27**(2), 156–163 (2018)

8. D.G. Bassinello, A.M. Tusset, R.T. Rocha, J.M. Balthazar, Dynamical analysis and control of a chaotic microelectromechanical resonator model. *J. Shock Vib.* **2018**, 4641629 (2018)
9. V. Kumar, J.W. Boley, Y. Yang, H. Ekowaluyo, J.K. Miller, G.T.C. Chiu, J.F. Rhoads, Bifurcation-based mass sensing using piezoelectrically-actuated microcantilevers. *Appl. Phys. Lett.* **98**(15), 153510 (2011)
10. A.M. Alneamy, M.E. Khater, A.K. Abdel-Aziz, G.R. Heppler, E.M. Abdel-Rahman, Electrostatic arch micro-tweezers. *Int. J. Non Linear Mech.* **118**, 103298 (2020)
11. S. Lenci, G. Rega, Control of pull-in dynamics in a nonlinear thermoelastic electrically actuated microbeam. *J. Micromech. Microeng.* **16**(2), 390 (2006)
12. M.A.A. Hafiz, L. Kosuru, M.I. Younis, Electrothermal frequency modulated resonator for mechanical memory. *J. Microelectromech. Syst.* **25**(5), 877–883 (2016)
13. A.Z. Hajjaj, N. Jaber, S. Ilyas, F.K. Alfosail, M.I. Younis, Linear and nonlinear dynamics of micro and nano-resonators: Review of recent advances. *Int. J. Non Linear Mech.* **119**, 103328 (2020)
14. K. Asadi, J. Yu, H. Cho, Nonlinear couplings and energy transfers in micro-and nano-mechanical resonators: Intermodal coupling, internal resonance and synchronization. *Philos. Trans. A Math. Phys. Eng. Sci.* **376**(2127), 20170141 (2018)
15. W. Yang, S. Towfighian, Internal resonance and low frequency vibration energy harvesting. *Smart Mater. Struct.* **26**(9), 095008 (2017)
16. A. Vyas, D. Peroulis, A.K. Bajaj, Dynamics of a nonlinear microresonator based on resonantly interacting flexural-torsional modes. *Nonlinear Dyn.* **54**(1–2), 31–52 (2008)
17. R. Potekin, S. Dharmasena, H. Keum, X. Jiang, J. Lee, S. Kim, L.A. Bergman, A.F. Vakakis, H. Cho, Multi-frequency atomic force microscopy based on enhanced internal resonance of an inner-paddled cantilever. *Sens. Actuators A Phys.* **273**, 206–220 (2018)
18. S.S.P. Nathangari, S. Dong, L. Medina, N. Moldovan, D. Rosenmann, R. Divan, D. Lopez, L.J. Lauhon, H.D. Espinosa, Nonlinear mode coupling and one to one internal resonances in a monolayer WS₂ nanoresonator. *Nano Lett.* **19**(6), 4052–4059 (2019)
19. E. Hacker, O. Gottlieb, Application of reconstitution multiple scale asymptotics for a two-to-one internal resonance in magnetic resonance force microscopy. *Int. J. Non Linear Mech.* **94**, 174–199 (2017)
20. C.R. Kirkendall, D.J. Howard, J.W. Kwon, Internal resonance in quartz crystal resonator and mass detection in nonlinear regime. *Appl. Phys. Lett.* **103**(22), 223502 (2013)
21. M.F. Daqaq, E.M. Abdel-Rahman, A.H. Nayfeh, Two-to-one internal resonance in microscanners. *Nonlinear Dyn.* **57**, 231 (2009)
22. H. Ouakad, H.M. Sedighi, M.I. Younis, One-to-one and three-to-one internal resonances in MEMS shallow arches. *J. Comput. Nonlinear Dyn.* **12**(5), 051025 (2017)
23. A. Sarrafan, S. Azimi, F. Golnaraghi, B. Bahreyni, A nonlinear rate microsensor utilising internal resonance. *Sci. Rep.* **9**(1), 8648 (2019)
24. A.Z. Hajjaj, N. Jaber, M.A.A. Hafiz, S. Ilyas, M.I. Younis, Multiple internal resonances in MEMS arch resonators. *Phys. Lett. A* **382**(47), 3393–3398 (2018)
25. L. Ruzziconi, N. Jaber, L. Kosuru, M.L. Bellaredj, M.I. Younis, Two-to-one internal resonance in the higher-order modes of a MEMS beam: Experimental investigation and theoretical analysis via local stability theory. *Int. J. Non Linear Mech.* **129**, 103664 (2021)
26. A. Nayfeh, D. Mook, *Nonlinear Oscillations* (Wiley, New York, 1979)
27. L. Ruzziconi, N. Jaber, L. Kosuru, M.L. Bellaredj, M.I. Younis, Experimental and theoretical investigation of the 2: 1 internal resonance in the higher-order modes of a MEMS microbeam at elevated excitations. *J. Sound Vib.* **499**, 115983 (2021)
28. L. Ruzziconi, N. Jaber, L. Kosuru, M.L. Bellaredj, M.I. Younis, Internal resonance in the higher-order modes of a MEMS beam: Experiments and global analysis. *Nonlinear Dyn.* **103**, 2197–2226 (2021)
29. M.I. Younis, *MEMS Linear and Nonlinear Statics and Dynamics* (Springer, 2011)

Nonlinear Dynamics of NEMS/MEMS Elements in the Form of Beams Taking into Account the Temperature Field, Radiation Exposure, Elastoplastic Deformations



Irina Papkova , Tatiana Yakovleva , Anton Krysko , and Vadim Krysko 

1 Introduction

In this work, we study the development problem of NEMS (nanoelectromechanical systems) as a continuation of the microelectromechanical devices' development (MEMS). One of the MEMS evolutionary ways is to reduce their mechanical components to nanoscale up to 10 nm and thereby decrease their mass, which leads to an increase in their resonance frequencies. This leads to a NEMS energy consumption decrease, a significant increase in the functionality of this kind of devices, and their application field expansion when taking into account dynamic, thermal, noise, and radiation effects, which entail the need to build mathematical models taking into account the dependence of material properties on these influences.

In the proposed work, a mathematical model is built taking into account physical nonlinearity, residual plastic deformations, and cyclic loading, and this is possible when constructing a mathematical model, the dependence of material properties on the deformations intensity, temperature, and radiation exposure; nanoeffects are taken into account. This model type does not exist in the literature known to us, since classical mechanics does not allow this.

The first attempt to construct an elasticity theory with an asymmetric stress tensor belongs to the Cosserat brothers [1]. In their work, the Cosserat brothers developed the elasticity theory, using a variational principle, which they called “L'Action Euclidienne.” In the 1960s, the Cosserat brothers' idea received the attention of researchers, and many continuum theories were proposed. These theories can

This work was supported by the RFBR (Grant No. 20-08-00354).

I. Papkova · T. Yakovleva (✉) · A. Krysko · V. Krysko
Yuri Gagarin State Technical University of Saratov, Saratov, Russia
e-mail: yan-tan1987@mail.ru

be divided into three classes: strain gradient theory, microelasticity theory, and nonlocal elasticity theory.

These theories account for the size effect using scale material length parameters.

The moment theory proposed by Toupin [2], Mindlin [3], and Koiter [4] considers only the rotation vector gradient in the strain energy, and therefore, only two scale parameters of the material length are required. In a modified moment theory proposed by Yang et al. [5], one scale parameter is used.

The microelasticity theory was proposed by Eringen [6] as a generalization of the Cosserat brothers' theory. The microelasticity theory made it possible to obtain the microinertia conservation law, which was lacking in previous theories, and that did not allow determining the change in body position during movement. For modeling small-sized structures, several nonclassical higher-order continuum theories have been developed, such as the moment theory [2, 3, 7–9].

After the first study of the microbeams, a static analysis based on the modified moment theory of Park S.K. and Gao X.L. [10], many studies were carried out to determine the static characteristics, stability, and vibrations for microbeams [11–17]. Nonlinear effects in fine structural elements have been studied by Xia W. [18], Ke L.L. [19], and Ghayes M.H. [20, 21] using the modified moment theory. All the theories discussed in the introduction are based on the theory of elasticity. The main problems in the literature known to us are devoted to the problem when the elastic characteristics change according to a given law. This is a functionally gradient theory [22–24]. In this paper, the material properties depend on the stress intensity diagram of the strain intensity and, as a result, on the x , z coordinates and temperature. Thus, the analysis theory of the elastic-plastic deformations is constructed on the basis of the modified moment theory.

The relationship between deformations and stresses is given according to experimental data and depends on temperature.

2 Problem Formulation

In the modified moment theory [5], the deformation potential energy Π in an elastic body occupying the region $\Omega = \{0 \leq x \leq a; -\frac{b}{2} \leq y \leq \frac{b}{2}; -h \leq z \leq h\}$, where a is the beam length, b beam width, h beam thickness, and x, y, z Cartesian coordinates (Fig. 1), at infinitesimal strains, is written in the form:

$$\Pi = \frac{1}{2} \int_0^a \int_{-b/2}^{b/2} \int_{-h}^h (\sigma_{ij} \varepsilon_{ij} + m_{ij} \chi_{ij}) dx dy dz \quad (1)$$

where σ_{ij} is the classical stress tensor, ε_{ij} strain tensor components, χ_{ij} components of the symmetric curvature gradient tensor, and m_{ij} the moment of higher orders. Accepted $b = 1$.

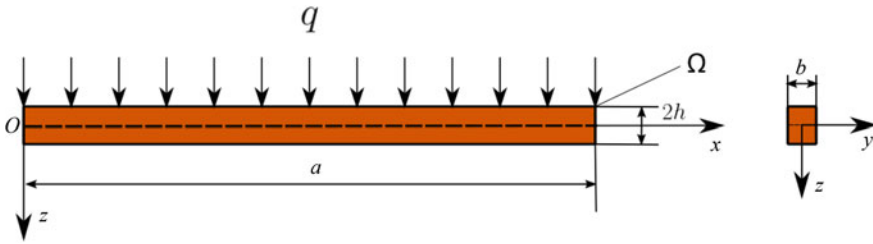


Fig. 1 Computational beam scheme

To build a mathematical model, the following hypotheses are accepted: The Bernoulli-Euler hypothesis is used. The material is isotropic, but inhomogeneous; its properties depend on the x, z coordinates, strain intensity e_i , temperature increment $\theta(x, z) = T(x, z) - T_0(x, z)$, where $T(x, z)$ is the specified temperature and $T_0(x, z)$ the initial temperature. The Duhamel-Neumann law is used. The deformation theory of plasticity and the von Mises plasticity criterion are used. The deformation diagram depends on temperature; the temperature field is determined from the solution of the two-dimensional stationary heat equation. The nanostructure is taken into account using the modified moment theory.

According to the modified moment theory, the symmetric curvature gradient tensor components χ_{ij} take the form

$$\chi_{12} = -\frac{1}{2} \frac{\partial^2 w}{\partial x^2}. \tag{2}$$

where w is deflection. The strain tensor components take the form $e_{xx} = -z \frac{\partial^2 w}{\partial x^2} + \alpha_t \theta(x, z)$, where α_t is the linear expansion of the material. Let's write Hooke's law: $\sigma_{xx} = \frac{E(1-\nu)}{(1+\nu)(1-2\nu)} e_{xx}$, where E is the elasticity modulus and ν Poisson's ratio.

Taking into account (Eq. 2), we obtain for m_{ij} : $m_{xy} = -\frac{El^2}{1+\nu} \frac{\partial^2 w}{\partial x^2}$. Loads and moments, taking into account the modified moment theory, are as follows: $M_{xx} = \int_{-h}^h \sigma_{xx} z dz$; $Y_{xy} = \int_{-h}^h m_{xy} dz$. The parameter l , which appears at the higher-order moment m_{ij} , is an additional independent material length parameter associated with the symmetric rotation gradient tensor. In this model, in addition to the usual Lamé parameters, it is necessary to take into account one more scale parameter of length l [1]. This is a direct consequence of the fact that, in the moment theory of elasticity, the strain energy density is a function of the strain tensor and the symmetric curvature tensor. It does not explicitly depend on rotation (the asymmetric part of the deformation gradient) and the asymmetric part of the curvature tensor.

From the Ostrogradsky-Hamilton variational principle, we obtain the equations of motion for a flexible shell element taking into account the modified moment theory:

$$\begin{aligned} & \frac{\partial^2}{\partial x^2} \left[- \left(\int_{-h}^h \left(\frac{E(1-\nu)}{(1+\nu)(1-2\nu)} z^2 + \frac{EI^2}{1+\nu} \right) dz \right) \frac{\partial^2 w}{\partial x^2} - \int_{-h}^h \frac{E\alpha_t(1-\nu)z\theta}{2(1+\nu)(1-2\nu)} dz \right] + q \\ & = \frac{\partial^2 w}{\partial t^2} \int_{-h}^h \rho dz + \varepsilon \frac{\partial w}{\partial t} \int_{-h}^h \rho dz \end{aligned} \quad (3)$$

where ε is the dissipation coefficient, ρ beam material density, and $q(x, t)$ external normal load.

To solve Eq. (3), the temperature θ should be determined. The θ value is not given, but is determined from the Eq. (4) solution with the corresponding boundary conditions of the first, second, and third kinds:

$$\frac{\partial^2 \theta}{\partial x^2} + \frac{\partial^2 \theta}{\partial z^2} = 0. \quad (4)$$

Boundary and initial conditions for the beam:

$$\text{Rigid clamping } w(0, t) = 0, \quad \frac{\partial w(0, t)}{\partial x} = 0, \quad w(a, t) = 0, \quad \frac{\partial w(a, t)}{\partial x} = 0, \quad (5)$$

$$\text{Articulated support } w(0, t) = 0, \quad \frac{\partial^2 w(0, t)}{\partial x^2} = 0, \quad w(a, t) = 0, \quad \frac{\partial^2 w(a, t)}{\partial x^2} = 0, \quad (6)$$

$$\text{Initial conditions } w|_{t=t_0} = \frac{\partial w}{\partial t}|_{t=t_0} = 0. \quad (7)$$

The required equations were reduced for a numerical solution to a dimensionless form in the usual way [25]. Integration of Eqs. (3)–(7) with respect to coordinate and time is carried out by the finite differences method of the second accuracy order.

The derivation of the governing equations on the theory of plasticity, where E and ν are coupled with the shear modulus G and the beam modulus of the volumetric deformation K , is obtained via the following relations:

$$E = \frac{9KG}{3K + G}, \quad \nu = \frac{1}{2} \frac{3K - 2G}{3K + G}. \quad (8)$$

We take $K = K_0 = \text{const}$. The Young module and the Poisson ratio depend on the coordinates $\{x, z\}$, temperature T , and the deformation intensity e_i . In the theory of small elastic-plastic deformations, the shear modulus is determined by the formula

$G = \frac{1}{3} \frac{\sigma_i(e_i)}{e_i}$, where σ_i stands for the stress intensity and e_i describes the deformation intensity:

$$e_i = \frac{\sqrt{2}}{3} \left(1 + \frac{\nu}{1-\nu} + \left(1 + \frac{\nu}{1-\nu} \right)^2 \right) |e_{xx}|. \tag{9}$$

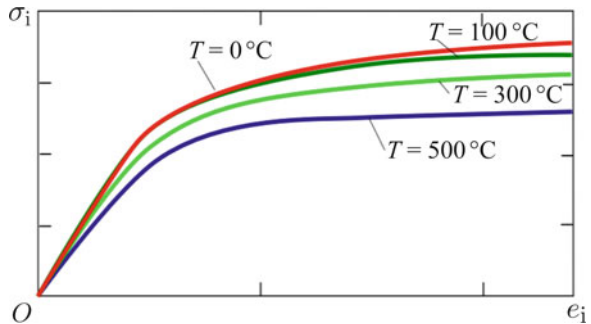
The convergence of the method in spatial and temporal coordinates is investigated. It was found that to obtain results with the required accuracy degree, it is sufficient to divide the integration interval $[0, 1]$ into 120 parts. The results were compared for 10, 20, 40, 80, 120, 160, and 200 sections of the segment division $[0, 1]$. The convergence conditions were set not only for the deflection function itself but also for its first and second derivatives. The Cauchy problem for the obtained results reliability was solved by the Runge-Kutta methods from the second to eighth order of accuracy: Runge-Kutta second and fourth order, Runge-Kutta-Felberg of the fourth-order method, Cache-Carp fourth order, Runge-Kutta Prince-Dormand eighth order, implicit Runge-Kutta second-order and fourth-order method, and Newmark method. For determining reliable decisions used the methodology described in [26, 27]. The Newmark method was chosen. The solution stability in time, i.e., time step, is carried out according to the Runge principle. At each time layer, an iterative procedure of the Birger variable parameters method of elasticity [23] is constructed; the value of Young’s modulus in the spatial grid in $\{x, z\}$ is specified. The material of the beam is steel with a deformation diagram:

$$\sigma_i = \begin{cases} G_0 e_i, & \text{if } e_i < e_s \\ G_0 e_s + G_1 (e_i - e_s), & \text{if } e_i \geq e_s \end{cases} \cdot \begin{cases} G = G_0 & \text{for } e_i < e_s, \\ G = G_0 \frac{e_s}{e_i} + G_1 \left(1 - \frac{e_s}{e_i} \right) & \text{for } e_i \geq e_s \end{cases} \tag{10}$$

where e_s is the yield strain.

Shear moduli G_0 and hardening modulus G_1 were determined experimentally [28] depending on temperature. The dependencies of the stress intensity on the deformations intensity and the temperature are shown in Fig. 2.

Fig. 2 Graphical dependency $\sigma_i(e_i)$



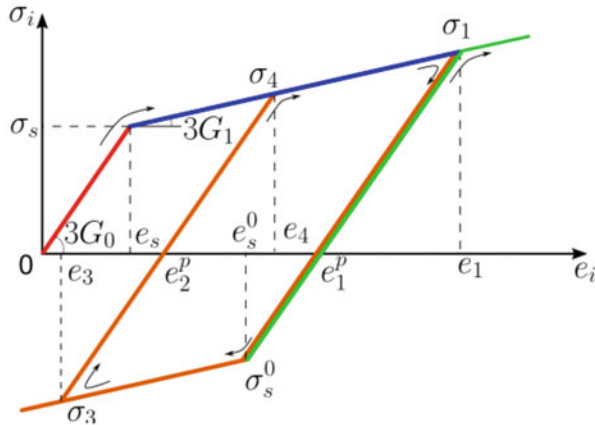


Fig. 3 Graphical dependency $\sigma_i(e_i)$ for Eq. (10)

3 Algorithms for Residual Plastic Deformation Accounting

Figure 3 shows the accounting of loading and unloading the shell element on the example of the relation $\sigma_i(e_i)$. A detailed description is in [29].

In what follows, we consider the neutron radiations of flexible rectangular beams' stability. Lenskiy [30] pointed out that metal radiation through the fast neutron flux implies a change in their physical and metallic properties. It has been observed that the largest radiation influence has been exhibited by the magnitude of the carbon silicate material flow limit σ_s . Radiation increase implies increase of σ_s . In the steel F-212 V case, the functional and nonlinear dependence of σ_s versus the total radiation flux is reported by Iliushin and Ogibalov [31].

4 Numeric Results

Let us present the numerical study results for an accelerometer-sensitive element in the form of a physically nonlinear rigidly clamped (Eq. 5) microbeam located in a stationary temperature field, and to this beam, a uniformly distributed transverse load is applied. A beam (Fig. 4) with the following geometric parameters is considered: length $a = 300 \mu\text{m}$, thickness $h = 10 \mu\text{m}$, and the material is steel. In this paper, the solution of static problems will be presented using the steady solution method, which is a special case of the parameter continuation method. Figs. 5 and 6 have shown the dependence of the static load on the deflection at different temperatures. Boundary conditions for the heat equation:

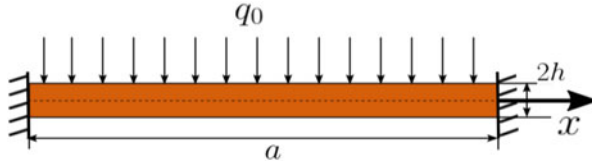


Fig. 4 Design scheme of the beam

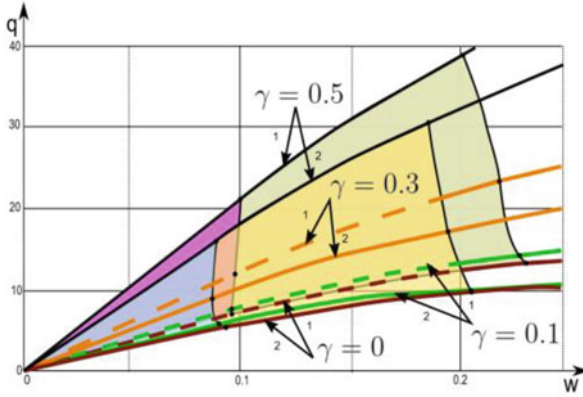


Fig. 5 Load-deflection graph for $T_1 = 0\text{ }^\circ\text{C}$ (line 1); $500\text{ }^\circ\text{C}$ (line 2) (blue – elastic deformations at $T_1 = 0\text{ }^\circ\text{C}$, yellow – elastic-plastic deformations at $T_1 = 0\text{ }^\circ\text{C}$, purple – elastic deformations at $T_1 = 500\text{ }^\circ\text{C}$, green – elastic-plastic deformations at $T_1 = 500\text{ }^\circ\text{C}$)

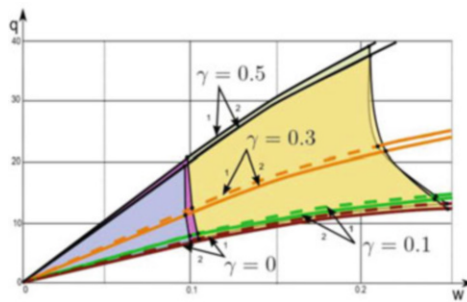


Fig. 6 Load-deflection graph for $T_1 = 100\text{ }^\circ\text{C}$ (line 1); $300\text{ }^\circ\text{C}$ (line 2) (blue – elastic deformations at $T_1 = 100\text{ }^\circ\text{C}$, yellow – elastic-plastic deformations at $T_1 = 100\text{ }^\circ\text{C}$, purple – elastic deformations at $T_1 = 300\text{ }^\circ\text{C}$, green – elastic-plastic deformations $T_1 = 300\text{ }^\circ\text{C}$)

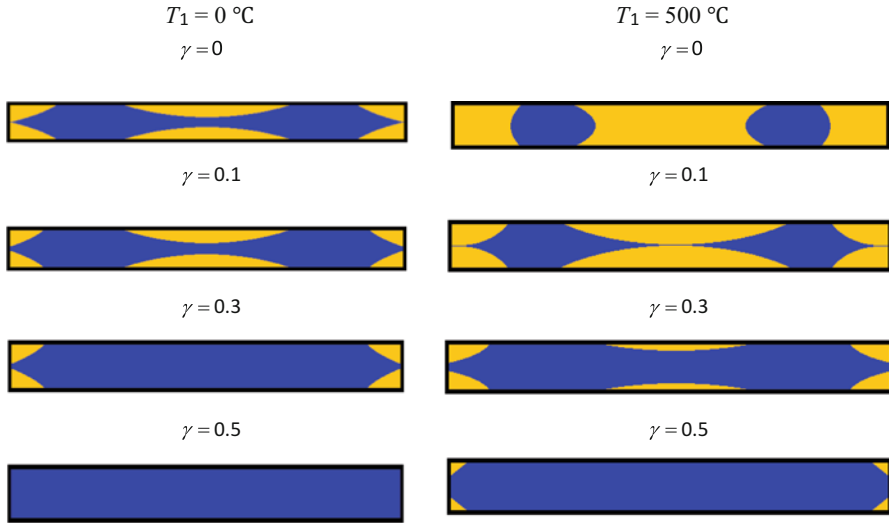


Fig. 7 Areas of elastic and plastic deformations

$$\theta = T_1 \text{ with } z = -\frac{h}{2}, x = [0; a]; T_1 = 0 \text{ with } z = \frac{h}{2}, x = [0; a]. \quad (12)$$

The heat equation was solved by the second-order finite difference method.

Consider the graphs “load-deflection” depending on the temperature $T_1 = 0 \text{ }^\circ\text{C}$, $500 \text{ }^\circ\text{C}$ (Fig. 5); $T_1 = 100 \text{ }^\circ\text{C}$, $300 \text{ }^\circ\text{C}$ (Fig. 6), the size-dependent parameter changed as $\gamma = \frac{l^2}{h^2} = 0; 0.1; 0.3; 0.5$. The graphs show the zones of elastic and elastic-plastic deformations. In graphs 4 and 5, the solid line marks the dependences at $T_1 = 0 \text{ }^\circ\text{C}$ and $T_1 = 100 \text{ }^\circ\text{C}$, and the dashed line at $T_1 = 500 \text{ }^\circ\text{C}$ and $T_1 = 300 \text{ }^\circ\text{C}$. An increase in temperature from $T_1 = 0 \text{ }^\circ\text{C}$ to $T_1 = 500 \text{ }^\circ\text{C}$ (Fig. 5) leads to a decrease in the load at which elastic-plastic deformations occur. Figure 6 shows the dependences $q(w)$ for $T_1 = 100 \text{ }^\circ\text{C}$ to $T_1 = 300 \text{ }^\circ\text{C}$. In the elastic part, the plots marked with the solid and dashed lines coincide at the same value of the size-dependent parameter; the difference begins in the elastoplastic part: at the same load, the deflection at $T_1 = 100 \text{ }^\circ\text{C}$ is less than at $T_1 = 300 \text{ }^\circ\text{C}$. With an increase in the parameter γ , the elastic deformations zone increases, and elastic-plastic deformations occur at a greater load. An increase in temperature leads to a decrease in the bearing capacity of the beam.

Figure 7 shows a comparison of the zones distribution for elastic and plastic deformations (the elastic deformation is designated in blue, and the plastic deformations are marked with a yellow) along beam thickness depending on the temperature and dimension-dependent parameter. Studies are shown under the load $q = 20$. At

$T_1 = 0$ °C, $\gamma = 0$, $\gamma = 0.1$, $T_1 = 500$ °C, $\gamma = 0$, $\gamma = 0.1$, a phenomenon of a plastic hinge is observed. With increasing temperature from 0 °C to 500 °C, zones of plastic deformations increase with any γ . With an increase in the dimension-dependent parameter, the zone of plastic deformations gradually decreases to a complete disappearance (at $T_1 = 0$ °C and $\gamma = 0.5$). At temperature $T_1 = 500$ °C and $\gamma = 0.5$, plastic deformations remain in the corners of the beams.

5 Conclusions

For the first time, a nonlinear dynamics general theory of physically nonlinear beams was constructed according to the modified moment theory in a temperature field. Algorithms and software packages have been created for the study of elastic and elastic-plastic deformations for micro and nanobeams. The stationary solution is obtained from dynamic solutions using the steady solution method. Numerical results are given for the nonlinear dynamics of a beam in a temperature field, when the beam material properties substantially depend on temperature. It is shown that with an increase in the size-dependent parameter, the zone of elastic and elastic-plastic deformations increases at any temperature in $T_1 = 0$ °C; 100 °C; 300 °C; 500 °C.

References

1. E. Cosserat, F. Cosserat, *Théorie des corps déformables* (Librairie Scientifique A. Hermann, 1909)
2. R.A. Toupin, Elastic materials with couple-stresses. *Arch. Ration. Mech. Anal.* **11**(1), 385–414 (1962)
3. R.D. Mindlin, H.F. Tiersten, Effects of couple-stresses in linear elasticity. *Arch. Ration. Mech. Anal.* **11**(1), 415–448 (1962)
4. W.T. Koiter, Couple-stress in the theory of elasticity. *Proc. K. Ned. Akad. Wet. North Holland Pub* **67**, 17–44 (1964)
5. F. Yang, A.C.M. Chong, D.C.C. Lam, Couple stress based strain gradient theory for elasticity. *Int. J. Solids Struct.* **39**(10), 2731–2743 (2002)
6. A.C. Eringen, Linear theory of micropolar elasticity. *J. Math. Mech.* **15**(6), 909–923 (1966)
7. R.D. Mindlin, Influence of couple-stresses on stress concentrations. *Exp. Mech.* **3**, 1–7 (1963)
8. W.T. Koiter, Couple-stresses in the theory of elasticity: I and II. *Proc. K. Ned. Akad. Wet. B.* **67**, 17–44 (1964)
9. H.A. Fleck, J.W. Hutchinson, A phenomenological theory for strain gradient effects in plasticity. *J. Mech. Phys. Solids* **41**, 1825–1857 (1993)
10. S.K. Park, X.L. Gao, Bernoulli–Euler beam model based on a modified couple stress theory. *J. Micromech. Microeng.* **16**, 2355–2359 (2006)
11. L.L. Ke, Y.S. Wang, Size effect on dynamic stability of functionally graded microbeams based on a modified couple stress theory. *Compos. Struct.* **93**, 342–350 (2011)
12. J.N. Reddy, Microstructure-dependent couple stress theories of functionally graded beams. *J. Mech. Phys. Solids* **59**, 2382–2399 (2011)

13. M. Salamat-talab, A. Nateghi, J. Torabi, Static and dynamic analysis of third-order shear deformation FG micro beam based on modified couple stress theory. *Int. J. Mech. Sci.* **57**, 63–73 (2012)
14. A. Nateghi, M. Salamat-talab, J. Rezapour, B. Daneshian, Size dependent buckling analysis of functionally graded micro beams based on modified couple stress theory. *Appl. Math. Model.* **36**, 4971–4987 (2012)
15. M. Simsek, J.N. Reddy, Bending and vibration of functionally graded microbeams using a new higher order beam theory and the modified couple stress theory. *Int. J. Eng. Sci.* **64**, 37–53 (2013)
16. M. Simsek, J.N. Reddy, A unified higher order beam theory for buckling of a functionally graded microbeam embedded in elastic medium using modified couple stress theory. *Compos. Struct.* **101**, 47–58 (2013)
17. B. Akgöz, O. Civalek, A size-dependent shear deformation beam model based on the strain gradient elasticity theory. *Int. J. Eng. Sci.* **70**, 1–14 (2013)
18. W. Xia, L. Wang, L. Yin, Nonlinear non-classical microscale beams: Static bending, postbuckling and free vibration. *Int. J. Eng. Sci.* **48**, 2044–2053 (2010)
19. L.L. Ke, Y.S. Wang, J. Yang, S. Kitipornchai, Nonlinear free vibration of size-dependent functionally graded microbeams. *Int. J. Eng. Sci.* **50**, 256–267 (2012)
20. M.H. Ghayes, M. Amabili, H. Farokhi, Nonlinear forced vibrations of a microbeam based on the strain gradient elasticity theory. *Int. J. Eng. Sci.* **63**, 52–60 (2013)
21. M.H. Ghayes, H. Farokhi, M. Amabili, Nonlinear dynamics of a microscale beam based on the modified couple stress theory. *Compos. Part B* **50**, 318–324 (2013)
22. J. Awrejcewicz, A.V. Krysko, S.P. Pavlov, M.V. Zhigalov, V.A. Krysko, Stability of the size-dependent and functionally graded curvilinear Timoshenko beams. *J. Comput. Nonlinear Dyn.* **12**, 041018 (2017). <https://doi.org/10.1115/1.4035668>
23. J. Awrejcewicz, A.V. Krysko, S.P. Pavlov, M.V. Zhigalov, V.A. Krysko, Chaotic dynamics of size dependent Timoshenko beams with functionally graded properties along their thickness. *Mech. Syst. Signal Process.* **93**, 415–430 (2017)
24. J. Awrejcewicz, V.A. Krysko, S.P. Pavlov, M.V. Zhigalov, Nonlinear dynamics size-dependent geometrically nonlinear Timoshenko beams based on a modified moment theory. *Appl. Math. Sci.* **11**(5), 237–247 (2017)
25. J. Awrejcewicz, V.A. Krysko, I.V. Papkova, A.V. Krysko, *Deterministic Chaos in One Dimensional Continuous Systems* (World Scientific, Singapore, 2016), 460 p. ISBN: 978-981-4719-69-8
26. A.V. Krysko, J. Awrejcewicz, A.A. Zakharova, I.V. Papkova, V.A. Krysko, Chaotic vibrations of flexible shallow axially symmetric shells. *Nonlinear Dyn. Springer Netherlands* **91**, 2271–2291 (2018)
27. I.A. Birger, General algorithms for solving the theory problems of elasticity, plasticity and creep, in *Advances in Mechanics of Deformable Media*, (Nauka, Moscow, 1975), pp. 51–73
28. Ю.Н. Шевченко, И.В. Прохоренко, *Теория упруго-пластических оболочек при неизотермических процессах нагружения* (Наук. думка, Киев, 1981), 296 с
29. A.V. Krysko, J. Awrejcewicz, I.V. Papkova, V.A. Krysko, Stability improvement of flexible shallow shells using neutron radiation. *Materials* **13**(14), 3187 (2020)
30. V.S. Lensky, The effect of reactive irradiation on the mechanical properties of solids. *Eng. Coll.* **28**, 17–23 (1960)
31. A.A. Ilyushin, P.M. Ogibalov, On the strength of the shells of a thick-walled cylinder and a hollow ball exposed to radiation. *Eng. Coll.* **28**, 134–144 (1960)

Single Input–Single Output MEMS Gas Sensor



A. Alneamy, N. Heidari, W. Lacarbonara, and E. Abdel-Rahman

1 Introduction

MEMS sensors have been widely used in several applications such as chemical, medical, and biological [1–3]. Gas sensors are designed to detect perilous gases in the environment. These sensors are coated with a functional layer to capture the target gas molecules [4]. The change in the response of such a device can be measured using several detecting mechanisms such as capacitively [5, 6], piezoelectrically [7, 8], and piezoresistively [9–11].

There are two commonly used detection modes in inertial gas sensors: static and dynamic. The static mode measures the mass absorbed by the detector material. This is done by measuring the change in structural displacement while the dynamic mode measures the shift in one of its resonance frequencies [12, 13]. The latter mode is significantly sensitive to changes in mass interpreted as changes in the location of the bifurcation points either linearly or nonlinearly.

Recently, there were several attempts to introduce different designs and configurations for gas sensors in order to enhance their performance. For example, Khater et al. [14] designed and fabricated a gas sensor consisting of a cantilever beam with a plate attached to its free end. The sensor was excited near the pull-in threshold.

A. Alneamy (✉)

Department of Mechanical Engineering, Jazan University, Jazan, Saudi Arabia
e-mail: alneamy@jazanu.edu.sa

N. Heidari · W. Lacarbonara

Department of Structural and Geotechnical Engineering, Sapienza University of Rome, Rome, Italy
e-mail: heidari.1783508@studenti.uniroma1.it; walter.lacarbonara@uniroma1.it

E. Abdel-Rahman

Department of Systems Design Engineering, University of Waterloo, Waterloo, ON, Canada
e-mail: eihab@uwaterloo.ca

The result showed that the sensor has the ability to detect 5 ppm of ethanol vapor in dry nitrogen.

Another design was proposed by Jaber et al. [15]. Their sensor consists of a clamped-clamped beam that is made of a metal-organic framework (MOF) and excited electrostatically. It was deployed to detect water vapor and acetone. The sensor was excited in the second bending mode resulting in a large frequency shift and exhibited a sensitivity to detect a mass change of 203.2 fg. A similar study was also proposed by Bouchaala et al. [13]. They studied the theoretical and experimental performance of gas sensors based on clamped-clamped beam configurations. Their analysis showed a measured quantity of 4.389 ng.

In this paper, a new design and implementation for gas sensors is presented based on earlier work by Cetraro [16]. The sensor consists of a shuttle mass and two resonant inner beams attached to it. The shuttle mass is excited via an external force that indirectly excites the inner beams. This design showed the ability to detect two different gases simultaneously. To further investigate this concept, a kinematic model was constructed to study the static and dynamic response of one of the sensor's cantilever beams accounting for the lowest two bending modes considering external and electrostatic forces.

2 Sensor Design

The single input–single output sensor (SISO) consists of a shuttle mass that supports two cantilever beams as shown in Fig. 1. It is electrostatically actuated by applying a voltage difference between the side-surface of the shuttle mass and the sidewall electrode marked as “drive electrode”. The shuttle mass is carrying two inner cantilever beams serving as sensors. The beams have been functionalized to detect similar or different gases depending on the detector material being used.

The gas sensor is designed to be operated in two modes. A static mode uses a bias voltage (V_{dc}) applied via the sidewall electrodes and a dynamic mode uses a biased time-varying voltage signal (V_{dc1} and V_{ac1}) to the drive electrode. The shuttle mass is grounded while a V_{dc} voltage (V_{dc2}) is applied to the sense electrode. A schematic diagram of the electrical connectivity is shown in Fig. 1. In this work, the sensor is excited by a single electrostatic force applied between the sensor and the drive electrode while the shuttle mass and sense electrode are grounded. This connection is only one actuation scenario, others are also possible given the sensor's electrical connectivity.

Actuating the shuttle mass results in the base excitation of the inner resonators. Two variable capacitances arise between the sensor and the drive electrode C_d and the sensor and the sense electrode C_s . The detection mechanism can be electrical through capacitance measurement or optical using a Laser-Doppler Vibrometer.

The former estimates the shuttle mass displacement indirectly by measuring the capacitance C_s or the capacitance difference $C_s - C_d$. On the other hand, the Laser-Doppler Vibrometer can measure the displacement of the inner beams directly. In

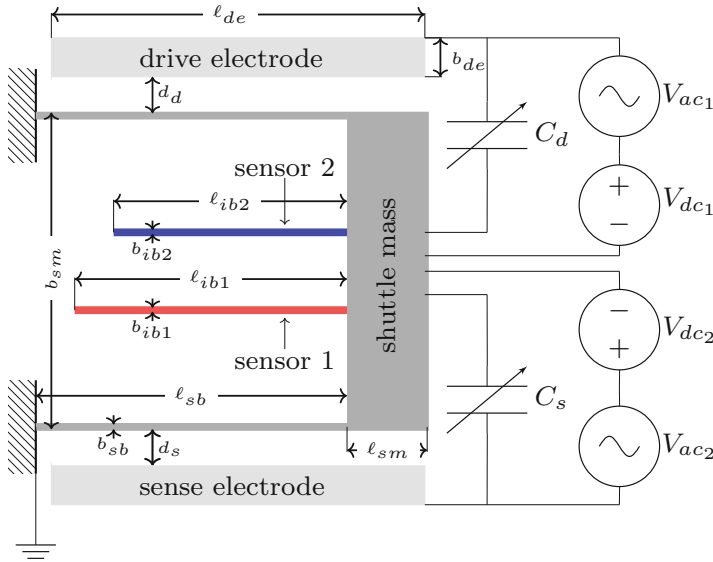


Fig. 1 A schematic of the proposed single input–single output electrostatic gas sensor, electrical connections, and the sensor parameters

both cases, a target gas concentration is measured as a shift in one of the sensor’s resonance frequencies. Equipping each of the inner beams with a distinct detector material and using multiple resonances allows for simultaneous detection of two gases.

The two beams supporting the shuttle mass are identical with a length of $\ell_{sb} = 620 \mu\text{m}$ and a width of $b_{sb} = 10 \mu\text{m}$, Fig. 1. The shuttle mass length and width are $\ell_{sm} = 70 \mu\text{m}$ and $b_{sm} = 200 \mu\text{m}$, respectively. One of the support beams is coupled electrostatically to the drive electrode. The electrostatic gap between the support beam and drive electrode is denoted d_d . This initial gap is $d_d = 2 \mu\text{m}$. On the other hand, the gap between the other support beam and the sense electrode is denoted by d_s set to $2 \mu\text{m}$. The sidewall electrodes are equal in length $\ell_{de} = \ell_{se} = 680 \mu\text{m}$ and similar to the sum of the support beam and shuttle mass lengths $\ell_{sb} + \ell_{sm}$. The structural layer thickness is $h = 10 \mu\text{m}$.

3 Problem Formulation

Two approaches were used in this study to examine the concept of single input–single output gas sensor: a finite-element (FE) model and a kinematic model based on a one-mode Reduced-Order model. The first approach was used to investigate the static response, eigenvalues, and corresponding mode shapes of the SISO. The second approach was deployed to study the static and dynamic response of the

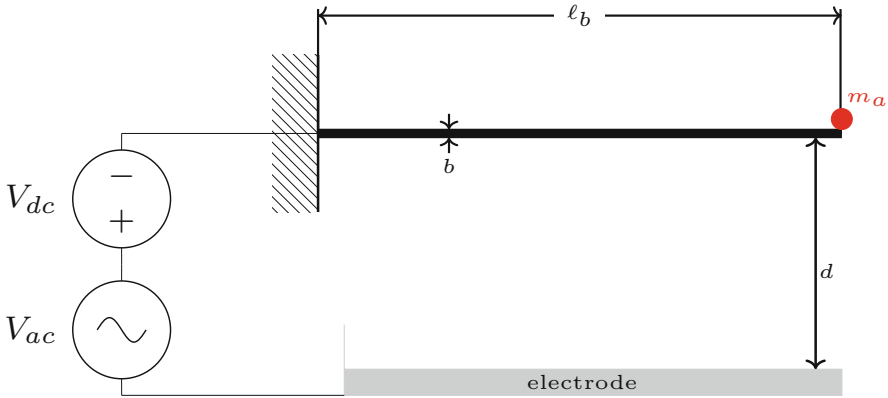


Fig. 2 A schematic of an electrically actuated cantilever beam with the added mass

sensor’s inner cantilever beams under external and electrostatic excitation. The latter model was also aimed to study the sensor’s sensitivity and, more broadly, dynamic response in the presence and absence of gas molecules. This is a necessary step to examine the sensor feasibility.

We assume that the cantilever beam has a cross-sectional area A_b and an area moment of inertia J and carrying an added mass, representing the gas molecules, located at the tip as shown in Fig. 2. The added mass m_a is treated as a point mass while its rotary inertia is neglected. The equation of motion describing the damped in-plane deflection $v(s, t)$ with the associated boundary conditions were derived using Euler-Bernoulli beam theory while ignoring the shear deformation. In this derivation, we accounted for the nonlinear inertia terms, the added mass and a harmonic excitation force. Following these assumptions, one can write the equation of motion as follows:

$$\begin{aligned}
 & \left[\rho A_b \left(1 - \frac{1}{2} v'^2 \right) + m_a \delta(s - \ell_b) \right] \ddot{v} + \rho A_b v' \int_0^s (v' \ddot{v}' + \dot{v}'^2) d\xi + c \dot{v} \\
 & + v'' \int_s^{\ell_b} \rho A_b \left[v' \ddot{v} - \int_0^\xi (v' \ddot{v}' + \dot{v}'^2) dz \right] d\xi \\
 & + M v'' - v'' \int_s^{\ell_b} M' v'' d\xi + m_a v'' \left[(v'|_{\ell_b} \ddot{v}|_{\ell_b}) - \int_0^{\ell_b} (v' \ddot{v}' + \dot{v}'^2) d\xi \right] = f(t)
 \end{aligned} \tag{1}$$

where the second term in Eq. (1) represents nonlinear inertia terms and the seventh term represents the effects of the added mass. The constitutive law for the bending moment is

$$M = EJ\kappa = EJ \left[v'' \left(1 + \frac{1}{2} v'^2 \right) \right] \tag{2}$$

The associated boundary conditions for the beam are the kinematic relations at the fixed-end

$$v(0, t) = 0 \quad , \quad v'(0, t) = 0 \tag{3}$$

and the mechanical boundary conditions at the free end

$$M(\ell_b, t) = 0 \quad , \quad Q(\ell_b, t) = -m_a \ddot{v}|_{s=\ell_b} \tag{4}$$

Thus, the mechanical boundary conditions at the tip can be expressed in terms of displacements as

$$EJv''(\ell_b, t) = 0 \quad , \quad EJv'''(\ell_b, t) = -m_a \ddot{v}|_{s=\ell_b} \tag{5}$$

Then, we nondimensionalize Eq. (1) by re-scaling the displacement $v(s, t)$ by the separation gap d and time t by a time-scale coefficient $\sqrt{\rho A_b \ell_b^4 / EJ}$ to yield

$$\begin{aligned} & \left[\left(1 - \frac{1}{2} \hat{v}^2 \right) + m^* \delta(\hat{s} - 1) \right] \ddot{\hat{v}} + \hat{v}' \int_0^{\hat{s}} (\hat{v}' \ddot{\hat{v}} + \dot{\hat{v}}'^2) d\hat{\xi} + \hat{c} \dot{\hat{v}} \\ & + \hat{v}'' \int_{\hat{s}}^1 \left[\hat{v}' \ddot{\hat{v}} - \int_0^{\hat{\xi}} (\hat{v}' \ddot{\hat{v}} + (\dot{\hat{v}}')^2) d\hat{z} \right] d\hat{\xi} \\ & + \alpha \left[\hat{v}'''' + \hat{v}'' \left(\frac{1}{2} \hat{v}'' \hat{v}^2 \right) - \hat{v}'' \int_{\hat{s}}^1 \hat{v}'' \hat{v}''' d\hat{\xi} \right] + m^* \hat{v}'' \left[(\hat{v}'|_1 \ddot{\hat{v}}|_1) - \int_0^1 (\hat{v}' \ddot{\hat{v}} + \dot{\hat{v}}'^2) d\hat{\xi} \right] = f(t) \end{aligned} \tag{6}$$

where $\hat{c} = 2\zeta \omega_n$, m^* is the ratio of the added mass to the beam mass and

$$\alpha = \begin{cases} 1 & , \quad \text{if } m^* = 0 \\ \frac{1}{1+m^*} & , \quad \text{if } m^* \neq 0 \end{cases}$$

Then, a ROM was developed to describe the beam motion using a one-mode projection in the Galerkin expansion which can be expressed as

$$\hat{v}(\hat{s}, \hat{t}) = \phi_i(\hat{s}) \hat{q}_i(\hat{t}) \tag{7}$$

where $\phi_i(\hat{s})$ is beam bending mode shape and $\hat{q}_i(\hat{t})$ is modal coordinate. Substituting this form into Eq. (6), multiplying the resulting equation by the mode shape ϕ_i and then integrating over the beam length, we obtained an ODE describing the transverse motion in terms of the generalized coordinate \hat{q}_i . For the sake of simplicity, we dropped ($\hat{\cdot}$) from the notation henceforth.

Projecting the equation of motion, Eq. (6), onto the first bending mode ϕ_1 yielded

$$(1 + 4 m^*) q_1'' + 12.3624 \alpha q_1 + 13.8134 \alpha q_1^3 + 2\zeta \omega_n q_1'$$

$$\begin{aligned}
& +(2.4428 + 0.7366 m^*)q_1^2 q_1'' \\
& +(4.5967 - 3.9889 m^*)q_1(q_1')^2 = f(t)
\end{aligned} \tag{8}$$

where the prime indicates differentiation with respect to time.

Similarly, the reduced-order model for the second mode shape ϕ_2 was found to be

$$\begin{aligned}
& (1 + 4 m^*)q_2'' + 485.519 \alpha q_2 - 2066.73 \alpha q_2^3 + 2\zeta \omega_n q_2' \\
& +(176.738 m^* + 112.832)q_2^2 q_2'' \\
& +(144.726 + 430.966 m^*)q_2(q_2')^2 = f(t)
\end{aligned} \tag{9}$$

Next, we compare the beam response under an external excitation of the form

$$f(t) = A \cos(\Omega t)$$

to its response under an electrostatic excitation of the form

$$f(t) = \frac{\beta V^2(t)}{(1 - \phi_i q_i)^2} \int_0^1 \phi_i(\xi) d\xi$$

where the nondimensional coefficient β is defined as

$$\beta = \frac{6\epsilon \ell_b^4}{(1 + 4 m^*)Eh^3 d^3}$$

and the voltage waveform is given by

$$V(t) = V_{dc} + V_{ac} \cos(\Omega t)$$

4 Results and Discussion

4.1 SISO Sensor

A 3D model for the SISO with the dimensions listed in Sect. 2 and the material described above was constructed using the FEM COMSOL Multiphysics. The drive and sense electrodes were placed parallel to the shuttle mass and support beams with a capacitor gap of $d_d = d_s = 2 \mu\text{m}$. The sensor was enclosed in an air box $(1000 \times 100 \times 270) \mu\text{m}^3$ in order to account for the electrostatic fringing field. The boundary conditions fixed the support beams to their anchors. To calculate the static response, the SISO was grounded while the drive electrode voltage and the sense electrode voltage were set to V_{dc} and zero, respectively.

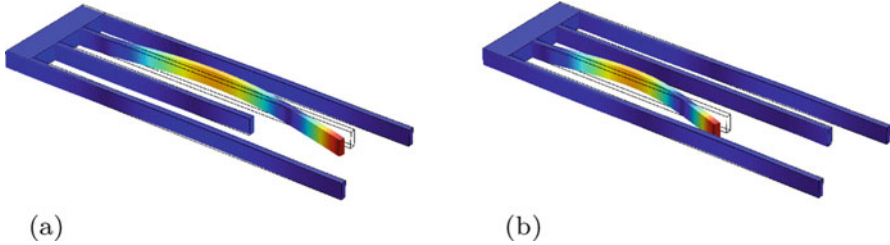


Fig. 3 The selected mode shapes for (a) sensor 2 and (b) sensor 1. (a) sensor 2: $f_1 = 288.31$ kHz. (b) sensor 1: $f_2 = 532.37$ kHz

The Electromechanics module was used to perform static and eigenvalue analyses. The drive electrode voltage was initially set to $V_{dc} = 0$ and gradually increased in steps of 2 V over the range [0–35] V. This iterative approach is necessary to capture the pull-in voltage accurately.

The displacement of the shuttle mass' tip-point was calculated without an added mass. The results show that the deflection at the tip-point increases as the applied voltage increases until it reaches the pull-in threshold where the sensor equilibrium loses stability and goes into contact with the drive electrode. We found that the sensor “pull-in” voltage corresponding to this threshold is 34.8 V.

We used the FEM module to evaluate the first eight natural frequencies and the corresponding mode shapes. This is an essential step to identify mode shapes where the inner cantilever beams' response is suitable for sensing applications. We found that some of the lowest eigenfrequencies are dominated by shuttle mass motions, whereas some of the higher modes are dominated by the cantilever beams' oscillations. We chose to operate the sensor at mode shapes dominated by the in-plane bending of the inner beams to reduce the squeeze-film damping which tends to increase the quality factor and, therefore, the sensor sensitivity.

The first selected mode ($f_1 = 288.31$ kHz) is dominated by the second in-plane bending vibrations of the inner beam marked “sensor 2” in Fig. 3a. The second selected mode ($f_2 = 532.37$ kHz) is dominated by the second in-plane bending vibrations of the inner beam marked as “sensor 1” in Fig. 3b. This difference in their resonance frequencies allows for simultaneous detection of two gases by equipping each of the inner beams with a distinct detector material.

4.2 Cantilever Beam Sensor

We investigated analytically the response of one of the SISO inner beams under external and electrostatic excitation. The sensor has a length of 200 μm , a width of 10 μm , thickness of 2 μm , and a separation gap of 2 μm , respectively. The reduced-order model (ROM) projected onto the first mode, Eq. (8), was first solved analytically for the static response.

Fig. 4 The cantilever beam tip deflection as a function of the V_{dc} obtained using the first mode projection. The branch of stable equilibria is shown as a solid blue line and the branch of unstable equilibria is shown as a dashed red line. The FE model deflection is marked by (green filled circle) symbol

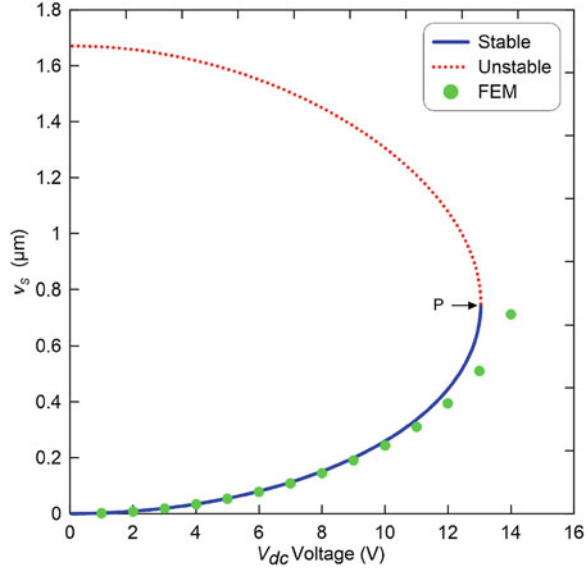
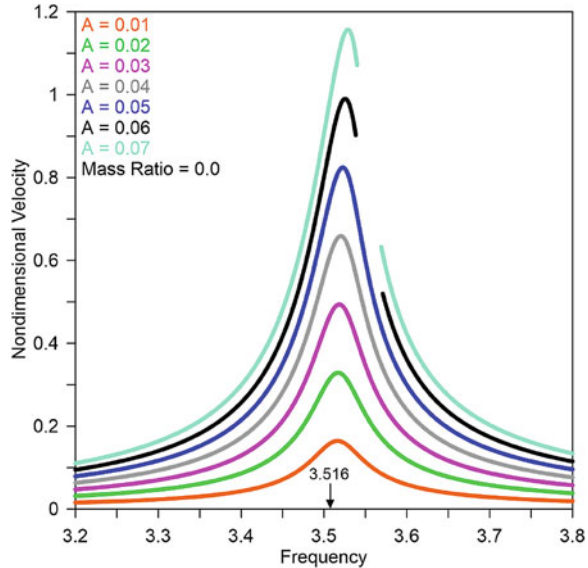


Figure 4 shows the cantilever tip deflection v as a function of V_{dc} . A branch of stable equilibria, shown as a solid blue line, and a branch of unstable equilibria, shown as a dashed red line, meet at a saddle-node bifurcation (point P). The figure shows that the tip deflection increases smoothly as the V_{dc} voltage increases along the branch of stable equilibria until it reaches the “pull-in instability” at point P ($V_{pin} = 13.1$ V). Beyond this point, there are no stable equilibria.

To validate the analytical static results, the FE model developed above was also used to solve for the static deflection of the cantilever beam. Figure 4 compares the tip deflection calculated by the FE model, marked by (green filled circle) symbols, to the ROM results. We found that, for lower V_{dc} voltages the two models are similar. However, as the applied voltage approaches the pull-in bifurcation point, differences emerge. This is due to the limited number of modes (one) used in the Galerkin expansion. For better convergence, a higher number of modes should be incorporated into the model.

The beam performance as a sensor was investigated by subjecting it to a frequency sweep in the vicinity of the first two in-plane fundamental frequencies ω_i with and without the added mass. In this analysis, the voltage signal frequency Ω was swept-up and down. The damping ratio ζ was set to 0.02 and two forcing signals were used: an external (linear) force and an electrostatic force. The frequency-response curves (FRCs) were generated by employing the shooting method to obtain the periodic orbits and to determine their stability by evaluating their Floquet multipliers.

Fig. 5 The nondimensional FRCs of the cantilever beam tip velocity in the vicinity of the first bending mode’s primary resonance in the absence of added mass under an external force with amplitude $A = 0.01–0.07$ as the signal frequency was swept-up and down in the range of 3.2–3.8



External Excitation

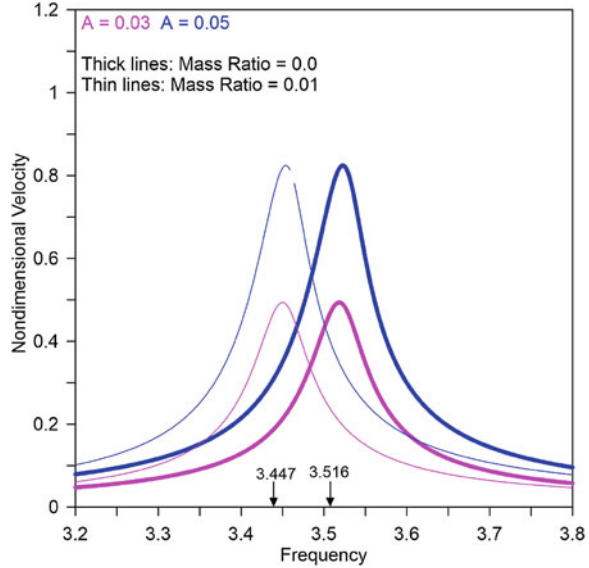
The first in-plane natural frequency of the cantilever beam was evaluated analytically by solving the eigenvalue problem associated with Eq. (8). The nondimensional frequency was found to be $\omega_1 = 3.516$. Then, to dynamically evaluate the response of the beam tip, Eq. (8) was integrated over a long time ($500 T_s$), where $T_s = 2\pi/\Omega$. The time-history of the last 100 periods was used to obtain the steady-state amplitude.

Variations in the amplitude of the beam tip velocity in the absence of added mass are shown in Fig. 5 as the amplitude of the external excitation force increases from $A = 0.01$ to 0.07 in steps of 0.01 and the signal frequency is swept-up and down in the vicinity of the first mode resonance (the frequency range of 3.2–3.8). The figure shows the stable response only. We found that the first mode is mildly hardening due to the contribution of the geometric and the nonlinear inertia terms.

The response was completely stable up to $A = 0.05$. The discontinuity in the frequency-response curves, corresponding to the forcing amplitudes of $A = 0.06$ shown as a black line and $A = 0.07$ shown as a light blue line in Fig. 5, are due to the appearance of the unstable solution branch along a stretch of those curves. However, these velocities are also corresponding to large displacements. Some of them in excess of the available nondimensional gap $v > 1$, at these forcing levels, indicate that they are not of interest.

To investigate the performance of the beam as a frequency-shift sensor, we repeated the previous procedure with the added mass $m^* = 0.01$. Figure 6 compares the FRCs of the tip velocity in the presence and absence of the added mass for excitation amplitudes of $A = 0.03$ and $A = 0.05$. The frequency shift in the vicinity of primary resonance of the first mode is significant for both excitation amplitudes.

Fig. 6 A comparison of the nondimensional tip velocity FRCs in the vicinity of the first bending mode's primary resonance in the absence and presence of an added mass under an external excitation with amplitudes of 0.03 and 0.05 as the signal frequency is swept-up and down in the range of 3.2–3.8. Thick lines represent the FRCs without the added mass and thin lines represent the FRCs with the added mass



We found that for this mass change, the natural frequency drops from $\omega_1 = 3.516$ to 3.447 corresponding to a frequency shift of 0.069. This confirms that the sensor can detect mass changes due to gas molecules. We also note that the response is still mildly hardening.

The nondimensional frequency of the second bending mode is obtained by solving the eigenvalue problem given by Eq. (9). It was found to be at $\omega_2 = 22.034$. We carried out a frequency sweep in the vicinity of the second bending mode's primary resonance to investigate its potential for sensing applications. We found that the response is always softening as shown in Fig. 7.

Introducing the added mass, the natural frequency of the second mode drops from $\omega_2 = 22.034$ to 21.61 corresponding to a frequency shift of 0.434. We also found that the response maintains its softening behavior in the presence of added mass. We conclude that the frequency shift of the second bending mode is more significant than that of the first bending mode. This is due to the minor effective mass of the second mode compared to the first mode.

Electrostatic Excitation

The same analysis was also carried out under the electrostatic excitation to investigate the effect of the electrostatic field on the frequency shifts and, therefore, the sensor performance. Variation of the beam tip velocity was obtained under various voltage waveforms as the signal frequency was swept-up and down in the range of 2.5–3.8 for the first mode and the range of 21–22.4 for the second mode, respectively.

The frequency-response curve of the sensor in the vicinity of the first mode's primary resonance under a voltage waveform of $V_{dc} = V_{ac} = 1$ V is shown in

Fig. 7 A comparison of the nondimensional tip velocity FRCs in the vicinity of the second bending mode’s primary resonance in the absence and presence of an added mass under external excitation with amplitudes equal to 0.01, 0.02, and 0.03 as the signal frequency is swept-up and down in the range of 21–22.4. Thick lines represent the FRCs without the added mass and thin lines represent the FRCs with the added mass.

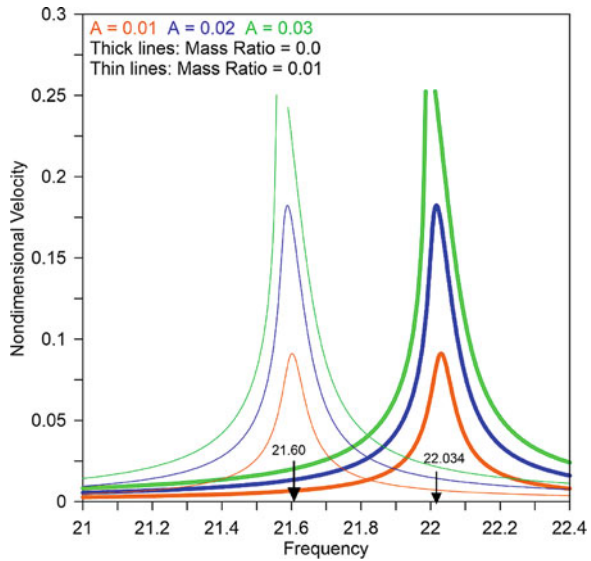


Fig. 8 A comparison of the nondimensional tip velocity FRCs in the vicinity of the first bending mode’s primary resonance with and without added mass under an electrostatic force as the signal frequency is swept-up and down in the range of 2.5–3.8. Thick lines represent the FRCs without the added mass and thin lines represent the FRCs with the added mass

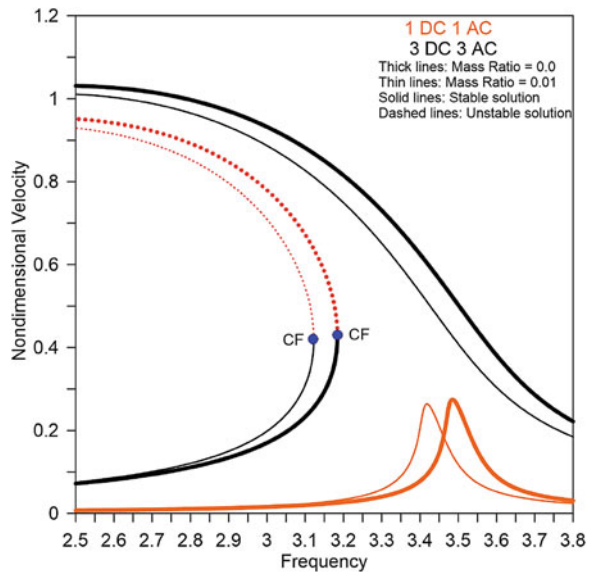


Fig. 8. The curves are shown with (thin orange line) and without added mass (thick orange line). We note that the first mode is mildly softening due to the electrostatic force which introduces linear and cubic softening terms as well as quadratic terms into the beam stiffness. Comparing these results to those obtained under the external force, we conclude that the effect of the electrostatic force dominates the effects of the geometric nonlinearity and nonlinear inertia term.

Increasing the voltage waveform to $V_{dc} = V_{ac} = 3 \text{ V}$ results in multi-valuedness. To examine the stability of co-existing orbits, we employed a combined shooting method to generate the periodic orbits and evaluate their Floquet multipliers. The maximum velocity for stable orbits is marked as a solid black line while that of unstable orbits is marked as a dashed red line, see Fig. 8. The frequency-response curves are shown with (thin lines) and without (thick lines) added mass.

In the absence of added mass, the maximum velocity increases smoothly with the signal frequency until it jumps up at $\Omega = 3.18$ to an upper stable branch of the solutions through a cyclic-fold bifurcation demarcated by CF (blue filled circle). At point CF, a Floquet multiplier exits the unit circle through $+1$ as the lower branch of stable solutions meets a branch of unstable solutions. On the other hand, all orbits are stable along the upper branch of solution as the frequency is swept-down from $\Omega = 3.8$ to 2.5 .

Adding a mass of $m^* = 0.01$, we found that the frequency shift in the resonance peak for the waveform $V_{dc} = V_{ac} = 1 \text{ V}$ was 0.07 which is almost equal to that realized under external excitation. We conclude that the performance of a traditional frequency-shift sensor would be very similar under either external or electrostatic excitation at this forcing level. On the other hand, increasing the electrostatic forcing level to $V_{dc} = V_{ac} = 3 \text{ V}$ creates an opportunity to implement a bifurcation sensor that exploits the shift in the frequency of a bifurcation point due to the added mass. This frequency shift was found to be 0.063 . While this indicates a lower sensitivity than that of a traditional sensor, bifurcation sensors facilitate simpler detection mechanisms that require only the identification of a large (discontinuous) jump in the response associated with the bifurcation.

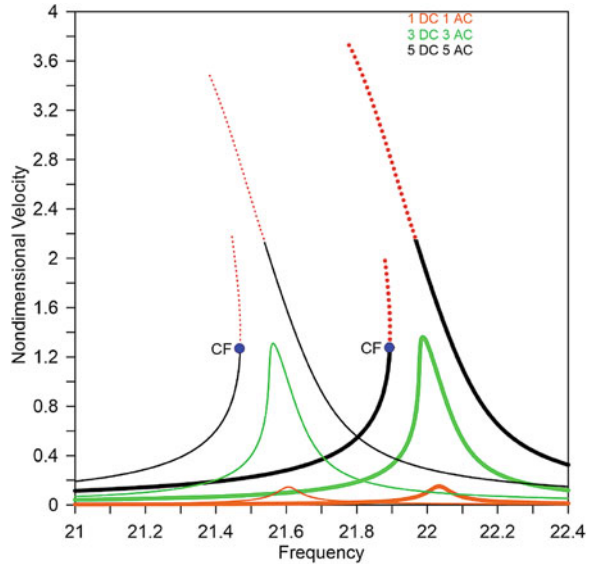
We carried out a similar analysis to investigate the sensor performance in the vicinity of the second mode's primary resonance using Eq. (9) and sweeping the signal frequency in the range 21 – 22.4 . In the absence of added mass, we found that the FRCs (thick lines) maintain their softening behavior, Fig. 9. The frequency response was single-valued for the voltage waveforms of $V_{dc} = V_{ac} = 1 \text{ V}$ and $V_{dc} = V_{ac} = 3 \text{ V}$. However, it becomes multivalued for $V_{dc} = V_{ac} = 5 \text{ V}$. At this forcing level, the motion is characterized by stable (solid lines) and unstable (dashed lines) branches of solution appear as shown in Fig. 9.

The tip velocity increases smoothly until it jumps up at $\Omega = 21.892$ to an upper branch of unstable solutions through a cyclic-fold bifurcation demarcated by CF (blue filled circle). At CF, a Floquet multiplier exits the unit circle through $+1$ as the lower branch of stable solutions meets a branch of unstable solutions. Interestingly, sweeping-down the frequency from $\Omega = 3.8$, the response increases along with an upper stable branch of solution until the orbits become unstable at $\Omega = 21.961$.

Introducing a mass of $m^* = 0.01$, we show the frequency-response curves for the same excitation conditions in Fig. 9 marked by thin lines. We found that the frequency shift in the resonant peak was 0.433 for the voltage waveform $V_{dc} = V_{ac} = 1 \text{ V}$ and 0.428 for the voltage waveform $V_{dc} = V_{ac} = 3 \text{ V}$ which are almost equal to that realized under external excitation.

On the other hand, the frequency shift in the bifurcation point for $V_{dc} = V_{ac} = 5 \text{ V}$ was found to be 0.425 which is similar in magnitude to the shifts in the resonant

Fig. 9 A comparison of the nondimensional tip velocity FRCs in the vicinity of the second bending mode's primary resonance with and without the added mass under an electrostatic force as the signal frequency is swept-up and down in the range of 21–22.4. Thick lines represent the FRCs without the added mass and thin lines represent the FRCs with an added mass.



under single-valued electrostatic excitation and the natural frequency under external excitation. We conclude that a bifurcation sensor would gain a simpler detection mechanism while maintaining a similar sensitivity to a frequency-shift sensor.

5 Conclusions

We presented a novel gas sensor made of multiple resonators excited via a single input signal and the data is collected through a single output signal. The sensor consists of a U-shaped shuttle mass carrying two micro-cantilever resonators serving as sensors. Actuation of the shuttle mass results in base excitation of the inner resonators. The preliminary results show that the shuttle mass can serve as an actuator and a sensor at the same time. We have shown that the inner cantilever beams can detect similar or different gases depending on the detector material used and whether the operating frequency is similar or different. We developed a simple model to study the dynamic behavior of one of the sensor's inner cantilever beams in the absence and presence of the added mass. The results show that the sensor can be operated as a traditional frequency-shift sensor or a bifurcation sensor. We found that a bifurcation sensor indicates a lower sensitivity than that of a traditional sensor. However, it facilitates a straightforward detection mechanism that requires only the identification of a significant jump in the response associated with the bifurcation point. We also found that the beam has a mildly hardening response under an external force (linear) in the first bending mode and a softening behavior

in the second mode. On the other hand, exciting the beam electrostatically results in a softening response for both the first and second modes.

Acknowledgments WL acknowledges partial support by the PRIN Grant n. 2017L7X3CS-002 (3D PRINTING: A BRIDGE TO THE FUTURE. Computational methods, innovative applications, experimental validations of new materials and technologies) and by the 2019 Sapienza Grant n. RG11916B8160BCCC (Vibration mitigation via advanced engineered devices and materials).

References

1. G. Ciuti, L. Ricotti, A. Menciacchi, P. Dario, Mems sensor technologies for human centred applications in healthcare, physical activities, safety and environmental sensing: a review on research activities in Italy. *Sensors* **15**(3), 6441–6468 (2015)
2. B. Ilic, Y. Yang, H.G. Craighead, Virus detection using nanoelectromechanical devices. *Appl. Phys. Lett.* **85**(13), 2604–2606 (2004)
3. K. Park, N. Kim, D.T. Morissette, N.R. Aluru, R. Bashir, Resonant mems mass sensors for measurement of microdroplet evaporation. *J. Microelectromech. Syst.* **21**(3), 702–711 (2012)
4. S. Cheng, H. Liu, S. Hu, D. Zhang, H. Ning, A survey on gas sensing technology Xiao Liu. *Sensors* **12**, 9635–9665 (2012)
5. W.-T.S. Chen, K.M.E. Stewart, C.K. Yang, R.R. Mansour, J. Carroll, A. Penlidis, Wearable rf sensor array implementing coupling-matrix readout extraction technique. *IEEE Trans. Microwave Theory Tech.* **63**(12), 4157–4168 (2015)
6. R.A. Potyrailo, Toward high value sensing: monolayer-protected metal nanoparticles in multivariable gas and vapor sensors. *Chem. Soc. Rev.* **46**(17), 5311–5346 (2017)
7. S. Tadigadapa, K. Mateti, Piezoelectric mems sensors: state-of-the-art and perspectives. *Meas. Sci. Technol.* **20**(9), 092001 (2009)
8. W. Pang, H. Zhao, E.S. Kim, H. Zhang, H. Yu, X. Hu, Piezoelectric microelectromechanical resonant sensors for chemical and biological detection. *Lab Chip* **12**(1), 29–44 (2012)
9. A. Mirzaei, J.-H. Lee, S.M. Majhi, M. Weber, M. Bechelany, H.W. Kim, S.S. Kim, Resistive gas sensors based on metal-oxide nanowires. *J. Appl. Phys.* **126**(24), 241102 (2019)
10. R. Raiteri, M. Grattarola, H.-J. Butt, P. Skládal, Micromechanical cantilever-based biosensors. *Sens. Actuators B Chem.* **79**(2–3), 115–126 (2001)
11. A. Boisen, S. Dohn, S.S. Keller, S. Schmid, M. Tenje, Cantilever-like micromechanical sensors. *Rep. Prog. Phys.* **74**(3), 036101 (2011)
12. Y. Aboelkassem, A.H. Nayfeh, M. Ghommem, Bio-mass sensor using an electrostatically actuated microcantilever in a vacuum microchannel. *Microsyst. Technol.* **16**(10), 1749–1755 (2010)
13. A. Bouchaala, A.H. Nayfeh, M.I. Younis, Frequency shifts of micro and nano cantilever beam resonators due to added masses. *J. Dyn. Syst. Meas. Control.* **138**(9), 091002 (2016)
14. M.E. Khater, M. Al-Ghamdi, S. Park, K.M.E. Stewart, E.M. Abdel-Rahman, A. Penlidis, A.H. Nayfeh, A.K.S. Abdel-Aziz, M. Basha, Binary mems gas sensors. *J. Micromech. Microeng.* **24**(6), 065007 (2014)
15. N. Jaber, S. Ilyas, O. Shekhah, M. Eddaoudi, M.I. Younis, Sensitive resonant gas sensor operating in air with metal organic frameworks coating, in *2017 19th International Conference on Solid-State Sensors, Actuators and Microsystems (TRANSDUCERS)* (IEEE, Piscataway, 2017), pp. 1081–1087
16. M. Cetraro, MEMS Multi mass sensor exploiting nonlinear resonances. Ph.D. Thesis, Sapienza University of Rome (2017)

A Numerical Study of Acoustic Radiation Forces for the Contactless Excitation of a Microcantilever



M. Akbarzadeh, S. Oberst, S. Sepehriahnama, Y. K. Chiang, B. J. Halkon, A. Melnikov, and D. A. Powell

1 Introduction

Both the study of acoustic forces and how waves propagate in fluids have a long history, dating back to the works of Rayleigh on the physical origins of radiation forces exerted by acoustic waves [1]. The acoustic radiation force (ARF) can be considered a time-averaged force acting on an object within a sound field. This force is caused by changing the energy density of its incident acoustic field. The magnitude of the acoustic radiation force depends on how much energy is absorbed or reflected by the object within the incident field. The ARF is known to be *static* when the incident field is continuous but, with constant amplitude, yet can become *dynamic* for time-varying intensity. In the last decades, the practical significance of the ARF was clarified in nonlinear acoustics. Many engineering applications and branches were developed to exploit this force, including but not limited to particle manipulation in microfluidic devices [2], vibro-acoustic spectrography for

M. Akbarzadeh (✉) · S. Sepehriahnama · B. J. Halkon
Centre for Audio, Acoustics and Vibration, University of Technology Sydney, Sydney, NSW,
Australia
e-mail: Mehdi.Akbarzadeh@student.uts.edu.au

S. Oberst
Centre for Audio, Acoustics and Vibration, University of Technology Sydney, Sydney, NSW,
Australia

School of Engineering and Information Technology, University of New South Wales, Canberra,
ACT, Australia

Y. K. Chiang · D. A. Powell
School of Engineering and Information Technology, University of New South Wales, Canberra,
ACT, Australia

A. Melnikov
Fraunhofer Institute for Photonic Microsystems IPMS, Dresden, Saxony, Germany

imaging an acoustic response of internal body tissues to mechanical excitation [3], acoustic levitation devices [4], acoustic manipulation/tweezing, e.g., for separating cancer cells from blood cells [5], sorting and separation of particles in open microfluidic channels [6], or experimental vibration testing [7–9]. To compute the static and dynamic ARF acting on simple geometries such as spheres, cylinders, and ellipsoids, closed-form formulae have been reported in the literature [10, 11]. These mathematical formulations are limited to acoustically small particles which are objects that are small compared to the wavelength of the sound in the surrounding fluid and to objects which display symmetry.

Examples of such small objects include microbeams which are often main components in resonators used as sensors and actuators in various applications. Some of these include the detection of temperature and humidity, toxic gases and vapors, mass and biological cells, or viral particles [12]. To measure the mechanical and vibration properties of microbeams, different means of excitation can be chosen, including electrostatic and electromagnetic, mechanical vibration, and acoustic radiation excitation [12].

Experimental methods for studying the behavior of microstructures such as microbeams are very valuable; accurate small-scale measurements require precise laboratory equipment and sensitive adjustments, which are, however, expensive, and to conduct practical experiments at this small scale is very difficult. Therefore, besides experimental studies, computer simulations are usually conducted. Measuring the dynamical properties of micro fabricated structures leads to problems such as that the properties do depend not only on constituent materials but also on the process of fabrication which again depends on the scale considered. Microcantilevers can be made from different materials, yet most often, silicon is found. Liu et al. [13] investigated the dimension effect on the mechanical behavior of a single-crystal silicon microcantilever. They fabricated various types of samples with different thicknesses and lengths to obtain their stress-strain relationship and to evaluate experimentally dimension effects on flexural strength, Young's modulus, and failure strain.

Measuring the resonant frequencies is another challenging aspect in works related to microcantilevers as it is actually not straightforward to excite these microstructures in a precise and controlled way, for example, determining the resonant frequencies by using the mechanical base excitation method disadvantageous as the oscillation of the base causes inaccuracies and resonances of the shaker as well as the support fixture may cause spurious resonances to be detected that are unrelated to the resonance frequencies of the microcantilever. Moreover, reliably fixing a microcantilever to a mechanical shaker may not be repeatable, is very time-consuming, and can damage the structure. Inaccurately clamping the structure will lead to wrong responses during the experiment caused by higher than usual anchor losses owing to contact separation, impact, and friction, e.g., micro-slip [14]. Considering all the difficulties related to measuring mechanical and dynamic properties of small structures, it is understandable that often, multiphysics simulations are applied prior to conducting any experiment.

2 Mathematical Formulation

The ARF can be modeled as a nonlinear acoustic phenomenon of second order and is defined as the integration of the radiation stresses over the surface of an object [15]:

$$F_{\text{rad}} = \iint_A S_{ij} dA \quad (1a)$$

$$S_{ij} = \langle \delta P \rangle \delta_{ij} + \rho \langle v_i v_j \rangle \quad (1b)$$

$$\langle \delta P \rangle = -\frac{\rho_0}{2} \langle |\nabla \phi|^2 \rangle + \frac{\rho_0}{2c_0^2} \left\langle \left(\frac{\partial \phi}{\partial t} \right)^2 \right\rangle + C' \quad (1c)$$

For an ideal fluid, the radiation stresses have two parts: the mean Eulerian excess pressure, $\langle \delta P \rangle$, and the Reynolds stresses, $\rho v_i v_j$. Here, δ_{ij} is the Kronecker delta, ρ is the equilibrium density, ϕ is the velocity potential, c_0 is the speed of sound in the fluid, dA is the surface element, C' is a constant in space and time, and $\langle \cdot \rangle$ is the time averaging operator.

2.1 Static Acoustic Radiation Force

Ignoring the Reynolds stresses and calculating $\langle \delta P \rangle$ and ϕ for spherical objects, King presented the first analytical model for the ARF acting on particles [16]. By applying a Tylor series to acoustic wave equations, for acoustically small particles ($ka \ll 1$), he calculated the ARF for a rigid sphere within an inviscid fluid. By neglecting the higher-order terms, two formulae are proposed, one for plane progressive wave and the second one for standing waves:

$$F = 2\pi\rho_0|\phi|^2(ka)^6 \frac{1 + \frac{2}{9}(1 - \rho_0/\rho_1)^2}{(2 + \rho_0/\rho_1)^2}, \quad \text{for progressive wave} \quad (2a)$$

$$F = 2\pi\rho_0|\phi|^2(ka)^3 \sin(2kh) \frac{1 + \frac{2}{3}(1 - \rho_0/\rho_1)}{(2 + \rho_0/\rho_1)}, \quad \text{for standing wave} \quad (2b)$$

where $|\phi|$ is the magnitude of the incident wave velocity potential, a is the radius of the rigid sphere, k is the wave number, h is the distance between the pressure antinode and the center of the sphere in the wave direction, and ρ_0 and ρ_1 are the densities of the fluid and that of the particle, respectively.

A more general theory of ARF to study compressible particles was reported in [17], and two analytical expressions for the force acting on small compressible spheres exposed to in-plane standing waves and progressive waves were presented:

$$F = 2\pi\rho_0|\phi|^2(ka)^6 \frac{\left(1 - \frac{1 + \frac{2}{3(\rho_0/\rho_1)^2\sigma^2}}{\rho_0/\rho_1}\right) + \frac{2}{9}(1 - \rho_0/\rho_1)^2}{(2 + \rho_0/\rho_1)^2}, \quad \text{for progressive wave} \quad (3a)$$

$$F = 2\pi\rho_0|\phi|^2(ka)^3 \sin(2kh) \left(\frac{1 + \frac{2}{3}(1 - \rho_0/\rho_1)}{(2 + \rho_0/\rho_1)} - \frac{\rho_0/\rho_1}{3\sigma^2} \right), \quad \text{for standing wave} \quad (3b)$$

where $\sigma = K_f/K_p$ is the ratio of the compressibility of the fluid to the particle and K_f, K_p are bulk modulus of fluid and particle, respectively.

A simplified formula in terms of time-averaged kinetic and potential energies of stationary acoustic fields of any geometries was presented using Gorkov's formula [18]. This formulation, when applied to small compressible fluid particles, provides the force as a gradient of a potential function:

$$U = 2\pi a^3 \rho_0 \left(\frac{1}{3} \frac{\langle p \rangle^2}{(\rho_0 c_0)^2} \left(1 - \frac{1}{\sigma} \right) - \frac{1}{2} \langle |u| \rangle^2 \frac{2 - \rho_0/\rho_1}{2 + \rho_0/\rho_1} \right) \quad (4)$$

where U is the force potential, so that the force can be written as $F = -\nabla U$. To calculate the ARF on particles, COMSOL Multiphysics uses Eq. (4), and this equation has been coded in the "Particle Tracing for Fluid Flow" interface. However, this formulation neglects thermoviscous effects and only applies to acoustically small particles.

The ARF exerted on elastic and viscoelastic infinite cylinders due to a quasi-standing wave has been reported in [19]. The ARF and torque on disk-shaped materials in ultrasonic standing waves are reported in [20, 21].

To investigate the ARF acting on objects or structures with more complex geometries, numerical simulations are required since analytical models are only developed for simple geometrical shapes. The numerical calculation of an ARF acting on a sphere in a viscous fluid based on multipoles and the Stokeslet method has been presented in [22]. The first-order velocity and the pressure originated from the multipole series solution, and the volumetric force in the acoustic streaming via the Stokeslet method is subsequently calculated from its first-order velocity and pressure. The use of the first three terms of the first-order potential series provides generally sufficiently accurate results to also explore the interparticle radiation forces due to more than two particles [22].

2.2 Dynamic Acoustic Radiation Force

Two methods have been used to produce experimentally dynamic ARF [3, 7–9]: by employing a single ultrasound beam with an amplitude being modulated at low frequency or by interfering with a pair of low-power, ultrasonic frequencies of different frequencies (dual beam mode). In comparison to the first, the latter method confines the ARF spatially by limiting it to a small region of the beam's intersection [7] which allows expressing the velocity potential function using the following expression [9]:

$$\phi = A \cos\left(2\pi f_a - \frac{\Delta\varphi}{2}\right)t + A \cos\left(2\pi f_b + \frac{\Delta\varphi}{2}\right)t \quad (5)$$

where A is the wave amplitude, with the frequencies being denoted by f_a and f_b and $\Delta\varphi$ being the phase difference of the two wave fields. The ARF acting on the object is always proportional to the square of the velocity potential function, while the mathematical formulation of the exerted dynamic ARF can be modeled using four terms. The first term corresponds to the frequency difference $\Delta f = f_b - f_a$, the second and third terms correspond to $2f_a$ and $2f_b$, and the fourth term is expressed as the $f_a + f_b$. By just using the first term [9], the acoustic radiation force can be expressed as:

$$F_{\text{rad}} = F_0 \cos[(2\pi \Delta f)t + \Delta\varphi] \quad (6)$$

3 Noncontact Excitation of Microcantilevers

Using the ARF, Huber et al. used focused acoustic waves to conduct a noncontact excitation of microcantilevers and coupled microcantilever arrays. The diameter of the focal spot produced by this transducer is 3 mm, which is much larger than the microcantilever's dimension, and covers presumably the entire structure (Mikromasch CSC12-E silicon AFM, $350 \times 35 \times 1 \mu\text{m}^3$) leading to uniform area excitation [8].

An operational modal analysis is conducted by using ARF to obtain the first three resonance frequencies of the microcantilever and the first resonance pick obtained at 11.2 kHz, the second resonance pick obtained at 72.4 kHz, and the third resonance pick obtained at 204 kHz [8], which show good agreement if compared with those obtained by base excitation as shown in Fig. 1. However, the base excitation spectrum includes undesired fixture resonances which can be seen in Fig. 1.

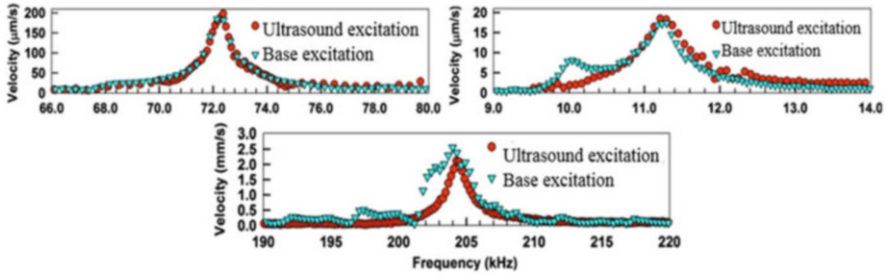


Fig. 1 A comparison between three first resonances for ultrasound radiation force and base excitation obtained in Huber’s experiment [8]

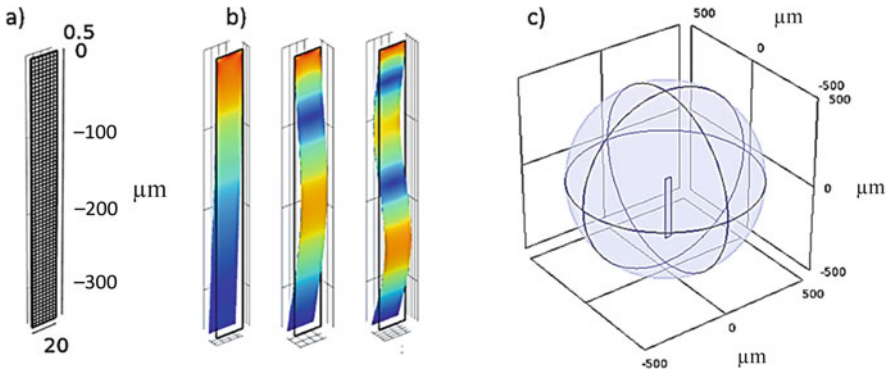


Fig. 2 (a) A 3D finite element model of the microcantilever. (b) Three first mode shapes. (c) A 3D finite element model of microcantilever surrounded in a fluid domain

3.1 Numerical Simulation

To obtain the first three resonance frequencies, the mode shapes, and the exerted radiation force, we conduct a numerical simulation modeling a microcantilever with its results compared to experiments conducted in [8]. Figure 2a shows the meshed microcantilever using COMSOL Multiphysics.

To perform modal analysis, two types of excitation, namely, boundary load and acoustic plane pressure waves, are used. According to [8], the dynamic ARF causes a uniform excitation of the entire microcantilever, so that an ARF can be assumed as a typical harmonic boundary load with a certain amplitude, as presented in Eq. (6). In Huber’s work, the frequency in Eq. (6) is known and can therefore be adjusted using amplitude modulation; yet, its amplitude remains unknown.

To conduct a modal analysis by boundary load excitation, the solid mechanics physics in COMSOL was selected, using a linear elastic microcantilever. A mapped mesh of 18,033 cube-shaped elements was generated, and fixed boundaries were

used to clamp the beam. A boundary pressure load of 1 N/m^2 amplitude and a frequency range of 5–210 kHz were applied using 1 kHz frequency steps.

Using both the pressure acoustics module and the solid mechanics module within the acoustic-structure interaction Multiphysics interface in the frequency domain, the microcantilever was excited using a plane acoustic wave of 10 Pa amplitude. The fluid domain has been modeled as a spherical region surrounding the microcantilever (Fig. 2c). Due to free tetrahedral meshing of both, the solid and fluid domains, this model includes with 127,003 tetrahedral elements many more elements than the boundary load excitation model in which the solid domain only was meshed. The boundary condition for the fluid at the outer boundary of the spherical domain is that of spherical wave radiation which allows acoustic waves to exit the domain without reflection (i.e., fulfilling the Sommerfeld radiation condition) [23].

The three first mode shapes are plotted in Fig. 2b. Figure 3a shows the frequency response of the microcantilever tip with the lowest three resonances obtained with *boundary load excitation*. The first three resonant peaks are determined at 11.4, 72.6, and 198 kHz and are in good agreement with Huber’s experimental results showing less than 0.5% difference (11.2, 72.4, and 204 kHz) [8]. Using *acoustic wave excitation*, the first three resonances are obtained at exactly the same frequencies obtained by boundary load excitation as shown in Fig. 3b.

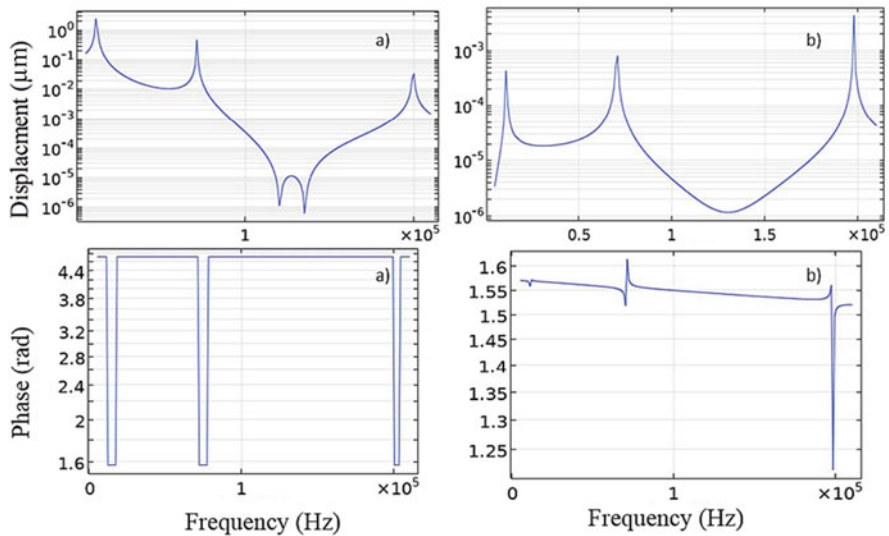


Fig. 3 The frequency response of the lowest three resonances of the microcantilever obtained with (a) boundary load excitation and (b) acoustic wave excitation

3.2 Estimating Acoustic Radiation Force

Based on the numerical simulation and the obtained resonant frequencies, the dynamic ARF can be estimated. By comparing different excitation methods, we can approximate the known response of the system. However, another unknown parameter in this experiment is damping, which has been considered in the following as “loss factor” in terms of material damping. The loss factor η depends on other parameters such as temperature or frequency, and by increasing frequency, the loss factor decreases [24]; for silicon, η is generally expected to lie between 0.001 and 0.1 [24]. According to Eq. (6), and ignoring the phase difference $\Delta\phi$, the ARF can be expressed as:

$$F_{\text{rad}} = F_0 \cos [(2\pi \Delta f) t] \tag{7}$$

with Δf being its resonance frequency. To estimate the amplitude F_0 of the ARF, we adjust the input force so that the output of the microcantilever tip speed corresponds to the value measured by Huber et al. [8] as presented in Fig. 1.

As shown in Fig. 4a, for the first resonant frequency and if $\eta = 0.04$ and $F_0 = 8.0 \times 10^{-5} \text{ N/m}^2$, the frequency responses of the computational model match well those of the experiments. For the first resonant frequency, f_1 , and the radiation force, we can hence write:

$$F_{\text{rad}}(f_1) = 8.0 \times 10^{-5} \cos \left[\left(2\pi \times \left(11.4 \times 10^3 \right) \right) t \right] \text{ N/m}^2. \tag{8a}$$

Similarly, as shown in Fig. 4b, for the second resonant frequency, if $\eta = 0.01$ and $F_0 = 2.45 \times 10^{-3} \text{ N/m}^2$, the response is similar to that found in experiments, and

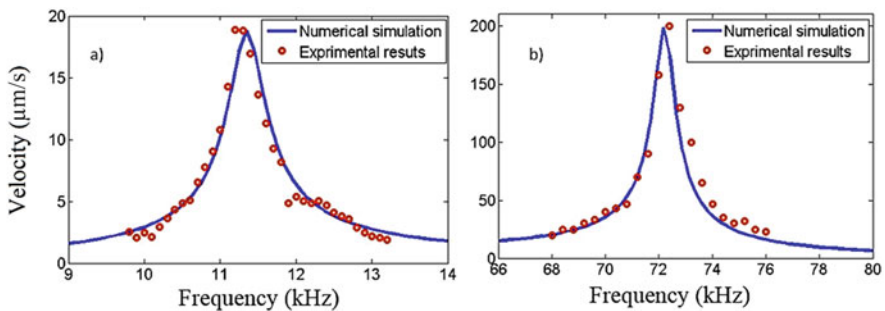


Fig. 4 A comparison between numerical simulation and some points of the experimental results presented in [8] near (a) the first resonance frequency and (b) the second resonance frequency when the amplitude of the boundary load excitation in numerical simulation is F_0

the radiation force can be written as:

$$F_{\text{rad}}(f_2) = 2.45 \times 10^{-3} \cos \left[\left(2\pi \times (72.1 \times 10^3) \right) t \right] \text{ N/m}^2. \quad (8b)$$

Finally, for the third resonant frequency, f_3 , if $\eta = 0.0055$, the radiation force expression becomes:

$$F_{\text{rad}}(f_3) = 6.54 \times 10^{-2} \cos \left[\left(2\pi \times (198 \times 10^3) \right) t \right] \text{ N/m}^2. \quad (8c)$$

Due to having at least two unknowns, forcing and damping, the latter having different components including anchor and radiation losses, or internal damping, which has not been studied experimentally, no clear answer can be obtained here. If one considered nonlinear vibrations of the microcantilever as related to nonlinear stiffness or nonlinear damping, the estimated acoustic radiation force would have to change. The absolute deviation between the magnitudes of the forces as calculated using linear and nonlinear assumptions depends on the kind, the degree, and the strength of the nonlinearity involved [25]. Knowing all those nonlinear parameters for stiffness, damping, etc., the finite element method could be used to calculate the radiation force exerted on a nonlinear microcantilever.

4 Conclusions

This chapter has set out some of the fundamentals for the determination of acoustic radiation forces. Using numerical simulations, both a dynamic boundary load excitation and an acoustic wave excitation technique were used to excite a microcantilever; these were compared with previously reported experimental findings [8]. The first three resonant frequencies and mode shapes obtained for both excitation techniques are in good agreement with those found experimentally. In the last step, the dynamic acoustic radiation force was estimated based on the experimental responses for the three resonant frequencies. It can be concluded that this experiment included some unknown parameters: the loss factor – and its dependency on physical conditions such as temperature and frequency – should be analyzed further in the future. Anchor losses may play an important role, but they are not discussed in [8]. Knowing all nonlinear parameters such as stiffness and damping and unknown parameters, the finite element method can be used to calculate the radiation force exerted on the microcantilever.

These new numerical results need to be validated experimentally with a focus on determining the correct boundary conditions and material properties of the silicon cantilever; these aspects were not a particular focus of the earlier experimental investigation [8]. Computer modeling alone is not enough to determine the system behavior, and because of the existence of some uncertainty in boundary conditions such as anchor and radiation losses, unknown internal damping, and nonlinear

properties, more information is required for proper modeling of the microcantilever vibration and estimating the ARF. The work presented in this paper provides a potential foundation on which the use of dynamic ARF might be used experimentally to excite microstructures in place of more traditionally implemented base excitation techniques to better extract their dynamic characteristics.

References

1. L. Rayleigh, On the pressure of vibrations. *Philos. Mag.* **3**, 338–346 (1902)
2. H. Bruus, Acoustofluidics 7: The acoustic radiation force on small particles. *Lab Chip* **12**(6), 1014–1021 (2012)
3. M. Fatemi, J.F. Greenleaf, Ultrasound-stimulated vibro-acoustic spectrography. *Science* **280**(5360), 82–85 (1998)
4. N. Brunetiere, M. Wodtke, Considerations about the applicability of the Reynolds equation for analyzing high-speed near field levitation phenomena. *J. Sound Vib.* **783**(29), 115496 (2020)
5. P. Li et al., Acoustic separation of circulating tumor cells. *Proc. Natl. Acad. Sci. U. S. A.* **112**, 4970–4975 (2015)
6. C. Devendran, I. Gralinski, A. Neild, Separation of particles using acoustic streaming and radiation forces in an open microfluidic channel. *Microfluid. Nanofluid.* **17**, 879–890 (2014)
7. T.M. Huber, Noncontact modal analysis of a pipe organ reed using airborne ultrasound stimulated vibrometry. *J. Acoust. Soc. Am.* **4**, 2476–2482 (2006)
8. T.M. Huber, D.C. Abell, C.B. Mellema, M. Spletzer, A. Raman, Mode-selective noncontact excitation of microcantilevers and microcantilever arrays in air using the ultrasound radiation force. *Appl. Phys. Lett.* **97**, 21410 (2010)
9. T.M. Huber, J.R. Beaver, N.M. Helps, Noncontact modal excitation of a classical guitar using ultrasound radiation force. *Exp. Tech.* **37**, 38–46 (2013)
10. G.T. Silva, S. Chen, J.F. Greenleaf, M. Fatemi, Dynamic ultrasound radiation force in fluids. *Phys. Rev. E* **71**, 056617 (2005)
11. X. Peng, W. He, F. Xin, G.M. Genin, J.L. Lu, The acoustic radiation force of a focused ultrasound beam on a suspended eukaryotic cell. *Ultrasonics* **108**, 106205 (2020)
12. A. Shooshtari, H. Kalhori, A. Masoodian, Investigation for dimension effect on mechanical behavior of a metallic curved micro-cantilever beam. *Measurement* **44**, 454–465 (2011)
13. H.K. Liu, C.H. Pan, P.P. Liu, Dimension effect on mechanical behavior of silicon micro-cantilever beams. *Measurement* **41**, 885–895 (2008)
14. S. Kruse, M. Tiedemann, B. Zeumer, P. Reuss, H. Hetzler, N. Hoffmann, The influence of joints on friction induced vibration in brake squeal. *J. Sound Vib.* **340**(31), 239–252 (2015)
15. C.P. Lee, T.G. Wang, Acoustic radiation pressure. *J. Acoust. Soc. Am.* **94**(2), 1099–1109 (1993)
16. L.V. King, On the acoustic radiation pressure on spheres. *Proc. R. Soc. A Math. Phys. Eng. Sci.* **147**, 212–240 (1934)
17. K. Yosioka, Y. Kawasima, Acoustic radiation pressure on a compressible sphere. *Acustica* **5**(3), 167–173 (1955)
18. L.P. Gorkov, On the forces acting on a small particle in an acoustical field in an ideal fluid. *Sov. Phys. Dokl.* **6**, 773 (1962)
19. F.G. Mitri, Theoretical calculation of the acoustic radiation force acting on elastic and viscoelastic cylinders placed in a plane standing or quasi-standing wave field. *Eur. Phys. J. B* **44**, 71–78 (2005)
20. A. Garbin, I. Leibacher, P. Hahn, H. Le Ferrand, S. Studart, J. Dual, Acoustophoresis of disk-shaped microparticles: A numerical and experimental study of acoustic radiation forces and torques. *J. Acoust. Soc. Am.* **138**(5), 2759–2769 (2015)

21. A.B. Wood, A correction to the theory of the Rayleigh disc as applied to the measurement of sound-intensity in water. *Proc. Phys. Soc.* (1926–1948) **47**(5), 779 (1935)
22. S. Sepehrirahnama, F.S. Chau, K.M. Lim, Numerical calculation of acoustic radiation forces acting on a sphere in a viscous fluid. *Phys. Rev. E* **92**, 063309 (2015)
23. S. Oberst, J.C.S. Lai, S. Marburg, Guidelines for numerical vibration and acoustic analysis of disc brake squeal using simple models of brake systems. *J. Sound Vib.* **332**(9), 2284–2299 (2013)
24. M. Colakoglu, Factors effecting internal damping in aluminum. *J. Theor. Appl. Mech.* **44**(1), 95–105 (2004)
25. Z. Zhang, S. Oberst, J.C.S. Lai, On the potential of uncertainty analysis for prediction of brake squeal propensity. *J. Sound Vib.* **377**(1), 123–132 (2016)

Approximate Solutions to Axial Vibrations of Nanobars in Nonlinear Elastic Medium



Ugurcan Eroglu

1 Introduction

If the characteristic external length of the structure is comparable to that of internal, predictions of the classical theory of elasticity may be erroneous. In such cases, nonlocal (quasicontinuum) theories shall be used, which are able to capture spatial wave dispersion and take into account the internal organization of the material. They are classified as strong or weak depending on the scale parameter, which is related to the smallest unit of interest of the structure, and considered wavelengths [1–4]. In the former, usually integro-differential operators are applied on the kinematic fields, due to axiom of causality, while for the latter, assuming smaller scale parameter, these operators are approximated with differential operators [5]. We may quote many different theories for these different classes of nonlocal models, beginning with the work by Cosserat brothers [6] (or even the works of Gabrio Piola [7]), Eringen [8], Kröner [4], Eringen and Edelen [9]; see also relatively recent monographs by Eringen [10, 11]. There are also new approaches to account for nonlocality, such as the so-called stress driven model [12] and models based on fractional calculus [13, 14].

The applications of this relatively new nonclassical theories usually include reduced-order structural elements, such as bars and beams. We may quote [15, 16] as studies examining behavior of bars of nano-size by utilizing nonclassical continuum models. In this contribution, we will examine axial vibrations of nanobars which are embedded in an elastic medium, the stiffness of which is amplitude-dependent. The size effects will be incorporated by Eringen's two-phase local/nonlocal model [17]. This model is basically one of the three variants of Eringen's, along with the original

U. Eroglu (✉)

Department of Mechanical Engineering, Izmir University of Economics, Balçova, Izmir, Turkey
e-mail: ugurcan.eroglu@ieu.edu.tr

integral model [8, 9] and differential model [18]. The latter model is a simplified version of the original for unbounded domains, where the boundary effects vanish. However, in bounded domains the differential model fails as expected, evidenced by paradoxical results reported in the literature [19, 20]. The original model, on the other hand, provides a mathematical description of the mechanical problem which brings the requirement for additional and spurious constraints, the so-called constitutive boundary conditions, in order to admit a solution in a certain form [21, 22], which may be satisfied only in limited number of practical applications [23]. Two-phase model enables the solution to fulfill constitutive boundary conditions; yet, it brings the question of motivation of enforcing conditions which are not physical [24]. Motivated by these considerations, we will look for a solution to axial vibrations of bars of nano-size by admitting the field functions depend on the fraction of the nonlocal part in constitutive equation, which is assumed to be a small quantity.

2 Axial Vibration of Nanobars

2.1 Governing Equations

The reference configuration of the bar, \mathcal{B}_0 , occupies the volume \mathcal{V}_0 and consists of planar sections, \mathcal{R} , continuously and orthogonally attached through their centroids to a portion of a straight line, \mathcal{C}_0 of length L ; $\mathcal{V}_0 = \mathcal{R} \times [0, L]$. Position of a generic point, $P \in \mathcal{C}_0$ is parameterized by $x \in [0, L]$. Another configuration, \mathcal{B} , is defined by only rigid translations of the sections along \mathcal{C}_0 , u .¹ Suitable measure of the axial strain, ε , assumed small in this case, and the balance of an infinitesimal portion of the bar in terms of the resultant of the axial stress over \mathcal{R} , N , induced due to relative placement of the cross-sections, are written as,

$$\varepsilon = \frac{du}{dx}, \quad \frac{dN}{dx} = -q, \quad (1)$$

where q is the distributed force along the bar axis, including both the body forces and the resultant of the external contact actions. The former component of q in our case is due to the inertial forces, q_i , and the latter one is due to reaction of the surrounding media which is assumed to behave nonlinearly elastic, q_e . These components are,

¹Depending on the exact geometry of \mathcal{R} , assumption of rigid translation may be violated due to the so-called *boundary effects* which is due to missing neighbor atoms at the boundaries. For a thin-walled tubular section, such as in carbon nanotubes, however, this assumption is valid as there is no missing neighbor atoms. In case of boundary effects on the cross-section, a proper definition of a generic configuration may be done with an additional scalar quantity representing the warping of the section.

$$q_i = -\rho A \ddot{u}, \quad q_e = -\alpha u - \beta u^3, \tag{2}$$

where ρ , A , α , and β denote the density of the material, area of the section, and parameters quantifying the stiffness of the surrounding media.

The constitutive equation is assumed to be linear and has two parts representing qualitatively different response of the material: local and nonlocal [17]. The former is in usual form providing stress at a point is related to the strain of the same while the latter suggests the stress is a convolution of the strain with a kernel function. Thus, we assume a strain-driven model which is a consequence of admitting it is the deformation which results in stress [11]. When simplified for bar structures, we have,

$$N(x)/B = (1 - \xi)\varepsilon(x) + \xi \int_0^L K(x, \varepsilon)\varepsilon(\varepsilon)d\varepsilon, \tag{3}$$

where B is a measure of the axial stiffness, which is the multiplication of modulus of elasticity and cross-sectional area in macro-scale. $K(x, \varepsilon)$ is called kernel, or attenuation function, representing the long-range interactions of particles. Among many alternatives, we use exponential kernel with the following form:

$$K(x, \varepsilon) = \frac{1}{2\kappa} \exp(|x - \varepsilon|/\kappa), \quad \kappa > 0, \tag{4}$$

where κ is called *nonlocal parameter* which is a measure of the distance of long-range interactions.

Inserting Eq. (1) into the derivative of (3), with a usual short notation for the convolution, we have,

$$\frac{\rho A}{B} \ddot{u} - (1 - \xi) u'' - \xi (K * u')' + \frac{\alpha}{B} u + \frac{\beta}{B} u^3 = 0. \tag{5}$$

Applying Galërkin technique in time domain, with $u(x, t) = \bar{u}(x) \cos(\sqrt{\lambda}t)$, (5) becomes

$$-\lambda \frac{\rho A}{B} u - (1 - \xi) u'' - \xi (K * u')' + \frac{\alpha}{B} u + \frac{3}{4} \frac{\beta}{B} u^3 = 0, \tag{6}$$

for which we will look for an approximate solution, under suitable boundary conditions, in subsequent sections.

2.2 Formal Expansions

According to *Fredholm alternative theorem*, Eq. (3) has a unique solution if and only if the homogeneous equation ($N = 0$) has only the trivial solution $\varepsilon = 0$ [25]. This is physically reasonable; as in our case it means that null incremental stress means null incremental strain. Then again, without relying on intuitive conclusions: existence, and uniqueness of the solution of (3) must be examined. Herein, however, we assume a solution exists and basically look for it in the form of a series.

Formal expansion of a function f up to m th-order with respect to a parameter, η about $\eta = \eta_0$ is,

$$f \approx \sum_{n=0}^m \frac{(\eta - \eta_0)^n}{n!} \frac{d^n f}{d\eta^n} = \sum_{n=0}^m \frac{(\eta - \eta_0)^n}{n!} f_n = f^m. \quad (7)$$

Accordingly, the formal expansions of field functions of our problem with respect to the fraction coefficient, ξ , about $\xi = 0$ (local elasticity);

$$u \approx \sum_{n=0}^m \frac{\xi^n}{n!} u_n = u^m, \quad N \approx \sum_{n=0}^m \frac{\xi^n}{n!} N_n = N^m, \quad \lambda \approx \sum_{n=0}^m \frac{\xi^n}{n!} \lambda_n = \lambda^m. \quad (8)$$

Such an expansion renders a hierarchy of equations, and boundary conditions. The first two sets are as follows:

$$\begin{aligned} -u_0'' - \lambda_0 \frac{\rho A}{B} u_0 + \frac{\alpha}{B} u_0 + \frac{3}{4} \frac{\beta}{B} u_0^3 &= 0 \\ u_0'' - u_1' - (K * u_0')' - \frac{\lambda_0 \rho A}{B} u_1 - \frac{\lambda_1 \rho A}{B} u_0 + \frac{9\beta}{4B} u_0^2 u_1 + \frac{\alpha}{B} u_1 &= 0. \end{aligned} \quad (9)$$

The first of (9) is the well-known equation for local bars, for which various strategies are available to obtain a solution, albeit approximate. The second of (9) provides the contribution of long-range interactions modeled with Eringen's two-phase constitutive equation.

3 Results

3.1 Zeroth-Order Solution

Admitting $u_0 = c \sin \frac{\pi x}{2L}$ in Eq. (9)₁, for a fixed-free bar, we have the following residual:

$$R(x) = \frac{c \sin \left(\frac{\pi x}{2L} \right) \left(3c^2 \beta L^2 \sin^2 \left(\frac{\pi x}{2L} \right) + \pi^2 B + 4L^2 (\alpha - \lambda_0 \rho A) \right)}{4BL^2}. \quad (10)$$

Applying Galérkin’s technique,

$$\int_0^L R(x) \sin\left(\frac{\pi x}{2L}\right) dx = 0 \Rightarrow \lambda_0 = \frac{9c^2\beta L^2 + 4\pi^2 B + 16\alpha L^2}{16L^2\rho A} \tag{11}$$

the zeroth-order eigenvalue is found. A dependance of this eigenvalue on the amplitude of vibration, c , through the coefficient of nonlinear part of the elastic medium, β , is apparent. In case of no elastic medium, e.g., $\alpha \equiv \beta = 0$, the well-known eigenvalue corresponding to small-amplitude vibrations of a fixed-free local bar, λ_L , is recovered.

$$\lambda_L = \frac{\pi^2 B}{4L^2\rho A} \tag{12}$$

Let us nondimensionalize λ_0 as follows:

$$\bar{\lambda}_0 = \frac{\lambda_0}{\lambda_L} = 1 + \frac{4\bar{\alpha} + \frac{9\bar{c}^2\bar{\beta}}{4}}{\pi^2}, \quad \bar{c} = \frac{c}{L}, \quad \bar{\alpha} = \frac{L^2\alpha}{B}, \quad \bar{\beta} = \frac{L^4\beta}{B}. \tag{13}$$

Figure 1 provides the dependance of the fundamental frequency on vibration amplitude for different behavior of the elastic medium. Hardening and softening effects are clearly visible for positive and negative values of $\bar{\beta}$, as clearly expected.

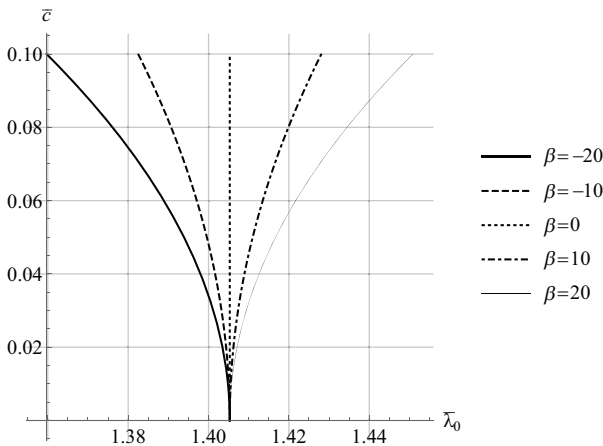


Fig. 1 Zeroth-order nondimensional frequency depending on amplitude. $\bar{\alpha} = 1$

3.2 First-Order Solution

To find the first-order increment in eigenvalue as a response to small nonlocality is to be found by using *Fredholm compatibility equation*. Accordingly,

$$\int_0^L \left(u_0'' - (K * u_0')' - \frac{\lambda_1 \rho A}{B} u_0 \right) u_0 dx = 0 \tag{14}$$

which provides,

$$\lambda_1 = \frac{\pi B e^{-\frac{1}{\kappa}} (32L^4 - 8\pi^2 \kappa^2 L^2 - \pi \kappa e^{L/\kappa} (\pi^4 \kappa^3 + 32L^3 + 4\pi^2 \kappa L^2))}{4\rho A (4L^3 + \pi^2 \kappa^2 L)^2} \tag{15}$$

or, in nondimensional form,

$$\bar{\lambda}_1 = \frac{\lambda_1}{\lambda_L} = \frac{e^{-\frac{1}{\bar{\kappa}}} \left(\pi \bar{\kappa} \left(-e^{\frac{1}{\bar{\kappa}}} (\pi^4 \bar{\kappa}^3 + 4\pi^2 \bar{\kappa} + 32) - 8\pi \bar{\kappa} \right) + 32 \right)}{\pi (\pi^2 \bar{\kappa}^2 + 4)^2}, \bar{\kappa} = \kappa/L. \tag{16}$$

Equation(16) provides the small effect of the long-distance interactions in materials on the eigenvalue. Note that it is independent of the amplitude of the vibration motion; however, consideration of higher-orders provides the effect of nonlocality coupled with the amplitude of the vibration.

The dependance of fundamental frequency on nonlocal parameter, κ , and on vibration amplitude for different elastic medium parameters is provided in Fig. 2.

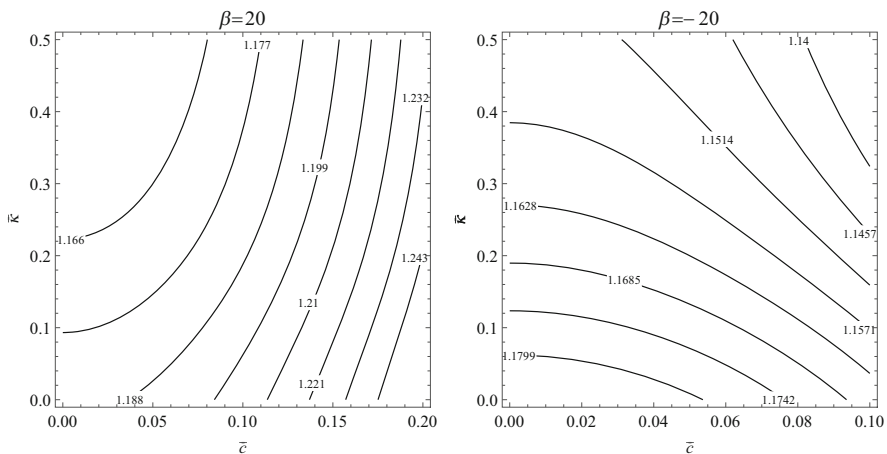


Fig. 2 Variation of fundamental frequency with amplitude and nonlocal parameter ($\bar{\alpha} = 1, \xi = 0.1$)

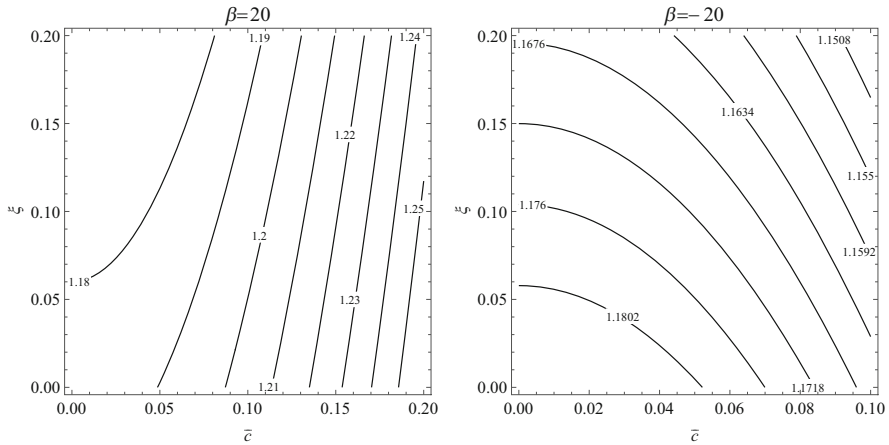


Fig. 3 Variation of fundamental frequency with amplitude and fraction coefficient ($\bar{\alpha} = 1, \bar{\kappa} = 0.1$)

The softening effect is clearly observed, which is even more appreciable for softening response of elastic medium depending on the vibration amplitude. In this particular parameter of $\beta = 20$, the hardening behavior of the medium seems to overpower the softening due to nonlocal parameter, especially for increasing vibration amplitudes.

Another graphical interpretation is provided in Fig. 3, in which the variation of fundamental frequency with amplitude and the fraction coefficient is plotted. Fraction coefficient plays a similar role to nonlocal parameter, although it must be limited since only the first-order terms are considered.

4 Conclusions

Nonclassical continuum theories are needed when the internal organization of the material plays a role in its macro behavior. Providing great simplifications in the analysis by continuum assumption, the mathematical operators appearing in the field equations are usually led to concerns about existence and uniqueness of solution. We showed herein the possibility of using the fraction coefficient as a parameter in terms of which the field functions and eigenvalues can expanded into series. Such a procedure provided a local elasticity problem at its lowest order, is free of any additional and spurious mathematical requirements. Moreover, the first-order contribution of nonlocality on eigenvalues of bars inside an elastic medium is found in closed-form. The results and solution technique provided here is thought to be a great tool for material identification problems as well as providing a benchmark of results for future studies.

References

1. P. Trovalusci, *Molecular Approaches for Multifield Continua: Origins and Current Developments* (Springer, Vienna, 2014), pp. 211–278
2. P. Trovalusci, *Discrete to Scale-Dependent Continua for Complex Materials: A Generalized Voigt Approach Using the Virtual Power Equivalence in Materials with Internal Structure: Multiscale and Multifield Modeling and Simulation*. Springer Tracts in Mechanical Engineering (Springer International, Berlin, 2015)
3. G. Maugin, *Generalized Continuum Mechanics: What Do We Mean by That? Mechanics of Generalized Continua: One Hundred Years After the Cosserats*. Advances in Mechanics and Mathematics, vol. 21 (Springer, New York, 2010)
4. E. Kröner, Elasticity theory of materials with long range cohesive forces. *Int. J. Solids Struct.* **3**(5), 731–742 (1967)
5. I. Kunin, *Elastic Media with Microstructure: One-Dimensional Models*. Elastic Media with Microstructure (Springer, Berlin, 1982)
6. E. Cosserat, F. Cosserat, *Théorie des corps déformables* (A. Hermann, Paris, 1909)
7. F. dell’Isola, A. Della Corte, R. Esposito, L. Russo, Some cases of unrecognized transmission of scientific knowledge: from antiquity to Gabrio Piola’s peridynamics and generalized continuum theories, in *Generalized Continua as Models for Classical and Advanced Materials*, ed. by H. Altenbach, S. Forest. Advanced Structured Materials, vol 42 (Springer, Berlin, 2016)
8. A.C. Eringen, A unified theory of thermomechanical materials. *Int. J. Eng. Sci.* **4**(2), 179–202 (1966)
9. A. Eringen, D. Edelen, On nonlocal elasticity. *Int. J. Eng. Sci.* **10**, 233–248 (1972)
10. A. Eringen, *Microcontinuum Field Theory* (Springer, Berlin, 1999)
11. A.C. Eringen, *Nonlocal Continuum Field Theories*, 1 edn. (Springer, Berlin, 2002)
12. G. Romano, R. Barretta, Nonlocal elasticity in nanobeams: the stress-driven integral model. *Int. J. Eng. Sci.* **115**, 14–27 (2017)
13. T.M. Atanackovic, B. Stankovic, Generalized wave equation in nonlocal elasticity. *Acta Mech.* **208**, 1–10 (2009)
14. A. Carpinteri, P. Cornetti, A. Sapora, Nonlocal elasticity: an approach based on fractional calculus. *Meccanica* **49**, 2551–2569 (2014)
15. M. Aydogdu, Axial vibration analysis of nanorods (carbon nanotubes) embedded in an elastic medium using nonlocal elasticity. *Mech. Res. Commun.* **43**, 34–40 (2012)
16. E. Benvenuti, A. Simone, One-dimensional nonlocal and gradient elasticity: closed-form solution and size effect. *Mech. Res. Commun.* **48**, 46–51 (2013)
17. A. Eringen, Linear theory of nonlocal elasticity and dispersion of plane waves. *Int. J. Eng. Sci.* **10**, 425–435 (1972)
18. A.C. Eringen, Screw dislocation in non-local elasticity. *J. Phys. D Appl. Phys.* **10**(5), 671–678 (1977)
19. J. Fernández-Sáez, R. Zaera, J. Loya, J. Reddy, Bending of Euler–Bernoulli beams using Eringen’s integral formulation: a paradox resolved. *Int. J. Eng. Sci.* **99**, 107–116 (2016)
20. N. Challamel, C.M. Wang, The small length scale effect for a non-local cantilever beam: a paradox solved. *Nanotechnology* **19**(34), 345703 (2008)
21. M. Tuna, M. Kirca, Exact solution of Eringen’s nonlocal integral model for bending of Euler–Bernoulli and Timoshenko beams. *Int. J. Eng. Sci.* **105**, 80–92 (2016)
22. G. Romano, R. Barretta, Comment on the paper exact solution of Eringen’s nonlocal integral model for bending of Euler–Bernoulli and Timoshenko beams by Meral Tuna and Mesut Kirca. *Int. J. Eng. Sci.* **109**, 240–242 (2016)
23. M. Tuna, M. Kirca, Respond to the comment letter by Romano and Barretta on the paper exact solution of Eringen’s nonlocal integral model for bending of Euler–Bernoulli and Timoshenko beams. *Int. J. Eng. Sci.* **116**, 141–144 (2017)

24. R. Zaera, Ó. Serrano, J. Fernández-Sáez, On the consistency of the nonlocal strain gradient elasticity. *Int. J. Eng. Sci.* **138**, 65–81 (2019)
25. K.E. Atkinson, *The Numerical Solution of Integral Equations of the Second Kind*. Cambridge Monographs on Applied and Computational Mathematics (Cambridge University Press, Cambridge, 1997)

Nonlinear Modeling for Thermal Behavior on Power Integrated Circuits



Arturo Buscarino, Carlo Famoso, and Luigi Fortuna

1 Introduction

The high temperature of electronic devices is one of the main causes of failure. Therefore, the formulation of an effective thermal model that allows to understand the heating of the device becomes fundamental in order to establish the conditions of its correct operation, its reliability and times work [1]. The modeling of temperature dynamics occurring over the surface of electronic devices can be performed considering various quality of approximation, however, in order to make the obtained models easily applicable, they must not be complex, they must not have a high order and should not significantly affect the computing resources of computers [2].

Our starting point is linked to the concept that the temperature dynamic behavior of electronic devices is a dynamic spatio-temporal process in which domains characterized by different materials, heat loads and geometries interact [3].

Essentially, two approaches to the problem can be considered: a Finite Element Methods (FEM), and a Lumped Parameters approach. The first one is considered the method of choice for simulating real systems with complex space-time dynamics linked to articulated geometric architectures. The second one captures the similarity between thermal and electrical phenomena and the thermal dynamics is modeled

A. Buscarino (✉) · L. Fortuna
DIEEI, University of Catania, Catania, Italy

CNR-IASI, Italian National Research Council, Institute for Systems Analysis and Computer Science, A. Ruberti, Rome, Italy
e-mail: arturo.buscarino@unict.it; luigi.fortuna@unict.it

C. Famoso
DIEEI, University of Catania, Catania, Italy
e-mail: carlo.famoso@dieei.unict.it

as the cascade of elementary RC circuits. Both methods have advantages and disadvantages [2].

The approach using FEM, while returning a very detailed view of the problem, can lead to a considerable increase in the complexity of the model, requiring the use of huge computing resources, so much so as to make their use not very useful in certain problems of thermal propagation, in view of the complexity of the procedure that leads to the complete definition of the model and its numerical simulation. On the other hand, the approach using Lumped Parameters, while ensuring a relative low level of complexity in realization of the model and the use of few computing resources [3], it is not very suitable for thermal systems in which the structure of the components is characterized by the presence of numerous materials with very different thermal characteristics and located in such a way as to give the device a considerable constitutive inhomogeneity. Furthermore, time-delays must be considered in the model since they often occur in modeling the propagation of the heat loads over surface, and they can be difficult to treat.

The basic idea discussed herein is to merge the FE methods with lumped parameter models. From the FEM approach we get the explicit consideration of the spatial extension of the device, while from the lumped parameter models we can exploit their usually lower orders. Starting from real datasets acquired in laboratory by using appropriate thermal acquisition devices providing spatial information of the temperature over the package surface of the real electronic device, or data numerically generated by the finite element model, the aim is to obtain a general reduced order thermal nonlinear model mimicking the thermal behavior of the dynamics under investigation, ensuring the precision of FEMs but lowering the degree of complexity of the model, which relies on the specific geometry, the materials, and the inhomogeneities of considered packages [4].

The paper is organized as follows: in Sect. 2 the modeling methodology is outlined, in Sect. 3 the numerical simulations to generate datasets are presented, while in Sect. 4 reduced order modeling results are discussed. The conclusions are drawn in Sect. 5.

2 Methodology

Considering the physics of the process, the initial hypothesis we make is that the thermal process is driven by a heat diffusion process over the package surface.

This leads to consider the device according to an overall vision, which requires to consider not only the point where the temperature is detected but also the temperatures in the nearby points, in the perspective that the thermal flow diffuses in relation to the conditions that are created in the immediate vicinity. In particular, the models of the phenomenon, which we will formulate, mimic the input–output relationship between the temperature on a specific point and the temperatures measured in an 8-neighborhood of that point [5].

The proposed approach combines well with the FEM modeling philosophy. In fact, once the mesh for the numerical solution of the problem has been defined, the dislocation and the distance between its points within the thermal system is well known and remains fixed. In this way, once the point on the surface of the device to be thermally characterized is assigned, the points positioned inside the region of influence with radius one are immediately identified and the contribution in temperature given by these points to sustain the superficial thermal diffusion process, that will influence the thermal dynamics in the point under examination, can be uniquely defined.

With regard to the finite elements model, which was implemented on the ANSYS 2019-R3, it must be said that it refers to a power electronics device made with SiC technology. The data provided by the solution of this finite element model, constitute the starting point for the implementation of the next step of our purpose, that is to use the same data to implement a process of identification of the phenomenon that allows the achievement of the same results, but with slightly reduced calculation and implementation efforts.

For the purpose we adopted two nonlinear models, namely a nonlinear autoregressive model with exogenous inputs (NARX), based on neural networks, and a Hammerstein-Wiener Model (H-WM).

3 Thermal Modeling from Numerical Simulations

The examined power electronics device is essentially an apparatus in which four overlapping structures define its geometry and functionality. The first layer, the lower one, is an aluminum parallelepiped, with a rectangular base whose maximum size does not exceed 20 mm, and which has a thickness of 0.25 mm. Superimposed on the aluminum layer, a structure is made up of three layers of three different materials, respectively, each having equal dimensions in width and depth.

The layer in contact with the aluminum base is a solder layer with a thickness of 0.25 mm. Superimposed, there is a copper layer with a thickness of 0.3 mm and, finally, a layer in Silicon Nitride, with a thickness of 0.32 mm, completes this structure. The Direct Bonded Copper (DBC) layer is made on the previous Silicon Nitride layer. A schematic representation of the device is reported in Fig. 1.

The active devices, four in number on the DBC, are identical in size and constituent materials. Essentially, these are four rectangular-based parallelepipeds with dimensions just over four millimeters, made up of three different layers of overlapping materials. The layer in contact with the DBC is the one solder layer with a thickness of 0.07 mm, followed by two layers of the same material, SiC, but with a different thickness, of 0.175 and 0.005 mm to close the structure.

The three-dimensional model was meshed with a rectangular mesh which is made up of 5556 nodes and 3968 elements, as reported in Fig. 2a.

The model defined in its geometry, characterized in the physical properties of the materials and discretized with the mesh, is now ready to be solved.

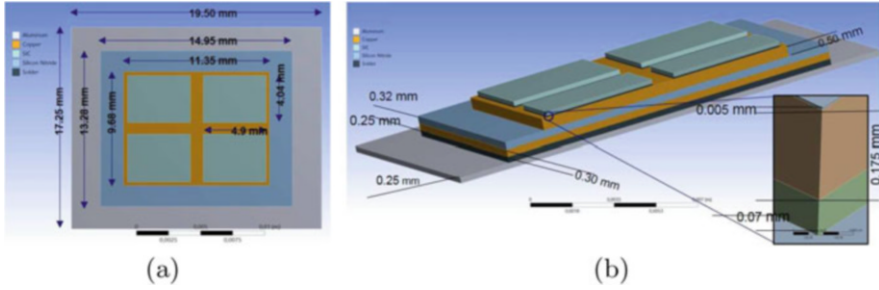


Fig. 1 FE 3D model for the considered package: (a) top view and (b) 3D projection

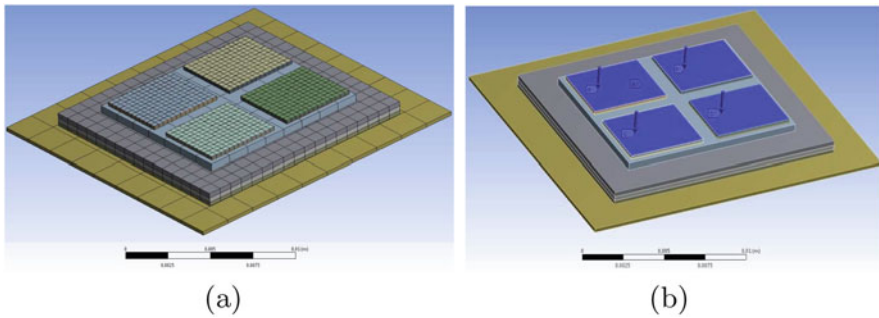


Fig. 2 (a) FE 3D Meshed model for the considered package. (b) Thermal flow defined on the surface of each individual device

The solution is obtained, imposing the initial temperature conditions and the dynamics of the sources. These are four different thermal flows uniformly applied on very small limited area of the upper surfaces of the corresponding active devices, as in Fig. 2b. The dynamics of the sources are different from each other in time evolution.

The thermal model has been studied in four different scenarios, providing for the combined and non-simultaneous activation of the devices. The activation of the device consists in applying to it, in a given instant of time, a step heat flow of 105 W. The simulations were conducted over a thirty-second time interval and the steady-state colored temperature on the four devices, in each operating scenarios, is shown in Fig. 3.

The FEM software allows to determine a steady-state temperature distribution taking into account the materials property. It is clear from a comparison of the dynamics, how the steady-state temperature distribution is not only linked to the dynamics of the source that is affecting the single device, but is clearly affected by the thermal flows of the neighboring devices, highlighting that the thermal process in question is essentially a diffusive process, in which neighboring processes influence each other. What emerges from the simulations conforms to what was

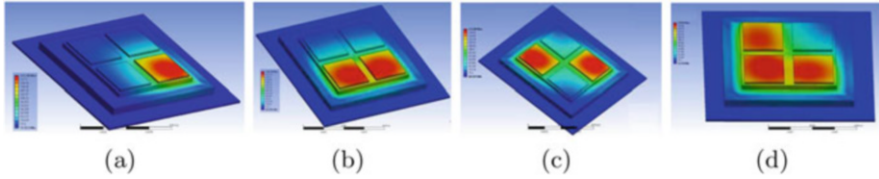


Fig. 3 Four different scenarios of the simulation: (a) 1: on, 2,3,4: off; (b) 1,2: on, 3,4: off; (c) 1,4: on, 2,3:off; (d) 1,2,4: on, 3: off

initially assumed in our discussion about the mutual interactions of the neighboring elements.

4 Reduced Order Nonlinear Modeling from Numerical Simulation Data

As already pointed out, the numerical data provided by the FEM simulation of the device constitute the starting point for the implementation of nonlinear reduced order models: NARX and H-WM.

As concerns the NARX model, it has been identified by using an artificial neural network.

In the Hammerstein-Wiener model, the input–output relationship of the system is decomposed into three interconnected elements: the dynamics of the system is represented by a linear transfer function, while the nonlinearities of the system are expressed by nonlinear functions of the input and of the linear system output. In our case the input and output nonlinearities were characterized by piecewise linear nonlinearities functions.

In order to validate the thesis of this work, it was decided to conduct the study on a point of the device whose thermal dynamics were physically linked as much as possible to that of nearby elements. For this reason it was decided to concentrate the study on the point located at the internal vertex of the device 4.

The order of the linear transfer function and the nonlinearity input/output signal were chosen experimentally and considering the shape and behavior of the signals.

Similar, the nonlinear blocks are configured with the test-error algorithm after each change validating the model and analyzing the results.

4.1 System Configuration I: 1: On; 2,3,4: Off

In the first thermal configuration of the system, only one of the four devices is considered thermally activated.

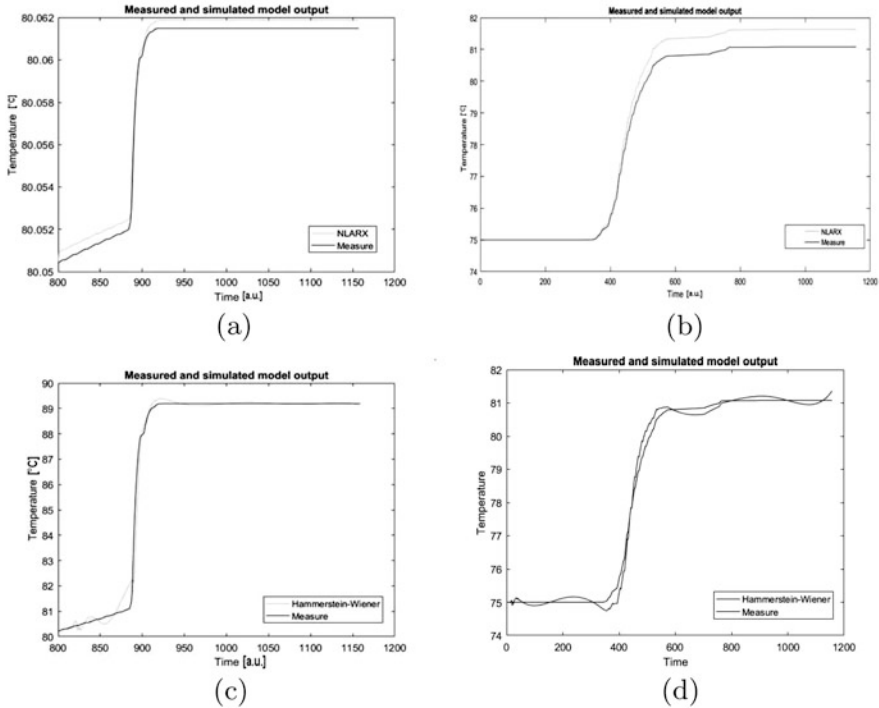


Fig. 4 Configuration 1. One-step-ahead prediction of the temperature over a single point: (a) NARX and (b) H-W. One-step-ahead prediction of the temperature over a single point internal to die 2: (c) NARX and (d) H-W. Time in arbitrary units

NARX Model The best NARX model, for the point under consideration, obtained by using a neural network with 3 units with sigmoid activation function and inserting a single regressor for inputs 5, 6, 7, and 8 and none for the other four, including the output. The delay has set by default to 1. The one-step-ahead prediction is reported in Fig. 4a, displaying a 90.83% accuracy, a Final Prediction Error (FPE): $4.58 \cdot 10^{-5}$, and a Mean Square Error (MSE): $4.32 \cdot 10^{-5}$.

Once the model was validated for the point under consideration, it was verified whether the same model continued to apply to another point that did not belong to the area of interest. An internal point has been identified in device 2, as shown in Fig. 4b. The one-step-ahead prediction is reported in Fig. 4b, displaying a 84.77% accuracy.

H-W Model The best Hammerstein-Wiener model was obtained using in the two nonlinear blocks 2 units with a piecewise activation function for each of the inputs and 1 unit for the output. The central linear block is characterized, for each of the 8 inputs, by a transfer function with 3 zeros and 4 poles. Delay set by default to 1. The one-step-ahead prediction is reported in Fig. 4c, displaying a 98.48% accuracy, a Final Prediction Error (FPE): $1.46 \cdot 10^{-4}$, and a Mean Square Error (MSE): $1.04 \cdot 10^{-4}$.

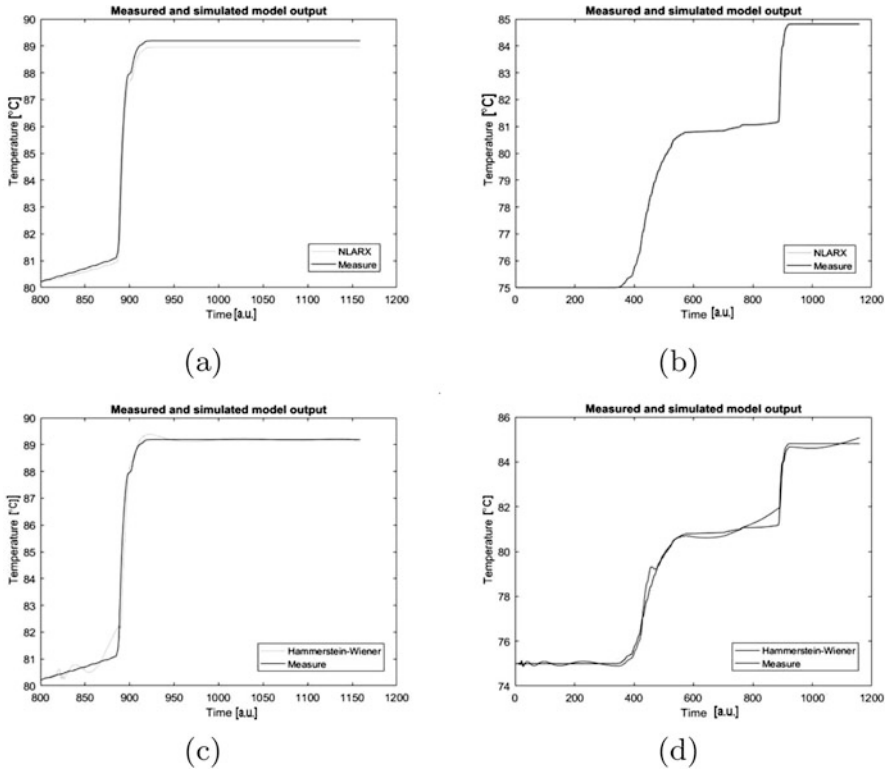


Fig. 5 Configuration 2. One-step-ahead prediction of the temperature over a single point: (a) NARX and (b) H-W. One-step-ahead prediction of the temperature over a single point internal at die 2: (c) NARX and (d) H-W. Time is in arbitrary units

Similarly, to the previous case, the model was tested in the internal point of device 2. The one-step-ahead prediction is reported in Fig. 4d, displaying a 93.51% accuracy.

4.2 System Configuration II: 1, 2: On; 3,4: Off

In the second thermal configuration of the system, only two of the four devices are considered thermally activated: two devices located on one side.

NARX Model The best NARX model, for the point under consideration, is obtained by using a network with 2 units with sigmoidal activation function and inserting a single regressor for inputs 5, 6, 7, and 8 and none for the other four, including the output. The delay has set by default to 1. The one-step-ahead prediction is reported in Fig. 5a, displaying a 92.77% accuracy, a Final Prediction Error (FPE): $5.01 \cdot 10^{-5}$, and a Mean Square Error (MSE): $4.79 \cdot 10^{-5}$.

The one-step-ahead prediction of the point internal at device 2 is reported in Fig. 5b, displaying a 98.83% accuracy.

H-W Model The best Hammerstein-Wiener model, defined for this operating condition of the system, has the same configuration as the model defined for the previous case. The one-step-ahead prediction is reported in Fig. 5c, displaying a 92.04% accuracy, a Final Prediction Error (FPE): $1.48 \cdot 10^{-4}$, and a Mean Square Error (MSE): $1.14 \cdot 10^{-4}$.

The one-step-ahead prediction related to at the point internal at device 2 is reported in Fig. 5d, displaying a 94.03% accuracy.

4.3 System Configuration III: 1, 4: On; 2, 3: Off

In the third thermal configuration of the system, only two devices located on the diagonal are considered thermally activated.

NARX Model The best NARX model, for the point under consideration, is obtained using 2 neurons with sigmoidal activation function and inserting four regressors for each of the eight inputs and none for the output. The delay has set by default to 1. The one-step-ahead prediction is reported in Fig. 6a, displaying a 96.25% accuracy, a Final Prediction Error (FPE): $8.21 \cdot 10^{-4}$, and a Mean Square Error (MSE): $6.23 \cdot 10^{-4}$.

Once the model was validated for the point under consideration, it was verified whether the same model continued to apply to another point that did not belong to the area of interest. An internal point of the device 2 located near the device 4 has been identified. The one-step-ahead prediction is reported in Fig. 6b, displaying a 83.83% accuracy. The result obtained shows how the model sufficiently follows the dynamics of the assigned system, even if it presents some uncertainty in the transitory phases.

H-W Model The best Hammerstein-Wiener model was obtained using in the two nonlinear blocks 2 units with a piecewise activation function for each of the inputs and 1 unit for the output. The central linear block is characterized, for each of the 8 inputs, by a transfer function with 2 zeros and 3 poles. Delay set by default to 1. The one-step-ahead prediction is reported in Fig. 6c, displaying a 92.04% accuracy, a Final Prediction Error (FPE): $7.05 \cdot 10^{-3}$, and a Mean Square Error (MSE): $5.71 \cdot 10^{-3}$.

The one-step-ahead prediction related to other point is reported in Fig. 6d, displaying a 94.73% accuracy.

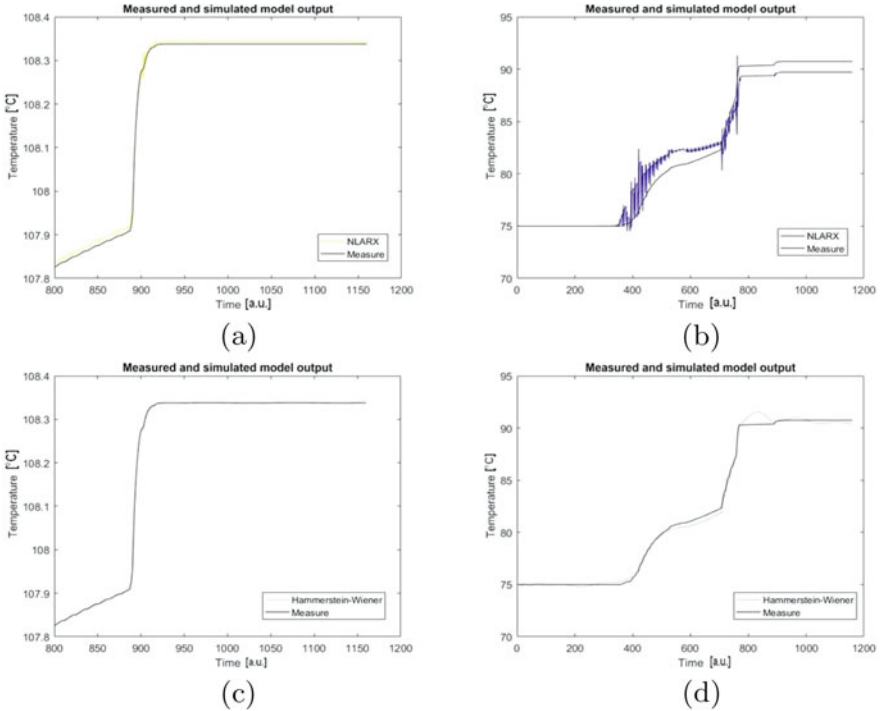


Fig. 6 Configuration 3. One-step-ahead prediction of the temperature over a single point: (a) NARX and (b) H-W. One-step-ahead prediction of the temperature over a single point internal at die 2: (c) NARX and (d) H-W. Time is in arbitrary units

4.4 System Configuration IV: 1, 2, 4: On; 3: Off

In the fourth and last thermal configuration of the system, three of the four devices are considered thermally activated.

NARX Model The best NARX model, for the point under consideration, is obtained using 5 neurons with sigmoidal activation function and inserting three regressors for all inputs except input 4 for which there are four regressors, and none for the output. The delay has set by default to 1. The one-step-ahead prediction is reported in Fig. 7a, displaying a 83.90% accuracy, a Final Prediction Error (FPE): $1.03 \cdot 10^{-3}$, and a Mean Square Error (MSE): $6.85 \cdot 10^{-4}$.

The one-step-ahead prediction of the point internal at device 2 is reported in Fig. 7b, displaying a 81.17% accuracy.

H-W Model The best Hammerstein-Wiener model was obtained using in the two nonlinear blocks 2 units with a piecewise activation function for each of the inputs and 1 unit for the output. The central linear block is characterized, for each of the 8 inputs, by a transfer function with 3 zeros and 4 poles. Delay set by default to 1.

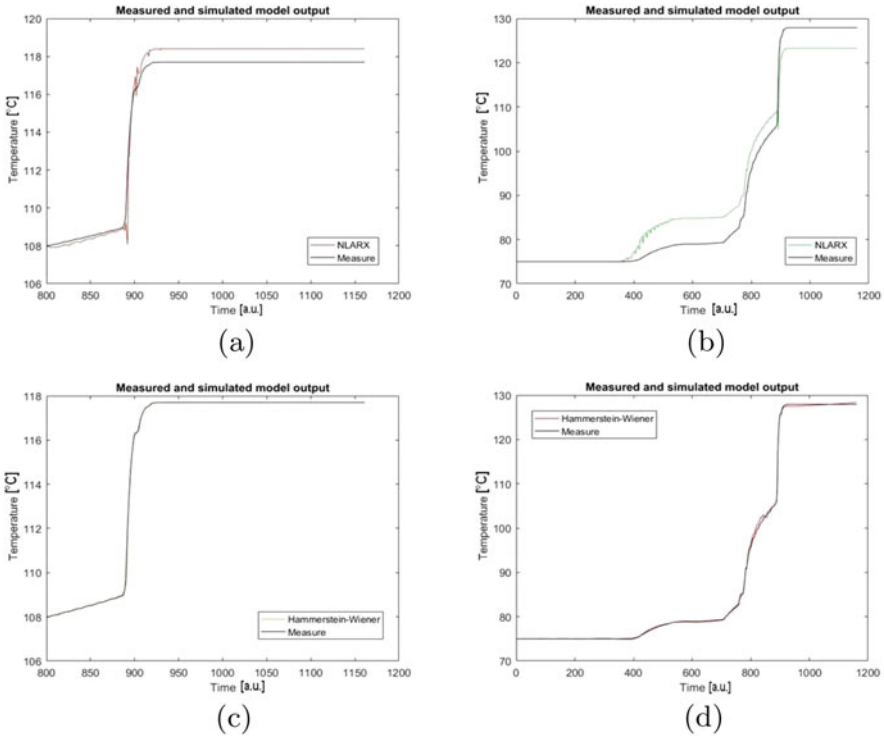


Fig. 7 Configuration 4. One-step-ahead prediction of the temperature over a single point: (a) NARX and (b) H-W. One-step-ahead prediction of the temperature over a single point internal at die 2: (c) NARX and (d) H-W. Time is in arbitrary units

The one-step-ahead prediction is reported in Fig. 7c, displaying a 98.99% accuracy, a Final Prediction Error (FPE): $1.42 \cdot 10^{-3}$, and a Mean Square Error (MSE): $1.11 \cdot 10^{-3}$.

The one-step-ahead prediction related to the point internal at device 2 is reported in Fig. 7d, displaying a 98.74% accuracy.

5 Conclusions

Comparing these results and highlighting the accuracy with which the model follows the temperature trend in a randomly assigned point of the FE mesh, the fundamental role that nonlinearities play in defining the exact thermal behavior of the system, clearly emerges. In all the thermal configurations in which the system has been studied, the best results have been obtained by adopting the Hammerstein-Wiener

models: this highlights how thermal processes are essentially linear, however, the inclusion of a weak nonlinear behavior improves the model performance.

In addition, the cost in terms of time to implement the H-W model (complexity of the model) and the processing cost to obtain the final results, are significantly lower in the H-W model, compared to the model implemented and solved considering the finite elements. Therefore, given the obtained results, the use of the H-W model proves to be a valid alternative to simulate the thermal behavior of a multichip power electronic device. The simple models proposed and investigated should be considered as simplified solution, the results discussed in this paper open the possibility to determine reduced order models of the thermal behavior of high density electronic devices keeping a suitable level of accuracy.


References

1. J.W. Kolar, J. Biela, S. Waffler, T. Friedli, U. Badstübner, Performance trends and limitations of power electronic systems, in *2010 6th International Conference on Integrated Power Electronics Systems* (IEEE, Piscataway, 2010), pp. 1–20
2. H.N. Koti, H. Chen, Y. Sun, N.A. Demerdash, On shortening the numerical transient in time-stepping finite element analysis of induction motors: method implementation, in *2019 IEEE International Electric Machines & Drives Conference (IEMDC)* (IEEE, Piscataway, 2019), pp. 1157–1162
3. M. Iachello, V. De Luca, G. Petrone, N. Testa, L. Fortuna, G. Cammarata, S. Graziani, M. Frasca, Lumped parameter modeling for thermal characterization of high-power modules. *IEEE Trans. Compon. Packag. Manuf. Technol.* **4**(10), 1613–1623 (2014)
4. L. Ljung, *System Identification: Theory for the User* (Prentice Hall, Upper Saddle River, 1999)
5. M.L. Apicella, A. Buscarino, C. Corradino, L. Fortuna, G. Mazzitelli, M.G. Xibilia, Temperature model identification of FTU liquid lithium limiter. *IEEE Trans. Control Syst. Technol.* **26**(3), 1132–1139 (2017)

Part V
Multifunctional Structures, Materials, and
Metamaterials

Modeling Asymmetric Hysteresis Inspired and Validated by Experimental Data



Jin-Song Pei, Biagio Carboni, and Walter Lacarbonara 

1 Introduction

Experimental data play an important role in this study. It first reveals the asymmetry of the restoring force, as shown in Fig. 1, where various symmetric cyclic displacement histories x (i.e., *inputs*) lead to asymmetric responses in terms of restoring force histories r (i.e., *outputs*). The obtained force-displacement measurements form *hysteresis loops*; the rheological element exhibiting this behavior can be conceptually called a *hysteresis spring*. The energy dissipation is different for the two loading directions.

The laboratory setup is shown in Fig. 2 where the tested device comprises two plates connected by two continuous steel wire ropes. It is manufactured by the company Enidine [1] and is used for vibrations isolation induced by vertical or horizontal excitations. Mechanical asymmetry in terms of force-displacement cycles can be introduced by materials, devices, or structures. The investigated device exhibits asymmetric hysteresis due to coupled geometric nonlinearities and inter-wire frictional dissipation. The restoring force is acquired by means of a Zwick-Roell testing machine under displacement control. One plate is cyclically moved with prescribed displacement histories while the other plate is fixed. A load-cell measures the restoring force provided by the ropes which exhibits an asymmetric constitutive response for positive and negative displacements. The

J.-S. Pei (✉)
University of Oklahoma, Norman, OK, USA
e-mail: jspei@ou.edu
https://www.researchgate.net/profile/Jin-Song_Pei

B. Carboni · W. Lacarbonara
DISG Department of Structural and Geotechnical Engineering, SAPIENZA University of Rome,
Rome, Italy
e-mail: biagio.carboni@uniroma1.it; walter.lacarbonara@uniroma1.it

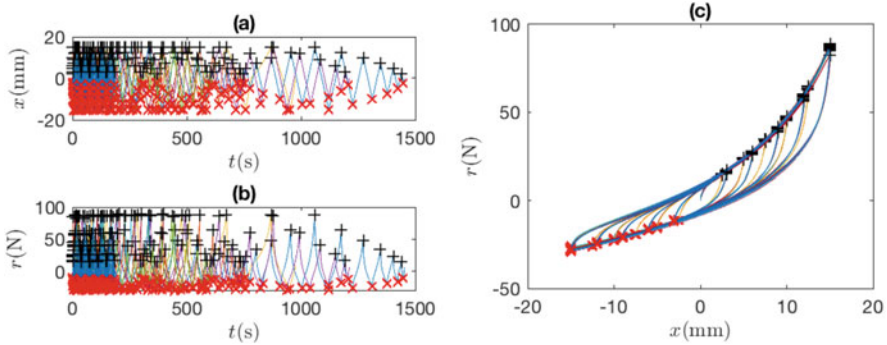


Fig. 1 (a) Displacement time histories $x(t)$, which is the input; (b) restoring force time histories $r(t)$, which is the output, and (c) the corresponding hysteresis loops $r(t)$ versus $x(t)$



Fig. 2 The wire rope-based device subject to the experimental testing campaign

experimental data are organized in four groups from A to D, all of which are displacement-controlled. These four test groups were designed to study loading rate-dependency of the responses [2]. Groups A and B consist of Tests 1–9 with different amplitude and velocity of sawtooth loading patterns. Group C consists of Tests 10–14 with a periodic frequency-modulated sawtooth loading pattern. Group D consists of Tests 15–22 with multiple cycles of both amplitude- and frequency-modulated sawtooth loading pattern. Figure 1 shows the inputs and outputs with all test data overlaid.

The experimental data are the evidence that motivates and inspires this modeling work, noting that there is not a specific phenomenological model at hand to simulate these particular asymmetric hysteresis responses. For the sake of model parameter

identification, a test belonging to Group D is more useful than those of the other groups given the richness of multiple loading/reloading and unloading curves. The identified parameter values from Group D will be validated by using the data from other groups.

Reference [2] quantifies a measure for loading rate-dependency and concludes that the responses shown in Fig. 1 are *rate-independent*. The rate-independency hints to the possibility of applying the classical Preisach operator. There are two benefits associated with the classical Preisach models. First, the classical Preisach models probably are the most general rate-independent hysteresis models. Next, we will adapt the extended Masing model [3, 4], a subset of the classical Preisach models [5], for asymmetric hysteresis.

Our objective is to explore the possibility of generalizing the existing extended Masing model. Since the extended Masing model has a concise format for symmetric hysteresis, we wonder if a concise format could also be achieved for asymmetric hysteresis.

The technical challenges are outlined in a brief literature review in Sect. 2, and a formal definition for asymmetrical hysteresis is proposed in Sect. 3. Section 4 focuses on the proposed problem formulations. Section 5 presents the nonlinear parametric identification results. Finally, Sect. 6 discusses the limitations and future improvements.

2 Technical Challenges

Asymmetric hysteretic responses have been studied with various modeling approaches [6–11]. Given the challenging nature of this problem, the number of parameters to be identified can be computationally demanding.

The classical Preisach models were originally developed for magnetic hysteresis [12, 13] but are in fact more general. The input-output relation of the classical Preisach model is given as follows:

$$y(t) = \iint_T v(\alpha, \beta) \mathcal{R}_{\alpha, \beta} u(t) d\alpha d\beta, \quad (1)$$

where $u(t)$ and $y(t)$ are the input and output, respectively. $\mathcal{R}_{\alpha, \beta}$ represents a relay hysteron operator with switching down and up thresholds in the input as α and β , respectively. $v(\alpha, \beta)$ is the Preisach (density, weighting, distribution) function. T denotes the Preisach triangle with $\beta \geq \alpha$.

It can be computationally demanding to identify $v(\alpha, \beta)$ for an asymmetric hysteresis because of the asymmetry required by the distribution [14]. We thus wonder if we could work with models simpler than the classical Preisach models to reduce the computational demand. The work of [5] shows that the Masing models (and more) are Preisach models and also indicates that for Masing models $v(\alpha, \beta)$ is a function of $\alpha - \beta$, reducing two parameters to one. Due to the fact that it is

a simpler model than the classical Preisach model, Masing model will be explored herein. We will pay a particular attention to the adequacy of this choice, which cannot be entirely answered in this study and will require a further study.

In terms of Masing models, an early paper by Masing [15] provided the stimulus for later development of models for softening hysteresis systems by researchers, for example, [3, 4, 16–22]. Masing models were originally proposed for steady-state hysteresis; the relationship between r and x was extended for arbitrary loading conditions via the so-called *Masing rules* with contributions from [3, 4, 21, 22], leading to the so-called extended Masing model, as reviewed in [23]. Masing Rule 1 deals with the relationship between the virgin loading curve and all other reloading and unloading curves, while Masing Rules 2 and 3 address the closure and fate of minor loops relevant to *nonlocal memory*.

Regarding Masing Rule 1, we have the experimental virgin loading curve along the positive but not the negative direction as shown in Fig. 1, thus not allowing us to examine this rule. Furthermore, there is not a concept corresponding to the virgin loading curve in the classical Preisach models, making us question if we should pay attention to the reloading and unloading branches only, i.e., disregard Masing Rule 1 for asymmetric hysteresis. Since the experimental data in this study do not involve minor loops, we cannot examine Masing Rules 2 and 3 for asymmetric hysteresis. Although we will not directly employ the Masing rules for modeling asymmetric hysteresis, this study could facilitate the topic in the future.

In the classical Preisach models, there are only piecewise monotonically increasing or decreasing input-output branches (e.g., [24]). This is consistent with the “monotone operators” and discussions on “vibro-correctness” in [13]. This monotonicity property will be instrumental for modeling asymmetric hysteresis as will be revealed in Sect. 4.

We have to further question whether the asymmetric hysteresis can be treated as a model assembly so that we could avoid developing a new model. [25] reviews a modified Masing model in terms of $r = (1 - \alpha)h(x) + \alpha z$, where the first and second terms are an odd nonlinear function and the hysteresis, respectively. Similarly, as reviewed in [23], the extended Masing models are fundamentally softening hysteresis systems. If a nonlinear hardening spring is connected in parallel with an extended Masing model, then hardening hysteresis can be described.

We thus investigate the feasibility of modeling asymmetric hysteresis by connecting a nonlinear asymmetric cubic spring (denoted as Duffing component) with an extended Masing model in parallel. With the same input displacement cycle, Fig. 3 gives two examples where $\lambda = 1$ and $\lambda = 5$ (for the Duffing component when $x \geq 0$ only) as in Fig. 3c, f, respectively, leading to $r = r_M + \lambda r_D$. The outputs r appear asymmetrical under symmetrical inputs x as shown in Fig. 3e, f; however, the *dissipated energy* enclosed by the hysteresis loop when $x \geq 0$ and $x < 0$ is the same because only the underlying extended Masing model contributes to the dissipated energy and provides symmetric hysteresis cycles as shown in Fig. 3a, b.

We numerically rule out this feasibility meaning that we cannot leverage a symmetric Masing model to describe the experimental response shown in Fig. 1. For example, Test 10 has the dissipated energy of 341.20 and 170.50 Nmm in the

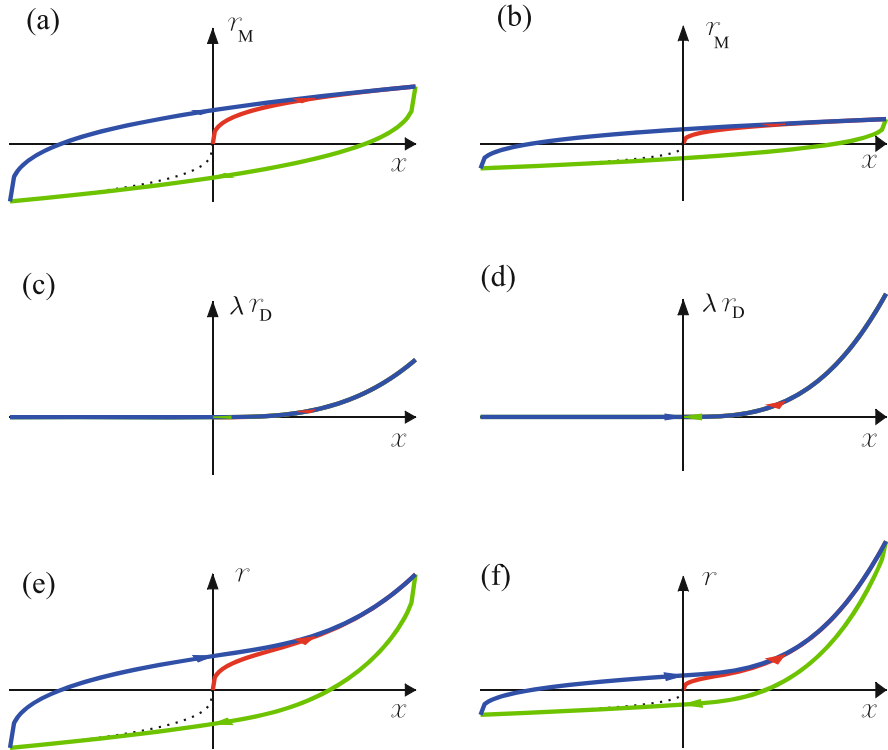


Fig. 3 Force-displacement cycles where the cycles shown in (e) and (f) are obtained by assuming a parallel connection of Masing in (a) and (b), with Duffing springs in (c) and (d), respectively. $r = r_M + \lambda r_D$ with the subscripts M and D for Masing and Duffing, respectively. r_D is assumed to be zero when $x < 0$ and $\lambda = 1, 5$ in (c) and (d), respectively

positive and negative x direction, respectively. In summary, we will have to provide an asymmetric hysteresis model instead, the first step of which is to define the asymmetric hysteresis.

3 Definition for Asymmetric Hysteresis

Asymmetry in a skeleton curve alone could be captured by introducing an asymmetric nonlinear spring into a modeling assembly as illustrated in the two examples given in Fig. 3; however, the experimental data in this study indicate the underlying hysteresis loops (as in Fig. 3a, b) being asymmetric instead. We thus cannot define the asymmetric hysteresis to be modeled by merely examining the amplitudes of $r(t)$ in both directions.

The dissipated energy measured by the enclosed area of hysteresis loops $\int r(t)dx(t)$ differ in the positive and negative directions of $x(t)$ in this study; however, the same dissipated energy in both directions does not guarantee symmetric hysteresis because the former is a sufficient condition to obtain the same dissipated energy—not a necessary condition.

With this analysis, the challenging asymmetric hysteresis to be modeled is defined as follows:

Definition 1 (Asymmetric Hysteresis in Restoring Force) When $x(t)$ has the same amplitude in both positive and negative directions, the differences in $r(t)$ between reloading and unloading for $+x(t)$ and $-x(t)$ are not the same for all $x(t)$. We name this asymmetric hysteresis in terms of restoring force $r(t)$.

4 Generalizing Extended Masing Model for Asymmetric Hysteresis

As shown in Fig. 1, the virgin loading curve appears only once in a test and for the positive loading direction only. After traversing the virgin curve, the device undergoes only unloading and reloading phases. So, we will focus on these two kinds of branches herein by following the monotonicity property.

For symmetric hysteresis in an extended Masing model [3, 4], these two kinds of branches are described by this *implicit function*:

$$\text{Branches of reloading or unloading: } f\left(\frac{x - x_{[j]}}{2}, \frac{r - r_{[j]}}{2}\right) = 0, \quad (2)$$

where $(x_{[j]}, r_{[j]})$ is the j th load reversal point, i.e., $\dot{x}_{[j]} = 0$ and $\dot{r}_{[j]} = 0$. Each branch is monotonically increasing or decreasing for reloading and unloading, respectively, following the so-called monotonicity and leading to a simultaneous occurrence of $\dot{x}_{[j]} = 0$ and $\dot{r}_{[j]} = 0$.

For symmetric hysteresis, the extended Masing model class may be written in a differential form [3, 4] by prescribing the tangent stiffness $\frac{dr}{dx}$, still, as an *implicit function*:

$$\text{Branches of reloading or unloading: } \frac{dr}{dx} = g\left(\frac{x - x_{[j]}}{2}, \frac{r - r_{[j]}}{2}\right). \quad (3)$$

An example of Eq. (3) but in an *explicit function* is given in [3] as follows:

$$\text{Branches of reloading or unloading: } \frac{dr}{dx} = K \left[1 - \left| \frac{r - r_{[j]}}{2r_u} \right|^n \right], \quad (4)$$

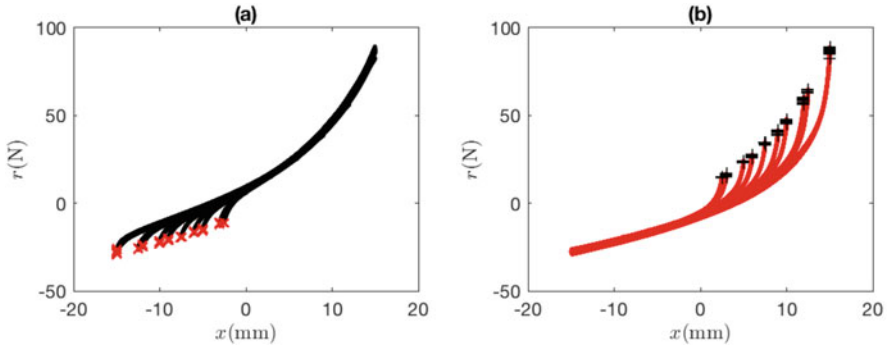


Fig. 4 Decomposed (a) reloading and (b) unloading branches from Fig. 1

where K , r_u , and n are model parameters. This is an *effort-controlled* formulation using the jargon in bond graph theory as introduced in [26], meaning that the quantity of r is natural to be solved first.

For the asymmetric hysteresis at hand, we decompose the hysteresis loops into reloading and unloading branches first and present them in Fig. 4:

We conjecture that, for an asymmetric extended Masing model, we could have two *implicit functions*:

$$\text{All reloading curves: } f_l \left(\frac{x - x_{[j]}}{2}, \frac{r - r_{[j]}}{2} \right) = 0. \tag{5}$$

$$\text{All unloading curves: } f_u \left(\frac{x - x_{[j]}}{2}, \frac{r - r_{[j]}}{2} \right) = 0. \tag{6}$$

Using *explicit functions*, we can have the following *flow-controlled* formulations from the bond graph theory meaning that the displacement x is natural to be solved first:

$$\text{All reloading curves: } r = r_l(x, x_{[j]}) \tag{7}$$

$$\text{All unloading curves: } r = r_u(x, x_{[j]}) \tag{8}$$

given that $r_{[j]}$ will be the starting or ending value of r of each branch thus can be dropped from the explicit functions. The feasibility of these two equations is tested in Fig. 5. It can be seen that each of these two surfaces is a one-to-one mapping and fairly smooth, being very promising.

We can also have the following *effort-controlled explicit functions*:

$$\text{All reloading curves: } x = x_l(r, r_{[j]}) \tag{9}$$

$$\text{All unloading curves: } x = x_u(r, r_{[j]}) \tag{10}$$

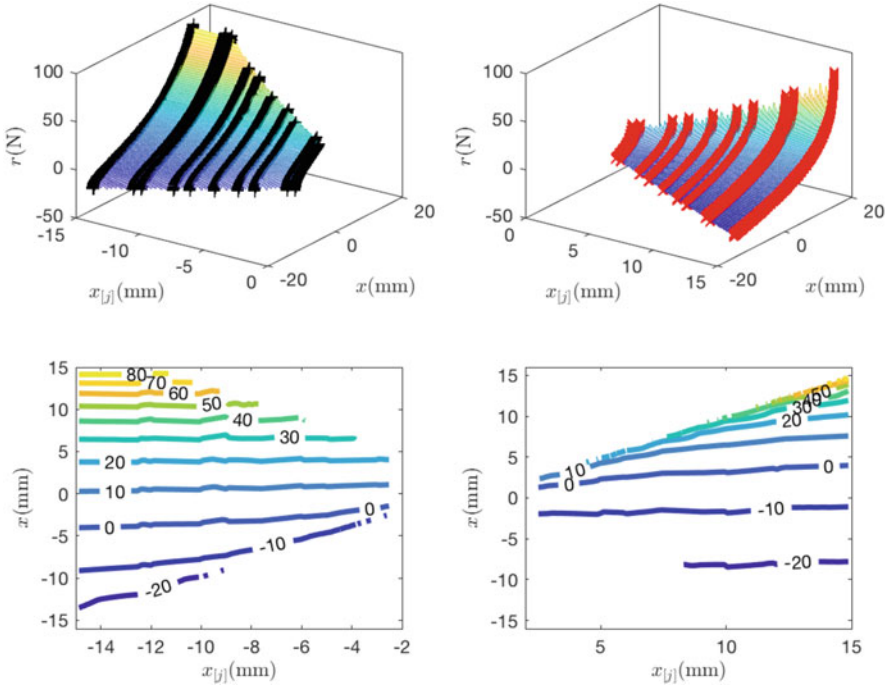


Fig. 5 All test data lumped together to examine the feasibility of Eqs. (7) and (8) for the left and right column, respectively; MATLAB meshgrid command is used for the approximated surfaces before obtaining their contour plots

given that $x_{[j]}$ will be the starting or ending value of x of each branch thus can be dropped from the explicit functions. The feasibility of these two equations is tested in Fig. 6 where each of these two surfaces is proved to be a one-to-one mapping and fairly smooth, thus being very promising.

5 Parameter Identification Using Neural Networks

To identify the explicit functions properly, the data are split into training and validation sets as normally done. As discussed previously, the only dataset used for training is Group D given its richness. For Eqs. (7) to (10), four separate multilayer feedforward neural networks (FFNN), each with three hidden nodes following [27, 28], were initialized and trained using the Nguyen-Widrow and Levenberg-Marquardt algorithm, respectively. In training each FFNN, a default division of Group D is 70, 15, and 15 percent for training, validation, and test, respectively. Samples of the trained weights and biases are given in Table 1. As an example, Group B is predicted using the four trained FFNN following Eqs. (7)–(10);

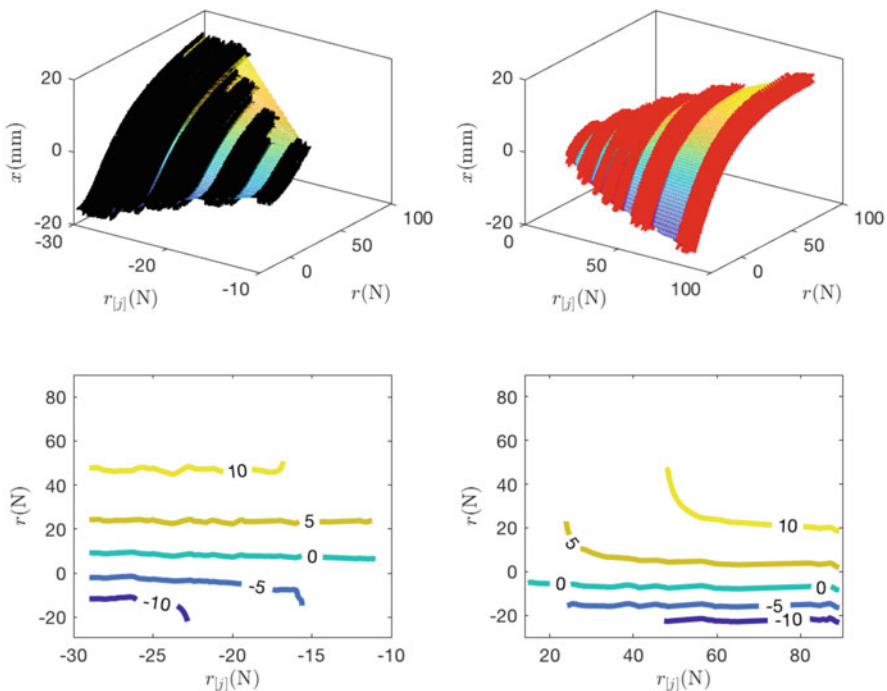


Fig. 6 All test data lumped together to examine the feasibility of Eqs. (9) and (10) for the left and right column, respectively; MATLAB meshgrid command is used for the approximated surfaces before obtaining their contour plots

Table 1 Samples of trained weights and biases of FFNNs

Following	Trained input weights IW and biases b , and output weights LW
Eq. (7)	$IW = \begin{bmatrix} -0.7420 & -0.0032 \\ 3.6985 & -1.8641 \\ -2.1808 & 0.8942 \end{bmatrix}, b = \begin{bmatrix} 1.8066 \\ 1.6135 \\ -3.0160 \end{bmatrix}, LW = \begin{bmatrix} -8.0476 \\ -0.1340 \\ -7.4041 \end{bmatrix}^T$
Eq. (8)	$IW = \begin{bmatrix} 2.8860 & 3.2264 \\ 7.2669 & -2.6694 \\ 0.5633 & -0.0156 \end{bmatrix}, b = \begin{bmatrix} 1.9592 \\ -5.7168 \\ -1.0901 \end{bmatrix}, LW = \begin{bmatrix} -0.0041 \\ 3.6266 \\ 2.5238 \end{bmatrix}^T$

the results are properly paired up to form entire loops as in Fig. 7. The normalized root mean squared error (NRMSE) corresponding to these four equations are 0.6%, 0.7%, 0.7%, and 1.0%.

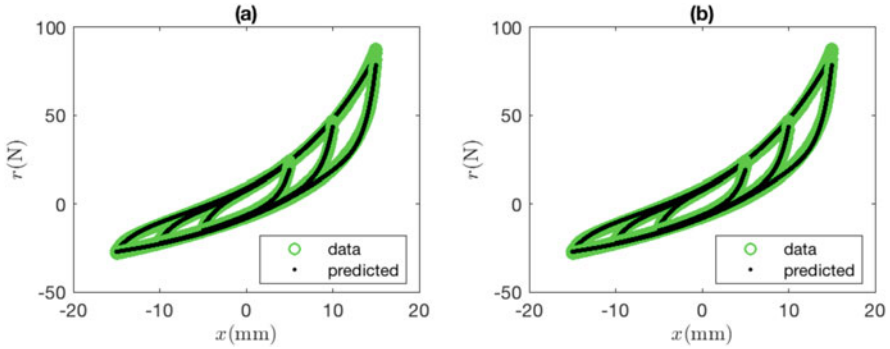


Fig. 7 All Group D test data lumped together to train a total of four separate neural networks following Eqs. (7)–(10), where the first and last two are used to predict Group B results given in (a) and (b), respectively

6 Discussion and Conclusions

A small step has been taken towards extending the Masing model for asymmetric hysteresis. Although the obtained results seem promising, the open question is centered on the robustness to minor loops. Possible future work includes updating the Masing rules, studying nonlocal memory, and validating the identified functions using new experimental datasets. Moreover, numerical simulations employing the asymmetric hysteresis spring inside a dynamical system will be part of future research efforts.

References

1. ITT Enidine Inc, Compact wire rope isolator (2020). <http://www.enidine.com>
2. M. Antonelli, B. Carboni, W. Lacarbonara, D. Bernardini, T. Kalmár-Nagy, Quantifying rate-dependence of a nonlinear hysteretic device, in *Nonlinear Dynamics of Structures, Systems and Devices*, ed. by W. Lacarbonara, B. Balachandran, J. Ma, J. Tenreiro Machado, G. Stepan (Springer, Berlin, 2020)
3. P. Jayakumar, Modeling and identification in structural dynamics. Ph.D. thesis, California Institute of Technology, Pasadena, CA (1987)
4. P. Jayakumar, J.L. Beck, System identification using nonlinear structural models, in *Structural Safety Evaluation Based on System Identification Approaches*, ed. by H.G. Natke, J.T.P. Yao (Friedr. Vieweg & Sohn, Braunschweig/Wiesbaden, 1988). Vieweg International Scientific Book Series, vol Proceedings of the 1987 Workshop at Lambrecht/Pfalz, pp. 82–102
5. V.A. Lubarda, D. Sumarac, D. Krajcinovic, Preisach model and hysteretic behaviour of ductile materials. *Eur. J. Mech. A/Solids* **12**(4), 445–470 (1993)
6. S. Dobson, M. Noori, Z. Hou, M. Dimentberg, T. Baber, Modeling and random vibration analysis of SDOF systems with asymmetric hysteresis. *Int. J. Non-Linear Mech.* **32**(4), 669–680 (1997)

7. J. Song, A. Der Kiureghian, Generalized Bouc-Wen model for highly asymmetric hysteresis. *ASCE J. Eng. Mech.* **132**(6), 610–618 (2006)
8. B. Carboni, W. Lacarbonara, P.T. Brewick, S.F. Masri, Dynamical response identification of a class of nonlinear hysteretic systems. *J. Intell. Mater. Syst. Struct.* **29**(13), 2795–2810 (2018)
9. A. Salvatore, B. Carboni, L.Q. Chen, W. Lacarbonara, Experimental dynamic response of a nonlinear wire rope isolator, in *Nonlinear Dynamics and Control* (Springer, Cham, 2020), pp 89–98
10. S. Xie, G. Ren, B. Wang, A modified asymmetric generalized Prandtl-Ishlinskii model for characterizing the irregular asymmetric hysteresis of self-made pneumatic muscle actuators. *Mech. Mach. Theory* **149**, 103836 (2020)
11. N. Vaiana, S. Sessa, L. Rosati, A generalized class of uniaxial rate-independent models for simulating asymmetric mechanical hysteresis phenomena. *Mech. Syst. Signal Process.* **146**, 106984 (2021)
12. F. Preisach, About the magnetic aftereffect. *Mag. Phys.* **94**(5–6), 277–302 (1935)
13. M.A. Krasnosel'skiĭ, A.V. Pokrovskii, *Systems with Hysteresis* (Springer, Berlin, 1989)
14. A. Stancu, B. Negulescu, R. Tanasa, L. Stoleriu, Preisach model for systems with asymmetric first order reversal curve (FORC) distribution. *Optoelectron. Adv. Mater. Rapid Commun.* **4**(3), 361–364 (2010)
15. G. Masing, Eigenspannungen und verfestigung beim messing, in *Proceedings of the 2nd International Congress for Applied Mechanics, Zurich* (1926), pp. 332–335, in German
16. P.C. Jennings, Response of simple yielding structures to earthquake excitation. Ph.D. dissertation, California Institute of Technology (1963)
17. P.C. Jennings, Periodic response of a general yielding structure. *J. Eng. Mech. Div. Proc. Am. Soc. Civ. Eng.* **90**(EM2), 131–166 (1964)
18. P.C. Jennings, Earthquake response of a yielding structure. *J. Eng. Mech. Div. Proc. Am. Soc. Civ. Eng.* **91**(EM4), 41–68 (1965)
19. W.D. Iwan, A distributed-element model for hysteresis and its steady-state dynamic response. *ASME J. Appl. Mech.* **33**(4), 893–900 (1966)
20. W.D. Iwan, On a class of models for the yielding behavior of continuous and composite systems. *ASME J. Appl. Mech.* **34**(3), 612–617 (1967)
21. W.R.S. Fan, The damping properties and the earthquake response spectrum of steel frames. Ph.D. thesis, University of Michigan, Ann Arbor, MI (1968)
22. R. Pyke, Nonlinear soil models for irregular cyclic loadings. *J. Geotech. Eng. Div. ASCE* **105**, 715–726 (1979)
23. J.L. Beck, J. L. and J.S. Pei, Demonstrating the power of extended Masing models for hysteresis through model equivalencies and numerical investigation, *Nonlinear Dynamics*, under review for publication
24. I. Mayergoyz, *Mathematical Models of Hysteresis and Their Applications*. Elsevier Series in Electromagnetism (Elsevier, Amsterdam, 2003)
25. W. Lacarbonara, F. Verstroni, Nonclassical responses of oscillators with hysteresis. *Nonlinear Dyn.* **32**, 235–258 (2003)
26. J.S. Pei, J.P. Wright, F. Gay-Balmaz, J.L. Beck, M.D. Todd, On choosing state variables for piecewise-smooth dynamical system simulations. *Nonlinear Dyn.* **95**(2), 1165–1188 (2019)
27. J.S. Pei, E.C. Mai, Constructing multilayer feedforward neural networks to approximate nonlinear functions in engineering mechanics applications. *ASME J. Appl. Mech.* **75**, 061002 (2008)
28. J.S. Pei, E.C. Mai, J.P. Wright, S.F. Masri, Mapping some functions and four arithmetic operations to multilayer feedforward neural networks. *Nonlinear Dyn.* **71**(1–2), 371–399 (2013)

Forced Transversal Vibrations of von Karman Plates with Distributed Spring-Masses



Aleksandra Gawlik, Andrzej Klepka, Vsevolod Vladimirov,
and Sergii Skurativskyi

1 Introduction

Studying the dynamics of complex multiphase, multicomponent, or hierarchical media [1, 2], it is necessary, as a rule, to modify the classical equations of continual mechanics in order to include additional degrees of freedom associated with the presence of the internal structure [3–7]. Today, there is a large number of diverse approaches enabling to take into account the influence of the structure of media on their dynamical properties [1, 5, 8, 9]. In this paper, we employ an approach based on the idea of interpenetrating continua [3, 10] leading to improved models of the elastic continuum with inclusions. Previous studies of such models have been mainly dedicated to the linear dynamics [3, 4, 6, 7], 1D problems of wave propagation [10, 11], beam vibrations [3, 12], in particular, when physical nonlinearity [10, 12] and spatio-temporal nonlocal effects [10, 13] were taken into account. Expanding this approach to the 2D problems, we are going to consider the dynamic response of a geometrically nonlinear plate containing elastic inclusions to the action of an external periodic force and to modify along the way the exploration methods applied for homogeneous plates [14–17]. In this way, our studies encompass resonant, antiresonant and hysteretic phenomena, bifurcation scenario, multi-mode and chaotic oscillations caused by the interaction of nonlinear effects with the dynamics of oscillating inclusions.

A. Gawlik (✉) · A. Klepka · V. Vladimirov
AGH University of Science and Technology, Krakow, Poland
e-mail: agawlik@agh.edu.pl; klepka@agh.edu.pl

S. Skurativskyi
Subbotin Institute of Geophysics, National Academy of Sciences of Ukraine, Kyiv, Ukraine

2 The Model for the Dynamics of Plate with Oscillating Inclusions and Boundary Value Problem Statement

Based on the approach proposed in the works [3, 4, 12], we describe an elastic medium with oscillatory inclusions by means of a coupled system of PDEs responsible for the description of a bulk medium in the von Karman approximation [14–16] and an ODE describing the dynamics of an oscillating inclusion with natural frequency ω . The system under study takes the following form:

$$\rho h u_{tt} + D \Delta \Delta u - h(F_{yy} u_{xx} + F_{xx} u_{yy} - 2F_{xy} u_{xy}) = -m \rho h w_{tt} \tag{1}$$

$$+ \rho h \Omega^2 \gamma \sin \Omega t,$$

$$\Delta \Delta F = E((u_{xy})^2 - u_{xx} u_{yy}), \tag{2}$$

$$w_{tt} + \omega^2(w - u) + \tau \omega^2(w - u)_t = 0, \tag{3}$$

where u is the plate deflection, F describes the stress field, w is the displacement of a partial oscillator, ρ is the plate density, h is the plate thickness, γ and Ω are the external force’s amplitude and frequency, respectively, $m \rho$ is the mass of an oscillating inclusion τ is the time of relaxation, Δ is the two-dimension Laplace operator, $D = \frac{E h^3}{12(1-\nu^2)}$, ν is the Poisson’s ratio.

Assume that the plate is the simply supported [15, 17] on all edges of the domain $\Lambda = \{0, a\} \times \{0, b\}$. In this case, the following constrains for the mid-plane displacements S, R hold

$$S = \int_0^{a/2} \left[\frac{1}{E} (F_{yy} - \nu F_{xx}) - \frac{1}{2} (u_x)^2 \right] dx = F_{xy} = 0, \tag{4}$$

$$R = \int_0^{b/2} \left[\frac{1}{E} (F_{yy} - \nu F_{xx}) - \frac{1}{2} (u_y)^2 \right] dy = F_{xy} = 0.$$

We are looking for the approximate solution to the boundary value problem (1)–(4) in the following form:

$$u = U(t) \sin \frac{\pi x}{a} \sin \frac{\pi y}{b}, \quad w = W(t) \sin \frac{\pi x}{a} \sin \frac{\pi y}{b}, \quad F = U(t)^2 \Phi(x, y). \tag{5}$$

Substituting (5) into Eq. (2), we get the equation

$$\Delta \Delta \Phi = \frac{E \pi^4}{2a^2 b^2} \left(\cos \frac{2\pi x}{a} + \cos \frac{2\pi y}{b} \right). \tag{6}$$

The solution to this equation takes the form

$$\Phi = \frac{p_x}{2} \left(y - \frac{b}{2} \right)^2 + \frac{p_y}{2} \left(x - \frac{a}{2} \right)^2 + \phi_{01} \cos \frac{2\pi x}{a} + \phi_{10} \cos \frac{2\pi y}{b},$$

where

$$\phi_{01} = \frac{a^2 E}{32b^2}, \quad \phi_{10} = \frac{b^2 E}{32a^2}.$$

From the boundary conditions (4) we can determine the remaining coefficient as follows:

$$p_x = \frac{E\pi^2(b^2 + a^2\nu)}{8a^2b^2(1 - \nu^2)}, \quad p_y = \frac{E\pi^2(a^2 + b^2\nu)}{8a^2b^2(1 - \nu^2)}. \tag{7}$$

Inserting expressions (5) into Eqs. (1), (3) and excluding Φ , we finally get the system of ODEs:

$$\begin{aligned} U'' + \mu_1 U + \mu_4 U^3 + \mu_2 W'' &= \mu_3 \Omega^2 \gamma \sin \Omega t, \\ W'' + \omega^2(W - U) + \omega^2 \tau(W' - U') &= 0, \end{aligned} \tag{8}$$

where $\mu_1 = \frac{D\pi^4(a^2+b^2)^2}{\rho h a^4 b^4}$, $\mu_2 = m$, $\mu_3 = \frac{16}{\pi^2}$, $\mu_4 = \frac{E\pi^4}{16\rho a^4 b^4(1-\nu^2)}(4\nu a^2 b^2 + (3 - \nu^2)(a^4 + b^4))$. Note that dependence of μ_1 and μ_4 on plate size allows one to avoid strong constraints concerning parameter selection. Thus, in the system obtained the parameter μ_2 is regarded as a coupling parameter, μ_4 characterizes the nonlinearity. We also use the scaling $\Omega t \rightarrow t$, allowing to eliminate the dependence of the external disturbance on the frequency Ω :

$$\begin{aligned} U'' + \frac{\mu_1}{\Omega^2} U + \mu_2 W'' + \frac{\mu_4}{\Omega^2} U^3 &= \mu_3 \gamma \sin t, \\ W'' + \frac{\omega^2}{\Omega^2} (W - U) + \omega^2 \frac{\tau}{\Omega} (W' - U') &= 0. \end{aligned} \tag{9}$$

Note that the first equation of the system (9) coincides with the classical Duffing equation as $\mu_2 = 0$. So we can expect that the whole system inherits some features of this equation. Of interest is the question of what additional properties demonstrates the system under consideration.

3 Model's Multiharmonic Solutions and Their Stability

At first we consider solutions which can be approximated by the trigonometric functions. To do this, the harmonic balance method is utilized. Since the system (9) contains cubic term, the approximate solution possesses the third harmonic in its Fourier expansion. In spite of its smallness, it should be incorporated into the approximation, for this helps to reduce the deviation of phase portrait in the (U, U') plane from elliptic shape and avoid the discrepancy between numerical and analytical results. Thus, we are looking for a solution to (9) in the following form:

$$U(t) = U_1 + U_3, \quad W(t) = W_1 + W_3, \tag{10}$$

where $U_j = c_j \sin jt + d_j \cos jt$, $W_j = s_j \sin jt + q_j \cos jt$, $j = 1, 3$ are the first and third Fourier harmonics, the parameters c_j , d_j , s_j , and q_j are constants.

Substituting formula (10) into the system (9), multiplying the obtained relations in turn by $\sin t$, $\cos t$, $\sin 3t$ or $\cos 3t$ and then integrating in the interval $(0, 2\pi)$, we obtain the following formulas relating hitherto undefined coefficients:

$$\begin{aligned} & 3c_1^3\mu_4 - 3c_1^2c_3\mu_4 + 3d_1^2c_3\mu_4 - 4(s_1\mu_2 + \gamma\mu_3)\Omega^2 \\ & + c_1(4\mu_1 + 3(d_1^2 - 2d_1d_3 + 2(c_3^2 + d_3^2))\mu_4 - 4\Omega^2) = 0, \\ & 3d_1^3\mu_4 - 3c_1^2d_3\mu_4 + 3d_1^2d_3\mu_4 - 4q_1\mu_2\Omega^2 \\ & + d_1(4\mu_1 + 3(c_1^2 + 2c_1c_3 + 2(c_3^2 + d_3^2))\mu_4 - 4\Omega^2) = 0, \\ & 4c_3\mu_1 - c_1(c_1^2 - 3d_1^2)\mu_4 + 3c_3(2c_1^2 + 2d_1^2 + c_3^2 + d_3^2)\mu_4 = 36(c_3 + s_3\mu_2)\Omega^2, \\ & 4d_3\mu_1 - d_1(3c_1^2 - d_1^2)\mu_4 + 3d_3(2c_1^2 + 2d_1^2 + c_3^2 + d_3^2)\mu_4 = 36(d_3 + q_3\mu_2)\Omega^2. \end{aligned} \tag{11}$$

The second equation of the system (9) yields the explicit relations for the quantities s_1 , q_1 and s_3 , q_3 :

$$\begin{aligned} s_1 &= \frac{\omega^2(d_1\Omega^3\tau + c_1(\omega^2 + \Omega^2(-1 + \omega^2\tau^2)))}{(\Omega^2 - \omega^2)^2 + \Omega^2\omega^4\tau^2}, \quad q_1 = \frac{\omega^2(-c_1\Omega^3\tau + d_1(\omega^2 + \Omega^2(-1 + \omega^2\tau^2)))}{(\Omega^2 - \omega^2)^2 + \Omega^2\omega^4\tau^2}, \\ s_3 &= \frac{\omega^2(27d_3\Omega^3\tau + c_3(\omega^2 + 9\Omega^2(-1 + \omega^2\tau^2)))}{(9\Omega^2 - \omega^2)^2 + 9\Omega^2\omega^4\tau^2}, \\ q_3 &= \frac{\omega^2(-27c_3\Omega^3\tau + d_3(\omega^2 + 9\Omega^2(-1 + \omega^2\tau^2)))}{(9\Omega^2 - \omega^2)^2 + 9\Omega^2\omega^4\tau^2}. \end{aligned} \tag{12}$$

Thus, taking into account Eqs.(12), we can reduce the system (11) to the cubic polynomial equations with respect to the parameters c_1 , d_1 , c_3 , and d_3 only. Fixing all the parameters but Ω and solving the system obtained, we evaluate the amplitudes of the first and the third harmonics. To reveal the general features of amplitude curves, let us specify the parameters as follows: $\mu_1 = 0.4$, $\mu_2 = 0.15$, $\mu_4 = 1.0$, $\omega = 0.65$, $\tau = 0.05$, $\gamma = 0.3$. The plate natural frequencies derived from the linearized problem are 0.526 and 0.781.

Fig. 1a, b exhibits the amplitude curve describing the maximal values of the first harmonic, i.e., $\max\{c_1 \sin t + d_1 \cos t\} = \max U_1 = \sqrt{c_1^2 + d_1^2}$, when the parameter Ω grows. The local minimum, appeared in the vicinity of $\Omega = \omega$, resonant peak, and hysteretic behavior are presented in Fig. 1a. At $\Omega > \omega$ (Fig. 1b), there are two separated branches of amplitude curves.

Fig. 1c, d presents $\max\{c_3 \sin 3t + d_3 \cos 3t\} = \max U_3 = \sqrt{c_3^2 + d_3^2}$ as a function of the parameter Ω . Note that the local minimum (antiresonance) is located at $\omega/3$, and two local maxima appear at 0.176 and 0.262.

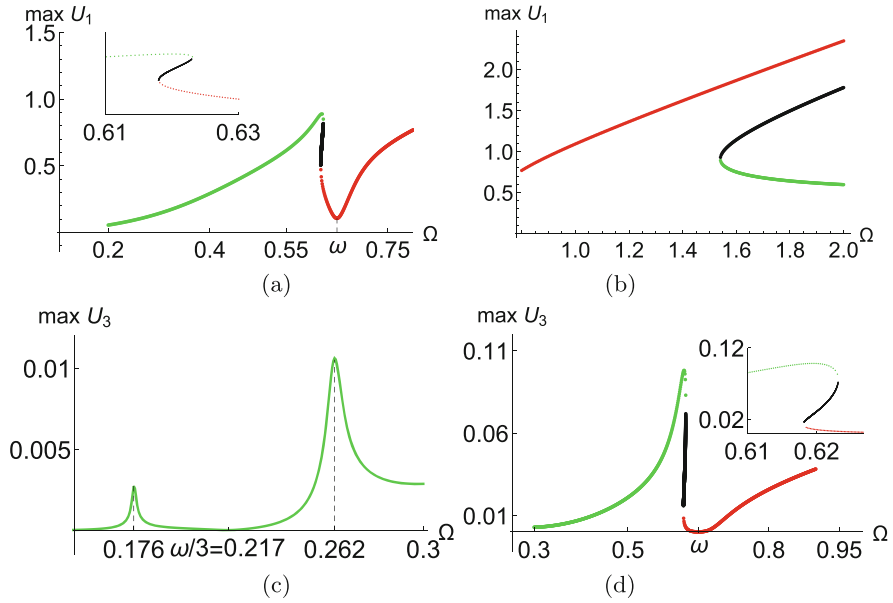


Fig. 1 The amplitude curves of the first harmonic (a, b) and the third harmonic (c, d). The insets exhibit detailed shape of the amplitude curves in the intervals with hysteresis

In studying the scenario of system’s evolution, it is important to investigate the stability of solutions (10). To do this, consider the evolution of small deviations from the functions $U_0(t)$, $W_0(t)$ satisfying the system (9)

$$U(t) = U_0(t) + \tilde{u}(t), \quad W(t) = W_0(t) + \tilde{w}(t). \tag{13}$$

Inserting (13) into (9) and dropping out the higher-order terms, we get the following linear system:

$$\tilde{u}'' + \frac{\mu_1}{\Omega^2} \tilde{u} + \mu_2 \tilde{w}'' + \frac{\mu_4}{\Omega^2} 3U_0^2 \tilde{u} = 0, \quad \tilde{w}'' + \frac{\omega^2}{\Omega^2} (\tilde{w} - \tilde{u}) + \omega^2 \frac{\tau}{\Omega^2} (\tilde{w}' - \tilde{u}') = 0. \tag{14}$$

Now we use the ansatz

$$\tilde{u} = e^{\lambda t} \varphi, \quad \tilde{w} = e^{\lambda t} \psi,$$

which being inserted into (14) produces the following system:

$$\begin{aligned} \lambda^2 \varphi + 2\lambda \varphi' + \varphi'' + \frac{\mu_1}{\Omega^2} \varphi + \mu_2 (\lambda^2 \psi + 2\lambda \psi' + \psi'') + \frac{\mu_4}{\Omega^2} 3U_0^2 \varphi &= 0, \\ \lambda^2 \psi + 2\lambda \psi' + \psi'' + \frac{\omega^2}{\Omega^2} (\psi - \varphi) + \omega^2 \frac{\tau}{\Omega^2} (\lambda \psi + \psi' - \lambda \varphi - \varphi') &= 0. \end{aligned} \tag{15}$$

Suppose that the solution of the system (15) can be found in the form

$$\varphi = \sin nt + \alpha_1 \cos nt, \quad \psi = \alpha_2 \sin nt + \alpha_3 \cos nt, \quad (16)$$

where $\alpha_i = \text{const}$, $i = 1, 2, 3$; $n \in N$.

First we restrict ourself to the case $n = 1$. Inserting (16) into (15) and equating the coefficients of $\cos t$ and $\sin t$ to zero, the algebraic system with respect to α_i and λ can be cast:

$$\begin{aligned} & \alpha_1 \lambda^2 + 2\lambda - \alpha_1 + \mu_2 \left(\alpha_3 \lambda^2 + 2\alpha_2 \lambda - \alpha_3 \right) + \frac{\alpha_1 \mu_1}{\Omega^2} \\ & + \frac{3\mu_4}{4\Omega^2} \left(c_1^2 \alpha_1 + 2d_1 c_3 + 2c_1 (d_1 + \alpha_1 c_3 - d_3) \right. \\ & \left. + \alpha_1 (3d_1^2 + 2d_1 d_3 + 2(c_3^2 + d_3^2)) \right) = 0, \\ & \lambda^2 - 2\alpha_1 \lambda - 1 + \mu_2 \left(\alpha_2 \lambda^2 - 2\alpha_3 \lambda - \alpha_2 \right) + \frac{\mu_1}{\Omega^2} \\ & + \frac{3\mu_4}{4\Omega^2} \left(3c_1^2 + d_1^2 + 2d_1 (\alpha_1 c_3 - d_3) + 2(c_3^2 + d_3^2) \right. \\ & \left. - 2c_1 (c_3 + (d_3 - d_1) \alpha_1) \right) = 0, \\ & \alpha_2 \lambda^2 - 2\alpha_3 \lambda - \alpha_2 + \left(\frac{\omega}{\Omega} \right)^2 [\alpha_2 - 1] + \frac{\omega^2}{\Omega} \tau [\alpha_1 - \alpha_3 + \lambda(\alpha_2 - 1)] = 0, \\ & \alpha_3 \lambda^2 + 2\alpha_2 \lambda - \alpha_3 + \left(\frac{\omega}{\Omega} \right)^2 [\alpha_3 - \alpha_1] + \frac{\omega^2}{\Omega} \tau [\alpha_2 - 1 + \lambda(\alpha_3 - \alpha_1)] = 0. \end{aligned} \quad (17)$$

Thus, each point of the amplitude curve depicted in Fig. 1 should be analyzed concerning its stability. Using the λ solutions of system (17), the stability of two-harmonic solution (10) is estimated. The resulting curve partitioning presented in Fig. 2 contains several bifurcation points. To validate the analytical findings, the results of numerical simulations (Fig. 2, solid red line) of parent system (9) at increasing Ω are presented as well. It is evident that two-harmonic approximation (10) fits the numerical periodic solutions, producing the smooth amplitude curve, very good. The upper and lower branches forming the hysteretic transition correspond to stable modes, whereas the middle one relates to the unstable movements. This is quite common case for hysteretic zones, whereas at larger forcing frequency Ω the two zones with unstable solutions are appeared.

When we fix $\Omega = 0.673$ belonging to the unstable zone, the Fourier spectrum of numerical solution shows the presence of forcing frequency Ω , additional frequency $\Omega_1 = 0.822\Omega$, and combination frequency $2\Omega - \Omega_1 = 1.178\Omega$ (Fig. 2, lower inset). From this it follows that two-dimensional torus exists in the phase space. It is interesting that the stable numerical solution has the same amplitude as the unstable mode of (10).

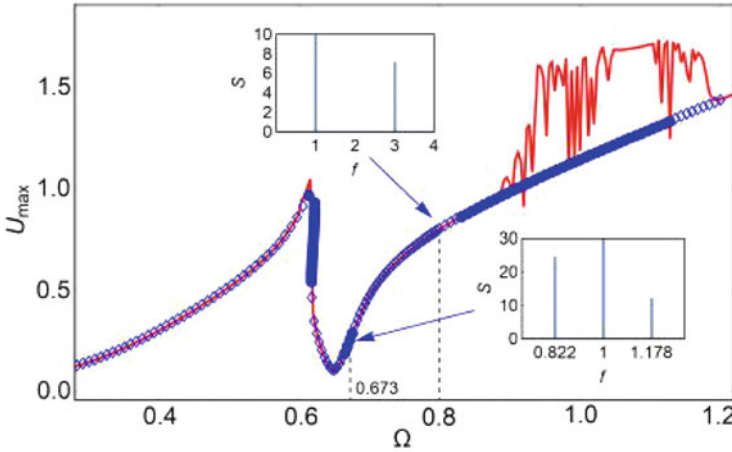


Fig. 2 Stability of two-harmonic solution (10). The marks “diamond” stand for stable modes, the marks “bullet” correspond to unstable modes. Blue marks and solid red curve correspond to the analytical and numerically derived amplitude curves, respectively. Insets represent the Fourier spectra of the numerical solutions derived at $\Omega = 0.673$ (lower inset) and $\Omega = 0.8$ (upper inset). The value $f = 1$ stands for the forcing frequency Ω

If we fix $\Omega = 0.8$ from the stable zone, the solution’s Fourier spectrum contains two maxima located at forcing frequency Ω and its tripled 3Ω that corresponds to two-harmonic solution (10).

Thus, in the stability zones, the bi-harmonic solution (10) describes the oscillation modes quite well. But when it loses the stability, the quasiperiodic oscillations with different number of partial and combination frequencies are realized. This produces the irregular deviations from the amplitude curve derived on the basis of solution (10).

4 The Structure of Solutions Approximated by the Four Harmonics

The careful observation of resonant peak with hysteretic zone shows the unstable solution existence at the top of curve. It is reasonable to assume that in case when the two-harmonic solution becomes unstable, the stable regime, enriched by additional harmonics, appears. To describe such a solution, we use the following expression

$$U(t) = z_1 + \sum_{j=1}^4 U_j(t), \quad W(t) = z_1 + \sum_{j=1}^4 W_j(t), \quad z_1 = const. \quad (18)$$

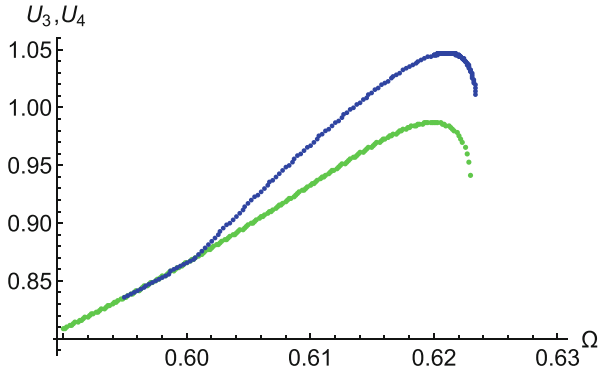


Fig. 3 Comparison of two- (lower curve) and four-harmonic (upper curve) solutions at $\mu_2 = 0.15$

By analogy, inserting this expression into the system (9), the algebraic system with respect to the coefficients is obtained. The resulting amplitude curve at the same parameters as in Fig. 2 is drawn in Fig. 3. So, there is a bifurcational point where solution (18) is cleaved from the two-harmonic regime, which in turn becomes unstable as it is shown in Fig. 2.

5 Additional Numerical Studies of System (9)

As is shown in Fig. 2, the periodic solutions of the system (9) can be described in detail by different finite harmonic approximations. When the forcing frequency, nonlinearity (μ_4) and connectivity (μ_2) are large, it is instructive to supplement the studies by numerical simulations.

The numerical simulations show that when $\Omega = O(1)$, in particular, if $\Omega = 1.6$, the coexistence of periodic and more complex attractors is encountered. Starting from the complex regime and varying Ω , the amplitude curve for this regime is plotted in Fig. 4a.

When we double the parameter μ_2 , i.e., take $\mu_2 = 0.3$, and derive the amplitude curves in the same manner, Fig. 4b is obtained. It is observed the increasing of irregularity which is most clear exposed in the vicinity of the resonant peak. The essential separation of zones with different quasiperiodic regimes is seen as well. Auxiliary information on the structure of solutions and their bifurcations can be obtained from the analysis of Poincare sections. Since the model (9) is the harmonically forced system, the Poincare section is defined as a set of points $U(t_j) : t_j = 2\pi j, j = 1, \dots, N$. Varying Ω and omitting transient processes, the

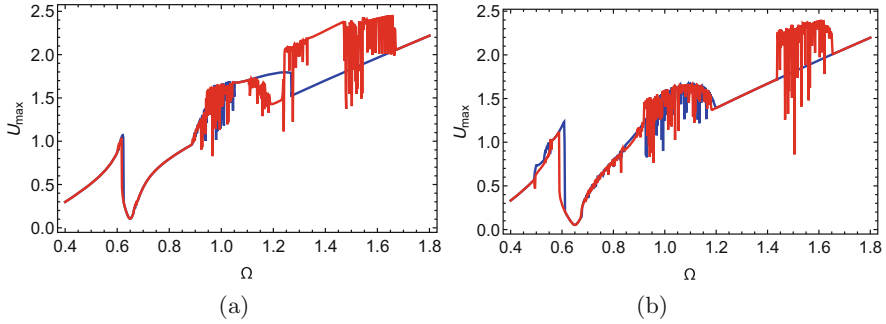


Fig. 4 The amplitude curves at $\mu_2 = 0.15$ (a) and $\mu_2 = 0.30$, when the parameter Ω increases from the leftmost point (blue points) and varies from the value $\Omega = 1.6$ (red line)

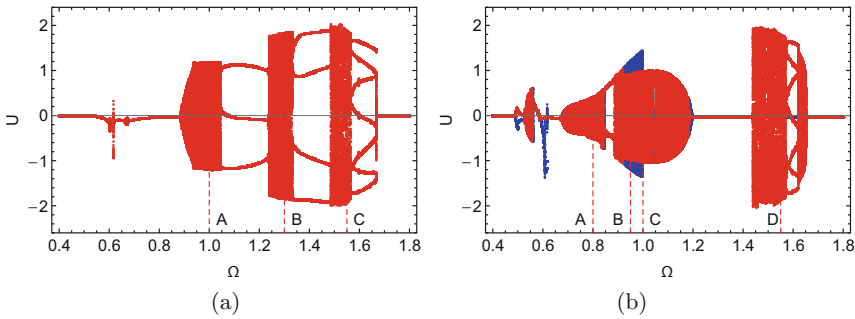


Fig. 5 The bifurcational diagrams at $\mu_2 = 0.15$ (a) and $\mu_2 = 0.3$, blue points correspond to the increasing Ω from the leftmost point (b). The letters stand for the Poincare sections presented below

bifurcation diagrams depicted in Fig. 5 are derived at $\mu_2 = 0.15; 0.3$. The way of diagram construction is the same to that employed when obtaining Fig. 4.

To find out the fine structure and types of existing regimes, the Poincare sections are analyzed in more detail. Specifying the values of forcing frequency $\Omega = 1; 1.3; 1.55$ and $\mu_2 = 0.15$, at which the complex regimes exist, the Poincare sections (Fig.6a) are derived. Closed forms of the sections tell us about the implementation of quasiperiodic regimes. Furthermore, the doubling torus bifurcation is observed (curve C at $\Omega = 1.55$).

Figure 6b exhibits the Poincare sections of the complex regimes at $\mu_2 = 0.3$. It follows from the diagrams presented that there are three types of quasiperiodic attractors in the given interval of values of the parameter Ω .

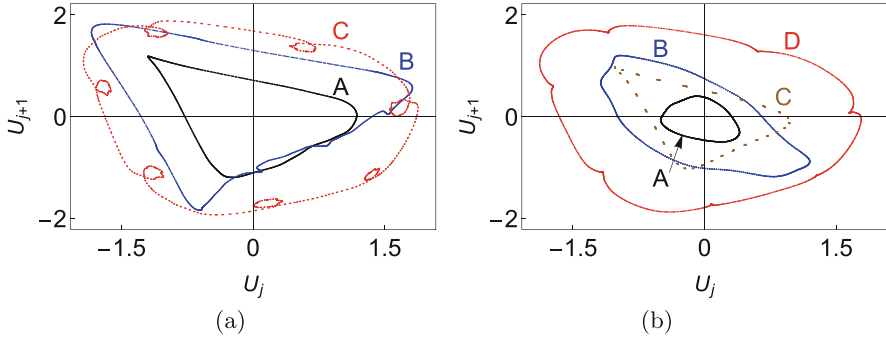


Fig. 6 The Poincaré sections at (a): $\Omega = 1$ (A); 1.3 (B); 1.55 (C); (b) $\Omega = 0.8$ (A); 0.95 (B, hidden attractor); 1.0 (C); 1.55 (D). The location of Poincaré sections is marked in Fig. 5

6 Conclusions

From the results presented above the following conclusions can be made:

- the approximate solution comprised of the first and third Fourier harmonics illustrates well enough some features of the dynamics of von Karman plate with inclusions for wide values of forcing frequency and measure of nonlinearity. Moreover, its stability allows one to estimate correctly the bifurcational values of forcing frequency;
- when two-harmonic solution is unstable, different scenarios of system's evolution are observed. It is shown, in particular, that the stable four-harmonic regime forming the resonant maximum is developed. Unstability of two-harmonic solution also gives rise to the quasiperiodic regime existence;
- incorporation of inclusions' dynamics causes the appearance of additional natural frequencies in the medium, the development of additional regimes and scenario, increasing the hysteretic window.

It is worth noting also that the results outlined above can be useful for improving the ultrasonic diagnostics methods [2, 8], new material (acoustic metamaterial) production [16], as well as in the development of vibro-protection [9, 18] and other civil engineering structures [7].

Acknowledgments The work presented in this paper was funded in part within the scope of the research project 2018/29/B/ST8/02207 "Identification and characterization of local resonances in inhomogeneous media with discontinuities" financed by the Polish National Science Centre.

References

1. A. Carcaterra, A. Akay, Transient energy exchange between a primary structure and a set of oscillators: Return time and apparent damping. *J. Acoust. Soc. Am.* **115**(2), 683–696 (2004)
2. I. Solodov, Resonant acoustic nonlinearity of defects for highly-efficient nonlinear NDE. *J. Nondestruct. Eval.* **33**, 252–262 (2014)
3. V.A. Palmov, *Vibrations of Elasto-Plastic Bodies* (Springer, Berlin, 1998)
4. G.S. Mishuris, A.B. Movchan, L.I. Slepyan, Waves in elastic bodies with discrete and continuous dynamic microstructure. *Phil. Trans. R. Soc.* **A378**, 20190313 (2019)
5. R.J. Nagem, I. Veljkovic, G. Sandri, Vibration damping by a continuous distribution of undamped oscillators. *J. Sound Vib.* **207**(3), 429–434 (1997)
6. R.L. Weaver, Multiple-scattering theory for mean responses in a plate with sprung masses. *J. Acoust. Soc. Am.* **101**(6), 3466–3474 (1997)
7. D. Zhou, T. Ji, Free vibration of rectangular plates with continuously distributed spring-mass. *Int. J. Solids Struct.* **43**, 6502–6520 (2006)
8. A. Klepka, K. Dziejciech, J. Spzytek, J. Mrowka, J. Gorski, Experimental investigation of hysteretic stiffness related effects in contact-type nonlinearity. *Nonlinear Dyn.* **95**, 1513–1528 (2019)
9. K. Xu, T. Igusa, Dynamic characteristics of multiple substructures with closely spaced frequencies. *Earthquake Eng. Struct. Dyn.* **21**, 1059–1070 (1992)
10. V.A. Danylenko, S.I. Skurativskiy, Peculiarities of wave dynamics in media with oscillating inclusions. *Int. J. Non-Linear Mech.* **84**, 31–38 (2016)
11. V.A. Danylenko, S.I. Skurativskiy, I.A. Skurativska, Asymptotic wave solutions for the model of a medium with Van Der Pol oscillators. *Ukrainian J. Phys.* **59**(9), 932–938 (2014)
12. V.A. Danylenko, S.I. Skurativskiy, Resonance modes of propagation of nonlinear wave fields in media with oscillating inclusions. *Dopov. Nat. Akad. Nauk Ukr.* **11**, 108–112 (2008)
13. V.A. Danylenko, S.I. Skurativskiy, Travelling wave solutions of nonlocal models for media with oscillating inclusions. *Nonlinear Dyn. Syst. Theory* **12**(4), 365–374 (2012)
14. J.G. Easley, Nonlinear vibration of beams and rectangular plates. *J. Appl. Math. Phys. (ZAMP)* **15**, 167–175 (1964)
15. E. Esmailzadeh, M.A. Jalali, Nonlinear oscillations of viscoelastic rectangular plates. *Nonlinear Dyn.* **18**, 311–319 (1999)
16. E. Mahmoudpour, Nonlinear resonant behavior of thick multilayered nanoplates via nonlocal strain gradient elasticity theory. *Acta Mech.* **231**, 2651–2667 (2020)
17. S.I. Chang, A.K. Bajaj, C.M. Krousgrill, Non-linear vibrations and chaos in harmonically excited rectangular plates with one-to-one internal resonance. *Nonlinear Dyn.* **4**, 433–460 (1993)
18. M. Strasberg, D. Feit, Vibration damping of large structures induced by attached small resonant 197 structures. *J. Acoust. Soc. Am.* **99**(1), 336–344 (1996)

Nonlinear Free Vibrations of Functionally Graded Microplates Based on the Modified Couple Stress Theory



Sinem Mızrak and Ender Ciğeroğlu

1 Introduction

Functionally graded materials (FGMs) are a special class of composites with mechanical properties varying smoothly in one direction due to continuous change in the volume fractions of the constituent phases from one surface to another. This provides superior properties and improved performance to FGMs in preferred directions when they are compared to homogenous materials. Therefore, FGMs are used in several areas, such as spaceplane bodies, rocket engine components, automotive engine components, living tissues like bones and teeth, armor plates, bulletproof vests, thermal barriers, protective coatings, turbine blades, and sensors. In recent years, FGMs are also used in micro/nanoscale applications such as micro/nano-electro-mechanical systems (M/NEMS), thin films, and probes for atomic force microscopes. Due to the widening area of use for micro/nano FGMs, it is important to obtain accurate results for the static and dynamic behavior of these materials. It is shown that the deformation behavior of such nanomaterials is size-dependent, and the use of the classical continuum theory, i.e., size-independent theory, for nanomaterials does not always provide accurate results [1]. Therefore, nonclassical higher-order continuum theories such as nonlocal elasticity theory [2], strain gradient theory [3], classical couple stress theory [4], and its modified version [5] are developed and used for nanostructures. In classical couple stress theory, the stress tensor is expressed as a summation of Cauchy stress tensor and couple stress tensor. Besides two classical material constants, two additional material constants are required to employ this theory. In the modified version, the couple stress tensor is constrained as symmetric due to the additional equilibrium relation explained

S. Mızrak · E. Ciğeroğlu (✉)
Middle East Technical University, Ankara, Turkey
e-mail: sinem.demirkaya_01@metu.edu.tr; ender@metu.edu.tr

by Yang et al. [5]. The modified couple stress theory (MCST) is advantageous when it is compared to other higher-order continuum theories since single material property, which is the length scale parameter, is enough to define material properties. The length-scale parameter is the ratio of the modulus of curvature to the shear modulus and can be obtained by experiments, i.e., torsion tests of slim cylinders, as indicated by Lam et al. [3]. The modified couple stress theory-based formulations are utilized by several researchers to investigate the static and dynamic behavior of size-dependent microbeams and microplates [6–10].

In the literature, there are also numerous models which have been developed by using MCST to represent the behavior of FGM microplates with different shapes. Asghari et al. [11] represented a size-dependent model for arbitrarily shaped FGM microplates by using the Kirchhoff plate model. Thai et al. [12] employed both Kirchhoff and Mindlin plate models to solve static bending, buckling, and free vibration problems for rectangular FGM microplates with geometric nonlinearity. The nonlinear bending and free vibration responses of an FG rectangular microplate lying on an elastic foundation were investigated by Lou et al. [13]. A unified size-dependent higher-order plate theory was developed for a rectangular FGM plate by Lou et al. [14], and this unified model can be degenerated to various shear deformable plate theories and refined plate theories. Wang et al. [15] examined the large amplitude free vibration of Kirchhoff circular plates by using the Kantorovich method for the elimination of time variable and shooting method for the solution of boundary value problem. Ke et al. [16] presented an annular microplate model for nonlinear free vibration analysis based on Mindlin plate theory and employed Differential Quadrature Method (DQM) to discretize the governing equations. The authors assumed that the strain energies for positive and negative vibration amplitudes are equal to each other and utilized a solution method that calculates different natural frequencies for positive and negative cycles. The authors used half-cycle periods, $T_1 = \pi/\omega_1$ and $T_2 = \pi/\omega_2$, in order to calculate the nonlinear frequency from $\omega = 2\pi/(T_1 + T_2)$. Esraghi et al. [17] represented a unified plate model for axisymmetric linear free vibrations and static deflections of FG annular and circular microplates. In their next study, through-the-thickness temperature variation and thermal strains were also taken into consideration [18].

The harmonic balance method (HBM) is a widely used method for solving nonlinear differential equations [19]. In this method, the set of nonlinear differential equations are transformed into a set of nonlinear algebraic equations by expressing the solution in the form of truncated Fourier series, and the solution of these algebraic equations yields Fourier coefficients. In the literature, there are several studies that utilize HBM for nonlinear free vibration of circular and annular plates with classical plate theories [20–22].

It should be noted that very limited literature is available for the nonlinear vibration of annular FGM plates at microscale. In this paper, the nonlinear free vibration problem of FGM annular microplates is studied by utilizing the Mindlin plate theory. The microstructure dependency is taken into account by using MCST in the formulation. Hamilton's principle is applied to obtain governing partial differential equations and boundary conditions. The nonlinear equations are discretized by

using DQM. The novelty of the present paper is that HBM is utilized to transform these discretized nonlinear equations to a set of nonlinear algebraic equations to investigate the vibration behavior of an annular microplate. An iterative eigenvalue solver is also employed to solve generated eigensystem similar to [23]. Numerical results obtained are compared with the results available in the literature in order to verify the procedure. Effects of inhomogeneity constant, vibration amplitude, and length scale parameter on the nonlinear natural frequencies of the FGM annular microplate are investigated.

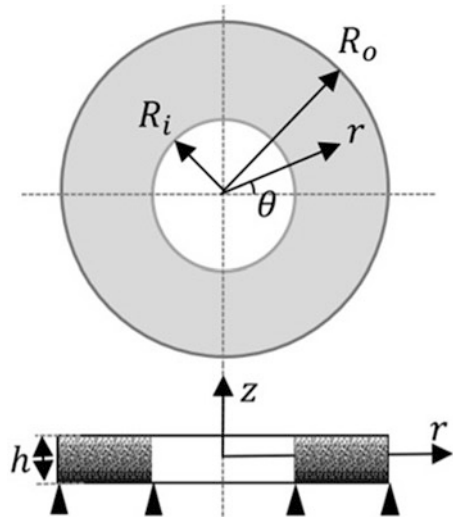
2 Formulation

The geometry of an annular FGM plate with an inner radius R_i , outer radius R_o , and thickness h is given in Fig. 1. The problem is considered axisymmetric since the material properties and the boundary condition is assumed as independent of θ . The composition of the lower surface ($z = -h/2$) is fully metallic, whereas the upper surface ($z = h/2$) is fully ceramic. Volume fractions of ceramic (subscript c) and metallic (subscript m) phases are expressed as

$$V_c(z) = \left(\frac{1}{2} + \frac{z}{h} \right)^\lambda, \tag{1}$$

$$V_m(z) = 1 - V_c(z) \tag{2}$$

Fig. 1 Schematic for a simply supported annular FGM plate



where λ is an inhomogeneity constant. The effective values of elastic modulus E , Poisson’s ratio ν , and mass density ρ can be found according to the Mori-Tanaka method [24].

According to the MCST [5], the strain energy can be written as

$$U = \frac{1}{2} \int_V (\sigma_{ij} \varepsilon_{ij} + m_{ij} \chi_{ij}) dV \tag{3}$$

where $\sigma_{ij} = 2\mu\varepsilon_{ij} + \lambda\delta_{ij}\varepsilon_{kk}$ is Cauchy stress tensor, $m_{ij} = 2\mu l^2 \chi_{ij}$ is deviatoric part of the couple stress tensor, and ε_{ij} and χ_{ij} stand for strain tensor and symmetric curvature tensor, respectively. l is a material length scale parameter, μ and λ are Lamé parameters.

According to Mindlin plate theory, the displacement field in the cylindrical coordinate system is expressed as

$$u_r(r, z, t) = u(r, t) - z \phi(r, t), \tag{4}$$

$$u_\theta(r, z, t) = 0, \tag{5}$$

$$u_z(r, z, t) = w(r, t) \tag{6}$$

where u_r, u_θ, u_z are radial, circumferential, and transverse displacements, respectively, and ϕ is rotation at the mid-plane. According to von Karman’s large deformation theory, strain tensors can be expressed in terms of displacements as follows

$$\varepsilon_{rr} = \frac{\partial u}{\partial r} - z \frac{\partial \phi}{\partial r} + \frac{1}{2} \left(\frac{\partial w}{\partial r} \right)^2, \tag{7}$$

$$\varepsilon_{\theta\theta} = \frac{u}{r} - z \frac{\phi}{r}, \tag{8}$$

$$\varepsilon_{\theta r} = \varepsilon_{\theta z} = 0, \tag{9}$$

$$\varepsilon_{rz} = \frac{1}{2} \left(\frac{\partial w}{\partial r} - \phi \right), \tag{10}$$

$$\chi_{r\theta} = \frac{1}{4} \left\{ \frac{1}{r} \frac{\partial w}{\partial r} + \frac{1}{r} \phi - \frac{\partial^2 w}{\partial r^2} - \frac{\partial \phi}{\partial r} \right\}, \tag{11}$$

$$\chi_{z\theta} = 0 \tag{12}$$

Introducing the following stiffness components and inertia related terms,

$$\{A_{11}, B_{11}, D_{11}\} = \int_{-\frac{h}{2}}^{\frac{h}{2}} \frac{E(z)}{1 - \nu(z)^2} \{1, z, z^2\} dz, \tag{13}$$

$$A_{552} = \int_{-\frac{h}{2}}^{\frac{h}{2}} \frac{EI^2}{2(1 + \nu(z))} dz, \tag{14}$$

$$\{A_{11}^*, B_{11}^*, D_{11}^*\} = \int_{-\frac{h}{2}}^{\frac{h}{2}} \frac{E(z) \nu(z)}{1 - \nu(z)^2} \{1, z, z^2\} dz, \tag{15}$$

$$F_{55} = \int_{-\frac{h}{2}}^{\frac{h}{2}} \frac{E(z)}{2(1 + \nu(z))} dz, \tag{16}$$

$$\{I_1, I_2, I_3\} = \int_{-\frac{h}{2}}^{\frac{h}{2}} \rho(z) \{1, z, z^2\} dz \tag{17}$$

and utilizing Hamilton’s principle [16], Gauss Divergence Theorem and variational principles, the differential equations of motion can be obtained as

$$A_{11} \left(\frac{\partial^2 u}{\partial r^2} + \frac{1}{r} \frac{\partial u}{\partial r} - \frac{u}{r^2} \right) + A_{11} \frac{\partial^2 w}{\partial r^2} \frac{\partial w}{\partial r} + (A_{11} - A_{11}^*) \frac{1}{2r} \left(\frac{\partial w}{\partial r} \right)^2 - B_{11} \left(\frac{\partial^2 \phi}{\partial r^2} + \frac{1}{r} \frac{\partial \phi}{\partial r} - \frac{1}{r^2} \phi \right) = I_1 \frac{\partial^2 u}{\partial t^2} - I_2 \frac{\partial^2 \phi}{\partial t^2} \tag{18}$$

$$\begin{aligned} & \left(-\frac{A_{552}}{4} \right) \left(r \frac{\partial^4 w}{\partial r^4} + 2 \frac{\partial^3 w}{\partial r^3} - \frac{1}{r} \frac{\partial^2 w}{\partial r^2} + \frac{1}{r^2} \frac{\partial w}{\partial r} \right) + (k_s F_{55}) \left(r \frac{\partial^2 w}{\partial r^2} + \frac{\partial w}{\partial r} \right) \\ & - \left(\frac{A_{552}}{4} \right) \left(r \frac{\partial^3 \phi}{\partial r^3} + 2 \frac{\partial^2 \phi}{\partial r^2} - \frac{1}{r} \frac{\partial \phi}{\partial r} + \frac{1}{r^2} \phi \right) - (k_s F_{55}) \left(r \frac{\partial \phi}{\partial r} + \phi \right) \\ & + A_{11} \left[\frac{1}{2} \left(\frac{\partial w}{\partial r} \right)^3 + \frac{3r}{2} \left(\frac{\partial w}{\partial r} \right)^2 \frac{\partial^2 w}{\partial r^2} \right] + A_{11} \left[\frac{\partial u}{\partial r} \frac{\partial w}{\partial r} \right. \\ & \left. + r \frac{\partial^2 u}{\partial r^2} \frac{\partial w}{\partial r} + r \frac{\partial u}{\partial r} \frac{\partial^2 w}{\partial r^2} \right] + A_{11}^* \left(\frac{\partial u}{\partial r} \frac{\partial w}{\partial r} + u \frac{\partial^2 w}{\partial r^2} \right) \\ & - B_{11} \left(\frac{\partial \phi}{\partial r} \frac{\partial w}{\partial r} + r \frac{\partial^2 \phi}{\partial r^2} \frac{\partial w}{\partial r} + r \frac{\partial \phi}{\partial r} \frac{\partial^2 w}{\partial r^2} \right) \\ & - B_{11}^* \left(\frac{\partial \phi}{\partial r} \frac{\partial w}{\partial r} + \phi \frac{\partial^2 w}{\partial r^2} \right) = I_1 r \frac{\partial^2 w}{\partial t^2} \end{aligned} \tag{19}$$

$$\begin{aligned} & - B_{11} \left(\frac{\partial^2 u}{\partial r^2} + \frac{1}{r} \frac{\partial u}{\partial r} - \frac{1}{r^2} u \right) + \left(\frac{A_{552}}{4} \right) \left(\frac{\partial^3 w}{\partial r^3} + \frac{1}{r} \frac{\partial^2 w}{\partial r^2} - \frac{1}{r^2} \frac{\partial w}{\partial r} \right) \\ & + (k_s F_{55}) \left(\frac{\partial w}{\partial r} - \phi \right) \\ & + \left(D_{11} + \frac{A_{552}}{4} \right) \left(\frac{\partial^2 \phi}{\partial r^2} + \frac{1}{r} \frac{\partial \phi}{\partial r} - \frac{1}{r^2} \phi \right) \\ & - (B_{11} - B_{11}^*) \left(\frac{1}{2r} \left(\frac{\partial w}{\partial r} \right)^2 \right) - B_{11} \frac{\partial w}{\partial r} \frac{\partial^2 w}{\partial r^2} \\ & = I_3 \frac{\partial^2 \phi}{\partial t^2} - I_2 \frac{\partial^2 u}{\partial t^2} \end{aligned} \tag{20}$$

where k_s is the shear correction factor which is $\pi^2/12$ for Mindlin Plate Theory. The boundary conditions at $r = R_i, R_o$ obtained by collecting terms which multiply $\delta u, \delta w, \frac{\partial \delta w}{\partial r}$ and $\delta \phi$ as follows

$$A_{11} \frac{\partial u}{\partial r} - B_{11} \frac{\partial \phi}{\partial r} + A_{11}^* \frac{u}{r} - B_{11}^* \frac{1}{r} \phi + \frac{1}{2} A_{11} \left(\frac{\partial w}{\partial r} \right)^2 = 0 \tag{21}$$

$$\begin{aligned} & \frac{-A_{552}}{4} \left(\frac{\partial^3 w}{\partial r^3} + \frac{1}{r} \frac{\partial^2 w}{\partial r^2} - \frac{1}{r^2} \frac{\partial w}{\partial r} \right) + k_s F_{55} \frac{\partial w}{\partial r} + A_{11} \frac{\partial u}{\partial r} \frac{\partial w}{\partial r} + A_{11}^* \frac{u}{r} \frac{\partial w}{\partial r} \\ & - B_{11} \frac{\partial \phi}{\partial r} \frac{\partial w}{\partial r} - B_{11}^* \frac{\phi}{r} \frac{\partial w}{\partial r} + \frac{1}{2} A_{11} \left(\frac{\partial w}{\partial r} \right)^3 \\ & - \frac{A_{552}}{4} \left(\frac{\partial^2 \phi}{\partial r^2} + \frac{1}{r} \frac{\partial \phi}{\partial r} - \frac{1}{r^2} \phi \right) - k_s F_{55} \phi = 0 \end{aligned} \tag{22}$$

$$\left(\frac{A_{552}}{4} \right) \left(r \frac{\partial^2 w}{\partial r^2} - \frac{\partial w}{\partial r} + r \frac{\partial \phi}{\partial r} - \phi \right) = 0 \tag{23}$$

$$\begin{aligned} & \left(\frac{A_{552}}{4} \right) r \frac{\partial^2 w}{\partial r^2} + \left(-\frac{A_{552}}{4} \right) \frac{\partial w}{\partial r} - B_{11} r \frac{\partial u}{\partial r} - B_{11}^* u + \left(D_{11} + \frac{A_{552}}{4} \right) r \frac{\partial \phi}{\partial r} \\ & + \left(D_{11}^* - \frac{A_{552}}{4} \right) \phi - B_{11} \frac{1}{2} r \left(\frac{\partial w}{\partial r} \right)^2 = 0 \end{aligned} \tag{24}$$

The dimensionless quantities can be defined as explained in Ref. [17] to simplify the solution process.

3 Solution Procedure

The differential quadrature method (DQM) is used to solve governing differential equations and boundary conditions. According to DQM, the m th order differential operator of one-dimensional function $f(x)$ can be written as

$$\left(\frac{\partial^m f(x, t)}{\partial x^m} \right)_{x=x_i} = \sum_{j=1}^N C_{ij}^{(m)} f(x_j, t), \quad i = 1, 2, \dots, N \tag{25}$$

where N is the total number of grid points, C_{ij}^m and x_i are called the weighting coefficients of the m th order derivative with respect to x and grid points in the DQM.

Redistributed Chebyshev-Gauss-Lobatto grid points are given by

$$\begin{aligned} r_k &= \frac{R_i}{R_o} + \frac{R_o - R_i}{R_o} \frac{1}{2} \left\{ 1 - \cos \left(\frac{\pi(k-1)}{N-1} \right) \right\}, \quad k = 3, 4, \dots, N - 2, \\ r_1 &= \frac{R_i}{R_o}, \quad r_2 = \frac{R_i}{R_o} + 0.0001, \quad r_{N-1} = 0.9999, \quad r_N = 1 \end{aligned} \tag{26}$$

By utilizing Eqs. (25) and (26) and substituting dimensionless quantities into Eqs. (18)–(24), the equations of motions and the boundary conditions can be expressed in matrix form as

$$(\mathbf{K}_L + \mathbf{K}_{NL}) \mathbf{x} + \mathbf{M} \ddot{\mathbf{x}} = \mathbf{0} \tag{27}$$

where $\mathbf{x} = \{\{\bar{u}_i\}^T, \{\bar{w}_i\}^T, \{\varphi_i\}^T\}$ is the displacement vector, \mathbf{K}_L is the linear stiffness matrix, \mathbf{K}_{NL} is nonlinear stiffness matrix which is a function of \mathbf{x} , and \mathbf{M} is the mass matrix.

The motion of the microplate is assumed as periodic, and the harmonic balance method with single and two harmonics is used to reduce the problem to a set of nonlinear algebraic equations in terms of the contribution coefficients. If only the first two harmonics are used in the solution, the displacement vector can be written as

$$\mathbf{x} = \mathbf{x}_1^* \cos(\omega t) + \mathbf{x}_2^* \cos(2\omega t) \tag{28}$$

where \mathbf{x}^* is the matrix for Fourier coefficients. If only the first harmonic is used, \mathbf{x}_2^* is taken as zero, and the size of the unknown displacement vector decreases from $6N$ to $3N$. Substituting Eq. (28) into Eq. (27) and neglecting higher order lead to

$$\left(\mathbf{K}_L + \mathbf{K}_{NL} - \omega^2 \mathbf{M}\right) \mathbf{x}^* = \mathbf{0}, \tag{29}$$

$$\omega = \sqrt{\frac{I_{10}}{A_{110}}} (R_o - R_i) \Omega \tag{30}$$

where Ω is the natural frequency of free vibrations. All quadratic nonlinear terms in equations disappear when only the first harmonic is used in the solution. The natural frequencies and mode shape vector can be obtained by solving Eq. (29). An iterate procedure is employed to obtain the solution. Firstly, the linear eigensystem is solved by neglecting \mathbf{K}_{NL} , and the scaling of the eigenvector is performed in a way such that the maximum transverse displacement is equal to w_{max} . Substituting the scaled eigenvector of the linear problem into \mathbf{K}_{NL} , the eigensystem is updated and solved again to obtain new eigenvalues and eigenvectors. The iterative procedure continues until the relative error between two frequencies found from subsequent iterations is smaller than 0.1%.

4 Numerical Results

Free vibration of a size-dependent annular plate with ceramic (SiC) and aluminum (Al) constituent phases is examined in this study. The boundary condition of the annular plate is hinged along the inner and outer radius (Fig. 1). The mechanical properties of the materials are taken as $E_c = 427$ GPa, $E_m = 70$ GPa, $\nu_c = 0.17$, $\nu_m = 0.3$, $\rho_c = 3100$ kg/m³, $\rho_m = 2702$ kg/m³ where subscript c and m are for ceramic and aluminum phases, respectively. The length scale parameter is assumed as 15 μ m.

4.1 Free Vibration Frequencies of the Linear Problem

The convergence of the solution is studied for a different number of grid points N , and the results obtained for $\lambda = 1.2, h/l = 5, R_i/R_o = 0.2, R_o/h = 10$ are represented in Table 1. As seen in Table 1, as the number of grid points increases, the accuracy of the result also increases. The results are identical for four significant figures for $N \geq 25$.

In order to verify the developed procedure, the dimensionless linear natural frequencies obtained for Mindlin plate theory are compared with the ones given in Ke et al. [16] and Eshraghi et al. [17] for $N = 25$. As it can be seen from Table 2, the results obtained in the present study agree well with the existing results in the literature.

4.2 Free Vibration Frequencies of the Nonlinear Problem

In this section, the dimensionless frequencies for free vibration of the simply supported annular FGM microplate are demonstrated. The results for the cases where only the first harmonic, and the first two harmonics are used in the solution are given in Table 3 and the results are compared with the frequencies calculated by Ke et al. [16] where the authors used a modified iteration procedure in which

Table 1 Effect of number of DQM points on the first dimensionless linear natural frequency of annular FGM microplate with hinged-hinged support, $\lambda = 1.2, h/l = 6, R_i/R_o = 0.2, R_o/h = 10$

N	10	15	20	25	30	35	40
ω_L	0.72498	0.75731	0.75825	0.75857	0.75861	0.75861	0.75861

Table 2 Comparison for first dimensionless linear natural frequency $\sqrt{I_{10}/A_{110}}R_o\Omega$ of annular FGM microplate with hinged-hinged support, $\lambda = 1.2, R_i/R_o = 0.2, R_o/h = 10$, Mindlin Plate Theory

h/l	1	1.5	2	3	6	10	16	Classical
Ke et al. [16]	1.5711	1.1996	1.0252	0.8718	0.7582	0.7301	0.7201	0.7141
Eshraghi et al. [17]	1.5710	1.1996	1.0252	0.8720	0.7586	0.7306	0.7206	0.7141
Present study	1.5710	1.1996	1.0252	0.8720	0.7586	0.7307	0.7206	0.7140

Table 3 The first dimensionless nonlinear frequency $\omega_{NL} = \sqrt{I_{10}/A_{110}}R_o\Omega$ of annular FGM microplate with the hinged-hinged condition, $\lambda = 1.2, h/l = 1, R_i/R_o = 0.2, R_o/h = 10$

SIn method	ω_L	w_{max}							
		0.1	0.2	0.3	0.4	0.5	0.6	0.7	0.8
Only first harmonic	1.5710	1.5758	1.5898	1.6128	1.6439	1.6824	1.7273	1.7777	1.8331
First two harmonics	1.5710	1.5750	1.5868	1.6062	1.6327	1.6658	1.7048	1.7490	1.7980
Ke et al. [16]	1.5711	1.5744	1.5841	1.6008	1.6242	1.6547	1.6918	1.7353	1.7849

Table 4 The effect of length scale parameter on first dimensionless nonlinear frequency $\omega_{NL} = \sqrt{I_{10}/A_{110}}R_0\Omega$ of annular FGM microplate with the hinged-hinged condition, $\lambda = 1.2$, $R_i/R_o = 0.2$, $R_o/h = 10$

h/l	ω_L	w_{max}								
		0.1	0.2	0.3	0.4	0.5	0.6	0.7	0.8	0.9
1	1.5710	1.5750	1.5868	1.6062	1.6327	1.6658	1.7048	1.7490	1.7980	1.8510
1.5	1.1996	1.2047	1.2198	1.2443	1.2775	1.3184	1.3659	1.4192	1.4773	1.5394
2	1.0252	1.0310	1.0481	1.0758	1.1130	1.1584	1.2108	1.2690	1.3320	1.3989
3	0.8720	0.8785	0.8979	0.9290	0.9704	1.0205	1.0778	1.1409	1.2088	1.2803
6	0.7586	0.7659	0.7875	0.8219	0.8673	0.9218	0.9835	1.0509	1.1227	1.1980
10	0.7307	0.7383	0.7606	0.7960	0.8427	0.8985	0.9614	1.0300	1.1029	1.1793
50	0.7147	0.7225	0.7452	0.7814	0.8289	0.8855	0.9493	1.0185	1.0920	1.1689
Classical	0.7140	0.7218	0.7446	0.7808	0.8283	0.8850	0.9488	1.0180	1.0916	1.1684

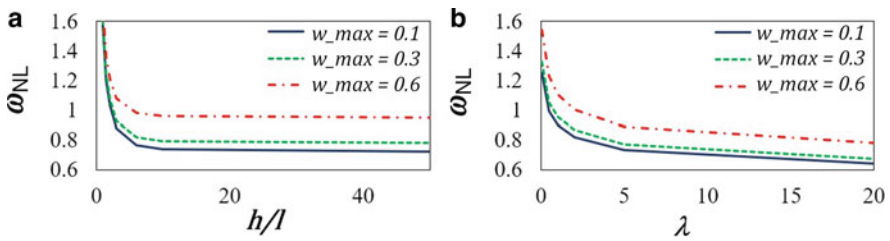


Fig. 2 The effect of (a) length scale parameter (b) inhomogeneity parameter on ω_{NL}

frequencies of negative and positive half-cycles are different and found by assuming the strain energies of the half cycles are equal. As can be seen from the results, the second harmonic term becomes more important when the vibration amplitude increases. From the results obtained, it can be seen that as the maximum vibration amplitude increases, so as the dimensionless nonlinear natural frequency.

In Table 4 and Fig. 2, the nonlinear frequencies with respect to different length scale parameters are presented for Mindlin plate theory, and λ is again taken as 1.2. The first two harmonics are used to obtain nonlinear natural frequencies. The linear natural frequencies are also listed to study the effect of nonlinearity. In addition, in the last row of the table, the dimensionless natural frequency for the classical plate theory is given for comparison. As expected, the results converge to classical plate theory as the plate thickness increases. The size effect becomes less important for h/l values greater than 50. Therefore, it can be concluded that the effect of size dependency is important if the thickness is in the order of length scale parameter or less.

The effect of inhomogeneity is demonstrated in Fig. 2 and Table 5 for eight different values of λ . The first value for λ corresponds to a pure SiC plate, while the last value is for a pure aluminum plate. Both linear and nonlinear frequencies of the microplate decrease while λ increases, since the rigidity of the plate decreases due to metal-rich content.

Table 5 The effect of inhomogeneity parameter on first dimensionless nonlinear frequency $\omega_{NL} = \sqrt{I_{10}/A_{110}}R_o\Omega$ of annular FGM microplate with the hinged-hinged condition, $h/l = 3$, $R_i/R_o = 0.2$, $R_o/h = 10$

λ	ω_L	w_{max}								
		0.1	0.2	0.3	0.4	0.5	0.6	0.7	0.8	0.9
SiC	1.3247	1.3350	1.3654	1.4141	1.4786	1.5564	1.6450	1.7423	1.8464	1.9559
0.05	1.2383	1.2482	1.2772	1.3237	1.3853	1.4595	1.5439	1.6364	1.7354	1.8395
0.5	0.9845	0.9923	1.0152	1.0520	1.1009	1.1598	1.2270	1.3008	1.3799	1.4631
1.0	0.8941	0.9009	0.9210	0.9533	0.9962	1.0481	1.1075	1.1728	1.2430	1.3169
2.0	0.8150	0.8209	0.8384	0.8664	0.9039	0.9493	1.0013	1.0587	1.1204	1.1856
5.0	0.7291	0.7342	0.7493	0.7736	0.8060	0.8453	0.8905	0.9403	0.9939	1.0506
20.0	0.6345	0.6395	0.6535	0.6759	0.7057	0.7418	0.7830	0.8284	0.8770	0.9283
Al	0.5737	0.5784	0.5924	0.6147	0.6443	0.6799	0.7204	0.7647	0.8120	0.8618

5 Conclusions

In this chapter, axisymmetric nonlinear free vibration analysis of simply supported FGM annular microplates is studied. The mechanical properties varying with thickness are calculated by using the Mori-Tanaka method. The developed formulation is based on the modified couple stress theory, von Kármán large deformation theory, and the Mindlin plate theory. Hamilton’s principle is used to derive partial differential equations. Differential quadrature and harmonic balance are the methods to solve these equations. The results for both linear and nonlinear natural frequencies are compared with the results that exist in the literature to prove the developed formulation is valid.

The effect of inhomogeneity constant, vibration amplitude, and length scale parameter on natural frequencies is investigated. The numerical results showed that increase in inhomogeneity constant causes a descent in both linear and nonlinear natural frequencies. As the vibration amplitude gets larger, the nonlinear natural frequency increase. The rise in the ratio between plate thickness and length scale parameter results in a decrease in nonlinear natural frequency.



References

1. B. Arash, S. Wang, Vibration of single- and double-layered graphene sheets. *J. Nanotechnol. Eng. Med.* **2**(011012), 1–7 (2011)
2. S.C. Pradhan, J.K. Phadikar, Nonlocal elasticity theory for vibration of nanoplates. *J. Sound Vib.* **325**, 206–223 (2009)
3. D.C.C. Lam, F. Yang, A.C.M. Chong, J. Wang, P. Tong, Experiments and theory in strain gradient elasticity. *J. Mech. Phys. Solids* **51**, 1477–1508 (2003)
4. R.D. Mindlin, H.F. Tiersten, Effects of couple-stresses in linear elasticity. *Arch. Ration. Mech. Anal.* **11**(1), 415–448 (1962)

5. F. Yang, A.C.M. Chong, D.C.C. Lam, P. Tong, Couple stress based strain gradient theory for elasticity. *Int. J. Solids Struct.* **39**, 2731–2743 (2002)
6. H.M. Ma, X.L. Gao, J.N. Reddy, A microstructure dependent Timoshenko beam model based on a modified couple stress theory. *J. Mech. Phys. Solids* **56**(12), 3379–3391 (2008)
7. G.C. Tsiasas, A new Kirchhoff plate model based on a modified couple stress theory. *Int. J. Solids Struct.* **46**(13), 2757–2764 (2009)
8. L. Yin, Q. Qian, L. Wang, W. Xia, Vibration analysis of micro scale plates based on modified couple stress theory. *Acta Mech. Solida Sin.* **23**(5), 386–393 (2010)
9. E. Jomehzadeh, H.R. Noori, A.R. Saidi, The size-dependent vibration analysis of micro plates based on a modified couple stress theory. *Phys. E Low Dimens. Syst. Nanostruct.* **43**(4), 877–883 (2011)
10. M. Asghari, Geometrically nonlinear micro-plate formulation based on the modified couple stress theory. *Int. J. Eng. Sci.* **51**, 292–309 (2012)
11. M. Asghari, E. Taati, A size-dependent model for functionally graded microplates for mechanical analyses. *J. Vib. Control.* **19**, 1614–1632 (2012)
12. H.T. Thai, D.H. Choi, Size-dependent functionally graded Kirchhoff and Mindlin plate models based on a modified couple stress theory. *Compos. Struct.* **95**, 142–153 (2013)
13. J. Lou, L. He, Closed-form solutions for nonlinear bending and free vibration of functionally graded microplates based on the modified couple stress theory. *Compos. Struct.* **131**, 810–820 (2015)
14. J. Lou, L. He, J. Du, A unified higher order plate theory for functionally graded microplates based on the modified couple stress theory. *Compos. Struct.* **133**, 1036–1047 (2015)
15. Y.G. Wang, W.H. Lin, N. Liu, Large amplitude free vibration of size-dependent circular microplates based on the modified couple stress theory. *Int. J. Mech. Sci.* **71**, 51–57 (2013)
16. L.L. Ke, J. Yang, S. Kitipornchai, M.A. Bradford, Y.S. Wang, Axisymmetric nonlinear free vibration of size-dependent functionally graded annular microplates. *Compos. B Eng.* **53**, 207–217 (2013)
17. I. Eshraghi, S. Dag, N. Soltani, Consideration of spatial variation of the length scale parameter in static and dynamic analyses of functionally graded annular and circular micro-plates. *Compos. B Eng.* **78**, 338–348 (2015)
18. I. Eshraghi, S. Dag, N. Soltani, Bending and free vibrations of functionally graded annular and circular micro-plates under thermal loading. *Compos. Struct.* **137**, 196–207 (2016)
19. A. Grolet, F. Thouverez, Computing multiple periodic solutions of nonlinear vibration problems using the harmonic balance method and Groebner bases. *Mech. Syst. Signal Process.* **52–53**, 529–547 (2015)
20. M. Haterbouch, R. Benamar, Geometrically nonlinear free vibrations of simply supported isotropic thin circular plates. *J. Sound Vib.* **280**, 903–924 (2005)
21. F. Hejripour, A.R. Saidi, Nonlinear free vibration analysis of annular sector plates using differential quadrature method. *Proc. Inst. Mech. Eng. C J. Mech. Eng. Sci.* **226**(2), 485–497 (2011)
22. B. Lhoucine, E.B. Khalid, B. Rhali, Geometrically non-linear axisymmetric free vibrations of thin isotropic annular plates. *Int. Sch. Sci. Res. Innov.* **7**(9), 1887–1893 (2013)
23. E. Cigeroglu, H. Samandari, Nonlinear free vibrations of curved double walled carbon nanotubes using differential quadrature method. *Phys. E Low Dimens. Syst. Nanostruct.* **64**, 95–105 (2014)
24. T. Mori, K. Tanaka, Average stress in matrix and average elastic energy of materials with misfitting inclusions. *Acta Metall.* **21**, 571–574 (1973)

The Development of a Dynamic Coupled Model for Aluminium Composite Sandwich Plates Under Thermoelastic Loading



Olga A. Ganiłova , Matthew P. Cartmell , and Andrew Kiley

1 Introduction

The materials used on the exterior of spacecraft are subjected to many degrading environmental threats. In terms of material degradation in space, low-Earth orbit (LEO) is a particularly harsh environment because of the presence of atomic oxygen (AO) along with all other environmental components [1]. As a spacecraft moves in and out of the sunlight during its orbit around Earth, the degree to which a material experiences thermal cycling temperature extremes depends on its thermo-optical properties (solar absorptance and thermal emittance), its view of the sun, the Earth, and other surfaces of the spacecraft, time in sunlight and eclipse, thermal mass and equipment or components that produce heat [1]. The cyclic temperature variations can range from -120 to $+120$ °C due to high solar absorptance with low infrared emittance, in the absence of spacecraft system thermal control. Sixteen thermal cycles a day, taking the case of the International Space Station (ISS) which orbits Earth approximately every 92 min, may lead to cracking, peeling, spalling or pinholes in the coating, allowing AO to attack the underlying material [1].

In [2], an experiment was performed to investigate the thermal behaviour of a sandwich panel deployable as an integral part of a satellite using a ground thermal-vacuum test. An interesting study carried out by [3] focused on the effect of thermal cycling in a simulated LEO environment on the microhardness of aluminium alloys and subjected these alloys to cycles ranging from -140 to $+110$ °C, to study thermal fatigue and resulting stress state. The study concluded that aluminium alloys

O. A. Ganiłova · M. P. Cartmell (✉)

Aerospace Centre of Excellence, Department of Mechanical & Aerospace Engineering,
University of Strathclyde, Glasgow, Scotland, UK

e-mail: olga.ganiłova@strath.ac.uk; matthew.cartmell@strath.ac.uk

A. Kiley

Airbus Defence & Space Ltd., Stevenage, Hertfordshire, UK

exposed to extended thermal cycling exhibited obvious softening behaviour, causing phase transformations leading to crack initiation. The principal finding was that aeronautical materials that undergo periodic heating and cooling can be damaged to varying degrees, with thermal fatigue having a great impact on the mechanical properties of the materials used.

For a spacecraft panel undergoing cyclic loading under the perspective of modelling, it is logical to propose that the structure must combine the effects of thermal loading as well as a mechanical disturbance. This is because from a physical point of view, the deformation of a body is connected to a change of heat inside it, so to a change of the temperature distribution in the body. So, a deformation of the body leads to temperature changes, and conversely. The internal energy of the body depends on both the temperature and the deformation and so, in the case of a spacecraft panel, it necessarily undergoes processes that are intrinsically coupled, defined collectively as thermoelasticity [4]. Many modelling approaches tend to separate the mechanical and thermal effects, but thermoelastic processes are not generally reversible because although the elastic part may be reversed, the deformations may be recoverable through cooling – the thermal part may not be reversible due to the dissipation of energy during heat transfer [5]. So, there is a strong need to couple the mechanical and thermal aspects of the problem to achieve results of meaningful accuracy. In order to reduce the computational cost, it was decided to adopt third-order von Kármán modelling with thermo-mechanical coupling (TTC), as described in [6], to an industrial application of an aluminium honeycomb sandwich panel. Such panels are routinely used within spacecraft structures, but this is also a common form of structural material encountered right across the aerospace industry. We consider an industrial case of thermodynamic loading with room temperature initial thermal conditions and gradual mechanical loading, both combined together for the first time. Working at the micro-vibration level tackles an important spacecraft phenomenon because even moderate thermo-mechanical loading conditions generate micro-vibration, which contributes to the all-important satellite de-point problem, in which precise orientation is lost due to thermo-mechanical perturbations and which industry is very keen to minimise as far as possible.

2 Problem Under Consideration

The sandwich panel to be considered is composed of two types of aluminium alloy. For the outer faces of thickness 0.4 mm, an Al-2024 alloy is used, whilst an Al-5056 alloy foil is used to form the hexagonal honeycomb core. This core is of depth 14.24×10^{-3} m and comprises a foil of thickness 0.0254×10^{-3} m. It has been decided to develop a partially coupled model, and although TTC in [6, 7] is a partially coupled model, it still demonstrates very high accuracy when compared with the fully coupled model [5, 8].

3 A Model for Mechanical and Thermal Behaviour of the Panel

The mechanical equations of motion are based on the Reddy plate theory development [6] noting that it is assumed that deflection due to shear is negligible with respect to flexure between the layers, and so, the basis for the model has been reduced to the interpretation given by [9],

$$\begin{aligned} N_{11,x} + N_{12,y} &= 0 \\ N_{12,x} + N_{22,y} &= 0 \end{aligned} \tag{1}$$

$$\begin{aligned} M_{11,xx} + 2M_{12,xy} + M_{22,yy} + N_{11}w_{,xx} + 2N_{12}w_{,xy} + N_{22}w_{,yy} \\ + q(x, y, t) - p_x w_{,xx} - p_y w_{,yy} = \rho h w_{,tt} + \delta w_{,t}. \end{aligned}$$

and where N_{ij} are membrane forces, M_{ij} are bending moments, p_x and p_y are forces applied along the x and y coordinate directions respectively, δ is a damping coefficient, $q(x, y, t)$ is a transversely distributed loading, ρ and h are the density and thickness of the panel, and $w(x, y, t)$ is the lateral deformation of the panel.

For a laminated plate with arbitrarily oriented plies, the thermoelastic linear constitutive relations for the k th orthotropic lamina in the principal material coordinates of the lamina are:

$$\begin{Bmatrix} \sigma_{11} \\ \sigma_{22} \\ \sigma_{12} \end{Bmatrix} = \begin{bmatrix} Q_{11} & Q_{12} & 0 \\ Q_{12} & Q_{22} & 0 \\ 0 & 0 & Q_{66} \end{bmatrix}^{(k)} \begin{Bmatrix} \varepsilon_{11} \\ \varepsilon_{22} \\ \varepsilon_{12} \end{Bmatrix} - \begin{Bmatrix} \beta_{11} \\ \beta_{22} \\ 0 \end{Bmatrix}^{(k)} T \tag{2}$$

where $\overline{Q}_{ij}^{(k)}$ are the plane stress-reduced elastic stiffnesses and $\overline{\beta}_{11}^{(k)} = \overline{Q}_{11}^{(k)}\alpha_1 + \overline{Q}_{12}^{(k)}\alpha_2$ and $\overline{\beta}_{22}^{(k)} = \overline{Q}_{12}^{(k)}\alpha_1 + \overline{Q}_{22}^{(k)}\alpha_2$ are the thermoelastic stiffnesses, with α_1 and α_2 being the coefficients of thermal expansion in the x and y directions, and ε_{ij} ($i, j = 1, 2$) are local plane strains. The relationships between strains and displacements are derived in detail in [6].

Following [6], we also assume that the temperature varies according to a cubic law, consistent with assumptions based on past observations:

$$T = T_0 + zT_1 + z^2T_2 + z^3T_3 \tag{3}$$

where $T(x, y, z, t)$ is the three-dimensional temperature variable, while $T_0(x, y, t)$, $T_1(x, y, t)$, $T_2(x, y, t)$ and $T_3(x, y, t)$ are the hitherto unknown components of the temperature of the two-dimensional model and cover the full profile up to a cubic distribution.

The thermal balance equations are introduced for the case of non-stationary conduction and thermoelastic coupling, as in [6, 7],

$$\begin{aligned} q_{1,x}^{(0)} + q_{2,y}^{(0)} - b_{,t}^{(0)} - a_{,t}^{(0)} + Q^{(0)} &= 0 \\ q_{1,x}^{(1)} + q_{2,y}^{(1)} - b_{,t}^{(1)} - a_{,t}^{(1)} + Q^{(1)} &= 0 \end{aligned} \quad (4)$$

where the $q_i(x, y, z, t)$ represents the three-dimensional heat flow along the x, y, z directions, $b(x, y, z, t)$ is the internal energy due to non-stationary conduction, and $a(x, y, z, t)$ is the interaction energy due to the thermoelastic coupling, all defined in detail in [6, 7].

A procedure for computing the solutions to the principal Eqs. (1) and (2) and invoking all the parameters that follow, defined with respect to the specified boundary and initial conditions, has been coded in Mathematica™.

Since we are interested in the temperature and displacement distribution in the z -direction for the structure when subjected to combined mechanical and thermal loading, the system can be reduced to the following equations to find the membrane temperature $T_0(t)$ and bending temperature $T_1(t)$ as defined in [7, 10], noting that T_∞ is the constant temperature difference between the absolute surrounding temperature and the reference temperature:

$$\begin{aligned} C_1 \ddot{W}(t) + C_2 \dot{W}(t) + [C_3 + C_4 P_x(t) + C_5 P_y(t) + C_6 T_0(t) + C_7 T_\infty(t)] W(t) \\ + C_8 W^3(t) + C_9 T_1(t) + Q(t) &= 0 \\ C_{10} \dot{T}_0(t) + C_{11} T_0(t) + C_{12} T_\infty(t) + C_{13} \dot{W}(t) W(t) &= 0 \\ C_{16} \dot{T}_1(t) + C_{17} T_1(t) + C_{18} T_\infty(t) + C_{19} \dot{W}(t) &= 0 \end{aligned} \quad (5)$$

In Ref. [6], this form of a system of equations was solved analytically obtaining a general solution using features within the Mathematica™ code. However, this was done by eliminating the nonlinear terms and for static values of the mechanical and thermal loading, thus,

$$\begin{aligned} C_1 \ddot{W}(t) + C_3 W(t) + C_9 T_1(t) &= 0 \\ C_{10} \dot{T}_0(t) + C_{11} T_0(t) &= 0 \\ C_{16} \dot{T}_1(t) + C_{17} T_1(t) + C_{19} \dot{W}(t) &= 0 \end{aligned} \quad (6)$$

Here, our overall aim has been to look for a solution for the system in its generalised form, as stated in full in Eq. (5).

Before starting to look for an analytical solution, it was decided to investigate whether the presence of the nonlinear terms eliminated in [6] would have a pronounced effect on the behaviour of the panel under consideration. Therefore, an

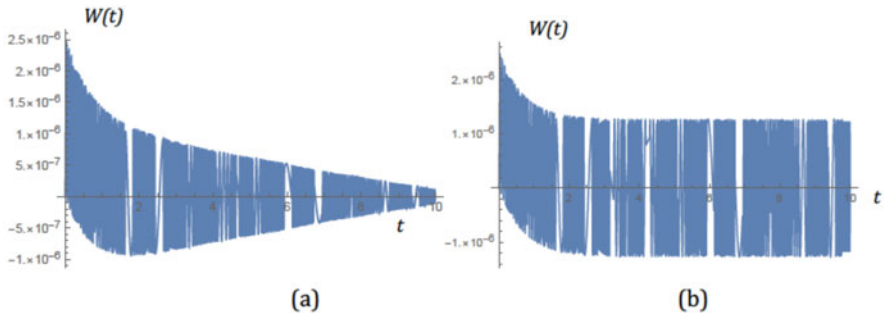


Fig. 1 Deflection $W(t)$ in metres for the panel under $Q = 1 \text{ N}$, $T = 70 \text{ }^\circ\text{C}$ based on the following solutions: (a) numerical solution of Eq. (5), (b) closed-form solution for Eq. (6)

analytical closed-form solution (using the DSolve function in Mathematica™) was found for the simplified system (Eq. 6), as well as a comparable numerical solution (using NDSolve in Mathematica™) for the full system with nonlinear terms in Eq. (5). As an initial test example, we assumed that the panel should be subjected to a small constant mechanical load, arbitrarily set to 1 N, and a thermal load in the form of an environmental soak temperature of 70 °C, and no mechanical damping.

The purely numerical solution to Eq. (5) for $W(t)$ and the closed-form analytical solution for $W(t)$ obtained for the reduced system of Eq. (6) are both plotted in the time domain in Fig. 1.

The two time domain plots of Fig. 1 suggest that for the data considered retaining the nonlinear and coupling terms provides a solution offering more detailed information about the behaviour of the panel, including an important internal energy transfer phenomenon arising from the interaction between the mechanical and thermal aspects of the problem, demonstrated in Fig. 1a as a transient decay in the displacement response. However, the numerical solution found for the full nonlinear system, obviously, does not offer any generic insight into the phenomenology of the problem and is restricted in use to specific data cases such as the one just discussed.

Given that this particular numerical solution, and others too, confirm the transient nature of the displacement response with time, as one would fully expect, the next logical step in the investigation would be to obtain a proper closed-form solution for the full nonlinear system. An immediate benefit of this would be the calculation of accurate and generalised responses and greatly reduced calculation times for different geometries, loading conditions and different material properties for the panel. Nevertheless, despite the limitations of Eq. (6), it should be mentioned that the predicted profile of the temperature distribution along the thickness was found to be phenomenologically accurate for this solution and can be used without any loss of accuracy.

4 Numerical Experiment

For the numerical study of the system (Eq. 5) with full nonlinear coupling terms, different forms of loading are considered: a constant thermal load only, a dynamic thermal load only, a constant mechanical load only, a combined thermo-mechanical load consisting of a dynamic thermal component and a constant mechanical component. In this paper, results are presented for constant and dynamic thermal loads and a combined thermo-mechanical load. The plate-like sandwich panel under consideration is of the dimensions $(100 \times 100) \times 10^{-3}$ m with variable thickness honeycomb and was considered to be simply supported. The thermal loading was applied by means of imposing a difference between the reference temperature and the environmental temperature, to represent free heat exchange conditions. The mechanical loading was taken as a normal constant force applied centrally to the top-face sheet.

4.1 The Case of Thermal Loading

When elevated temperature conditions apply at the outer faces of the sandwich panel to represent the free heat exchange condition, these faces will heat up first of all, with the heat then distributing from the outer faces inwards towards the centre of the core. To understand the process of the displacement emerging due to this changing thermal equilibrium, as well as the characteristics of the thermal gradient along with the thickness, a constant environmental surround temperature of 100 °C was initially applied with the ambient reference (start) temperature set to 22 °C, and a solution for the system of Eq. (5) was obtained using the NDSolve function in Mathematica™.

The principal features of the displacement response are the transient over time and the largely symmetrical peak to peak amplitude over the time of the transient's decay (Fig. 2). This accords with practical expectations for a plate under this form of loading.

In Fig. 3, discrete snapshots between 0.001 s through to 5 s are given for the time history of the thermal gradient across the thickness of the panel, to understand the thermal changes that the panel undergoes, and the conditions under which it stabilises.

By fixing the time steps and observing the progression of the temperature distribution through the plate, we see the main stages of the temperature stabilising process described in [6]. By applying heat to the plate through an elevated environmental soak temperature, the temperature distributes through the thickness as shown in Fig. 3a with the intermediate temperature of the honeycomb core being very close to the top skin temperature (Fig. 3b), and after 1 s, this stabilises and settles within the range of 1.1 °C with a small difference between that of the skin temperature and the honeycomb core. The process of equilibrating temperature is reflected in the behaviour of $T_0(t)$ in Fig. 2b where we clearly see that after 5 s,

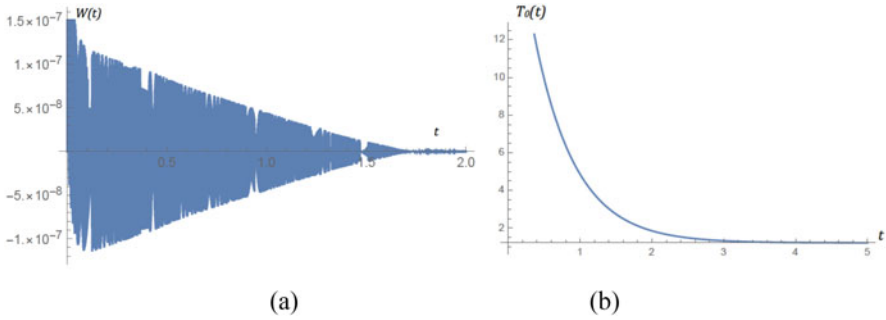


Fig. 2 (a) Displacement response (in metres) in the time domain and (b) time history of the distribution of the thermal component $T_0(t)$ (in $^{\circ}\text{C}$) when subjected solely to a thermal load defined by an environmental temperature of 100°C and with a core thickness of 0.01424 m and total plate thickness of 0.015 m

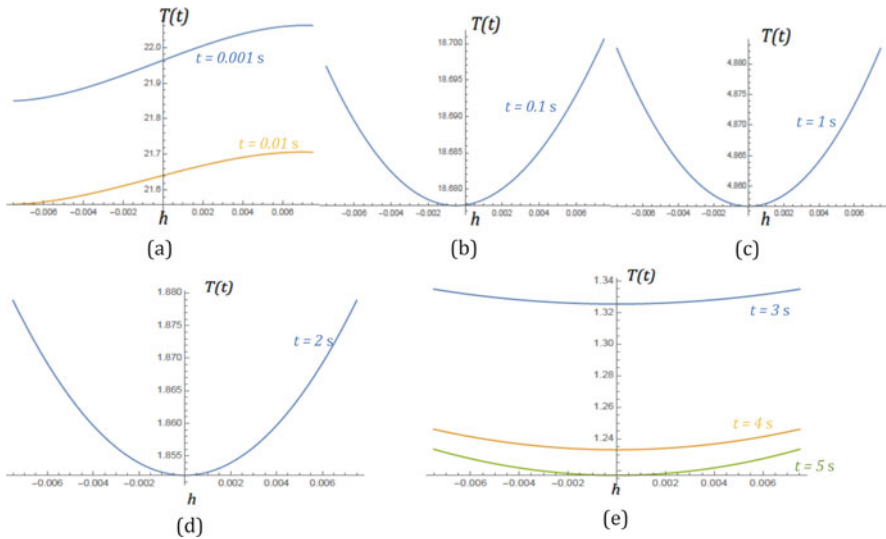


Fig. 3 Plots of the temperature (in $^{\circ}\text{C}$) distribution through the thickness h (in metres) of the panel under a thermal load due to an environmental soak temperature of 100°C , for (a) $t = 0.001\text{ s}$, (b) $t = 0.1\text{ s}$, (c) $t = 1\text{ s}$, (d) $t = 2\text{ s}$, (e) $t = 3\text{ s}$

the equilibrium temperature is reached and the profile thereafter remains constant in time. The process of obtaining the solution for $T_0(t)$ can in itself be a useful tool for finding out if the temperature stabilises at a certain equilibrium, and what the temperature of that equilibrium might be, as well as to determine how long it takes for the panel to reach an equilibrium state. To investigate the behaviour of the panel when the environmental temperature varies under the prescribed dynamic condition, Eq. (5) is solved for $T(t) = 20 + 10t$ with the reference temperature set to 22°C , as in the previous case.

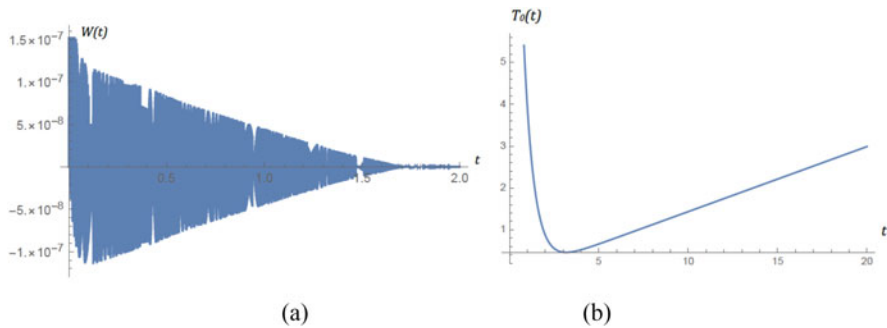


Fig. 4 (a) Displacement response (in metres) in the time domain (in seconds); (b) Time history of the thermal component $T_0(t)$ (in °C) for the panel under a thermal load of $(20 + 10t)$ °C with a core thickness of 0.01424 m and for a total plate thickness of 0.015 m. Time is in seconds

The same qualitative conditions prevail for the response to this form of load, and the transient dies out after about 1.75 s. Analysing the history of the thermal gradient over time shows that the sample underwent the same process of stabilisation and reached equilibrium after 3 s; however, due to the linearly increasing thermal load $(20 + 10t)$ °C, the temperature in the sample rapidly increased after equilibrium. This is clear from the distribution of the middle plane thermal component $T_0(t)$ in Fig. 4b.

4.2 The Case of Thermo-mechanical Loading

For the case of thermo-mechanical loading, the physics of the separate thermal and mechanical loading scenarios are combined using the model discussed previously.

An initial check on the combined effect of a constant mechanical load of 1 N and a dynamic thermal load initiated by the environmental temperature which obeys the linear law given by $(20 + 10t)$ °C was carried out. This showed that the deformation under these conditions is virtually the same as when undergoing purely the linear thermal load law, but the structure experiences a generally greater level of principal stress than for the case of the isolated mechanical load. This is due to the additional compressive stress caused by the thermal expansion of the panel. The deformation response, thermal gradient and general correspondence to the cases of purely dynamic thermal loading can all be observed for very thin and thick panels, with the results given in Fig. 5.

A more pronounced dc offset occurs in the displacement response when the constant mechanical load is increased up to more realistic values, such as 10 N or 100 N, and this phenomenon is shown very clearly in Fig. 6.

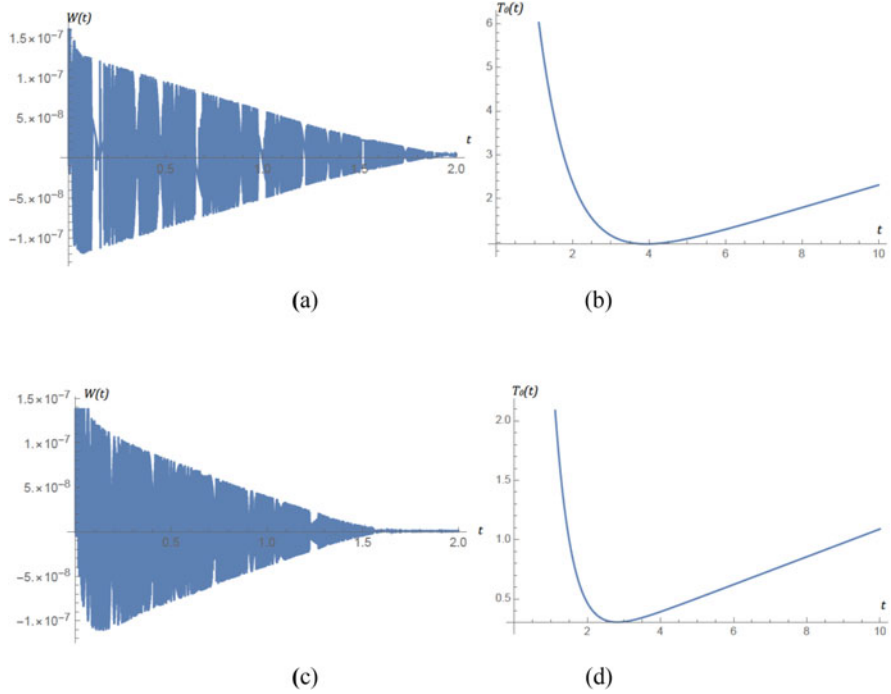


Fig. 5 (a), (c) Displacement response (in metres) in the time domain and (b), (d) time history of the distribution of the thermal component $T_0(t)$ (in $^{\circ}\text{C}$): (a), (b) for core thickness of 0.00824 m and total plate thickness of 0.009 m and (c), (d) for core thickness of 0.01924 m and total plate thickness of 0.02 m when subjected to a thermal load of $(20 + 10t)$ $^{\circ}\text{C}$ and a constant mechanical loading of 1 N

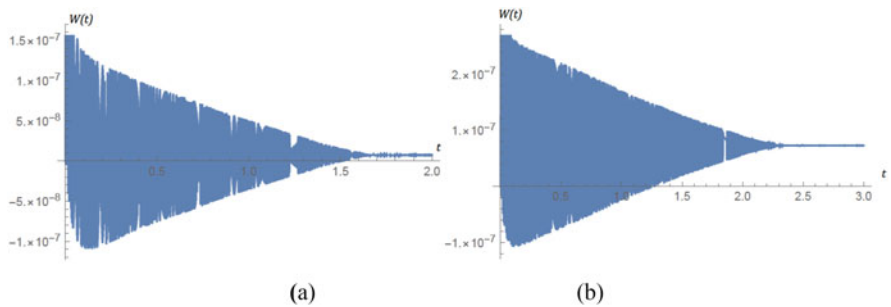


Fig. 6 Displacement response (in metres) in the time domain when subjected to a thermal load of $(20 + 10t)$ $^{\circ}\text{C}$ and a constant mechanical load of (a) 10 N and (b) 100 N, with a core thickness of 0.01924 m and a total plate thickness of 0.02 m

5 Conclusions

A new modelling strategy for aluminium honeycomb composite panels has been suggested, in which the physics of dynamic thermal and mechanical loadings are integrated into a partially coupled modelling procedure which can easily accommodate different boundary conditions and dynamically varying thermal properties. The nonlinear thermo-mechanical model comprises three coupled nonlinear ordinary differential equations for which an analytical closed-form solution can only be obtained for the linearised equations and static thermal and mechanical loads, and so a comparison has been undertaken between this solution and a corresponding numerical solution for the full nonlinear model. The simplified analytical solution obtained in [6] has been found to be useful for predicting the temperature profile through the thickness of panels with no appreciable loss of accuracy. However, for the simulation of displacement, the system of coupled equations can be solved numerically; results for this are discussed here. An approximate closed-form analytical solution for this equation could be sought using an asymptotic method such as the perturbation method of multiple scales. A full set of numerical results have been obtained for a simply supported aluminium honeycomb composite panel commonly used within the industry, undergoing thermal, mechanical and thermo-mechanical loading conditions. The thermal load mechanism involves free heat exchange, and the mechanical loading in all cases comprises a normal constant force exerted centrally on the top surface of the panel. When the panel is subjected solely to a thermal load, applied by means of a fixed environmental temperature, then the solution for the displacement of the panel shows transient oscillation over time at a commensurately small amplitude. The thermal gradient through the thickness of the panel is also calculated based on the coupled system (Eq. 5) using the numerical solution derived, and thermal stabilisation emerges over time, as one would expect. Broadly, the same qualitative responses are observed for a linearly increasing thermal load temperature, but with the stabilisation showing close coupling to the rising environmental temperature. Core thickness affects the results, with the thinner panels displaying a more pronounced thermo-mechanical response than thicker ones. In the case of pure mechanical loading, at a constant but arbitrary low level initially, the panel behaves as normal theory would predict, with a small dc offset in the displacement once the very small transient has decayed. The temperature profile shows a thermal response that reduces to zero in time, indicating that the internal and environmental temperatures are equal. This is a persistent effect for different geometry and mechanical load magnitude. Finally, in the case of combined dynamic thermo-mechanical loading, the panel is subjected to a linearly increasing thermal load temperature and a constant arbitrary mechanical load. The increasing thermal equilibrium over time and the dc offset in the displacement amplitude are strongly persistent features of the results despite different core thicknesses, with the level of the dc offset increasing significantly with the applied mechanical load.

Acknowledgements The first two authors would like to acknowledge the financial support made available by Airbus Defence & Space Ltd. and also the award of funding from the Strathclyde Centre for Doctoral Training. The authors would also like to thank Airbus Defence & Space Ltd. for confidential access to data, noting that no disclosure of any such data whatsoever has been made within this paper.

References

1. M.M. Finckenor, K.K. Groh, *A Researcher's Guide to Space Environmental Effects*. NP-2015-03-015-JSC (International Space Station. NASA, 2015)
2. J.B. Bai, R.A. Sheno, J.J. Xiong, Thermal analysis of thin-walled deployable composite boom in simulated space environment. *Compos. Struct.* **173**, 210–218 (2017)
3. P. Lv, Z. Zhang, L. Ji, X. Hou, Q. Guan, Microstructure evolution of 2024 and 7A09 aluminium alloys subjected to thermal cycling in simulated LEO space environment. *Mater. Res. Innov.* **18**(3), 169–175 (2013)
4. W. Nowacki, *Thermoelasticity*, 2nd edn. (Pergamon Press, 1986)
5. S. Brischetto, E. Carrera, Coupled thermo-mechanical analysis of one-layered and multilayered plates. *Compos. Struct.* **92**, 1793–1812 (2010)
6. E. Saetta, G. Rega, Third order thermomechanically coupled laminated plate: 2D nonlinear modeling, minimal reduction, and transient/post-buckled dynamics under different thermal excitations. *Compos. Struct.* **174**, 420–441 (2017)
7. E. Saetta, G. Rega, Unified 2D continuous and reduced order modeling of thermomechanically coupled laminated plate for nonlinear vibrations. *Meccanica* **49**, 1723–1749 (2014)
8. S. Brischetto, E. Carrera, Thermomechanical effect in vibration analysis of one-layered and two-layered plates. *Int. J. Appl. Mech.* **3**(1), 161–185 (2011)
9. Y.-L. Yeh, Chaotic and bifurcation dynamic behavior of a simply supported rectangular orthotropic plate with thermo-mechanical coupling. *Chaos Solutions Fractals* **24**, 1243–1255 (2015)
10. E. Saetta, G. Rega, Modeling, dimension reduction, and nonlinear vibrations of thermomechanically coupled laminated plates. *Procedia Eng.* **144**, 875–882 (2016)

On the Vibration Attenuation Properties of Metamaterial Design Using Negative Stiffness Elements



Kyriakos Alexandros Chondrogiannis, Vasilis Dertimanis, Boris Jeremic, and Eleni Chatzi

1 Introduction

A decisive aspect in the design of civil structures lies in their behavior under dynamic excitation. Aiming to ensure safety and structural protection, the engineering community has focused on the development of vibration attenuation systems, which can limit the effects of the dynamic excitation on a target structure.

The mitigation of structural vibration has been frequently treated via use of passive linear devices. Many of the well established practices for this purpose include the concept of tuned mass dampers [1]. Although passive linear systems have proven potential in vibration mitigation, their effectiveness is limited within a narrow range of frequencies, while unfavorable results (e.g., amplification) can be observed outside this range. A need thus exists for technological developments that can mitigate vibration within broad frequency ranges.

In materializing such a goal, novel designs have been recently proposed within the framework of metamaterials [2, 3]. These types of configurations are characterized by extraordinary properties regarding prevention of wave propagation within a specific frequency range, the so-called band-gap, or guidance of propagating waves [4]. A challenge that arises when considering earthquake excitation is related to seismic motions, which are typically described by a low frequency content, which lies well outside the most common applications of metamaterials, which were initially studied for electromagnetic waves, therefore high frequency spectra. In recent literature, however, the idea of metastructures has emerged, i.e., periodic

K. A. Chondrogiannis (✉) · V. Dertimanis · E. Chatzi
Institute of Structural Engineering, ETH Zürich, Zurich, Switzerland
e-mail: Chondrogiannis@ibk.baug.ethz.ch; v.derti@ibk.baug.ethz.ch; chatzi@ibk.baug.ethz.ch

B. Jeremic
Department of Civil and Environmental Engineering, University of California, Davis, CA, USA
e-mail: jeremic@ucdavis.edu

arrangements, which are able to inhibit low frequency wave propagation [5–7], also relating to seismic excitation. An extensive study over linear configuration options reveals that the creation of wide band-gaps is a highly challenging task, which has led to the investigation of nonlinear systems [8, 9]; a concept which is extended to nonlinear metamaterials and periodically arranged structures [10, 11]. A promising variant of nonlinear vibration mitigation solutions is delivered by incorporation of negative stiffness elements that can lead to highly efficient energy absorption and can also be used within the concept of metamaterials [12, 13]. Exploring negative stiffness elements, in the works of Al-Shudeifat et al. and Chen et al. [14–16] shallow arch configurations have been investigated. In the work of Antoniadis et al. [12] negative stiffness elements are incorporated in the metastructure configuration, taking into consideration vertical vibration isolation, resulting to static loading capacity limitations to ensure resistance against gravitational loads. To the contrary, this study aims at vibration attenuation in the horizontal direction, releasing the negative stiffness effects to intervene in the connection between the unit cells.

2 Metamaterial Configuration

In the current work, geometric nonlinearities are utilized as a basis for metamaterial development. Geometrically nonlinear behavior is produced with the use of a triangular shallow arch that is undergoing large displacements and that can, under specific conditions, trigger negative stiffness effects. The system under investigation consists of multiple, identical, and elastically interconnected unit cells that form a lattice, as shown in Fig. 1. Each cell is composed of a rigid support, connected to the nonlinear element. One end of the configuration is connected to the ground and the other to a primary mass, subjected to protection from incoming vibration. Moreover, the system is excited by a harmonic force, applied to the primary mass, or input ground acceleration.

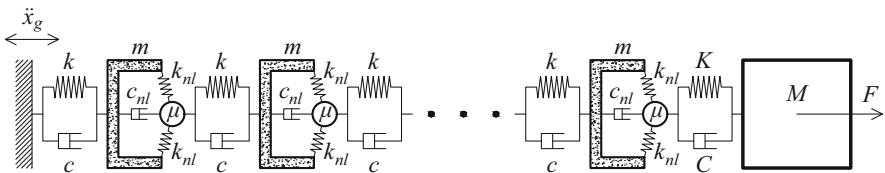


Fig. 1 Nonlinear metamaterial lattice

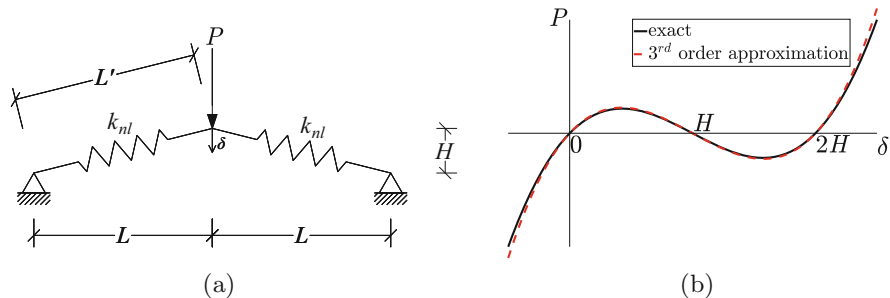


Fig. 2 Triangular arch: (a) Geometry (b) Force-Displacement relation

3 Nonlinear Behavior of the Triangular Arch

The nonlinear behavior in the unit cell scale is produced with the use of a triangular arch. A triangular arch (Fig. 2a) that undergoes large displacements develops a nonlinear force-displacement relation. This results from the change in the stiffness of the system with evolution of the vertical displacement, δ . This behavior can be calculated analytically via Eq. (1) and forms a function of the geometrical and stiffness parameters of the system.

$$P(\delta) = 2k_{nl}L' \left(1 - \sqrt{\frac{\left(\frac{L}{H}\right)^2 + \left(1 - \frac{\delta}{H}\right)^2}{\left(\frac{L}{H}\right)^2 + 1}} \right) \frac{1 - \frac{\delta}{H}}{\sqrt{\left(\frac{L}{H}\right)^2 + \left(1 - \frac{\delta}{H}\right)^2}} \quad (1)$$

The bi-stable geometry of Fig. 2 comprises two stable equilibrium points, at which both springs remain undeformed (no tension or compression). This system can trigger negative stiffness effects as the tip of the arch undergoes large displacements. The equilibrium path of the configuration is plotted in Fig. 2b, which reveals the two stable equilibrium points, where the springs are unloaded, for $\delta = 0$ and $\delta = 2H$. For displacement $\delta = H$, the springs are aligned in the horizontal position, while being compressed, thus establishing the system unstable for this position [14].

4 Analytical Derivations

4.1 Nonlinear Force-Displacement Relation

In order to study the dynamic behavior of the system, the dispersion relation and the frequency response function are analytically derived. A useful practice is

the polynomial approximation of the nonlinear force-displacement relation of the triangular arch, in order to simplify the calculations. Performing Taylor-expansion about $\delta = H$ yields the polynomial approximation of the nonlinear relation [14], a 3rd order of which is used in this study, as shown in Eq. (2). Satisfactory compliance of the polynomial approximation, compared to the exact behavior, can be achieved with a 3rd order approximation, as shown in Fig. 2b.

$$\begin{aligned}
 P(\delta) &\approx k_1 (\delta - H) + k_2 (\delta - H)^3 \\
 k_1 &= -2k_{nl} \left(\frac{L'}{L} - 1 \right), \quad k_2 = \frac{k_{nl}L'}{L^3}
 \end{aligned}
 \tag{2}$$

4.2 Dispersion Relation

A useful indication of the performance of a metamaterial configuration against vibration mitigation is the dispersion relation, between the wave number and respective frequency, that reveals the propagating and evanescent wave frequencies. To calculate this relation, the infinite lattice should be studied with Bloch boundary conditions applied, as noted in Fig. 3. The assumed solution, enforcing Bloch’s periodicity [13, 17], is considered to be of the form of Eq. (3).

$$\begin{aligned}
 u_{j\pm 1}(t) &= \left(U_1 e^{i\omega t} + \bar{U}_1 e^{-i\omega t} \right) e^{\pm iq} \\
 v_{j\pm 1}(t) &= \left(V_1 e^{i\omega t} + \bar{V}_1 e^{-i\omega t} \right) e^{\pm iq} \\
 v(t) &= u(t) - y(t)
 \end{aligned}
 \tag{3}$$

where $u(t)$ is the displacement of mass m , $y(t)$ is the displacement of mass μ , $v(t)$ is the relative displacement of these nonlinearly connected masses, q is the reduced wave number and ω is the angular frequency.

The nonlinear force-displacement approximation is considered to be of the form of Eq. (4), which corresponds to initial conditions of the system, defined as $y(0) = H$. Parameters k_1 and k_2 are calculated according to Eq. (2).

$$F_{nl}(t) = k_1 v(t) + k_2 v(t)^3
 \tag{4}$$

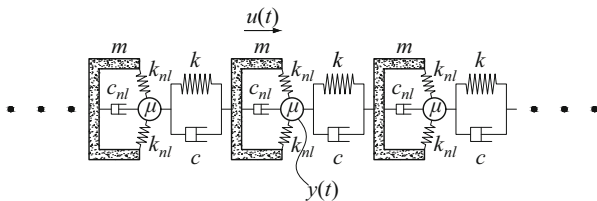


Fig. 3 Infinite lattice

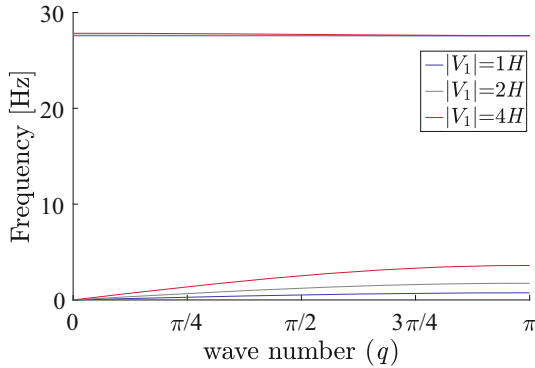


Fig. 4 Dispersion curves of the infinite lattice ($m = 1, k = 10^4, \mu = 0.5, k_{nl} = 100, H = 0.1, L = 0.5$)

Therefore, the equations of motion for the j th unit cell, in the absence of damping, take the form of Eq. (5).

$$\begin{aligned}
 m\ddot{u}_j(t) + k[u_j(t) - (u_{j-1}(t) - v_{j-1}(t))] + k_1v_j(t) + k_2v_j(t)^3 &= 0 \\
 \mu(\ddot{u}_j(t) - \ddot{v}_j(t)) + k(u_j(t) - v_j(t) - u_{j+1}(t)) - k_1v_j(t) - k_2v_j(t)^3 &= 0
 \end{aligned}
 \tag{5}$$

Substitution of Eq. (3) in Eq. (5), collecting terms of $e^{i\omega t}$ and balancing of the harmonics, according to the steps of the Harmonic Balance Method, yields the dispersion relation of the infinite lattice in Eq. (6).

$$\cos(q) = \frac{2k(k_1 + 3k_2V_1\bar{V}_1) - (m + \mu)(k + k_1 + 3k_2V_1\bar{V}_1)\omega^2 + m\mu\omega^4}{2k(k_1 + 3k_2V_1\bar{V}_1)}
 \tag{6}$$

It is observed that the resulting dispersion curves and the corresponding band-gap are depended on the relative displacement V_1 ($|V_1| = \sqrt{V_1\bar{V}_1}$) of the nonlinearly connected masses, as shown in Fig. 4. The dispersion branches appear to shift into higher frequencies as the nonlinearity term k_2 has more dominant contribution for increasing $V_1\bar{V}_1$ values, which results to stiffening of the system. The determination of the resulting band-gap is a nontrivial procedure. Incoming vibrations that fall within this stop-band are attenuated, thus their intensity is altered, which results in a revision of the activated level of nonlinearity, subsequently altering the band-gap [13].

4.3 Frequency Response

An important means for evaluating the behavior of a system under dynamic excitation is its response under varying frequencies. For nonlinear systems, response

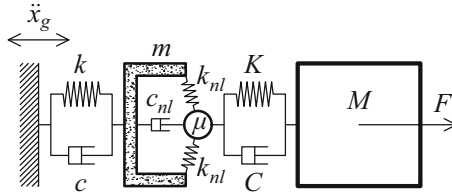


Fig. 5 Single unit cell setup

characteristics form a function of not only the frequency, but also of the amplitude of the excitation. To calculate this relation analytically, a finite lattice is considered, which is comprised of a single unit cell and the primary mass, as depicted in Fig. 5. The input excitation is considered to be harmonic of the form $F(t) = Y \cos(\omega t)$ and $\ddot{x}_g(t) = X \cos(\omega t)$.

The assumed solution for the harmonic oscillation of the response for each degree of freedom is considered to be of the form of Eq. (7).

$$x_i(t) = A_i \cos(\omega t) + B_i \sin(\omega t) \tag{7}$$

where $i = 1, 2, 3$ for mass m, μ, M , respectively.

The nonlinear force-displacement relation of the triangular arch follows what was already described in Sect. 4.1. Therefore, the equations of motion are formed as in Eq. (8).

$$M\ddot{x}_3(t) + C(\dot{x}_3(t) - \dot{x}_2(t)) + K(x_3(t) - x_2(t)) = F(t) \tag{8a}$$

$$\begin{aligned} &\mu\ddot{x}_2(t) + C(\dot{x}_2(t) - \dot{x}_3(t)) + c_{nl}(\dot{x}_2(t) - \dot{x}_1(t)) + \\ &+ K(x_2(t) - x_3(t)) + k_1(x_2(t) - x_1(t)) + k_2(x_2(t) - x_1(t))^3 = 0 \end{aligned} \tag{8b}$$

$$\begin{aligned} &m\ddot{x}_1(t) + c(\dot{x}_1(t) - \dot{x}_g(t)) + c_{nl}(\dot{x}_1(t) - \dot{x}_2(t)) + \\ &+ k(x_1(t) - x_g(t)) + k_1(x_1(t) - x_2(t)) + k_2(x_1(t) - x_2(t))^3 = 0 \end{aligned} \tag{8c}$$

Substitution of Eq. (7) in Eqs. (8) and balancing of the harmonics yields a nonlinear system of equations, the numerical solution of which determines the coefficients $A_1, A_2, A_3, B_1, B_2, B_3$ for given angular frequency ω and input coefficients Y, X .

To calculate the amplitude of the displacement for each mass i , Eq. (9a) is used. Moreover, the acceleration amplitude of each mass is calculated according to Eq. (9b). In Figs. 6 and 7 the solutions of Q_3^{dis} and Q_3^{acc} are plotted, which result from the solution of the nonlinear system of equations for discrete frequencies.

$$Q_i^{dis} = (A_i^{(2)} + B_i^{(2)})^{(1/2)} \tag{9a}$$

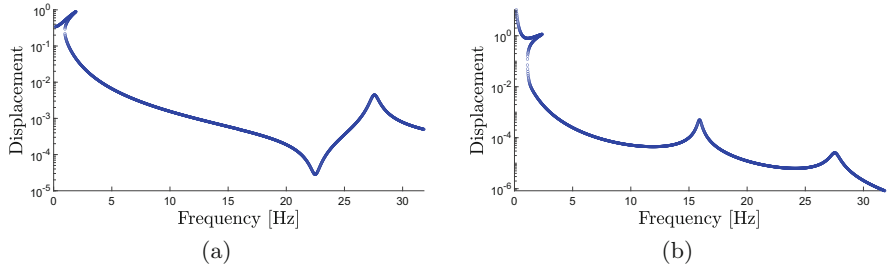


Fig. 6 Analytical solution of the displacement amplitude of mass M for varying frequencies: **(a)** $Y = 10, X = 0$ and **(b)** $Y = 0, X = 10$ ($M = 1, C = 1, K = 10^4, m = 1, c = 1, k = 10^4, \mu = 0.5, k_{nl} = 100, c_{nl} = 1, H = 0.1, L = 0.5$)

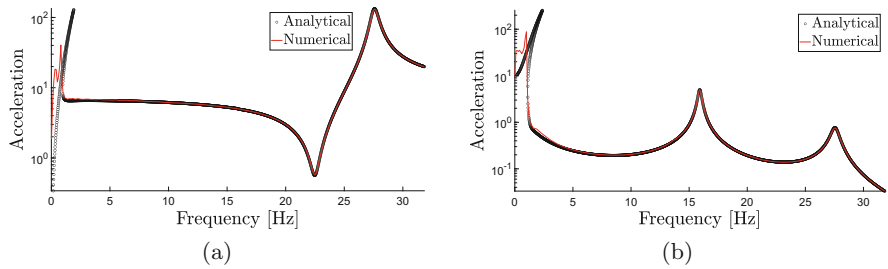


Fig. 7 Numerical to analytical comparison of maximum acceleration of mass M for varying frequencies and single unit cell setup: **(a)** $Y = 10, X = 0$ and **(b)** $Y = 0, X = 10$ ($M = 1, C = 1, K = 10^4, m = 1, c = 1, k = 10^4, \mu = 0.5, k_{nl} = 100, c_{nl} = 1, H = 0.1, L = 0.5$)

$$\mathbf{Q}_i^{acc} = \left[(\boldsymbol{\omega}^{(2)} \circ \mathbf{A}_i)^{(2)} + (\boldsymbol{\omega}^{(2)} \circ \mathbf{B}_i)^{(2)} \right]^{(1/2)} \tag{9b}$$

where \circ and $(^p)$ denote element-wise multiplication and p -th power, respectively.

5 Numerical Simulations

The response of the system of Fig. 1 is now simulated numerically. The equations of motion are formed for each unit cell and the primary mass in Eqs. (10)–(13). For the numerical simulations the exact nonlinear force-displacement relation was considered according to Eq. (1). The differential equations of motion were solved numerically, after arranging the system in a nonlinear state space form. The analyses were performed using MATLAB® environment, with integration carried out by means of the *ode45* function. Moreover, the harmonic excitation was applied to the system incrementally as $F(t) = t/t_{\max} Y \cos(\omega t)$ and $\ddot{x}_g(t) = t/t_{\max} X \cos(\omega t)$, within a time period of $t_{\max} = 30$ seconds, for discrete angular frequencies, for

which the time history of the response was recorded. Finally, the maximum values of acceleration response were obtained as a function of the input excitation frequency.

The equations of motion for the first unit cell can be formulated as:

$$\begin{aligned} m\ddot{u}_1(t) + c(\dot{u}_1(t) - \dot{x}_g(t)) + c_{nl}(\dot{u}_1(t) - \dot{y}_1(t)) + k(u_1(t) - x_g(t)) + F_{nl}^1(t) &= 0 \\ \mu\ddot{y}_1(t) + c(\dot{y}_1(t) - \dot{u}_2(t)) + c_{nl}(\dot{y}_1(t) - \dot{u}_1(t)) + k(y_1(t) - u_2(t)) - F_{nl}^1(t) &= 0 \end{aligned} \quad (10)$$

The equations of motion for the i -th unit cell, $i = 2, \dots, N - 1$, are

$$\begin{aligned} m\ddot{u}_i(t) + c(\dot{u}_i(t) - \dot{y}_{i-1}(t)) + c_{nl}(\dot{u}_i(t) - \dot{y}_i(t)) + k(u_i(t) - y_{i-1}(t)) + F_{nl}^i(t) &= 0 \\ \mu\ddot{y}_i(t) + c(\dot{y}_i(t) - \dot{u}_{i+1}(t)) + c_{nl}(\dot{y}_i(t) - \dot{u}_i(t)) + k(y_i(t) - u_{i+1}(t)) - F_{nl}^i(t) &= 0 \end{aligned} \quad (11)$$

For the last (N -th) unit cell the equations of motion are

$$\begin{aligned} m\ddot{u}_N(t) + c(\dot{u}_N(t) - \dot{y}_{N-1}(t)) + c_{nl}(\dot{u}_N(t) - \dot{y}_N(t)) + k(u_N(t) - y_{N-1}(t)) + F_{nl}^N(t) &= 0 \\ \mu\ddot{y}_N(t) + C(\dot{y}_N(t) - \dot{U}(t)) + c_{nl}(\dot{y}_N(t) - \dot{u}_N(t)) + K(y_N(t) - U(t)) - F_{nl}^N(t) &= 0 \end{aligned} \quad (12)$$

For the primary structure they are formed as:

$$M\ddot{U}(t) + C(\dot{U}(t) - \dot{y}_N(t)) + K(U(t) - y_N(t)) = F(t) \quad (13)$$

where $F_{nl}^i(t) = P(x_{rel}^i(t))$ and $x_{rel}^i(t) = u_i(t) - y_i(t)$

In Fig. 7 the numerical results of the maximum acceleration amplitude are compared to the analytical derivations of Sect. 4.3, where a single unit cell configuration is considered (Fig. 5). Sufficient agreement is observed for most frequency ranges for the two curves. However, some discrepancies are observed for low frequencies (<1 Hz), where the corresponding displacements are significantly increased ($\sim 10H$, H : height of triangular arch at rest), as can be inferred from Fig. 6. This results from the increase in the discrepancy between the polynomial approximation and the exact nonlinear equilibrium path for high displacement values. Overall, the agreement between the numerical and the analytical results is considered to be sufficient. Therefore, the derived dispersion curves in Fig. 4 can offer a useful indication of the resulting band-gap potential for the proposed configuration.

In order to evaluate the effect of an increasing number of unit cells on the response of the system, parametric analyses with varying number of unit cells were performed. Figure 8 illustrates the maximum recorded acceleration in the primary mass across varying frequencies. The results of the nonlinear lattice indicate mitigation of accelerations within frequency ranges >1 Hz, thus revealing the beneficial effects of increasing number of unit cells in vibration attenuation.

The results are further compared with the response of the unprotected primary mass, as well as with an equivalent linear system consisting of 5 unit cells. In the latter, a linear spring was considered in the connection of masses m and μ . Its stiffness was determined from the tangential stiffness of Eq.(1) for

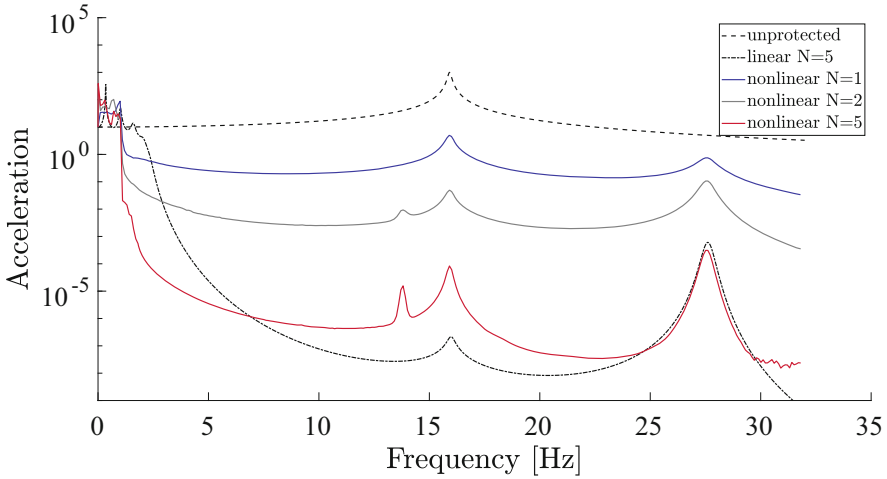


Fig. 8 Numerical calculation of the maximum acceleration of mass M for varying frequencies and number of unit cells ($M = 1, C = 1, K = 10^4, m = 1, c = 1, k = 10^4, mu = 0.5, k_{nl} = 100, c_{nl} = 1, H = 0.1, L = 0.5, Y = 0, X = 10$). Comparison to the acceleration response of the unprotected mass M and to a linear system

displacement equal to the ground displacement amplitude at frequency of 1 Hz, ($\omega = 2\pi, x_g(t) = -X/\omega^2 \cos(\omega t)$), which is the limit frequency for vibration attenuation in the nonlinear lattice. It is observed that the nonlinear lattice can offer vibration mitigation properties in lower frequencies than the equivalent linear one. It can be pointed that the acceleration reduction is more intense for the linear case, compared to the nonlinear system with 5 cells for certain frequencies. However, this is observed for frequency ranges for which the reduction in the response is significant for both the linear and the nonlinear design.

6 Conclusions

The current study investigates the vibration attenuation properties of a geometrically nonlinear metastructure configuration. Utilization of triangular arch setups results in a nonlinear equilibrium path and under specific circumstances negative stiffness effects are observed. An investigation on the resulting band-gap was performed, determining the effect of increasing oscillation amplitude, which results to a shift of this stop-band to higher frequencies, mainly affecting the lower branch of the dispersion relation. Moreover, an analytical study on the system’s response for varying input frequencies was performed and compared to numerical results, revealing sufficient compliance. Finally, the effect of the inclusion of multiple unit cells on the system’s response was investigated. The results revealed favorable

effects within a broad frequency range, thus promising great potential toward structural vibration mitigation.

Acknowledgments This project has received funding from the European Union's Horizon 2020 research and innovation programme under the Marie Skłodowska-Curie grant agreement No INSPIRE-813424.

References

1. Z. Zhou, X. Wei, Z. Lu, B. Jeremic, Influence of soil-structure interaction on performance of a super tall building using a new eddy-current tuned mass damper. *Struct. Design Tall Special Build.* **27**(14), e1501 (2018). <https://doi.org/10.1002/tal.1501>
2. A. Palermo, S. Krödel, K.H. Matlack, R. Zaccherini, V.K. Dertimanis, E.N. Chatzi, A. Marzani, C. Daraio, Hybridization of guided surface acoustic modes in unconsolidated granular media by a Resonant Metasurface. *Phys. Rev. Appl.* **9**, 054026 (2018). <https://doi.org/10.1103/PhysRevApplied.9.054026>
3. R. Zaccherini, A. Colombi, A. Palermo, V.K. Dertimanis, A. Marzani, H.R. Thomsen, B. Stojadinovic, E.N. Chatzi, Locally resonant metasurfaces for shear waves in granular media. *Phys. Rev. Appl.* **13**, 034055 (2020). <https://doi.org/10.1103/PhysRevApplied.13.034055>
4. V. Fedotov, *Metamaterials* (Springer, Cham, 2017). https://doi.org/10.1007/978-3-319-48933-9_56
5. V.K. Dertimanis, I.A. Antoniadis, E.N. Chatzi, Feasibility analysis on the attenuation of strong ground motions using finite periodic lattices of mass-in-mass barriers. *J. Eng. Mech.* **142**(9), 04016060 (2016). [https://doi.org/10.1061/\(ASCE\)EM.1943-7889.0001120](https://doi.org/10.1061/(ASCE)EM.1943-7889.0001120)
6. P.R. Wagner, V.K. Dertimanis, I.A. Antoniadis, E.N. Chatzi, On the feasibility of structural metamaterials for seismic-induced vibration mitigation. *Int. J. Earthquake Impact Eng.* **1**(1/2), 20–56 (2016). <https://doi.org/10.1504/ijeie.2016.10000957>
7. R. Zaccherini, A. Palermo, S. Krödel, V.K. Dertimanis, A. Marzani, C. Daraio, E.N. Chatzi, Resonant metabarriers as seismic attenuators in granular media, in *Proceedings of ISMA 2018 - International Conference on Noise and Vibration Engineering and USD 2018 - International Conference on Uncertainty in Structural Dynamics* (2018), pp. 3047–3057
8. A.F. Vakakis, O.V. Gendelman, L.A. Bergman, D.M. McFarland, G. Kerschen, Y.S. Lee, *Nonlinear Targeted Energy Transfer in Mechanical and Structural Systems I* (Springer, Netherlands, 2008). <https://doi.org/10.1007/978-1-4020-9130-8>
9. D.M. McFarland, L.A. Bergman, A.F. Vakakis, Experimental study of non-linear energy pumping occurring at a single fast frequency. *Int. J. Non-Linear Mech.* **40**(6), 891–899 (2005). <https://doi.org/10.1016/j.ijnonlinmec.2004.11.001>
10. S. Fiore, G. Finocchio, R. Zivieri, M. Chiappini, F. Garescì, Wave amplitude decay driven by anharmonic potential in nonlinear mass-in-mass systems. *Appl. Phys. Lett.* **117**(12), 124101 (2020). <https://doi.org/10.1063/5.0020486>
11. V.K. Dertimanis, S.F. Masri, E.N. Chatzi, On the vibration attenuation properties of finite periodic lattices of impact dampers, in *9th ECCOMAS Thematic Conference on Smart Structures and Materials (SMART 2019)*, Paris, France (2019), pp. 1146–1154
12. I.A. Antoniadis, A. Paradeisiotis, Acoustic meta-materials incorporating the KDamper concept for low frequency acoustic isolation. *Acta Acustica United Acustica* **104**(4), 636–646 (2018). <https://doi.org/10.3813/AAA.919203>
13. M. Wenzel, O.S. Bursi, I. Antoniadis, Optimal finite locally resonant metafoundations enhanced with nonlinear negative stiffness elements for seismic protection of large storage tanks. *J. Sound Vib.* **483**, 115488 (2020). <https://doi.org/10.1016/j.jsv.2020.115488>

14. M.A. Al-Shudeifat, Highly efficient nonlinear energy sink. *Nonlinear Dyn.* **76**(4), 1905–1920 (2014). <https://doi.org/10.1007/s11071-014-1256-x>
15. Y. Chen, Z. Qian, K. Chen, P. Tan, S. Tesfamariam, Seismic performance of a nonlinear energy sink with negative stiffness and sliding friction. *Struct. Control Health Monitor.* **26**(11), e2437 (2019). <https://doi.org/10.1002/stc.2437>
16. S. Chen, B. Wang, S. Zhu, X. Tan, J. Hu, X. Lian, L. Wang, L. Wu, A novel composite negative stiffness structure for recoverable trapping energy. *Composites Part A: Appl. Sci. Manufact.* **129**, 105697 (2020). <https://doi.org/10.1016/j.compositesa.2019.105697>
17. A. Palermo, A. Marzani, A reduced Bloch operator finite element method for fast calculation of elastic complex band structures. *Int. J. Solids Struct.* **191–192**, 601–613 (2020). <https://doi.org/10.1016/j.ijsolstr.2019.12.011>

Long-Range Resonator-Based Metamaterials



A. S. Rezaei, F. Mezzani, and A. Carcaterra

1 Introduction

Metamaterials are artificial composites capable of presenting unusual behaviour in terms of waves, unlike conventional materials. An arbitrary arrangement for constructing elements of metamaterials can be adopted, which is proper for the intended use. Activating communication among non-neighbouring parts of a system on the macro scale provides the opportunity for steering waves within the domain. In fact, long-range metamaterials (LRM), a subcategory of mechanical metamaterials, borrow the concept of nonlocal interactions from the nonlocal elasticity [1–3] and disclose some intriguing features. For example, Carcaterra et al. [4] demonstrated that the presence of long-range forces imposed by magnetic interactions among distant points would give rise to a rich variety of wave propagation phenomena including wave-stopping and superluminality. Other contributions [5–7] examine the effects induced by the long-range interactions, when different operators are responsible for establishing communication among non-adjacent parts of a system. Note that the term “operator” refers to the constructing elements of the long-range superstructure, which enables distant communication within the domain and which could be either a structural or a contactless link, such as springs or magnets, respectively, and that are here the resonator units.

An important point to be understood is the key role of connectivity pattern in the response of the system. The pattern implies how points of a short-range configuration are engaged in the long-distant interactions, producing nonlocal forces, which modifies the corresponding dynamics. Long-range interaction patterns found in nature are often inspirations for scientists and engineers, seeking to replicate

A. S. Rezaei (✉) · F. Mezzani · A. Carcaterra

Department of Mechanical and Aerospace Engineering, Sapienza University of Rome, Rome, Italy

e-mail: amirsajjad.rezaei@uniroma1.it

through nonlinear mathematical models. Such models are found, for example, in the swarm control of cooperative robots which, thanks to suitable nonlinear control logics, are able to create stable swarm formations [8–10].

Locally resonant acoustic metamaterials (LARM), another class of mechanical metamaterials, provide band structures with single/multiple complete gaps with the help of substructures attached to a host body. The units at their resonant frequency absorb the energy, inducing the generation of complete bandgaps. Resonators, being the constructing elements of the long-range superstructure, could include different configurations of different degrees-of-freedom. Clearly, the number of emerging gaps in the band structure of the entire long-range structure is in direct correspondence with the degrees of freedom of the associated resonators. Many researchers have devoted their focus towards the understanding of underlying mechanisms for generation of the bandgaps and examining the impact of involved parameters on the properties of the corresponding gaps [11–14]. Furthermore, the possibility of controlling elastic waves in nonlinear acoustic metamaterials was investigated in several contributions [15–18] during the past few years. Various applications including acoustic cloaking, acoustic diode, and ultrasonic metamaterial lens [19–22] are provided by the remarkable gift of acoustic metamaterials, capable of manipulating the mechanical waves.

This work is an attempt to accommodate the core concept of locally resonant acoustic metamaterials within the framework of long-range metamaterials. The idea is to employ resonators as long-range operators to develop a structure, which simultaneously benefits from the principal characteristics of both classes, namely, LRAMs and LRMs. For that matter, a very simple resonator unit is considered, and the dynamic description of the system is extracted. The respective dispersion relation entails the birth of a single bandgap in the frequency-wavenumber map of the system. Interestingly, some anomalies are evident in the group velocity response associated with the acoustic and optical dispersion branches, typical of long-range configurations.

2 Long-Range Resonator-Based Metamaterials

In the current section, a homogenous long-range configuration is introduced, wherefore the long-range superstructure is composed of resonator units. The term “homogenous” refers to the physics of the problem, being the long-range operators homogeneously distributed across the domain. Such long-range operators add extra degrees-of-freedom to those of the host structure. Therefore, additional equations are required to fully analyse the dynamics of the system, like locally resonant acoustic metamaterials. Here, a conventional one-dimensional waveguide is selected as the host structure and single-degree-of-freedom (SDOF) resonator units act as long-range operators, taking the responsibility for developing communication among distant cross-sections of the waveguide.

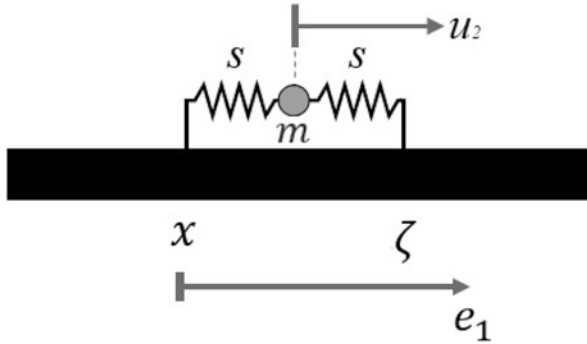


Fig. 1 A simple model for long-range resonator-based waveguides

2.1 Mathematical Model

A simple configuration for the resonator unit is considered, as shown in Fig. 1, which may be viewed as a basic subset of a generalized layout. As mentioned earlier, the composing elements of the long-range superstructure are identical resonator units of the type displayed in Fig. 1. Each unit is made of a single mass m and two springs of the stiffness s . It is worth mentioning that the mass exclusively moves in the axial direction.

The long-range interaction between the distant points x and ζ in the horizontal Cartesian direction e_1 is made possible via the resonator units, as shown in Fig. 1. The long-range operator contributes to the system’s overall degrees-of-freedom unlike those proposed in the literature [5], where the operators are modelled by springlike links. In fact, simple springs do not alter the system’s overall degrees of freedom, and the associated dynamics is controlled by the pre-existing kinematic variables of the host structure.

The dynamic description for the long-range resonator-based waveguide is:

$$\rho A \ddot{u}_1(x, t) - EA u_1''(x, t) - \int_{-\infty}^{\infty} \mathcal{N}_x(x, \zeta, t) \|(x - \zeta) d\zeta = 0 \tag{1}$$

The super dot convention refers to the temporal differentiation, and $'$ denotes the spatial differentiation, here with respect to x . The Young’s modulus, cross-section area, and mass density are represented by E , A and ρ , respectively. The integral term in Eq. (1) explains the overall long-range force induced by the long-range operators, and accordingly, $\mathcal{N}_x(x, \zeta, t)$ is the force imposed by the constituents of the long-range superstructure. To avoid infinite values for the integral term, an arbitrary confining kernel $\|(x)$ is considered, which follows the common notion of decaying interaction intensity with distance. This implies that the hub point x can only interact nonlocally with points ζ , which fall within the interaction region defined by $\|(x)$ via the resonator units.

From a physical point of view, distant communication can be made by different means including actual elastic links, resonator units, or electromagnetic interaction forces. For instance, by integrating a solid cylinder with a co-axial thin shell via some stiffeners, as extensively discussed in Ref. [23], the interaction among distant points can take place. However, for developing setups with full connectivity, as the one under studying, precise design of the structure as well as state-of-the-art manufacturing techniques is required.

To investigate the dynamics of the system, Eq. (1) must be explicitly determined, i.e., the expression of $\mathcal{N}_x(x, \zeta, t)$ and $\|(x)$ defined. The long-range force $\mathcal{N}_x(x, \zeta, t)$ is:

$$\mathcal{N}_x(x, \zeta, t) = s [u_2(\zeta, t) - u_1(x, t)] \tag{2}$$

Here, u_2 is the axial displacement of the mass. The second necessary equation regarding the motion of the mass is:

$$m \ddot{u}_2(\zeta, t) + 2s u_2(\zeta, t) - s [u_2(x, t) + u_1(\zeta, t)] = 0 \tag{3}$$

The expression for $u_2(\zeta, t)$ in the temporal Fourier domain is:

$$\hat{u}_2(\zeta, \omega) = \frac{s [\hat{u}_1(x, \omega) + \hat{u}_1(\zeta, \omega)]}{2s - m\omega^2} \tag{4}$$

Here, the frequency is represented by ω .

Regarding the selection of $\|(x)$, a confining rectangular window of the active length $2L$ is considered throughout this study with L being an arbitrary length parameter. Considering the rectangular window $H(x)$, Eq. (1), after applying temporal Fourier transform, becomes:

$$-\rho A \omega^2 \hat{u}_1(x, \omega) = EA \hat{u}_1''(x, \omega) + 2Ls \left\{ \frac{s \hat{u}_1(x, \omega)}{2s - m\omega^2} - \hat{u}_1(x, \omega) \right\} + \frac{s^2 \hat{u}_1(x, \omega)}{2s - m\omega^2} * H(x) \tag{5}$$

Here, the symbol $*$ denotes the convolution operation. Expressing Eq. (5) in the spatial Fourier domain provides the dispersion relation as:

$$\Omega^2 = K^2 + 2\chi \left\{ 1 - \frac{\Omega_0^2}{2\Omega_0^2 - \Omega^2} \left[1 + \frac{\sin(K)}{K} \right] \right\} \tag{6}$$

where

$$K = kL \quad (7a)$$

$$\Omega = \omega L \sqrt{\rho/E} \quad (7b)$$

$$\Omega_0 = \omega_0 L \sqrt{\rho/E} \quad (7c)$$

$$\chi = sL^3/E A \quad (7d)$$

and $\omega_0 = \sqrt{s/m}$ is a natural frequency parameter, while k is the wavenumber. Equation (6) is the nondimensional dispersion relation of the long-range resonator-based waveguide discussed above, and the related nondimensional groups are defined in Eq. (7).

The dispersion relation (6) is a fourth-order equation in terms of the nondimensional frequency Ω , and its peculiar mathematical form suggests the existence of two dispersion branches, namely, acoustic branch and optical branch. In fact, the acoustic branch (AB) is that part of the dispersion relation, which explains the propagation at low frequencies. The optical branch (OB), on the other hand, is concerned with propagation at higher frequencies, placing higher with respect to the acoustic branch on the dispersion map.

2.2 Results and Discussion

The dispersion relation is controlled by the nondimensional frequency parameter Ω_0 and the nondimensional regulating parameter χ . The parameter χ provides a measure of the intensity of long-range interactions, which has a significant impact on the curve trend of each branch, especially in the long wavelength range.

To exhibit the dispersion map of the system, Fig. 2 is provided, where the variation of the nondimensional frequency Ω is plotted against the nondimensional wavenumber K for fixed values of χ and Ω_0 . The figure confirms the emergence of a complete bandgap between the acoustic and optical branches. Within the bandgap bandwidth, neither acoustic nor optical phonon can propagate. This is a new phenomenon in the context of homogenous long-range metamaterials, which cannot be observed in systems with zero degree-of-freedom long-range operators.

Table 1 gives the width of the gap \mathcal{W} for configurations with different natural frequency parameter Ω_0 and the nondimensional regulating parameter χ . Based on the tabulated data, the gap shrinks as the Ω_0 rises regardless of the value χ adopts. For instance, for a system characterised by $\chi = 10$, the value of \mathcal{W} experiences a sharp drop, nearly 80%, when the frequency parameter gets decoupled. Therefore, tuning the width of the gap can be done by manipulating Ω_0 since \mathcal{W} is highly

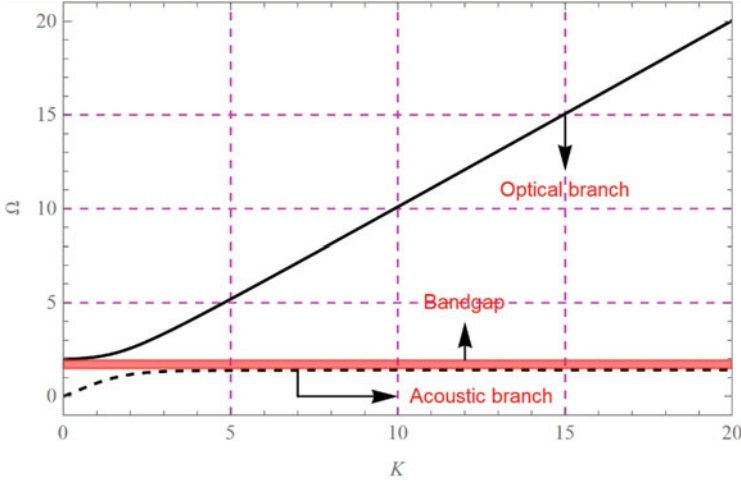


Fig. 2 A simple model for long-range resonator-based waveguides ($\chi = 1$ and $\Omega_0^2 = 1$)

Table 1 Effect of χ and Ω_0 on the width of bandgap

χ	Ω_0	\mathcal{W}
1	1	0.586
	5	0.150
	10	0.071
10	1	3.277
	5	1.299
	10	0.697
50	1	8.689
	5	5.194
	10	3.214

sensitive to Ω_0 . This is further confirmed by Fig. 3, which shows the trend of how the band structure changes according to the variation of Ω_0 . Note that the physical parameters of the resonator units are directly related to Ω_0 , and thereby, a different value for Ω_0 acknowledges a new resonator unit.

Table 1 provides information about the effect of χ on the width of the gap. To clearly demonstrate this effect, Fig. 4 compares the band structure of a long-range resonator-based waveguide for two different values of χ . In accordance with the results of Table 1, the gap grows significantly with the increase of χ . The red-shaded region exhibits the bandgap corresponding to the system with $\chi = 100$, which is considerably wider than the gap between the acoustic and optical dispersion branches of the waveguide with $\chi = 10$. This sensitivity also provides the chance to tune the width of the gap.

The key distinction between this research and those in the context of locally resonant acoustic metamaterials is the alteration of the curve path in long wavelength bandwidth for both dispersion branches. As portrayed in Fig. 4, the ripples

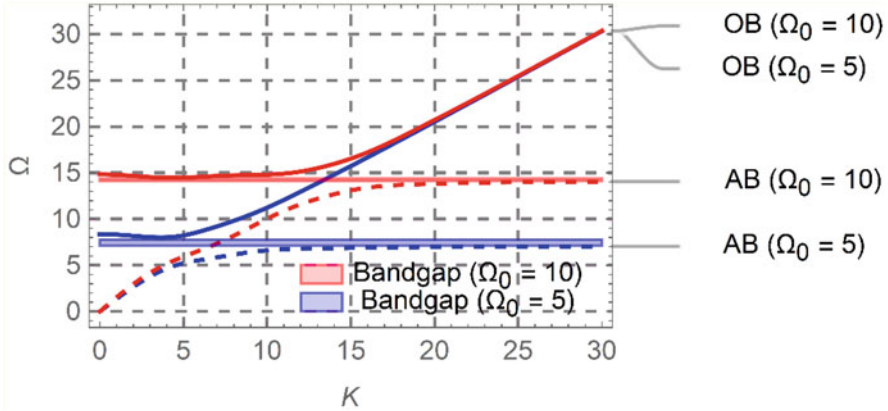


Fig. 3 Band structure of a long-range resonator-based waveguide ($\chi = 10$)

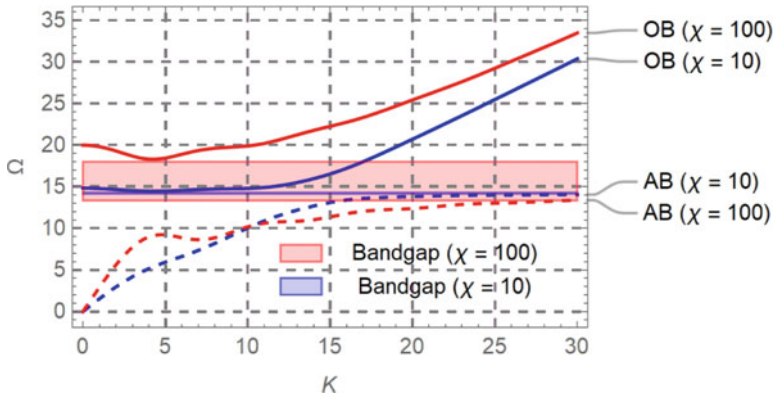


Fig. 4 Band structure of a long-range resonator-based waveguide ($\Omega_0^2 = 100$)

on the curves become more pronounced in the aforementioned range as the nondimensional regulating parameter χ has a larger value. Since distortions along the curve are usually accompanied by intriguing phenomena associated with the speed of phonons, the group velocity response $C_g = d\Omega/dK$ corresponding to the acoustic and optical dispersion branch is examined in Figs. 5 and 6, respectively.

Based on the above figures, zero/negative group velocity can be reached for a given a large enough value of χ . In fact, Fig. 5 demonstrates that the curves neither touch nor cross the horizontal axis unless the adopted value for χ exceeds a critical value χ_{cr}^{AB} . This means that relatively stiffer springs are required within the configuration of the resonator unit to push the system towards conditions presenting unusual behaviours such as wave-stopping and negative group velocity. For a system characterized by supercritical values of χ , wave-stopping phenomena are

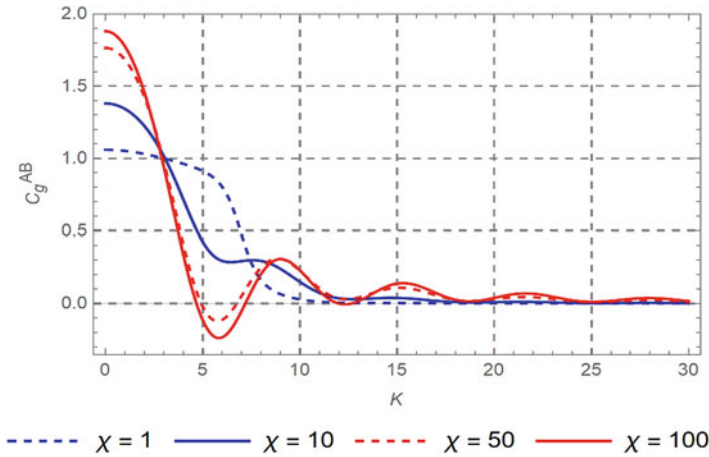


Fig. 5 Group velocity response associated to acoustic branch ($\Omega_0^2 = 25$)

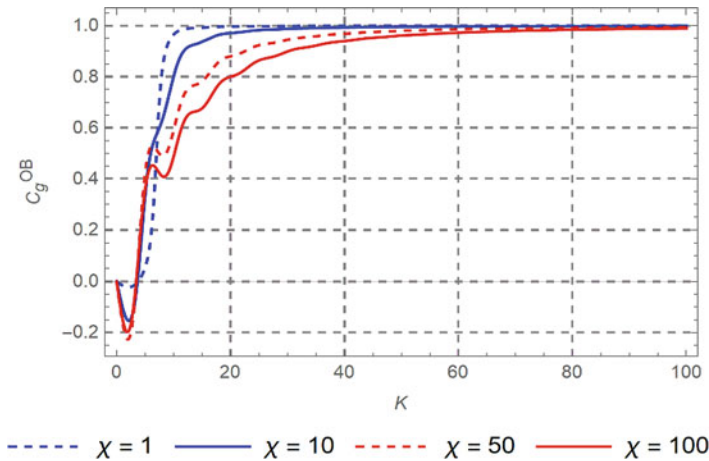


Fig. 6 Group velocity response associated to optical branch ($\Omega_0^2 = 25$)

achieved at two distinct wavenumbers/frequencies, and backward travelling wave envelopes are met within the band recognized by two consecutive wave-stopping wavenumbers/frequencies at the extremes. Interestingly, the curves shown in Fig. 6 present negative values within a certain band for all considered values of χ . Note that group velocity curve paths can be highly influenced by the natural frequency parameter Ω_0 , which is assumed to be fixed in both figures.

Since group velocity is in one-to-one correspondence with the speed of phonons, beneficial information can be extracted from Figs. 5 and 6. For example, both acoustic and optical phonons travel backwardly in the low-frequency range provided

that the nondimensional regulating parameter oversteps χ_{cr}^{AB} . For a subcritical value of χ , acoustic and optical phonons move in the opposite direction in the referred range.

3 Concluding Remarks

This paper considers simple resonator units as the constructing elements of the long-range superstructure in long-range configurations. However, the system also includes properties like those of locally resonant acoustic metamaterials, and accordingly, new characteristics emerge within the band structure of long-range systems. The current study covers the plane wave analysis of a conventional one-dimensional long-range resonator-based waveguide. Communication among the distant cross-sections of the waveguide is made by identical single-degree-of-freedom resonator units, guaranteeing the long-range property of the system. It is assumed that the interaction region for any arbitrary point is confined. The corresponding dispersion relation is controlled by two nondimensional parameters, a frequency parameter, linked to the mechanical properties of the resonator unit, and a regulating parameter, the measure of the intensity of long-range interactions. The dispersion map suggests the generation of one complete bandgap, where the width of the gap is tuned by the nondimensional parameters. The bandgap provides the chance to attenuate the vibrational energy within a targeted frequency band. More importantly, the long-range print can be traced along the acoustic and optical dispersion curves especially in the low-frequency range, where curve paths imply the potentials for driving the wave envelopes, associated with both branches, in the backward direction within certain bands. Such signature phenomena emerge as the consequence of long-range property, being absent in the response of locally resonant acoustic metamaterials.

References

1. A.C. Eringen, D.G.B. Edelen, On nonlocal elasticity. *Int. J. Eng. Sci.* **10**, 233–248 (1972). [https://doi.org/10.1016/0020-7225\(72\)90039-0](https://doi.org/10.1016/0020-7225(72)90039-0)
2. A.C. Eringen, Plane waves in nonlocal micropolar elasticity. *Int. J. Eng. Sci.* **22**, 1113–1121 (1984). [https://doi.org/10.1016/0020-7225\(84\)90112-5](https://doi.org/10.1016/0020-7225(84)90112-5)
3. A.C. Eringen, Linear theory of nonlocal elasticity and dispersion of plane waves. *Int. J. Eng. Sci.* **10**, 425–435 (1972). [https://doi.org/10.1016/0020-7225\(72\)90050-X](https://doi.org/10.1016/0020-7225(72)90050-X)
4. A. Carcaterra, F. Coppo, F. Mezzani, S. Pensalfini, Long-range retarded elastic metamaterials: Wave-stopping, negative, and hypersonic or superluminal group velocity. *Phys. Rev. Appl.* **11**, 014041 (2019). <https://doi.org/10.1103/PhysRevApplied.11.014041>
5. F. Mezzani, A.S. Rezaei, A. Carcaterra, Wave propagation phenomena in nonlinear elastic metamaterials, in *New Trends in Nonlinear Dynamics*, (Springer International Publishing, 2020), pp. 31–40

6. F. Mezzani, F. Coppo, S. Pensalfini, N. Roveri, A. Carcaterra, Twin-waves propagation phenomena in magnetically-coupled structures, in *Procedia Engineering*, (Elsevier, 2017), pp. 711–716
7. S. Pensalfini, F. Coppo, F. Mezzani, G. Pepe, A. Carcaterra, Optimal control theory based design of elasto-magnetic metamaterial, in *Procedia Engineering*, (Elsevier, 2017), pp. 1761–1766
8. N. Roveri, A. Carcaterra, L. Molinari, G. Pepe, Safe and secure control of swarms of vehicles by small-world theory. *Energies* **13**, 1043 (2020). <https://doi.org/10.3390/en13051043>
9. M. Pinto, G. Pepe, N. Roveri, A. Carcaterra, Swarm of robot attacking an acoustic source: Detection and trapping, in *48th International Congress and Exhibition on Noise Control Engineering. Institute of Noise Control Engineering*, (Sociedad Española de Acústica, 2019)
10. L. Nesi, G. Pepe, M. Bibuli, E. Zereik, A. Carcaterra, M. Caccia, A new tow maneuver of a damaged boat through a swarm of autonomous sea drones, in *IFAC-PapersOnLine*, (Elsevier, 2019), pp. 360–366
11. F.R. Montero de Espinosa, E. Jiménez, M. Torres, Ultrasonic band gap in a periodic two-dimensional composite. *Phys. Rev. Lett.* **80**, 1208–1211 (1998). <https://doi.org/10.1103/PhysRevLett.80.1208>
12. P.F. Pai, Metamaterial-based broadband elastic wave absorber. *J. Intell. Mater. Syst. Struct.* **21**, 517–528 (2010). <https://doi.org/10.1177/1045389X09359436>
13. H. Sun, X. Du, P.F. Pai, Theory of metamaterial beams for broadband vibration absorption. *J. Intell. Mater. Syst. Struct.* **21**, 1085–1101 (2010). <https://doi.org/10.1177/1045389X10375637>
14. P. Wang, F. Casadei, S. Shan, J.C. Weaver, K. Bertoldi, Harnessing buckling to design tunable locally resonant acoustic metamaterials. *Phys. Rev. Lett.* **113**, 014301 (2014). <https://doi.org/10.1103/PhysRevLett.113.014301>
15. X. Fang, J. Wen, J. Yin, D. Yu, Y. Xiao, Broadband and tunable one-dimensional strongly nonlinear acoustic metamaterials: Theoretical study. *Phys. Rev. E* **94**, 052206 (2016). <https://doi.org/10.1103/PhysRevE.94.052206>
16. W.J. Zhou, X.P. Li, Y.S. Wang, W.Q. Chen, G.L. Huang, Spectro-spatial analysis of wave packet propagation in nonlinear acoustic metamaterials. *J. Sound Vib.* **413**, 250–269 (2018). <https://doi.org/10.1016/j.jsv.2017.10.023>
17. S.G. Konarski, M.R. Haberman, M.F. Hamilton, Frequency-dependent behavior of media containing pre-strained nonlinear inclusions: Application to nonlinear acoustic metamaterials. *J. Acoust. Soc. Am.* **144**, 3022–3035 (2018). <https://doi.org/10.1121/1.5078529>
18. X. Fang, J. Wen, B. Bonello, J. Yin, D. Yu, Wave propagation in one-dimensional nonlinear acoustic metamaterials. *New J. Phys.* **19**, 053007 (2017). <https://doi.org/10.1088/1367-2630/aa6d49>
19. S. Zhang, C. Xia, N. Fang, Broadband acoustic cloak for ultrasound waves. *Phys. Rev. Lett.* **106**, 024301 (2011). <https://doi.org/10.1103/PhysRevLett.106.024301>
20. S. Zhang, L. Yin, N. Fang, Focusing ultrasound with an acoustic metamaterial network. *Phys. Rev. Lett.* **102**, 194301 (2009). <https://doi.org/10.1103/PhysRevLett.102.194301>
21. P. Kerrian, A. Hanford, B. Beck, D. Capone, Underwater acoustic ground cloak development and demonstration. *J. Acoust. Soc. Am.* **143**, 1918–1918 (2018). <https://doi.org/10.1121/1.5036252>
22. D. Cresse, A one-way system for sound. *Nature* (2010). <https://doi.org/10.1038/news.2010.559>
23. A.S. Rezaei, F. Mezzani, A. Carcaterra, Wave propagation with long-range forces and mistuning effects. *Proc. Inst. Mech. Eng. C J. Mech. Eng. Sci.* (2021). <https://doi.org/10.1177/0954406221989743>

Part VI
Nonlinear Waves

KdV, Extended KdV, 5th-Order KdV, and Gardner Equations Generalized for Uneven Bottom Versus Corresponding Boussinesq's Equations



Piotr Rozmej and Anna Karczewska

1 Introduction

Nonlinear waves are the subject of a vast number of studies in many fields of science. They appear in hydrodynamics, propagation of optical and acoustic waves, plasma physics, electrical circuits, biology. These equations usually appear as approximations of more basic laws describing relevant systems' behavior, usually too complicated for non-numerical analysis. These approximations assume that some parameters characterizing the system are small, and then a perturbative approach can be used. In this way, one can derive various nonlinear wave equations, e.g., the *Korteweg-de Vries equation* (KdV), the *extended Korteweg-de Vries equation* (KdV2), *5th-order KdV*, or the *Gardner equation* [1], though the original derivations were different. All these equations can be derived from the Euler equations describing the model of the irrotational motion of an inviscid and incompressible fluid in a container with a flat, impenetrable bottom.

In the past, there were many attempts to take into account bottom variations. Article [2] is the only one known to us (apart from our approach) in which the authors introduce besides two small standard parameters, the third one associated with an uneven bottom. In [3], we presented a broader discussion of some of the attempts and methods to account for uneven bottoms.

P. Rozmej (✉)

Faculty of Physics and Astronomy, University of Zielona Góra, Zielona Góra, Poland

e-mail: P.Rozmej@if.uz.zgora.pl

<http://staff.uz.zgora.pl/prozmej>

A. Karczewska

Faculty of Mathematics, Computer Science and Econometrics, University of Zielona Góra, Zielona Góra, Poland

e-mail: a.karczewska@wmie.uz.zgora.pl

In [3], we derived four new wave equations, which generalize for the case of uneven bottom Korteweg-de Vries equation (KdV), extended KdV (KdV2), fifth-order KdV, and Gardner equation (combined KdV–mKdV). The first is obtained for $\alpha = O(\beta)$, $\delta = O(\beta)$, the second for $\alpha = O(\beta)$, $\delta = O(\beta^2)$, the third for $\alpha = O(\beta^2)$, $\delta = O(\beta^2)$, and the fourth for $\beta = O(\alpha^2)$, $\delta = O(\beta^2)$. In all cases, the generalized wave equations could be derived only for a particular class of bottom functions, namely the piecewise linear ones. Moreover, the additional term originating from the uneven bottom has the same form in all four generalized wave equations. On the way to these results, we derived corresponding sets of the Boussinesq equations, which are valid for bottoms of arbitrary shapes. The parameters α , β , δ have the following meaning. Besides standard small parameters $\alpha = \frac{a}{H}$ and $\beta = \left(\frac{H}{l}\right)^2$ we introduced the third one, defined as $\delta = \frac{a_h}{H}$. Here a represents the wave amplitude, H —average depth of the basin, l —average wavelength and a_h —amplitude of bottom variations. For the perturbation approach all of them should be small. Only in the case of KdV2, which contains terms second order in α , β , can these parameters take larger values. All derived equations are written in scaled dimensionless variables. For all details of the derivations of Boussinesq equations and final KdV-type equations for the uneven bottom, we refer to the article [3].

In numerical calculations, we adapted the finite difference code (FDM), which proved to be very efficient in our earlier papers [3–7]. In all simulations, we considered long time evolution over the bottom in a shape of an extended bump

$$h(x) = \frac{1}{2} (\tanh[0.055(x - 50)] + \tanh[0.055(220 - x)]) . \quad (1)$$

Two cases of initial conditions are considered. In the first case, the initial condition is taken in the form of a soliton solution appropriate for the particular equation. In the second case, it is assumed that the initial wave is in the form of a Gaussian with a deflection opposite to the soliton (e.g., depression instead elevation or vice versa) and with the mass (volume) three times the soliton mass. In the figures presenting the simulations, the first case is always displayed in the upper row, and the second case is shown in the lower row. The left column always shows the time evolution obtained according to the particular single wave equation, whereas the right one shows the time evolution obtained according to the particular set of the Boussinesq equations.

It is worth emphasizing that numerical studies on KdV-type equations still belong to active research fields (see, e.g., [8, 9]). An extensive discussion of problems presented in this article, with exact derivations and many other numerical examples, was referred to in [10].

2 Generalized KdV Equation

When the parameters α, β, δ are of the same order, and terms only up to first order are retained, one obtains Boussinesq equations in the form [3]

$$\eta_t + w_x + \alpha(\eta w)_x - \frac{1}{6}\beta w_{3x} - \delta(hw)_x = 0, \tag{2}$$

$$w_t + \eta_x + \alpha w w_x - \frac{1}{2}\beta w_{2xt} = 0. \tag{3}$$

Elimination of w from (2)–(3) in order to obtain a single wave equation for η appears to be possible only when $h_{2x} = 0$, that is when the bottom function is the piecewise linear one. In such case the system (2)–(3) can be made compatible, and can be reduced to the single KdV-type equation

$$\eta_t + \eta_x + \frac{3}{2}\alpha\eta\eta_x + \frac{1}{6}\beta\eta_{3x} - \frac{1}{4}\delta(2h\eta_x + h_x\eta) = 0. \tag{4}$$

Since Boussinesq equations do not require the condition $h_{2x} = 0$, the bottom function h can be arbitrary. From this point of view Boussinesq equations (2)–(3) are more general (more fundamental) than the single wave equation (4). For the flat bottom case, when $\delta = 0$, Eq. (4) reduces to the usual Korteweg-de Vries equation. It is natural to consider a motion in which a KdV soliton, formed on the flat bottom region,

$$\eta(x, t) = A \operatorname{sech}^2 \left[\sqrt{\frac{3\alpha}{4\beta}} A \left(x - t \left(1 + A \frac{\alpha}{2} \right) \right) \right] = A \operatorname{sech}^2 [B(x - vt)]. \tag{5}$$

enters a region with the varying bottom. Therefore, in the top row of Fig. 1, the initial condition has the form of the KdV soliton (5). Here and in the following, A denotes soliton's amplitude. In the calculation, $A = 1$ was used.

We were curious about the answer to the following question: What will be the time evolution of the wave in which the initial shape is drastically different from that of the soliton? So, for simulations shown in the bottom row of Fig. 1, the initial condition is chosen as the Gaussian with the triple volume of the KdV soliton, the same velocity, the same amplitude but the opposite deflection. The soliton's volume is equal to $\int_{-\infty}^{\infty} \eta(x, 0) dx$. This value determines the width of the Gaussian when the amplitude is given. Precisely, the initial profile is taken as $u(x, 0) = -A e^{(x-x_0)^2/\sigma^2}$.

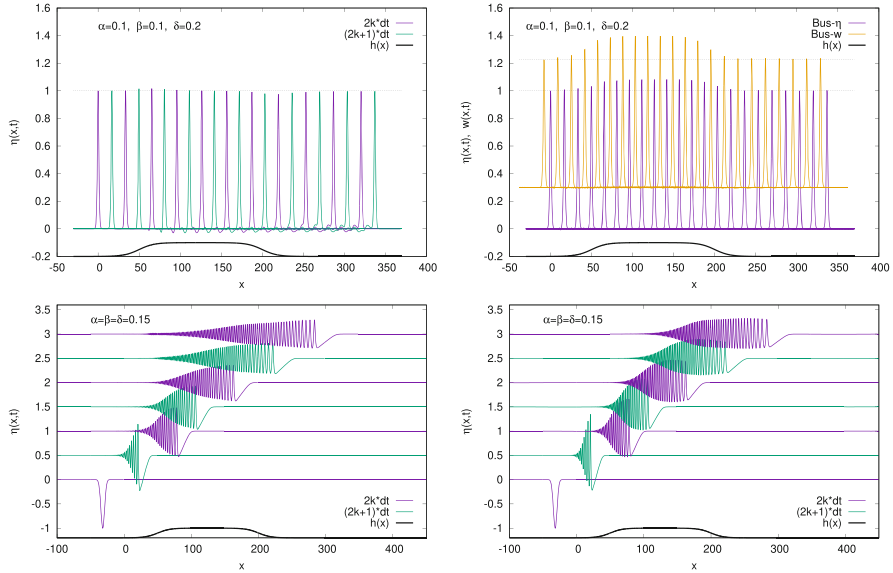


Fig. 1 Top: Left part—time evolution of the KdV soliton (5) obtained according to the KdV-type equation (4) for the bottom given by (1) with $\delta = 0.2$. Subsequent profiles correspond to times $t_n = n * 16$, with $n = 0, 1, \dots, 21$. Right part—the same obtained according to the Boussinesq set (2)–(3). To avoid overlaps, profiles of w function are shifted by 0.3 up and by 8 left. The shape of the bottom function is drawn in an arbitrary scale. Bottom: Left part—time evolution obtained according to the KdV-type equation (4). Initial profile is a Gaussian with the triple volume of the KdV soliton, the same velocity, the same amplitude but the opposite deflection. Here, time step between the consecutive profiles (shifted up by 0.5) is $dt = 64$. Right part—the same obtained according to the Boussinesq set (2)–(3)

3 Generalized KdV2 Equation

When $\alpha = O(\beta)$, $\delta = O(\beta^2)$, keeping terms up to second order one obtains Boussinesq equations in the following form [3]

$$\eta_t + w_x + \alpha(\eta w)_x - \frac{1}{6}\beta w_{3x} - \frac{1}{2}\alpha\beta(\eta w_{2x})_x + \frac{1}{120}\beta^2 w_{5x} - \delta(hw)_x = 0, \tag{6}$$

$$w_t + \eta_x + \alpha w w_x - \frac{1}{2}\beta w_{2xt} + \frac{1}{24}\beta^2 w_{4xt} + \frac{1}{2}\alpha\beta(-2(\eta w_{xt})_x + w_x w_{2x} - w w_{3x}) = 0. \tag{7}$$

Also, in this case, the elimination of w appears possible when w has a piecewise linear form. Then one can make Eqs. (6)–(7) compatible and obtain the single wave equation

$$\eta_t + \eta_x + \alpha \frac{3}{2} \eta \eta_x + \beta \frac{1}{6} \eta_{3x} - \alpha^2 \frac{3}{8} \eta^2 \eta_x + \alpha \beta \left(\frac{23}{24} \eta_x \eta_{2x} + \frac{5}{12} \eta \eta_{3x} \right) + \beta^2 \frac{19}{360} \eta_{5x} - \frac{1}{4} \delta (2h \eta_x + h_x \eta) = 0. \tag{8}$$

The term originating from the uneven bottom has the same form as that in (4), but now it belongs to terms of second order. When $\delta = 0$, that is for the flat bottom, Eq. (8) reduces to the well known *extended KdV* (KdV2) equation [11].

In [4], we showed that KdV2 equation has the single soliton solution of the same form as the KdV soliton, but with slightly different coefficients when amplitudes are the same. Precisely, $B_{KdV} = \sqrt{\frac{3}{4} \frac{\alpha}{\beta}} A$, whereas $B_{KdV2} \approx \sqrt{0.6 \frac{\alpha}{\beta}} A$, and $v_{KdV} = 1 + \frac{\alpha}{2} A$, whereas $v_{KdV2} \approx 1.11455$ is fixed. Moreover, $A_{KdV2} \approx \frac{0.02424}{\alpha}$ [4], therefore in simulations we used $\alpha = 0.2424$ to have KdV2 soliton with an amplitude equal to 1. With $A = 1$, such soliton was chosen as the initial condition for numerical evolution presented in the top row of Fig. 2. In the bottom row of Fig. 2, the initial condition is the Gaussian with the triple volume of the KdV2 soliton, the same velocity, but the amplitude equal to -1 .

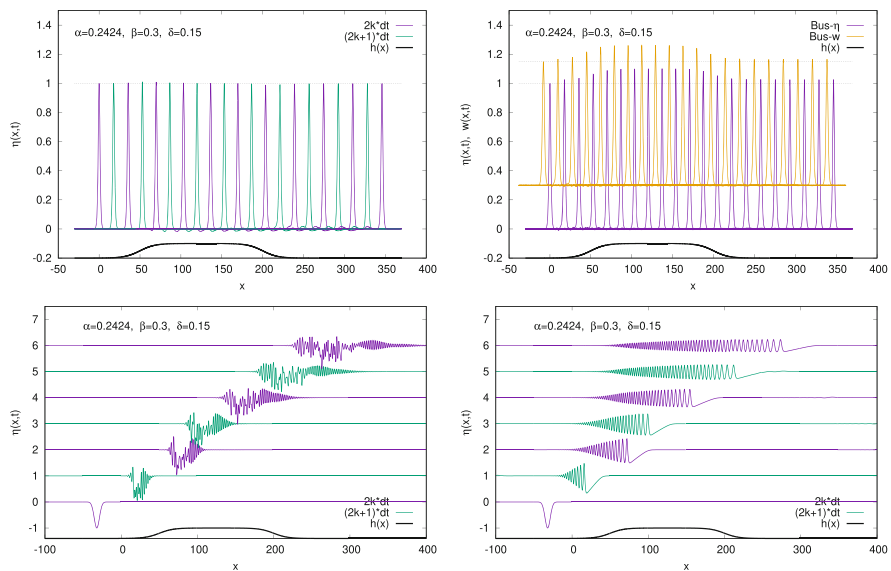


Fig. 2 The same as in Fig. 1, but for the extended KdV (KdV2) Eq. (8)—left part and for the corresponding Boussinesq set (6)–(7)

4 Generalized Fifth-Order KdV-Type Equations

When α and δ are both of the order of β^2 , Boussinesq equations (obtained by keeping all terms up to second order) receive the form [3]

$$\eta_t + w_x - \frac{1}{6}\beta w_{3x} + \alpha(w\eta)_x + \frac{1}{120}\beta^2 w_{5x} - \delta(hw)_x = 0, \quad (9)$$

$$w_t + \eta_x - \beta \left(\frac{1}{2}w_{2xt} + \tau\eta_{3x} \right) + \alpha w w_x + \frac{1}{24}\beta^2 w_{4xt} = 0. \quad (10)$$

Like in the previous cases, elimination of the w function (possible when h is a piecewise linear function) leads to the single wave equation

$$\begin{aligned} \eta_t + \eta_x + \frac{3}{2}\alpha\eta\eta_x + \beta\frac{1-3\tau}{6}\eta_{3x} + \beta^2\frac{19-30\tau-45\tau^2}{360}\eta_{5x} \\ - \frac{1}{4}\delta(2h\eta_x + h_x\eta) = 0. \end{aligned} \quad (11)$$

In (9)–(11), the Bond number $\tau = \frac{T}{\rho gh^2}$ appears, where T is the surface tension coefficient. For surface gravity waves, this term can be safely neglected, since $\tau < 10^{-7}$ (when the fluid depth is of the order of meters), but it is important for waves in thin fluid layers. For the flat bottom ($\delta = 0$), Eq. (11) reduces to a *fifth-order KdV-type equation* derived by Hunter and Sheurle in [12] as a model equation for gravity-capillary shallow water waves of small amplitude. It is known [13] that a fifth-order KdV-type equation has a soliton solution in the form

$$\eta(x, t) = A \operatorname{sech}^4[B(x - vt)], \quad (12)$$

where coefficients A , B , v are known functions of the equation parameters α , β , τ . Real soliton solutions require $\tau > \frac{1}{3}$. So, for initial condition in the top row of Fig. 3 we took the soliton (12) of the fifth-order KdV equation for $\alpha = 0.24$, $\beta = 0.3$ and $\tau = 0.35$. For this value of τ the amplitude A in (12) is negative, therefore the soliton has the shape of a depression. The parameter $\delta = 0.15$ was used in the calculations.

5 Generalized Gardner Equations

When both β and δ are of the order of α^2 and terms up to second order are retained, the resulting Boussinesq equations receive the form [3]

$$\eta_t + w_x + \alpha(\eta w)_x - \frac{1}{6}\beta w_{3x} - \delta(hw)_x = 0, \quad (13)$$

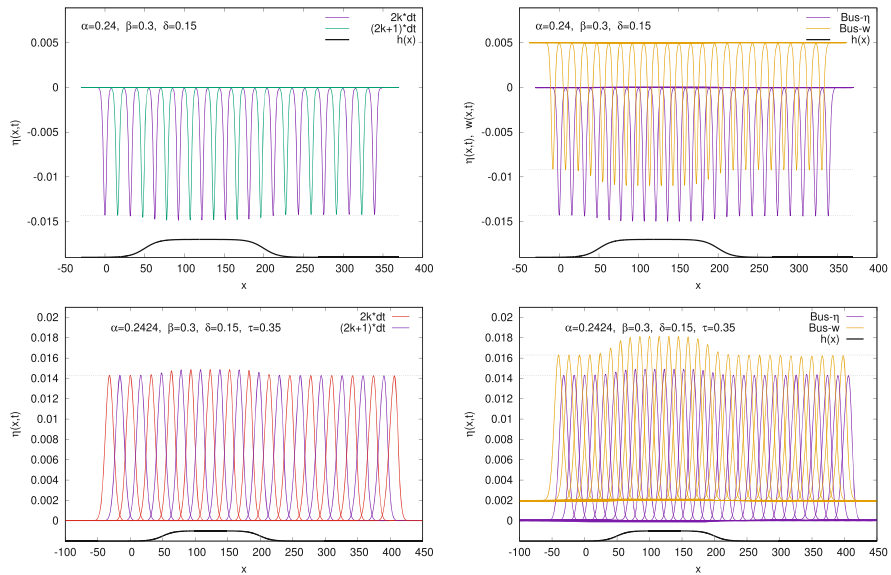


Fig. 3 The same as in Fig. 1 but for the 5th order KdV equation (11)—left part and for the corresponding Boussinesq set (9)–(10)—right part

$$w_t + \eta_x + \alpha w w_x - \beta \left(\tau \eta_{3x} + \frac{1}{2} w_{2xt} \right) = 0. \tag{14}$$

Elimination of the w function (possible when h is a piecewise linear function) leads to the single wave equation

$$\eta_t + \eta_x + \frac{3}{2} \alpha \eta \eta_x + \alpha^2 \left(-\frac{3}{8} \eta^2 \eta_x \right) + \frac{1 - 3\tau}{6} \beta \eta_{3x} - \frac{1}{4} \delta (2h \eta_x + h_x \eta) = 0, \tag{15}$$

which for $\delta = 0$ reduces to the well known Gardner equation (combined KdV-mKdV equation). It is well known, e.g., [14, 15], that for Gardner equation, there exists a one-parameter family of analytic solutions in the form

$$\eta(x, t) = \frac{A}{1 + B \cosh[(x - vt)/\Delta]}. \tag{16}$$

When Δ is chosen as the independent parameter, the other three coefficients determining the solution, A, B, v , are functions of the parameters of the equation α, β, τ , and the arbitrary Δ . When very small effects from surface tension are neglected, Gardner equation can be used for shallow water gravity waves by setting $\tau = 0$. On the other hand, when $\tau > \frac{1}{3}$, Gardner equation applies for surface waves in thin fluid layers.

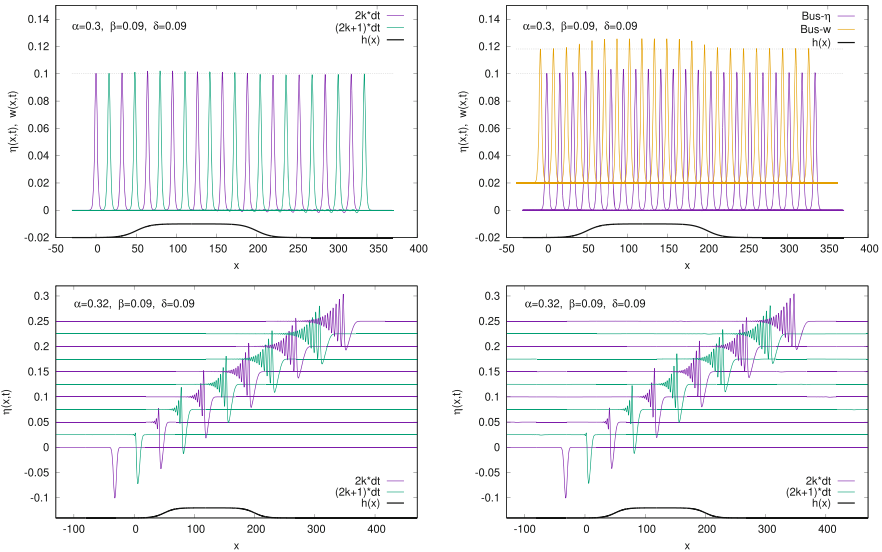


Fig. 4 The same as in Fig. 1 but for the Gardner equation (15)—left part and for the corresponding Boussinesq set (13)–(14)—right part. Parameters $\alpha = 0.3, \beta = \delta = 0.09, \tau = 0$ of the equation were used. The value $\Delta^2 = 1$ was chosen for the initial soliton (16)

5.1 Shallow Water Case, Small τ

In Fig. 4, we present simulations of the time evolution according to Eq. (15)—left, and (13)–(14)—right, with $\tau = 0$. According to the same convention initial conditions in the upper row correspond to soliton of Gardner equation (16) and to Gaussian with triple soliton’s volume and opposite amplitude in the lower row.

5.2 Thin Liquid Layer Case, $\tau > \frac{1}{3}$

In this case, the coefficient $\frac{1-3\tau}{6}\beta$ is negative, which implies a negative amplitude A of the Gardner soliton. In Fig. 5, we present the result of numerical simulations in this case. Parameters $\alpha = 0.3, \beta = \delta = 0.09, \tau = 1$ of the equations were used.

6 Do We Have Chaos in KdV2 Case?

In cases when the initial conditions were substantially different from appropriate solitons, the time evolutions according to KdV-type equations and the corresponding Boussinesq equations are qualitatively similar. The case of KdV2 is the only

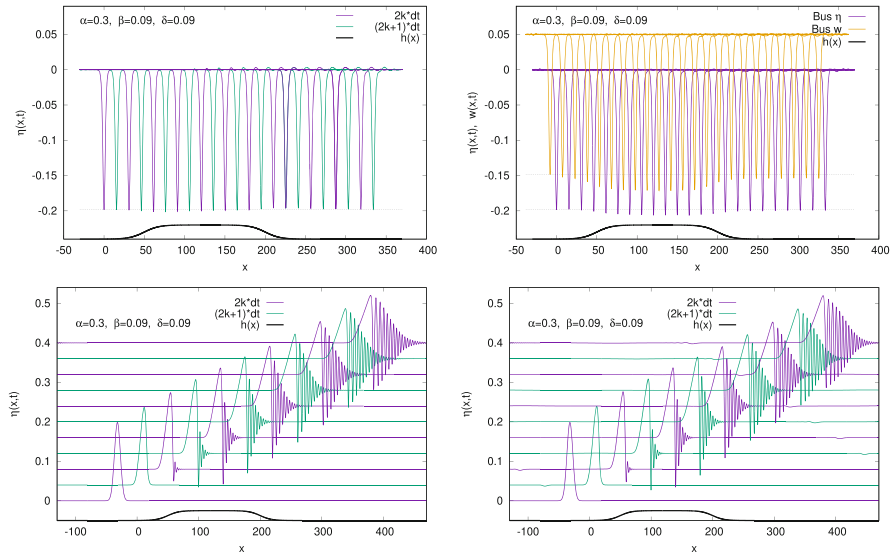


Fig. 5 The same as in Fig. 4 but when $\tau = 1$

exception. It seems that the reason is the following. The KdV, fifth-order KdV, and Gardner equations are **integrable**. Their exact solutions form one-parameter families. Contrary, the KdV2 equation (Eq. (8) with $\delta = 0$) is **non-integrable**. Moreover, as found in [4], given α, β determine the unique soliton. Therefore, the motion of the wave, initially much different from this soliton, could be **chaotic**. In Fig. 6, we present a preliminary study of this property.

Define the distance between two different trajectories $\eta_1(x, t)$ and $\eta_2(x, t)$ by $M_1(t) = \int_{-\infty}^{\infty} |\eta_1(x, t) - \eta_2(x, t)| dx \approx \sum_{i=1}^N |\eta_1(x_i, t) - \eta_2(x_i, t)| dx$. For $\eta_1(x, t = 0)$ we chose the Gaussian distortion having the same amplitude $A_1 = 1$ as the KdV2 soliton, but with the width σ_1 ensuring multiple soliton's volume. For $\eta_2(x, t = 0)$ we chose the similar Gaussian form but with parameters slightly changed, namely with $A_2 = A_1(1 + \varepsilon)$ and $\sigma_2 = \sigma_1/(1 + \varepsilon)$, which ensures the same initial volume. In both cases the initial velocity is chosen the same as the velocity of KdV2 soliton. Figure 6 shows that distances between considered trajectories seem to increase exponentially at least for times considered. Analogous results are obtained for $M_2 = \int_{-\infty}^{\infty} [\eta_1(x, t) - \eta_2(x, t)]^2 dx$ measure. More detailed studies of this problem are in preparation.

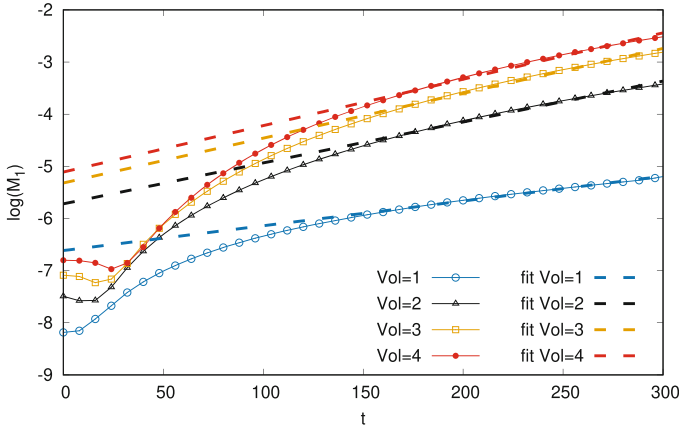


Fig. 6 Time dependence of measures M_1 for $\varepsilon = 10^{-4}$ and different volumes of initial conditions in forms of Gaussians with different volumes

7 Conclusions

In all considered cases for the uneven bottom, the nonlinear wave equations (4), (8), (11), and (15) are non-integrable. Therefore the influence of the bottom variations on surface waves has to be analyzed numerically. The main property of the results is that the uneven bottom’s influence on the surface wave $\eta(x, t)$ obtained from Boussinesq equations is always substantially more significant than that obtained from single KdV-type wave equations. It is worth emphasizing that Boussinesq equations are valid for an arbitrary form of the bottom function, whereas the compatibility condition, necessary for the existence of single KdV-type wave equations, requires $\frac{d^2h}{dx^2} = 0$. On the other hand, in numerics, the bottom function h enters only by its values in the mesh points, as it is a piecewise linear function.

In all cases discussed above, when the initial conditions were chosen in the form of soliton solutions to particular wave equations, the wave profiles appear extremely resistant to disturbances introduced by varying bottom.

References

1. G.I. Burde, A. Sergyeyev, Ordering of two small parameters in the shallow water wave problem. *J. Phys. A Math. Theor.* **46**, 075501 (2013). <https://doi.org/10.1088/1751-8113/46/7/075501>
2. R.R. Rosales, G.C. Papanicolau, Gravity waves in a channel with a rough bottom. *Stud. Appl. Math.* **68**(2), 89–102 (1983). <https://doi.org/10.1002/sapm198368289>
3. A. Karczewska, P. Rozmej, Can simple KdV-type equations be derived for shallow water problem with bottom bathymetry? *Commun. Nonlinear Sci. Numer. Simulat.* **82**, 105073 (2020). <https://doi.org/10.1016/j.cnsns.2019.105073>

4. A. Karczewska, P. Rozmej, E. Infeld, Shallow water soliton dynamics beyond Korteweg-de Vries equation. *Phys. Rev. E* **90**, 012907 (2014). <https://doi.org/10.1103/PhysRevE.90.012907>
5. A. Karczewska, P. Rozmej, E. Infeld, Energy invariant for shallow-water waves and the Korteweg-de Vries equation: Doubts about the invariance of energy. *Phys. Rev. E* **92**, 053202 (2015). <https://doi.org/10.1103/PhysRevE.92.053202>
6. A. Karczewska, P. Rozmej, E. Infeld, G. Rowlands, Adiabatic invariants of the extended KdV equation. *Phys. Lett. A* **381**, 270–275 (2017). <https://doi.org/10.1016/j.physleta.2016.11.035>
7. G. Rowlands, P. Rozmej, E. Infeld, A. Karczewska, Single soliton solution to the extended KdV equation over uneven depth. *Eur. Phys. J. E* **40**, 100 (2017). <https://doi.org/10.1140/epjje/i2017-11591-7>
8. T. Ak, Numerical experiments for long nonlinear internal waves via Gardner equation with dual-power law nonlinearity. *Int. J. Mod. Phys. C* **30**, 1950066 (2019). <https://doi.org/10.1142/S0129183119500669>
9. T. Ak, A. Saha, S. Dhawan, A.H. Kara, Investigation of Coriolis effect on oceanic flows and its bifurcation via geophysical Korteweg–de Vries equation. *Numer. Methods Part Diff. Eq.* **36**, 1234–1253 (2020). <https://doi.org/10.1002/num.22469>
10. A. Karczewska, P. Rozmej, Generalized KdV-type equations versus Boussinesq's equations for uneven bottom – numerical study (2020). arXiv:2007.01267
11. T.R. Marchant, N.F. Smyth, The extended Korteweg-de Vries equation and the resonant flow of a fluid over topography. *J. Fluid. Mech.* **221**, 263–288 (1990). <https://doi.org/10.1017/S0022112090003561>
12. J.K. Hunter, J. Scheurle, Existence of perturbed solitary wave solutions to a model equation for water waves. *Physica D* **32**, 253–268 (1988). [https://doi.org/10.1016/0167-2789\(88\)90054-1](https://doi.org/10.1016/0167-2789(88)90054-1)
13. B. Dey, A. Khare, C.N. Kumar, Stationary solitons of the fifth order KdV-type. *Equations and their stabilization. Phys. Lett. A* **223**, 449–452 (1996). [https://doi.org/10.1016/S0375-9601\(96\)00772-4](https://doi.org/10.1016/S0375-9601(96)00772-4)
14. R. Grimshaw, E. Pelinovsky, T. Talipova, Solitary wave transformation in medium with sign-variable quadratic nonlinearity and cubic nonlinearity. *Physica D* **132**, 40–62 (1999). [https://doi.org/10.1016/S0167-2789\(99\)00045-7](https://doi.org/10.1016/S0167-2789(99)00045-7)
15. L. Ostrovsky, E. Pelinovsky, V. Shrira, Y. Stepanyants, Beyond the KdV: post-explosion development. *CHAOS* **25**, 097620 (2015). <https://doi.org/10.1063/1.4927448>

Modified Non-linear Schrödinger Models, $\mathcal{CP}_s\mathcal{T}_d$ Symmetry, Dark Solitons, and Infinite Towers of Anomalous Charges



Harold Blas, Martín Cerna, and Luis dos Santos

1 Introduction

Some non-linear field theory models with important physical applications and solitary wave solutions are not integrable. Recently, some deformations of integrable models, such as sine-Gordon, Korteweg-de Vries, and non-linear Schrödinger models [1–4], which exhibit soliton-type properties, have been put forward. Quasi-integrability properties of the deformations of the integrable models have recently been examined in the frameworks of the anomalous zero-curvature formulations [1, 4, 5] and the deformations of the Riccati-type pseudo-potential approach [2, 3, 6]. Recently, it has been considered the properties of the modified (focusing) non-linear Schrödinger model with bright solitons [6]. Here we tackle the problem of constructing, analytically and numerically, new towers of anomalous charges for the modified (defocusing) non-linear Schrödinger model with dark solitons; so extending the results of [5] by providing novel infinite towers of quasi-conservation laws. Both types of models (focusing and defocusing) differ in the relevant signs (+/–) of their coupling constants and the boundary conditions (b.c.) imposed on their soliton solutions. So, in the focusing (defocusing) case one has bright (dark) solitons with vanishing (non-vanishing) b.c..

H. Blas (✉)
Instituto de Física, UFMT, Cuiabá, MT, Brazil
e-mail: blas@ufmt.br

M. Cerna
Departamento de Matemática, FC-UNASAM, Huaraz, Peru
e-mail: bcernam@unasam.edu.pe

L. dos Santos
CEFET-RJ, Campus Angra dos Reis, RJ, Brazil
e-mail: luis.santos@cefet-rj.br

2 Quasi-Conservation Laws and Anomalous Charges

Consider the modified non-linear Schrödinger models (MNLS)

$$i \partial_t \psi(x, t) + \partial_x^2 \psi(x, t) - \left[\frac{\delta V(|\psi|^2)}{\delta |\psi|^2} \right] \psi(x, t) = 0, \tag{1}$$

where $\psi \in C$ and $V : R_+ \rightarrow R$ is the deformed potential.

Let us consider a special space-time reflection around a fixed point (x_Δ, t_Δ) as a symmetry of soliton-type solutions of the model

$$\tilde{\mathcal{P}} : (\tilde{x}, \tilde{t}) \rightarrow (-\tilde{x}, -\tilde{t}); \quad \tilde{x} = x - x_\Delta, \quad \tilde{t} = t - t_\Delta. \tag{2}$$

The transformation $\tilde{\mathcal{P}}$ defines a shifted parity \mathcal{P}_s for the spatial variable x and a delayed time reversal \mathcal{T}_d for the time variable t . It is assumed that the ψ solution of the deformed NLS model (1) possesses the following property under the transformation (2)

$$\tilde{\mathcal{P}} \equiv \mathcal{P}_s \mathcal{T}_d, \quad \tilde{\mathcal{P}}(\psi) = e^{i\delta} \bar{\psi}, \quad \tilde{\mathcal{P}}(\bar{\psi}) = e^{-i\delta} \psi, \quad \bar{\psi} \equiv \psi^*, \quad \delta = \text{constant}. \tag{3}$$

In [6] it has been provided a method to construct an infinite number of towers of quasi-conservation laws. Here we consider the lowest order and the first three towers of quasi-conservation laws and discuss them in the context of the defocusing NLS with dark soliton solutions.

The first order charge and its generalization becomes¹

$$\frac{d}{dt} Q_1(t) = \int dx \hat{\alpha}_1, \quad \hat{\alpha}_1 \equiv 2F^{(1)}(I) \partial_x [\partial_x \bar{\psi} \partial_x \psi] \tag{4}$$

$$Q_1(t) = \int_{-\infty}^{\infty} dx \left[iF(I) \frac{\bar{\psi} \partial_x \psi - \psi \partial_x \bar{\psi}}{\bar{\psi} \psi} \right], \quad I \equiv |\psi|^2, \tag{5}$$

where $F^{(n)}(I) \equiv \frac{d^n}{dI^n} F(I)$. For $F = 1$ one has $\hat{\alpha}_1 = 0$ in (4) and the relevant charge Q_1^{top} turns out to be the topological charge of the dark soliton's phase. For arbitrary F and the special solutions satisfying the parity property (2)–(3) one has

$$\int_{-\tilde{t}}^{\tilde{t}} dt \int_{-\tilde{x}}^{\tilde{x}} dx \hat{\alpha}_1 = 0, \quad \text{for } \tilde{t} \rightarrow \infty, \quad \tilde{x} \rightarrow \infty. \tag{6}$$

Therefore, integrating in t on the b.h.s. of (4) one can get

$$Q_1(\tilde{t}) = Q_1(-\tilde{t}), \quad \tilde{t} \rightarrow \infty. \tag{7}$$

¹Formally, one can assume $\text{deg}(\psi^{\pm 1}) = \text{deg}(\bar{\psi}^{\pm 1}) = \pm 1, \text{deg}(\partial_x) = \frac{1}{2} \text{deg}(\partial_t) = 1$.

The special function $F(I) = e^{-I^2}$ has been used in [7] to study the first integrals in the study of soliton-gas and integrable turbulence.

A tower of infinite number of quasi-conservation laws can be constructed on top of a given lowest order exact (quasi-)conservation law. Next, we will present the first few of them.

First Tower

One can construct a tower of quasi-conserved charges on top of the exact conserved charge $\mathcal{Q}_1 = \frac{1}{2} \int dx (\bar{\psi} \psi)$. So, one has

$$\frac{d}{dt} \mathcal{Q}_n = \int dx \hat{\beta}_n; \quad \hat{\beta}_n \equiv -\frac{1}{2n} \partial_x [(\bar{\psi} \psi)^{n-1}] i (\bar{\psi} \partial_x \psi - \psi \partial_x \bar{\psi}), \quad n = 2, 3, \dots \quad (8)$$

$$\mathcal{Q}_n = \frac{1}{2n} \int dx (\bar{\psi} \psi)^n. \quad (9)$$

For the field ψ satisfying (2)–(3) the anomaly density $\hat{\beta}_n$ possesses an odd parity for any n . Therefore, one must have the vanishing of the space-time integral of the anomaly $\hat{\beta}_n$ and then, the asymptotically conserved charges satisfy

$$\mathcal{Q}_n(\tilde{t}) = \mathcal{Q}_n(-\tilde{t}), \quad \tilde{t} \rightarrow \infty, \quad n = 2, 3, \dots \quad (10)$$

Second Tower

The next tower of quasi-conserved charges is constructed on top of the exact conserved charge $\tilde{\mathcal{Q}}_1(t) = i \int dx (\bar{\psi} \partial_x \psi - \psi \partial_x \bar{\psi})$. So, one has

$$\begin{aligned} \frac{d}{dt} \tilde{\mathcal{Q}}_n &= \int dx \hat{\gamma}_n; \quad \hat{\gamma}_n \equiv -\frac{(i)^n}{n} \partial_x [(\bar{\psi} \partial_x \psi - \psi \partial_x \bar{\psi})^{n-1}] \\ &\times \left[2\partial_x \psi \partial_x \bar{\psi} - \psi \partial_x^2 \bar{\psi} - \bar{\psi} \partial_x^2 \psi + 2V^{(1)} |\psi|^2 - 2V \right], \end{aligned} \quad (11)$$

$$\tilde{\mathcal{Q}}_n(t) = \int dx \frac{(i)^n}{n} (\bar{\psi} \partial_x \psi - \psi \partial_x \bar{\psi})^n, \quad n = 2, 3, \dots \quad (12)$$

Similarly, one has the asymptotically conserved charges

$$\tilde{\mathcal{Q}}_n(\tilde{t}) = \tilde{\mathcal{Q}}_n(-\tilde{t}), \quad \tilde{t} \rightarrow \infty, \quad n = 2, 3, \dots \quad (13)$$

Third Tower

The next tower of quasi-conserved charges is constructed on top of a fourth order one, which is itself quasi-conserved. One has

$$\frac{d}{dt} K_n = \int dx \hat{\delta}_n, \quad n = 1, 2, \dots \quad (14)$$

$$K_n = \int dx [\partial_x \bar{\psi} \partial_x \psi]^n. \tag{15}$$

The general form of the anomalies $\hat{\delta}_n$ are provided in [6]. Below we will consider the case $n = 1$

$$\hat{\delta}_1 \equiv i[(\bar{\psi} \partial_x \psi)^2 - (\psi \partial_x \bar{\psi})^2]V^{(2)}(I), \quad V^{(2)} \equiv \frac{d^2}{dI^2}V(I). \tag{16}$$

Regarding the standard (defocusing) NLS model one can argue that all the anomalies will vanish upon integration in space-time provided that the N-dark solitons satisfy (2)–(3). Consequently, their associated charges will be asymptotically conserved even for the standard NLS model. In fact, these types of solutions have been constructed in [6] for N-bright solitons. We already have those results for standard NLS dark solitons and they will appear elsewhere. So, those examples show an analytical, and not only numerical, demonstration of the vanishing of the space-time integrals of the anomalies associated to the infinite towers of infinitely many quasi-conservation laws in soliton theory.

3 Numerical Simulations

We consider the non-integrable cubic-quintic NLS (CQNLS) model

$$i \frac{\partial \psi(x, t)}{\partial t} + \frac{\partial^2 \psi(x, t)}{\partial x^2} - \left(2\eta |\psi(x, t)|^2 - \frac{\epsilon}{2} |\psi(x, t)|^4\right) \psi(x, t) = 0, \tag{17}$$

where $\eta > 0$, $\epsilon \in R$. The model (17) possesses a solitary wave solution of the form $\psi(x, t) = \Phi(z)\exp[i\Theta(z) + i\omega t]$, $z = x - vt$ (see [5])

$$\Phi_{\pm}^2(z) = \frac{\xi_1 + r\xi_2 \tanh^2 [k^{\pm}(z - z_0)]}{1 + r \tanh^2 [k^{\pm}(z - z_0)]} \tag{18}$$

$$\Theta_{\pm}(z) = \mp \arctan \left[\sqrt{r \frac{\xi_2}{\xi_1}} \tanh [k^{\pm}(z - z_0)] \right], \tag{19}$$

where

$$r \equiv \frac{|\psi_0|^2 - \xi_1}{\xi_2 - |\psi_0|^2}, \quad k^{\pm} \equiv \sqrt{\frac{|\epsilon|}{6}} \sqrt{(\pm)(\xi_2 - |\psi_0|^2)(|\psi_0|^2 - \xi_1)}, \tag{20}$$

$$\xi_1 = \frac{B - \sqrt{B^2 - 6v^2\epsilon}}{2\epsilon}, \quad \xi_2 = \frac{B + \sqrt{B^2 - 6v^2\epsilon}}{2\epsilon}, \quad B \equiv 6\eta - 2\epsilon|\psi_0|^2. \tag{21}$$

Fig. 1 Collision of two-dark solitons of the CQNLS model (17) for $\epsilon = +0.005$, $|\psi_0| = 6$, $\eta = 2.5$. The initial solitons ($t_i =$ green line) travel with velocities $v_1 \approx -4.7\sqrt{2}$ (right soliton) and $v_2 \approx 13\sqrt{2}$ (left soliton), respectively. They completely overlap ($t_c =$ blue line) in their closest approximation and then transmit to each other. The dark solitons after collision are plotted as a red line (t_f)

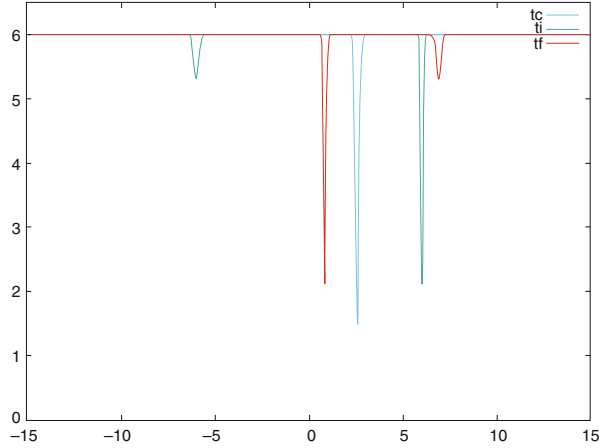
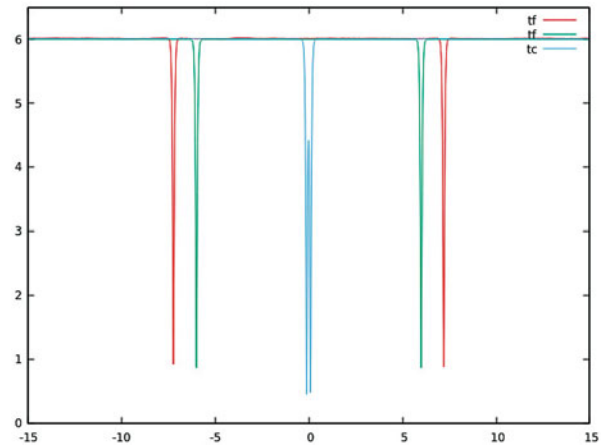


Fig. 2 Reflection of two-dark solitons of the cubic-quintic NLS model (17) plotted for $\epsilon = -0.01$, $|\psi_0| = 6$, $\eta = 2.5$. The initial solitons ($t_i =$ green line) travel in opposite direction with velocity $|v| \approx 1.97\sqrt{2}$. They partially overlap ($t_c =$ blue line) in their closest approximation and then reflect to each other. The dark solitons after collision are plotted as a red line (t_f)



The notations Φ_{\pm} and Θ_{\pm} correspond to $\epsilon > 0$ and $\epsilon < 0$, respectively. So, we will take two one-dark solitary waves located some distance apart as the initial condition for our numerical simulations of two-dark soliton collisions. Below, we numerically compute the space and space-time integrals of the anomaly densities $\hat{\alpha}_1$, $\hat{\beta}_2$, $\hat{\gamma}_2$, and $\hat{\delta}_1$, appearing in (4), (8), (11), and (16), respectively, for two type of two-soliton collisions of the CQNLS model (17) (Figs. 1 and 2).

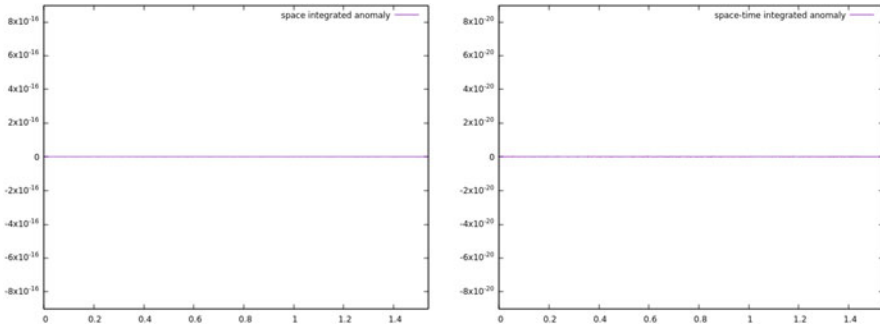


Fig. 3 The left figure shows the plot $\int_{-\tilde{x}}^{+\tilde{x}} \hat{\alpha}_1 dx$ vs t and the right one shows the plot $\int_{-\tilde{t}}^{+\tilde{t}} dt \int_{-\tilde{x}}^{+\tilde{x}} dx \hat{\alpha}_1$ vs t for the anomaly $\hat{\alpha}_1$ in (4) and for the 2-soliton collision of Fig. 1

3.1 Transmission of Two-Dark Solitons and Anomalous Charges

We numerically compute the space and space-time integrals of the anomaly densities $\hat{\alpha}_1$, $\hat{\beta}_2$, $\hat{\gamma}_2$, and $\hat{\delta}_1$, as shown in Figs. 3, 4, 5, and 6, respectively, for the transmission of two-dark solitons of the CQNLS model (17) as plotted in Fig. 1.

3.2 Reflection of Two-Dark Solitons and Anomalous Charges

Next, we numerically simulate the space and space-time integrals of the anomaly densities $\hat{\alpha}_1$, $\hat{\beta}_2$, $\hat{\gamma}_2$, and $\hat{\delta}_1$, as shown in Figs. 7, 8, 9, and 10, respectively, for the reflection of two-dark solitons of the CQNLS model (17) as plotted in Fig. 2.

Some comments are in order here. First, in our numerical simulations of the 2-dark soliton collisions of the CQNLS model (17) we have not observed appreciable emission of radiation during the collisions; so, it can be argued that the linear superposition of well separated two solitary waves of the CQNLS model is an adequate initial condition. Second, we have shown the vanishing of the space-time integrals of the anomaly densities $\hat{\alpha}_1$, $\hat{\beta}_2$, $\hat{\gamma}_2$ and $\hat{\delta}_1$, appearing in (4), (8), (11) and (16), respectively, within numerical accuracy. Third, we have performed extensive numerical simulations for a wide range of values in the parameter space; i.e., the deformation parameter $|\epsilon| < 1$ and coupling constant $\eta \approx 2.5$, several amplitudes and relative velocities for 2-soliton collisions, obtaining the vanishing of those anomalies, within numerical accuracy.

Sometimes the vanishing of the anomaly, within numerical accuracy, already happens for the space integration alone, e.g., as in Figs. 3 and 7. In fact, in Fig. 7 one has $\int_{-\tilde{x}}^{+\tilde{x}} dx \hat{\alpha}_1 \approx 10^{-16}$. This fact can be explained by some symmetry considerations of the anomalies [5] written in a new parametrization of the field

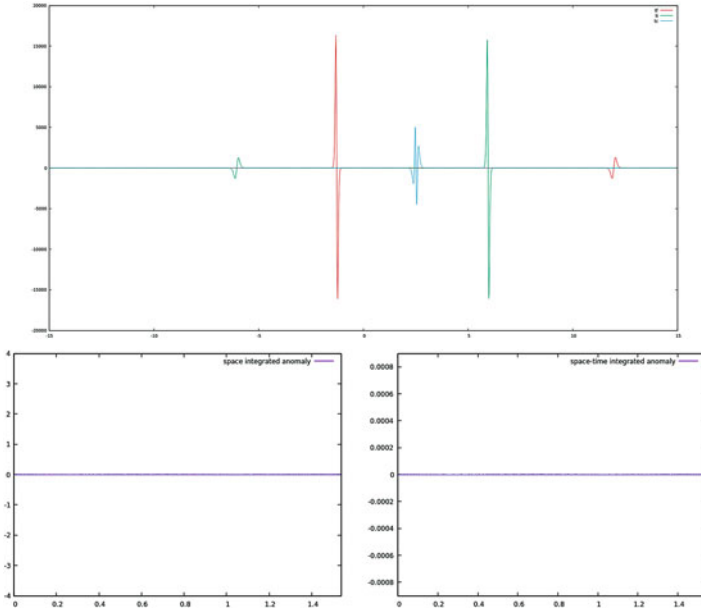


Fig. 4 Top figure shows the profile at initial (green), collision (blue) and final (red) times of the anomaly density $\hat{\beta}_2$ in (8) for the 2-soliton collision of Fig. 1. In the bottom the left figure shows the plot $\int_{-\tilde{x}}^{+\tilde{x}} \hat{\beta}_2 dx$ vs t and the right one shows the plot $\int_{-\tilde{t}}^{+\tilde{t}} dt \int_{-\tilde{x}}^{+\tilde{x}} dx \hat{\beta}_2$ vs t

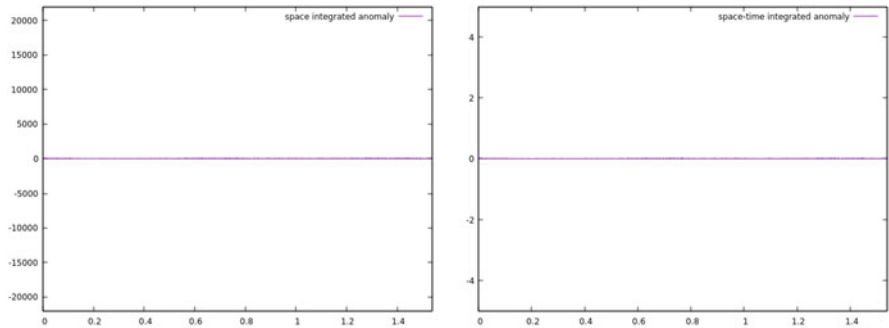


Fig. 5 The left figure shows the plot $\int_{-\tilde{x}}^{+\tilde{x}} \hat{\gamma}_2 dx$ vs t and the right one shows the plot $\int_{-\tilde{t}}^{+\tilde{t}} dt \int_{-\tilde{x}}^{+\tilde{x}} dx \hat{\gamma}_2$ vs t of the anomaly density $\hat{\gamma}_2$ in (11) for the 2-soliton collision of Fig. 1

ψ . So, let us write the anomaly density of Eq. (4) $\hat{\alpha}_1$ as

$$\hat{\alpha}_1 = 2F^{(1)}(I)\partial_x \left[\frac{(\partial_x I)^2}{4I} + \frac{1}{2}I(\partial_x \varphi)^2 \right], \quad \psi \equiv \sqrt{I}e^{i\varphi/2}. \quad (22)$$

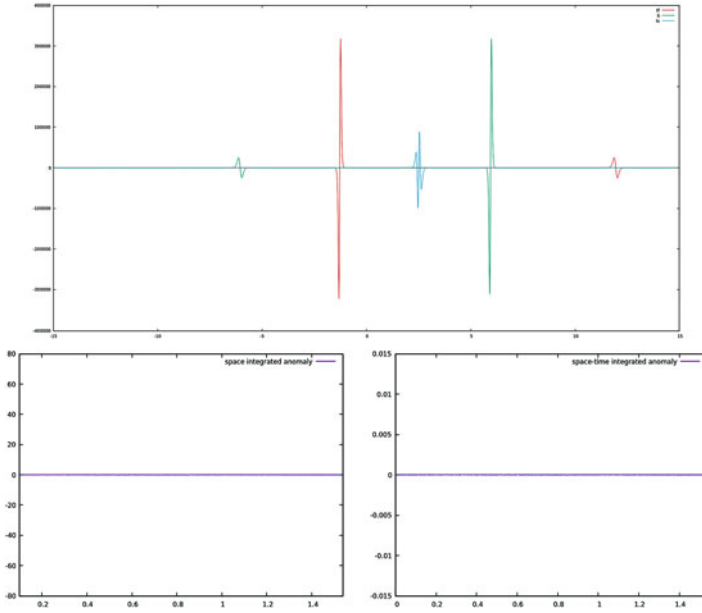


Fig. 6 Top figure shows the profile at initial (green), collision (blue) and final (red) times of the anomaly density $\hat{\delta}_1$ in (16) for the 2-soliton collision of Fig. 1. The bottom left shows the plot $\int_{-x}^{+x} \hat{\delta}_1 dx$ vs t and the right one shows the plot $\int_{-t}^{+t} dt \int_{-x}^{+x} dx \hat{\delta}_1$ vs t

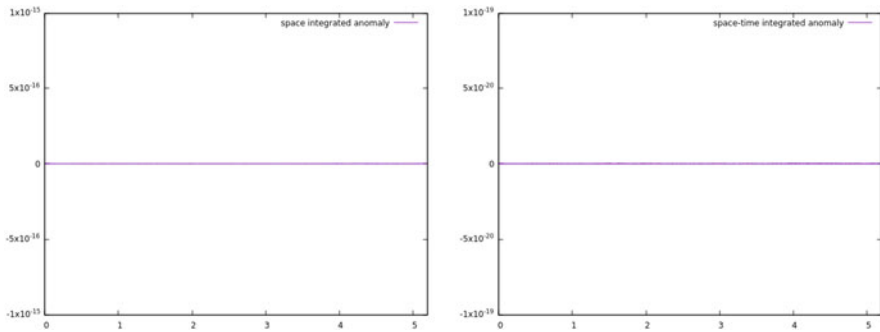


Fig. 7 The left figure shows the plot $\int_{-x}^{+x} \hat{a}_1 dx$ vs t and the right one shows the plot $\int_{-t}^{+t} dt \int_{-x}^{+x} dx \hat{a}_1$ vs t , for the anomaly \hat{a}_1 in (4) computed for the soliton reflection in Fig. 2

Notice that this anomaly density is an odd function under the space reflection $x \rightarrow -x$, provided that $I \rightarrow I$ and $\varphi \rightarrow \varphi$. In Fig 2. for the collision of two-dark solitons one has the plot of the modulus $|\psi| = \sqrt{I}$ for three successive times which shows this type of symmetry for each time.

On the other hand, the vanishing $\int_{-x}^{+x} dx \hat{a}_1 \approx 10^{-16}$ in Fig. 3 might happen for some other reasons than the existence of some symmetry arguments as above,

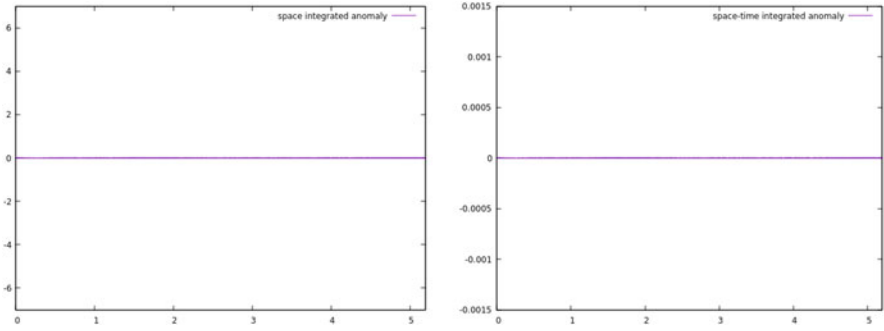


Fig. 8 The left figure shows the plot $\int_{-\tilde{t}}^{+\tilde{x}} \hat{\beta}_2 dx$ vs t and the right one shows the plot $\int_{-\tilde{t}}^{+\tilde{x}} dt \int_{-\tilde{x}}^{+\tilde{x}} dx \hat{\beta}_2$ vs t for the anomaly $\hat{\beta}_2$ in (8) computed for the soliton reflection in Fig. 2

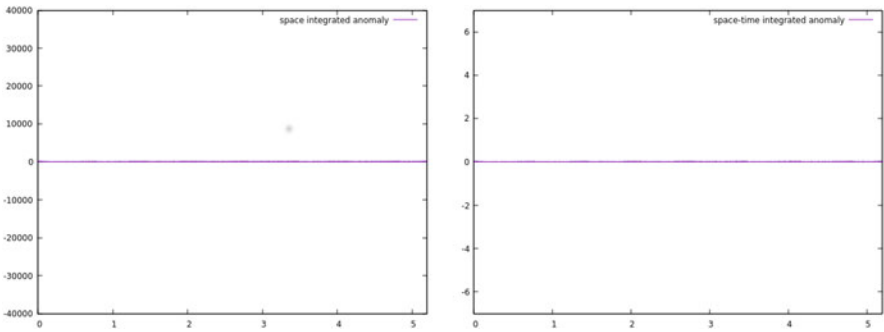


Fig. 9 The left figure shows the plot $\int_{-\tilde{t}}^{+\tilde{x}} \hat{\gamma}_2 dx$ vs t and the right one shows the plot $\int_{-\tilde{t}}^{+\tilde{x}} dt \int_{-\tilde{x}}^{+\tilde{x}} dx \hat{\gamma}_2$ vs t for the anomaly $\hat{\gamma}_2$ in (11) computed for the soliton reflection in Fig. 2

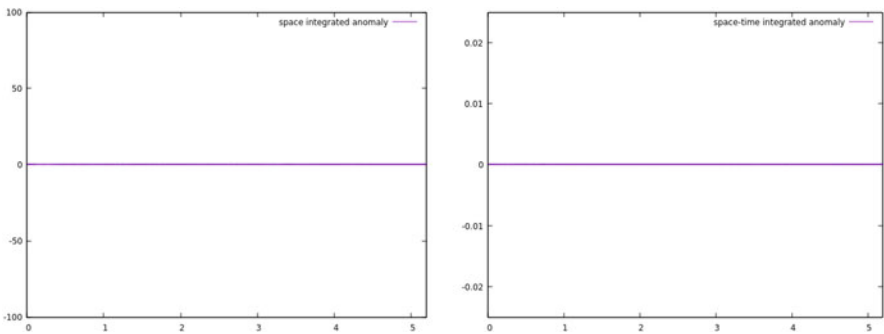


Fig. 10 The left figure shows the plot $\int_{-\tilde{t}}^{+\tilde{x}} \hat{\delta}_1 dx$ vs t and the right one shows the plot $\int_{-\tilde{t}}^{+\tilde{x}} dt \int_{-\tilde{x}}^{+\tilde{x}} dx \hat{\delta}_1$ vs t for the anomaly $\hat{\delta}_1$ in (16) computed for the soliton reflection in Fig. 2

since this fact cannot be visualized qualitatively in the collision of two-dark solitons in Fig. 1. In fact, the exact analytic 2-soliton solutions of the modified NLS model (17) are not known, so it is not possible to show this type of symmetries for the explicit field configurations. However, in the case of the standard NLS model the analytic N-soliton solutions are available and the relevant space-time symmetries can be examined for the solutions and the various anomalies [4, 5].

The true understanding of the vanishing of the space-time integral of the anomalies and the relevance of them for the dynamics of the collision of the solitons of the modified NLS model are under current investigations. The only explanation, so far, for the vanishing of the integrated anomalies, is the symmetry argument as presented above.

Remarkably, infinite number of anomalies and the related quasi-conserved charges are also present in the standard NLS model [6]. So, an exact conserved charge of certain order can be constructed as a linear combination of some quasi-conserved charges of the same order, and when a linear combination of their related anomalies vanish, even before the space-time integration of them are performed.

4 Discussion and Conclusions

Quasi-integrability properties of the CQNLS model have been examined by providing novel anomalous charges related to infinite towers of quasi-conservation laws. The anomaly densities exhibit odd parities under the special space-time symmetry (2)–(3) of the field configurations.

Through numerical simulations of 2–dark soliton collisions we have checked the quasi-conservation properties of the lowest order charges of the CQNLS model defined in (4), (8), (11), and (14), respectively. So, we computed the space and space-time integrals of their associated anomaly densities $\hat{\alpha}_1$, $\hat{\beta}_2$, $\hat{\gamma}_2$, and $\hat{\delta}_1$, for two types of two-soliton collisions of the CQNLS model (17) as plotted in Figs. 1 and 2, respectively. In our numerical simulations presented in Figs. 3, 4, 5, 6, 7, 8, 9 and 10 we have observed that the space-time integrals of the set of anomalies $\hat{\alpha}_1$, $\hat{\beta}_2$, $\hat{\gamma}_2$, and $\hat{\delta}_1$ vanish within numerical accuracy. So, one can conclude that for 2-dark solitons the relevant charges are asymptotically conserved and their collisions are elastic within numerical accuracy, for a wide range of values of the set $\{\eta, \epsilon\}$ and a variety of amplitudes, velocities, and relative initial phases. Since the modified NLS equations are quite ubiquitous, our results may find potential applications in several areas of non-linear science.

References

1. L.A. Ferreira, W.J. Zakrzewski, JHEP05 **130**, (2011); L.A. Ferreira, G. Luchini, W.J. Zakrzewski, JHEP09 **103** (2012); F. ter Braak, L.A. Ferreira, W.J. Zakrzewski, NPB **939**, 49 (2019)

2. H. Blas, H.F. Callisaya, J.P.R. Campos, Riccati-type pseudo-potentials, conservation laws and solitons of deformed sine-Gordon models. *Nucl. Phys. B* **950**, 114852–114905 (2020)
3. H. Blas, R. Ochoa, D. Suarez, Quasi-integrable KdV models, towers of infinite number of anomalous charges and soliton collisions. *JHEP03* **136**, 1–48 (2020)
4. H. Blas, A.C.R. do Bonfim, A.M. Vilela, Quasi-integrable non-linear Schrödinger models, infinite towers of exactly conserved charges and bright solitons. *JHEP05* **106**, 1–28 (2017)
5. H. Blas, M. Zambrano, Quasi-integrability in the modified defocusing non-linear Schrödinger model and dark solitons. *JHEP03* **005**, 1–47 (2016)
6. H. Blas, M. Cerna, L.F. dos Santos, Modified non-linear Schrödinger models, CPT invariant N-bright solitons and infinite towers of anomalous charges (2020). arXiv:2007.13910 [hep-th]
7. G. Roberti, G. El, S. Randoux, P. Suret, *PRE* **100**, 032212 (2019); A.A. Gelash, D.S. Agafontsev, *PRE* **98**, 042210 (2018)

Effect of Vorticity on Peregrine Breather for Interfacial Waves of Finite Amplitude



Shibam Manna and Asoke Kumar Dhar

1 Introduction

The stability of two-dimensional (2D) finite amplitude steady waves to arbitrary small 3D perturbations on the surface of infinite depth of water has been analysed numerically by Maclean et al. [1]. This analysis discloses that there are two different types of instabilities for finite amplitude gravity waves. The first is predominantly 2D and is associated with all the known results for particular cases as for example Benjamin–Feir instability. The second is predominantly 3D and becomes dominant when the steepness of the wave is very large. This work in the case of interfacial waves is then extended by Yuen [2]. The 2D instability of interfacial gravity waves in the particular case of long wave length perturbation and small wave steepness has been studied analytically by Grimshaw and Pullin [3] from the cubic NLSE. Later, Pullin and Grimshaw [4] have extended this analysis for interfacial gravity waves including the effect of basic current shear in the superposition of either or both the inviscid fluids and have reported both the analytical and numerical results. Later on, Dhar and Das [5] analysed the stability of gravity interfacial waves of infinite depth including the effect of shear current. There are many cases in which we observed that currents are not uniform with the water depth. In view of the above, many situations such as air–water interfaces and jet-like ebb flows can be cited, which incorporates non-uniformity of the currents with depth. In the presence of linear shear current for which velocity is uniform, it was theoretically observed that the motion of the wave continues to be irrotational and also constant vorticity can only effect the dispersion relation at first order of approximation. Choi [6] applied a pseudospectral process to analyse the interaction of nonlinear surface

S. Manna (✉) · A. K. Dhar
Indian Institute of Engineering Science and Technology, Shibpur, India
e-mail: fake5@nodycon2021.it

gravity waves including linear shear currents and observed that the maximum wave amplitude for positive shear current is much smaller than that in the absence of any shear, while the effect reverse to this is found for a negative shear current. A fully nonlinear boundary integral method to present the interaction between gravity waves and shear currents including the arbitrary distribution of vorticity was suggested by Nwogu [7]. He observed that the vorticity can significantly affect the development of modulated wave trains. It is to be noted that for analysing the nonlinear evolution of water waves, nonlinear Schrodinger equations are generally applied due to its proper reflection of modulational instability. Ever since the experimental validation of the analytical soliton like solution of NLSE, there has been much of an interest shown by the researchers towards the Peregrine Breather [8] like solution of the NLSE. Considering the case of infinite depth superposed fluids, the instances of air–water interface as well as the Boussinesq approximation have been analysed in that paper. According to Liao et al. [9], being a theoretical solution of third-order NLSE, the PB can be viewed as a prototype of Rogue waves and as such the impact of basic current shear for finite amplitude interfacial waves on PB is of considerable interest of this paper. In this chapter, we first derived a third-order NLSE for a gravity wave travelling at the interface of two superposed fluids having finite depths including the effect of basic current shear. From this evolution equation, we then performed a stability analysis in the cases of air–water interface as well as the Boussinesq approximation. Later, the effect of vorticity on Peregrine Breather has also been examined.

2 Governing Equations

We consider the interface between two inviscid and incompressible fluids in the perturbed state by the equation $y = \zeta(x, t)$. The two fluids having densities ρ_1 and ρ_2 ($\rho_1 < \rho_2$), respectively, are bounded by the horizontal planes at $y = h_1$ and $y = -h_2$. In each fluid, the basic current has constant vorticity ω_1 and ω_2 , respectively. As three space dimensional perturbations to the primary wave are not vorticity preserving, the stability analysis presented here is limited to two space dimensional that can be considered as irrotational. Now, we employ the following transformations for dimensionless variables:

$$\begin{aligned} \sqrt{k_0^3/g}(\phi, \phi', \psi, \psi') &\rightarrow (\phi, \phi', \psi, \psi'), \quad k_0(x, y, \zeta, h_1, h_2) \rightarrow (x, y, \zeta, h_1, h_2), \\ \sqrt{1/k_0g}(\omega_1, \omega_2) &\rightarrow (\omega_1, \omega_2), \quad \sqrt{k_0gt} \rightarrow t, \quad r = \rho_1/\rho_2. \end{aligned} \quad (1)$$

The governing equations can be expressed as

$$\nabla^2\phi' = 0, \quad \nabla^2\psi' = 0, \quad \text{in } \zeta < y < h_1 \quad (2)$$

$$\nabla^2\phi = 0, \quad \nabla^2\psi = 0, \quad \text{in } -h_2 < y < \zeta \quad (3)$$

$$\phi'_y - \zeta_t = (\phi'_x - \omega_1 \zeta) \zeta_x, \quad \text{for } y = \zeta \tag{4}$$

$$\phi_y - \zeta_t = (\phi_x - \omega_2 \zeta) \zeta_x, \quad \text{for } y = \zeta \tag{5}$$

$$\begin{aligned} &\phi_t - r\phi'_t + (1-r)\zeta + \omega_2\psi - r\omega_1\psi' \\ &= \frac{r}{2}(\nabla\phi')^2 - \frac{1}{2}(\nabla\phi)^2 + \omega_2y\phi_x - r\omega_1y\phi'_y, \quad \text{for } y = \zeta \end{aligned} \tag{6}$$

$$\phi_y = 0, \psi = 0, \text{ on } y = -h_2 \text{ and } \phi'_y = 0, \psi' = 0, \text{ on } y = h_1, \tag{7}$$

where ψ' and ψ are the stream functions for the upper and lower fluids satisfying the Cauchy–Riemann relations as follows:

$$\phi'_x = \psi'_y, \phi'_y = -\psi'_x, \phi_x = \psi_y, \phi_y = -\psi_x. \tag{8}$$

A solution can be found in the following form:

$$P = P_0 + \sum_{n=1}^{\infty} [P_n \exp\{in(kx - \sigma t)\} + c.c.], \tag{9}$$

where P symbolises for $\phi', \phi, \psi', \psi, \zeta$, and “c.c.” means complex conjugate. Here $\phi'_n, \phi_n, \psi'_n, \psi_n$ ($n = 0, 1, 2$) are functions of $y, x_1 = \epsilon x, t_1 = \epsilon t$, whereas the ζ_n are functions of x_1, t_1 , and ϵ is a slow ordering parameter. The linear dispersion relation for a plane progressive wave is given by

$$f(\sigma, k) = \sigma_1\sigma^2 + r\sigma_2\sigma^2 - (\omega_2 - r\omega_1)\sigma\sigma_1\sigma_2 - k(1-r)\sigma_1\sigma_2, \tag{10}$$

where $\sigma_i = \tanh kh_i, (i = 1, 2)$. We assume that the primary wave has the wave number k_0 . Therefore, we have $k = 1$, and the relation (10) for finding σ thus reduces to

$$(\sigma_1 + r\sigma_2)\sigma^2 - (\omega_2 - r\omega_1)\sigma\sigma_1\sigma_2 - (1-r)\sigma_1\sigma_2 = 0. \tag{11}$$

From the dispersion relation, the group velocity c_g of the primary wave can be found as

$$c_g = \frac{-\delta_0\sigma^2 + \{(\omega_2 - r\omega_1)\sigma + (1-r)\}\delta_1 + (1-r)\sigma_1\sigma_2}{2(\sigma_1 + r\sigma_2)\sigma - (\omega_2 - r\omega_1)\sigma_1\sigma_2}, \tag{12}$$

where $\delta_0 = h_1(1 - \sigma_1^2) + rh_2(1 - \sigma_2^2)$ and $\delta_1 = \sigma_1h_2(1 - \sigma_2^2) + \sigma_2h_1(1 - \sigma_1^2)$.

3 Derivation of Evolution Equation

By inserting the expansions of (9) into (2) and (3), we obtain the following solutions:

$$\phi'_n = \operatorname{sech}(h_1 k_n) \cosh[(y - h_1)k_n] C'_n, \quad \psi'_n = \operatorname{sech}(h_1 k_n) \sinh[(y - h_1)k_n] D'_n, \tag{13}$$

$$\phi_n = \operatorname{sech}(h_2 k_n) \cosh[(y + h_2)k_n] C_n, \quad \psi_n = \operatorname{sech}(h_2 k_n) \sinh[(y + h_2)k_n] D_n, \tag{14}$$

where $C'_n, D'_n, C_n, D_n, (n = 1, 2)$ are functions of x_1, t_1 and $k_n = n - i\epsilon \frac{\partial}{\partial x_1}$. For $n = 0$, we get the solutions of zeroth harmonic terms after taking Fourier transforms of (2) and (3)

$$\overline{\phi'_0} = \operatorname{sech}(h_1 \epsilon \bar{k}) \cosh[(y - h_1)\epsilon \bar{k}] C'_0, \quad \overline{\psi'_0} = \operatorname{sech}(h_1 \epsilon \bar{k}) \sinh[(y - h_1)\epsilon \bar{k}] D'_0, \tag{15}$$

$$\overline{\phi_0} = \operatorname{sech}(h_2 \epsilon \bar{k}) \cosh[(y + h_2)\epsilon \bar{k}] C_0, \quad \overline{\psi_0} = \operatorname{sech}(h_2 \epsilon \bar{k}) \sinh[(y + h_2)\epsilon \bar{k}] D_0, \tag{16}$$

in which $\overline{\phi'_0}, \overline{\phi_0}, \overline{\psi'_0}, \overline{\psi_0}$ represent the Fourier transforms of the corresponding quantities defined by

$$(\overline{\phi'_0}, \overline{\phi_0}, \overline{\psi'_0}, \overline{\psi_0}) = \iint_{-\infty}^{\infty} (\phi'_0, \phi_0, \psi'_0, \psi_0) e^{-i(\bar{k}x_1 - \bar{\sigma}t_1)} dx_1 dt_1, \tag{17}$$

in which C'_0, D'_0, C_0, D_0 are functions of $\bar{k}, \bar{\sigma}$.

To solve three sets of equations corresponding to $n = 1, 2, 0$, we consider the perturbation expansion as follows:

$$F_m = \sum_{n=1}^{\infty} \epsilon^n F_{mn}, \quad (m = 0, 1), \quad F_2 = \sum_{n=2}^{\infty} \epsilon^n F_{2n}, \tag{18}$$

where F_m represents $C'_m, D'_m, C_m, D_m, \zeta_m (m = 0, 1, 2)$.

Inserting (18) in the three sets of equations and equating different powers of ϵ , we obtain a sequence of equations; from the first set ($n = 1$) of equations, corresponding to (4) and (5), we obtain solutions of $C'_{11}, C'_{12}, C_{11}, C_{12}$, respectively. Similarly, from second set ($n = 2$) and third set ($n = 0$), corresponding to (4), (5) and (2), we obtain solutions of $C'_{22}, C_{22}, \zeta_{22}$ and $C'_{01}, C'_{02}, C_{01}, C_{02}, \zeta_{01}, \zeta_{02}$, respectively. It is to be noted that the coefficients of D'_n and $D_n (n = 1, 2, 0)$ can be expressed in terms of C'_n, C_n by using the Cauchy–Riemann relations (8). Finally,

the equation resulting from (2) of the first set of equations can be expressed in the form as follows:

$$f(W_1, K_1)\zeta_1 = -ir\sigma_2(W_1 + \omega_1\sigma_1)a_1 - i(W_1 - \omega_2\sigma_2)\sigma_1b_1 - \sigma_1\sigma_2K_1c_1, \quad (19)$$

where $W_1 = \sigma + i\epsilon \frac{\partial}{\partial t_1}$, $K_1 = 1 - i\epsilon \frac{\partial}{\partial x_1}$ and a_1, b_1, c_1 are quantities due to nonlinear terms. Now, inserting solutions of several perturbed quantities that appear right side of (19), applying the transformations,

$$\xi = x_1 - c_g t_1, \quad \tau = \epsilon t_1 \quad (20)$$

and setting $\zeta = \zeta_1 = \zeta_{11} + \epsilon \zeta_{12}$, we obtain the following third-order nonlinear evolution equation:

$$i\zeta_\tau + \alpha\zeta\xi\xi + \mu\zeta^2\zeta^* = 0, \quad (21)$$

in which the coefficients are available in the Appendix. It is to be noted that the nonlinear term μ of (21) comes from the interaction of primary wave with the wave-induced mean flow and the second harmonic, respectively.

4 Modulational Instability analysis

The solution of Eq. (21) is

$$\zeta = (\zeta_0/2) \exp(-i\Delta\sigma\tau), \quad (22)$$

where ζ_0 is a real number, and the frequency shift $\Delta\sigma$ due to nonlinearity is

$$\Delta\sigma = (\mu/4)\zeta_0^2. \quad (23)$$

We now introduce the perturbation on the above solution given by

$$\zeta = (\zeta_0/2)(1 + \zeta' + i\theta') \exp(-i\Delta\sigma\tau), \quad (24)$$

in which ζ' and θ' are small real perturbations of amplitude and phase, respectively. Next, we assume that $(\zeta', \theta') \propto \exp(-i\Omega\tau)$. Inserting (24) in (21), linearising with respect to ζ', θ' and taking the Fourier transformation of the resulting equations given by

$$(\bar{\zeta}', \bar{\theta}') = \int_{-\infty}^{\infty} (\zeta', \theta') e^{(-i\lambda\xi)} d\xi,$$

we obtain the nonlinear dispersion as follows:

$$\overline{R_1} = \sqrt{\overline{R_2}(\overline{R_2} - \zeta_0^2 \mu/2)}, \quad (25)$$

in which

$$\overline{R_1} = \Omega - c_g \lambda, \quad \overline{R_2} = \alpha \lambda^2. \quad (26)$$

There is an instability when

$$\lambda^2 < (\mu/2\alpha)\zeta_0^2. \quad (27)$$

At marginal stability, the perturbed wave number λ is given as

$$\lambda = \sqrt{\mu/2\alpha}\zeta_0. \quad (28)$$

If this condition (27) is satisfied, then the maximum growth rate is

$$G_r = \mu\zeta_0^2/4. \quad (29)$$

5 Effect of Vorticity on Peregrine Breather

The non-dimensional form of Eq. (21) is

$$i \frac{\partial \zeta'}{\partial \tau'} + \frac{\partial^2 \zeta'}{\partial \xi'^2} + 2|\zeta'|^2 \zeta' = 0, \quad (30)$$

which is obtained by employing the following transformations on the variables:

$$\xi' = \frac{1}{2} \tilde{\zeta} \sqrt{\frac{2\mu}{\alpha}} \xi, \quad \tau' = \frac{1}{2} \mu \tilde{\zeta}^2 \tau, \quad \zeta' = \frac{\zeta}{\tilde{\zeta}}, \quad (31)$$

where ξ' denotes the normalised coordinate and the normalised time is denoted as τ' . The Peregrine Breather solution of Eq. (30) is

$$\zeta'(\xi', \tau') = \left[\frac{4(1 + 4i\tau')}{1 + 4\xi'^2 + 16\tau'^2} - 1 \right] \exp(2i\tau'). \quad (32)$$

This solution (32) is localised in both space and time. Applying the transformation (31) in (32), we obtain the Peregrine solution in its dimensional form as

$$\zeta(x_1, t_1) = \tilde{\zeta} \exp(i\mu\tilde{\zeta}^2 t_1) \left[\frac{4\alpha(1 + 2i\mu\tilde{\zeta}^2 t_1)}{\alpha + 2\mu\tilde{\zeta}^2(x_1 - c_g t_1)^2 + 4\alpha\mu^2\tilde{\zeta}^4 t_1^2} - 1 \right] \tag{33}$$

6 Discussion and Conclusions

A third-order NLSE is established for gravity waves travelling at the interface of two superposed fluids of finite depth under the circumstance of a shear current. Using this equation, the instability analysis is then investigated for air–water interface ($r = 0.00129$) as well as the Boussinesq approximation ($r \rightarrow 1$). Furthermore, the effect of vorticity on the peregrine breather has been taken into account. For an air–water interface from Fig. 1, we observed that G_r increases as $|\omega_1|$ decreases for fixed depth h_2 of the lower fluid, that is, the basic current shear in the air decreases G_r for fixed values of h_2 . Also, for fixed $|\omega_1|$, G_r increases as h_2 increases. Now, from Fig. 2, we found that G_r increases as ω_2 decreases, but the reverse effect is observed for $-ve$ vorticity. Also, for fixed $+ve$ vorticity, G_r decreases as h_2 increases, and the reverse effect is observed for fixed values of $-ve$ vorticity. Here, we found that sufficiently big value of the $+ve$ basic current shear (ω_2) in the water removes the modulational instability for surface gravity waves of fixed finite depth of water, but $-ve$ basic current shear increases G_r . For the case of Boussinesq approximation, we see from Fig. 3 that G_r increases with the increment of ω_1 for fixed values of h_1 . In Fig. 4, we have plotted curves for several values of $h_1, h_2, \omega_1, \omega_2$ for both air–water interface and the Boussinesq approximation. As $h_1, h_2 \rightarrow \infty$, the four curves of Fig. 4 are similar as those of Dhar and Das [5]. Here, we see that the basic current shear in the air (ω_1) decreases G_r for surface waves of infinite depths. Furthermore, for $r \rightarrow 1$, which corresponds to potential oceanic or atmospheric application, we found that G_r increases as ω_1 increases for deep water surface gravity waves. For $r = 0.00129$ as well as $r \rightarrow 1$, wave number λ at marginal stability has been depicted in Fig. 5 for several values of $h_1, h_2, \omega_1, \omega_2$. For the case of air–water interface, from Fig. 6, we see that the breather span increases as h_2 decreases, while the breather span increases as $|\omega_1|$ increases. From Fig. 7, it is observed that h_1 has similar influence on breather span as that of the case in Fig. 6 for h_2 and the breather span increases for increasing $+ve$ values of ω_2 , while the reverse effect is encountered for $-ve$ values of ω_2 . For the Boussinesq approximation, Fig. 8 depicts that the span of the breather decreases as h_1 increases whereas the breather span decreases as ω_1 increases. In Fig. 9, we have plotted breather solution for several finite values of $h_1, h_2, \omega_1, \omega_2$. From Figs. 10 and 11 for air–water interface, we find that for fixed value of ω_1, ω_2 , the breather width increases both in space and in time as h_2 decreases. In Figs. 12 and 13, we have plotted the breather solution for several

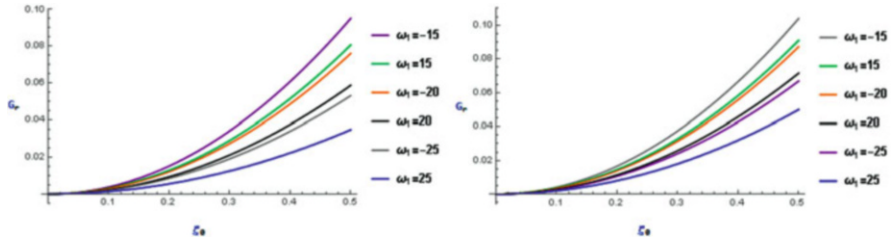


Fig. 1 G_r vs. ζ_0 plot for $r = 0.00129$, $h_1 \rightarrow \infty$, $\omega_2 = 0$ and $h_2 = 2$ (left) and $h_2 = 5$ (right)

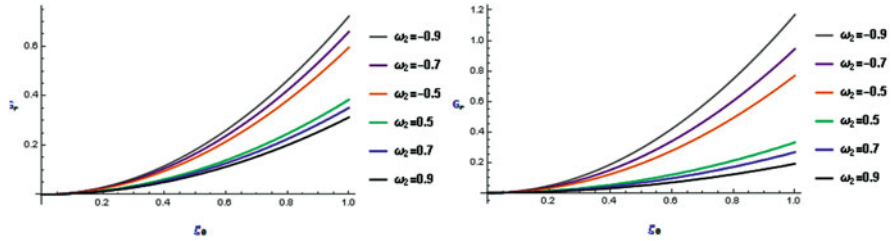


Fig. 2 G_r vs. ζ_0 plot for $r = 0.00129$, $h_1 \rightarrow \infty$, $\omega_1 = 0$ and $h_2 = 2$ (left) and $h_2 = 5$ (right)

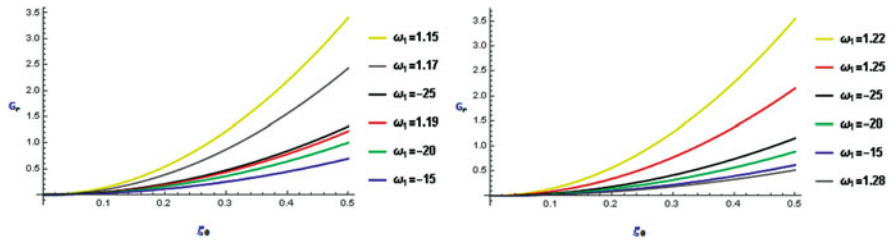


Fig. 3 G_r vs. ζ_0 plot for $r = 0.00129$, $h_2 \rightarrow \infty$, $\omega_2 = 0$ and $h_1 = 2$ (left) and $h_1 = 5$ (right)

finite values of h_1 , h_2 , ω_1 , ω_2 , and we observe that the breather span increases in space when h_1 , h_2 , ω_1 , ω_2 increases for air–water interface and that the breather amplitude increases in time when h_1 , h_2 , ω_1 , ω_2 decreases for the Boussinesq approximation.

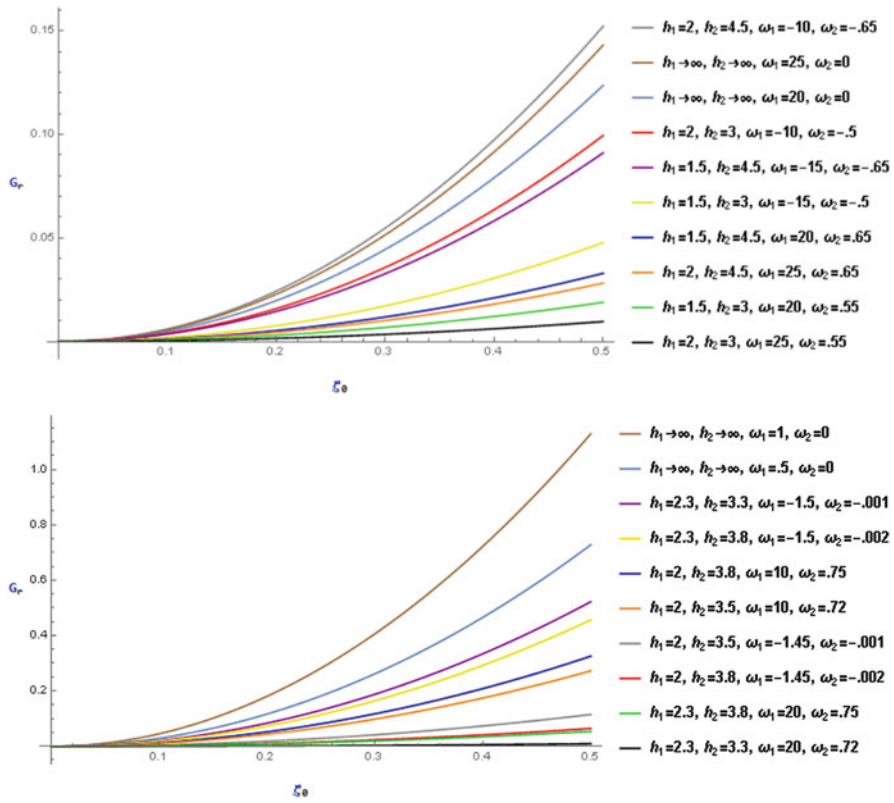


Fig. 4 G_r vs. ζ_0 plot for $r = 0.00129$ (left) and $r \rightarrow 1$ (right)

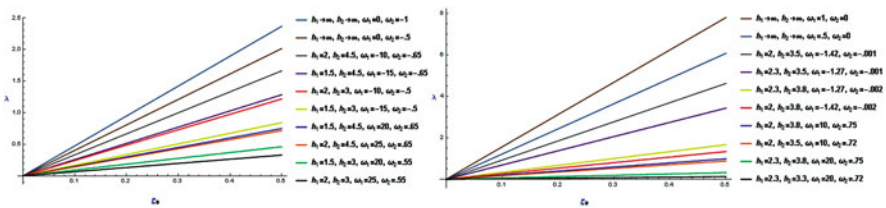


Fig. 5 λ vs. ζ_0 plot for $r = 0.00129$ (left) and $r \rightarrow 1$ (right). The region above each line indicates stable region and that of the below region indicates unstable region

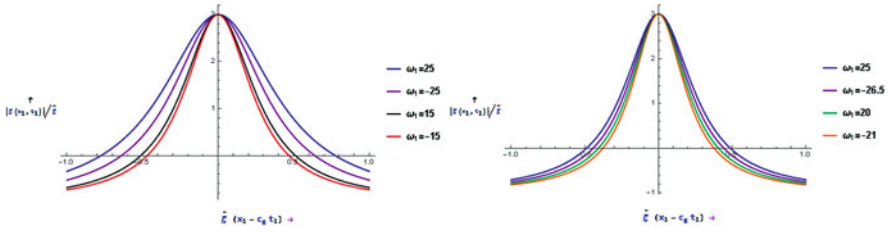


Fig. 6 $|\zeta(x_1, t_1)|/\tilde{\zeta}$ vs. $\tilde{\zeta}(x_1 - c_g t_1)$ plot for $r = 0.00129$, $h_1 \rightarrow \infty$, $\omega_2 = 0$ and $h_2 = 2$ (left) and $h_2 = 5$ (right)

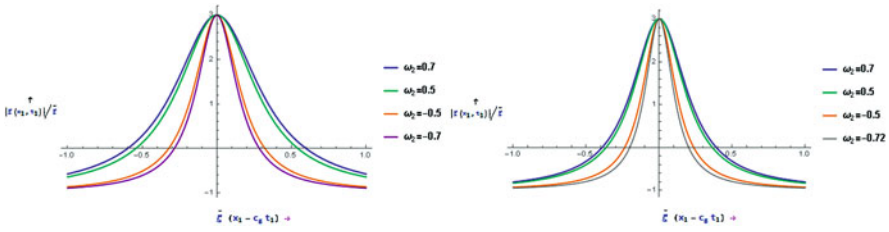


Fig. 7 $|\zeta(x_1, t_1)|/\tilde{\zeta}$ vs. $\tilde{\zeta}(x_1 - c_g t_1)$ plot for $r = 0.00129$, $h_1 \rightarrow \infty$, $\omega_1 = 0$ and $h_2 = 2$ (left) and $h_2 = 5$ (right)

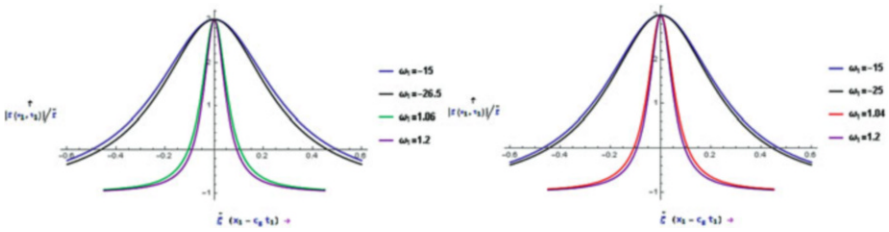


Fig. 8 $|\zeta(x_1, t_1)|/\tilde{\zeta}$ vs. $\tilde{\zeta}(x_1 - c_g t_1)$ plot for $r \rightarrow 1$, $h_2 \rightarrow \infty$, $\omega_2 = 0$ and $h_1 = 1.4$ (left) and $h_1 = 1.5$ (right)

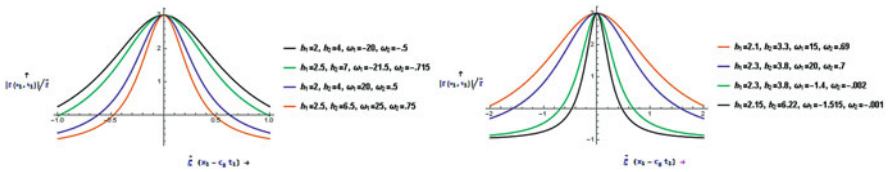


Fig. 9 $|\zeta(x_1, t_1)|/\tilde{\zeta}$ vs. $\tilde{\zeta}(x_1 - c_g t_1)$ plot for $r = 0.00129$ (left) and $r \rightarrow 1$ (right)

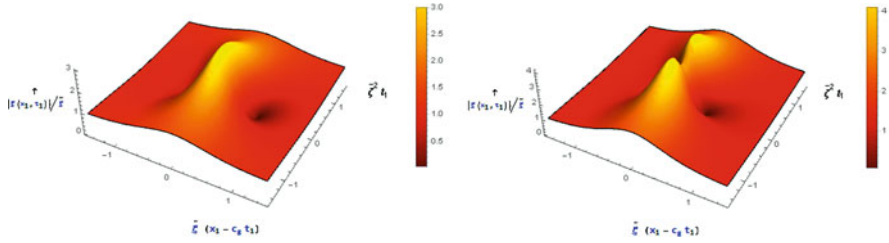


Fig. 10 The Peregrine Breather for $r = 0.00129$, $h_1 \rightarrow \infty$, $\omega_2 = 0$ and $h_2 = 2$, $\omega_1 = 20$ (left) and $h_2 = 5$, $\omega_1 = 20$ (right)

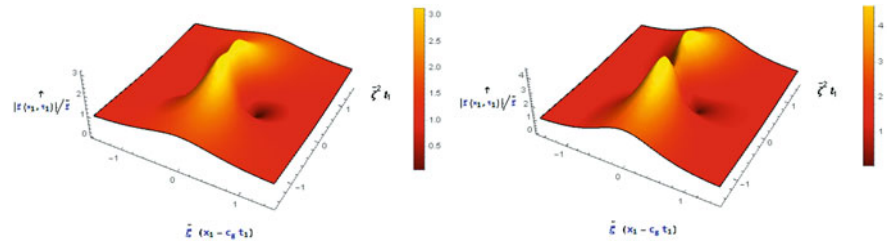


Fig. 11 The Peregrine Breather for $r = 0.00129$, $h_1 \rightarrow \infty$, $\omega_1 = 0$ and $h_2 = 3$, $\omega_2 = 0.65$ (left) and $h_2 = 5$, $\omega_2 = 0.65$ (right)

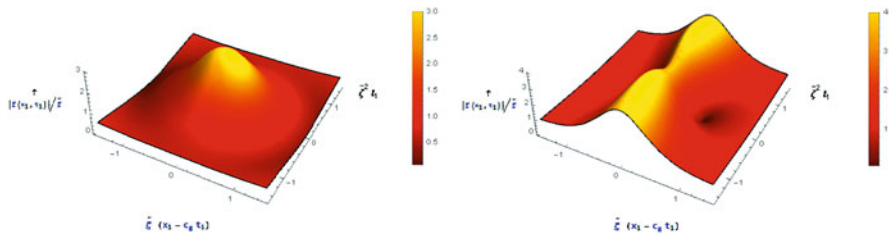


Fig. 12 The Peregrine Breather for $r = 0.00129$, $h_1 = 2$, $h_2 = 4$, $\omega_1 = 20$, $\omega_2 = 0.5$ (right) and $r \rightarrow 1$, $h_1 = 2.3$, $h_2 = 3.8$, $\omega_1 = 20$, $\omega_2 = 0.7$ (left)

Appendix

The coefficients appearing in Eq. (21) are

$$\begin{aligned} \alpha &= \frac{1}{2} \left(\frac{dc_g}{dk} \right)_{k=1} = \frac{1}{f\sigma} [(\sigma_1 + r\sigma_2)c_g^2 \\ &+ \{2\sigma h_1(1 - \sigma_1^2) + 2\sigma r h_2(1 - \sigma_2^2) - (\omega_2 - r\omega_1)\delta_1\}c_g \\ &- \sigma^2\{\sigma_1 h_1^2(1 - \sigma_1^2) + r\sigma_2 h_2^2(1 - \sigma_2^2)\} \\ &- \{(\omega_2 - r\omega_1)\sigma + (1 - r)\}(\delta_3 - \delta_4) - (1 - r)\delta_1], \end{aligned}$$

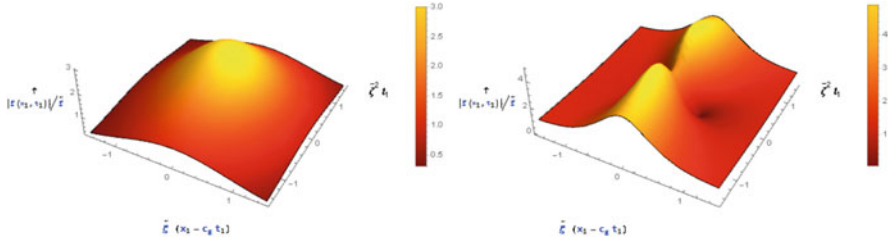


Fig. 13 The Peregrine Breather for $r = 0.00129, h_1 = 2.5, h_2 = 6.5, \omega_1 = 25, \omega_2 = 0.75$ (right) and $r \rightarrow 1, h_1 = 2.1, h_2 = 3.3, \omega_1 = 15, \omega_2 = 0.69$ (left)

$$\begin{aligned} \mu = & \frac{1}{2\sigma_1^3\sigma_2^3f_\sigma} \left[\frac{2\{\sigma^2\sigma_1^2(1-\sigma_2^2) - r\sigma^2\sigma_2^2(1-\sigma_1^2) + \frac{\sigma_2\sigma_1^2\delta_5(c_g-h_2\omega_2)}{h_2} - \frac{r\sigma_1\sigma_2^2\delta_6(c_g+h_1\omega_1)}{h_1}\}^2}{\frac{c_g^2}{h_2} + \frac{rc_g^2}{h_1} - \delta_7} \right. \\ & + \frac{\{\sigma^2\sigma_1^2(3-\sigma_2^2) - r\sigma^2\sigma_2^2(3-\sigma_1^2) - \omega_2\sigma_1^2\sigma_2(\delta_5 + \sigma + \sigma\sigma_2^2) - r\omega_1(\delta_6 + \sigma + \sigma\sigma_1^2)\}^2}{\sigma^2\sigma_2 + r\sigma^2\sigma_1} \\ & - \frac{2\sigma_1^2\sigma_2^2(h_1\delta_5^2\sigma_1^2 + rh_2\delta_6^2\sigma_2^2)}{h_1h_2} - \sigma_1\sigma_2\{4\sigma^2\sigma_1^3(1-2\sigma_2^2) + 4r\sigma^2\sigma_2^3(1-2\sigma_1^2) \\ & - \omega_2\sigma_2\sigma_1^3(4\sigma(1-\sigma_2^2) - \omega_2\sigma_2(1+\sigma_2^2)) \\ & \left. + r\omega_1\sigma_1\sigma_2^3(4\sigma(1-\sigma_1^2) + \omega_1\sigma_1(1+\sigma_1^2))\right], \end{aligned}$$

$$\begin{aligned} \delta_1 &= \sigma_1h_2(1-\sigma_2^2) + \sigma_2h_1(1-\sigma_1^2), & \delta_2 &= \sigma_1 + h_1(1-\sigma_1^2), \\ \delta_3 &= h_1h_2(1-\sigma_1^2)(1-\sigma_1^2), \end{aligned}$$

$$\begin{aligned} \delta_4 &= \sigma_1\sigma_2\{h_1^2(1-\sigma_1^2) + h_2^2(1-\sigma_2^2)\}, & \delta_5 &= 2\sigma - \sigma_2\omega_2, & \delta_6 &= 2\sigma + \sigma_1\omega_1, \\ \delta_7 &= 1 - r + (\omega_2 - r\omega_1)c_g. \end{aligned}$$

References

1. J.W. McLean, Y.C. Ma, D.U. Martin, P.G. Saffman, H.C. Yuen, Three-dimensional instability of finite-amplitude water waves. *Phys. Rev. Lett.* **46**, 817 (1981). <https://doi.org/10.1103/PhysRevLett.46.817>
2. H.C. Yuen, Nonlinear dynamics of interfacial waves. *Phys. D Nonlinear Phenomena* **12**(1–3), 71–82 (1984). [https://doi.org/10.1016/0167-2789\(84\)90515-3](https://doi.org/10.1016/0167-2789(84)90515-3)
3. R. Grimshaw, D. Pullin, Stability of finite-amplitude interfacial waves. Part 1. Modulational instability for small-amplitude waves. *J. Fluid Mech.* **160**, 297–315 (1985). <https://doi.org/10.1017/S0022112085003494>

4. D. Pullin, R. Grimshaw, Stability of finite-amplitude interfacial waves. Part 3. The effect of basic current shear for one-dimensional instabilities. *J. Fluid Mech.* **172**, 277–306 (1986). <https://doi.org/10.1017/S002211208600174X>
5. A.K. Dhar, K.P. Das, Stability analysis from fourth order evolution equation for small but finite amplitude interfacial waves in the presence of a basic current shear. *J. Austral. Math. Soc. Ser. B. Appl. Math.* **35**(3), 348–365 (1994). <https://doi.org/10.1017/S0334270000009346>
6. W. Choi, Nonlinear surface waves interacting with a linear shear current. *Math. Comput. Simul.* **80**(1), 29–36 (2009). <https://doi.org/10.1016/j.matcom.2009.06.021>
7. O.G. Nwogu, Interaction of finite-amplitude waves with vertically sheared current fields. *J. Fluid Mech.* **627**, 179–213 (2009). <https://doi.org/10.1017/S0022112009005850>
8. D.H. Peregrine, Water waves nonlinear Schrödinger equations and their solutions. *Austral. Math. Soc. Ser. B.* **25**, 16 (1983). <https://doi.org/10.1017/S0334270000003891>
9. B. Liao, G. Dong, Y. Ma, J.L. Gao, Linear-shear-current modified Schrödinger equation for gravity waves in finite water depth. *Phys. Rev. E* **96**, 043111 (2017). <https://doi.org/10.1103/PhysRevE.96.043111>

Construction of Soliton Solutions of the Matrix Modified Korteweg–de Vries Equation



Sandra Carillo and Cornelia Schiebold

1 Introduction

This chapter is a sequel to [1], where a general approach to the solution theory of the matrix mKdV is outlined and certain solutions are explicitly constructed. Actually, these solutions are part of a family for which a complete classification will be given in the forthcoming article [2].

Here, the focus is on solutions beyond the setting of [1, 2]. In a somewhat experimental spirit, we will examine ways to weaken the assumptions in [2] and initialize the study of some novel solution classes. The emphasis does not lie on completeness, but on a qualitative study of phenomena, discussed mainly for the first interesting cases.

The result to start from is a general solution formula presented in Theorem 1, building on work in [3, 4]. Solution formulas of this kind have been studied for quite a while, see [5–8] and the references therein. Here, the use of Bäcklund techniques should also be mentioned [9–12]. Closely related formulas for scalar equations are known to generate very large solution classes, roughly speaking the solutions accessible by the standard inverse scattering method [13]. As the situation for matrix equations is much less transparent, the case studies made here are also

S. Carillo (✉)

Università di Roma La Sapienza, Dip. S.B.A.I., Rome, Italy

I.N.F.N. - Sezione Roma1, Gr. IV - M.M.N.L.P., Rome, Italy

e-mail: sandra.carillo@uniroma1.it

<https://www.sbai.uniroma1.it/~sandra.carillo/index.html>

C. Schiebold

Department of Mathematics and Science Education MOD, Mid Sweden University, Sundsvall, Sweden

e-mail: cornelia.schiebold@miun.se

meant as a step towards better understanding the range of our methods. Finally, we mention some alternative approaches to matrix solutions in [14–17].

2 An Explicit Solution Class of the $\mathbf{d} \times \mathbf{d}$ -Matrix Modified Korteweg–de Vries Equation Depending on Matrix Parameters and N -Solitons

We start with stating an explicit solution class for the modified Korteweg–de Vries equation with values in the $\mathbf{d} \times \mathbf{d}$ -matrices,

$$V_t = V_{xxx} + 3\{V^2, V_x\}, \tag{1}$$

depending on matrix parameters.

Theorem 1 For $N \in \mathbb{N}$, let k_1, \dots, k_N be complex numbers such that $k_i + k_j \neq 0$ for all i, j , and let B_1, \dots, B_N be arbitrary $\mathbf{d} \times \mathbf{d}$ -matrices.

Define the $N\mathbf{d} \times N\mathbf{d}$ -matrix function $L = L(x, t)$ as block matrix $L = (L_{ij})_{i,j=1}^N$ with the $\mathbf{d} \times \mathbf{d}$ -blocks

$$L_{ij} = \frac{\ell_i}{k_i + k_j} B_j,$$

where $\ell_i = \ell_i(x, t) = \exp(k_i x + k_i^3 t)$.

Then,

$$V = (B_1 \ B_2 \ \dots \ B_N) \left(I_{N\mathbf{d}} + L^2 \right)^{-1} \begin{pmatrix} \ell_1 I_{\mathbf{d}} \\ \vdots \\ \ell_N I_{\mathbf{d}} \end{pmatrix}$$

is a solution of the matrix modified KdV equation (1) with values in the $\mathbf{d} \times \mathbf{d}$ -matrices on every open set Ω on which $\det(I_{N\mathbf{d}} + L^2) \neq 0$.

The proof of Theorem 1, which is based on results in [3, 4], is provided in [2]. Here, we focus on applications and discuss some interesting examples.

Remark 1

- (a) In [4], it is shown that the solution class for the matrix KdV equation which corresponds to the class in Theorem 1 comprises the N -soliton solutions as derived by the inverse scattering method in [15].
- (b) In contrast to (1), the non-commutative mKdV in the form

$$V_t = V_{xxx} + 3 (V V^T V_x + V_x V^T V) = 0$$

(as for example derived from reduction of the non-commutative AKNS system) admits also non-square matrix interpretation. We refer to [8] for a fairly complete asymptotics of 2-solitons in the vector case.

3 Explicit Solutions

Motivated by Carillo et al. [1], the subclass of solutions arising from choosing $k_1, \dots, k_N \in \mathbb{R}$ and B_1, \dots, B_N as (real) multiples of a real matrix B which has real Jordan canonical form is discussed thoroughly in [2], the main result being a complete classification of this subclass up to a possible (common) change of coordinates. It should be stressed that all solutions in [1] belong to this subclass.

In the present section, a variety of solutions beyond this case are presented.

3.1 The Matrix Parameter B Does Not Have a Real Jordan Form

A prototypical example for a real matrix without real Jordan form in the case $d = 2$ is rotations. Consider

$$B = \begin{pmatrix} \frac{1}{\sqrt{2}} & \frac{1}{\sqrt{2}} \\ -\frac{1}{\sqrt{2}} & \frac{1}{\sqrt{2}} \end{pmatrix},$$

the rotation with the angle $\frac{\pi}{4}$, and let $N = 1$.

The corresponding solution according to Theorem 1 is

$$\begin{aligned} V &= B \left(I_2 + \left(\frac{1}{2k} \ell B \right)^2 \right)^{-1} \ell I_2 \\ &= 2k g B \left(I_2 + (gB)^2 \right)^{-1}, \end{aligned}$$

where $g = \ell/(2k)$. Since B^2 is the clockwise rotation by $\pi/2$, i.e. $B^2 = \begin{pmatrix} 0 & 1 \\ -1 & 0 \end{pmatrix}$, this is very easily computed explicitly, giving

$$\begin{aligned} V &= \sqrt{2}k g \begin{pmatrix} 1 & 1 \\ -1 & 1 \end{pmatrix} \begin{pmatrix} 1 & g^2 \\ -g^2 & 1 \end{pmatrix}^{-1} = \sqrt{2}k \frac{g}{1+g^4} \begin{pmatrix} 1 & 1 \\ -1 & 1 \end{pmatrix} \begin{pmatrix} 1 & -g^2 \\ g^2 & 1 \end{pmatrix} \\ &= \sqrt{2}k \frac{g}{1+g^4} \begin{pmatrix} 1+g^2 & 1-g^2 \\ -(1-g^2) & 1+g^2 \end{pmatrix}. \end{aligned}$$

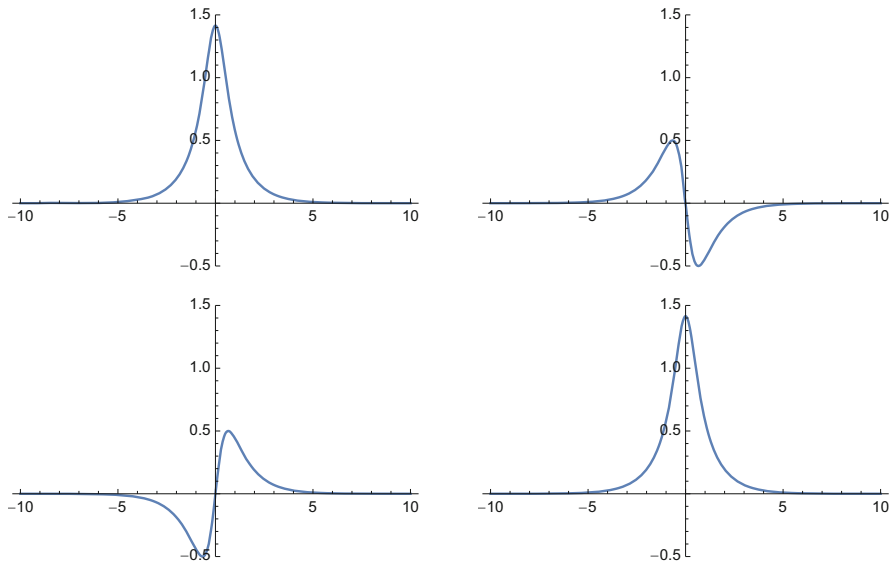


Fig. 1 Snapshot of the solution in Sect. 3.1 for $k = 1$ at $t = 0$

Note that this solution is regular and moves, without changing shape, with velocity constant $-k^2$, see Fig. 1.

3.2 Unequal Matrix Parameters

Next, we consider the case $N = 2$ with matrix parameters B_1 and B_2 such that $B_1 \neq cB_2$ (for all $c \in \mathbb{R}$). In this case, we get from Theorem 1

$$V = (B_1 \ B_2) \left(I_{2d} + M^2 \right)^{-1} \begin{pmatrix} \ell_1 I_d \\ \ell_2 I_d \end{pmatrix} \text{ where } M = \begin{pmatrix} \frac{1}{2k_1} \ell_1 B_1 & \frac{1}{k_1+k_2} \ell_1 B_2 \\ \frac{1}{k_1+k_2} \ell_2 B_1 & \frac{1}{2k_2} \ell_2 B_2 \end{pmatrix}.$$

Let us first focus on the case that

$$B_1 B_2 = 0 = B_2 B_1.$$

Using this assumption, it is straightforward to verify that

$$(B_1 \ B_2) M = (B_1 \ B_2) R, \tag{2}$$

$$M^2 = MR, \tag{3}$$

where

$$R = \begin{pmatrix} \frac{1}{2k_1} \ell_1 B_1 & 0 \\ 0 & \frac{1}{2k_2} \ell_2 B_2 \end{pmatrix}.$$

From (3), we get $M^3 R = M M^2 R = M(MR)R = M^2 R^2$. Thus, $M^2(I_{2d} + R^2) = (I_{2d} + M^2)MR$, showing $(I_{2d} + M^2)^{-1}M^2 = MR(I_{2d} + R^2)^{-1}$, and hence

$$(I_{2d} + M^2)^{-1} = I_{2d} - (I_{2d} + M^2)^{-1}M^2 = I_{2d} - MR(I_{2d} + R^2)^{-1}.$$

Together with (2), this implies

$$\begin{aligned} (B_1 \ B_2) (I_{2d} + M^2)^{-1} &= (B_1 \ B_2) (I_{2d} - MR(I_{2d} + R^2)^{-1}) \\ &= (B_1 \ B_2) (I_{2d} - R^2(I_{2d} + R^2)^{-1}) = (B_1 \ B_2) (I_{2d} + R^2)^{-1}. \end{aligned}$$

As a result,

$$\begin{aligned} V &= (B_1 \ B_2) \begin{pmatrix} \left(I_d + \frac{1}{(2k_1)^2} \ell_1^2 B_1^2\right)^{-1} & 0 \\ 0 & \left(I_d + \frac{1}{(2k_2)^2} \ell_2^2 B_2^2\right)^{-1} \end{pmatrix} \begin{pmatrix} \ell_1 I_d \\ \ell_2 I_d \end{pmatrix} \\ &= \sum_{j=1,2} \ell_j B_j \left(I_d + \frac{1}{(2k_j)^2} \ell_j^2 B_j^2\right)^{-1} \\ &=: \sum_{j=1,2} V_j. \end{aligned}$$

Observe that V_j is precisely the solution one obtains from the input data $N = 1$ with parameters k_j and B_j in Theorem 1. In this sense, V_j can be interpreted as a matrix 1-soliton. In the case $B_1 B_2 = 0 = B_2 B_1$, the solution V therefore is a linear superposition of the two matrix 1-solitons.

Example 1 In Figs. 2 and 3, the solution is depicted in the case $d = 2$, for $k_1 = 1$, $k_2 = \sqrt{2}$, and the matrix parameters are

- (a) Figure 2 $B_1 = \begin{pmatrix} 1 & 0 \\ 0 & 0 \end{pmatrix}$, $B_2 = \begin{pmatrix} 0 & 0 \\ 0 & 1 \end{pmatrix}$ and
- (b) Figure 3 $B_1 = \begin{pmatrix} 1 & 1 \\ 1 & 1 \end{pmatrix}$, $B_2 = \begin{pmatrix} 1 & -1 \\ -1 & 1 \end{pmatrix}$.

Of course, there is a huge variety of solutions not covered by the cases above. We conclude this subsection with one additional example.

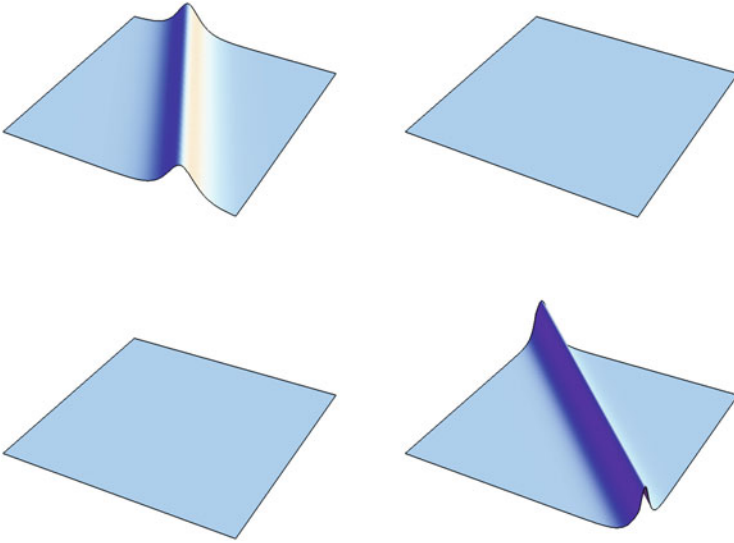


Fig. 2 The solution in Example 1(a) depicted for $-10 \leq x \leq 10$ and $-5 \leq t \leq 5$ with plot range between $-\sqrt{2}$ and $\sqrt{2}$

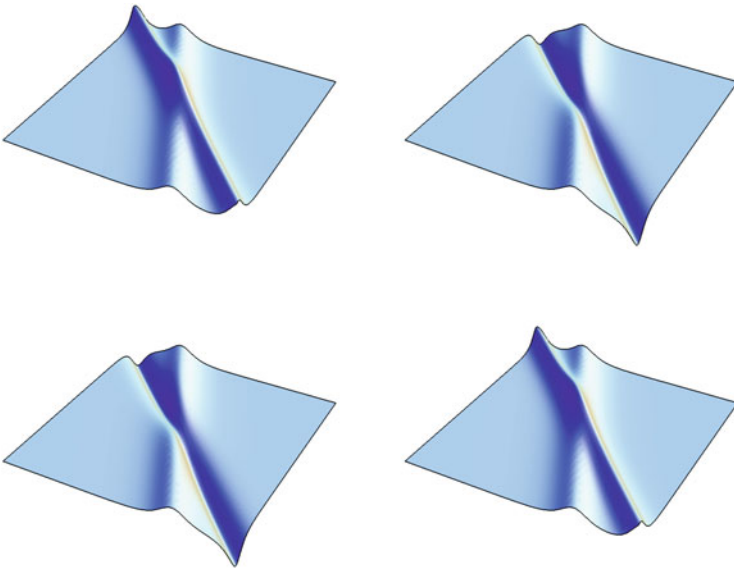


Fig. 3 The solution in Example 1(b) depicted for $-10 \leq x \leq 10$ and $-5 \leq t \leq 5$ with plot range between $-\sqrt{2}$ and $\sqrt{2}$

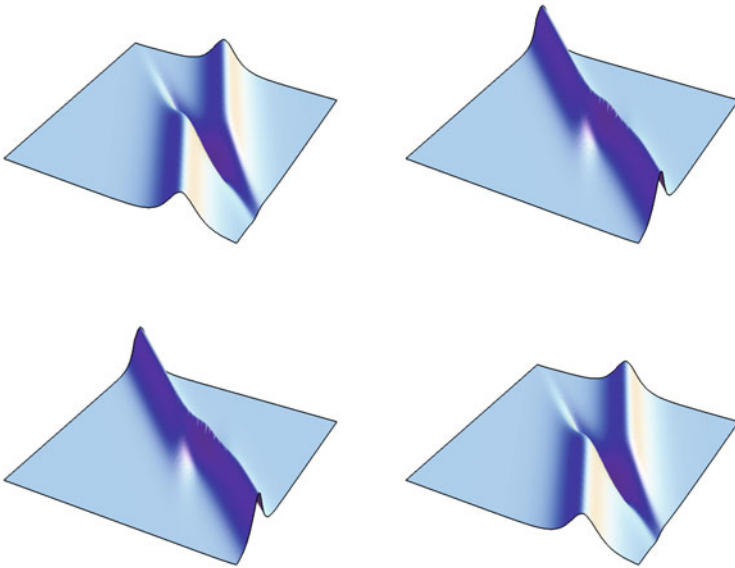
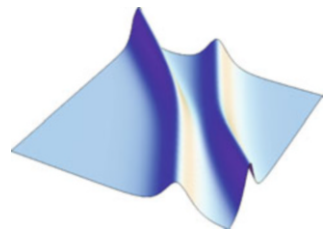


Fig. 4 The solution in Example 2 depicted for $-10 \leq x \leq 10$ and $-5 \leq t \leq 5$ with plot range between $-\sqrt{2}$ and $\sqrt{2}$

Example 2 In Fig. 4, the solution is depicted in the case $d = 2$, for $k_1 = 1, k_2 = \sqrt{2}$, and with the matrix parameters

$$B_1 = \begin{pmatrix} 1 & 0 \\ 0 & 1 \end{pmatrix}, B_2 = \begin{pmatrix} 0 & 1 \\ 1 & 0 \end{pmatrix}.$$

For comparison, we also depict the *scalar* 2-soliton.¹ The frame is the same as in Fig. 4.



¹As generated in the case $d = 1$ with the input data $N = 2, k_1 = 1, k_2 = \sqrt{2}$, and $b_1 = b_2 = 1$ in Theorem 1.

Remark 2 In [18], a Bäcklund chart of KdV-type equations is introduced, linking in particular the KdV with its singularity equation (For a generalization of this link to the operator level, we refer to [19], see also [20]). It is then indicated how this can be used to generate explicit solutions. It would be interesting to compare the solution in Example 2, see Fig. 4, with the (scalar) interacting soliton in [12, Fig. 3].

3.3 Complex Parameters: A Breather Solution

Finally, we would like to mention that also complex parameters can lead to real solutions. This is well known in the case of the scalar modified KdV equation where the input data k, \bar{k}, b, \bar{b} results in a breather,² a solution consisting of a bound state of a soliton and an antisoliton [21]. The same holds true in the case of the matrix modified KdV equation as the following argument shows.

Starting from Theorem 1 with $N = 2$ and the parameters chosen to as $k_1 = k, k_2 = \bar{k}$ (such that $\ell_1 = \ell, \ell_2 = \bar{\ell}$) and $B_1 = B, B_2 = \bar{B}$, our solution reads

$$V = (B \bar{B}) \left(I_{2d} + M^2 \right)^{-1} \begin{pmatrix} \ell I_d \\ \bar{\ell} I_d \end{pmatrix} \text{ with } M = \begin{pmatrix} \frac{1}{2k} \ell B & \frac{1}{k+\bar{k}} \ell \bar{B} \\ \frac{1}{k+\bar{k}} \bar{\ell} B & \frac{1}{2\bar{k}} \bar{\ell} \bar{B} \end{pmatrix}.$$

Introducing $D = \begin{pmatrix} 0 & I_d \\ I_d & 0 \end{pmatrix}$, such that

$$(B \bar{B}) = (\bar{B} B) D \quad \text{and} \quad D \begin{pmatrix} \ell I_d \\ \bar{\ell} I_d \end{pmatrix} = \begin{pmatrix} \bar{\ell} I_d \\ \ell I_d \end{pmatrix}$$

and

$$\begin{aligned} DMD &= \begin{pmatrix} 0 & I_d \\ I_d & 0 \end{pmatrix} \begin{pmatrix} \frac{1}{2k} \ell B & \frac{1}{k+\bar{k}} \ell \bar{B} \\ \frac{1}{k+\bar{k}} \bar{\ell} B & \frac{1}{2\bar{k}} \bar{\ell} \bar{B} \end{pmatrix} \begin{pmatrix} 0 & I_d \\ I_d & 0 \end{pmatrix} \\ &= \begin{pmatrix} \frac{1}{2\bar{k}} \bar{\ell} \bar{B} & \frac{1}{k+\bar{k}} \bar{\ell} B \\ \frac{1}{k+\bar{k}} \ell B & \frac{1}{2k} \ell B \end{pmatrix}. \end{aligned}$$

²Here, \bar{k} denotes the complex conjugate of k .

Observe that $D^{-1} = D$. Hence, since $D(I_{2d} + M^2)^{-1}D = (I_{2d} + DM^2D)^{-1} = (I_{2d} + (DMD)^2)^{-1}$, we find

$$V = (\bar{B} \ B) \left(I_{2d} + \left(\begin{array}{cc} \frac{1}{2k} \bar{\ell} \bar{B} & \frac{1}{k+k} \bar{\ell} B \\ \frac{1}{k+k} \ell \bar{B} & \frac{1}{2k} \ell B \end{array} \right)^2 \right)^{-1} \begin{pmatrix} \bar{\ell} I_d \\ \ell I_d \end{pmatrix} = \bar{V},$$

showing that the solution V is real.

Example 3 For illustration, we add two random examples. In both examples, $k = 1 + i$. For the corresponding scalar breather, this implies velocity = 2, and hence the plots are drawn for $(x, x + 2t)$ giving a stationary picture. The matrix parameter is

Figure 5 $B = \begin{pmatrix} i & -2 \\ 1 + i & 2 - i \end{pmatrix},$

Figure 6 $B = \begin{pmatrix} i & -2i \\ 3i - 1 & -1 \end{pmatrix}.$

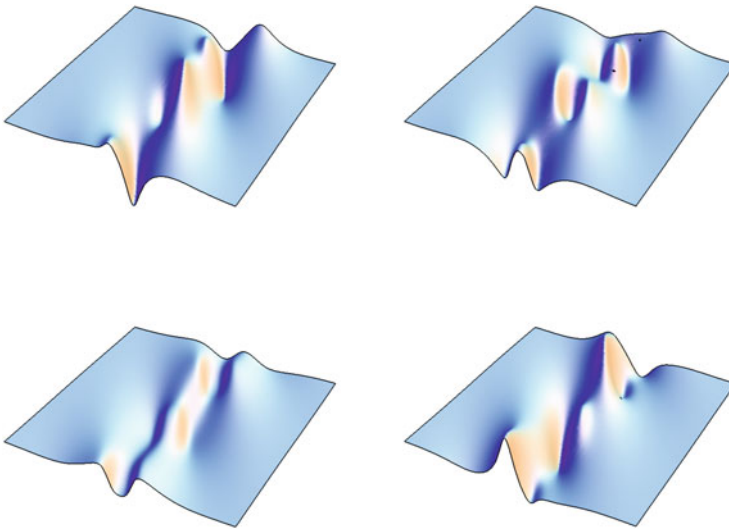


Fig. 5 The solution in Example 3(a) is depicted for $-5 \leq x \leq 5$ and $0 \leq t \leq 2$ with plot range between -3.5 and 3.5

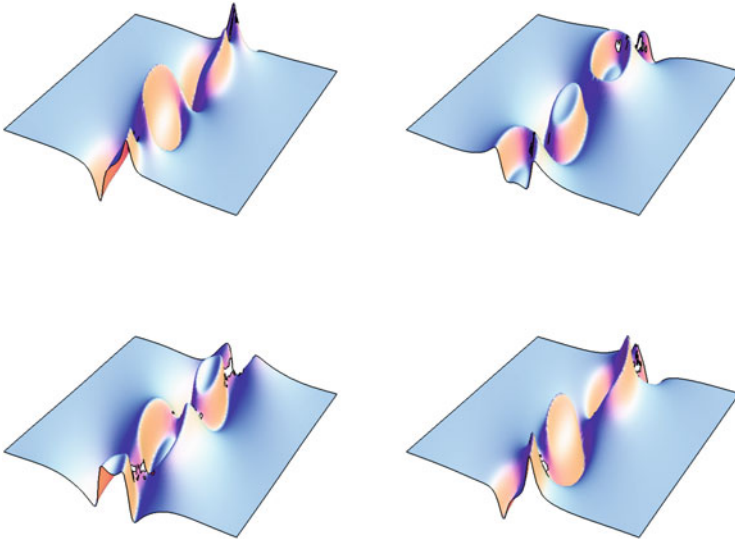


Fig. 6 The solution in Example 3(b) is depicted for $-5 \leq x \leq 5$ and $-1 \leq t \leq 1$ with plot range between -5.5 and 5.5

Acknowledgments The financial support of G.N.F.M.-I.N.d.A.M., I.N.F.N. and Università di Roma LA SAPIENZA, Rome, Italy are gratefully acknowledged. C. Schiebold acknowledges Dip. S.B.A.I., Università di Roma LA SAPIENZA, for the kind hospitality. A preliminary version of this work was posted as an arXiv preprint [22].

References

1. S. Carillo, M. Lo Schiavo, C. Schiebold, Matrix solitons solutions of the modified Korteweg-de Vries equation, in *Nonlinear Dynamics of Structures, Systems and Devices*, ed. by W. Lacarbonara, B. Balachandran, J. Ma, J. Tenreiro Machado, G. Stepan (Springer, Cham, 2020), pp. 75–83
2. S. Carillo, M. Lo Schiavo, C. Schiebold, N -soliton matrix mKdV solutions: a step towards their classification. Preprint 2021
3. S. Carillo, C. Schiebold, Noncommutative Korteweg-de Vries and modified Korteweg-de Vries hierarchies via recursion methods. *J. Math. Phys.* **50**, 073510 (2009)
4. S. Carillo, C. Schiebold, Matrix Korteweg-de Vries and modified Korteweg-de Vries hierarchies: noncommutative soliton solutions. *J. Math. Phys.* **52**, 053507 (2011)
5. B. Carl, C. Schiebold, Ein direkter Ansatz zur Untersuchung von Solitongleichungen. *Jahresber. Deutsch. Math.-Verein.* **102**, 102–148 (2000). (for a translation see <http://apachepersonal.miun.se/~corsch/JahresberichteDMV.PDF>)
6. V.A. Marchenko, *Nonlinear Equations and Operator Algebras* (Reidel, Dordrecht, 1988)
7. A.L. Sakhnovich, L.A. Sakhnovich, I. Ya. Roitberg, Inverse problems and nonlinear evolution equations, in *Solutions, Darboux Matrices and Weyl-Titchmarsh Functions*. *Studies in Mathematics*, vol. 47 (De Gruyter, Berlin 2013)

8. C. Schiebold, Matrix solutions for equations of the AKNS system, in *Nonlinear Systems and their Remarkable Mathematical Structures*, ed. by N. Euler (CRC Press, Boca Raton, 2018), Chapter B.5, pp. 256–293
9. F. Calogero, A. Degasperis, Spectral transform and solitons: Tools to solve and investigate nonlinear evolution equations, in *Studies in Mathematics and Its Applications*, vol. 13 (North-Holland, Amsterdam, 1982)
10. C. Gu, H. Hu, Z. Zhou, Darboux transformations in integrable systems, in *Theory and Their Applications to Geometry*. Mathematical Physics Studies, vol. 26 (Springer, Dordrecht, 2005)
11. C. Rogers, W. Schief, Bäcklund and darboux transformations, in *Geometry and Modern Applications in Soliton Theory*. Cambridge Texts in Applied Mathematics, vol. 30 (Cambridge University Press, Cambridge, 2002)
12. C. Rogers, W.F. Shadwick, *Bäcklund Transformations and Their Applications*. Mathematics in Science and Engineering, vol. 161 (Academic, New York, 1982)
13. H. Blohm, Solution of nonlinear equations by trace methods. *Nonlinearity* **13**, 1925–1964 (2000)
14. X. Chen, Y. Zhang, J. Liang, R. Wang, The N-soliton solutions for the matrix modified Korteweg-de Vries equation via the Riemann-Hilbert approach. *Eur. Phys. J. Plus* **135**, 574 (2020)
15. V.M. Goncharenko, Multisoliton solutions of the matrix KdV equation. *Theor. Math. Phys.* **126**, 81–91 (2001)
16. D. Levi, O. Ragnisco, M. Bruschi, Continuous and discrete matrix Burgers' hierarchies. *Il Nuovo Cimento B* **74**, 33–51 (1983)
17. C. Schiebold, Noncommutative AKNS systems and multisoliton solutions to the matrix sine-Gordon equation. *Discrete Contin. Dyn. Syst.* **2009**, 678–690 (2009)
18. B. Fuchssteiner, S. Carillo, Soliton structure versus singularity analysis: Third-order completely integrable nonlinear differential equations in 1+1-dimensions. *Physica A* **154**, 467–510 (1989)
19. S. Carillo, M. Lo Schiavo, E. Porten, C. Schiebold, A novel noncommutative KdV-type equation, its recursion operator, and solitons. *J. Math. Phys.* **59**, 043501 (2018)
20. S. Carillo, M. Lo Schiavo, and C. Schiebold, Abelian versus non-Abelian Bäcklund charts: Some remarks. *Evol. Equ. Control Theory* **8**, 43–55 (2019)
21. V.E. Zakharov, A. Shabat, Exact theory of two-dimensional self-focusing and one-dimensional self-modulation of waves in nonlinear media. *Sov. Phys. JETP* **34**, 62–69 (1972)
22. S. Carillo, C. Schiebold, Construction of soliton solutions of the matrix modified Korteweg-de Vries equation (2020). Preprint arXiv:2011.12677

Part VII
Chaotic Systems, Stochasticity, and
Uncertainty

Frequency Locking, Quasiperiodicity, and Chaos Due to Special Relativistic Effects



Derek C. Gomes and G. Ambika

1 Introduction

Most of the studies in nonlinear dynamical systems deal with non-relativistic regime and chaos exists in such systems due to their inherent nonlinearity. The study of chaos in relativistic systems is an interesting area of research both for its own nature as well as for its applications in many experimental contexts where particle oscillations occur at effectively very high velocities [1, 2]. The addition of relativistic corrections to linear dynamical systems can induce nonlinearity in them and hence has been reported recently to exhibit chaotic dynamics [3–6]. The classical and quantum dynamics of kicked relativistic particle in a box and driven oscillator are also studied recently [7]. The 2-dimensional relativistic anisotropic, harmonic oscillator is shown to be chaotic [3]. Also the dynamics of a quartic oscillator at relativistic energies exhibits bifurcations and chaos and is found to have a transition to periodic regular motion for large forcing [8]. The nonlinear dynamics of the constant-period oscillator under external periodic forcing displays nonlinear resonances and chaos when the driving force is sufficiently strong [9].

While it is thus established that chaos must appear in most integrable classical systems due to special relativistic corrections to the dynamics, the details of the dynamical states and route to chaos in them are still not fully understood. In our study of the one-dimensional forced harmonic oscillator we show how the natural frequency varies with increasing relativistic effects. We then find that the system exhibits frequency locked and quasiperiodic states as the natural frequency changes. We also indicate a novel route to chaos in this system as the effects of relativistic

D. C. Gomes · G. Ambika (✉)

Department of Physics, Indian Institute of Science Education and Research (IISER) Tirupati,
Tirupati, India

e-mail: derekgomes@students.iisertirupati.ac.in; g.ambika@iisertirupati.ac.in

corrections are tuned. When damping is present, we report that the system exhibits multi-stable states due to nonlinear effects induced by relativistic corrections. Also, to the best of our knowledge, our study for the first time on the relativistic version of the Hénon-Heiles system reports an enhancement of chaotic regions in the relativistic regime.

2 Relativistic Forced Harmonic Oscillator

The harmonic oscillator is a popular prototype, widely used in all branches of Physics to understand periodic oscillations as well as to approximate a variety of vibrations in real systems. One of the reasons for this is the extreme simplicity with which it can be used both in classical and quantum regimes giving analytic solutions. This means harmonic oscillator is integrable in classical mechanics and analytically solvable in quantum mechanics and this holds true in many dimensions even with damping and forcing. However, in the special relativistic regime, even the 1-d harmonic oscillator is not integrable and we see the relativistic harmonic oscillator under forcing and damping can give rise to nonlinear dynamical states due to the nonlinearity introduced by special relativistic effects.

The Hamiltonian for the relativistic forced harmonic oscillator (with rest mass unity) is

$$H = \sqrt{p^2 c^2 + c^4} + \frac{1}{2} k x^2 + x F \cos \omega t \quad (1)$$

which leads to the equations of motion

$$\frac{dx}{dt} = \frac{p}{\sqrt{1 + \frac{p^2}{c^2}}} \quad (2)$$

$$\frac{dp}{dt} = -kx - F \cos \omega t \quad (3)$$

It is clear that the above system (all variables in suitable units) is nonlinear, with the spring constant (k), the forcing amplitude (F), and the driving frequency (ω). As reported by Kim and Lee [6], we control the relativistic effects in the system by treating the speed of light, c , as an additional parameter. As we will see in the next section, the relativistic corrections occur as functions of p/c (where p is the momentum) and decreasing the value of c for similar values of p effectively increases the impact of relativistic effects in the system.

3 Shift in Natural Frequency

One of the main changes in the system in Eq. (1) from its non-relativistic counterpart is that its natural frequency is no longer constant with amplitude, just like a nonlinear oscillator. In order to get a better understanding of how this change occurs and the factors that influence this, we expand Eq. (2) up to first order, to get

$$\frac{dx}{dt} = p(1 - p^2/2c^2) \tag{4}$$

neglecting higher-order terms since $c \gg p$. In this limit the relativistic effects act like a perturbation as in Eq. (4). In this context, perturbation approaches can be used as reported in the case of the constant-period oscillator [9] using canonical perturbation theory. We use a different (but equivalent) approach developed by Lindstedt [10] to calculate the effect of the perturbation on the natural frequency. Then the expression for the frequency, $\omega_{0,rel}$ (up to first order) is

$$\omega_{0,rel} = \omega_0 \left[1 - \frac{3}{16c^2} \left\{ p(0)^2 + \omega_0^2(x(0) + \frac{F}{\omega_0^2 - \omega^2})^2 \right\} - \frac{3\omega^2 F^2}{8c^2(\omega_0^2 - \omega^2)^2} \right] \tag{5}$$

Here (ω_0) is the natural frequency in the non-relativistic limit ($c \rightarrow \infty$). We find that the resultant frequency decreases due to the perturbation. Although we consider the case of a weak relativistic perturbation for the analytical calculation in Eq. (5), the approach is suggestive of the parameters that play a role in the shift in frequency. We present this effect more explicitly by computing the power spectra from the numerically obtained time series of the position variable of the system.

In Fig. 1 we show the power spectra for increasing relativistic effects in the system. It is clear that the natural frequency decreases, while, as expected, the driving frequency (taken as $\omega = 4$) remains the same. We note that the greater the relativistic correction (i.e., smaller the parameter c), the smaller is the natural frequency corresponding to the largest peak. The dynamical states corresponding to the three values of c used are clear from the Poincaré plots in Fig. 1d.

By tuning c as a parameter, we compute the shift in natural frequency from the power spectra and plot this shift with c in Fig. 2. The solid curve in the figure shows the numerical fit to the variation of shift in frequency ($\omega_0 - \omega_{0,rel}$) $\approx \omega_0(1 + (c/a)^2)^{-1}$, where $\omega_0 = 1$. The fitting parameter, $a = 122.6$, is estimated by the nonlinear least squares method. We note up to first order, this relation agrees with the nature of variation obtained in Eq. (5) from the perturbation theory approach. In the next section, we present how the shift in the natural frequency can lead to different dynamical states in the system.

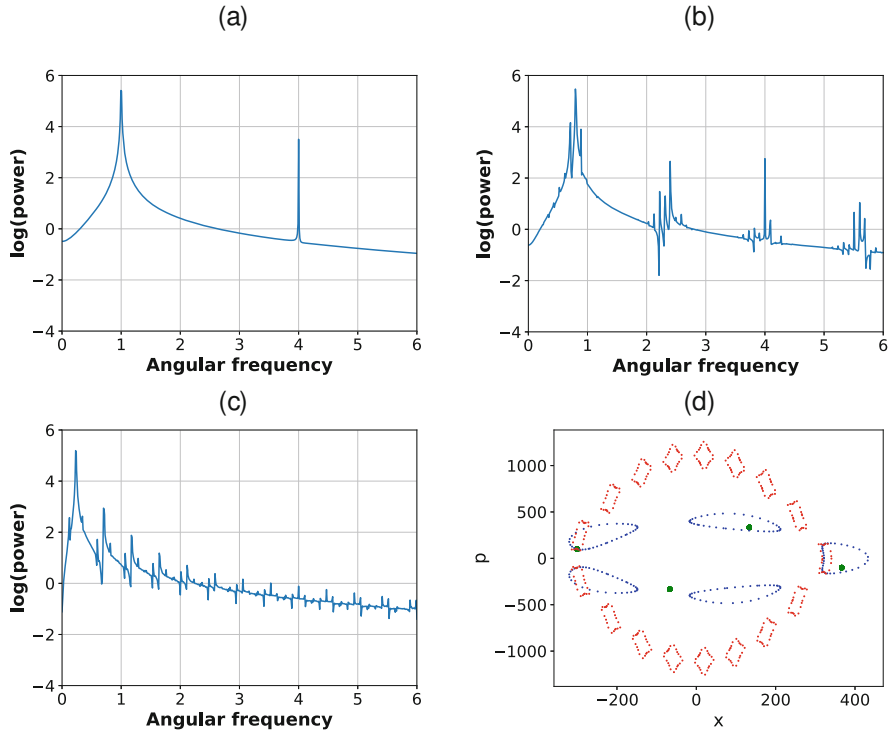


Fig. 1 Power spectra of $x(t)$ for varying c . (a) $c = 300000$ (b) $c = 300$ (c) $c = 50$, the other parameters are fixed as $k = 1, F = 500, \omega = 4, x(0) = -300, p(0) = 100$. (d) Poincaré plot of the phase space showing resonances corresponding to the parameters in the power spectra, color coded as the red points correspond to (c), the blue points to (b) and the green points (enlarged for visualization) to (a)

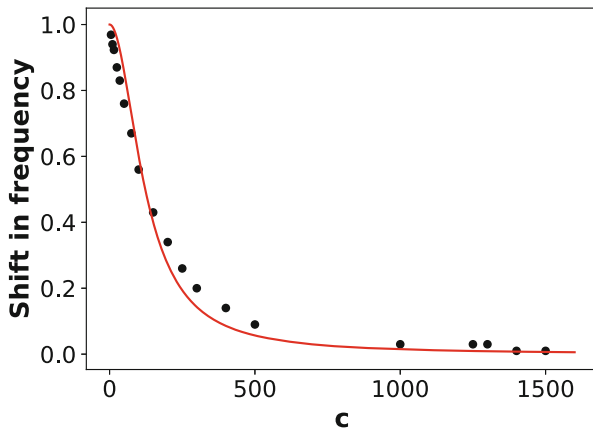


Fig. 2 Shift in the natural frequency of the relativistic harmonic oscillator as a function of c

4 Frequency Locked and Quasiperiodic States

The fact that the natural frequency continuously decreases makes it possible for the system to get into rational and irrational ratios with the driving frequency and therefore the dynamics also leads to frequency locked and quasiperiodic states. The frequency locked states corresponding to rational ratios and the values of c at which they occur are clear from the plateaus in the Devil’s Staircase plot in Fig. 3. The most prominent plateau is for $w_{0,rel} = 0.8$, with the driving frequency at 4 giving a ratio of 5. As the natural frequency continuously decreases, the ratios 6, 7, 8, etc. also appear. Also it is equally likely that as the ratios of frequencies vary due to changes in c , they enter into irrational ratios and hence can give rise to quasiperiodic dynamics in the system.

The structure of the trajectories corresponding to both types of dynamical states discussed above are clear from the Poincaré plots that show trajectories in phase space sampled at the driving frequency. The resonances corresponding to the rational ratios of frequencies are shown in Fig. 4. As the natural frequency decreases with decrease in c , the ratio of frequencies and hence the number of resonances also increase. We note that the odd-numbered (corresponding to odd ratio) resonances are more prominent than their even-numbered counterparts. The occurrence of only odd-numbered resonances (up to first order) has been attributed to the symmetry of the potential in the earlier work on the relativistic driven harmonic oscillator [6] as well as in similar relativistic systems [9]. We observe the even-numbered resonances arise from higher-order effects but are confined to very small regions of phase space. The continuous trajectories shown in Fig. 5 indicate occurrence of quasiperiodic states for two different values of c .

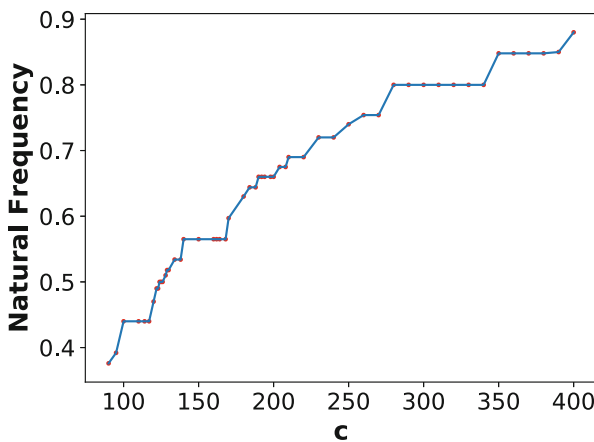


Fig. 3 Devil’s staircase plot of natural frequency as c is varied, keeping forcing amplitude constant. The other parameters are the same as in Fig. 1

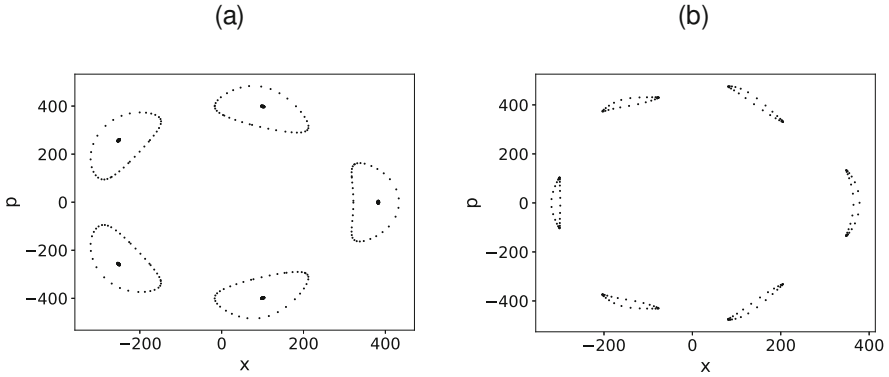


Fig. 4 Poincaré plots showing frequency locked states with their islands (a) $c = 300$, number of resonances, $N = 5$ (b) $c = 200$, $N = 6$

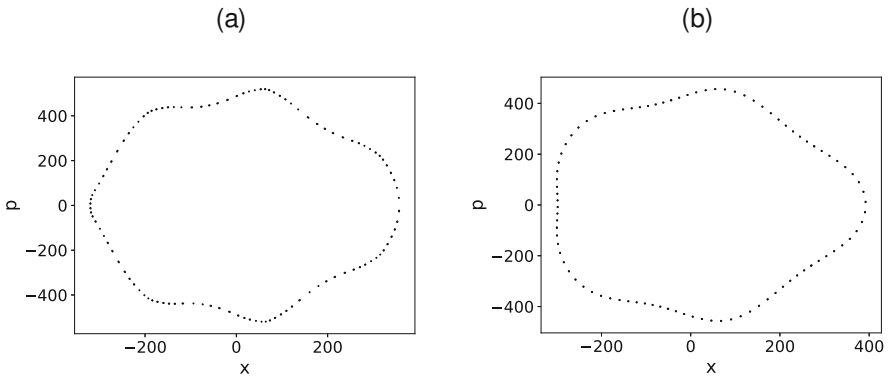


Fig. 5 Poincaré plots showing quasiperiodic states. In (a) $c = 175$ and in (b) $c = 250$

5 Chaos Induced by Relativistic Effects

We observe the occurrence of chaos induced by relativistic effects in regions confined between the other types of trajectories. We plot in Fig. 6 the Poincaré plots of the phase space of the system with the same set of initial conditions and parameters but reducing the value of c . It is clear from Fig. 6 that as c decreases the chaotic regions appear in phase space due to disappearance of the even-resonance states. Thus in Fig. 6b. the chaotic trajectory occurs near the $N = 10$ resonance while the nearby trajectories of $N = 9$ and $N = 11$ resonances are still preserved. In Fig. 6c. where c is decreased even further, only odd resonances are visible in between chaotic regions. To further visualize chaos in this system we plot in Fig. 6d. the power spectrum corresponding to a chaotic trajectory in Fig. 6b.

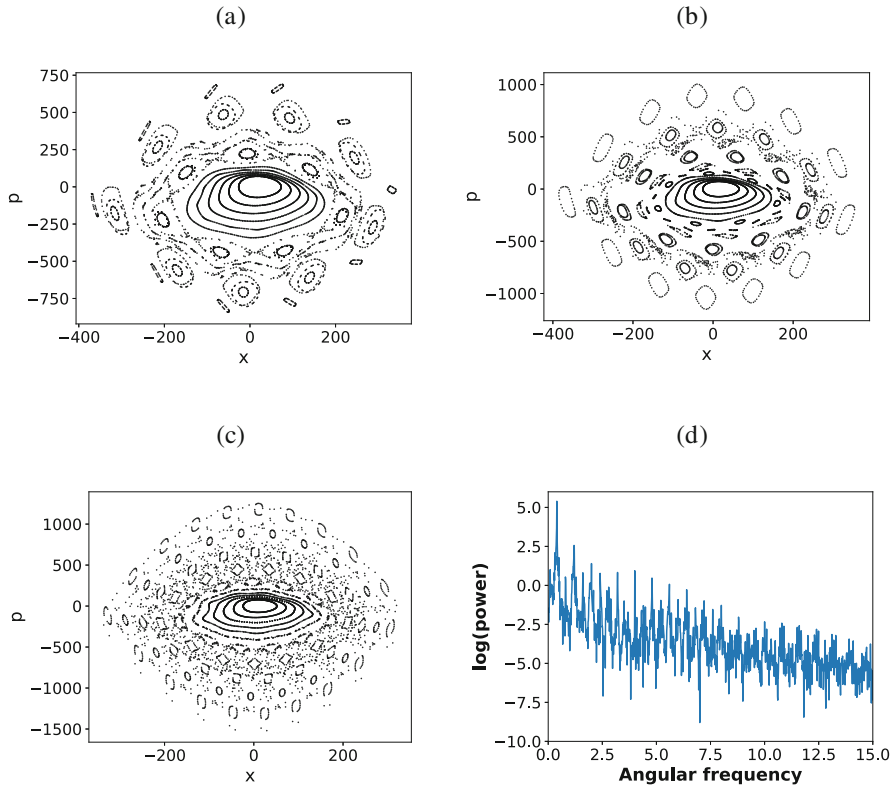


Fig. 6 Poincaré plots of the phase space trajectories indicating the appearance of chaotic regions as c is decreased (a) $c = 100$ (b) $c = 75$ (c) $c = 45$, (d) Power spectrum for a chaotic trajectory from (b)

6 Multi-Stability in Damped Relativistic Oscillator

In this section we consider the damped harmonic oscillator in the relativistic regime with the following equations

$$\frac{dx}{dt} = \frac{p}{\sqrt{1 + \frac{p^2}{c^2}}}; \frac{dp}{dt} = -kx - bp - F \cos \omega t \tag{6}$$

where the additional term is $-bp$, with b as the damping parameter. We find that relatively small damping in the system, with relativistic effects leads to multi-stable states, very different from the damped driven non-relativistic oscillator. This is seen in Fig. 7 where the phase space structure for the same set of 20 different initial conditions are shown for the undamped non-relativistic, damped non-relativistic, and damped relativistic cases. In the damped relativistic case, we find the system

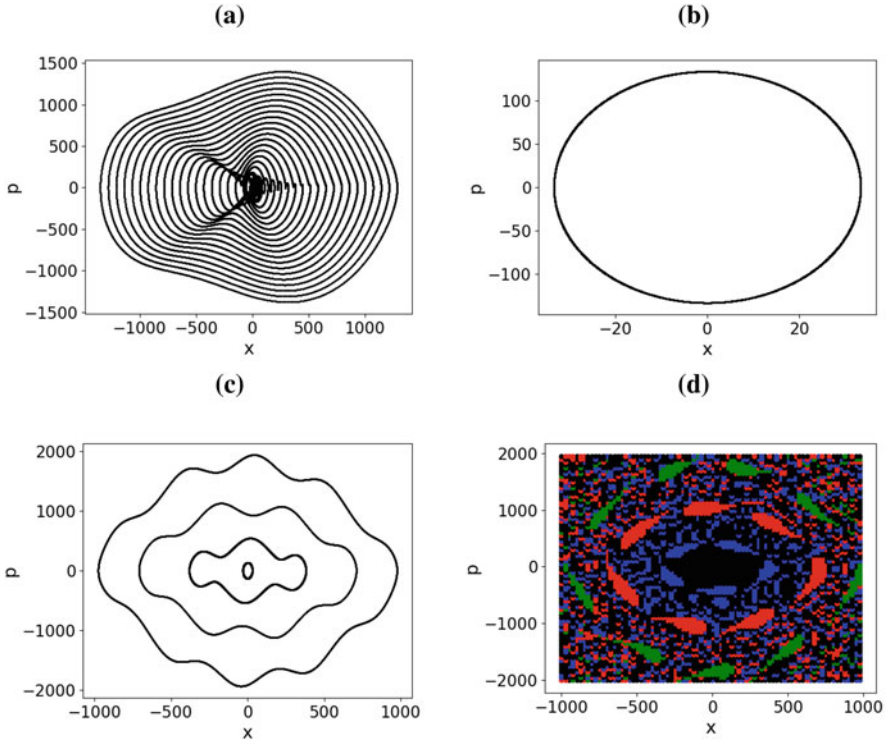


Fig. 7 Phase space trajectories starting from the same set of 20 initial conditions for (a) undamped non-relativistic (b), damped non-relativistic (c) damped relativistic oscillator. Here $b = 0.01$ and $c = 300$. In (d) we plot the basin structure for the system where the four different colors correspond to the basins of the four different attractors in the damped relativistic case in (c) (the colors black, blue, red, and green represent the smallest to largest attractor, respectively)

settles to four different states or attractors. To confirm multi-stability, we present the basin structure corresponding to these four attractors.

7 Relativistic Hénon-Heiles System

As another system of interest, we study the effects of special relativity in an intrinsically nonlinear and nonintegrable system, the Hénon-Heiles system. This system models the stellar motion about a galactic center and is known to have a rich dynamics [11]. The potential of the system models the galactic potential centered around the galactic center in the $x - y$ plane given by

$$V(x, y) = \frac{1}{2}(x^2 + y^2) + \lambda \left(x^2y - \frac{y^3}{3} \right) \tag{7}$$

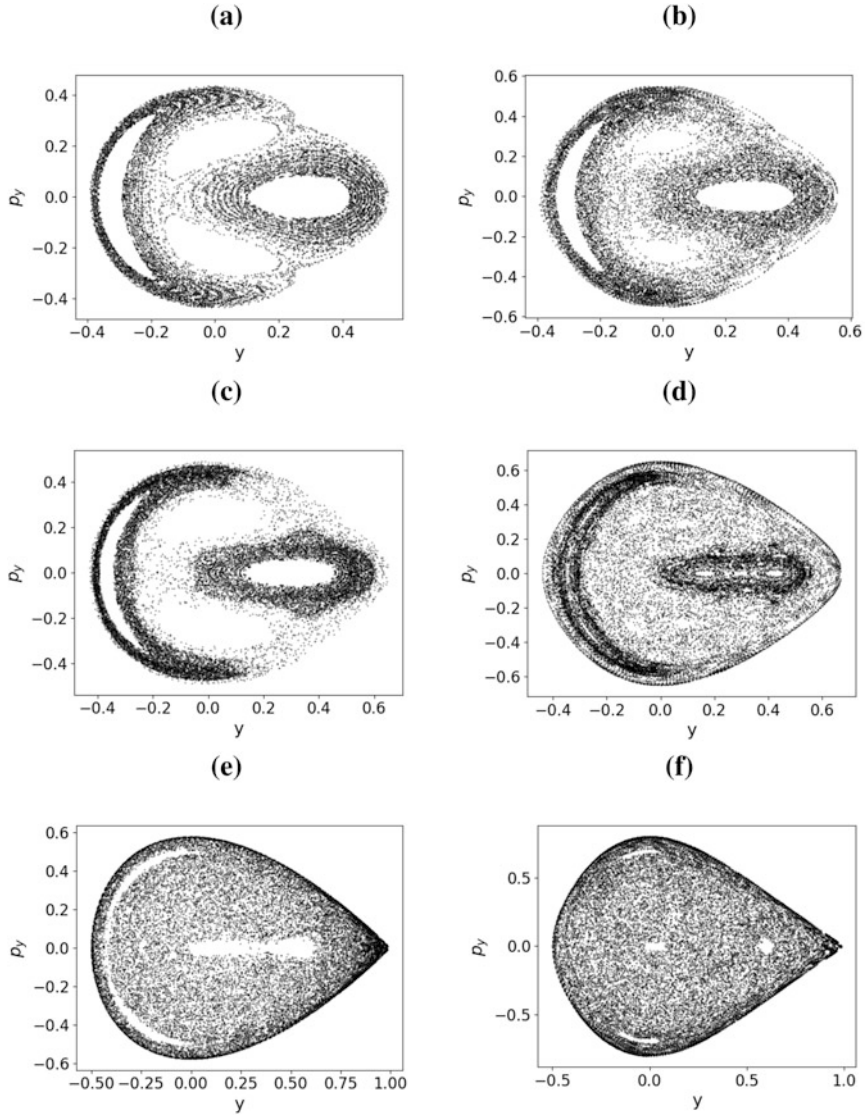


Fig. 8 Phase space structure in the $y - p_y$ plane for the relativistic Hénon-Heiles system (right) compared with that of the non-relativistic system(left) **(a)** $E = 0.10$, non-relativistic **(b)** $E = 0.10$, relativistic **(c)** $E = 0.125$,non-relativistic **(d)** $E = 0.125$, relativistic **(e)** $E = 1/6$,non-relativistic **(f)** $E = 1/6$, relativistic, where relativistic cases correspond to $c = 0.3$

The relativistic Hamiltonian is

$$H = \sqrt{p^2 c^2 + c^4} - c^2 + V(x, y) \tag{8}$$

where rest mass is unity and we have subtracted the rest energy(c^2) from the Hamiltonian as it is usually not considered in measuring energy in the non-relativistic case. In general, this has no significance in the equations of motion and as the total energy E is treated as a parameter in studying the Hénon-Heiles system [11] and for making comparison with well-studied non-relativistic case, it is important to subtract this contribution. We note that in the limit as $c \rightarrow \infty$ the Hamiltonian in Eq. (8) reduces to the non-relativistic one. Our main result in this study is that adding relativistic corrections leads to enhanced chaos in the system. This is clear from the phase space structures shown in the $y - p_y$ plane of phase space in Fig. 8 for both non-relativistic and the corresponding relativistic regimes for three different values of E (we take $\lambda = 1$ and p_y corresponds to momentum conjugate to y).

8 Conclusions

We report the different dynamical states induced by special relativistic effects in a harmonic oscillator with sinusoidal forcing. We present perturbation methods and numerical computations to show how the relativistic corrections shift the natural frequency and consequently generate frequency locked and quasiperiodic states. We also show how reducing the value of c can lead to chaos with the disappearance of even resonances. In the presence of small damping, the forced harmonic oscillator exhibits multi-stable states with an interesting basin structure [12]. In an inherent nonlinear system like Hénon-Heiles system, we report the enhancement of chaos as the relativistic effects are tuned.

References

1. M. Billardon, Storage ring free-electron laser and chaos. *Phys. Rev. Lett.* **65**, 713–716 (1990)
2. K.M. Fujiwara, Z.A. Geiger, K. Singh, R. Senaratne, S.V. Rajagopal, M. Lipatov, T. Shimasaki, D.M. Weld, Experimental realization of a relativistic harmonic oscillator. *New J. Phys.* **20**, 063027 (2018)
3. R.S.S. Vieira, T.A. Michtchenko, Relativistic chaos in the anisotropic harmonic oscillator. *Chaos, Solitons and Fractals* **117**, 276–282 (2018)
4. S.P. Drake, C.P. Dettmann, N.E. Frankel, N.J. Cornish, Chaos in special relativistic dynamics. *Phys. Rev. E.* **53**, 1351–1361 (1996)
5. A.L. Harvey, Relativistic harmonic oscillator. *Phys. Rev. D.* **6**, 1474–1476 (1972)
6. J.H. Kim, H.W. Lee, Relativistic chaos in the driven harmonic oscillator. *Phys. Rev. E.* **51**, 1579–1581 (1995)
7. J.R. Yusupov, D.M. Otajanov, V.E. Eshniyazov, D.U. Matrasulov, Classical and quantum dynamics of a kicked relativistic particle in a box. *Phys. Rev. A.* **382**, 633–638 (2018)
8. S.W. Kim, H.W. Lee, Bifurcation and chaos in a periodically driven quartic oscillator at relativistic energies. *Int. J. Bifurc. Chaos* **7**, 945–949 (1996)

9. S.W. Lee, J.H. Kim, H.W. Lee, Relativistic nonlinear dynamics of a driven constant-period oscillator. *Phys. Rev. E*. **56**, 4090–4096 (1997)
10. M.A. Lieberman, A.J. Lichtenberg, *Regular and Chaotic Dynamics* (Springer, Berlin, 1983)
11. R.C. Hilborn, *Chaos and Nonlinear Dynamics* (Oxford University Press, Oxford, 1985)
12. D.C. Gomes, G. Ambika, Frequency locking, Quasi periodicity and Chaos due to special relativistic effects (2021). Preprint arXiv:2101.00139v2

High Frequency Chaotic Behavior in Non-ideal Operational Amplifier



**Maide Bucolo, Arturo Buscarino, Carlo Famoso, Luigi Fortuna,
and Salvina Gagliano**

1 Introduction

The simplest ideal electronic circuit producing a chaotic behavior must include three memory elements and a nonlinear device. The nonlinear device can be a diode, and the nonlinearity of parasitic capacitance of the diode determines the occurrence of chaos, such as in the inductor-capacitor-diode circuit discussed [1]. A consideration can be performed on the basis of this standard example: chaotic behavior and nonlinear dynamics arise thanks to an imperfection in the diode manufacturing process [2].

Therefore, parasitic nonlinearities, which often represent undesired effects, actually make the device an *imperfect* element, thus enhancing its characteristics and allowing for richer dynamics that would otherwise not be observable [3, 4].

In the following, we examine two electronic circuits based on an Operational Amplifier (OpAmp). We use two off-the-shelf integrated circuits implementing the OpAmp. Both realizations display manufacturing imperfections, which, in the end, allow the observation of unexpected high frequency chaotic oscillations [5].

The paper is organized as follows. In Sect. 2, the two circuits are discussed. In Sect. 3, experimental results proving the occurrence of high frequency chaos are shown. Conclusive remarks are discussed in Sect. 4.

M. Bucolo · A. Buscarino · L. Fortuna (✉)
DIEEI, University of Catania, Catania, Italy

CNR-IASI, Italian National Research Council Institute for Systems Analysis and Computer
Science, Rome, Italy
e-mail: maide.bucolo@unict.it; arturo.buscarino@unict.it; luigi.fortuna@unict.it

C. Famoso · S. Gagliano
DIEEI, University of Catania, Catania, Italy
e-mail: carlo.famoso@dieei.unict.it; salvina.gagliano@unict.it

2 The Circuits

The first system we examine is based on the integrated circuit *LM311p*, manufactured by Texas Instruments. It is a high-speed differential voltage comparator.

A voltage comparator is a circuit that serves to compare two voltage values, i.e., the value applied at the input (V_{in}) is compared with a fixed threshold value (V_{REF}). If the applied input value is different from the threshold value, the circuit changes the output logic state providing, as appropriate, a logic level 1 (maximum positive voltage) or a logic level 0 (zero voltage).

However, to verify that the device imperfections can enrich the dynamics of a circuit, the chaotic circuit proposed in this contribution is realized by designing an electronic system with an integrated voltage comparator circuit *LM311p*. The schematic circuit diagram used for our experiment is shown in Fig. 1.

Its extreme simplicity of construction emerges from the physical implementation obtained using the *LM311p* integrated device, as reported in Fig. 2.

The circuit encompasses mainly passive elements, as a variable resistor R_5 , which acts as a bifurcation parameter, and, most notably, no reactive elements

Fig. 1 Single OpAmp voltage comparator

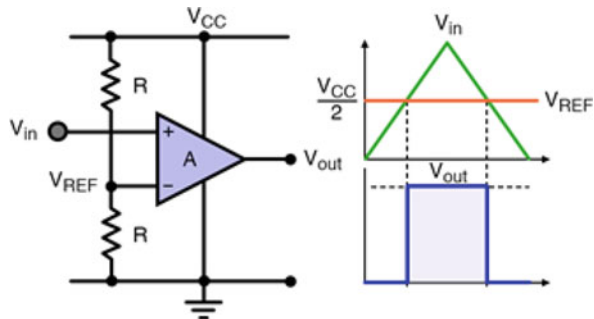
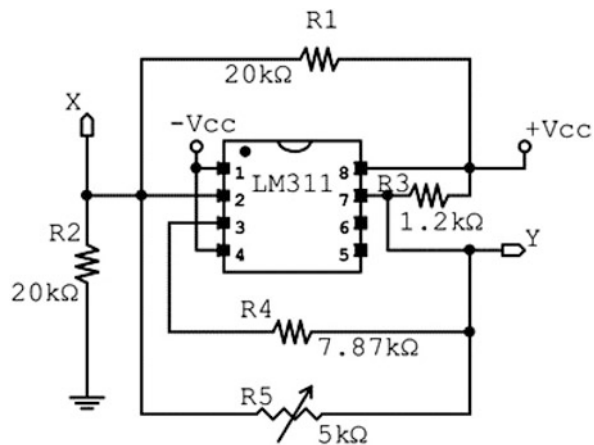


Fig. 2 Schematic diagram of the circuit based on the voltage comparator



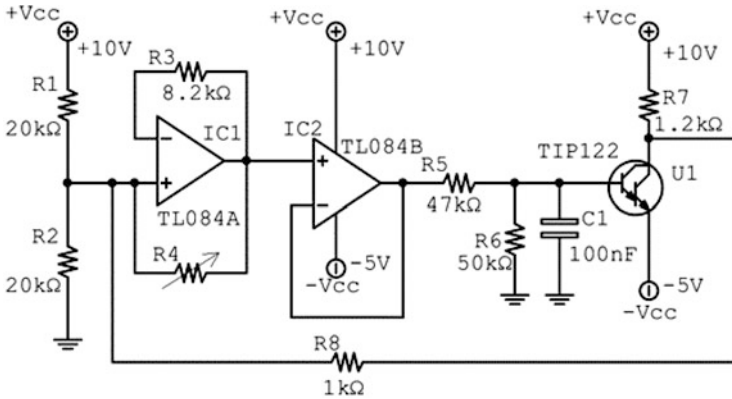


Fig. 3 Schematic diagram of the circuit based on TL084 and TIP122

(capacitors or inductors) are explicitly present. The supply voltage is fixed $V_+ = 9.98\text{ V}$ and $V_- = -3.99\text{ V}$.

The observed dynamical behavior is investigated by varying R_5 . We acquired the voltage at points labeled X, and Y, in Fig. 1, by using the digital oscilloscope Agilent DSOX4052A at a sampling frequency of 1 MHz.

The second system we examined was realized joining a high-speed operational amplifier TL084 (manufactured by STMicroelectronics) and a NPN Darlington Power Transistor TIP122 (manufactured by STMicroelectronics). The circuit is shown in Fig. 3.

It consists, besides the integrated device and the NPN Power Darlington Transistor, only in resistors and a capacitor $C_1 = 100\text{ nF}$. The input of the transistor is decoupled through the use of a voltage follower. The supply voltage is fixed at $V_+ = 10\text{ V}$ and $V_- = -5\text{ V}$.

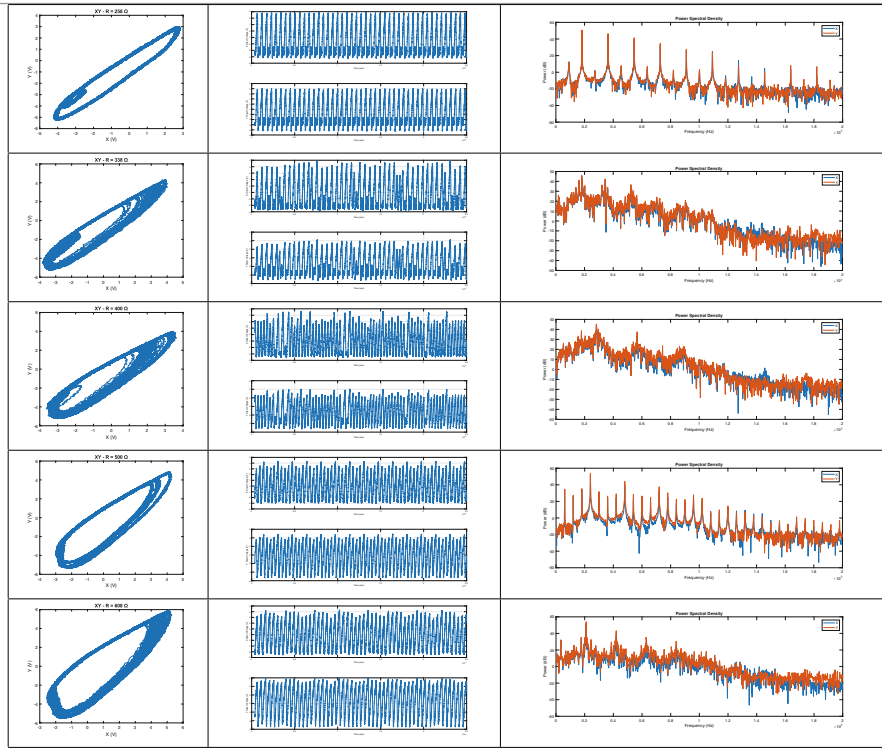
The nonlinear dynamical behavior of this circuit is investigated when the potentiometer R_4 , realized by a 1 kΩ trimmer, is varied. The voltages at the non-inverting input of the OpAmp and at the collector of the transistor have been acquired at a sampling frequency of 1 MHz.

3 Results

The behavior of the first circuit has been examined for a wide range of values of R_5 , from 250 to 600 Ω and typical examples of the temporal behavior of signals at point X and Y are displayed in Table 1.

The signals for $R_5 = 338\text{ Ω}$ and $R_5 = 40\text{ Ω}$ have a larger spectral content with respect to those related to $R_5 = 258\text{ Ω}$ and $R_5 = 50\text{ Ω}$, thus ranging from chaos to a limit-cycle behavior. Notably, the spectral content is up to 10 MHz.

Table 1 Nonlinear dynamics obtained varying R_5 in the circuit with the LM311p. From left to right: reconstructed attractors, temporal trends, frequency spectrum. From top to bottom: $R_5 = 258 \Omega$, $R_5 = 338 \Omega$, $R_5 = 400 \Omega$, $R_5 = 500 \Omega$, $R_5 = 608 \Omega$



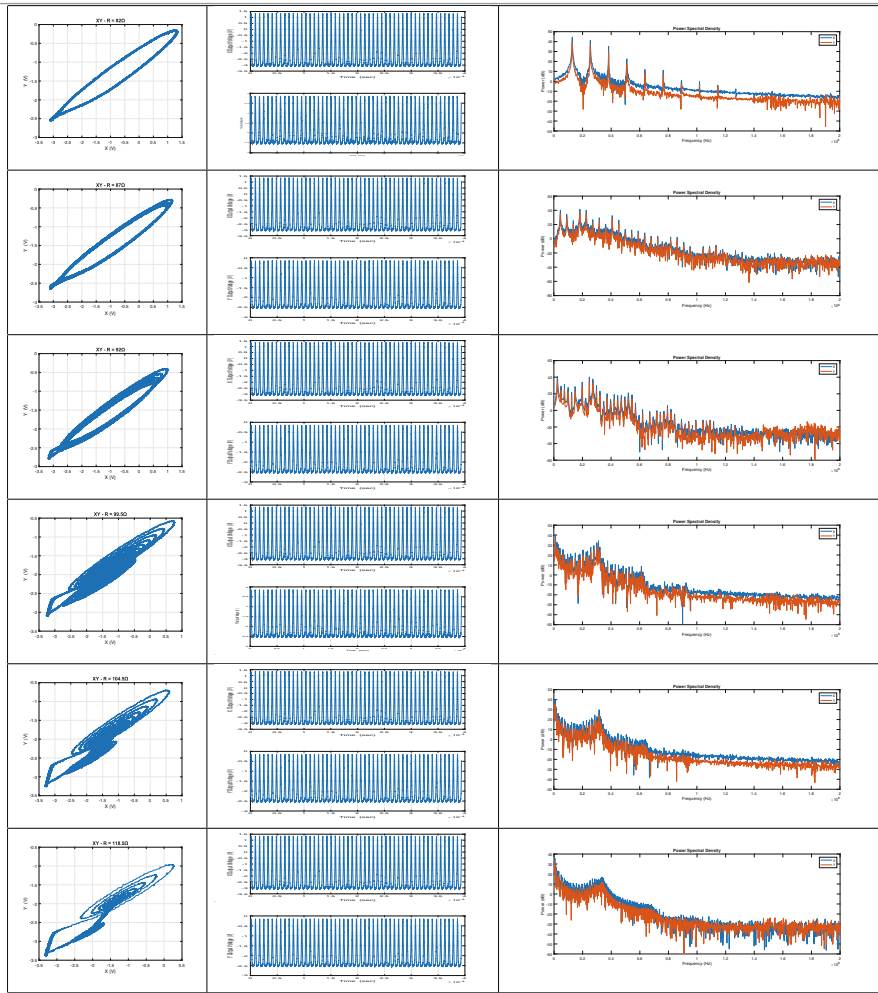
With a similar methodology we examined the second circuit. The trimmer R_4 assumes values between 82 and 118.5Ω . The temporal behavior and the spectral analysis of the acquired signals are displayed in Table 2.

As it can be inferred for the spectral analysis, the dynamics of the system is richer when R_4 is increased, ranging from a periodic motion to a chaotic flow. Spectral content is up to a 1 MHz bandwidth.

4 Conclusions

The occurrence of chaos due to imperfections in two integrated circuits from different manufacturers (Texas Instruments, STMicroelectronics) has been unveiled in this paper. It has been observed that each sample leads to different chaotic and periodic windows in the parameter space, still maintaining the occurrence of nonlinear oscillations.

Table 2 Nonlinear dynamics obtained varying R_4 by the circuit with TL084 and TIP122. From left to right: reconstructed attractors, temporal trends, frequency spectrum. From top to bottom: $R_4 = 82 \Omega$, $R_4 = 87 \Omega$, $R_4 = 92 \Omega$, $R_4 = 100 \Omega$, $R_4 = 104 \Omega$, $R_4 = 120 \Omega$



The fundamental conceptual difference of the circuits under consideration with respect to other simple chaos generators is that the complex dynamics emerges from the imperfections of the active device. It is due to these imperfections that bring out dynamics that would otherwise remain latent, enriching the collection of possible behaviors.

Moreover, the simplicity and cheapness of the implementations proposed make them good candidates as paradigmatic examples of imperfect nonlinear electronic systems.

References

1. M.J. Hasler, Electrical circuits with chaotic behavior. *Proc. IEEE* **75**(8), 1009–1021 (1987).
2. M. Bucolo, A. Buscarino, C. Famoso, L. Fortuna, M. Frasca, Control of imperfect dynamical systems. *Nonlinear Dyn.* **98**(4), 2989–2999 (2019).
3. A. Buscarino, C. Corradino, L. Fortuna, M. Frasca, J.C. Sprott, Nonideal behavior of analog multipliers for chaos generation. *IEEE Trans. Circ. Syst. II Express Briefs* **63**(4), 396–400 (2015)
4. G.S. Yim, J.W. Ryu, Y.J. Park, S. Rim, S.Y. Lee, W.H. Kye, C.M. Kim, Chaotic behaviors of operational amplifiers. *Phys. Rev. E* **69**(4), 045201 (2004)
5. A. Buscarino, L. Fortuna, M. Frasca, *Essentials of Nonlinear Circuit Dynamics with MATLAB and Laboratory Experiments* (CRC Press, Boca Raton, 2017)

Multiple Hysteresis Jump Resonance in a Class of Oscillators with Nonic Polynomial Nonlinearity



Maide Bucolo, Arturo Buscarino, Carlo Famoso, Luigi Fortuna, and Salvina Gagliano

1 Introduction

Jump resonance is a fundamental topic in the area of nonlinear control systems. It consists in a peculiar behavior of the frequency response in forced nonlinear systems involving the occurrence of jumps of the output amplitude when the frequency of the input signal is varied [1, 2]. Since jump resonance may represent a desirable “memory” effect, guidelines to design and implement circuits with multijump resonance can be outlined [3]. Furthermore, with the term multiple hysteresis jump resonance, we indicate a specific case of jump resonance where the frequency response undergoes different hysteresis windows within the same range, thus leading to multiple jump paths. In this contribution we highlight the occurrence of a complex pattern of multiple hysteresis in a nonlinear oscillator involving a nonic nonlinearity.

Recently, analytic results to unveil the conditions ensuring a multiple hysteresis behavior in nonlinear oscillators involving a quintic polynomial nonlinearity have been presented [4]. In this contribution, we focus on determining the existence of a higher order multiple hysteresis behavior, characterizing its robustness with respect to system parameters.

M. Bucolo · A. Buscarino (✉) · L. Fortuna
Dipartimento di Ingegneria Elettrica Elettronica e Informatica, University of Catania, Catania, Italy

CNR-IASI, Italian National Research Council Institute for Systems Analysis and Computer Science, Rome, Italy
e-mail: arturo.buscarino@unict.it

C. Famoso · S. Gagliano
Dipartimento di Ingegneria Elettrica Elettronica e Informatica, University of Catania, Catania, Italy

The rest of the paper is organized as follows: in Sect. 2 the oscillator scheme, based on a Lur’e decomposition, is presented and the analytical approach to determine the nonic multiple hysteresis is discussed, in Sect. 3 the numerical characterization of the nonic multiple hysteresis jump resonance is presented, showing an interesting connection with the onset of chaos. Concluding remarks are given in Sect. 4.

2 Oscillators with Nonic Polynomial Nonlinearities

Given a generic second-order linear system with transfer function $G(s)$, it can be put in a closed-loop scheme where the feedback loop introduces a given nonlinear function $\psi(x)$. This scheme is commonly referred to as Lur’e form [5] of nonlinear feedback systems, where $G(s)$ represents the transfer function of the linear part from which the nonlinearity can be isolated.

Let us consider the Lur’e representation reported in Fig. 1, where the linear is a general second-order transfer function

$$G(s) = \frac{K \omega_0^2}{s^2 + 2\xi \omega_0 s + \omega_0^2} \tag{1}$$

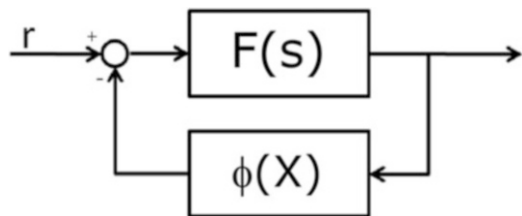
characterized by a gain K , a natural frequency ω_0 , and a damping factor ξ . Furthermore, we consider a nonic polynomial nonlinearity

$$\phi(x) = \bar{A}x^9 + \bar{B}x^7 + \bar{C}x^5 + \bar{D}x^3 \tag{2}$$

where \bar{A} , \bar{B} , \bar{C} , \bar{D} are suitable gains.

A widely used approach to analyze the frequency response of a nonlinear oscillator forced by a sinusoidal input is the so-called describing function approach [1], which, similarly to other classical methods [6], is based on two assumptions: the system variables can be approximated as the sum of a finite number of sinusoidal terms, and a low-pass filtering effect occurs in the loop. Under these assumptions, the nonlinear terms of the system can be represented by functions of the amplitude of their input, as their action is considered as linear. The describing function approach

Fig. 1 Lur’e representation of a nonlinear forced oscillator: $G(s)$ represents the linear part, while $\phi(x)$ is the nonlinearity



has been demonstrated to be effective also in presence of higher harmonics to determine the occurrence of nonlinear behavior, including chaotic oscillations [7].

Referring again to the system in Fig. 1, the signal x can be written as $x(t) = U \sin(\omega t + \psi)$, with U and ψ the amplitude and the phase of $x(t)$. The describing function of the odd nonlinearity $\phi(x)$ depends only on the amplitude U [8], as

$$N(U) = \bar{A} \frac{63}{128} U^8 + \bar{B} \frac{35}{64} U^6 + \bar{C} \frac{5}{8} U^4 + \bar{D} \frac{3}{4} U^2 = AU^8 + BU^6 + CU^4 + DU^2 \quad (3)$$

in which we have defined $A = \frac{63}{128} \bar{A}$, $B = \frac{35}{64} \bar{B}$, $C = \frac{5}{8} \bar{C}$, $D = \frac{3}{4} \bar{D}$. The input signal $r(t) = \bar{R} \sin(\omega t)$ is a solution for the closed-loop system if it occurs:

$$N(U)U + G^{-1}(j\omega)U = \bar{R}e^{-j\psi} \quad (4)$$

Assuming a zero phase, i.e., $\psi = 0$, and indicating with R and I the real and imaginary part of $G^{-1}(j\omega)$, the modulus of Eq. (4) is calculated as:

$$(AU^9 + BU^7 + CU^5 + DU^3 + RU)^2 + (IU)^2 = \bar{R}^2 \quad (5)$$

and thus

$$\begin{aligned} &A^2U^{18} + (2AB)U^{16} + (B^2 + 2AC)U^{14} + (2BC + 2AD)U^{12} \\ &+ (C^2 + 2BD + 2AR)U^{10} + (2CD + 2BR)U^8 + (D^2 + 2CR)U^6 \\ &+ (2DR)U^4 + (I^2 + R^2)U^2 - \bar{R}^2 = 0 \end{aligned} \quad (6)$$

Define now $X = U^2$, so that

$$\begin{aligned} p(X) &= A^2X^9 + (2AB)X^8 + (B^2 + 2AC)X^7 + (2BC + 2AD)X^6 \\ &+ (C^2 + 2BD + 2AR)X^5 + (2CD + 2BR)X^4 + (D^2 + 2CR)X^3 \\ &+ (2DR)X^2 + (I^2 + R^2)X - \bar{R}^2 = 0 \end{aligned} \quad (7)$$

Since jump resonance occurs when the frequency response is a multi-valued function of ω , system parameters must be chosen accordingly. In particular, the multiple hysteresis jump resonance window corresponds to a range of ω for which Eq. (7) admits nine positive real solutions.

A numerical procedure to determine the values of A , B , C , D , R , I , and \bar{R} leading to this condition can be outlined starting from the principle of polynomial identity. We can, thus, fix the nine positive real solutions and determine the corresponding polynomial and solving a system of ten nonlinear equations in six unknowns. Obviously this solution is based on searching an admissible set of positive real solutions for Eq. (7). A different approach is searching for the

limit conditions where three pairs of coincident solutions occur. This means to impose that the ratios between the polynomial $p(x)$ in (7) and the second-order polynomials $p_1(x) = x^2 - 2a_{L,1}x + a_{L,1}^2$, $p_2(x) = x^2 - 2a_{L,2}x + a_{L,2}^2$, and $p_3(x) = x^2 - 2a_{L,3}x + a_{L,3}^2$ have a remainder equal to zero. Therefore it follows

$$\frac{p(X)}{p_1(X)p_2(X)p_3(X)} = q_1(X) + r_1(X) \tag{8}$$

where the quotient is a third order polynomial on which the Cardano conditions [9] can be applied to guarantee three positive real solutions.

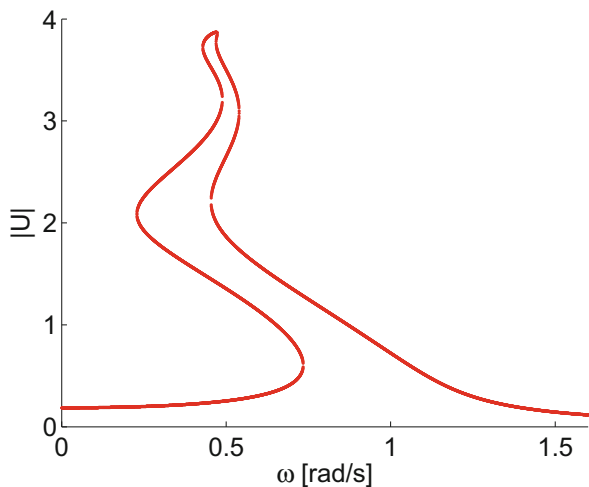
Once retrieved suitable values of parameters, R and I can be used to determine the parameters of the linear part ξ , ω_n , and K .

3 Characterization of Multiple Hysteresis Jump Resonance

A suitable set of nine positive real solutions can be selected as [15.0, 14.5, 13.9, 9,] [4, 2]. The resulting nonlinear systems of ordinary equations can be solved using numerical tools, leading to a set of parameters $A = 1$, $B = -38.09$, $C = 499.68$, $D = -2569.09$, and $\bar{R} = 951.92$. The multiple hysteresis frequency response obtained with this set of parameters, and fixing $K = 0.00019$ and $\xi = 0.05$ for the linear part, is reported in Fig. 2.

The parameter space $K - \xi$, determining the dynamics of the linear part of the oscillator, is now explored by means of numerical simulations to unveil the regions in which multiple hysteresis resonance occurs. The map reported in Fig. 3 characterizes the number of positive and real solutions found for Eq. (7) varying K and ξ . The area of the parameter space in which three, five, seven, or nine solutions

Fig. 2 Multiple hysteresis jump resonance with nine windows of hysteresis in the nonic nonlinear oscillator. Parameters are selected as: $A = 1$, $B = -38.09$, $C = 499.68$, $D = -2569$, $K = 0.00019$, $\xi = 0.05$, $\omega_n = 1$, $\bar{R} = 951.92$



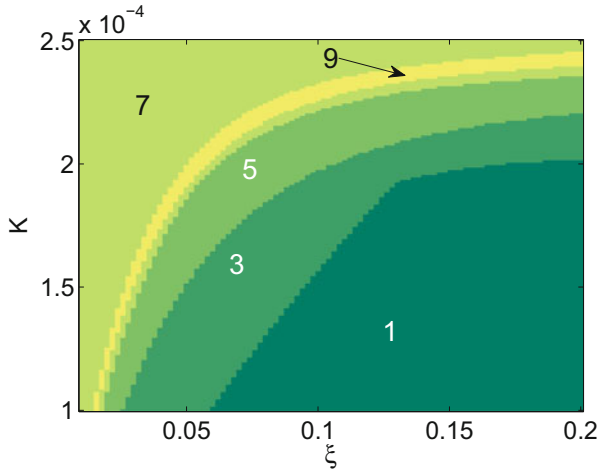


Fig. 3 Multiple hysteresis jump resonance: multiple solutions for Eq. (7) in the parameter space $K-\xi$. Other parameters: $A = 1, B = -38.09, C = 499.68, D = -2569, \omega_n = 1,$ and $\bar{R} = 951.92$

are retrieved correspond to the regions of multiple hysteresis jump resonance. Interestingly, multiple hysteresis jump resonance appears as a robust phenomenon with respect to the considered parameter, even the number of jump paths changes.

An example of multijump range is reported in Fig. 2. In order to further characterize the robustness of the behavior, we calculated the width of the frequency range in which multiple solutions can be retrieved. Let us define the parameters $\Delta\omega_3, \Delta\omega_5, \Delta\omega_7,$ and $\Delta\omega_9$ as the width of the frequency range in which three, five, seven, and nine positive real solutions, respectively, are found. The values of these parameters are reported in the maps reported in Figs. 4, 5, 6, and 7.

A further element of interest is that the trends of hysteresis width varying K are nontrivial. To account for this, we show $\Delta\omega(K)$ in Fig. 8, fixing $\xi = 0.15$. We can assess that the behavior of $\Delta\omega$ is non-monotone.

Multiple hysteresis jump resonance appears to be strictly linked to the onset of chaotic behavior. In fact, fixing ω within the range of multiple hysteresis and increasing the amplitude \bar{R} of the forcing signal, a bifurcation route to chaos can be observed. In Fig. 9, we report in red the limit cycle corresponding to $\bar{R} = 950$ and in blue the chaotic attractor obtained increasing \bar{R} .

4 Conclusions

The characterization of multiple hysteresis jump resonance in forced oscillators with nonic polynomial nonlinearity has been reported in this paper, discussing and evaluating the robustness of the multiple hysteresis jump resonance behavior.

Fig. 4 $\Delta\omega_3$ evaluated in the parameter space $K - \xi$. Other parameters as: $A = 1$, $B = -38.09$, $C = 499.68$, $D = -2569$, $\omega_n = 1$, $\bar{R} = 951.92$

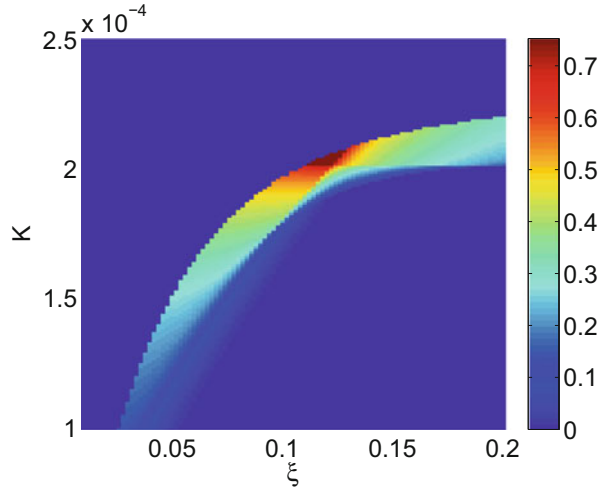
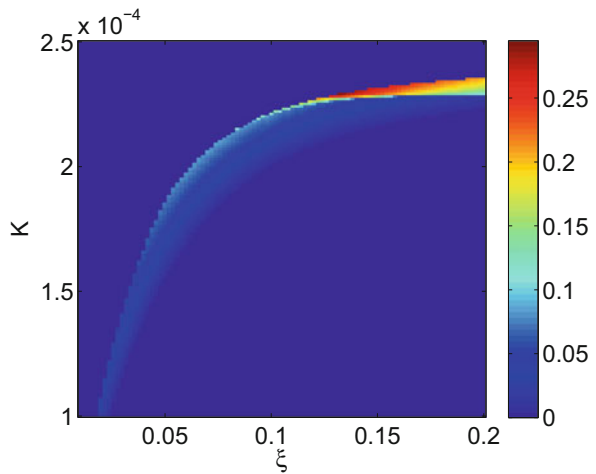


Fig. 5 $\Delta\omega_5$ evaluated in the parameter space $K - \xi$. Other parameters as: $A = 1$, $B = -38.09$, $C = 499.68$, $D = -2569$, $\omega_n = 1$, $\bar{R} = 951.92$



The robustness of the obtained multiple hysteresis windows has been investigated by means of numerical simulations retrieving that the multiple hysteresis jump resonance with different nested windows can be retrieved in the proposed oscillator with given parameters, acting only on the linear part of the oscillator.

Moreover, the possibility to link the occurrence of multiple jump resonance with chaos has been investigated detecting a route to chaos based on varying solely the amplitude of the input signal when the frequency is fixed within the range of jump resonance. This result paves the way to a novel bifurcation scenario typical for nonlinear driven oscillators.

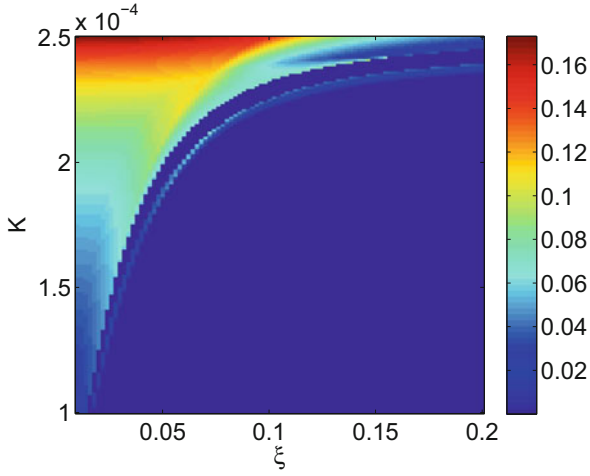


Fig. 6 $\Delta\omega_7$ evaluated in the parameter space $K - \xi$. Other parameters as: $A = 1, B = -38.09, C = 499.68, D = -2569, \omega_n = 1, \bar{R} = 951.92$

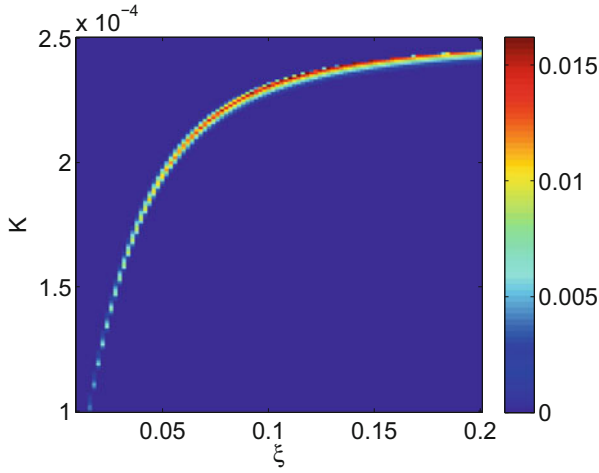


Fig. 7 $\Delta\omega_9$ evaluated in the parameter space $K - \xi$. Other parameters as: $A = 1, B = -38.09, C = 499.68, D = -2569, \omega_n = 1, \bar{R} = 951.92$

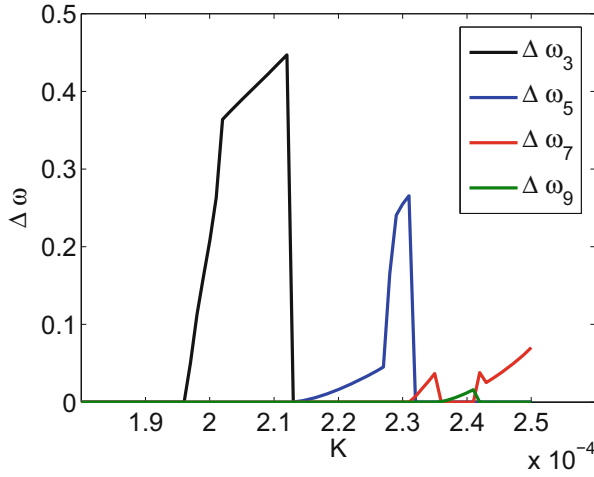


Fig. 8 Width of the jump resonance (three, five, seven, and nine solutions) frequency range for $\xi = 0.15$. Other parameters as: $A = 1$, $B = -38.09$, $C = 499.68$, $D = -2569$, $\omega_n = 1$, and $\bar{R} = 951.92$

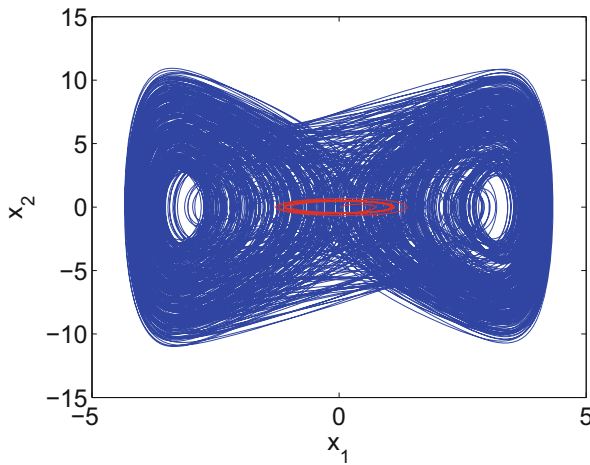


Fig. 9 Multiple hysteresis jump resonance and chaotic behavior. Parameters are selected as: $A = 1$, $B = -38.09$, $C = 499.68$, $D = -2569$, $\omega_n = 1$. The input is a sinusoidal signal with amplitude $\bar{R} = 951.92$ (red curve) and $\bar{R} = 95192$ (blue attractor) and frequency ω

References

1. D.P. Atherton, *Nonlinear Control Engineering* (Van Nostrand Reinhold, Wokingham, 1982)
2. F. Cairone, P. Anandan, M. Bucolo, Nonlinear systems synchronization for modeling two-phase microfluidics flows. *Nonlinear Dyn.* **92**(1), 75–84 (2018)
3. A. Buscarino, C. Famoso, L. Fortuna, M. Frasca, Multi-jump resonance systems. *Int. J. Control* **93**(2), 282–292 (2018)
4. M. Bucolo, A. Buscarino, L. Fortuna, M. Frasca, Multiple Hysteresis Jump Resonance in a Class of Forced Nonlinear Circuits. *Int. J. Bifur. Chaos* **30**(15), 1–13 (2020)
5. A. Buscarino, L. Fortuna, M. Frasca, *Essentials of Nonlinear Circuit Dynamics with MATLAB® and Laboratory Experiments* (CRC Press, Boca Raton, 2017)
6. N.N. Bogoliubov, Y.A. Mitropolski, *Asymptotic Methods in the Theory of Non-linear Oscillations* (Hindustan Publishing, Delhi, 1961)
7. R. Genesio, A. Tesi, Harmonic balance methods for the analysis of chaotic dynamics in nonlinear systems. *Automatica* **28**(3), 531–548 (1992)
8. P.A. Cook, *Nonlinear Dynamical Systems* (Prentice Hall, Hoboken, 1994).
9. Zwillinger, D. (Ed.), *CRC Standard Mathematical Tables and Formulae* (CRC Press, Boca Raton, 2011)

Environmentally Induced Chaos and Amplitude Death in Neuronal Network Activity



Evgeniya V. Pankratova

1 Introduction

Communication of neurons performs detecting, processing, and transmission of any information by the living organisms. For a lot of researchers dealing with biological experiments, mathematical modeling and neural network hardware design, the mechanisms involved into these processes are of particular interest. Due to significant development of the technical opportunities of experimental study of the real neuronal networks activity, new aspects for information processing in the brain are revealed, new influencers on this process are specified.

On the one hand it is known that, astrocytes whose main function was believed to be a biochemical support for the neurons can modify the neuronal response by the release of various gliotransmitters [1, 2]. In particular, the neuronal synchronization considered within the frame of tripartite synapse concept allowed to show glutamate and D-serine impacts on synaptic signal transmission leading to non-trivial changes in neuronal activity [3].

On the other hand, the extracellular matrix components deposited in the space between neurons and astrocytes in the form of a net-like structure, also can regulate the neuronal excitability and synaptic connectivity. Particularly, it was shown that experimentally observed absence of synaptic contacts along neuronal surfaces neighboring with the hyaluronic acid-lecticans-tenascin complexes is due to formation of repulsive barrier between axons and dendrites [4]. Scientific investigations in this direction provoked the development of the tetrapartite theory of synaptic signaling [5]. Recent results within the frame of this theory were presented in [6, 7]. It was shown that, the feedback between the neuronal firing activity and

E. V. Pankratova (✉)

Lobachevsky State University of Nizhni Novgorod, Nizhny Novgorod, Russia

e-mail: pankratova@neuro.nnov.ru

protease-dependent concentration of extracellular matrix (ECM) molecules may lead to different types of bistability that can play crucial role in brain homeostasis maintaining and memory function implementation.

Finally, a narrow gap separating the cells in the brain, besides perineuronal nets, ECM, and other secreted molecules, also contains interstitial fluid. As shown recently, the properties of the latter (interstitial viscosity, steric hindrance, physical drag, etc.) play significant role in brain health and disease, because it provides an environment for the well-being of neural network components [8, 9]. For instance, accumulation of proteins released into the extracellular space, namely α -synuclein or amyloid- β , may initiate the progression of neurodegenerative diseases [10].

The structure of the paper is as follows. In the second section, description of the considered model is presented. In the third section, stability of the stationary state is analyzed. The accuracy of the analytical estimation for the threshold interstitial viscosity that defines the boundary between quiescent and oscillatory network activity is compared with the results of direct numerical integration. In the fourth section, scenarios for chaos emergence are performed. The last section contains some conclusions and discussions.

2 Mathematical Model

In the present work, we are interested in the dynamics of a network of n identical neuronal-type systems, which are described by FitzHugh–Rinzel equations, and coupled both directly and via an environmental media:

$$\begin{aligned} \dot{x}_i &= x_i - x_i^3/3 - y_i + z_i + \varepsilon(w - x_i) + \xi \sum_{j=1}^n g_{ij}x_j, \\ \dot{y}_i &= \gamma(x_i - by_i), \\ \dot{z}_i &= \mu(c - x_i - dz_i), \\ \dot{w} &= -hw + \varepsilon \sum_{j=1}^n (x_j - w), \quad i = 1, \dots, n, \end{aligned} \tag{1}$$

where x_i represents the membrane potential of i -th cell, variables y_i and z_i take into account the transport of ions across the membrane through fast and slow ion channels, respectively, w is the state of the environment. In this study, we assume that $\gamma = 0.08$, $b = 0.8$, $d = 1$, and small parameter $\mu = 0.0001$ [11]. The parameter c defines the regime of an isolated neuron behavior. Particularly, in [11], it was theoretically obtained that generation of bursts in FitzHugh–Rinzel model occurs for c belonging to some interval (c_q, c_s) . For $c < c_q$, each individual cell is in quiescence, while for $c > c_s$, each neuron demonstrates tonic spiking. In this study, we focus on three possible regimes of individual neuronal activity: two different periodic bursting regimes taking place for $c = -1.18$ and $c = -1.28$, and a chaotic one observed for $c = -1.21$. For these regimes, we analyze the impact of interstitial viscosity h on behavior of neuronal network with two types of coupling between the elements. The parameter ξ is the coefficient of direct coupling, and ε is the coupling coefficient defining the strength of interaction between the cells and

the environment. Matrix $\mathbf{G} = \{g_{ij}\}$ is the $n \times n$ symmetric connectivity matrix with off-diagonal elements equaling to 1 or 0, namely $g_{ij} = 1$ indicates that i -th and j -th cells of the network are coupled, while $g_{ij} = 0$ stands for an uncoupled pair of oscillators. As in [11–13], we assume that diagonal elements of the matrix \mathbf{G} are $g_{ii} = -(n - k_i - 1)$, where k_i is the number of elements that are uncoupled with the i -th cell.

2.1 Cessation of Network Oscillations

In order to obtain stationary state of the network, we equate the righthand side of equations (1) to zero

$$\begin{aligned} x_i - x_i^3/3 - y_i + z_i + \varepsilon(w - x_i) + \xi \sum_{j=1}^n g_{ij}x_j &= 0, \\ \gamma(x_i - by_i) &= 0, \\ \mu(c - x_i - dz_i) &= 0, \\ -hw + \varepsilon \sum_{j=1}^n (x_j - w) &= 0, \quad i = 1, \dots, n. \end{aligned} \tag{2}$$

Substituting $y_i(x_i)$, $z_i(x_i)$, and $w(\sum x_j)$ into the first group of equations (2), one can obtain the following equalities:

$$x_i - \frac{x_i^3}{3} - \frac{x_i}{b} + \frac{c}{d} - \frac{x_i}{d} + \frac{\varepsilon^2}{h + n\varepsilon} \sum_{j=1}^n x_j - \varepsilon x_i + \xi \sum_{j=1}^n g_{ij}x_j = 0. \tag{3}$$

As was shown in [11], the expressions for pairwise differences between the equations for x_i and x_j can be written in the following form:

$$(x_i - x_j) \left[1 - (x_i^2 + x_i x_j + x_j^2)/3 - 1/b - 1/d - \varepsilon - n\xi \right] = 0. \tag{4}$$

For standard set of FitzHugh–Rinzel parameters ($d = 1$, $b = 0.8$), the second multiplier in (4) is always negative. Therefore, the equality (4) holds only for the state placed on the synchronous manifold. This means that the equalities (3) can be rewritten in the following form:

$$x^3 + 3 \left(\frac{1}{b} + \frac{1}{d} + \frac{\varepsilon h}{\varepsilon n + h} - 1 \right) x - \frac{3c}{d} = 0. \tag{5}$$

Since the discriminant $D = (-1 + 1/b + 1/d + \varepsilon h/(\varepsilon n + h))^3 + 9c^2/4d^2$ is positive, the Eq. (5) has only one real root. To find this steady state, we substitute

$$x = \eta + \frac{1}{\eta} \left(\frac{1}{b} + \frac{1}{d} + \frac{\varepsilon h}{\varepsilon n + h} - 1 \right) \tag{6}$$

into (5) and obtain the following tri-quadratic equation:

$$\eta^6 - \frac{3c}{d}\eta^3 - \left(\frac{1}{b} + \frac{1}{d} + \frac{\varepsilon h}{\varepsilon n + h} - 1\right)^3 = 0. \quad (7)$$

Substitution of its solution

$$\eta_+ = \sqrt[3]{\frac{1}{2} \left(\frac{3c}{d} + \sqrt{\frac{9c^2}{d^2} + 4 \left(\frac{1}{b} + \frac{1}{d} + \frac{\varepsilon h}{\varepsilon n + h} - 1 \right)^3} \right)} \quad (8)$$

into equality (6) yields

$$x_s = \sqrt[3]{\frac{1}{2} \left(\frac{3c}{d} + \sqrt{\frac{9c^2}{d^2} + 4 \left(\frac{1}{b} + \frac{1}{d} + \frac{\varepsilon h}{\varepsilon n + h} - 1 \right)^3} \right)} + \sqrt[3]{\frac{1}{2} \left(\frac{3c}{d} - \sqrt{\frac{9c^2}{d^2} + 4 \left(\frac{1}{b} + \frac{1}{d} + \frac{\varepsilon h}{\varepsilon n + h} - 1 \right)^3} \right)}. \quad (9)$$

Therefore, the steady network state has the following coordinates

$$O \left(x_s, \frac{x_s}{b}, \frac{c - x_s}{d}, \frac{n \varepsilon x_s}{n \varepsilon + h} \right), \quad (10)$$

and its stability can be analyzed by linearizing the vector field of the system(1) taken on the synchronous manifold. Particularly, in [11], the necessary condition for the threshold value of the network scale defining the transition from the quiescent to oscillatory network activity, was obtained. Using the similar technique, one can write the estimation for interstitial viscosity threshold value:

$$h_{th} = \frac{n \varepsilon (q_1 - q_2) - q_1 q_2 + \mu d \gamma b + \gamma + \mu - n \varepsilon^2}{q_2 - q_1}, \quad (11)$$

where $q_1 = \mu d + \gamma b$, $q_2 = 1 - x_s^2 - \varepsilon$, $q_1 + x_s^2 < 1$. The curve obtained using (11) is shown in Fig. 1a. Obviously, this estimation cannot give strict boundary, but it provides rather good prediction guaranteeing an oscillatory network activity for $h < h_{th}$. To obtain strict $h_{th}(\varepsilon)$ -dependence, one can use the Routh–Gurvtz stability conditions for the steady-state mode. The data obtained numerically are shown in Fig. 1a by blue symbols. The boundary of this domain corresponds to cessation of network oscillations, or *amplitude death* in oscillatory network [14–16]. The firing mode transition with the increase of h is demonstrated in Fig. 1b (for $h = 1.6$) and Fig. 1c (for $h = 0.4$). It is worth noticing that due to the small

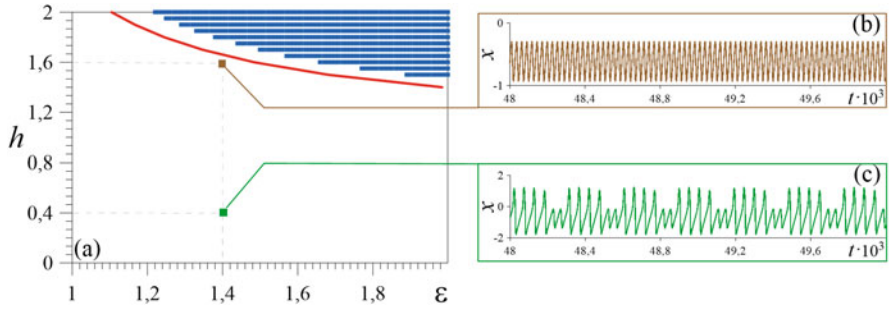


Fig. 1 (a) Cessation of network oscillations is observed for the points shown by blue symbols in (ϵ, h) parameter plane (numerical data). Red curve obtained from (11) is the boundary guaranteeing the network oscillatory activity for $h < h_{th}$. Time traces of $x(t)$ for various values of interstitial viscosity h : (b) $h = 1.6$, (c) $h = 0.4$; $\epsilon = 1.4$, $c = -1.18$

value of the parameter μ , the transition to the quiescent state can take large time interval. Therefore, to obtain the correct stability boundary by the direct numerical integration, it is necessary to use long-time accurate calculations.

3 Chaos Emergence

FitzHugh–Rinzel model is well known mathematical model that is used for description of the so-called elliptic bursting neuronal behavior [17–20]. Two examples of such type of firing are presented in Fig. 2. In both cases amplitude of oscillations gradually waxes and wanes. The difference is in the duration of the so-called silent phase and in number of spikes in each burst. Particularly, the time series data for $c = -1.18$ presented in Fig. 2a illustrates the trace with four spikes in each burst and small duration of the silent phase. While for $c = -1.28$, Fig. 2b, each burst contains three spikes and duration of the silent phase becomes significantly larger.

Further, we consider the change of such behavior in the presence of environment. Particularly, Fig. 3 shows the values of maxima of $x(t)$ in time traces calculated with the change of interstitial viscosity h . As seen from this bifurcation diagram, for high values of h (for example, the phase portrait for $h = 0.62$ is shown in Fig. 4a) the periodic oscillations are observed. With the decrease of h , a cascade of period doubling bifurcations takes place. Particularly, for $h = 0.58$ the oscillations with the doubled period are observed, Fig. 4b, for $h = 0.55$ period-4 oscillations occur, Fig. 4c. As a result of such sequence of doublings, for smaller values of h the neuronal activity becomes chaotic. Chaotic attractor observed, for example, for $h = 0.52$, is shown in Fig. 4d.

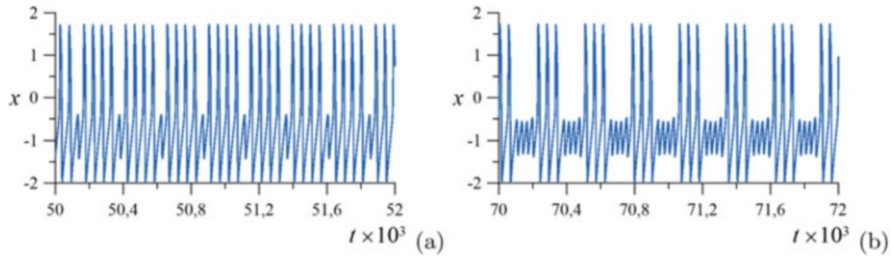


Fig. 2 Elliptic bursting behavior observed in uncoupled FitzHugh–Rinzel system for (a) $c = -1.18$ and (b) $c = -1.28$

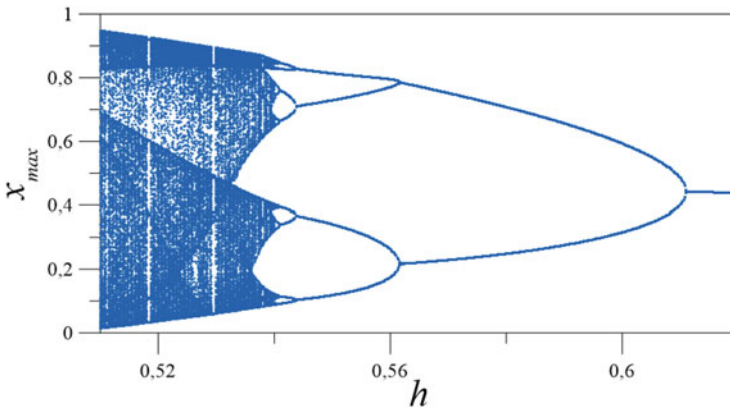


Fig. 3 Bifurcation diagram showing the maximal values of $x(t)$ with the change of interstitial viscosity h for $c = -1.18$, $\varepsilon = 1.5$

When $c = -1.28$, and individual elements of the network demonstrate the dynamics shown in Fig. 2b, the interstitial viscosity h changes the network activity mode in another way. Bifurcation diagram shown in Fig. 5, presents another scenario for chaos emergence. Again, for large values of h a simple periodic oscillation of $x(t)$ is observed, Fig. 6a. With the decrease of interstitial viscosity, the behavior of $x(t)$ becomes complicated: the birth of an invariant torus occurs via Neimark–Sacker bifurcation [21, 22]. To show this, the Poincaré maps of both the limit cycle observed for $h = 0.76$ (green point) and the torus observed for $h = 0.745$ (blue invariant curve) are presented in Fig. 6b. Quasi-periodic time trace of $x(t)$ obtained for $h = 0.74$ is shown in Fig. 6c. In Fig. 6d, three-dimensional projection of the torus calculated for $h = 0.72$ is demonstrated. Further decrease of h leads to appearance of periodicity windows in bifurcation diagram and finally to chaos, Fig. 6e.

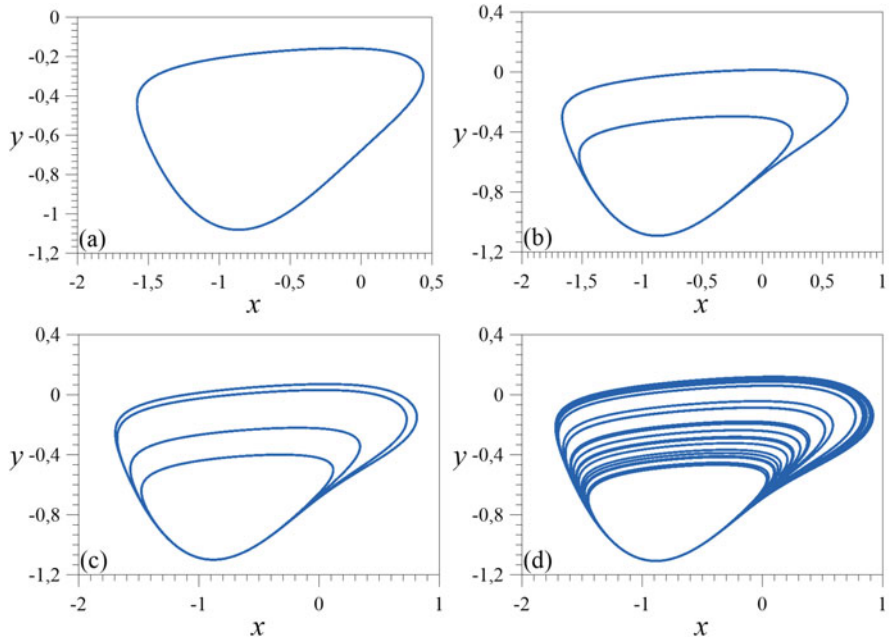


Fig. 4 Two-dimensional projections of phase portraits of the system (1) for various values of interstitial viscosity h : (a) $h = 0.62$, (b) $h = 0.58$, (c) $h = 0.55$, (d) $h = 0.52$; $c = -1.18$, $\varepsilon = 1.5$

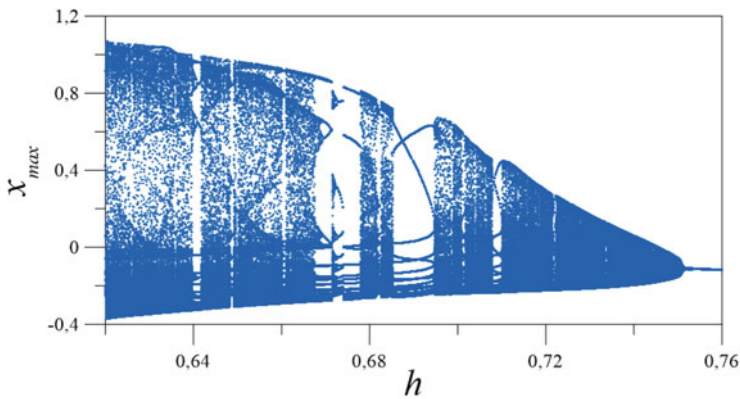


Fig. 5 Bifurcation diagram showing the maximal values of $x(t)$ with the change of interstitial viscosity h for $c = -1.28$, $\varepsilon = 1.5$

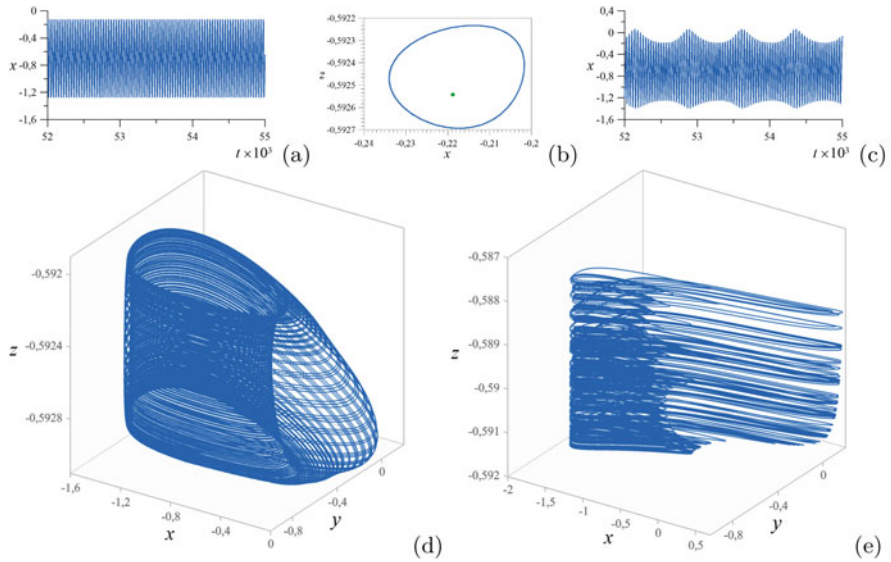


Fig. 6 (a) Time trace of $x(t)$ for $h = 0.78$. (b) Two-dimensional projections of phase portraits in the Poincaré section by surface $y = -0.8$ for two values of the parameter h : $h = 0.745$ (blue invariant curve corresponding to the torus) and $h = 0.76$ (green point corresponding to the limit cycle) (c) Time trace of $x(t)$ for $h = 0.74$. Three-dimensional projections of phase portraits of the system (1) for (d) $h = 0.72$ (torus), (e) $h = 0.6$ (chaotic attractor)

4 Multistability in Dynamics of the Neuronal Network

Multistability means coexistence of several attractors in the phase space of the system [23–26]. In neurodynamics, possible switchings from one stable state to the other are associated with implementing memory function of a network or with existence of some latent disease states.

In system (1), multistable regimes are also observed. Particularly, the bifurcation diagram in Fig. 7 illustrates possible coexistence of either two regular attractors with different characteristics, Fig. 8a, or regular oscillations with chaos, Fig. 8b.

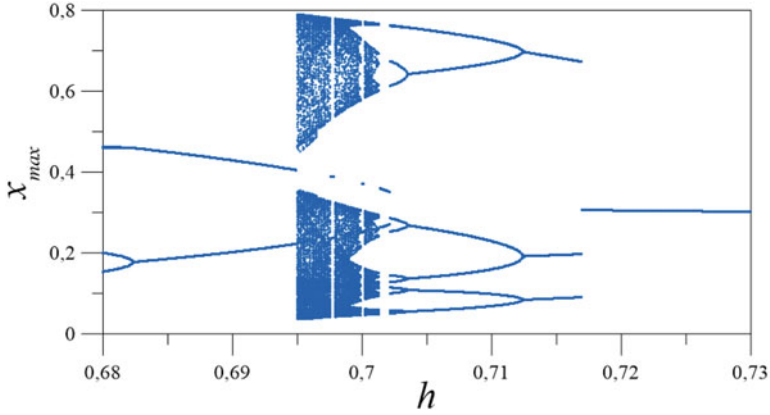


Fig. 7 Bifurcation diagram showing the maximal values of $x(t)$ with the change of interstitial viscosity h for $c = -1.21, \varepsilon = 1$

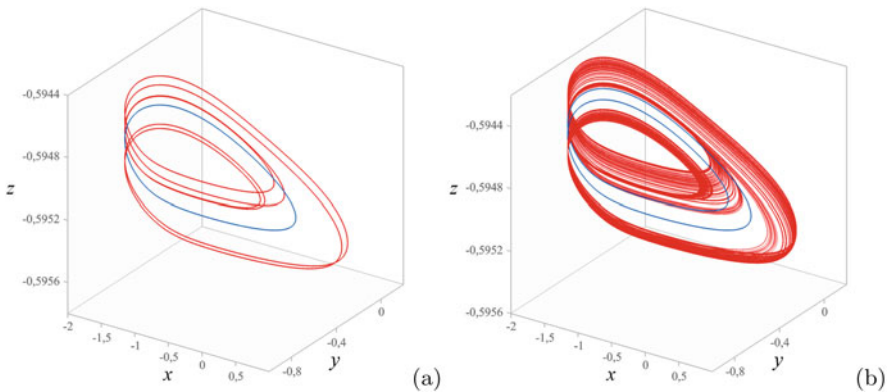


Fig. 8 Three-dimensional projections of phase portraits of the system (1) for various values of interstitial viscosity h and initial conditions $(x_0; y_0; z_0; w_0)$: **(a)** $h = 0.71, (0.6; -0.5; -0.5; 0.1)$ (blue cycle) and $(-0.2; 0; 0; 0.1)$ (red cycle of period 6); **(b)** $h = 0.697, (0.2; 0; 0; 0.1)$ (blue cycle of period 2) and $h = 0.697, (1.6; -0.5; -0.5; 0.1)$ (chaotic attractor)

5 Conclusions

Recently, simple phenomenological model for the network with the coupling between the neuronal cells that takes into account the role of the interstitial viscosity was introduced [11]. For small-scale networks, the phenomenon of amplitude death was revealed, and analytical estimation for the threshold network scale providing the neuronal activity was obtained.

In this study, the impact of interstitial viscosity on network activity was analyzed. An estimation for its threshold value guaranteeing the network oscillatory regime was obtained. Firing modes transition with the change of parameters in coupling

via environmental media was shown. For different individual (if the neurons are uncoupled) regular dynamical regimes, the role of the common environment in emergence of chaos in neuronal network dynamics was examined. It was shown that transition to irregular firing activity can occur via different bifurcation scenarios. Moreover, the range of parameters was obtained where the coexistence of both regular and chaotic regimes of neuronal activity is observed. Since the properties of connections between neural cells can have a dramatic influence on neural activity, the study of complex rhythms and firing transitions arising from various interaction schemes are of particular importance [27–29]. The results obtained within the frame of recently introduced mathematical model [11] demonstrate that the properties of interstitial fluid can contribute to a dual character of neuronal activity related with the development of hidden stages of some disease.

Acknowledgments The work was supported by grant of the President of the Russian Federation for state support of leading scientific schools No. NSh-2653.2020.2.

References

1. A. Verkhratsky, A. Butt, *Glial Neurobiology. A Textbook*, 1st edn. (Wiley, Hoboken, 2007), p. 224
2. S.Y. Gordleeva, S.V. Stasenko, A.V. Semyanov, A.E. Dityatev, V.B. Kazantsev, Bi-directional astrocytic regulation of neuronal activity within a network. *Front. Comput. Neurosci.* **6**(92), 1–11 (2012)
3. E.V. Pankratova, A.I. Kalyakulina, S.V. Stasenko, S.Y. Gordleeva, I.A. Lazarevich, V.B. Kazantsev, Neuronal synchronization enhanced by neuron-astrocyte interaction. *Nonlinear Dyn.* **97**(1), 647–662 (2019)
4. Y. Yamaguchi, Lecticans: organizers of the brain extracellular matrix. *Cell Mol. Life Sci.* **57**, 276–289 (2000)
5. A. Dityatev, M. Schachner, Extracellular matrix molecules and synaptic plasticity. *Nat. Rev. Neurosci.* **4**, 456–468 (2003)
6. V. Kazantsev, S. Gordleeva, S. Stasenko, A. Dityatev, A homeostatic model of neuronal firing governed by feedback signals from the extracellular matrix. *PLoS ONE* **7**(7), e41646 (2012)
7. I. Lazarevich, S. Stasenko, M. Rozhnova, E. Pankratova, A. Dityatev, V. Kazantsev, Activity-dependent switches between dynamic regimes of extracellular matrix expression. *PLoS ONE* **15**(1), e0227917 (2020)
8. F. Caserta, R.E. Hausman, W.D. Eldred, C. Kimmel, H.E. Stanley, Effect of viscosity on neurite outgrowth and fractal dimension. *Neurosci. Lett.* **136**, 198–202 (1992)
9. E. Sykova, C. Nicholson, Diffusion in brain extracellular space. *Physiol. Rev.* **88**, 1277–1340 (2008)
10. J.J. Iliff, M.J. Chen, B.A. Plog, D.M. Zeppenfeld, M. Soltero, L. Yang, I. Singh, R. Deane, M. Nedergaard, Impairment of glymphatic pathway function promotes tau pathology after traumatic brain injury. *J. Neurosci.* **34**, 16180–16193 (2014)
11. E.V. Pankratova, A.I. Kalyakulina, Environmentally induced amplitude death and firing provocation in large-scale networks of neuronal systems. *Regul. Chaot. Dyn.* **21**, 840–848 (2016)
12. V.N. Belykh, E.V. Pankratova, Chaotic synchronization in ensembles of coupled neurons modeled by the FitzHugh-Rinzel system. *Radiophys. Quant. Electron.* **49**(11), 910–921 (2006)

13. V.N. Belykh, E.V. Pankratova, E. Mosekilde, Dynamics and synchronization of noise perturbed ensembles of periodically activated neuron cells. *Int. J. Bifur. Chaos* **18**(9), 2807–2815 (2008)
14. A. Prasad, M. Dhamala, B.M. Adhikari, R. Ramaswamy, Amplitude death in nonlinear oscillators with nonlinear coupling. *Phys. Rev. E* **81**, 027201 (2010)
15. V. Resmi, G. Ambika, R.E. Amritkar, G. Rangarajan, Amplitude death in complex networks induced by environment. *Phys. Rev. E* **85**, 046211 (2010)
16. A. Gjurchinovski, A. Zakharova, E. Scholl, Amplitude death in oscillator networks with variable-delay coupling. *Phys. Rev. E* **89**, 032915 (2014)
17. J. Rinzel, A formal classification of bursting mechanisms in excitable systems, in *Proceedings of International Congress of Mathematics*, ed. by A.M. Gleason (AMS, Providence, 1987), p. 157893
18. C.A. Del Negro, C.-F. Hsiao, S.H. Chandler, A. Garfinkel, Evidence for a novel bursting mechanism in rodent trigeminal neurons. *Biophys. J.* **75**, 174 (1998)
19. E.M. Izhikevich, Synchronization of elliptic bursters. *SIAM Rev.* **43**(2), 315–344 (2001)
20. J. Wojcik, A. Shilnikov, Voltage interval mappings for an elliptic bursting model, in *Nonlinear Dynamics New Directions: Models and Applications*, ed. by H. Gonzalez-Aguilar, E. Ugalde, Chap. 9, vol. 12 (Springer, Berlin, 2015), pp. 195–213
21. E. Kolemen, N.J. Kasdin, P. Gurfil, Multiple Poincaré sections method for finding the quasiperiodic orbits of the restricted three body problem. *Celest Mech. Dyn. Astrogr.* **112**, 47–74 (2012)
22. N. Stankevich, A. Kuznetsov, E. Popova, E. Seleznev, Chaos and hyperchaos via secondary Neimark–Sacker bifurcation in a model of radiophysical generator. *Nonlinear Dyn.* **97**(4), 2355–2370 (2019)
23. T. Malashchenko, A. Shilnikov, G. Cymbalyuk, Six types of multistability in a neuronal model based on slow calcium current. *PLoS ONE* **6**(7), e21782 (2011)
24. M.E.B. Ngouonkadi, H.B. Fotsin, L.P. Fotso, K.V. Tamba, H.A. Cerdeira, Bifurcations and multistability in the extended Hindmarsh–Rose neuronal oscillator. *Chaos Solitons Fract.* **85**, 151–163 (2016)
25. J. Ma, F. Wu, G. Ren, J. Tang, A class of initials-dependent dynamical systems. *Appl. Math. Comput.* **298**, 65–76 (2017)
26. N.V. Stankevich, E.I. Volkov, Multistability in a three-dimensional oscillator: tori, resonant cycles and chaos. *Nonlinear Dyn.* **94**, 2455–2467 (2018)
27. A.O. Komendantov, O.G. Komendantova, S.W. Johnson, C.C. Canavier, A modeling study suggests complementary roles for GABA_A and NMDA receptors and the SK channel in regulating the firing pattern in midbrain dopamine neurons. *J. Neurophys.* **91**, 346–357 (2004)
28. G. Katriel, Synchronization of oscillators coupled through an environment. *Phys. D* **237**, 2933–2944 (2008)
29. F. Wu, Y. Zhang, X. Zhang, Regulating firing rates in a neural circuit by activating memristive synapse with magnetic coupling. *Nonlinear Dyn.* **98**, 971–984 (2019)

Chaos-Type Identification in the Contact Interaction of Closed Cylindrical Nanoshells Embedded One into the Other with a Gap Between Them



Irina Papkova , Tatiana Yakovleva , Anton Krysko , and Vadim Krysko 

1 Introduction

Closed cylindrical shells are widely used in various engineering structures, instrumentation, medicine, aircraft, and rocket construction. In this regard, works on theoretical studies of such structures in the world literature are presented very widely [1–4]. Cylindrical nanoshells are the structural members of nanoelectromechanical structures (NEMS). Contact interaction of individual elements affects the operating mode of the entire device [5, 6]. In these works, the contact interaction of plates and beams was studied taking into account nanoscale effects. Previously, the analysis of the chaotic oscillations type was mainly considered in physics and radiophysics [7]. In mechanics, the chaotic state type was studied using the example of classical systems [8]. In [9, 10], chaotic vibrations of a single-layer cylindrical shell are studied. However, the chaos-type studying issue of closed cylindrical nanostructures with contact has not received much attention in the literature.

This aim of this work is to construct a contact interaction theory of closed cylindrical nanoshells nested one into the other with a small gap between them and under the external load action. This work is the first to analyze the chaotic oscillations type of these nanoshells as a result of their contact.

This work was supported by the Russian Science Foundation (Grant No. 19-19-00215).

I. Papkova · T. Yakovleva (✉) · A. Krysko · V. Krysko
Yuri Gagarin State Technical University of Saratov, Saratov, Russia
e-mail: yan-tan1987@mail.ru

2 Formulation of the Problem

A mathematical model for nonlinear dynamics of complex mechanical systems in the form of two closed cylindrical nanoshells nested one into the other is built. The structural elements are separated by small gaps, and the interaction between the elements is taken into account in the boundary conditions (Figs. 1 and 2).

A distributed alternating strip load $q(x, y, t) = q_0 \sin(\omega_p t)$ acts on the nanoshell outer surface, where ω_p is frequency and q_0 is forced oscillations amplitude.

The mathematical model of closed cylindrical shells is based on the Kirchhoff-Love kinematic model, taking into account the geometric nonlinearity according to the T. von Karman model. The shells are isotropic, homogeneous, and elastic and obey Hooke's law. Nanoscale effects are taken into account according to the modified couple stress theory [11, 12]. The contact pressure is taken into account according to the B. Ya. Kantor model [13]. For this, the term $(-1)^i Kk(w_1 - w_2 - h_k)\Psi$ has been introduced into the system of equations (Eq. 2), where $i = 1, 2$ is nanoshell index; w_1 and w_2 are deflections of the outer and inner cylindrical nanoshell, respectively; Kk is rigidity coefficient of transversal compression in the contact zone; h_k is the gap between the cylindrical nanoshells. The function Ψ is defined as $\Psi = 1/2 [1 + \text{sign}(w_1 - h_k - w_2)]$. If $w_1 > w_2 + h_k$, then contact exists and $\Psi = 1$; otherwise, there is no contact and $\Psi = 0$.

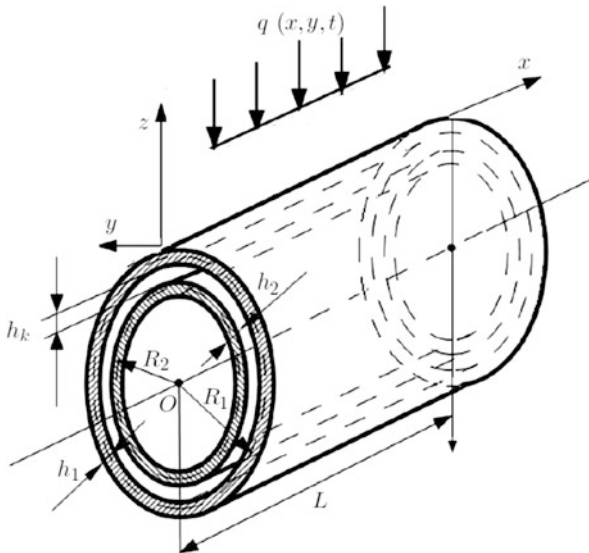
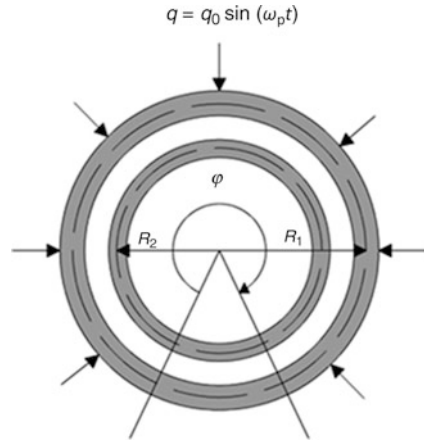


Fig. 1 Scheme of closed cylindrical nanoshells

Fig. 2 Shell loading diagram



The nonlinear partial differential equations system, boundary, and initial conditions are derived from the Hamilton-Ostrogradsky energy principle:

$$\int_{t_0}^{t_1} (\delta K - \delta U + \delta W) dt = 0 \tag{1}$$

In Eq. (1), K is the kinetic energy, U is the potential energy, and W is the external work related to distributed forces and energy dissipation.

The partial differential equations system for a two-layer packet of closed cylindrical nanoshells is given in the following (Eq. 2):

$$\begin{cases} D \Delta^2 w_i - k_{y_i} \frac{\partial^2 F_i}{\partial x^2} - L(w_i, F_i) + \frac{\partial^2 w_i}{\partial t^2} + \varepsilon \frac{\partial w_i}{\partial t} \\ \quad = q(x, y, t) + (-1)^i K(w_1 - w_2 - h_k) \Psi, \\ \frac{1}{Eh} \Delta^2 F_i = -\frac{1}{2} L(w_i, w_i) - k_{y_i} \frac{\partial^2 w_i}{\partial x^2}, \\ i = 1, 2, \end{cases} \tag{2}$$

where $D = \frac{Eh^3}{12(1-\nu^2)} + \frac{Eh\gamma^2}{2(1+\nu)}$, $\Delta^2(\cdot) = \frac{\partial^4(\cdot)}{\partial x^4} + 2\frac{\partial^4(\cdot)}{\partial x^2\partial y^2} + \frac{\partial^4(\cdot)}{\partial y^4}$, $L(w, F) = \frac{\partial^2 w}{\partial x^2} \frac{\partial^2 F}{\partial y^2} + \frac{\partial^2 w}{\partial y^2} \frac{\partial^2 F}{\partial x^2} - 2\frac{\partial^2 w}{\partial x\partial y} \frac{\partial^2 F}{\partial x\partial y}$, and $L(w, w) = 2\left[\frac{\partial^2 w}{\partial x^2} \frac{\partial^2 w}{\partial y^2} - \left(\frac{\partial^2 w}{\partial x\partial y}\right)^2\right]$ are known nonlinear operators.

Boundary and initial conditions must be added to the equations system (Eq. 2).

Further, Eq. (2) is reduced to dimensionless form using the following parameters: $w = h\bar{w}$, $F = Eh^2\bar{F}$, $t = t_0\bar{t}$, $\varepsilon = \bar{\varepsilon}/\tau$, $x = L\bar{x}$, $y = R\bar{y}$, $k_y = \bar{k}_y \frac{h}{R^2}$, $q = \bar{q} \frac{Eh^4}{L^2R^2}$, $\tau = \frac{LR}{h} \sqrt{\frac{\rho}{Eg}}$, and $\lambda = \frac{L}{R}$, where L and $R = R_y$ are shell length and radius. Here, t is time, ε is resistance coefficient of the medium in which the shell moves, $\nu = 0.3$ is Poisson's ratio, E is Young's modulus, g is acceleration of gravity, ρ is material density, γ is size-dependent coefficient, and $q(x, y, t)$ is strip load.

3 Solution Methods

Systems of nonlinear partial differential equations are reduced to a system of ordinary differential equations by the Faedo-Galerkin method in higher approximations and finite differences method of the second accuracy order. Previously, the authors compared the results of calculating nonlinear oscillations for rectangular layout cylindrical panels [14] using these methods, and preference was given to the Faedo-Galerkin method.

The Cauchy problem is solved by several methods: the Runge-Kutta-type methods from the second to the eighth accuracy order and the Newmark method to confirm the results' reliability. Further results investigation is carried out by means of nonlinear dynamics with the construction of signals, phase portraits, Fourier power spectra, and the wavelet analysis use. The Morlet, Gauss 8, Gauss 32, and Haar wavelets were used as the mother wavelets. The Morlet wavelet is the most informative for this class of problems, since it gives the best frequency localization at every moment in time. It is worth noting that the Fourier power spectrum gives a general picture of the nanoshell oscillations nature over the entire time interval.

An analysis of the nanoshell chaotic oscillations type is carried out according to the chaos criterion given by Gulik [15], as well as on the basis of the Lyapunov exponents (Le) spectrum signs calculated by the Sano-Sawada method [16]. To confirm the reliability of the results obtained, the largest Lyapunov exponents are calculated by several methods: Wolf [17], Kantz [18], Rosenstein [19], and Sano-Sawada [16].

4 Numeric Results

In the framework of numerical simulations, the following cases were considered: (1) vibrations of one closed cylindrical nanoshell and (2) vibrations of two closed cylindrical nanoshells with a small gap between them.

We attach to the system (Eq. 2) the boundary conditions for articulated support at the ends:

$$w_i = 0; \frac{\partial^2 w_i}{\partial x^2} = 0; F_i = 0; \frac{\partial^2 F_i}{\partial x^2} = 0 \quad \text{at } x = 0; 1, \quad (3)$$

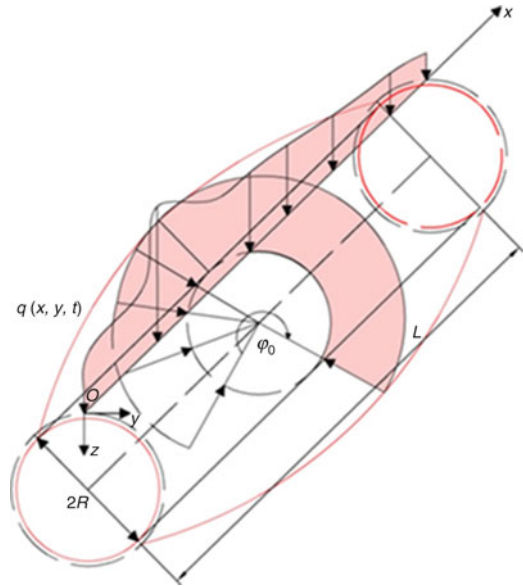
and periodicity condition at

$$y \in [0; 2\pi].$$

In addition to the boundary conditions, we add to Eq. (2) the initial conditions:

$$w_i|_{t=0} = 0, \dot{w}_i|_{t=0} = 0 \quad (4)$$

Fig. 3 Scheme of one closed cylindrical nanoshell



The functions w_i and F_i in system (Eq. 2) are approximated by an analytical expression containing a finite number of arbitrary parameters, represented as a functions product depending on time and coordinates:

$$w_i = \sum_{k=1}^N \sum_{l=0}^N A_{kl}(t) \sin(k\pi x) \cos(l y), \quad F_i = \sum_{k=1}^N \sum_{l=0}^N B_{kl}(t) \sin(k\pi x) \cos(l y) \tag{5}$$

1. A chaotic oscillations-type analysis of one closed cylindrical nanoshell under the action of a transverse distributed alternating strip load $q(x, y, t) = q_0 \sin(\omega_p t)$ is carried out (Figs. 3 and 4).

The Faedo-Galerkin method convergence is investigated depending on the terms number in the series $N = 5, 7, 9, 11, 13, 15$.

With the values of the parameters $\omega_p = 20.3, \lambda = 1, q_0 = 0.05, \gamma = 0$ in the harmonic oscillations shell region, the Faedo-Galerkin method convergence is achieved at $N = 9$ in all characteristics: signal, Fourier power spectrum, phase portrait, and wavelet spectrum (Fig. 5).

With an increase of the external load intensity $q_0 = 0.18575$ in the chaotic oscillations zone, to achieve the method convergence $N = 13$, members of the series are required, while the convergence is achieved by the signal (Fig. 6).

With an increase in the size-dependent parameter to $\gamma = 0.7$ and the same load intensity $q_0 = 0.18575$, the nanoshell oscillations acquire a harmonic character, and

Fig. 4 Shell loading diagram

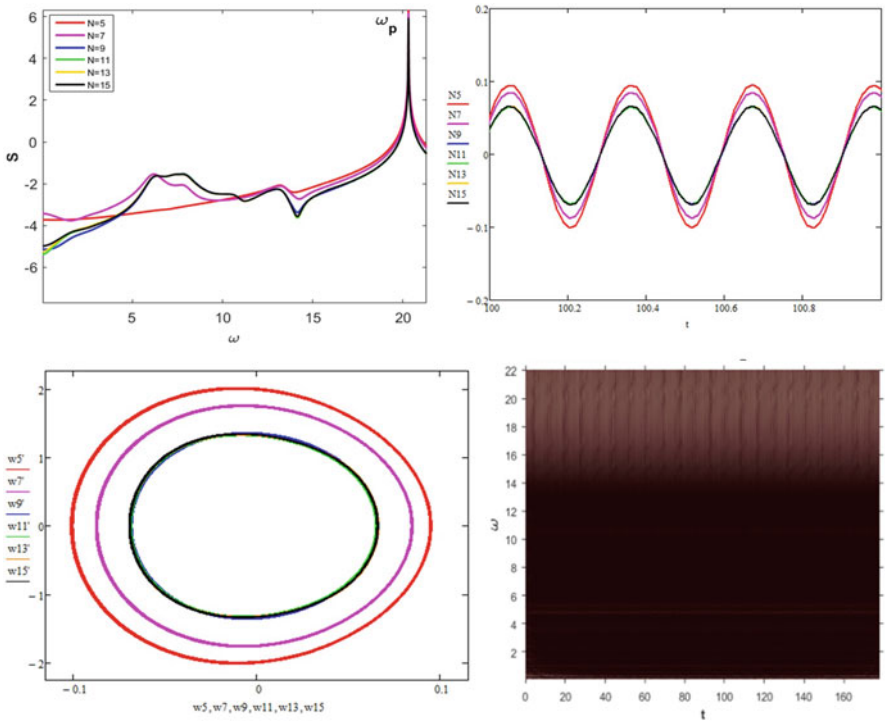
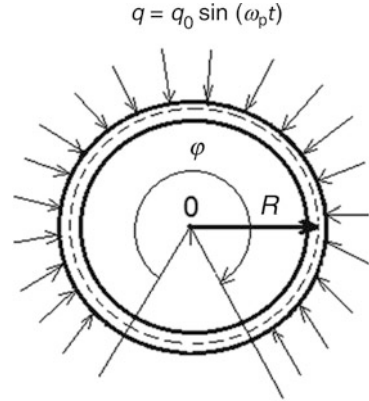


Fig. 5 The dynamic characteristics of a cylindrical shell at $q_0 = 0.05$, $\gamma = 0$. (a) Fourier power spectrum. (b) Signal. (c) Phase portrait. (d) Morlet wavelet spectrum

for the Faedo-Galerkin method to converge, $N = 9$ terms of the series are required. In this case, the convergence is achieved for all dynamic characteristics.

The six Lyapunov exponents (Le) spectrum was calculated for each value of the size-dependent coefficient $\gamma = 0, 0.1, 0.3, 0.5$, and 0.7 and for each series members

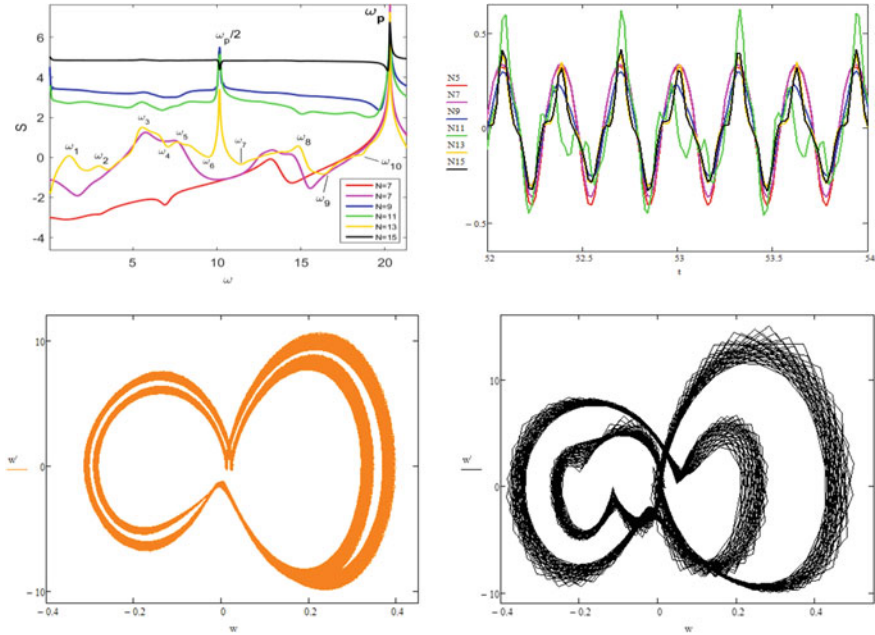


Fig. 6 The dynamic characteristics of a cylindrical shell at $q_0 = 0.18575$, $\gamma = 0$. (a) Fourier power spectrum. (b) Signal. (c) Phase portrait ($N = 13$). (d) Phase portrait ($N = 15$)

number in the Faedo-Galerkin method $N = 5, 7, 9, 11, 13$, and 15 , using the Sano-Sawada method (Table 1). The largest Lyapunov exponents signs calculated by the methods of Sano-Sawada, Wolf, Rosenstein and Kantz coincide with each other, which confirms the reliability of the results obtained.

2. The chaotic oscillations-type analysis of two closed cylindrical nanoshells embedded in one another under the transverse distributed band alternating load action is carried out (Figs. 1 and 2). The following parameter values are selected: $\omega_p = 24.75$, $\lambda = 2$, $R_1 = 112.5$, $\varepsilon = 1$, and $N = 13$. The influence of the size-dependent coefficient $\gamma = 0, 0.1, 0.3, 0.5, 0.7$ and the gap h_k on the nanoshells' complex vibrations nature is studied. In case $\gamma = 0$ and $h_k = 5 \cdot 10^{-2}$ ($R_2 = 112.45$) with load intensity $q_0 < 5 \cdot 10^{-3}$, the outer cylindrical shell performs harmonic vibrations; the inner shell is at rest due to the contact absence. The initial contact interaction of two nanoshells occurs when the load intensity is $q_0 = 5 \cdot 10^{-3}$; in this case, the outer nanoshell vibrations type is chaos (the largest Lyapunov exponent in the spectrum is positive; the rest are negative) and, for inner nanoshell, hyperchaos (the first two Lyapunov exponents in the spectrum are positive; the rest are negative). With a further increase in the load amplitude, the oscillations of both nanoshells are chaotic. In case $\gamma = 0.5$ and $h_k = 5 \cdot 10^{-2}$,

Table 1 The six Lyapunov exponents (Le) spectrum

	$q_0 = 0.05, \gamma = 0$	$q_0 = 0.18575, \gamma = 0$	$q_0 = 0.18575, \gamma = 0.7$
$N = 5$	7.726E-05; -0.0057909; -0.012276; -0.051032; -0.29507; -0.55542	-1.2875E-05; -0.0089335; -0.023767; -0.096256; -0.3141; -0.60404	1.1465E-05; -0.011262; -0.031348; -0.11782; -0.28377; -0.57246
$N = 7$	-0.00013904; -0.0080526; -0.015589; -0.069708; -0.27177; -0.55871	0.00029168; -0.010187; -0.03306; -0.10171; -0.30532; -0.62321	0.00022776; -0.010066; -0.03787; -0.12541; -0.32275; -0.61648
$N = 9$	9.6392E-05; -0.0086043; -0.016231; -0.072893; -0.29503; -0.5899	0.029539; 0.00608; -0.010725; -0.040297; -0.10398; -0.39182	0.00016187; -0.0093437; -0.027208; -0.11468; -0.28653; -0.55081
$N = 11$	-0.00033533; -0.0070116; -0.01556; -0.076991; -0.29532; -0.59248	0.047862; 0.0099957; -0.0010835; -0.015825; -0.084216; -0.29974	0.00016303; -0.0099494; -0.030293; -0.096564; -0.30091; -0.57837
$N = 13$	-0.00010453; -0.0084115; -0.015257; -0.076523; -0.30191; -0.58053	0.00064615; 8.5552E-05; -0.0030763; -0.021158; - 0.063622; -0.30458	9.706E-05; -0.010467; -0.027157; -0.10316; -0.30306; -0.57453
$N = 15$	0.00017664; -0.0070715; -0.016254; -0.072304; -0.29406; -0.59545	0.050099; 0.011308; -0.0034314; -0.023925; -0.083613; -0.36851	0.00028967; -0.010402; -0.028612; -0.10227; -0.30145; -0.58463
❖ - Harmonic oscillations ❖ - Hyperchaos			

Table 2 The seven Lyapunov exponents (Le) spectrum at $q_0 = 5 \cdot 10^{-2}$

	$\gamma = 0, h_k = 5 \cdot 10^{-2}$	$\gamma = 0.5, h_k = 5 \cdot 10^{-2}$	$\gamma = 0.5, h_k = 1 \cdot 10^{-1}$
Nanoshell 1	0.05658; -0.0028601; -0.082153; -0.15186; -0.25404; -0.39762; -0.7706	0.096271; 0.040125; -0.027847; -0.10125; -0.20026; -0.36232; -0.82294	0.066958; -0.002844; -0.056679; -0.11116; -0.19303; -0.32473; -0.73897
Nanoshell 2	0.054688; -0.0033813; -0.074719; -0.14699; -0.24656; -0.38881; -0.74392	0.10344; 0.041036; -0.03342; -0.096655; -0.18356; -0.34017; -0.78899	0.56729; 0.15778; -0.019058; -0.10313; -0.19339; -0.33994; -1.1403
❖ - Chaos ❖ - Hyperchaos			

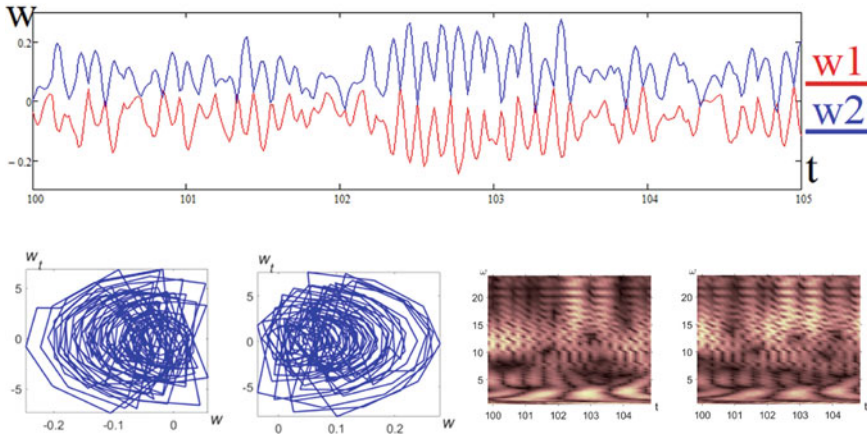


Fig. 7 The dynamic characteristics of a cylindrical shells at $\gamma = 0.5$; $q_0 = 5 \cdot 10^{-2}$; $h_k = 5 \cdot 10^{-2}$. (a) Signal. (b) Phase portrait. (c) Morlet wavelet spectrum

the initial contact interaction of two nanoshells occurs when the load intensity is $q_0 = 5 \cdot 10^{-2}$; the fluctuations type of both nanoshells is hyperchaos. When the gap between the cylindrical nanoshells value is $h_k = 1 \cdot 10^{-1}$ and the same values $\gamma = 0.5$ and $q_0 = 5 \cdot 10^{-2}$, the oscillations deflections increase. A contact interaction is observed, and the outer nanoshell is in chaos state and the inner in hyperchaos (Table 2).

Figure 7 shows the joint vibrations graph of both nanoshells as their contact interaction result, phase portraits, and Morlet wavelet spectra for the outer and inner nanoshells, respectively, at parameters $\gamma = 0.5$; $q_0 = 5 \cdot 10^{-2}$; $h_k = 5 \cdot 10^{-2}$. Phase portraits are strange attractors. On the wavelet spectra, there is frequencies intermittency in the range $\omega_p \in [1; 24.75]$. The largest Lyapunov exponent by the Rosenstein method for the outer nanoshell is $Le1 = 0.23132$, and for the inner $Le1 = 0.21642$.

5 Conclusions

In this work, a mathematical model for the contact interaction of two closed cylindrical nanoshells nested one into the other is constructed. An integrated approach is proposed for the nanoshell nonlinear dynamics studying and analyzing the type of their chaotic oscillations. The question of results' reliability and method convergence is investigated. The solution is considered with an almost infinite number of degrees, when the solution obtained for N and $N - 2$ coincides. As an example, a particular case of the problem is considered, namely, the chaos-type analysis of a single-layer closed cylindrical nanoshell under the external transverse

distributed strip load action is carried out. It was revealed that the oscillations type significantly depends on the amplitude and frequency of the load, size-dependent and geometric parameters, and the series members number in the Faedo-Galerkin method. The cylindrical nanoshell can perform harmonic or chaotic oscillations, while depending on the number of positive Lyapunov spectrum exponents, two types of chaos are observed: chaos and hyperchaos. A dynamic characteristic analysis of a cylindrical nanoshell nonlinear oscillation showed that the Ruelle-Takens-Newhouse oscillations transition scenario from harmonic to chaotic is typical for all considered cases. For $\lambda = 1$ at $\gamma = 0, 0.1, \text{ and } 0.3$, the Hopf bifurcation presence at $N = 9, 11, 13, \text{ and } 15$ is also a characteristic. At $\lambda = 3$, the Hopf bifurcation was observed at $\gamma = 0.3$ for $N = 5$; at $\gamma = 0.5$, the Hopf bifurcation was observed for all N . Also, within the numerical modeling framework, the vibrations-type analysis of two nested cylindrical nanoshells is carried out. It is revealed that the nanoshells' contact interaction leads to a chaotic oscillations mode. At the same time, depending on the size-dependent parameter γ and the gap between nanoshells h_k and the load intensity q_0 , the chaotic oscillations type changes: chaos or hyperchaos. It is also revealed that with an increase in the size-dependent parameter γ , the two-layer cylindrical nanostructure is more stable, that is, contact interaction and as a consequence, chaotic oscillations occur under greater intensity loads.

References

1. M.P.M. Amabili, Review of studies on geometrically nonlinear vibrations and dynamics of circular cylindrical shells and panels, with and without fluid-structure interaction. *Appl. Mech. Rev.* **56**, 349–381 (2003)
2. F. Alijani, M. Amabili, Non-linear vibrations of shells: A literature review from 2003 to 2013. *Int. J. Non Linear Mech.* **58**, 233–257 (2014)
3. A.V. Krysko, J. Awrejcewicz, O.A. Saltykova, S.S. Vetsel, V.A. Krysko, Nonlinear dynamics and contact interactions of the structures composed of beam-beam and beam-closed cylindrical shell members. *Chaos, Solitons Fractals* **91**, 622–638 (2016)
4. O.A. Saltykova, O.A. Afonin, T.V. Yakovleva, A.V. Krysko, The chaotic dynamics of closed cylindrical nanoshells under local loading. *Nonlinear World* **16**(5), 3–15 (2018)
5. V. Krysko Jr., J. Awrejcewicz, T. Yakovleva, A. Kirichenko, O. Szymanowska, V. Krysko, Mathematical modeling of MEMS elements subjected to external forces, temperature and noise, taking account of coupling of temperature and deformation fields as well as a nonhomogenous material structure. *Commun. Nonlinear Sci. Numer. Simul.* **72**, 39–58 (2019). <https://doi.org/10.1016/j.cnsns.2018.12.001>
6. T. Yakovleva, V. Krysko Jr., V. Krysko, Nonlinear dynamics of the contact interaction of a three-layer plate-beam nanostructure in a white noise field. *J. Phys. Conf. Ser.* **1210**, 012160 (2019)
7. S. Shurygina, On the behavior of one of the positive Lyapunov exponent in mutually coupled chaotic oscillators. Papers from the conference for young scientists “Presenting Academic Achievements to the World”, 2010, pp. 129–132
8. J. Awrejcewicz, A. Krysko, N. Erofeev, V. Dobriyan, M. Barulina, V. Krysko, Quantifying chaos by various computational methods. Part 1: Simple systems, in *Entropy in Dynamic Systems*, (MDPI, 2018), pp. 124–137

9. M. Amabili, P. Balasubramanian, G. Ferrari, Travelling wave and non-stationary response in nonlinear vibrations of water-filled circular cylindrical shells: Experiments and simulations. *J. Sound Vib.* **381**, 220–245 (2016)
10. M. Amabili, A. Sarkar, M.P. Païdoussis, Chaotic vibrations of circular cylindrical shells: Galerkin versus reduced-order models via the proper orthogonal decomposition method. *J. Sound Vib.* **290**(3–5), 736–762 (2006)
11. F. Yang, A.C.M. Chong, D.C.C. Lam, P. Tong, Couple stress based strain gradient theory for elasticity. *Int. J. Solids Struct.* **39**, 2731–2743 (2002)
12. R. Mindlin, H. Tiersten, Effects of couple-stresses in linear elasticity. *Arch. Ration. Mech. Anal.* **11**, 415–448 (1962)
13. B.Y. Kantor, *Contact Problems of the Nonlinear Theory of Shells of Revolution* (Nauk. Dumka, Kiev, 1990) [in Russian]
14. J. Awrejcewicz, A.V. Krysko, V.A. Krysko, I.V. Papkova, Routes to chaos in continuous mechanical systems. Part 1: Mathematical models and solution methods. *Chaos Solitons Fractals* **45**, 687–708 (2012)
15. D. Gulick, *Encounters with Chaos* (McGraw-Hill, New York, 1992)
16. M. Sano, Y. Sawada, Measurement of Lyapunov spectrum from a chaotic time series. *Phys. Rev. Lett.* **55**, 1082 (1985)
17. A. Wolf, J.B. Swift, H.L. Swinney, J.A. Vastano, Determining Lyapunov exponents from a time series. *Physica* **16D**, 285–317 (1985)
18. H. Kantz, A robust method to estimate the maximal Lyapunov exponent of a time series. *Phys. Lett. A* **185**(1), 77–87 (1994)
19. M.T. Rosenstein, J.J. Collins, C.J. de Luca, A practical method for calculating the largest Lyapunov exponent from small data sets. *Physica D* **65**, 117 (1993)

Scaling Wavelet Analysis of Chaotic Systems



L. E. Reyes-López, J. S. Murguía, H. González-Aguilar, and H. C. Rosu

1 Introduction

The Wavelet Transform (WT) is a mathematical tool for analyzing a wide variety of signal at different frequencies and different resolutions. In wavelet analysis, the signal is decomposed into certain types of functions, which are scaled and translated versions. The latter is usually referred to in the analysis of the wavelet base function, or simply the mother wavelet function. According to the Fourier analysis procedure, the closely-related forms or its transform, namely the continuous wavelet transform. Considering a finite number of wavelet functions, the discrete wavelet transform (DWT) is formed [1, 2]. It is known that, the class of hyper-chaotic systems, i.e., those dynamical systems having at least two positive Lyapunov exponents, have not been directly studied by means of wavelet transforms [3]. This motivated us to provide here a wavelet scaling analysis to different hyper-chaotic systems such as: Chen, Chua, Lorenz, and Rössler. All these systems are reviewed in Sect. 2, where briefly present their systems of equations and attractors for values of the parameters corresponding to the hyper-chaotic regime.

L. E. Reyes-López (✉) · J. S. Murguía · H. González-Aguilar
Facultad de Ciencias, Universidad Autónoma de San Luis Potosí (UASLP), San Luis Potosí,
México
e-mail: eduardo.reyes@uaslp.mx

H. C. Rosu
IPICyT, Instituto Potosino de Investigación Científica y Tecnológica, San Luis Potosí, México

2 Hyper-chaotic Dynamical Systems

This section is devoted to a brief presentation of the four hyper-chaotic systems which we will consider in this work. These systems, despite their relative simplicity, exhibit a more complex dynamics than the chaotic systems, and the key have received wide coverage in different areas of mathematics, physics, and engineering, among others.

2.1 Chen’s Hyper-chaotic System

The hyper-chaotic dynamics of Chen’s system is modeled by the set of differential equations

$$\begin{aligned}
 \dot{x}_1 &= a(y - x), \\
 \dot{x}_2 &= x(d - z) + cy - w, \\
 \dot{x}_3 &= xy - bz, \\
 \dot{x}_4 &= x + k.
 \end{aligned}
 \tag{1}$$

If $a = 36$, $b = 3$, $c = 28$, $d = -16$, and $k = 0.7$, the system is in the hyper-chaotic regime. In fact, to check the existence of hyper-chaos, there must be at least two positive Lyapunov exponents. The numerically calculated exponents are $(\lambda_1, \lambda_2, \lambda_3, \lambda_4) \approx (1.39, 1.43, 0, -13.34)$, which confirms such hyper-chaotic situation. In Fig. 1a, we display the hyper-chaotic attractor generated by the Chen system with $k = 0.5$ projected onto the plane $x - y$.

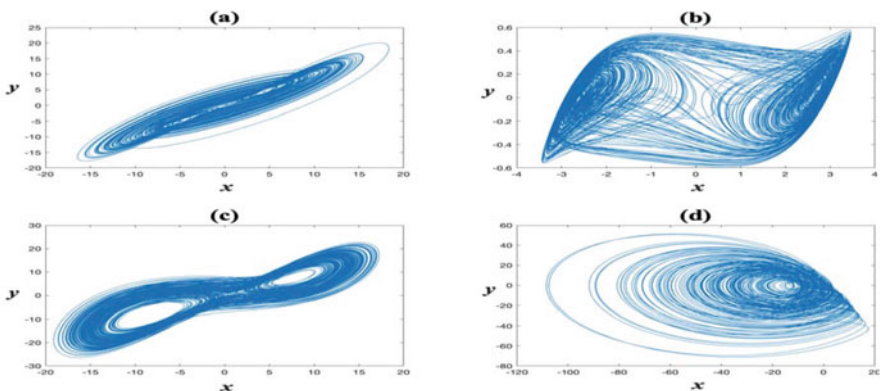


Fig. 1 The hyper-chaotic attractors projected on the plane $x - y$ of (a) Chen’s system for $k = 0.5$, (b) Chua’s system, (c) Lorenz’s system, and (d) Rössler system

2.2 Chua's Hyper-chaotic System

We also consider the four-dimensional hyper-chaotic system based on Chua's system as defined in [4]

$$\begin{aligned}\dot{x}_1 &= a(y - f(x)), \\ \dot{x}_2 &= x - y + z, \\ \dot{x}_3 &= -by - cz + 2, \\ \dot{x}_4 &= -dx + yz,\end{aligned}\tag{2}$$

with parameters values $(a, b, c, d) = (30, 50, 0.32, 0.1111)$, where the non-linear function is defined as $f(x_1) = px_1 + (1 + q)x_1^3$ with $p = 0.03$ and $q = -1.2$. With these values in the parameters, we obtain the Lyapunov exponents $\lambda_1 \approx 1.42$, $\lambda_2 \approx 1.11$, $\lambda_3 \approx 0$, and $\lambda_4 \approx -4.14$, which confirms the hyper-chaotic behavior. Figure 1b shows one hyper-chaotic attractor projected on the plane $x - y$.

2.3 Lorenz's Hyper-chaotic System

The hyper-chaotic dynamics of Lorenz's is modeled by the set of differential equations [5]

$$\begin{aligned}\dot{x} &= \sigma(y - x), \\ \dot{y} &= \rho x + y - xz + w, \\ \dot{z} &= xy - \beta z, \\ \dot{w} &= \phi x,\end{aligned}\tag{3}$$

where σ , ρ , β , and ϕ are parameters of the system. The σ , ρ are called Prandtl and Rayleigh parameters, respectively [6]. If $\sigma = 10$, $\rho = 28$, $\beta = 8/3$, and $\phi = 5$. With these values in the parameters, we obtained the Lyapunov exponents $\lambda_1 \approx 0.38$, $\lambda_2 \approx 0.41$, $\lambda_3 \approx 0$, and $\lambda_4 \approx -14.37$, which confirms the hyper-chaotic behavior. The $x - y$ projection of the hyper-chaotic attractor for this system is shown in Fig. 1c.

2.4 Rössler's Hyper-chaotic System

This is the first system that has been shown to display hyper-chaotic behavior [3]. It is described by the equations

$$\begin{aligned}\dot{x} &= -(y + x), \\ \dot{y} &= x + ay + 2, \\ \dot{z} &= b + xz, \\ \dot{w} &= -cz + dw,\end{aligned}\tag{4}$$

with parameters values $(a, b, c, d) = (0.23, 3, 0.5, 0.05)$, for which the corresponding four Lyapunov exponents are $\lambda_1 \approx 0.10$, $\lambda_2 \approx 0.12$, $\lambda_3 \approx 0$, and $\lambda_4 \approx -17.26$. Figure 1d shows one projection of this 4-D hyper-chaotic attractor.

3 The Discrete Wavelet Transform

In the context of the DWT, for a function $\chi(t)$, it is given in terms of dilated and translated versions of the wavelet function, $\Psi(t)$ [1, 2]. Considering the above, the wavelet function is defined as

$$\Psi_{m,n}(t) = 2^{m/2}\Psi(2^m t - n), \quad \text{for } m, n = 0, \pm 1, \pm 2, \dots\tag{5}$$

form an orthonormal basis, one can then write the expansion of $\chi(t)$ as

$$\chi(t) = \sum_{m,n} d_{m,n}\Psi_{m,n}(t),\tag{6}$$

where the wavelet coefficients $d_{m,n}$

$$d_{m,n} = \langle \chi(t), \Psi_{m,n}(t) \rangle = \int_{-\infty}^{\infty} \chi(t)\Psi_{m,n}(t)dt,\tag{7}$$

with m and n denoting the dilation and translations indices, respectively. To calculate $d_{m,n}$ in a practical numerical analysis, the DWT utilizes the so-called multiresolution analysis (MRA) approach. The key point of MRA is a multiscale, admissibility condition satisfying an approximation design originally developed by Mallat and Meyer [2] whose theoretical foundation would ultimately develop into what is known as the fast wavelet transform (FWT).

3.1 Wavelet Variance

According to [7], the power spectrum $P(\omega)$ for self-similar random processes, which corresponds to the Fourier transform of the autocorrelation function, presents the behavior

$$P(\omega) \sim |\omega|^{-\beta}, \quad (8)$$

where ω corresponds to the angular frequency and beta is the spectral parameter. In fact, the beta exponent is related to the statistically self-similar random processes called $1/f$ processes by the expression $\beta = 2H + 1$, where H is named as a self-similarity parameter. Even more important, the variance of the wavelet coefficients $\text{var}\{d_{m,n}\}$ is related to the decay levels m through the following power law [8]

$$\text{var}\{d_{m,n}\} \approx (2^m)^{-\beta}. \quad (9)$$

In order to estimate the scale exponent β the least squares fit of the following linear model is used [7, 9, 10]

$$\log_2(\text{var}\{d_{m,n}\}) = -m\beta + (K + v_m), \quad (10)$$

where K and v_m are constants related to the linear fitting procedure. The Eq. (9) is suitable for studying discrete chaotic time series, because their log variance plot has a well-defined form as pointed out in [7, 10]. If the log variance plot shows a maximum at a particular wavelet level, or a bump over a group of wavelet levels, which means a high energy concentration, it will often correspond to a fundamental *carrier frequency*. In addition, if the log variance of the wavelet of the wavelet coefficients plotted against level m shows a slope $-\beta$, thus the signal presents a fractal behavior, which is consistent with the statistically self-similar structure of the signal [7].

4 Results

In this section, the scaling dynamics of the above-mentioned hyper-chaotic systems is evaluated with the wavelet variance scaling analysis. The hyper-chaotic systems are simulated numerically with the classical fourth-order Runge–Kutta algorithm. To carry out the wavelet analysis, we use the Daubechies wavelet function db2 [1, 2].

We first examine the hyper-chaotic Chen's system (1). Fig. 2a shows a part of the time series of the x variable, whereas Fig. 2b displays a semi-logarithmic plot of the wavelet coefficient variances as a function of level m , which is known as the variance plot of the wavelet coefficients. In this figure it can be seen that the eighth level is the one with the greatest amplitude, i. e., the major share of signal energy

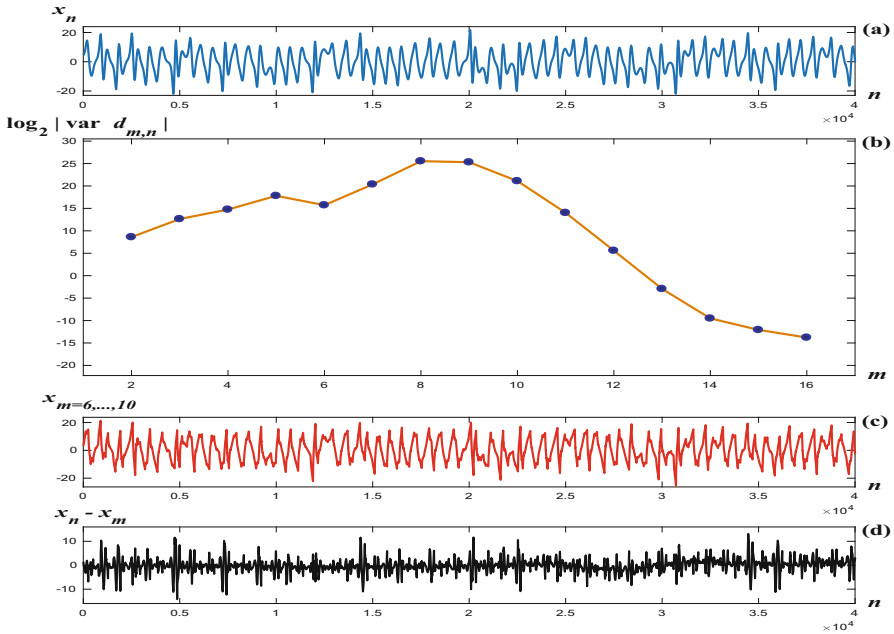


Fig. 2 (a) Time series of the x variable of hyper-chaotic Chen’s system. (b) logarithmic variance of wavelet coefficients $d_{m,n}$, (c) the reconstructed time series based on the sequence from 6th to 10th wavelet levels, and (d) the error between the reconstructed and the original time series

goes into this wavelet level. However, to catch almost the entire energy, we add together the five neighbor wavelet levels, $m = 6, \dots, 10$. The reconstruction of the signal at these wavelet levels is shown in Fig. 2c, where the structure of the original signal can be showed. Finally, Fig. 2d shows the error between the reconstruction and the original time series.

Another case was the Chua’s system. In this case, some samples of the time series of the state y are shown in Fig. 3a, while the wavelet variance plot is given in Fig. 3b, we can see that the levels $m = 6$ to $m = 10$ we are able to have a good reconstruction. The error between the reconstruction is depicted in Fig. 3c. The error between the reconstruction and the original time series is shown in Fig. 3d. According to the above, this case has a fundamental *carrier frequency*.

A different scenario is presented in the time series corresponding to state w , which is shown in Fig. 3a. The variance of the coefficients is shown in Fig. 3b, in which there is a line with a negative slope which indicates a behavior of the fractal type. The fractal coefficient is given by the slope and its numerically calculated values is $\beta \approx 2.26$. This implies that this variable is statistically self-similar and corresponds to the classical Brownian motion. It is worth mentioning that this scenario does not occur in chaotic three-dimensional systems [7, 10] (Fig. 4).

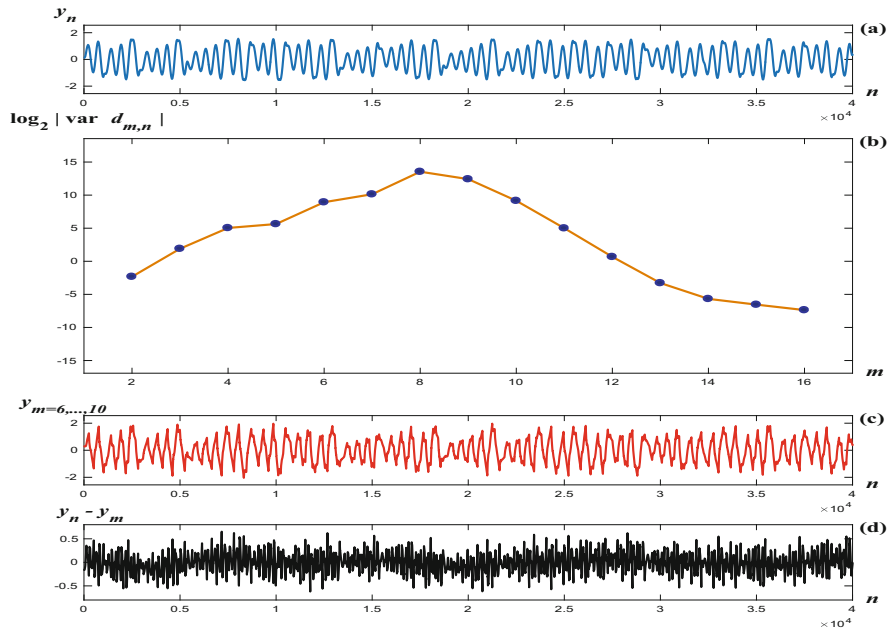


Fig. 3 (a) Time series of the y variable of hyper-chaotic Chua's system. (b) logarithmic variance of wavelet coefficients $d_{m,n}$. (c) the reconstructed time series pf the sum from 6th to 10th level, and (d) the difference between the reconstruction and the original time series

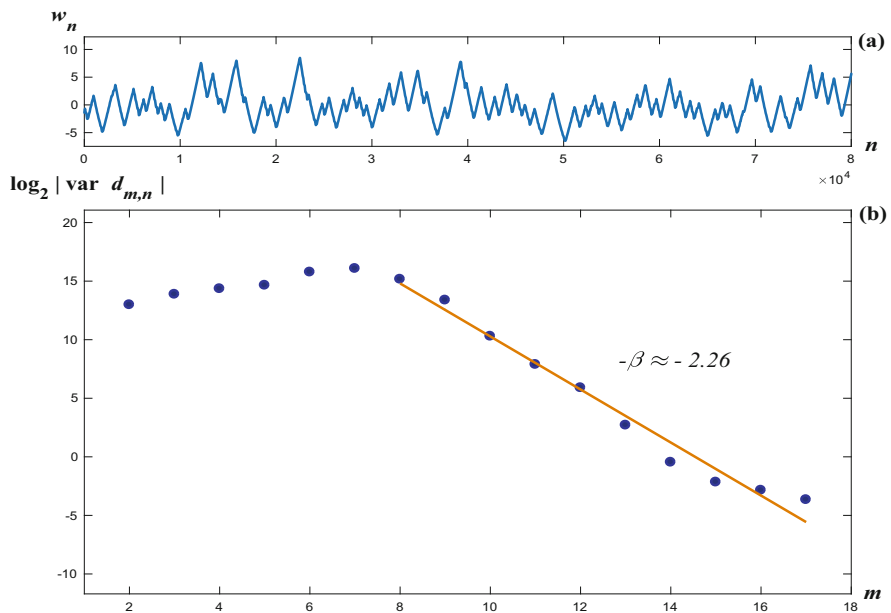


Fig. 4 (a) Time series of the w variable of hyper-chaotic Chua's system, and (b) the respective logarithmic variance of its wavelet coefficients $d_{m,n}$

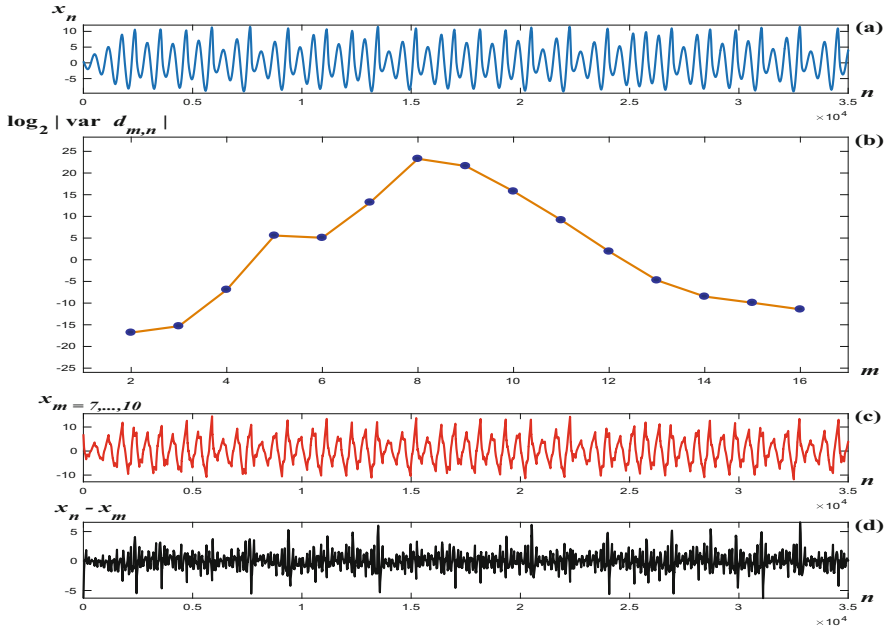


Fig. 5 (a) Time series of the x variable of hyper-chaotic Rössler system, (b) logarithmic variance of its wavelet coefficients $d_{m,n}$, (c) the reconstructed time series based on the sum from the 7th to 10th wavelet levels, and (d) difference point to point between the reconstructed and original time series

Table 1 Results of wavelet analysis. CF, F, and GN stand for carrier frequency, fractal, and Gaussian noise behaviors, respectively

Dynamical system	States			
	x	y	z	w
Chen	CF	CF	CF	F
Chua	GN	CF	GN	F
Lorenz	CF	CF	CF	GN
Rössler	CF	CF	CF	F

The last case we analyzed the hyper-chaotic Rössler’s system (4). In Fig. 5a displays the time series of the x state, whereas Fig. 5b illustrates the wavelet variance plot. We notice a substantial energy concentration from the 7th to 10th wavelet levels. Based in this range of levels, the reconstructed time series is shown in Fig. 5c. A similar situation occurs with the y and z variables. Finally, the difference between the reconstruction and the original time series is shown in Fig. 5d.

As a summary, the Table 1 shows the numerical results of the wavelet analysis of the time series of all studied hyper-chaotic systems.

5 Conclusions

In this work, the variance of the wavelet coefficients is used to analyze hyperchaotic time series from different systems. It appears that the wavelet approach is a very illustrative means of revealing some dynamical properties of the hyperchaotic systems. The results show a trend in most of the time series of the dynamical systems in the high concentration of energy at certain levels of transformation, which can be interpreted as a carrier frequency in the time series. On the other hand, for the fourth variable, a Brownian motion behavior is observed for the majority of the time series. Also, we found a fractal behavior in the fourth variable of the hyperchaotic time series. Finally, the information provided by the wavelet scaling analysis may be used to choose appropriate hyperchaotic dynamical system for whatever application. Such as in the image encryption system, because the behavior presented by the time series can help us to create a selection criteria of time series so that the operation of the encryption system has a better performance.

Acknowledgments L.E. Reyes-López is a CONACyT doctoral fellow at FC-IICO-UASLP. This paper was partially supported by CONACyT funds from grant CB 2017–2018 A1-S-45697.

References

1. I. Daubechies, *Ten Lectures on Wavelets* (Society for Industrial and Applied Mathematics, Philadelphia, 1992)
2. S. Mallat, *A Wavelet Tour of Signal Processing* (Elsevier, Amsterdam, 1999)
3. O.E. RöSSLer, An equation for hyperchaos. *Phys. Lett. A* **71**(2–3), 155–157 (1979)
4. T. Gao, Z. Chen, A new image encryption algorithm based on hyper-chaos. *Phys. Lett. A* **372**(4), 394–400 (2008)
5. C. Shen, S. Yu, J. Lü, G. Chen, Constructing hyperchaotic systems at will. *Int. J. Circuit Theory Appl.* **43**(12), 2039–2056 (2015)
6. E.N. Lorenz, Deterministic nonperiodic flow. *J. Atmos. Sci.* **20**(2), 130–141 (1963)
7. W.J. Staszewski, K. Worden, Wavelet analysis of time-series: coherent structures, chaos and noise. *Int. J. Bifur. Chaos* **9**(3), 455–471 (1999)
8. G.W. Wornell, A.V. Oppenheim, Wavelet-based representations for a class of self-similar signals with application to fractal modulation. *IEEE Trans. Inf. Theory* **38**(2), 785–800 (1992)
9. E. Campos-Cantón, J.S. Murguía, H.C. Rosu, Chaotic dynamics of a nonlinear electronic converter. *Int. J. Bifur. Chaos* **18**(10), 2981–3000 (2008)
10. J.S. Murguía, E. Campos-Cantón, Wavelet analysis of chaotic time series. *Rev. Mexicana de Física* **52**(2), 155–162 (2006)
11. J.S. Murguía, Scaling analysis of hyperchaotic time series. *Int. J. Mod. Phys. C* **28**(07), 1750094 (2017)
12. O.E. RöSSLer, An equation for continuous chaos. *Phys. Lett. A* **57**(5), 397–398 (1976)

Weakness Analyzing and Performance Improvement for Image Encryption with Chaos Across Cylinder



Chaofeng Zhao and Haipeng Ren

1 Introduction

Due to the attracting features, such as the extreme sensitivity to initial conditions and system parameters, ergodicity and random like behaviors, chaos is considered as one of the ideal tools for image encryption [1–9]. Although the chaos-based image encryption algorithm in [4–9] has achieved some encryption function, they have some security weaknesses. The image encryption algorithm [7] designed by Farhan et al., which has only two operations of pixels shuffling and XOR, lacking effective diffusion operation, brings security weakness. The present paper analyses and evaluates the security performance of the image encryption algorithm in [7] to show the weakness. To overcome the security weaknesses, an improved image encryption algorithm is proposed by adding the diffusion operation and creating a connection between plain-text images and security keys in order to resist chosen plain-text attack and differential attack.

The rest of this paper is organized as follows. The review and cryptanalysis of the Farhan's algorithm [7] is presented in Sect. 2. In Sect. 3, an improved image encryption algorithm is proposed, and the performance of the improved image encryption algorithm is evaluated to show the improved performances with respect to the original and comparison algorithms in Sect. 4. Finally, conclusions are given in Sect. 5.

C. Zhao · H. Ren (✉)

Shaanxi Key Laboratory of Complex System Control and Intelligent Information Processing,
Xi'an University of Technology, Xi'an, P.R. China
e-mail: tufei210@126.com; renhaipeng@xaut.edu.cn

2 The Review and Cryptanalysis of Farhan's Algorithm

2.1 The Chaotic System

In Farhan's algorithm [7], the authors proposed a new chaotic system [7] crossing inside and outside of a predefined cylinder, repeatedly, which is

$$\begin{cases} \dot{x} = z, \\ \dot{y} = x^2 + y^2 - a^2, \\ \dot{z} = 0.4z + 3xy, \end{cases} \quad (1)$$

where x , y , z are the state variables, a is the system parameter. The system is chaotic for $a = 1.7$, as shown in Fig. 1a, where the attractor is starting from the initial conditions $\{x_0, y_0, z_0\} = \{0.29, -1.81, 0.17\}$. Figure 1b shows the chaotic attractor that crosses the inside and outside of the cylinder defined by $x^2 + y^2 = a^2$, repeatedly.

2.2 The Original Image Encryption Algorithm

Farhan's algorithm [7] consists of three operations, including chaotic sequences processing, shuffling pixel positions, and pixel values encryption. The process of the algorithm is explained as follows.

Step a1: Parameter a and initial values $\{x_0, y_0, z_0\}$ are entered into system (1), evolving for a proper time T to obtain the state sequences.

Step a2: Input the plain-text image P with the size $M \times N$ (256×256).

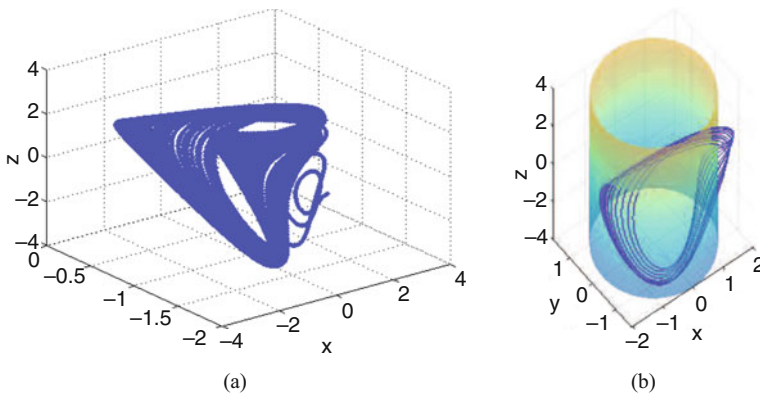


Fig. 1 (a) Chaotic attractor of system (1) with $a = 1.7$ and $\{x_0, y_0, z_0\} = \{0.29, -1.81, 0.17\}$; (b) The cylinder $x^2 + y^2 = a^2$ and the chaotic attractor

Step a3: The float values of the state sequences x , y , and z are transferred into 32-bit binary values with 3 bits for the integer part and 29 bits for the fraction part, and then select 20 least significant bits to generate the random numbers, i.e., “0” or “1”, and put in a vector, i.e., x' , y' , and z' represent vectors that sufficiently long binary numbers. Here, every eight bits conversion value of x' , y' , and z' form the final used random vectors, respectively, i.e., vectors x_1 , y_1 , and z_1 of length $M * N$ and values in $[0, 255]$.

Step a4: A random line mixing refers to shuffle image pixel positions (row or column) according to the indices generated by random sequences, which is used to shuffle rows and columns of the plain-text image and get the shuffled image P_s . The indices X_1 and Z_1 are generated by vectors x_1 and z_1 . Specifically, the duplication numbers within vectors x_1 and z_1 are removed until 256 distinct numbers between 0 and 255 are generated and recorded as indices X_1 and Z_1 , respectively. Where the random index X_1 is used to shuffle the rows of the plain-text image and the random index Z_1 is used to shuffle the columns of the image.

Step a5: After the shuffling process, the shuffled image P_s is row or column wise converted into a vector P_v , and a vector K_h is generated by XOR operation of the vector x_1 and y_1 . Finally, the values of P_v are XOR ed with K_h to obtain C_v , i.e., $C_v = P_v \oplus K_h = P_v \oplus (x_1 \oplus y_1)$. Where \oplus is XOR operation.

Step a6: Reshape C_v into matrix to obtain the encrypted image C of size $M \times N$ (256×256).

By carefully checking the process of Farhan’s algorithm [7], we learn that (A) the diffusion, one of the Shannon’s two basic principles including permutation and diffusion, does not exist, which made it impossible to resist chosen plain-text attack. (B) The keys used in Farhan’s algorithm [7] are irrelevant to the plain-text image to be encrypted. Therefore, Farhan’s algorithm [7] cannot resist differential attack. (C) As an encryption algorithm, the security keys analysis is of vital importance. In Farhan’s algorithm [7], there is no clear security keys, no definition of key space, and no analysis of key sensitivity, which leads to unpredictable security performance.

2.3 Recover the Target Plain-Text Image by Chosen Plain-Text Attack

According to Kerckhoffs’ principle, chosen plain-text attack means that an attacker is able to temporary access to the encryption machinery but does not know the security keys. Hence, the attacker can choose any plain-text and obtain the corresponding cipher-text, that is, the attacker’s goal is to obtain some information about the encryption algorithm through this process, so that the attacker can more effectively crack the encrypted information in the future. In the worst case, the keys can be easily obtained and used for decryption [10].

(1) Selecting the parameter a and initial conditions $\{x_0, y_0, z_0\}$ of the chaotic system (1) as the security keys, which are unknown to the attacker, and choosing

three known images P_{k1} (referred to as “all zero elements”), P_{k2} (referred to as “the same row elements”), and P_{k3} (referred to as “the same column elements”) with size of $M \times N$ (here, $M = N = 256$), which are

$$P_{k1} = \begin{pmatrix} 0 & 0 & \cdots & 0 \\ 0 & 0 & \cdots & 0 \\ \vdots & \vdots & \ddots & \vdots \\ 0 & 0 & \cdots & 0 \end{pmatrix}; P_{k2} = \begin{pmatrix} a_1 & a_2 & \cdots & a_N \\ a_1 & a_2 & \cdots & a_N \\ \vdots & \vdots & \ddots & \vdots \\ a_1 & a_2 & \cdots & a_N \end{pmatrix}; P_{k3} = \begin{pmatrix} b_1 & b_1 & \cdots & b_1 \\ b_2 & b_2 & \cdots & b_2 \\ \vdots & \vdots & \ddots & \vdots \\ b_M & b_M & \cdots & b_M \end{pmatrix},$$

where a_1, a_2, \dots, a_N , and b_1, b_2, \dots, b_M , are arbitrary integers that belong to $\{0, 1, \dots, 255\}$.

- (2) Farhan’s algorithm [7] is used to encrypt images P_{k1} , P_{k2} , and P_{k3} , and corresponding encrypted images are C_{k1} , C_{k2} , and C_{k3} , respectively, which are

$$C_{k1} = P_{k1}^{rc} \oplus K_{c1}. \quad (2)$$

$$C_{k2} = P_{k2}^{rc} \oplus K_{c2}. \quad (3)$$

$$C_{k3} = P_{k3}^{rc} \oplus K_{c3}, \quad (4)$$

where P_{k1}^{rc} , P_{k2}^{rc} , and P_{k3}^{rc} are the images of P_{k1} , P_{k2} , and P_{k3} after the shuffling of row and column elements, respectively, and K_{c1} , K_{c2} , and K_{c3} are the corresponding XOR key matrices, respectively, and the superscripts r and c represent the shuffling of row elements and the shuffling of column elements, respectively, i.e., P_{k1}^{rc} is the image of P_{k1} after the shuffling both row and column elements.

- (3) Assuming that the encrypted image C' is attacked, Farhan’s algorithm [7] is subjected to the chosen plain-text attack to recover the plain-text image P' . The detailed decryption process is as follows:

Step b1: Image shuffling is performed for image P_{k1} according to the Step a4 to get the shuffled image P_{k1}^{rc} . In fact, P_{k1}^{rc} is still composed of zero, i.e., $P_{k1}^{rc} = P_{k1}$. Therefore, we can get the encrypted image $C_{k1} = P_{k1}^{rc} \oplus K_{c1} = P_{k1} \oplus K_{c1} = K_{c1}$, i.e., $K_{c1} = C_{k1}$. Thus, $P^{rc} = C' \oplus K_{c1} = C' \oplus C_{k1}$, and $K_{c1} = K_{c2} = K_{c3}$.

Step b2: The shuffling of row elements of image P_{k2} is performed to get the shuffled image P_{k2}^r . In fact, P_{k2}^r is P_{k2} itself. So, after the shuffling of column elements, we can get $P_{k2}^c = P_{k2}^{rc}$. Thus, $P_{k2}^c = P_{k2}^{rc} = C_{k2} \oplus K_{c2} = C_{k2} \oplus K_{c1} = C_{k2} \oplus C_{k1}$.

By comparing P_{k2} and P_{k2}^c , we can calculate the equivalent key vector $c1$ of shuffling of column elements. Therefore, P^{rc} is obtained by the inverse shuffling of column elements of P^{rc} .

Step b3: The shuffling of row elements for image P_{k3} is performed to get the image P_{k3}^r , and then P_{k3}^r is shuffled in column elements to get the shuffled image

P_{k3}^{rc} . In fact, P_{k3}^{rc} is P_{k3}^r itself. Thus, $P_{k3}^r = P_{k3}^{rc} = C_{k3} \oplus K_{c3} = C_{k3} \oplus K_{c1} = C_{k3} \oplus C_{k1}$.

By comparing P_{k3} and P_{k3}^r , the equivalent key vector $r1$ of shuffling of row elements can be calculated. Therefore, P' is obtained by the inverse shuffling of row elements of P'' .

Taking the gray-scale plain-text image ‘‘Cameraman’’ with size of 256×256 as example to encrypt and decrypt, this process takes about 12 s to crack the encrypted image by our desktop computer. The time spend is very low. In conclusion, Farhan’s algorithm [7] is not able to resist chosen plain-text attack.

2.4 Differential Attack of Farhan’s Algorithm

In order to verify the differential attack resistance performance of Farhan’s algorithm [7], two commonly used indices are used, i.e., Number of Pixel Changing Rate (NPCR) and Unified Averaged Changed Intensity (UACI) [1, 3, 12]. For an excellent encryption algorithm, the ideal value of NPCR and UACI are 99.6094% and 33.4635%, respectively, for one bit plain-text change.

NPCR and UACI values of Farhan’s algorithm [7] derived by the average value of 200 times running for different images with size of 256×256 are given in the second row of Table 1. As seen from Table 1, NPCR and UACI values by Farhan’s algorithm [7] are far from the expected values, which indicates the weak resistance to differential attack. In Table 1, The value using bold font indicates the best value of

Table 1 The performance analysis of quantitative indices

Algorithms	Indices	Cameraman	Boat	5.3.01	All zero elements	The same row elements	The same column elements
Zhan [2]	NPCR	49.8043	67.9806	54.1472	73.6923	41.8472	55.3830
	UACI	20.5461	20.4679	13.5957	18.4986	20.1649	25.0541
	IE	7.9964	7.9989	7.9940	3.9998	7.9951	7.9973
	Time	42.564	174.298	754.431	48.468	55.382	47.228
Farhan [7]	NPCR	0.0015	–	–	0.0015	0.0015	0.0015
	UACI	5.9838e–06	–	–	5.9838e–06	4.0451e–05	2.6449e–05
	IE	7.9973	–	–	7.9971	7.9969	7.9973
	Time	0.0153	–	–	0.0148	0.0147	0.0150
Zhou [11]	NPCR	99.7971	99.7055	99.6009	99.5956	99.5850	99.3256
	UACI	33.7390	33.8777	33.4617	33.7873	33.1199	33.2512
	IE	7.9974	7.9992	7.9998	7.9974	7.9973	7.9976
	Time	0.364	0.831	3.268	0.369	0.356	0.387
Improved algorithm	NPCR	99.6582	99.6132	99.6032	99.6063	99.6170	99.6353
	UACI	33.4743	33.4632	33.4630	33.4659	33.4625	33.4707
	IE	7.9971	7.9993	7.9998	7.9968	7.9972	7.9969
	Time	0.0861	0.399	1.371	0.0894	0.0856	0.0875

the corresponding index within the same column. For example, in the Cameraman (picture) column, for the time index, Farhan [7] is the best, for the IE index, Zhou [11] is the best, for NPCR and UACI indices, the improved algorithm is the best.

3 The Improved Image Encryption Algorithm

One of the shortcomings of Farhan’s algorithm [7] is that it is not application to different size of image. In order to obtain the random sequence for the different size image, the randomization process described in Step a2 and a4 can be modified according to the size of image, as shown in Algorithm 1. The specific process of Algorithm 1 is as follow: For the image of size $M \times N$, two sufficiently long sequences x' and z' generated by system (1) are obtained according to the 20 least significant bits method in Step a2, we calculate $m = \text{ceil}(\log_2(M))$ and $n = \text{ceil}(\log_2(N))$ and convert the two sequences x' and z' into integers sequences X'_1 and Z'_1 according to every m -bit and n -bit, i.e., $[0, 2^m - 1]$ and $[0, 2^n - 1]$. Finally, we remove the duplicates until M and N distinct numbers between 1 and M and N are generated to obtain indexes X_1 and Z_1 , respectively.

Figure 2 gives the flowchart of the improved algorithm, where the blocks with black frame are the same as Farhan’s algorithm [7], while the blocks with red frame are added for the diffusion operation to improve the performance of the algorithm. Here, Steps c4 and c5 of the improved algorithm are given, and Steps c1, c2, c3, and c6 are the same as Steps a1, a2, a3, and a6. The procedure of Steps c4 and c5 is as follows:

Step c4: A random line mixing is used to get the shuffled image P_s . x' and z' are preprocessed using Algorithm 1, the random number indexes X_1 and Z_1 are obtained to shuffle the rows and the columns of the plain-text image, respectively.

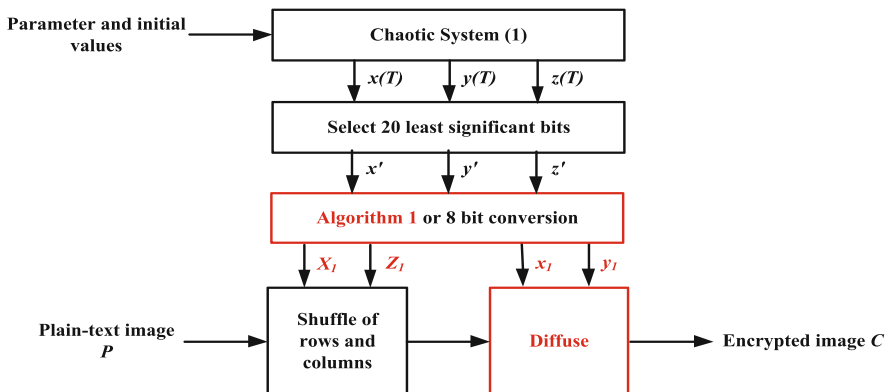


Fig. 2 The flowchart of the improved algorithm

Step c5: After the line mixing process, the following diffusion operation is performed.

First, the shuffled image P_s is row or column wise converted to a vector P_v .

Second, the pixel sum of P_v (recorded as Sum) is obtained by $Sum = \sum_{i=1}^{M*N} P_v(i)$.

Third, the initial intermediate key $C0(1)$ is calculated by

$$C0(1) = round((Sum - P_v(1))/(M * N - 1)).$$

Sum is updated by $Sum = Sum - P_v(i)$, where $i = 1$.

Fourth, calculate the remaining intermediate key vector by

$$C0(i) = bitxor((mod(P_v(i) + x_1, 256), mod(C0(i - 1) + y_1 + Sum * 10^3, 256))),$$

and update $Sum = Sum - P_v(i)$, where $i = 2, 3, \dots, length(P_v)$.

Fifth, $C_v = C0$.

4 Security Analysis of the Improved Image Encryption Algorithm

4.1 Security Key Space and Sensitivity Analysis

The security keys of the improved algorithm are composed of one parameter a and initial values $\{x_0, y_0, z_0\}$. If the precision of the parameter and initial values is 10^{-14} , the security key space of the improved image encryption algorithm is $(10^{14})^4 = 10^{64} \approx 2^{213}$, which is greater than 2^{100} and can resist brutal force attack [1, 3].

In order to demonstrate the key sensitivity of the improved algorithm, the number of bit change rate (NBCR) [13] is introduced, which is defined as

$$L(B_1, B_2) = \frac{Ham(B_1, B_2)}{len}, \quad (5)$$

where $Ham()$ is the Hamming distance of two images B_1 and B_2 , and len is total number of bits of B_1 and B_2 . If the NBCR values approach to 50%, B_1 and B_2 are completely different images with no correlations.

In the following experiments, 200 key groups $K(i) = \{a(i), x_0(i), y_0(i), z_0(i)\}$, ($i = 1, 2, 3, \dots, 200$) are selected from the security key space randomly and used to encrypt the plain-text image "Cameraman" to obtain 200 encrypted images denoted as $C_1(i)$. Second, each key group under the same condition except a security key mismatch (10^{-14}) on a, x_0, y_0, z_0 , respectively, denoted as $K1(i)$. And then, $K1(i)$ are used to encrypt the same plain-text image to obtain another 200 encrypted images denoted as $C_2(i)$, and calculate NBCR of $C_1(i)$ and $C_2(i)$; Third, decrypt a same cipher image $C_1(1)$ using $K1(i)$ and $K2(i)$ to generate two decrypted images

Table 2 NBCR of the parameter and three initial values (%)

Parameter/initial values	a	x_0	y_0	z_0
$L(C_1, C_2)$	49.9961	49.9965	49.9942	50.0014
$L(E_1, E_2)$	50.0004	50.0003	50.0038	49.9958

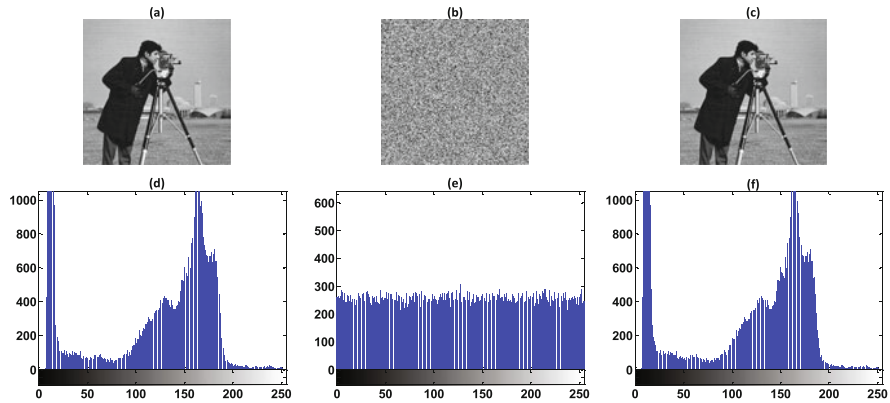


Fig. 3 Histograms of plain-text image “Cameraman” and its corresponding encrypted image and decryption image. (a) plain-text image; (b) the encrypted image; (c) the decryption image; (d) histogram of the plain-text image; (e) histogram of the encrypted image; (f) histogram of the decryption image

$E_1(i)$ and $E_2(i)$ and then calculate their NBCR. Table 2 gives the average of NBCR values of parameter a and three initial values x_0 , y_0 , z_0 . From Table 2, we learn that the NBCR values of parameter a and three initial values x_0 , y_0 , z_0 are very closed to 50%, which reveals that two encrypted images and two decryption images in the improved encryption algorithm are completely different. Therefore, the security keys are extremely sensitive.

4.2 Statistical Analysis

4.2.1 Histograms of Encryption Images

We give a typical example to show the plain-text image, the corresponding encrypted image, decryption image, and its corresponding histograms, respectively, as shown in Fig. 3. As seen from Fig. 3, the encrypted image in Fig. 3b is noise-like, hiding the original information very well. In Fig. 3e, all the gray-scale values of the encrypted image are distributed uniformly over the interval $[0, 255]$, which is significantly different from the original distribution shown in Fig. 3d.

4.2.2 Information Entropy (IE)

The most commonly used information entropy is the Shannon entropy [2, 3], which is regarded as the vital feature of randomness. It is easy to prove that a random gray-scale image with uniformly distributed pixels over the interval [0, 255] can achieve the ideal Shannon entropy equal to 8. The information entropy of the image in Fig. 3b is $IE = 7.9971$, which is very close to the ideal value. Table 1 gives information entropy of encrypted images by different image encryption algorithms, which indicates that the rate of information leakage from the improved algorithm is more close to zero, and shows competitive performance with [2, 7] in most cases, and very close to the ideal one and that in [11].

4.3 Differential Analysis

Table 1 shows NPCR and UACI values of the encrypted images for different images with different sizes. As seen from Table 1, the improved algorithm has NPCR and UACI values close to the expected values, i. e., 99:6094 and 33:4635%. So it is very sensitive to small changes in the plain-text images. In other words, it has a good ability to resist differential attack. As compared to the algorithms in [2, 7], the improvement is significant. It has comparable performance to the algorithm in [11].

4.4 Robustness to Partial Data Loss

When an encrypted image is subjected to partial data loss, the encryption algorithm should be robust enough to recover the plain-text image without significantly decreasing its visual quality. Figure 4 shows the results of the data loss using the improved algorithm. Although the decryption images being partially lost, from Fig. 4, we know that most of the plain-text images can be recovered, which indicates that the improved algorithm has good robustness.

4.5 Resistance to Chosen Plain-Text Attack of the Improved Algorithm

In the improved algorithm, the intermediate keys are related to the plain-text image to be encrypted. Even if the attacker cracked the keys with some special chosen plain-text images, the intermediate keys cannot be used to decrypt the target encrypted image, because different images have different intermediate keys. For diffusion process, the encrypted pixel value is not only related to the corresponding

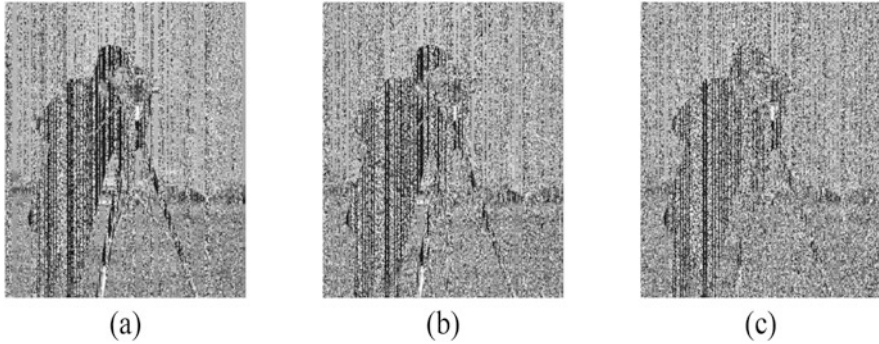


Fig. 4 The decrypted images from the encrypted “Cameraman” images with data loss. (a) 5% data loss; (b) 15% data loss; (c) 25% data loss

plain-text pixel value and the security key but also related to the former plain-text pixel values and former encrypted pixel values. This means different encrypted images have different former plain-text values and former encrypted values. The chosen plain-text attack test of the algorithms in [2, 7, 11] and the improved algorithm is conducted. The result shows that the algorithms in [2, 7] have weak ability to resist chosen plain-text attack, while the improved algorithm and the algorithm in [11] have strong resistance to chosen plain-text attack. So, the improved algorithm can resist chosen plain-text attack.

4.6 Efficiency

We test the average time cost of the improved algorithm on our desktop computer. Table 1 gives the time cost of the improved algorithm with respect to various size images. The results indicate that the cost of the improved algorithm is acceptable although these are extra cost as compared to Farhan’s algorithm [7].

5 Conclusions

In this chapter, Farhan’s algorithm [7] with some security weaknesses is analyzed and is found that it cannot resist chosen plain-text attack, differential attack and not fit for different size of image. Further, improvement operations are proposed to improve the performance. The simulation results show that the improved algorithm significantly improves the security of encryption images while still keeps all the merits of Farhan’s algorithm [7].

References

1. W.J. Cao, Y.J. Mao, Y.C. Zhou, Designing a 2D infinite collapse map for image encryption. *Signal Process.* **171**, 107457 (2020)
2. K. Zhan, D. Wei, J.H. Shi, J. Yu, Cross-utilizing hyperchaotic and DNA sequences for image encryption. *J. Electron. Imag.* **26**(1), 013021 (2017)
3. C.F. Zhao, H.P. Ren, Image encryption based on hyper-chaotic multi-attractors. *Nonlinear Dyn.* **100**(1), 679–698 (2020)
4. S. Wang, C. Wang, C. Xu, An image encryption algorithm based on a hidden attractor chaos system and the Knuth-Durstenfeld algorithm. *Opt. Laser. Eng.* **128**, 105995 (2020)
5. H. Liu, X. Wang, Color image encryption using spatial bit-level permutation and high-dimension chaotic system. *Opt. Commun.* **284**(16–17), 3895–3903 (2011)
6. X. Wu, B. Zhu, Y. Hu, A novel color image encryption scheme using rectangular transform-enhanced chaotic tent maps. *IEEE Access* **5**, 6429–6436 (2017)
7. A.K. Farhan, N.M.G. Al-Saidi, A.T. Maolood, F. Nazarimehr, I. Hussain, Entropy analysis and image encryption application based on a new chaotic system crossing a cylinder. *Entropy* **21**(10), 958 (2019)
8. C. Xu, J. Sun, C. Wang, An image encryption algorithm based on random walk and hyperchaotic systems. *Int. J. Bifurcat. Chaos* **30**(4), 2050060 (2020)
9. G. Cheng, C. Wang, C. Xu, A novel hyper-chaotic image encryption scheme based on quantum genetic algorithm and compressive sensing. *Multimed. Tools Appl.* **79**(39–40), 29243–29263 (2020)
10. L. Zhao, A. Adhikari, D. Xiao, On the security analysis of an image scrambling encryption of pixel bit and its improved scheme based on self-correlation encryption. *Commun. Nonlinear Sci.* **17**(8), 3303–3327 (2012)
11. Y.C. Zhou, L. Bao, C.L.P. Chen, A new 1D chaotic system for image encryption. *Signal Process.* **97**(7), 172–182 (2014)
12. Y. Wu, J.P. Noonan, NPCR and UACI randomness tests for image encryption. *Cyber. J.* **1**(2), 31–38 (2011)
13. J.C.H. Castro, J.M. Sierra, A. Seznec, The strict avalanche criterion randomness test. *Math. Comput. Simul.* **68**(1), 1–7 (2005)

A Surrogate Approach for Stochastic Modeling of a Crash Box Under Impact Loading in the Time Domain



Biswarup Bhattacharyya, Eric Jacquelin, and Denis Brizard

1 Introduction

The crash box is one of the important parts in a car body for providing safety to the passengers during a crash. Therefore, a proper design of a crash box can reduce the chance of the life loss. All the parameters of a crash box should be designed properly and often the design parameters are uncertain in nature. Therefore, uncertainty quantification (UQ) is one of the possible ways to design the crash box under uncertain parameters.

Monte Carlo simulation (MCS) can be used for UQ of such complex problem, however, to avoid the crude MCS approach, researchers have developed surrogate modeling approaches which maintains a trade-off between accuracy and efficiency. The surrogate modeling approach includes polynomial chaos expansion (PCE) [1], Kriging [2], among other less popular methods. Most surrogate models till date have considered static problems; however, the analysis of a crash box is an impact dynamics problem. As a result, the uncertainty in the response quantity is time-dependent. Therefore, the available surrogate models must be computed at each time-step for a crash box problem.

PCE is the most used surrogate model in many contexts. PCE model has been improved in several ways to adapt it for the dynamical systems. A time-dependent PCE model [3] was proposed to account the time-dependent nonlinear behavior of dynamical systems. However, it was observed that the time-dependent PCE was updated almost at each time-step for a single degree of freedom dynamical system and it is highly computationally expensive. Further, to reduce the computational cost, the time domain and the randomness were decoupled [4] using a nonlinear

B. Bhattacharyya (✉) · E. Jacquelin · D. Brizard
Univ Lyon, Université Claude Bernard Lyon 1, Univ Gustave Eiffel, IFSTTAR, LBMC
UMRT9406, Lyon, France

autoregressive with exogenous (NARX) model and the PCE model, respectively. However, due to the unavailability of a generalized NARX model for the impact dynamical system, a proper orthogonal decomposition (POD) approach has been used in [5, 6] to decouple the time-dependent behavior and the randomness. Therefore, the uncertain parameters were propagated by the PCE model. An attempt is made in this paper to propagate uncertain parameters through a crash box problem by the POD-PCE model.

2 Review of PCE and POD Approaches

2.1 PCE Approach

The input uncertain parameters of a system are given by $x = \{x_1, x_2, \dots, x_d\}$ and all the parameters are considered independent. For a crash box problem, the response quantity depends on time and it is given by $y(x, t)$. t can be considered as the continuous time or the discretized time vector with n_t time-steps. The PCE model for a dynamical system is given by

$$y(x, t) = \sum_{\alpha \in \mathbb{N}^d} a_\alpha(t) \psi_\alpha(x) \quad (1)$$

where $\psi_\alpha(x)$ are the multivariate orthonormal polynomials and $a_\alpha(t)$ are the time-dependent coefficients. $\alpha \in \mathbb{N}^d$ is a multi-index over all the uncertain parameters. The multivariate orthonormal polynomials are constructed using the tensor product of the univariate orthonormal polynomials with respect to the corresponding marginal probability density function (PDF). The univariate orthonormal polynomials are constructed according to the PDF of the input random variables [1], e.g., Legendre polynomial is used for the uniformly distributed random variables.

For applying the PCE model in a real context, the PCE model is truncated with a finite number of terms in the expansion and the truncated PCE is given by

$$y(x, t) \approx \sum_{\alpha \in \mathcal{D}} a_\alpha(t) \psi_\alpha(x) \quad (2)$$

where \mathcal{D} is a finite set of indices and the total number of terms in the PCE model is determined as:

$$\text{card } \mathcal{D} = n = \frac{(d+p)!}{d!p!} \quad (3)$$

where p is the maximum polynomial degree of the PCE model.

In this paper, the PCE model is used in a non-intrusive way. As a result, the response quantity must be computed at some predefined sample points (a.k.a. exper-

imental design points). The predefined samples of the input uncertain parameters can be given by a matrix $X = \{\mathbf{x}_1, \mathbf{x}_2, \dots, \mathbf{x}_d\} \in \mathbb{R}^{N \times d}$ and the corresponding response matrix is given by $Y(X, t) \in \mathbb{R}^{N \times n_t}$; N being the number of predefined samples. The polynomial basis matrix is given by $\Psi(X) \in \mathbb{R}^{N \times n}$. The PCE coefficients are usually determined by the ordinary least square (OLS) approach:

$$a(t) = \left(\Psi^T(X) \Psi(X) \right)^{-1} \Psi^T(X) Y(X, t) \quad (4)$$

where T in the superscript represents the transpose of the matrix.

2.2 POD Approach

Proper orthogonal decomposition (POD) is mainly used to identify the low order bases for a given set of snapshots [7]. In our case, the time-dependent stochastic response quantities behave almost similarly: each column of matrix Y contains the stochastic response at each time-step. The stochastic response can be projected on the lower order vectors either by performing eigenvalue decomposition on a kind of correlation matrix [8] or by performing singular value decomposition (SVD) on the response matrix [8]. The SVD approach is used in this paper for its efficiency:

$$Y = V \Sigma U \quad (5)$$

where V is the matrix having the lower order POD vectors and i -th column of V is given by i -th POD vector. The diagonal terms of Σ represent the kind of energy involved in the corresponding POD vectors. Usually the POD vectors are organized according to the involved energy in the descending order. Then, the POD vectors are normalized as follows:

$$V_i = \frac{V_i}{\|V_i\|} \quad (6)$$

where $\|\bullet\|$ is the L2-norm. Having the orthonormal POD vectors, the stochastic response can be represented by N POD vectors. However, in reality, quite low number of POD vectors $n_b < N$ is required to keep 99.99% of the energy [7]. Therefore, the stochastic response quantity is given by

$$y(x, t) \approx \sum_{i=1}^{n_b} b_i(x) V_i^T(t) \quad (7)$$

where $b_i(x)$ is the POD coefficient that needs to be computed. The POD coefficients are computed by projecting the stochastic response on the orthonormal POD vectors:

$$b_i (X) = Y (X, t) V_i (t); \quad i = 1, \dots, n_b \tag{8}$$

3 POD-PCE Model

It is evident from Eq. 7 that the randomness and the time domain are decoupled using the POD approach. The POD coefficients are only dependent on the uncertain parameters. Therefore, each POD coefficient is represented by the PCE model:

$$b_i (x) \approx \sum_{j=1}^n a_{j,i} \psi_j (x) \tag{9}$$

Furthermore, the PCE coefficients for each POD coefficient are computed using the OLS approach. Once the PCE coefficients are computed, the POD-PCE model is given by

$$y (x, t) \approx \sum_{i=1}^{n_b} \sum_{j=1}^n a_{j,i} \psi_j (x) V_i (t) \tag{10}$$

The usefulness of the POD-PCE model is that the time-dependent statistical moments (i.e., mean and standard deviation) can be computed just by post-processing the PCE coefficients and the POD vectors:

$$\hat{\mu} (y (x, t)) = \sum_{i=1}^{n_b} a_{1,i} V_i (t) \tag{11}$$

$$\hat{\sigma} (y (x, t)) = \sqrt{\sum_{i=1}^{n_b} \left[\sum_{1 \leq |\alpha| \leq p} a_{\alpha,i}^2 \right] V_i^2 + 2 \sum_{1 \leq i_1 < i_2 \leq n_b} \left[\sum_{1 \leq |\alpha| \leq p} a_{\alpha,i_1} a_{\alpha,i_2} \right] V_{i_1} (t) V_{i_2} (t)} \tag{12}$$

where $a_{1,i}$ is the PCE coefficient corresponding to the constant polynomial basis function for the i -th POD vector and $|\alpha| = \sum_{i=1}^d \alpha_i$.

4 UQ of Crash Box

4.1 Problem Statement

A quarter crash box, shown in Fig. 1, was considered for the present study to further reduce the computational cost compared to the full crash box. A similar kind of study has been reported in the previous researches [9]. The numerical model was obtained from <https://www.dynaexamples.com/> and the simulation was performed with the LS-DYNA finite element program. The crash box is fixed on the left side in Fig. 1c and a rigid mass (m_I) strikes the right side (in negative z direction) with some velocity (v). Additionally, two free sides have symmetric conditions. At the beginning of the simulation, the impacting mass was close to the crash box, but not in contact with it. The mass is known as the impactor for the present work. The contact was modeled with the “automatic single surface” contact option available in the LS-DYNA software because the crash pattern is usually not predefined for a crash box and it can detect the penetration of a shell element from both sides. The FE model was constructed with 469 four-node shell elements (*ELEMENT_SHELL keyword was used in LS-DYNA) and a total 518 nodes were there in the quarter crash box.

The nominal thickness of the crash box is 5 mm. The crash box is made of steel with the modulus of elasticity and the Poisson’s ratio of 200 GPa and 0.3, respectively. The crash box was modeled with an elasto-plastic material behavior (*MAT_PIECEWISE_LINEAR_PLASTICITY keyword was used in LS-DYNA). The effective plastic stress-strain curve is shown in Fig. 2.

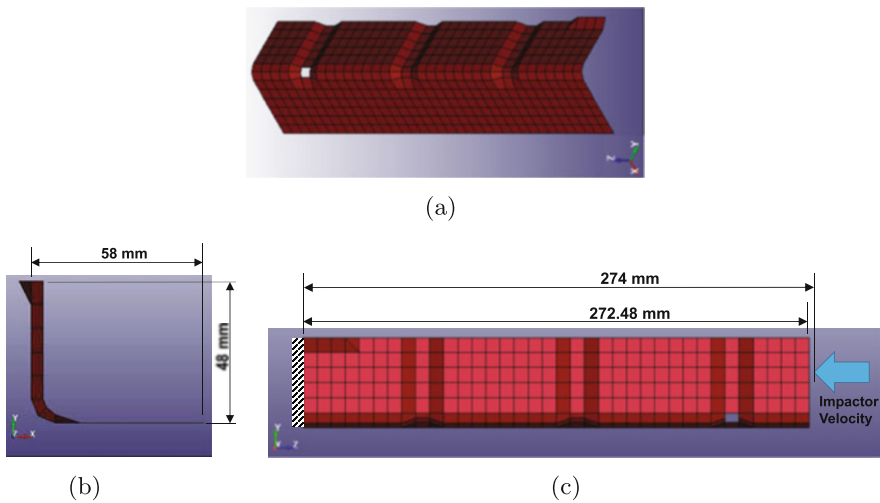


Fig. 1 Geometrical views of FE model of the quarter crash box. (a) Isometric view. (b) Plan view. (c) Front view

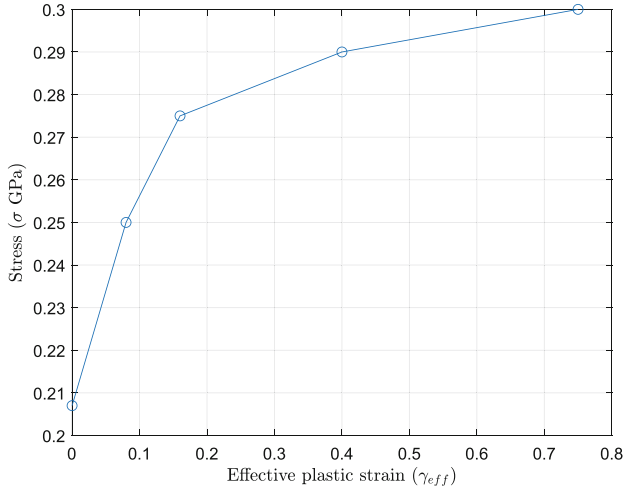


Fig. 2 Plastic stress-strain diagram

Table 1 Parameters of the uniformly distributed random variables for the crash box

Variable name	Symbol	Bounds	Unit
Impactor mass	m_I	[225,275]	kg
Crash box thickness	H	[5,6]	mm
Stress multiplying factor	c_σ	[0.8,1.2]	–

The crash box was analyzed considering three uncertain parameters, namely the impactor mass (m_I), the thickness (H) of the crash box, and the material property. The uncertainty was considered in the material property by a multiplicative constant applied to the stress component in the stress-strain curve, i.e., the stress axis values in Fig. 2 were multiplied with a constant (c_σ). All the uncertain parameters were considered uniformly distributed and the distribution parameters are listed in Table 1. The initial impactor velocity was set at $v = 10 \text{ m s}^{-1}$ and the time integration was performed in the time domain $t \in [0 \text{ ms}, 60 \text{ ms}]$ at a time-step of $\Delta t = 0.01 \text{ ms}$.

4.2 Uncertainty Quantification of a Quarter Crash Box

UQ was performed using the POD-PCE model for the above-mentioned crash box. Legendre polynomials were used for the uncertain parameters. The degree of the polynomials was chosen as $p = 5$. As a result, the number of terms in the PCE was $n = 56$. The reference result was computed by the MCS approach using 10^3 Latin hypercube samples (LHS), which took 18.23 h CPU time. As a single model evaluation was considered computationally expensive, the maximum number of model evaluations was restricted to 200 for the construction of the POD-PCE

model. For the construction of the POD-PCE model, Sobol sequence was used to generate samples sequentially. The initial number of samples was set as $N = 15$, then it was increased by 5 samples in each step. In each incremental step, a leave-one-out (LOO) error was computed to check the accuracy of the fitted POD-PCE model. The relative LOO error for the j -th sample is computed as [10]:

$$\epsilon_{\text{LOO},j} = \frac{\sum_{i=1}^{n_t} [Y(t_i, X_j) - \hat{Y}^{-j}(t_i, X_j)]^2}{\sum_{i=1}^{n_t} [Y(t_i, X_j) - \bar{Y}(X_j)]^2} \quad (13)$$

where $\hat{Y}^{-j}(t_i, X_j)$ is the predicted response at the j -th sample with the POD-PCE model constructed using all the samples without the j -th sample point. The mean relative LOO error for each step is computed as:

$$\bar{\epsilon}_{\text{LOO}} = \frac{1}{N} \sum_{j=1}^N \epsilon_{\text{LOO},j} \quad (14)$$

$\bar{\epsilon}_{\text{LOO}}$ is computed for all the samples in each step.

UQ was performed for contact force, impactor displacement, and impactor velocity. The POD-PCE model was constructed for two threshold values of the LOO error $\epsilon_{\text{POD-PC}} = 1 \times 10^{-2}$ and $\epsilon_{\text{POD-PC}} = 1 \times 10^{-3}$ separately.

4.2.1 Impactor Displacement

The evolution of the LOO error and the number of POD vectors with the increase of samples for the impactor displacement is shown in Fig. 3. It is seen the threshold LOO error of 1×10^{-2} was achieved using only 25 samples, whereas it took 80 samples to achieve an accuracy of 1×10^{-3} . Nevertheless, the number of POD vectors remained constant at $n_b = 3$. As a result, only $N_T = n \times n_b = 168$ PCE coefficients were computed for the PCE model.

The impactor displacement was predicted by the POD-PCE model at the reference samples and furthermore, the statistical moments were compared with the reference results. The mean and standard deviation are shown in Fig. 4. It is seen that the mean was predicted quite well even when the POD-PCE model reached an accuracy of 1×10^{-2} ; however, the standard deviation predicted at the same accuracy is not following the reference result in the later time. On the contrary, the standard deviation is quite accurate when the POD-PCE model reached an accuracy of 1×10^{-3} .

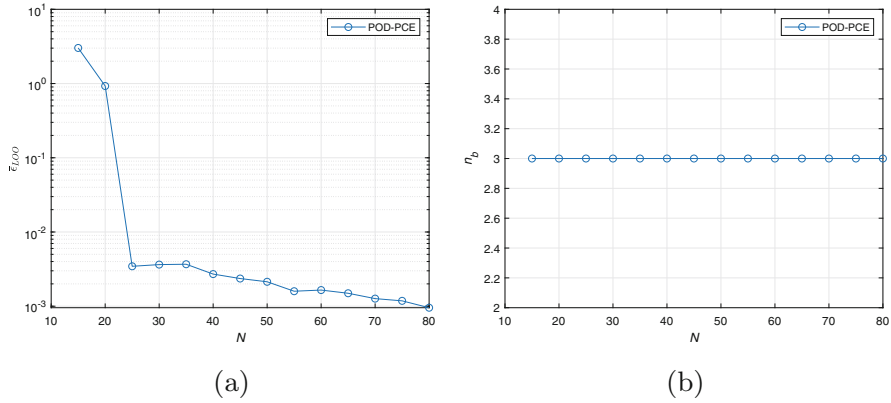


Fig. 3 Evolution of LOO error and the number of POD vectors for the impactor displacement of crash box. (a) LOO error. (b) POD vectors

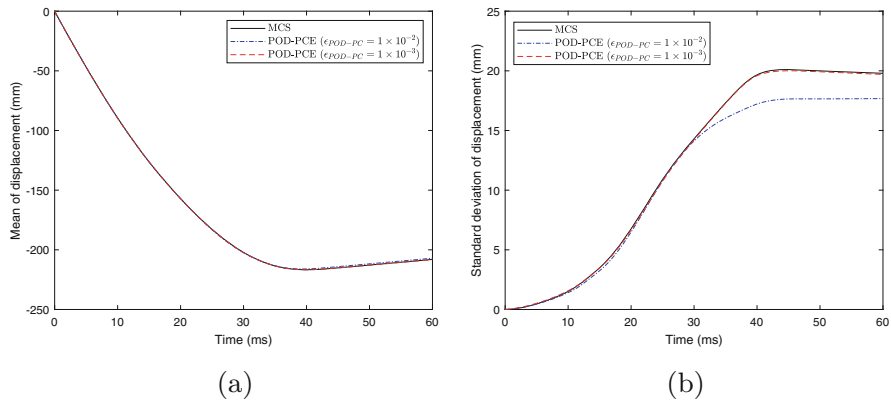


Fig. 4 Time-dependent statistical moments of the impactor displacement. (a) Mean. (b) Standard deviation

4.2.2 Impactor Velocity

In a similar way to the previous one, the evolution of the LOO error and the POD vectors were obtained and are shown in Fig. 5 for the impactor velocity. It is seen that the POD-PCE model took a little more samples ($N = 105$) than the previous one to reach a LOO error of 1×10^{-3} . The required number of POD vectors was $n_b = 8$ and therefore, $N_T = 448$ in this case.

The statistical moments predicted by the POD-PCE model for the impactor velocity are shown in Fig. 6. In this case also, the accuracy of the predicted standard deviation is quite better when the POD-PCE model reached an accuracy of 1×10^{-3} compared to an accuracy of 1×10^{-2} . The time-dependent mean is quite well predicted using both specified LOO errors.

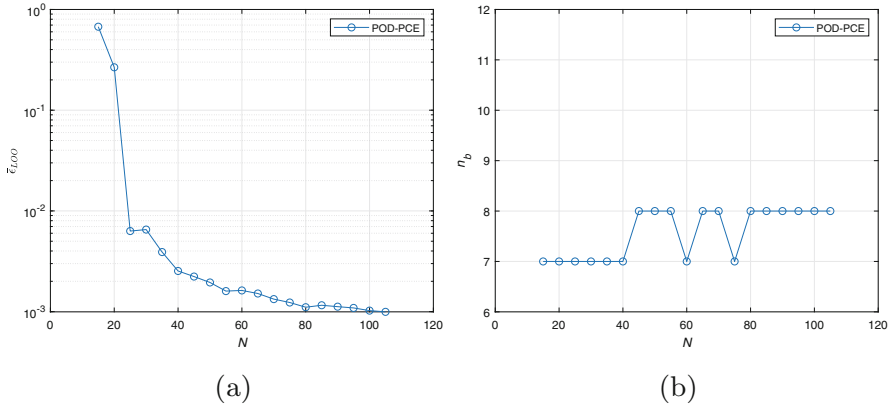


Fig. 5 Evolution of LOO error and the number of POD vectors for the impactor velocity of crash box. (a) LOO error. (b) POD vectors

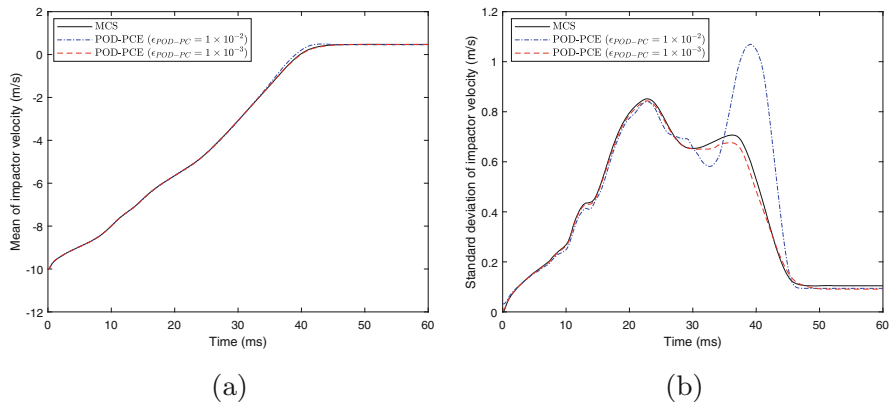


Fig. 6 Time-dependent statistical moments of the impactor velocity. (a) Mean. (b) Standard deviation

4.2.3 Contact Force

The evolution of the LOO error for the contact force is shown in Fig. 7 along with the number of POD vectors. It is observed that the LOO error is decreasing with the increase of samples; however, the lowest specified accuracy was not achieved even using the maximum allocated samples. The number of POD vectors was also increasing with the sample points and $n_b = 79$ POD vectors were required to represent the contact force, which is quite higher as compared to the previous responses.

The mean and standard deviation were predicted by the POD-PCE model constructed with $N = 200$ samples and are shown in Fig. 8. The mean was predicted quite well even without achieving a good accuracy. However, the accuracy of the

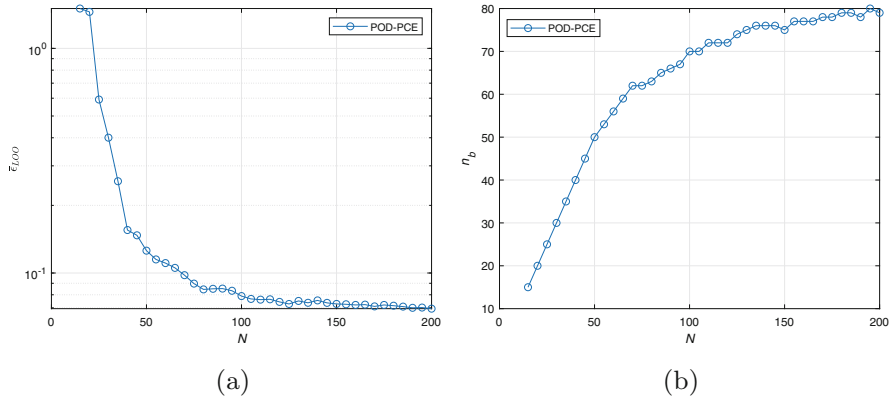


Fig. 7 Evolution of LOO error and the number of POD vectors for the contact force of crash box. (a) LOO error. (b) POD vectors

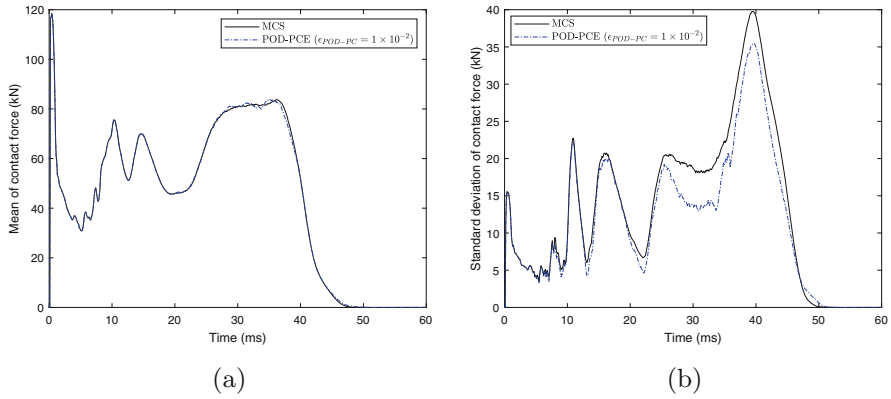


Fig. 8 Time-dependent statistical moments of the contact force. (a) Mean. (b) Standard deviation

standard deviation in the later time is lower. Nevertheless, the accuracy of the predicted standard deviation is acceptable.

5 Conclusions

A POD-PCE model has been used for propagating and quantifying uncertainty through a crash box problem. The POD approach was used to decouple the time domain and the randomness, and the PCE approach was used to propagate the uncertain parameters through the system. A LOO error was computed to measure the accuracy of the obtained POD-PCE model. A good LOO error was obtained

using lower number of samples than the maximum specified samples for impactor displacement and impactor velocity. On the contrary, the obtained LOO error for the contact force was higher even using the maximum number of samples as compared to the other responses. For all the cases, the time-dependent mean was predicted quite well even with a LOO error of 1×10^{-2} . However, a good accuracy for the standard deviation was obtained when the POD-PCE model achieved a LOO error of 1×10^{-3} .

References

1. D. Xiu, G.E. Karniadakis, The Wiener-Askey polynomial chaos for stochastic differential equation. *SIAM J. Sci. Comput. Sci. Comput.* **24**(2), 619–644 (2002)
2. I. Kaymaz, Application of kriging method to structural reliability problems. *Struct. Safety* **27**(2), 133–151 (2005)
3. M. Gerritsma, J.B.V.D. Steen, P. Vos, G. Karniadakis, Time-dependent generalized polynomial chaos. *J. Comput. Phys.* **229**(22), 8333–8363 (2010)
4. M. Spiridonakos, E. Chatzi, Metamodeling of dynamic nonlinear structural systems through polynomial chaos NARX models. *Comput. Struct.* **157**, 99–113 (2015)
5. E. Jacquelin, N. Baldanzini, B. Bhattacharyya, D. Brizard, M. Pierini, Random dynamical system in time domain: a POD-PC model. *Mech. Syst. Signal Process.* **133**, 106251 (2019)
6. B. Bhattacharyya, E. Jacquelin, D. Brizard, Uncertainty quantification of stochastic impact dynamic oscillator using a proper orthogonal decomposition-polynomial chaos expansion technique. *J. Vibr. Acoust.* **142**(6), 1–13 (2020)
7. L. Sirovich, Turbulence and the dynamics of coherent structures part I: coherent structures. *Quart. Appl. Math.* **45**(3), 561–571 (1987)
8. A. Chatterjee, An introduction to the proper orthogonal decomposition. *Curr. Sci.* **78**(7), 808–817 (2000)
9. J. Song, Y. Zhou, F. Guo, A relationship between progressive collapse and initial buckling for tubular structures under axial loading. *Int. J. Mech. Sci.* **75**, 200–211 (2013)
10. B. Bhattacharyya, E. Jacquelin, D. Brizard, A Kriging-NARX model for uncertainty quantification of nonlinear stochastic dynamical systems in time domain. *J. Eng. Mech.* **146**(7), 1–21 (2020)

Nonlinear Dynamics of a Hyperelastic Cylindrical Shell Composed of the Incompressible Rivlin-Saunders Material



Wenzheng Zhang, Zhentao Zhao, and Datian Niu

1 Introduction

The original intention of bifurcations and chaos theory is to study the qualitative behaviors of the nonlinear problems which are difficult to be solved analytically. But so far, more complex nonlinear problems could be investigated [1–3]. Moreover, the Lyapunov exponent, bifurcation diagram, and correlation dimension are commonly used to describe chaos and its different routes [4–6]. This paper focuses on the bifurcations and chaos related to hyperelastic materials.

Hyperelastic materials are also known as Green elastic materials [7], and their constitutive relations can be characterized by the strain energy functions. Particularly, as a typical hyperelastic material, rubber is widely used in seal ring, axle sleeve, tire and rubber bearing for bridge construction for sealing, vibration isolation, and so on. In addition, hyperelastic materials are also widely used in biomedical researchers [8–10].

The dynamic problems under suddenly applied constant loads originated from the work of Knowles [11]. Subsequently, the researches in this field have been extended furtherly by relevant scholars, including the periodic oscillation and amplitude jumping of cylindrical and spherical structures. Based on the existing researches, it is found that for the time-dependent loads, the system is nonautonomous, and the dynamic phenomena are more abundant. In this aspect of investigations, Yuan et al. [12] studied the condition of periodic oscillations of the spherical membrane under periodic step loads. Ren [13] studied the failure of spherical shells composed of the neo-Hookean material under periodic loads. The

W. Zhang (✉) · D. Niu
Dalian Minzu University, Dalian, P. R. China

Z. Zhao
Dalian University of Technology, Dalian, P. R. China

concept of the average load is introduced to describe the effect of external loads on structural oscillations, and the critical average load for structural failure was given. Yong et al. [14] studied the nonlinear oscillation of the pre-stretched thick spherical shell in constant and periodic electric fields. The authors pointed out that the increasing thickness parameter with the constant voltage enhances the stability of the structure, and the system performs quasiperiodic motion under periodic voltages. Regarding the more complex dynamic phenomena under time-dependent loads. Aranda-Iglesias et al. [15] studied the large amplitude axisymmetric free oscillations of a hyperelastic cylindrical structure. Zhao et al. [16] studied the dynamic behaviors of the spherical membrane under periodic perturbances in detail and explained the quasiperiodic and chaotic phenomena of the system from the perspective of subharmonic resonances. More researches on the dynamics of hyperelastic structures can be referred to the reviews of Alijan and Amabili [17].

In this paper, the dynamic behaviors of incompressible Rivlin-Saunders cylindrical shell under periodic perturbances are studied, and the influence of non-integer power-law material parameter on the qualitative behaviors of the system is analyzed. Different from other hyperelastic models, because the exponential part of the second principal invariant of the right Cauchy-Green tensor is not limited to integers, some singularities will be introduced in the process of investigations, which also enriches the phenomena. Particularly, this paper studies the dynamic behaviors of the cylindrical shell from the aspect of material parameters, such as the bifurcations of equilibrium curves under constant loads and the quasiperiodic and chaotic phenomena under periodic perturbances.

2 Mathematical Model

For an infinitely long cylindrical shell composed of an isotropic incompressible hyperelastic material, the radial symmetric motion is investigated when the inner surface of the shell is subjected to a class of uniform radial periodically perturbed loads. In the cylindrical coordinate system, the initial configuration and the deformed configuration of the shell are expressed as

$$D_0 = \{(R, \Theta, Z) | R_1 \leq R \leq R_2, 0 < \Theta \leq 2\pi, -\infty < Z < +\infty\}$$

$$D = \{(r, \theta, z) | r = r(R, t) > 0, \theta = \Theta, z = Z\} \quad (1)$$

where R_1 and R_2 are the inner and outer radii of the undeformed structure, respectively. The deformation gradient tensor used to describe the mapping relationship between two configurations is

$$\mathbf{F} = \text{Diag} \{\lambda_r, \lambda_\theta, \lambda_z\} = \text{Diag} \{\partial r / \partial R, r/R, 1\} \quad (2)$$

where λ_r is the principal stretch ratio in the radial direction and λ_θ is the principal stretch ratio in the circumferential direction.

The incompressibility condition implies that $\lambda_r \lambda_\theta \lambda_z = 1$; integrating it gives

$$r(R, t) = \left(R^2 + r_1^2(t) - R_1^2 \right)^{1/2} \tag{3}$$

where $r_1(t) = r(R_1, t)$ is an undetermined function; it describes the radial motion of the inner surface with time.

In the absence of the body force, the differential equations describing the radial motion of the structure may be reduced to a single equation, as follows:

$$\frac{\partial \sigma_{rr}(r, t)}{\partial r} + \frac{1}{r} (\sigma_{rr} - \sigma_{\theta\theta}) = \rho_0 \frac{\partial r^2(R, t)}{\partial t^2} \tag{4}$$

where

$$\sigma_{rr}(r, t) = \lambda_r \frac{\partial W}{\partial \lambda_r} - p(r, t), \quad \sigma_{\theta\theta}(r, t) = \lambda_\theta \frac{\partial W}{\partial \lambda_\theta} - p(r, t) \tag{5}$$

are the principal values in the radial and circumferential direction of the Cauchy stress tensor associated with the incompressible hyperelastic material, $W = W(\lambda_r, \lambda_\theta)$ is the associated strain energy function, $p(r, t)$ is the hydrostatic pressure associated with the incompressible condition, and ρ_0 is material density.

In this paper, a time-dependent pressure $p(t)$ at the inner surface and a free outer surface are considered; thus, the boundary conditions are given by

$$\sigma_{rr}(r(R_1, t), t) = -p(t), \quad \sigma_{rr}(r(R_2, t), t) = 0, \quad t \geq 0 \tag{6}$$

For convenience, we introduce the following notations:

$$\lambda(t) = \frac{r_1(t)}{R_1} \geq 0, \quad \delta = \frac{R_2^2}{R_1^2} - 1 \tag{7}$$

Substitute Eqs. (5) and (7) into Eq. (4), and then, integrate the equation with respect to r , and use the boundary condition (6); we have

$$\lambda \ddot{\lambda} \ln \left(\frac{\delta + \lambda^2}{\lambda^2} \right) + \dot{\lambda}^2 \ln \left(\frac{\delta + \lambda^2}{\lambda^2} \right) - \dot{\lambda}^2 \frac{\delta}{\delta + \lambda^2} + g(\lambda, \delta) = \frac{2}{\rho R_1^2} p(t) \tag{8}$$

where

$$g(\lambda, \delta) = \frac{2}{\rho R_1^2} \int_{r_2}^{r_1} \left(\lambda_1 \frac{\partial W}{\partial \lambda_1} - \lambda_2 \frac{\partial W}{\partial \lambda_2} \right) \frac{dr}{r} = \frac{2}{\rho R_1^2} \int_{\left(\frac{\delta+\lambda^2}{1+\delta}\right)^{1/2}}^{\lambda} \frac{W'(k)}{k^2 - 1} dk \tag{9}$$

The hyperelastic material in this paper is described by the incompressible Rivlin-Saunders model, which works well especially for vulcanized rubbers, and the specific form of the strain energy function is

$$W = \mu [(I_1 - 3) + \beta(I_2 - 3)^\alpha] = \mu \left[(\lambda_r^2 + \lambda_\theta^2 - 2) + \beta(\lambda_r^2 + \lambda_\theta^2 - 2)^\alpha \right] \tag{10}$$

where μ, α, β are material parameters. It is worth noting that the material parameter α in Eq. (10) may be taken as a non-integer, whose value is determined by relevant experiments.

Another important factor for the system (8) is the uniform radial periodically perturbed loads at the inner surface of the cylindrical shell given by

$$p(t) = p_0 + \varepsilon \sin \Omega t \tag{11}$$

where p_0 is a constant pressure, ε is a perturbation parameter, and Ω is an external excitation frequency.

Thus, the radial symmetric motion of an incompressible Rivlin-Saunders cylinder under periodically perturbed loads can be completely described by Eqs. (8) and (9).

3 Qualitative Analyses

For the given constant pressure, i.e., $\bar{p}(\tau) = p_0$, Eq. (8) reduces to an autonomous system, and the first integral is given by

$$H_0(\lambda, p_0, \alpha, \beta, \delta) = \frac{\rho R_1^2}{4} \lambda^2 \ln \left(\frac{\delta + \lambda^2}{\lambda^2} \right) \dot{\lambda}^2 + \int_1^\lambda \left(\int_{\left(\frac{\delta+s^2}{1+\delta}\right)^{1/2}}^s \frac{2(k^4-1)[1+\alpha\beta(k^2+k^{-2}-2)^{\alpha-1}]}{k^3(k^2-1)} dk \right) ds - \frac{p_0}{2} (\lambda^2 - 1) \tag{12}$$

where H_0 is the energy constant determined by the initial condition. Let

$$V(\lambda, p_0, \alpha, \beta, \delta) = \int_1^\lambda \left(\int_{\left(\frac{\delta+s^2}{1+\delta}\right)^{1/2}}^s \frac{2(k^4-1)[1+\alpha\beta(k^2+k^{-2}-2)^{\alpha-1}]}{k^3(k^2-1)} dk \right) ds - \frac{p_0}{2} (\lambda^2 - 1) \tag{13}$$

be the potential energy of the autonomous system, which satisfies $V(1, p_0) = 0$.

The equilibrium point of the system can be determined by the following equation:

$$p_0(\lambda) = \frac{1}{\lambda} \int_{\left(\frac{\delta+\lambda^2}{1+\delta}\right)^{1/2}}^\lambda \frac{2(k^4-1)[1+\alpha\beta(k^2+k^{-2}-2)^{\alpha-1}]}{k^3(k^2-1)} dk \tag{14}$$

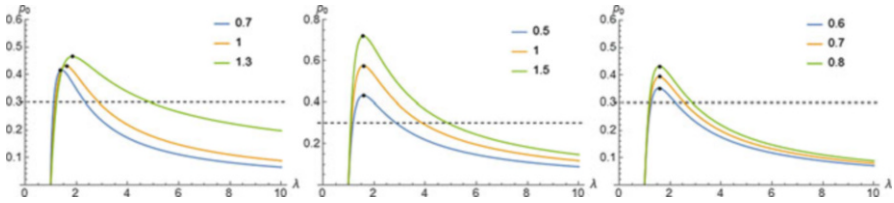


Fig. 1 Equilibrium curves for different values of α , β and δ

Note that the equilibrium curves given by Eq. (14) of the autonomous system are closely related to the material parameters α and β and the structure parameters δ for the given pressure p_0 . Therefore, this section mainly discusses the bifurcation behaviors of the system.

3.1 $0 < \alpha < 1.5$

In this case, $\lim_{\lambda \rightarrow +\infty} p_0(\lambda) = 0$; there exists only a zero horizontal asymptote. Let $p_0'(\lambda) = 0$; the maximum point of the deformation curve can be obtained, given by (λ_{cr}, p_{0cr}) , where λ_{cr} is the critical stretch of the structure and p_{0cr} is the maximal pressure. Moreover, it can be concluded that for $0 < p_0 < p_{0cr}$, if the equilibrium point $(\lambda_{eq}, 0)$ satisfies $1 < \lambda_{eq} < \lambda_{cr}$, it is a center; if the equilibrium point $(\lambda_{eq}, 0)$ satisfies $\lambda_{eq} > \lambda_{cr}$, it is a saddle point, as shown in Fig. 1.

3.2 $\alpha = 1.5$

It can be verified that there exists a nonzero horizontal asymptote, given by $p_0 = p_{0h}$, which is mainly influenced by β . When β is small, the curve also has a maximum point, which means each group of material parameters (β, δ) is corresponding to a critical stretch λ_{cr} . At this time, the situation is similar to the situation of $0 < \alpha < 1.5$, so no explanation will be given. In addition, when β is larger, there is no maximum point, and the system has only one equilibrium point $(\lambda_{eq}, 0)$, which is a center.

3.3 $\alpha > 1.5$

The deformation curve has no horizontal asymptote. For $\lim_{\lambda \rightarrow +\infty} p_0(\lambda) = +\infty$, it could have zero or two extreme points; in other words, the number of equilibrium points of the system could be one or three (Figs. 2, 3, and 4).

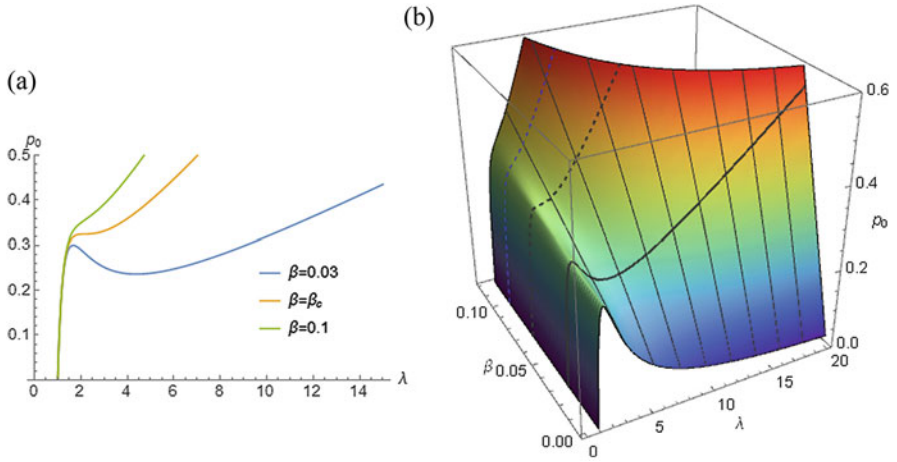


Fig. 2 For $\alpha = 3$ and $\delta = 0.8$, equilibrium curves with (a) $\beta = 0.03, \beta_c, 0.1$, and (b) $0 < \beta < 0.12$.

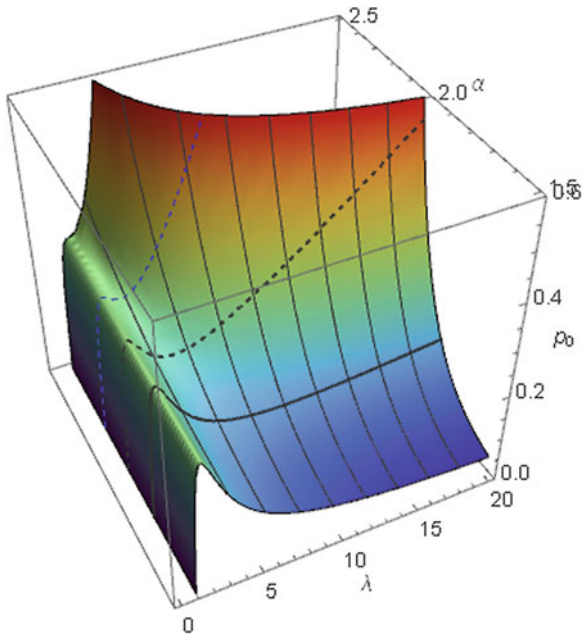
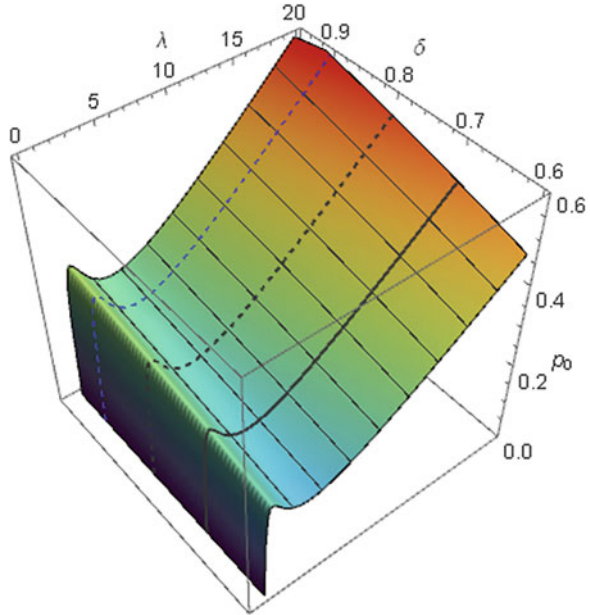


Fig. 3 For $\beta = 0.03$ and $\delta = 0.8$, equilibrium curves for $\alpha = 1.8, 2.0, 2.2$

It can be verified that there is a critical parameter β_c , which satisfies the following:

- (i) As $\beta < \beta_c$, the curve has a maximum value and a minimum value, denoted as $(\lambda_{cr1}, p_{0cr1}), (\lambda_{cr2}, p_{0cr2})$. If $0 < p_0 < p_{0cr2}$, the system has only a center; if

Fig. 4 For $\alpha = 2$ and $\beta = 0.03$, equilibrium curves for $\delta = 0.7, 0.8, 0.9$



$p_{0cr2} < p_0 < p_{0cr1}$, the system has three equilibrium points, in which there are two centers and a saddle point, and there exists the asymmetric homoclinic orbit of “ ∞ ” type in the phase plane. If $p_0 > p_{0cr1}$, the system also has only a center.

(ii) As $\beta \geq \beta_c$, the curve is monotonically increasing, there is no maximum point, and the system has only an equilibrium point, which is a center.

4 Analyses on Nonlinear Oscillations

According to the previous discussion, the case that only one equilibrium point can be analyzed in the latter two cases, this section only studies the dynamic behavior of the latter two systems with saddle points and discusses the influence of relevant parameters.

Firstly, the frequency of the periodic oscillations related to initial conditions of the integrable Hamilton system can be derived by Eq. (15), as follows:

$$\omega = \pi / \int_{\lambda_1}^{\lambda_2} \frac{d\lambda}{\sqrt{2(H_0 - V(\lambda, \alpha, \beta, p_0))}} \tag{15}$$

where λ_1 and λ_2 are the minimum and maximum stretches, respectively.

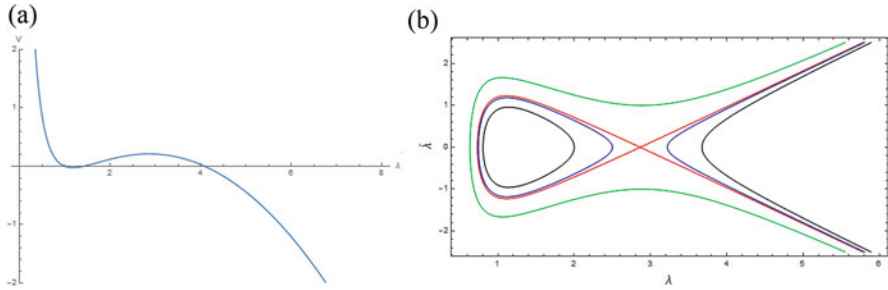


Fig. 5 For $\alpha = 1, \beta = 0.5, \delta = 0.8$, (a) the potential energy curve and (b) phase orbits

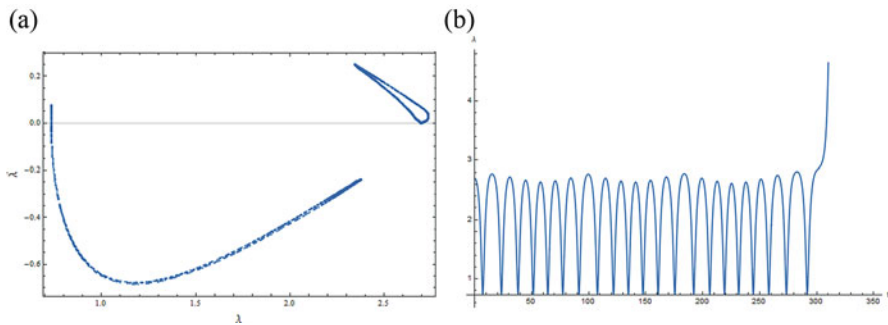


Fig. 6 For $\lambda_0 = 2.5$, (a) Poincaré section with $n = 2, p_1 = 0.0005$ and (b) time response curve with $n = 2, p_1 = 0.001$

4.1 System with Two Equilibrium Points

For the given material parameters, $\alpha = 1, \beta = 0.5, \delta = 0.8$, this subsection studies the system with two equilibrium points.

Figure 5 shows the potential energy curve and phase orbits of the autonomous system under the pressure $p_0 = 0.3$.

Figure 6 shows the perturbed oscillations with initial conditions near the saddle point. As $n = 2$, if the perturbation value is small enough ($p_1 = 0.0005$), the projection of the phase orbits in the Poincaré section is still two closed curves, and the system performs the quasiperiodic oscillation, as shown in Fig. 6a, while if the perturbation value increases to a certain extent (e.g., $p_1 = 0.001$), the motion of the system is extended beyond the separatrix, and the original quasiperiodic motion with a finite amplitude is destroyed, which leads the stretch of the structure to increase continuously until it breaks down, as shown in Fig. 6b.

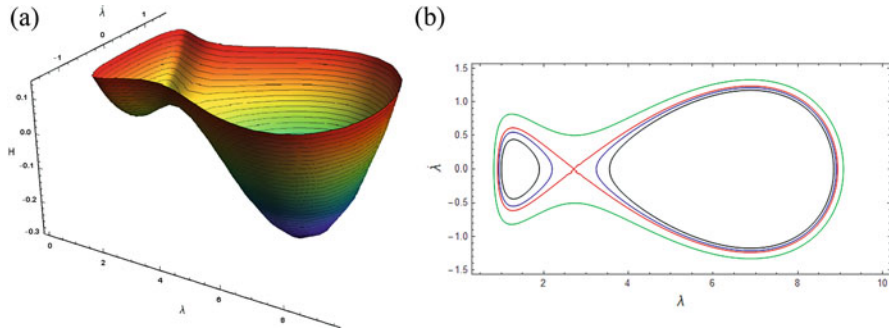


Fig. 7 (a) The double-well potential and (b) phase orbits

4.2 System with Three Equilibrium Points

For $\alpha > 1.5$ and $\beta < \beta_c$, there are two extreme points on the equilibrium curve. Only if $p_{0cr2} < p_0 < p_{0cr1}$ (p_{0cr1} , p_{0cr2} are the maximum and minimum on the equilibrium curve, respectively), there exists three equilibrium points and the asymmetric homoclinic orbit of “ ∞ ” type in the phase plane.

Figure 7 illustrates double-well potential with $p_0 = 0.26$, $\alpha = 2$, $\beta = 0.03$, $\delta = 0.8$. It can be seen that if the energy constant is appropriate, the system oscillates periodically only around any one well potential or around both, where the well potential corresponds to the center. Subsequently, the dynamic analyses of the system with double-well potential, that is, the system with the asymmetric homoclinic orbit of “ ∞ ” type, are carried out.

On this basis, the influence of α on the rupture of the level curves near the saddle point is discussed. Particularly, as $\alpha = 2$ and $p_0 = 0.26$, the equilibrium points are $(1.31, 0)$, $(2.72, 0)$, $(6.89, 0)$, respectively.

Figure 8 shows the motions with the initial stretch near the saddle point ($\lambda_0 = 2.8$) under periodic perturbations. According to the time response curve shown in Fig. 8a, it can be clearly seen that it is no longer a periodic oscillation; moreover, the phase orbit shown in Fig. 8b is distributed in the neighborhood of the homoclinic orbit. Furthermore, the maximal Lyapunov exponent is positive, as shown in Fig. 8c, so it is a chaotic motion. If the external excitation period is taken as the sampling parameter in the Poincaré sections shown in Fig. 8d, the scattered points distributed near the homoclinic orbit can be obtained, which is quite different from the quasiperiodic motion.

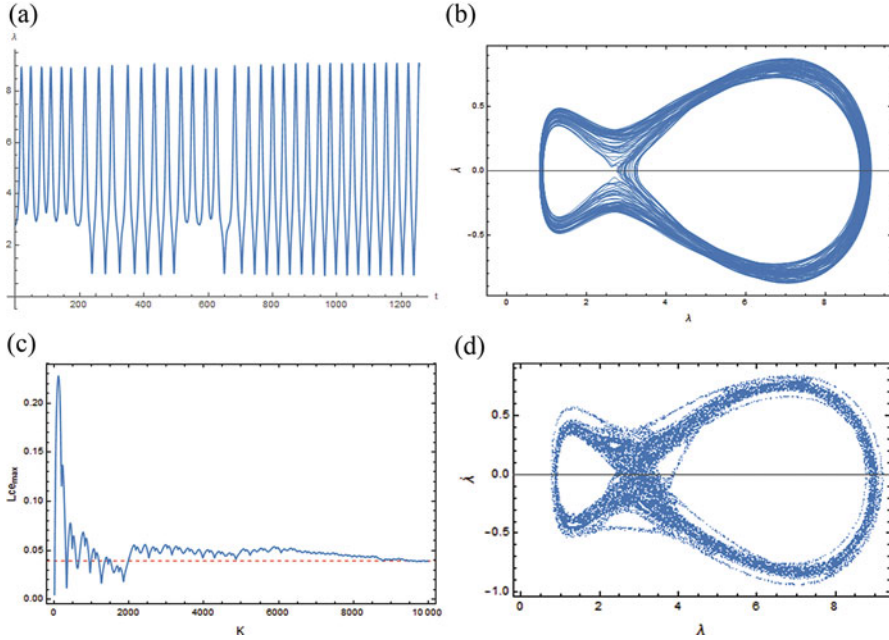


Fig. 8 For $\alpha = 2$, $\varepsilon = 0.005$, and $\lambda_0 = 2.8$, (a) the time response curve, (b) phase orbits, (c) maximal Lyapunov exponents, and (d) Poincaré sections

5 Conclusions

This chapter investigates the large-amplitude oscillations of the hyperelastic cylindrical shell, which is composed of the Rivlin-Saunders model. The main conclusions are given as follows.

First, under constant pressures, the equilibrium curves have various bifurcation behaviors, especially the secondary turning bifurcation. Moreover, the material parameter α affects the existence of the asymptotes, including the horizontal and vertical ones.

Second, under the periodic perturbations, if the external excitation frequency and the fundamental frequency satisfy the relation that $\Omega = n\omega$, when the initial condition is far away from the saddle point, the projection of the phase orbits in the Poincaré section is n closed curves. Particularly, for the system with two equilibrium points, when the initial condition is near the center, the system performs periodic oscillations; when the initial condition is near the saddle point, the system diverges rapidly with the perturbation. However, for the system with three equilibrium points, the system performs the chaotic motions with the perturbations when the initial condition is near the saddle point, and the structure will not be destroyed, which means that the system with three equilibrium points has better stability than that with two equilibrium points.

Acknowledgments This work is supported by the National Natural Science Foundation of China (nos. 11672069, 11702059, 11872145).

References

1. Z. Faghani, F. Nazarimehr, S. Jafari, J.C. Sprott, *Int. J. Bifurcation Chaos* **29**, 1950116 (2019)
2. Y. Chang, X. Wang, Z. Feng, W. Feng, *Int. J. Bifurcation Chaos* **30**, 2050024 (2020)
3. J. Liang, L. Tang, Y. Xia, Y. Zhang, *Int. J. Bifurcation Chaos* **30**, 2050004 (2020)
4. A. Wolf, J.B. Swift, H.L. Swinney, J.A. Vastano, *Physica D* **16**, 285–317 (1985)
5. M.T. Rosenstein, J.J. Collins, C.J. De Luca, *Physica D* **65**, 117–134 (1993)
6. T. Jiang, Z. Yang, Z. Jing, *Int. J. Bifurcation Chaos* **27**, 1750125 (2017)
7. R.W. Ogden, *Non-linear elastic deformations* (Dover Publications, New York, 1997)
8. H.W. Haslach, J.D. Humphrey, *Int. J. Non Linear Mech.* **39**, 399–420 (2004)
9. C. Zeng, X. Gao, *Int. J. Non Linear Mech.* **124**, 103510 (2020)
10. N. Gundiah, M.B. Ratcliffe, L.A. Pruitt, *J. Biomech.* **40**, 586–594 (2007)
11. J.K. Knowles, *Q. Appl. Math.* **18**, 71–77 (1960)
12. X.G. Yuan, H.W. Zhang, J.S. Ren, Z.Y. Zhu, *Appl. Math. Mech.* **31**, 903–910 (2010)
13. J.S. Ren, *Int. J. Eng. Sci.* **47**, 745–753 (2009)
14. H. Yong, X. He, Y. Zhou, *Int. J. Eng. Sci.* **49**, 792–800 (2011)
15. D. Aranda-Iglesias, J.A. Rodríguez-Martínez, M.B. Rubin, *Int. J. Non Linear Mech.* **99**, 131–143 (2018)
16. Z.T. Zhao, W.Z. Zhang, H.W. Zhang, X.G. Yuan, *Acta Mech.* **230**, 3003–3018 (2019)
17. F. Alijani, M. Amabili, *Int. J. Non Linear Mech.* **58**, 233–257 (2013)

Dynamical Analysis of a Memristor–Inductor–Capacitor Nonlinear Circuit



Marcelo Messias and Alisson C. Reinol

1 Introduction

For more than 150 years, the known fundamental passive circuit elements were the capacitor (discovered in 1745), the resistor (1827), and the inductor (1831). Then, in a seminal paper [1], professor Leon Chua, from University of California at Berkeley, predicted the existence of a fourth fundamental device, which he called a memristor, contraction of “memory resistor.” Despite this theoretical prediction, the physical realization of a memristor was possible only in 2007, when Stanley Williams and his team at HP Labs constructed a nanoelectronic device showing certain characteristics of a memristor [2]. Since then, the interest in studying memristive circuits increased exponentially, due to its potential applications in several technological areas. Indeed, as memristive circuits exhibit several different nonlinear phenomena, beyond the development of memory technology, they play an important role in the development of new nonlinear information processing methods and their physical implementation in hardware systems. They could be used, for instance, as cells of cellular nonlinear networks (or CNN) aiming to study microcirculation applications and other problems, as considered in [3]. Furthermore, major efforts are being made to develop neuromorphic memristor technology aiming to build complex brain-like computing structures [4]. As the cost of building memristive devices in industrial scale is still very high, the theoretical study of

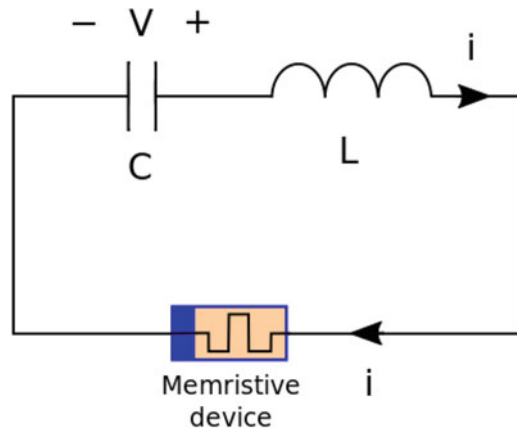
M. Messias (✉)

Universidade Estadual Paulista (UNESP), Faculdade de Ciências e Tecnologia, Departamento de Matemática e Computação, Presidente Prudente, Brazil
e-mail: marcelo.messias1@unesp.br

A. C. Reinol

Universidade Tecnológica Federal do Paraná (UTFPR), Departamento Acadêmico de Matemática, Apucarana, Brazil
e-mail: alissonreinol@utfpr.edu.br

Fig. 1 Schematic of MLC circuit



their properties, including computational simulations and emulations, becomes very important to better understand their behavior.

In this paper, we consider a memristive circuit, called *MLC circuit*, consisting of three elements (see Fig. 1): a passive linear inductor, a passive linear capacitor, and an active memristive device (or memristor). This circuit was proposed by Itoh and Chua in [5] and is described by the following nonlinear system of ordinary differential equations (for details, see [5]):

$$\dot{x} = -x(y + \beta), \quad \dot{y} = -\omega z - \alpha(x^2 - \mu)y, \quad \dot{z} = \omega y, \quad (1)$$

where $\alpha, \beta, \mu, \omega \in \mathbb{R}$ are control parameters, x, y , and z are state variables, which are proportional to the internal state of memristor, to the current, and to the voltage in the circuit, respectively, and the dot denotes derivative with respect to the time t .

Numerical simulations of the solutions of system (1) were presented by Itoh and Chua in [5]. Here, through an algebraic and numerical analysis we show that, for certain parameter values, system (1) presents first integrals and invariant algebraic surfaces. This implies the existence of certain global structures in its phase space, which are studied in Sect. 2.2. Varying the parameter values, these structures are broken and system (1) exhibits rather complex behaviors, as shown in Fig. 2. In our analysis, we consider the control parameters α, β, γ , and μ all positive.

Our main results about system (1) are given below.

Theorem 1 *For all parameter values, the x -axis and the yz -plane are invariant under the flow of system (1), which is symmetrical about the yz -plane.*

In Sect. 2.1 we prove Theorem 1 and describe the dynamical behavior of system (1) on the x -axis and on the yz -plane.

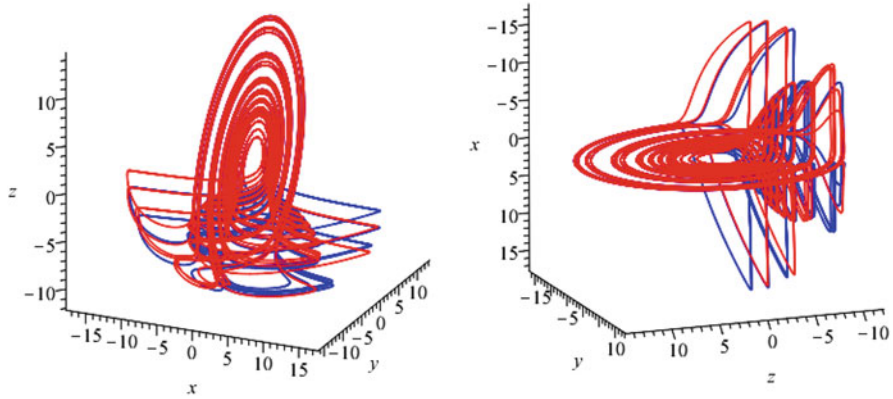


Fig. 2 Two orbits of system (1) for $\alpha = 0.1, \beta = 0.1, \omega = 0.5$ and $\mu = 0.7$, with initial conditions $(1, 1, 1)$ (red) and $(-1, 1, 1)$ (blue), $t \in [1900, 2350]$, from two different perspectives. An attractor can be observed

In the next result we consider the cases in which system (1) has *first integrals*, which are functions $H : \mathbb{R}^3 \rightarrow \mathbb{R}$ such that

$$\dot{x} \frac{\partial H}{\partial x} + \dot{y} \frac{\partial H}{\partial y} + \dot{z} \frac{\partial H}{\partial z} \equiv 0,$$

where $(x(t), y(t), z(t))$ is a solution curve of system (1) and $H = H(x(t), y(t), z(t))$, for all $t \in \mathbb{R}$. The following result holds.

Theorem 2 *System (1) has first integrals in the following cases:*

- (b.i) *For $\omega = 0$, the functions $H_1(x, y, z) = y + \beta \ln |y| - \alpha \frac{x^2}{2} + \alpha \mu \ln |x|$ and $H_2(x, y, z) = z$ are first integrals of system (1). In this case, the system is completely integrable.*
- (b.ii) *For $\alpha = 0$, the function $H_3(x, y, z) = y^2 + z^2$ is a polynomial first integral of system (1) and its phase space is foliated by the invariant cylinders $y^2 + z^2 = c$, with $c \in \mathbb{R}_+$.*

When a differential system has a polynomial first integral $H(x, y, z)$, the surfaces $H(x, y, z) = c$, with $c \in Im(H)$, are invariant under the flow of the system. In Sect. 2.2 we prove Theorem 2 and describe the flow on the invariant algebraic surfaces that foliate the phase space of system (1), in some interesting cases.

The next results describe the dynamics of system (1) considering two cases: when it has an infinite number of equilibrium points and when it has a finite number of equilibrium points.

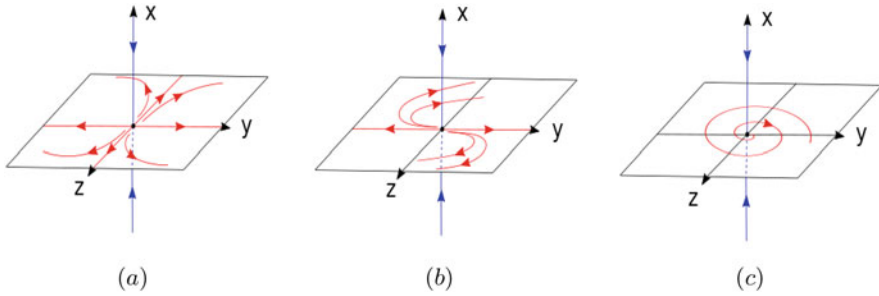


Fig. 3 Local behavior of system (1) near of the origin when it is an isolated equilibrium point. In (a) and (b) the origin is a saddle and in (c) the origin is a saddle-focus

Theorem 3 *System (1) has an infinite number of equilibrium points in the following cases:*

- (c.i) *For $\beta = 0$ and $\omega \neq 0$, the x -axis is formed by equilibrium points of the system;*
- (c.ii) *For $\beta \neq 0$, $\omega = 0$, and $\alpha\mu \neq 0$, the z -axis and the straight lines r_1 and r_2 given by $(\pm\sqrt{\mu}, -\beta, z)$, with $z \in \mathbb{R}$, are formed by equilibrium points of the system;*
- (c.iii) *For $\beta \neq 0$, $\omega = 0$, and $\alpha\mu = 0$, the yz -plane is formed by equilibrium points of the system;*
- (c.iv) *For $\beta = \omega = 0$ and $\alpha \neq 0$, the xz -plane is formed by equilibrium points of the system;*
- (c.v) *For $\beta = \omega = \alpha = 0$, the xz -plane and the yz -plane are formed by equilibrium points of the system.*

Theorem 3 is proved in Sect. 2.3, where we also describe the behavior of the orbits of system (1) near of these equilibrium points.

Theorem 4 *For $\beta\omega \neq 0$, the origin is the unique equilibrium point of system (1) and it is a saddle if $0 < \omega \leq \alpha\mu/2$ or a saddle-focus if $\omega > \alpha\mu/2$.*

Theorem 4 is proved in Sect. 2.4. The dynamics of system (1) near of the origin in the cases described by Theorem 4 are illustrated in Fig. 3.

Also in Sect. 2.4, we numerically describe the dynamics of system (1) when all the parameter values are positive, consequently the invariant sets described in the previous results are broken and the system has only one equilibrium point at the origin. In this case, interesting and complex dynamical behaviors can be observed. Finally, some concluding remarks are given in Sect. 3.

2 Dynamical Analysis of System (1)

In this section we perform a detailed study of the dynamical behavior of system (1), aiming to prove Theorems 1–4.

2.1 Symmetry, Invariant Straight Lines, and Invariant Planes

It is easy to see that system (1) is invariant under the coordinates transformation $(x, y, z) \rightarrow (-x, y, z)$, which persists for all parameter values. In this way, system (1) has a symmetry about the yz -plane. Then, in order to understand the dynamical behavior of the system it is enough to study its orbits in the semi-space $\{(x, y, z) \in \mathbb{R}^3/x \geq 0\}$. Furthermore, for all parameter values, the x -axis and the yz -plane are invariant under the flow of system (1). Indeed, for $y = z = 0$, system (1) becomes

$$\dot{x} = -\beta x, \quad \dot{y} = \dot{z} = 0,$$

which implies that the x -axis is invariant under the flow of the system and the orbits on it tend to the origin if $\beta > 0$ or this axis is formed by equilibrium points of the system if $\beta = 0$. Moreover, for $x = 0$ system (1) becomes

$$\dot{x} = 0, \quad \dot{y} = -\omega z + \alpha \mu y, \quad \dot{z} = \omega y,$$

which implies that the yz -plane is invariant under the flow of the system. Note that the restriction of system (1) to yz -plane is a linear system, whose origin is an equilibrium point with eigenvalues

$$\lambda_{1,2} = \frac{\alpha \mu \pm \sqrt{\alpha^2 \mu^2 - 4\omega^2}}{2}.$$

Hence, we have that:

- (a.i) For $\alpha \mu = 0$, the origin is a linear center;
- (a.ii) For $\alpha \mu > 0$ and $0 < \omega < \alpha \mu/2$, the origin is an unstable node;
- (a.iii) For $\alpha \mu > 0$ and $\omega = \alpha \mu/2$, the origin is an unstable improper node;
- (a.iv) For $\alpha \mu > 0$ and $\omega > \alpha \mu/2$, the origin is an unstable focus;

This proves Theorem 1.

2.2 First Integrals and Invariant Surfaces

Now we consider the cases in which system (1) has first integrals, as described in Theorem 2 statements.

Case (b.i) For $\omega = 0$, $H_1(x, y, z) = z$ and $H_2(x, y, z) = y + \beta \ln |y| - \alpha \frac{y^2}{2} + \alpha\mu \ln |x|$ are functionally independent first integrals of system (1), since we have

$$\dot{x} \frac{\partial H_i}{\partial x}(\varphi(t)) + \dot{y} \frac{\partial H_i}{\partial y}(\varphi(t)) + \dot{z} \frac{\partial H_i}{\partial z}(\varphi(t)) \equiv 0,$$

for $i = 1, 2$, where $\varphi(t)$ is a solution of the system. In this case, system (1) is completely integrable and its phase space can be completely determined. An interesting case occurs when $\omega = 0$, $\beta \neq 0$, and $\alpha\mu \neq 0$: the z -axis and the straight lines r_1 and r_2 parallel to the z -axis and given by $(\pm\sqrt{\mu}, -\beta, z)$, with $z \in \mathbb{R}$, are formed by equilibrium points of system (1). The eigenvalues of the linear part of the system at the equilibrium points on the z -axis are $\lambda_1 = -\beta$, $\lambda_2 = \alpha\mu$, and $\lambda_3 = 0$, then these equilibrium points are saddles, for $\alpha\mu \neq 0$ (see Fig. 4 left). The eigenvalues of the linear part of the system at the equilibrium points on r_1 and r_2 are $\lambda_{1,2} = \pm i\sqrt{2\alpha\mu\beta}$ and $\lambda_3 = 0$, then these equilibrium points are nonlinear centers, since the system is integrable in this case (see Fig. 4 right). Hence, system (1) has an infinity of periodic nonlinear oscillations.

Case (b.ii) For $\alpha = 0$, the phase space is foliated by the invariant cylinders $y^2 + z^2 = c$, around the x -axis. Recall that the plane $x = 0$ is invariant under the flow of system (1) and the system is symmetric about this plane. Hence, the solutions on the cylinders cannot cross the yz -plane, which has a center at the origin (see case

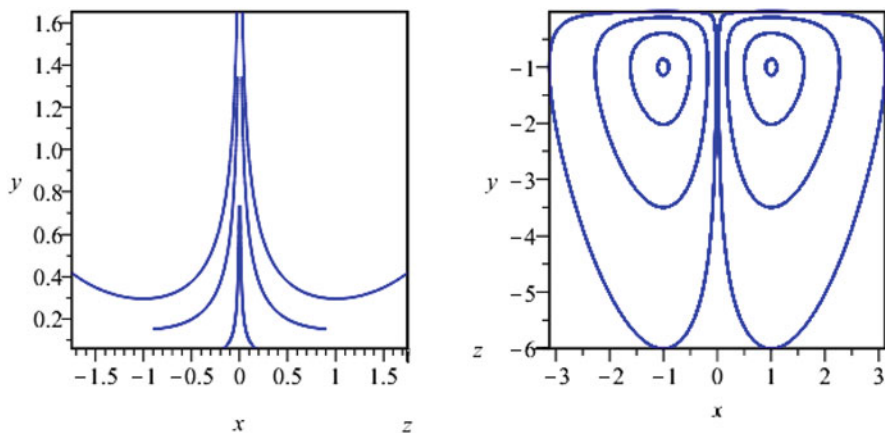


Fig. 4 Orbits of system (1) with $\alpha = \beta = \mu = 1$ and $\omega = 0$: there is a saddle at the origin and two centers at $(\pm\sqrt{\mu}, \beta, c)$, in each invariant plane $z = c \in \mathbb{R}$

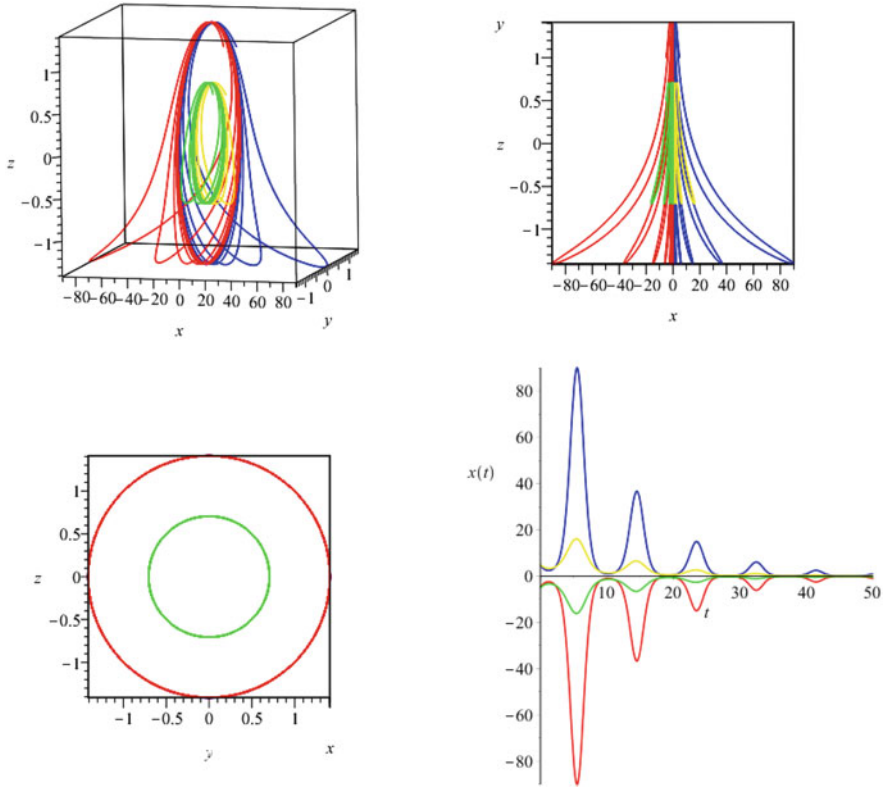


Fig. 5 Four orbits of system (1) with $\alpha = 0, \beta = 0.1, \omega = 0.7, \mu = 0.7$, initial conditions $(\pm 5, 1/2, 1/2), (\pm 5, 1, 1)$, its projections on the xz and yz -planes, and the coordinate $x(t)$ of these solutions. Observe the symmetry about the yz -plane

(a.i) above). Consequently, as the flow of the system on the x -axis are given by $\dot{x} = -\beta x$, with $\beta > 0$, the solutions on each invariant cylinder $y^2 + z^2 = c$, in the semi-spaces $x < 0$ and $x > 0$, tend to one of the periodic orbits which form the center in the yz -plane, as can be seen in Fig. 5.

In Fig. 6 we present the x, y , and z coordinates of two solutions of system (1) with $\mu = 0$. We can observe that the x -coordinate, which is related to the internal state of memristor (see [5] for details), presents spikes before tending to the periodic orbit in the yz -plane (see also Fig. 5). These spikes occur exactly when the voltage in circuit, given by the z -coordinate, is most negative and the current, given by the y -coordinate, crosses the zero value from negative to positive, see Fig. 6. Also, the x -coordinate passes near null value when the current is null, crossing the zero value from positive to negative. Furthermore, the largest the cylinder in which the orbit is contained, the largest the spikes.

This proves Theorem 2.

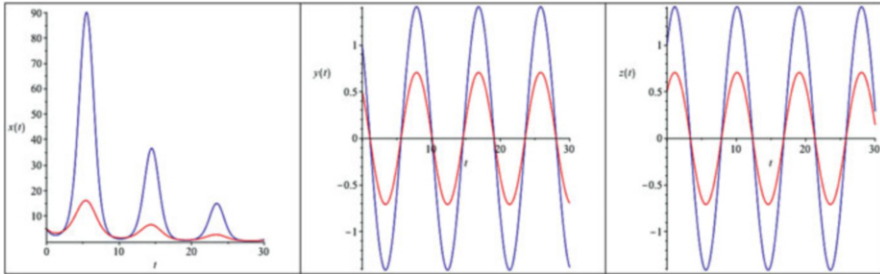


Fig. 6 x , y , and z -coordinates of two orbits of system (1) with $\alpha = 0$, $\beta = 0.1$, $\omega = 0.7$, and $\mu = 0.7$. Initial conditions $(5, 1/2, 1/2)$ in red and $(5, 1, 1)$ in blue, $t \in [0, 30]$

We continue this analysis considering two cases: when system (1) has an infinite number of equilibrium points and when it has a finite number of equilibrium points.

2.3 Infinite Number of Equilibrium Points

System (1) has an infinite number of equilibrium points in the following cases:

- (c.i) For $\beta = 0$ and $\omega \neq 0$, the x -axis is formed by equilibrium points of system (1) and the eigenvalues of the linear part of the system at these points are

$$\lambda_{1,2} = \frac{\alpha(\mu - x^2) \pm \sqrt{\alpha^2 x^4 - 2\alpha^2 \mu x^2 + \alpha^2 \mu^2 - 4\omega^2}}{2}, \quad \lambda_3 = 0.$$

Note that the classification of these equilibrium points depends on the value of the parameters α , μ , and ω and the position of the equilibrium point on the x -axis. Due to the great number of possibilities, we highlight some interesting cases:

- (c.i.i) If $\alpha = 0$, then all these equilibrium points are nonlinear centers, as $\lambda_{1,2} = \pm i\omega$ and the phase space of the system is foliated by the invariant cylinders $y^2 + z^2 = c$, with $c \in \mathbb{R}_+$ (case (b.ii) above).
- (c.i.ii) If $\mu = 0$, then $\lambda_{1,2} = (-\alpha x^2 \pm \sqrt{\alpha^2 x^4 - 4\omega^2})/2$ and these points are stable nodes for $0 < \omega \leq \alpha x^2/2$ or stable foci for $\omega > \alpha x^2/2$.
- (c.i.iii) The equilibrium points on the position $(\pm\sqrt{\mu}, 0, 0)$ are always nonlinear centers or weak foci, as $\lambda_{1,2} = \pm i\omega$ at these points.
- (c.ii) For $\beta \neq 0$, $\omega = 0$, and $\alpha\mu \neq 0$, the z -axis and the straight lines r_1 and r_2 parallel to the z -axis and given by the points $(\pm\sqrt{\mu}, -\beta, z)$, with $z \in \mathbb{R}$, are formed by equilibrium points of system (1).
- (c.ii.i) The eigenvalues of the linear part of the system at the equilibrium points on the z -axis are $\lambda_1 = -\beta$, $\lambda_2 = \alpha\mu$, and $\lambda_3 = 0$, then these equilibrium points are saddles, as $\alpha\mu \neq 0$.

- (c.ii.ii) The eigenvalues of the linear part of the system at the equilibrium points on r_1 and r_2 are $\lambda_{1,2} = \pm i\sqrt{2\alpha\mu\beta}$ and $\lambda_3 = 0$, then these equilibrium points are nonlinear centers, since the system is integrable (case (b.i)).
- (c.iii) For $\beta \neq 0$, $\omega = 0$, and $\alpha\mu = 0$, the yz -plane is formed by equilibrium points of system (1). Given an equilibrium point $(0, y, z)$ on this invariant plane the eigenvalues of the linear part of the system at this point are $\lambda_1 = -y - \beta$ and $\lambda_2 = \lambda_3 = 0$. Hence orbits tend to this equilibrium point if $y > -\beta$ or move away from it if $y < -\beta$. Moreover, for $\alpha = 0$ the plane $y = -\beta$ is also formed by equilibrium points and, in this plane, all equilibrium points are degenerate, as $\lambda_1 = \lambda_2 = \lambda_3 = 0$.
- (c.iv) For $\beta = \omega = 0$ and $\alpha \neq 0$, the xz -plane is formed by equilibrium points of system (1). Given an equilibrium point $(x, 0, z)$ on this invariant plane the eigenvalues of the linear part of the system at this point are $\lambda_1 = -\alpha(x^2 - \mu)$ and $\lambda_2 = \lambda_3 = 0$. Hence orbits tend to this equilibrium point if $x < -\sqrt{\mu}$ or $x > \sqrt{\mu}$ or move away from it if $-\sqrt{\mu} < x < \sqrt{\mu}$.
- (c.v) For $\beta = \omega = \alpha = 0$, the xz -plane and the yz -plane are formed by equilibrium points of system (1). All equilibrium points on the xz -plane are degenerate, as the eigenvalues of the linear part of the system at these points are $\lambda_1 = \lambda_2 = \lambda_3 = 0$. Given an equilibrium point $(0, y, z)$ on the yz -plane orbits tend to it if $y > 0$ or move away from it if $y < 0$, since, the eigenvalues are $\lambda_1 = -y$ and $\lambda_2 = \lambda_3 = 0$.

This proves Theorem 3.

2.4 Finite Number of Equilibrium Points and Complex Dynamics

System (1) has a finite number of equilibrium points for $\beta\omega \neq 0$. In this case the origin is the unique equilibrium point and the eigenvalues of the linear part of the system at this point are

$$\lambda_1 = -\beta, \quad \lambda_{2,3} = \frac{\alpha\mu \pm \sqrt{\alpha^2\mu^2 - 4\omega^2}}{2}.$$

We have the following cases (see Fig. 3):

- (d.i) For $0 < \omega \leq \alpha\mu/2$, the origin is a saddle, as $\lambda_1 < 0$, $\lambda_2 > 0$ and $\lambda_3 > 0$.
- (d.ii) For $\omega > \alpha\mu/2$, the origin is a saddle-focus, as $\lambda_1 < 0$ and $\lambda_{2,3} \in \mathbb{C}$ with $Re(\lambda_{2,3}) > 0$.

This proves Theorem 4.

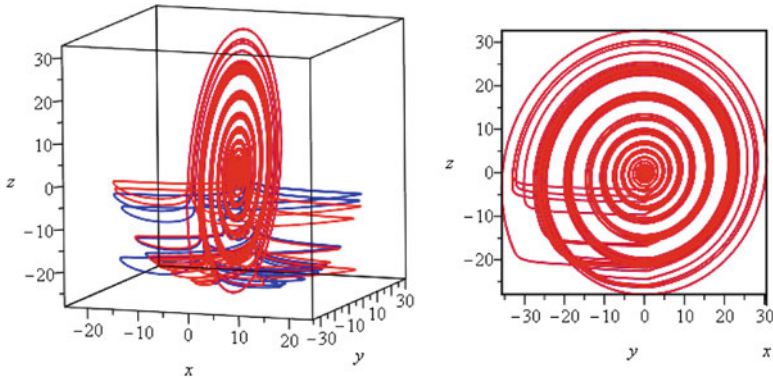


Fig. 7 Orbits of system (1) with $\alpha = 0.1$, $\beta = 0.5$, $\omega = 1.0$, and $\mu = 1.0$. Initial conditions $(\pm 1, 1, 1)$ and its projections on the plane- yz . $t \in [300, 650]$

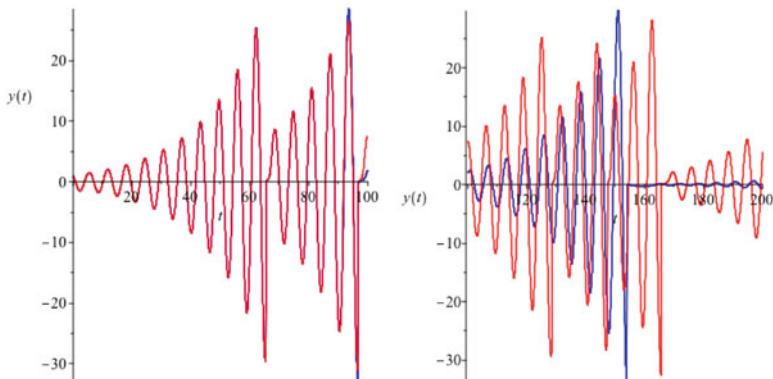


Fig. 8 Coordinate y of two orbits of system (1) with $\alpha = 0.1$, $\beta = 0.5$, $\omega = 1.0$, and $\mu = 1.0$. Initial conditions $(1, 1, 1)$ and $(1, 1.0001, 1)$. Left: $t \in [0, 100]$. Right: $t \in [100, 200]$. We can observe sensitivity to the initial conditions starting from $t = 100$

When all the parameters are different from zero, system (1) has only smaller one equilibrium point at the origin and the dynamics can be rather complex. We made several simulations in this case, showing the complex behavior of the solutions, which is shown in Fig. 7 (see also Fig. 2). In Fig. 8 is shown the sensitive dependence on initial conditions of two solutions which tend to the attractor shown in Fig. 7.

3 Concluding Remarks

System (1) presents the rare and interesting property of having possible chaotic behavior coexisting with an invariant plane (the yz -plane), in which the flow is linear. Although the focus at the origin in the invariant plane is unstable, meaning that all the solutions in this plane but the origin tend to infinity, there is a kind of attractor in the phase space, to which the solutions out the invariant plane tend as $t \rightarrow +\infty$ (see Figs. 2 and 7). We are further studying the interesting system (1), theoretical and numerically, and new results will appear in a near future paper. As in this paper, the aim is to contribute to the understanding of system (1) dynamics and, consequently, to the electronic behavior of the memristive circuit in Fig. 1.

References

1. L.O. Chua, Memristor: the missing circuit element. *IEEE Trans. Circuit Theory* **18**, 507–519 (1971)
2. D.B. Strukov, G.S. Snider, D.R. Stewart, R.S. Williams, The missing memristor found. *Nature* **453**, 80–83 (2008)
3. F. Sapuppo, M. Bucolo, M. Intaglietta, L. Fortuna, P. Arena, Cellular non-linear networks for microcirculation applications. *Int. J. Circ. Theor. Appl.* **34**, 471–488 (2006)
4. R. Tetzlaff (Ed.), *Memristors and Memristive Systems* (Springer, New York, 2014)
5. M. Itoh, L.O. Chua, Memristor Hamiltonian circuits. *Int. J. Bifur. Chaos* **21**, 2395–2425 (2011)

Periodic Solutions of Mathieu Oscillator, Induced by Fuzzy Uncertainty



Xiao-Ming Liu , Xiao-Ping Tian, Ling Hong, and Yue Shu

1 Introduction

The Mathieu equation was introduced by Mathieu to research the oscillation of an elliptic membrane. It is rich in the dynamics and can characterize many engineering problems [1, 2]. Inevitably, the practical system is subjected to uncertainties. An uncertainty can be modeled as a random variable if the probability density distribution function is known. However, many uncertainties only have incomplete or vague information, which should be modeled as a fuzzy uncertainty. Thus, it has practical significance to study the dynamics of the Mathieu oscillator with fuzzy uncertainty.

The fuzzy dynamical system is usually described by the fuzzy differential equation (FDE). The solution of the FDE varies with different interpretations which mainly fall into three categories based on the understanding of the derivative of the fuzzy variable. The first interpretation defines the fuzzy derivative as Hukuhara [3] or generalized Hukuhara derivative [4]. The second one expresses the FDE as the fuzzy differential inclusions where the fuzzy derivative is an ordinary one which belongs to a fuzzy set determined by a fuzzy function [5, 6]. The third interpretation directly applies the Zadeh's extension on the solution of the ordinary differential equation [7]. Among the solutions of the three interpretations, the latter

X.-M. Liu (✉) · Y. Shu
State Key Laboratory of Compressor Technology, Hefei General Machinery Research Institute,
Hefei, Anhui, P.R. China
e-mail: liuxiaoming_4109@163.com

X.-P. Tian
Chinese Flight Test Establishment, Xi'an, Shaanxi, P.R. China

L. Hong
State Key Laboratory for Strength and Vibration of Mechanical Structures, Xi'an Jiaotong
University, Xi'an, Shaanxi, P.R. China

two are consistent with the deterministic system in terms of stability, periodicity, and bifurcation [8, 9]. In general, the solution obtained by applying the Zadeh’s extension is the subset of that by the fuzzy differential inclusions [6].

To analytically solve the FDE is very difficult, especially for nonlinear systems. Thus, a numerical method is the main approach to obtain the fuzzy solution [5, 10]. However, numerically solving the FDE is a computationally intensive and data-intensive task, which results in the most numerical examples in the literature being limited to one-dimensional fuzzy system or short-time span computing [8, 11]. Liu proposed an effective numerical method of fuzzy differential inclusions by transforming them into the governing equation of the membership function and then calculating the membership function to obtain the fuzzy solution [12]. Since the method does not need comparison or data storage, it has high computational efficiency and low memory cost. With the above method, the long-term behavior of the Mathieu oscillator with fuzzy uncertainty is studied. By comparing the fuzzy and the deterministic solutions, the periodic part embedded in the fuzzy solution induced by the fuzzy uncertainty is revealed.

2 Preliminaries

Denote by $(\mathcal{F}_C)^n$ the space of convex and compact fuzzy sets on R^n , the fuzzy set $W \in (\mathcal{F}_C)^n$ is described by its membership function $\mu_W : R^n \rightarrow [0, 1]$. W is a fuzzy number when $W \in \mathcal{F}_C$ and μ_W is upper semi-continuous. Furthermore, W is a triangular fuzzy number if μ_W is

$$\mu_W(w) = \begin{cases} \frac{w-a}{b-a}, & w \in (a, b) \\ \frac{c-w}{c-b}, & w \in [b, c) \\ 0, & \text{otherwise} \end{cases} .$$

Besides the membership function, W can be delineated by its α -levels

$$[W]^\alpha = \begin{cases} \{w \in R^n | \mu_W(w) \geq \alpha\}, & \alpha \in (0, 1] \\ cl\{w \in R^n | \mu_W(w) > \alpha\}, & \alpha = 0 \end{cases} ,$$

in which $cl(E)$ stands for the closure of the subset E . The space of the fuzzy set W satisfying $[W]^0 \subset \Lambda \subset R^n$ is denoted as $(\mathcal{F}_C)^n(\Lambda)$.

Consider the initial value problem

$$\begin{cases} \dot{x} = f(t, x, w) \\ x(0) = x_0 \end{cases} , \tag{1}$$

in which $f : [0, T] \times R^n \times R^m \rightarrow R^n$ is a continuous function. Assume that the initial condition x_0 and the parameter w are disturbed by fuzzy uncertainties but limited in the regions $\Upsilon \subset R^n$ and $\Omega \subset R^m$, respectively, then they should be

replaced by the fuzzy sets $X_0 \in (\mathcal{F}_C)^n(\Upsilon)$ and $W \in (\mathcal{F}_C)^m(\Omega)$. Let $\mu_{X_0} : \Upsilon \rightarrow [0, 1]$ and $\mu_W : \Omega \rightarrow [0, 1]$ are upper semi-continuous membership functions of X_0 and W , respectively, then the problem becomes a fuzzy initial value problem and can be expressed by the FDE in the form of differential inclusions:

$$\begin{cases} \dot{x} \in f(t, x, [W]^\alpha) \\ x(0) = x_0 \in [X_0]^\alpha \end{cases}, \tag{2}$$

where $\alpha \in [0, 1]$. Let $\mathcal{X}(t)$ be Eq. (2)'s solution, according to [6, 13], there is $[\mathcal{X}(t)]^\alpha = \{x(t, x_0, c(t)) | x_0 \in [X_0]^\alpha, c(t) \in [W]^\alpha\}$ where $x(t, x_0, c(t))$ is the solution of the ordinary differential equation

$$\begin{cases} \dot{x} = f(t, x, c(t)) \\ x(0) = x_0 \end{cases}. \tag{3}$$

Notice that Eq. (3) degenerates into Eq. (1) while $c(t)$ is a constant. In the next section, we will use the method proposed in [12] to numerically obtain $\mathcal{X}(t)$.

3 Numerical Method for Fuzzy Differential Inclusions

For Eq. (2), let $[U(t, x)]^\alpha = f(t, x, [W]^\alpha)$ to define a fuzzy set $U(t, x) \in (\mathcal{F}_C)^n$. According to the extension principle [14], the membership function of $U(t, x)$ is

$$\mu_{U(t,x)}(u) = \begin{cases} \sup_{w \in f^{-1}(u)} \{\mu_W(w)\}, & \text{if } f^{-1}(u) \neq \emptyset \\ 0, & \text{if } f^{-1}(u) = \emptyset \end{cases},$$

where $f^{-1}(u) = \{w | w \in \Omega, f(w) = u\}$. Following [12, 15], if

- (1) the function f is continuous in $[0, T] \times R^n \times \Omega$,
- (2) the initial condition $\mu_{\mathcal{X}(0)}(x)$ is piece-wise smooth in R^n ,
- (3) $\mu_{U(t,x)}(u)$ is piece-wise smooth in (t, x) and can be expressed as $\mu_{U(t,x)}(u) = g(\Delta u^T(u, t, x)D(t, x)\Delta u(u, t, x))$, in which $D(t, x) = \begin{bmatrix} D^*(t, x) & \mathbf{O} \\ \mathbf{O} & \mathbf{O} \end{bmatrix}$ is an $n \times n$ matrix where $D^*(t, x)$ is a positive-definite $k \times k$ matrix, and $\Delta u = u(t, x) - u^1(t, x)$ where $u^1(t, x) = [U(t, x)]^1$.

then the membership function $\mu_{\mathcal{X}(t)}$ can be acquired by solving $\Phi(t, x)$ from the governing equation of the membership function

$$\begin{cases} \frac{\partial \Phi(t,x)}{\partial t} + (u^1(t, x))^T \nabla_x \Phi(t, x) + \Phi(t, x) \sqrt{(\nabla_x \Phi(t, x))^T \tilde{D}(t, x) \nabla_x \Phi(t, x)} = 0 \\ \Phi^2(0, x_0) = g^{-1}(\mu_{\mathcal{X}(0)}(x_0)) \end{cases} \tag{4}$$

where $\tilde{D}(t, \mathbf{x}) = \begin{bmatrix} D^{*-1}(t, \mathbf{x}) & \mathbf{O} \\ \mathbf{O} & \mathbf{O} \end{bmatrix}$, and substituting $\Phi(t, \mathbf{x})$ into the equation

$$\mu_{\mathcal{X}(t)}(\mathbf{x}) = g(\Phi^2(t, \mathbf{x})) . \tag{5}$$

It should be noticed that when $\Delta \mathbf{u}(\mathbf{u}(t, \mathbf{x}), t, \mathbf{x}) = \mathbf{0}$ and $D = \mathbf{O}$, which means $U(t, \mathbf{x})$ becomes a crisp value, the conclusion is maintained by making $\tilde{D} = \mathbf{O}$.

Equation (4) can be solved by integrating its characteristic equations:

$$\begin{cases} \frac{dx}{dt} &= \mathbf{u}^1 + \frac{\Phi}{q} \tilde{D} \boldsymbol{\psi} \\ \frac{d\xi}{dt} &= -\boldsymbol{\psi}^T \frac{\partial \mathbf{u}^1}{\partial t} - \frac{\Phi}{2q} \boldsymbol{\psi}^T \frac{\partial \tilde{D}}{\partial t} \boldsymbol{\psi} - q \zeta \\ \frac{d\boldsymbol{\psi}}{dt} &= -\boldsymbol{\psi}^T \frac{\partial \mathbf{u}^1}{\partial \mathbf{x}} - \frac{\Phi}{2q} \boldsymbol{\psi}^T \frac{\partial \tilde{D}}{\partial \mathbf{x}} \boldsymbol{\psi} - q \boldsymbol{\psi} \\ \frac{d\Phi}{dt} &= 0 \end{cases} \tag{6}$$

with the initial conditions

$$\begin{cases} \mathbf{x}_0 &\in [X_0]^0 \\ \Phi(0, \mathbf{x}_0) &= \sqrt{g^{-1}(\mu_{\mathcal{X}(0)}(\mathbf{x}_0))} \\ \boldsymbol{\psi}(0, \mathbf{x}_0) &= \nabla_{\mathbf{x}} \Phi(0, \mathbf{x}_0) \\ \zeta(0, \mathbf{x}_0) &= -(\mathbf{u}^1(0, \mathbf{x}_0))^T \boldsymbol{\psi}(0, \mathbf{x}_0) - \Phi(0, \mathbf{x}_0) \sqrt{(\boldsymbol{\psi}(0, \mathbf{x}_0))^T \tilde{D}(0, \mathbf{x}_0) \boldsymbol{\psi}(0, \mathbf{x}_0)} \end{cases}$$

where $q = \sqrt{\boldsymbol{\psi}^T \tilde{D} \boldsymbol{\psi}}$, $\mathbf{x} = [x_1, \dots, x_n]^T$, $\zeta = \partial \Phi / \partial t$, and $\boldsymbol{\psi} = [\psi_1, \dots, \psi_n]^T = \nabla_{\mathbf{x}} \Phi = [\partial \Phi / \partial x_1, \dots, \partial \Phi / \partial x_n]^T$.

It can be seen that the solution of Eq. (6) is the function of (t, \mathbf{x}_0) . Thus, by taking considerable samples from $[X_0]^0$ and calculating the solutions of Eq. (6) at time t and substituting Φ into Eq. (5), $\mathcal{X}(t)$ is numerically obtained.

4 Mathieu Oscillator with Fuzzy Uncertainty

To investigate the influence of the fuzzy uncertainty on the system, we start with the brief dynamical analysis of the deterministic Mathieu oscillator

$$\begin{cases} \dot{x}_1(t) &= x_2 \\ \dot{x}_2(t) &= -2.62x_1 - 25x_1^3 - 0.173x_2 + w(1 - \cos 2t)(0.456x_1 + 0.92) \end{cases} \tag{7}$$

A series of the bifurcations experienced by the Mathieu oscillator in the variation of w from 3.3 to 4.3 is shown in the bifurcation diagram Fig. 1a. It can be seen that there are two attractors when $w \in [3.509, 4.259]$. Specifically, the attractor marked by the upper branch converts to chaotic twice through period-doubling cascades

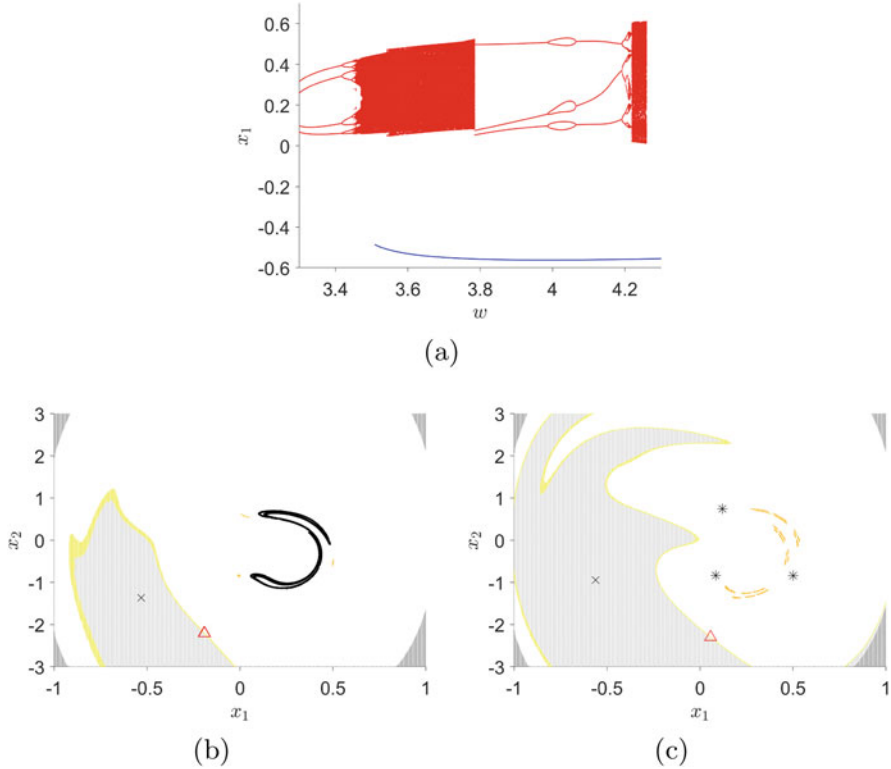


Fig. 1 (a) is the bifurcation diagram of the Mathieu oscillator Eq.(7) while $w \in [3.3, 4.3]$. The upper and lower branches marked in red and blue, respectively, represent two different attractors. (b) and (c) illustrate the global dynamical structures of the system when $w = 3.6$ and $w = 3.9$, respectively. The symbols, crosses, asterisks and dots, successively indicate the period-1, the period-3, and the chaotic attractor. The basins of the attractors are distinguished with gray and white, the basin boundaries are delineated by yellow curves, the period-1 saddles on basin boundary are represented by red triangle and the chaotic saddle in basin is represented by orange dots

as w is swept forward from 3.3 and vanishes at $w = 4.259$ due to a boundary crisis. As for the attractor represented by the lower branch, it remains period-1 while w is swept backwards from 4.3 and disappears at $w = 3.509$ with a saddle-node bifurcation. More details of the dynamical structures of the system Eq. (7) are shown in Fig. 1b, c, where two cases of $w = 3.6$ and $w = 3.9$ are chosen to reveal their global dynamics by the method of Generalized Cell Mapping with Sampling-Adaptive Interpolation [16]. As shown in Fig. 1b, there are a period-1 attractor and a chaotic one when $w = 3.6$. And Fig. 1c shows that there exist a period-1 attractor and a period-3 one while $w = 3.9$.

Now we come to the Mathieu oscillator when the parameter w is disturbed by fuzzy uncertainty and the system is described by the fuzzy differential inclusions:

$$\begin{cases} \dot{x}_1(t) = x_2 \\ \dot{x}_2(t) \in -25x_1^3 - 0.173x_2 - 2.62x_1 + [W]^\alpha(1 - \cos 2t)(0.456x_1 + 0.92), \end{cases} \tag{8}$$

where $W \in \mathcal{F}_C(R)$ is a triangular fuzzy number with the membership function

$$\mu_W(w) = \begin{cases} 1 - \frac{|w-w_p|}{0.1}, & w_p - 0.1 < w < w_p + 0.1 \\ 0, & \text{otherwise} \end{cases}.$$

In addition, the initial condition is $\mathbf{x}(0) \in [X_0]^\alpha$, where X_0 is a fuzzy set with the membership function as below

$$\mu_{X_0}(\mathbf{x}(0)) = \begin{cases} 1 - \frac{\sqrt{(x_1(0)-a)^2+(x_2(0)-b)^2}}{0.01}, & \sqrt{(x_1(0) - a)^2 + (x_2(0) - b)^2} < 0.01 \\ 0, & \text{otherwise} \end{cases}.$$

To solve Eq. (8) numerically, let

$$[U]^\alpha = \begin{bmatrix} x_2 \\ -25x_1^3 - 0.173x_2 - 2.62x_1 + [W]^\alpha(1 - \cos 2t)(0.456x_1 + 0.92) \end{bmatrix}$$

for all $\alpha \in [0, 1]$ to define a fuzzy set U . Then, for

$$\mathbf{u} = \begin{bmatrix} u_1 \\ u_2 \end{bmatrix} = \begin{bmatrix} x_2 \\ -25x_1^3 - 0.173x_2 - 2.62x_1 + w(1 - \cos 2t)(0.456x_1 + 0.92) \end{bmatrix}$$

in which $w \in R$, we have

$$\Delta \mathbf{u}(\mathbf{u}, t, \mathbf{x}) = \mathbf{u} - \mathbf{u}^1 = \begin{bmatrix} 0 \\ (w - w_p)(1 - \cos 2t)(0.456x_1 + 0.92) \end{bmatrix},$$

where

$$\mathbf{u}^1 = \begin{bmatrix} u_1^1 \\ u_2^1 \end{bmatrix} = \begin{bmatrix} x_2 \\ -25x_1^3 - 0.173x_2 - 2.62x_1 + w_p(1 - \cos 2t)(0.456x_1 + 0.92) \end{bmatrix}$$

and

$$\mu_{U(t,\mathbf{x})}(\mathbf{u}) = \begin{cases} 1 - 10\sqrt{\frac{\|\Delta \mathbf{u}(\mathbf{u}, t, \mathbf{x})\|^2}{(1 - \cos 2t)^2(0.456x_1 + 0.92)^2}}, & (1 - \cos 2t)(0.456x_1 + 0.92) \neq 0 \\ 1, & \text{otherwise} \end{cases}.$$

Furthermore, $\mu_{U(t,x)}(\mathbf{u})$ can be rewritten as the form

$$\mu_{U(t,x)}(\mathbf{u}) = 1 - 10\sqrt{\Delta \mathbf{u}^T(\mathbf{u}, t, \mathbf{x})D(t, \mathbf{x})\Delta \mathbf{u}(\mathbf{u}, t, \mathbf{x})},$$

where $D(t, \mathbf{x}) = \begin{bmatrix} 0 & 0 \\ 0 & D^*(t, \mathbf{x}) \end{bmatrix}$ and

$$D^*(t, \mathbf{x}) = \begin{cases} \frac{1}{(1-\cos 2t)^2(0.456x_1+0.92)^2}, & (1 - \cos 2t)(0.456x_1 + 0.92) \neq 0 \\ 0, & \text{otherwise} \end{cases}$$

Therefore,

$$\tilde{D} = \begin{bmatrix} 0 & 0 \\ 0 & (1 - \cos 2t)^2(0.456x_1 + 0.92)^2 \end{bmatrix},$$

and the characteristic equations are

$$\begin{cases} \frac{dx_1}{dt} = u_1^1 \\ \frac{dx_2}{dt} = u_2^1 + 2\Phi \text{sign}(\psi_2) \sin^2 t |0.456x_1 + 0.92| \\ \frac{d\zeta}{dt} = -4\psi_2 w_p \sin t \cos t (0.456x_1 + 0.92) \\ \quad -4\Phi \sin t \cos t |\psi_2(0.456x_1 + 0.92)| - q\zeta \\ \frac{d\psi_1}{dt} = \psi_2 (75x_1^2 + 2.62 - 0.912w_p \sin^2 t) \\ \quad -0.912\Phi \sin^2 t |\psi_2 \text{sign}(0.456x_1 + 0.92)| - q\psi_1 \\ \frac{d\psi_2}{dt} = -\psi_1 + 0.173\psi_2 - q\psi_2 \\ \frac{d\Phi}{dt} = 0 \end{cases}, \tag{9}$$

where $q = 2 \sin^2 t |\psi_2(0.456x_1 + 0.92)|$. With the initial conditions

$$\begin{cases} \mathbf{x}_0 \in [\mathbf{X}_0]^0 \\ \Phi(0, \mathbf{x}_0) = 0.1(1 - \mu_{X_0}(\mathbf{x}_0)) \\ \boldsymbol{\psi}(0, \mathbf{x}_0) = -0.1\left[\frac{\partial \mu_{X_0}(\mathbf{x}_0)}{\partial x_1}, \frac{\partial \mu_{X_0}(\mathbf{x}_0)}{\partial x_2}\right]^T \\ \zeta(0, \mathbf{x}_0) = -u_1^1(0, \mathbf{x}_0)\psi_1(0, \mathbf{x}_0) - u_2^1(0, \mathbf{x}_0)\psi_2(0, \mathbf{x}_0) \end{cases},$$

the fuzzy solution $\mathcal{X}(t)$ of Eq. (8) can be calculated by integrating Eq (9) with Runge–Kutta method. And the stable long-term solutions, which are approximated by the fuzzy solutions at $t = n\pi$ (n is a very large positive integer), are investigated. Through comparing the fuzzy and deterministic solutions, we can reveal the influence of the fuzzy uncertainty on the Mathieu oscillator.

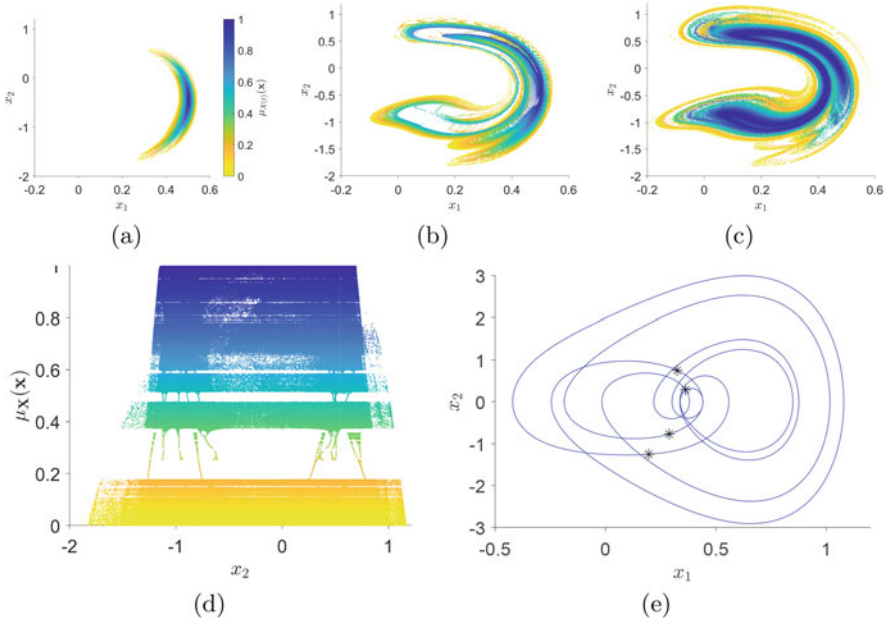


Fig. 2 When $w_p = 3.6$ and $(a, b) = (0.4379, -0.2811)$, the transient fuzzy solutions $\mathcal{X}(t)$ of the Mathieu oscillator with fuzzy uncertainty at (a) $t = 2\pi$ and (b) $t = 5\pi$. (c) The fuzzy attractor and (d) its x_2 - $\mu_{\mathcal{X}}(\mathbf{x})$ view. (e) The phase portrait and Poincaré map of the deterministic Mathieu oscillator with $c(t)$ satisfying Eq. (11), where $\Phi = 0.0788$ and $\psi_2(t)$ is solved from Eq. (9). In (a)–(d), the values of the membership function $\mu_{\mathcal{X}(t)}(\mathbf{x})$ from 0 to 1 are represented by different colors from yellow to blue. In (e), the phase portrait and the Poincaré map are represented by the curve and asterisks, respectively

4.1 Periodic Parts Induced from the Chaotic Solution

Let $w_p = 3.6$ first, which means the fuzzy uncertainty effects the system Eq. (7) of the case $w = 3.6$, and $(a, b) = (0.4379, -0.2811)$, the fuzzy solutions at $t = 2\pi$ and $t = 5\pi$ are shown successively in Fig. 2a, b. The stable long-term fuzzy solution is asymptotically reached at $t = 1100\pi$. Unless the long-term solution is a fixed point, the transient solution always changes over time. To obtain the full view of the fuzzy attractor, an enormous amount of fuzzy solutions at $t = n\pi$ ($n = 1101, 1102, \dots$) are drawn in the single picture Fig. 2c. And the x_2 - $\mu_{\mathcal{X}}(\mathbf{x})$ view of the fuzzy attractor is exhibited in Fig. 2d. It can be found that some parts of the fuzzy attractor are not chaotic but periodic. For instance, the part of $\mu_{\mathcal{X}}(\mathbf{x}) \in (0.181, 0.251)$ is period-4.

Since $[\mathcal{X}(t)]^\alpha$ is the set of the solutions of the ordinary differential equations:

$$\begin{cases} \dot{x}_1(t) &= x_2 \\ \dot{x}_2(t) &= -25x_1^3 - 0.173x_2 - 2.62x_1 + c(t)(1 - \cos 2t)(0.456x_1 + 0.92) \end{cases}, \tag{10}$$

where $c(t) : [0, T] \rightarrow [W]^\alpha$ is a measurable function, the periodic parts in the fuzzy attractor tell us that the counterparts must exist in the deterministic system when some conditions are satisfied. In other words, we can find $c(t)$ to make the deterministic Mathieu oscillator avoid chaotic long-term behavior. By comparing Eq. (10) and the first two equations of Eq. (9), $c(t)$ is deduced as

$$c(t) = w_p + \text{sign}(\psi_2(t))\text{sign}(0.456x_1(t) + 0.92)\Phi, \tag{11}$$

where $\Phi \in [0, 0.1)$ and $\psi_2(t)$ is obtained by integrating Eq. (9). Taking $\Phi = 0.0788$ and $x_0 = (0.4379, -0.2811)$ (around the deterministic chaotic attractor illustrated in Fig. 1b) as an example, the transient solutions of Eq. (10) are calculated in the time range of 10500π and the trajectory of the later 500π is plotted in Fig. 2e, where the curve outlines the phase portrait and the asterisks represent the Poincaré map at $t = n\pi (n = 10001, 10002, \dots, 10500)$. It shows that the solution of the deterministic Mathieu oscillator Eq. (10) is stable at the period-4 attractor, which agrees with the period-4 part of the fuzzy attractor found in Fig. 2d.

4.2 Periodic Parts Induced from the Period-1 Solution

Secondly, we study the other case of Eq. (8) as $w_p = 3.9$, i.e., the fuzzy uncertainty acts on the system Eq. (7) with $w = 3.9$. Additionally, taking $(a, b) = (-0.5615, -0.9493)$ to make the initial condition sit around the deterministic period-1 attractor (see Fig. 1c), the numerical transient solutions at the moment $t = 2\pi, t = 32\pi$ are demonstrated, respectively, in Fig. 3a, b. The long-term solution is asymptotically reached at $t = 1101\pi$. By simultaneously drawing enough transient fuzzy solutions at $t = n\pi (n = 1101, 1102, \dots)$ in the same picture, the fuzzy attractor and its $x_2-\mu_{\mathcal{X}}(x)$ view are illustrated in Fig. 3c, d. In Fig. 3c, five arms are found to run out from the center part of the fuzzy attractor and form a period-5 structure, which is very different from the deterministic period-1 attractor in Fig. 1c. It can be seen that the period-5 part ranges from $\mu_{\mathcal{X}}(x) \approx 0.284$ to $\mu_{\mathcal{X}}(x) \approx 0.65$.

It is similar to the case of $w_p = 3.6$, if the eligible $c(t)$ satisfies Eq. (11), the deterministic Mathieu oscillator Eq. (10) should have a period-5 stable long-term behavior while $\Phi \in (0.0284, 0.065)$. Taking $\Phi = 0.0536$ and $x_0 = (-0.5615, -0.9493)$ (around the period-1 attractor illustrated in Fig. 1c) as an example, the transient solution of Eq. (10) is calculated in the time range of 10500π and the trajectory of the later 500π is plotted in Fig. 3e, where the curve outlines the phase portrait and the asterisks represent the Poincaré map at $t = n\pi (n = 10001, 10002, \dots, 10500)$. It shows that the solution of the deterministic Mathieu oscillator is stable at a period-5 attractor, which agrees with the period-5 part of the fuzzy attractor found in Fig. 3c, d

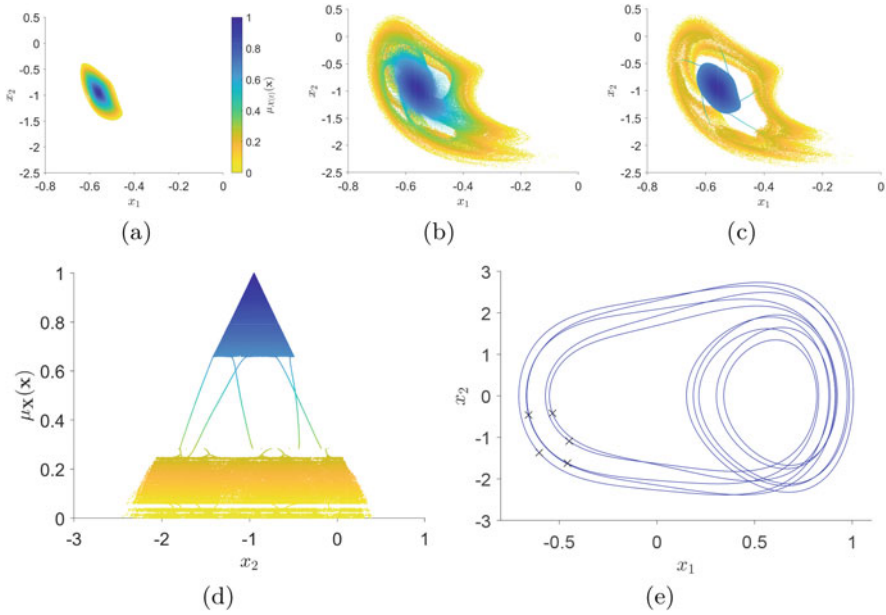


Fig. 3 When $w_p = 3.9$ and $(a, b) = (-0.5615, -0.9493)$, the transient fuzzy solutions $\mathcal{X}(t)$ of the Mathieu oscillator with fuzzy uncertainty at (a) $t = 2\pi$ and (b) $t = 32\pi$. (c) The fuzzy attractor with (d) its x_2 - $\mu_{\mathcal{X}}(x)$ view. (e) The phase portrait and Poincaré map of the deterministic Mathieu oscillator with $c(t)$ satisfying Eq. (11), where $\Phi = 0.0536$ and $\psi_2(t)$ is solved from Eq. (9). In (a)–(d), the values of the membership function $\mu_{\mathcal{X}(t)}(x)$ from 0 to 1 are represented by different colors from yellow to blue. In (e), the phase portrait and the Poincaré map are represented by the curve and crosses, respectively

5 Results and Discussion

By numerically solving the Mathieu oscillator with fuzzy uncertainty and studying the stable long-term fuzzy solution, it is found that the fuzzy uncertainty applied to the parameter of the system can excite the periodic part of the fuzzy solution which is very different from the original deterministic solution. Since the fuzzy solution is a set of solutions of infinitely many deterministic systems with different parameters, the periodic part means that a counterpart possessing the same period exists in some deterministic system with the parameter satisfying some conditions. In other words, if we can find some part of the fuzzy solution having the desired properties, we get a way of designing the parameter to obtain the expected stable long-term behavior in the deterministic system.

Acknowledgments This work was supported by the National Key Research and Development Program of China (Grant No. 2019YFB1504601) and the Youth Project of Provincial Natural Science Foundation of Anhui, China (Grant No. 1908085QE234).

References

1. D. Frenkel, R. Portugal, Algebraic methods to compute Mathieu functions. *J. Phys. A Math. Gen. Phys.* **34**(17), 3541–3551 (2001)
2. X.-M. Liu, J. Jiang, L. Hong, Z. Li, D. Tang, Fuzzy noise-induced codimension-two bifurcations captured by fuzzy generalized cell mapping with adaptive interpolation. *Int. J. Bifur. Chaos* **29**(11), 1950151 (2019)
3. O. Kaleva, Fuzzy differential equations. *Fuzzy Sets Syst.* **24**(3), 301–317 (1987)
4. B. Bede, S.G. Gal, Solutions of fuzzy differential equations based on generalized differentiability. *Commun. Math. Anal.* **9**(2), 22–41 (2010)
5. E. Hüllermeier, Numerical methods for fuzzy initial value problems. *Int. J. Uncertain. Fuzz. Knowl.-Based Syst.* **7**(5), 439–461 (1999)
6. Y. Chalco-Cano, H. Román-Flores, Some remarks on fuzzy differential equations via differential inclusions. *Fuzzy Sets Syst.* **230**, 3–20 (2013)
7. M. Oberguggenberger, S. Pittschmann, Differential equations with fuzzy parameters. *Math. Comput. Model. Dyn. Syst.* **5**(3), 181–202 (1999)
8. P. Diamond, P. Watson, Regularity of solution sets for differential inclusions quasi-concave in a parameter. *Appl. Math. Lett.* **13**(1), 31–35 (2000)
9. V. Lakshmikantham, R.N. Mohapatra, *Theory of Fuzzy Differential Equations and Inclusions* (Taylor & Francis, Milton Park, 2003)
10. A. Ahmadian, S. Salahshour, C.S. Chan, D. Baleanu, Numerical solutions of fuzzy differential equations by an efficient Runge–Kutta method with generalized differentiability. *Fuzzy Sets Syst.* **331**, 47–67 (2018)
11. S. Abbasbandy, J.J. Nieto, M. Alavi, Tuning of reachable set in one dimensional fuzzy differential inclusions, *Chaos Solitons Fract.* **26**(5), 1337–1341 (2005)
12. X.-M. Liu, J. Jiang, L. Hong, A numerical method to solve a fuzzy differential equation via differential inclusions. *Fuzzy Sets Syst.* **404**, 38–61 (2021)
13. J.P. Aubin, A. Cellina, *Differential Inclusions: Set-Valued Maps and Viability Theory*, 1st edn. (Springer, Berlin, 1984)
14. L.A. Zadeh, The concept of a linguistic variable and its application to approximate reasoning-I. *Inf. Sci.* **8**(3), 199–249 (1975)
15. Y. Friedman, U. Sandler, Evolution of systems under fuzzy dynamic laws. *Fuzzy Sets Syst.* **84**(1), 61–74 (1996)
16. X.-M. Liu, J. Jiang, L. Hong, D. Tang, Studying the global bifurcation involving Wada boundary metamorphosis by a method of generalized cell mapping with sampling-adaptive interpolation. *Int. J. Bifur. Chaos* **28**(2), 1830003 (2018)

Index

A

Acoustic radiation force (ARF)
 mathematical formulation
 dynamic acoustic radiation force, 339
 static acoustic radiation force, 337–338
 microbeams, 336
 microfluidic devices, 335
 noncontact excitation of microcantilevers
 estimation, 342–343
 numerical simulation, 340–341
 resonant frequencies, 336
 time-varying intensity, 335
 vibro-acoustic spectrography imaging,
 335–336
AEMM-based energy harvester, 202
“Agilent 33521A”, 298
Agroecosystems
 impact of insects and pests, 147
 model system, 150
 numerical simulations, 157–160
 reaction–diffusion system, 149
 spatial random movement of species, 160
 spatiotemporal system
 dispersion relation, 154
 linearized form, 153
 Routh–Hurwitz criterion, 154
 Turing instability, 155–157, 160
 temporal system
 boundedness, 149–150
 equilibria and stability analysis,
 150–152
Aluminum Nitride, 291
Amplitude death, 526
ANSYS WORKBENCH Transient Structural
 module, 128

Asymmetric damping coefficients, 211
Asymmetric hysteresis
 classical Preisach models, 373
 definition for, 375–376
 experimental data, 371
 extended Masing model, 373
 force-displacement cycles, 375
 masing models, 374
 rate-independency, 373
 technical challenges, 373–375
Atomic oxygen, 407
Autoregressive (AR) model, 7
Auxiliary oscillator, 234–237
Axial vibrations, of nanobars
 constitutive boundary conditions, 348
 Eringen’s two-phase local/nonlocal model,
 347
 first-order solution, 352–353
 formal expansions, 349
 governing equations, 348–349
 zeroth-order solution, 350–351

B

Bandgap, 201, 202, 205–208, 222, 432, 435,
 436, 439
Bandwidths, 263–265
Basic reproduction number, 28–29
Basins of attraction, 305–306
Beddington–DeAngelis incidence function, 51
Bernoulli–Euler hypothesis, 313
Bidirectional vibration, 250
Bifurcation diagram of systems, 66, 67, 69
Bifurcation sensor, 333
Birger variable parameters method, 315

- Birth control, *see* Optimal birth control
- Bistable electromagnetic energy harvester (BEEH), resonance circuit
- bifurcation diagram of output voltage, 226, 227
 - different resonance frequencies, 229
 - electromagnetic coupling, 223
 - equation of motion, 223–224
 - excitation condition, 226, 227
 - frequency response, 224, 228, 229
 - vs.* load resistance, 227
 - output voltage, 224–230
 - parameters, 224
 - phase orbit, 228, 229
 - Poincaré map, 224, 228, 229
 - potential energy, 222
 - vs.* pure resistance, 224, 225
 - schematic diagram, 222
- Bouc-Wen damping, 179
- Boussinesq equations, 445, 452, 473
- Brownian motion behavior, 555
- Buckled piezoelectric beam
- beam configuration, 278
 - electromechanical analysis
 - beam center structural displacement, 285
 - output voltage, 285
 - standard deviation of voltage output, 285
 - finite element model, 278–279
 - reduced order modeling
 - construction of basis functions, 282
 - formulation, 280–281
 - stiffness and electromechanical coupling coefficients, 282–283
 - validation results
 - critical buckling load and modes, 283
 - nonlinear dynamic responses, 284
 - nonlinear static responses, 283–284
- C**
- Ca^{2+} -mediated exosomal dynamics
- mathematical model
 - ATPase pump-dependent, 86
 - decoding synaptic exocytosis mechanism, 85
 - gating variables, 86
 - Hill function, 86
 - Hodgkin–Huxley neuron model, 87
 - membrane capacitance, 87
 - thermal inhibition, 87
 - time constants, 86
 - Watts–Sherman and Montefusco–Pedersen models, 85
 - results and discussion
 - exosomes in neurons, 88, 90
 - induced control signals/currents, 88, 89
 - microdomain calcium concentrations, 88, 90, 91
 - parameter set, 89
- Cantilever beam sensor
- electrostatic excitation, 330–333
 - external excitation, 329–330
- Capsule dynamics, 128
- Carrier frequency, 551, 552
- Cartesian coordinates, 312
- Cauchy–Riemann relations, 469
- Cauchy’s stress tensor, 292, 395
- Cellular nonlinear networks (CNN), 593
- Changchun Automobile Research Institute, 245
- Chaos-based image encryption algorithm, 557
- Chaotic behavior in biological systems, 63, 65
- Chaotic motion, 227, 229, 230, 250, 251, 590
- Chaotic oscillations, 535
- of one closed cylindrical nanoshell, 539
 - of two closed cylindrical nanoshell, 540
- Chen’s hyper-chaotic system, 548
- Chromosomal theory, 63
- Chua’s hyper-chaotic system, 549, 552, 553
- Classical couple stress theory, 395
- Classical Duffing equation, 385
- Closed cylindrical nanoshells, 535
- dynamic characteristics, 540, 541, 543, 544
 - formulation of problem, 536–537
 - Lyapunov exponents (Le) spectrum, 541, 542
 - solution methods, 538
 - vibrations of, 538–545
- Closed-loop scheme, 514
- Communication of neurons, 523
- Comprehensive transmission error, 242, 243, 247, 249
- Cooperative epidemiological model
- COVID-19 pandemic, 40
 - infectious dynamical processes, 40
 - mathematical analysis and modeling, 39
 - SIRD infectious disease model, 41
- Cooperative SIRD model, 45
- Coronavirus (COVID-19) epidemic, 3–4, 11
- Coupled bistable oscillators, 178
- Couple stress tensor, 395
- CQUAD4 shell element, 278
- Crash box, stochastic modeling of, 569–570
- PCE approach, 570–571

- POD approach, 571
- POD-PCE model, 572, 578
- UQ of
 - contact force, 577–578
 - impactor displacement, 575–576
 - impactor velocity, 576–577
 - Latin hypercube samples, 574
 - leave-one-out error, 575
 - problem statement, 573–574
- Crowley–Martin incidence function, 51
- Cryptanalysis of Farhan’s algorithm
 - chaotic system, 558
 - original image encryption algorithm, 558–559
 - target plain-text image, recover, 559–561
- Cyclic loading, 311
- Cylindrical coordinate system, 582

- D**
- Damping coefficient, 116, 130, 211, 217–219, 223, 235, 281, 308
- Damping force, 215, 216, 219, 242
- Damping matrix, 281, 295
- Data inference
 - Monte Carlo simulation, 42–43
 - physical time, 44
 - PSO method, 44, 45
 - RMS value, 43
 - SIRD model, 43
- Deformation, 408
- Design innovations, 127
- Devil’s Staircase plot, 499
- Dielectric constant, 308
- Differential quadrature method (DQM), 396, 400–401
- Dirichlet boundary conditions, 293
- Discrete wavelet transform (DWT), 547, 550–551
- Disease-free equilibrium, 29
- Dispersion relation, 422–423
- “Draft Representation Method for Descriptive Roughness”, 245
- Dual-resonator design, 202
- Duhamel-Neumann law, 313
- Dynamical analysis of system
 - memristor–inductor–capacitor nonlinear circuit
 - equilibrium points and complex dynamics, finite number of, 601–602
 - equilibrium points, infinite number of, 600–601
 - first integrals and invariant surfaces, 598–600
 - symmetry, invariant straight lines and invariant planes, 597
- Dynamic coupling method, 242
- Dynamic spatio-temporal process, 357

- E**
- Econometric Modeler toolbox, 9
- Effort-controlled explicit functions, 377
- Effort-controlled formulation, 377
- Ekeland’s variational principle, 163, 172, 174
- Elastic deformations, 317, 318
- Electrical equation of harvester, 257
- Electric energy regeneration device
 - bifurcation diagram of system changing with meshing frequency, 249, 251, 252
 - device structure design, 243–244
 - flow chart of nonlinear dynamic analysis, 243
 - gear system parameters, 250
 - generator parameters, 250
 - mass concentration method, 243, 247
 - Poincaré cross-sectional diagram, 249, 250, 252
 - road incentive, 244–246
 - system dynamics model
 - dimensionless differential equation of motion, 249
 - mechanical electromagnetic power regeneration system, 246
 - relative displacement of each meshing pair, 247
 - reserve clearance of roller one-way clutch, 247
 - side clearance of gear meshing pair, 248
 - time-varying meshing stiffness, 248
 - time domain, 244–246
- Electromechanical coupling coefficients, 221, 223, 282, 285, 291
- Electromechanical energy regeneration device, 242
- Electromechanics module, 327
- Electromotive voltage constant, 215, 216
- Electrostatic micromirrors, 291
- Electrostatic micro-tweezers, 302
- Elliptic bursting neuronal behavior, 527
- Endemic equilibrium
 - directed graph, 31
 - unique, 31–32
 - weighted digraph, 33
- Energy dissipation mechanism, 242

- Energy harvesting
- BEEH (*see* Bistable electromagnetic energy harvester (BEEH), resonance circuit)
 - 2D array (*see* 2D array of harvesters)
 - EHSA (*see* Energy harvesting shock absorber (EHSA))
 - magnetoelastic system (*see* Magneto piezo elastic oscillators)
 - metamaterials/metastructures (*see* Metastructures for vibration attenuation)
 - NES (*see* Vibration absorber energy harvester, NES)
 - reduced order modeling (*see* Buckled piezoelectric beam)
 - for wave energy harvesting (*see* Two-to-one internally resonant WEC)
- Energy harvesting shock absorber (EHSA)
- damping force, 216
 - downward stroke, 211, 212, 214, 218, 219
 - electromotive force voltage, 215
 - equivalent damping coefficient, 217, 218
 - equivalent stiffness, 217
 - force-displacement loops, 216
 - force-velocity loops, 216
 - frequency effect, 218
 - harmonic oscillations, 213
 - key parameters, 214
 - lumped model of, 213
 - output force, 214
 - rectified sine curve, 219
 - structure, 212
 - torque, 215
 - upward stroke, 211–215, 218, 219
- Energy localization, 202, 265
- Epithelial–mesenchymal transition, 63
- Equilibrium points
- finite number of, 601–602
 - infinite number of, 600–601
- Equivalent damping coefficient, 217–219
- Euler-Bernoulli beam theory, 324
- Euler equations, 443
- Excitation amplitude, 206
- Experimental testing campaign, 372
- Explicit function, 376
- Extended KdV (KdV2), 444, 446–447
- Extracellular matrix (ECM) molecules, 524
- F**
- Faedo-Galerkin method, 539, 545
- Faraday's law, 223, 234
- Farhan's algorithm, cryptanalysis of
- chaotic system, 558
 - original image encryption algorithm, 558–559
 - target plain-text image, recover, 559–561
- Fast Fourier transform (FFT), 303–305
- Feedforward neural networks (FFNN), 378
- FGM microplates, 396
- Field coupling, H-R neuron model
- collective behaviors, 108
 - control law, 108–111
 - dynamic equations, 106
 - error dynamics, 110
 - Lyapunov function, 110, 111
 - MATLAB platform, 106
 - modes of electrical activity, 106–108
 - stability of synchronization, 111–112
 - synchronization errors, 110
 - time series analysis, 109
 - TLEs of coupled, 112
- Fifth-order KdV-type equations, 448
- Final Prediction Error (FPE), 362
- Finite amplitude, interfacial waves of, 467
- Boussinesq approximation, 473–474
 - coefficients, 477
 - derivation of evolution equation, 470–471
 - governing equations, 468–469
 - modulational instability analysis, 471–472
 - Peregrine Breather, vorticity on, 472–473, 477
- Finite difference code (FDM), 445
- Finite Element Methods (FEM), 323, 357
- thermal modeling, 359–361
 - thermal propagation, 358
- Finite Element (FE) model
- ANSYS WORKBENCH Transient
 - Structural module, 128
 - apparatus and procedure, 131–132
 - capsule–intestine contact coupling, 128
 - capsule's displacement, 133, 134
 - contour map of pressure distribution, 135
 - friction coefficient, 134
 - intestinal deformation, 134
 - material properties, 129
 - mesh convergence test, 130–131
 - physical parameters, 130
 - results and analysis, 132–135
 - 2D conceptual design, 130
 - 3D conceptual design, 129, 130
- FitzHugh–Nagumo (FHN) model
- fixed input
 - Lyapunov function analysis, 98
 - measurement effects, 100, 101
 - second testing situation, 99
 - forward sensitivity method (FSM), 94

- inherent sensitivity analysis, 94
 - neuronal spike discharges, 94
 - parameter estimation framework
 - continuous-time dynamics, 95
 - forecast error, 96–97
 - forward sensitivities, 95–96
 - placement of observations using
 - forward sensitivity, 97–98
 - varying input, 100–102
 - FitzHugh–Rinzel equations, 524, 525, 527, 528
 - Flutter-based vibration, 189
 - Fo-ASEIR model, *see* Fractional-order age-structured SEIR (Fo-ASEIR) model
 - Focal circuit, 75–76
 - Force-displacement loops, 216
 - Force-displacement relation, 421
 - Force-velocity loops, 216
 - Forward sensitivity method (FSM), 94
 - Fourier analysis procedure, 547
 - Fourier coefficient vector, 269
 - Fourier–Galerkin–Newton method (FGNM), 272
 - Fourier harmonics
 - amplitude curves of, 387, 388
 - approximation, structure of solutions, 389–390
 - bi-harmonic solution, 389
 - cubic polynomial equations, 386
 - stability of, 389
 - two-harmonic approximation, 388
 - Fourier series, 269, 272, 295, 396
 - Fourier spectrum, 228, 229, 388, 389
 - Fourier transform, 551
 - Fractional-order age-structured SEIR (Fo-ASEIR) model, 14
 - age group data, 20
 - COVID-19 pandemic, 15
 - infection rate, 15
 - psychological effect factors, 19
 - Riemann–Liouville derivative, 14–15
 - simulations and discussions, 20
 - analysis, 22–23
 - fitting and forecast, 21
 - mobility and psychological effect factors, 21–22
 - symptom rate, 16
 - Fractional-order generalized SEIQRD model
 - COVID-19, 4
 - parameters, 6
 - transmission diagram, 5
 - Fredholm compatibility equation, 352
 - Free vibration frequencies
 - harmonic balance method for, 396
 - of Kirchhoff circular plates, 396
 - of linear problem, 402
 - natural frequency of, 401
 - nonlinear bending, 396
 - of nonlinear problem, 402–404
 - Frequency Response Function (FRF), 297–298
 - Full-order nonlinear piezoelectric model
 - device geometry, 296
 - experimental FRFs, 299
 - Frequency Response Function, 297–298
 - harmonic balance method, 295–296
 - Landau-Devonshire theory of ferroelectrics, 293
 - numerical simulations, 298
 - piezoelectric film measurements, 298
 - piezoelectric force, 294
 - Piola-Kirchhoff stress tensor, 293
 - polarization, 293–294
 - quality factor, 295
 - quality factor values, 299
 - Rayleigh damping, 295
 - theory of finite elasticity, 293
 - virtual power, 292
 - Functionally graded materials (FGMs)
 - MCST, 396
 - micro/nanoscale applications, 395
 - nonlinear vibration of, 396
 - Fuzzy differential equation (FDE), 605, 606
 - Fuzzy uncertainty, 605
 - Mathieu oscillator with, 608–612
 - chaotic solution, periodic parts induced from, 612–613
 - period-1 solution, periodic parts induced from, 613–614
- ## G
- Galerkin
 - discrete method, 191
 - expansion, 325
 - procedure, 270, 272, 308
 - Gardner equations, 448–451
 - Gas sensors, 321
 - Gauss Divergence Theorem, 399
 - Gaussian distortion, 451
 - Gear system parameters, 250
 - Generalized harmonic energy balance method (HEBM), 268–271
 - Geometric nonlinearities, 420
 - Geometric parameters, 316
 - Geometry, 421
 - Global stability
 - of disease-free equilibrium, 55
 - of the endemic equilibria, 55–56

Graphical dependency, 315–316
 Gravity waves, 473
 Green elastic materials, 581
 Gronwall inequality, 168

H

Hamilton-Ostrogradsky energy, 537
 Hamilton's principle, 399
 Hammerstein-Wiener Model (H-WM), 359, 362–363
 Harmonic balance finite element code, 299
 Harmonic balance method (HBM), 268, 271–274, 292, 295–296, 300, 396
 Harmonic excitation force, 178, 324
 Harmonic oscillations, 178, 213, 424, 539
 Hénon-Heiles system, 502–504
 High frequency chaotic behavior
 in non-ideal operational amplifier, 507
 circuits, 508–509, 511
 nonlinear dynamics, 509–511
 Hill function, 86
 Hill-type mathematical equation, 41
 Hindmarsh–Rose neuron model, field coupling
 collective behaviors, 108
 control law, 108–111
 dynamic equations, 106
 error dynamics, 110
 Lyapunov function, 110, 111
 MATLAB platform, 106
 modes of electrical activity, 106–108
 stability of synchronization, 111–112
 synchronization errors, 110
 time series analysis, 109
 TLEs of coupled, 112
 Hodgkin–Huxley neuron model, 87, 105
 Holographic lenses, 291
 Hopf bifurcation, 545
 Hukuhara derivative, 605
 Hyaluronic acid-lecticans-tenascin complexes, 523
 Hyper-chaotic dynamical systems, 548, 551
 Chen's hyper-chaotic system, 548
 Chua's hyper-chaotic system, 549, 552, 553
 Lorenz's hyper-chaotic system, 549
 Rössler's hyper-chaotic system, 550
 Hyper-chaotic Rössler system, 554
 Hyperelastic cylindrical shell, nonlinear
 dynamics of, 582
 mathematic model, 582–584
 nonlinear oscillations, analyses on, 587–590

 system with three equilibrium points, 589–590
 system with two equilibrium points, 588
 qualitative analyses, 584–587
 $\alpha = 1.5$, 585
 $\alpha > 1.5$, 585–587
 $0 < \alpha < 1.5$, 585

I

Image encryption, 557
 cryptanalysis of Farhan's algorithm
 chaotic system, 558
 original image encryption algorithm, 558–559
 target plain-text image, recover, 559–561
 Implicit functions, 376, 377
 Incremental harmonic balance (IHBM), 272
 Inertial gas sensors, 321
 Influenza viruses, 7
 Interfacial waves, finite amplitude
 Boussinesq approximation, 473–474
 coefficients, 477
 derivation of evolution equation, 470–471
 governing equations, 468–469
 modulational instability analysis, 471–472
 Peregrine Breather, vorticity on, 472–473, 477
 Intracellular calcium (Ca^{2+}) concentration, 83, 84

J

Jump resonance, multiple hysteresis, 513–514
 characterization of, 516–520
 occurrence of, 518
 oscillators with nonic polynomial
 nonlinearities, 514–516

K

Kantor model, 536
 Kerckhoffs' principle, 559
 Kinetic energy optimization
 coefficients of adjacent modal functions, 195
 differential equations, 195
 equation of energy harvester, 193
 i segment of beam, 194
 iteration results of PSO optimization process, 196

optimal beam model, 196, 197
 variable cross-sectional piezoelectric energy harvester, 194
 Z matrix, 195
 Kirchhoff-Love kinematic model, 536
 Korteweg-de Vries equation (KdV), 443, 445–446
 kth orthotropic lamina, 409

L

LabView™, 298
 LabWorks electrodynamic shaker, 236
 Lagrange's method, 255
 Lamé parameters, 313
 Landau-Devonshire theory, 293
 Lead-Zirconate Titanate (PZT), 291
 Leave-one-out (LOO) error, 575
 Limbic seizures
 focal circuit, 75–76
 mesoscale model, 74
 model design, 74–75
 normal circuit, 76–78
 schematic representation, 78
 simplifications, 74–75
 spike-wave discharges, 74
 time series and spectra of network, 78
 Linear stiffness coefficient of resonator, 206–207
 Locally resonant acoustic metamaterials (LARM), 431
 Long-range metamaterials (LRM), 431
 Long-range resonator-based metamaterials
 mathematical model, 433–435
 results, 435–439
 Lorenz's hyper-chaotic system, 549
 Low-Earth orbit (LEO), 407
 LS-DYNA finite element program, 573
 Lumped Parameters approach, 357
 Lur'e representation, 514
 Lyapunov exponent, 63, 65, 68, 111, 112, 182, 184, 185, 242, 538, 540, 541, 543, 547–550, 581, 589, 590
 closed cylindrical nanoshells, 545
 diagram, 242
 spectrum signs, 538
 Lyapunov function, 33, 98

M

Magneto piezo elastic oscillators
 mathematical model, 179–180
 numerical analysis
 bifurcation diagram, 183

chaotic behavior, 182
 coupling behavior between two trajectories, 181
 Lyapunov exponent, 182
 maximum average power, 184
 parameter, 181
 phase portrait with Poincaré points, 184, 185
 power output, 181, 182
 structure, 179
 Magnet oscillation, 202
 Masing rules, 380
 Mass lattice system, 202
 Mathieu equation, 605
 Mathieu oscillator, 605–606
 fuzzy differential inclusions, numerical method for, 607–608
 with fuzzy uncertainty, 608–612
 chaotic solution, periodic parts induced from, 612–613
 period-1 solution, periodic parts induced from, 613–614
 preliminaries, 606–607
 Matrix modified Korteweg–de Vries (mKdV) equation, 481
 class of the $d \times d$, 482–483
 explicit solutions, 483
 matrix parameter B, 483–484
 Peregrine Breather, 488–490
 unequal matrix parameters, 484–488
 Peregrine Breather, 488–490
 Mechanical asymmetry, 371
 Memory resistor, 593
 Memristor–inductor–capacitor nonlinear circuit, 593–596
 dynamical analysis of system
 equilibrium points and complex dynamics, finite number of, 601–602
 equilibrium points, infinite number of, 600–601
 first integrals and invariant surfaces, 598–600
 symmetry, invariant straight lines and invariant planes, 597
 equilibrium points, infinite number of, 596
 first integrals, 595
 parameter values, 594–595
 unique equilibrium point of system, 596
 MEMS gas sensor
 inertial gas sensors, 321
 metal-organic framework (MOF), 322
 Meshing damping, 243, 247, 249
 Meshing pair, 243, 247–249

- Metamaterial
 acoustic metamaterials, 432
 configuration, 420–421
- Metastructures for vibration attenuation
 bandgap, 201, 202, 205–208
 coupling coefficient β , 206
 electromechanical equations, 203, 204
 excitation amplitude X_g , 206
 linear stiffness coefficient of resonator Γ ,
 206–207
 nonlinear stiffness coefficient λ , 204–205
 schematic representation, 203
- Microelasticity theory, 312
- Microelectromechanical devices' development
 (MEMS), 311
- Micro-Electro-Mechanical Systems (MEMS)
 piezoelectric actuation (*see* Full-order
 nonlinear piezoelectric model)
 2:1 internal resonance, 302–303
- Micro-epsilon laser Doppler vibrometers, 236
- Mindlin plate theory, 396, 398, 399
- Mistuning patterns, 257–260, 263
- MLC circuit, 594
- Modified couple stress theory (MCST), 396
- Modified moment theory, 312
- Modified non-linear Schrödinger models
 (MNLS), 456–458
- Modified SIDARTH model
 epidemic components, 26–27
 improved, 27
- Monte Carlo simulation (MCS), 42–43, 569
- Mori-Tanaka method, 398
- Morlet wavelet, 538
- Multi-Island Genetic Algorithm (MIGA), 118
- Multiple hysteresis jump resonance, 513–514
 characterization of, 516–520
 occurrence of, 518
 oscillators with nonic polynomial
 nonlinearities, 514–516
- N**
- Nanoelectromechanical structures (NEMS),
 535
- Nano-mechanical resonators, 301
- NARX model, 362, 365
- Nastran, 278, 282–284, 286
- Natural frequencies, 235–236
- Neimark–Sacker bifurcation, 528, 529
- Neural networks, 378–380
- Neurodegenerative disorders, 83
- Neuronal network activity, 523–524
 chaos emergence, 527–530
 interstitial viscosity, 531
 mathematical model, 524–525
 multistability, dynamics of, 530–531
 network oscillations, cessation of,
 525–527
- Neuronal synchronization, 523
- Neurons communication, 523
- Newmark method, 315
- Newton Raphson method, 270
- NI-DAQ data acquisition system, 237
- Nodal piezoelectric forces, 295
- Nonclassical higher-order continuum theories,
 395
- Nonic polynomial nonlinearity, 514, 517
 oscillators with, 514–516
- Non-ideal operational amplifier
 high frequency chaotic behavior in, 507
 circuits, 508–509, 511
 nonlinear dynamics, 509–511
- Non-integrable cubic-quintic NLS (CQNLS)
 model, 458
- Nonlinear algebraic equations, 295, 396,
 401
- Nonlinear autoregressive with exogenous
 (NARX) model, 569–570
- Nonlinear energy sink (NES), 267–269,
 271–274
- Nonlinear force-displacement relation,
 421–422
- Nonlinear free vibration analysis, 396
- Nonlinear incidence function, 51
- Nonlinear stiffness coefficient, 204–205
- Nonlocal elasticity theory, 395
- Non-monotonic incidence function, 51
- Normal circuit, 76–78
- Normalized root mean squared error
 (NRMSE), 379
- Numerical analysis
 diagnosed cumulative infections, 33
 parameters estimation, 33–35
 sensitivity analysis, 35–37
- Numerical integration (NI), 271
- Numerical simulations, 390–392
 equations of motion, 426
 MATLAB[®] environment, 425
 maximum acceleration amplitude, 426
 two-dark solitons and anomalous charges
 reflection of, 460–464
 transmission of, 460
- O**
- Ohm's law, 215
- One-mode Reduced-Order model, 323
- Operational Amplifier (OpAmp), 507

- Optimal birth control
 - Ekeland's variational principle, 170, 172, 174
 - mild solution, 165–169
 - model formulation, 164–165
 - objective functional/energy functional, 170
 - optimal birth control problem, 170–174
- Optimization design
 - algorithms and flow path, 118–119
 - flow chart, 119
 - forward movement with medium speed, 119–123
 - parameter settings, 120
 - reliability verification, 120–123
 - results, 123–124
 - steps for capsule movement, 123
- Original image encryption algorithm, 558–559
- Ostrogradsky-Hamilton variational principle, 314
- P**
- Parameter estimation framework, FHN model
 - continuous-time dynamics, 95
 - forecast error, 96–97
 - forward sensitivities, 95–96
 - placement of observations using forward sensitivity, 97–98
- Parameter identification, 378–380
- Particle swarm optimization (PSO) method, 42, 43, 190, 196
- Peak power plots, 260–263
- Peregrine Breather, 468, 472–473, 478
 - matrix modified Korteweg–de Vries (mKdV) equation, 488–490
- Petra Thin-Film-Piezoelectric technology, 296
- Phase portraits of systems, 67, 68
- Phenomenological cooperative model, 41
- Physical nonlinearity, 311
- Pico projectors, 291
- Piezoceramic patches (PZT), 177, 178
- Piezoelectric cantilever beam, 190–192
- Piezoelectric energy harvester
 - kinetic energy optimization
 - coefficients of adjacent modal functions, 195
 - differential equations, 195
 - equation of energy harvester, 193
 - i segment of beam, 194
 - iteration results of PSO optimization process, 196
 - optimal beam model, 196, 197
 - variable cross-sectional piezoelectric energy harvester, 194
 - Z matrix, 195
 - optimized piezoelectric cantilever beam, 198
 - parallel synchronous switch interface circuit, 197
 - wind energy optimization
 - boundary conditions, 191
 - column section model, 192
 - critical velocity, 192
 - fluid force coefficients, 192
 - galloping critical velocity, 192
 - GPEH-V system, 191
- critical flow rate, 193
- output energy, 193
 - models and critical velocity, 193
 - V-groove, 191, 192
- Piezoelectric film measurements, 298
- Piezoelectric transduction mechanism, 267, 268
- Piola-Kirchhoff stress tensor, 293
- Plain-text attack, 559
- Plastic deformations, 317, 318
- POD-PCE model, 572
- Poincaré cross-sectional diagram, 250–252
- Poincaré plot, 500
- Point wave energy absorbers (PWAs), 233, 234, 239
- Poisson ratio, 314
- Policymakers, 23
- Polynomial chaos expansion (PCE), 569–571
- Population density, 158, 159, 164
- Power FRFs, 261, 262
- Power plots, 259, 260
- Power take-off unit (PTO), 234, 235, 237
- Predator–prey interaction models, 148
- Primary oscillator, 234, 235, 237
- Probability density function (PDF), 570
- Proper orthogonal decomposition (POD)
 - approach, 282, 570, 571
- PSO techniques, *see* Particle swarm optimization (PSO) techniques
- Q**
- Quality factor, 295, 298, 299, 327
- Quintic polynomial nonlinearity, 513
- R**
- Reduced order modeling method
 - buckled piezoelectric beam for energy harvesting, 278

- Reduced order modeling method (*cont.*)
 construction of basis functions, 282
 formulation, 280–281
 stiffness and electromechanical coupling coefficients, 282–283
See also Buckled piezoelectric beam
- Reduced order nonlinear modeling, 361–366
- Regression analysis, 47
- Relativistic forced harmonic oscillator, 496
- Relativistic Hénon-Heiles System, 502–504
- Relativistic systems, chaos in, 495
 damped relativistic oscillator, multi-stability in, 501–502
 frequency locked and quasiperiodic states, 499, 500
 natural frequency, shift in, 497–498
 relativistic effects, chaos induced by, 500, 501
 relativistic forced harmonic oscillator, 496
 relativistic Hénon-Heiles System, 502–504
- Reserve clearance of one-way clutch, 243, 247, 249, 251
- Residual plastic deformations, 311, 316
- Resonance frequency, 224, 226, 227, 229, 230, 295, 342
- Resonant gas sensor, 301
- Resonant pressure sensors, 301
- Restoring force, 371
- Reynolds number, 190
- Riccati-type pseudo-potential approach, 455
- Rivlin-Saunders cylindrical shell, 582
 mathematic model, 582–584
 nonlinear oscillations, analyses on, 587–590
 system with three equilibrium points, 589–590
 system with two equilibrium points, 588
 qualitative analyses, 584–587
 $\alpha = 1.5$, 585
 $\alpha > 1.5$, 585–587
 $0 < \alpha < 1.5$, 585
- Road displacement excitation, 246
- Road unevenness, 245
- Root mean square error (RMS), 43
- Rössler's hyper-chaotic system, 550
- Roughness coefficient, 245
- Runge–Kutta method, 34, 75, 98, 181, 204, 249, 251, 315, 538, 551, 611
- S**
- Saint-Venant Kirchhoff model, 299
- Sawyer-Tower circuit, 295, 298
- Scaling wavelet analysis of chaotic systems, 547
 discrete wavelet transform, 550–551
 hyper-chaotic dynamical systems, 548, 551
 Chen's hyper-chaotic system, 548
 Chua's hyper-chaotic system, 549
 Lorenz's hyper-chaotic system, 549
 Rössler's hyper-chaotic system, 550
 wavelet variance, 551
- Seasonal ARIMA (SARIMA) model, 7–8
 ACF and PACF, 8
 autoregressive, 8
 COVID-19, 10
 estimation results, 10
 fitting and prediction results, 9
 prediction results, 9
 residual and Q-Q plot, 10
- Secondary oscillators, 234, 236
- Semigroup theory, 163
- Sensitivity analysis
 parameter values, 35
 prevention and control strategy, 35
 transmission parameters, 35–36
 vaccination, 37
- Shock absorber, *see* Energy harvesting shock absorber (EHSA)
- Simulink design optimization toolbox (SLDO), 6
- Single input–single output sensor (SISO)
 electromechanics module, 327
 electrostatic fringing field, 326
 FEM module, 327
 inner resonators, 322
 Laser-Doppler Vibrometer, 322
 sensor's resonance frequencies, 323
 shuttle mass, 322
 shuttle mass length and width, 323
 static mode, 322
- SIRD models, 46
 classical, 46–47
 cooperative virus-pool, 47
- Six Sigma algorithm, 118
- Size-structured population models, 163–174
- Sol-gel-deposited piezoelectric patches, 296
- Sommerfeld effect, 213
- Spatial frequency, 245
- Stability analysis
 equilibrium, 29
 global, 30
 endemic equilibrium (*see* Endemic equilibrium)
- STMicronicsTM, 296
- Strain gradient theory, 395

- Strain tensors, 398
- Stress driven model, 347
- Strongly modulated response (SMR), 272, 274
- Susceptible–infected–recovered (SIR) epidemic model, 49
- Symmetric hysteresis, 376–378
- Symptom data challenge
- analyses, 17
 - COVID-19, 16
 - COVID-19 symptom datasets, 17
 - incidence functions, 19
 - incidence rates, 18
 - nonlinear incidence functions, 18
 - psychological factor and interventions, 18
- T**
- Tangent stiffness matrix, 281, 282
- Targeted energy transfer (TET), 267
- Thermal loading, 408, 412–415
- Thermoelastic coupling, 410
- Thermo-mechanical coupling (TTC), 408
- Three-strain COVID-19 SEIR epidemic model
- Beddington–DeAngelis incidence function, 51
 - Crowley–Martin incidence function, 51
 - flowchart, 51
 - global stability of disease-free equilibrium, 55
 - global stability of the endemic equilibria, 55–56
 - incidence functions, 50
 - nonlinear incidence function, 51
 - non-monotonic incidence function, 51
 - numerical simulations, 56–58
 - problem well-posedness, 51–53
 - steady states, 53–55
 - susceptible individuals, 50
 - two-strain reproduction numbers, 57
- Time-frequency power spectral density, 245
- Time-varying diffusion rate, birth control, 163–174
- Time-varying meshing stiffness, 243, 247–249
- Tooth side clearance, 243, 247, 249
- Torque, 191, 212–216, 247, 338
- Transverse Lyapunov exponents (TLEs), 111, 112
- Triangular arch, 421
- Tumor growth model
- bifurcation diagram, 66, 67, 69
 - chaotic behavior, 65
 - coexisting attractors, 69
 - dynamical model, 64–65
 - Lyapunov exponents, 65, 68
 - phase portraits, 67–68
 - phenomenon of antimonotonicity, 65
- Tuned mass dampers, 201, 419
- Turing instability, 148, 155–157, 160
- 2D array of harvesters
- bandwidth optimization, 264–265
 - bandwidths in different mistuning patterns, 263–264
 - harmonic excitation, 259
 - mathematical equations
 - electrical equation, 257
 - equations of motion, 257
 - mistuning patterns, 257–258
 - peak power plots, 259–263
 - power plots, 259, 260
 - system model, 256–257
- Two-dimensional (2D) finite amplitude, 467
- 2:1 Internal resonance
- basins of attraction, 305–307
 - experimental response, 303–304
 - mechanical model, 307–308
 - MEMS device, 302–303
 - simulated response, 304–305
- Two-to-one internally resonant WEC
- advantages, 238
 - backward frequency sweep, 237
 - experimental setup, 237
 - forward frequency sweep, 237
 - governing equations, 235
 - natural frequencies, 235–236
 - schematic diagram, 234
- U**
- Ultrasonic diagnostics methods, 393
- Uncertainty quantification (UQ)
- of crash box
 - contact force, 577–578
 - impactor displacement, 575–576
 - impactor velocity, 576–577
 - Latin hypercube samples, 574
 - leave-one-out error, 575
 - problem statement, 573–574
- V**
- Vehicle’s suspension system, 241
- Vehicle vibration energy, 241
- Vehicle Vibration Input-Standard for Road Surface Roughness Representation Method, 245
- V-groove, 191, 192

- Vibration absorber energy harvester, NES
 - generalized harmonic energy balance method, 269–270
 - harmonically excited primary system, 268, 269
 - HBM for frequency response, 272–274
 - numerical analysis, 271–272
 - Vibration absorbers, 201, 267
 - Vibrational energy, 222, 255, 268, 439
 - Vibration attenuation
 - in nonlinear lattice, 427
 - nonlinear vibration mitigation solutions, 420
 - seismic motions, 419
 - shallow arch configurations, 420
 - tuned mass dampers, 419
 - types of configurations, 419
 - vertical vibration isolation, 420
 - Vibro-impact capsule system
 - locomotion system
 - anisotropic friction, 138
 - experimental setup, 139–141
 - internal mass oscillation, 138
 - isotropic assumption, 138
 - rectilinear motion, 137
 - results and discussion, 141–143
 - mathematical model
 - dynamic model, 116–117
 - physical model, 116
 - optimization design
 - algorithms and flow path, 118–119
 - flow chart, 119
 - forward movement with medium speed, 119–123
 - parameter settings, 120
 - reliability verification, 120–122
 - results, 123–124
 - steps for capsule movement, 123
 - Vibro-impact self-propulsion technique, 128
 - Voltage comparator, 508
 - von Karman
 - approximation, 384
 - plate, 393
 - Vortex-induced vibration (VIV), 189
- W**
- Watts–Sherman and Montefusco–Pedersen models, 85
 - Wave energy harvesting, 233–239
 - Wave focusing, 202
 - Waveguiding, 202
 - Wavelet Transform (WT), 547
 - Wave-stopping, 438
 - Wind energy optimization
 - boundary conditions, 191
 - column section model, 192
 - critical velocity, 192
 - fluid force coefficients, 192
 - galloping critical velocity, 192
 - GPEH-V system, 191
 - critical flow rate, 193
 - output energy, 193
 - models and critical velocity, 193
 - V-groove, 191, 192
 - Wind-induced vibration energy, 189, 193, 198
 - Wireless capsule endoscopy detection technology, 115
 - Wireless sensors, 255, 277
- Y**
- Young's modulus, 129, 279, 299, 308, 315, 336, 433, 537